Cellular and subcellular localised fluorescent probes to image mobile Zn^{2+}

Name: Le Fang

Supervisors: Dr. Christopher Jones

Dr. Rachel Crespo-Otero

Prof. Michael Watkinson

Submitted in partial fulfilment of the requirements of the Degree of Doctor of Philosophy

Statement of originality

I, Le Fang, confirm that the research included within this thesis is my own work or that where it has been carried out in collaboration with, or supported by others, that this is duly acknowledged below and my contribution indicated. Previously published material is also acknowledged below.

I attest that I have exercised reasonable care to ensure that the work is original, and does not to the best of my knowledge break any UK law, infringe any third party's copyright or other Intellectual Property Right, or contain any confidential material.

I accept that the College has the right to use plagiarism detection software to check the electronic version of the thesis.

I confirm that this thesis has not been previously submitted for the award of a degree by this or any other university.

Signature: Le Fang

Date: July 2020

Details of collaboration and publications:

This work is done in collaboration with Dr. Giuseppe Trigiante, Barts and The London School of Medicine and Dentistry, Queen Mary University of London. The publications are listed below.

1. **L. Fang**, G. Trigiante, R. Crespo-Otero, C. S. Hawes, M. P. Philpott, C. R. Jones and M. Watkinson. Endoplasmic reticulum targeting fluorescent probes to image mobile Zn^{2+}. *Chem. Sci.*, 2019, 10, 10881-10887.

2. **L. Fang,** G. Trigiante, R. Crespo-Otero, M. P. Philpott, C. R. Jones and M. Watkinson. An alternative modular 'click-S_NAr-click' approach to develop subcellular localised fluorescent probes for mobile Zn^{2+}. *Org. Biomol. Chem.*, 2019, 17, 10013-10019. (Front cover)
3. **L. Fang**, G. Trigiante, R. Crespo-Otero, M. P. Philpott, C. R. Jones and M. Watkinson. Biotin-tagged fluorescent sensor to visualize 'mobile' Zn^{2+} in cancer cells, *Chem. Commun.*, 2018, 54, 9619-9622.
4. **L. Fang**, R. Crespo-Otero, C. R. Jones and M. Watkinson. Protect to detect: A Golgi apparatus targeted probe to image mobile zinc through the use of a lipophilic cell-labile protecting group strategy, submitted.

Abstract

Zn^{2+}, as the second most abundant d-block metal in the human body, plays an important role in a wide range of biological processes, and the dysfunction of its homeostasis is related to many diseases, including Type 2 diabetes, Alzheimer's disease, prostate and breast cancers. Small molecule fluorescent probes, as effective tools for real-time imaging, have been widely used to study Zn^{2+} related processes. However, the failure to control the small molecule probes' localisation in cells has limited their utility somewhat, as they are generally incapable of studying individual processes in a specific cellular location.

This thesis presents efforts to develop cellular and subcellular localised fluorescent probes for mobile Zn^{2+} imaging. Previously reported successful efforts towards cell-localised probes are outlined in Chapter 1 together with other relevant background information. These include genetically encoded site-directing proteins and the use of site-targeting peptides, which show very good targeting behaviour but are not without some disadvantages.

In Chapter 2, the development of a biotin-tagged probe is reported, which can be used to specifically detect mobile Zn^{2+} in breast cancer cells. Chapter 3 describes two novel endoplasmic reticulum (ER) targeting probes through the incorporation of a cyclohexane sulfonylurea group into the probes with different Zn^{2+} binding ligands. Both show excellent ER localisation and good fluorescence response to Zn^{2+} in a number of cell lines. In Chapter 4, a new Golgi apparatus localised probe employing a trityl protected cysteine residue as the targeting group is presented in which the trityl protecting group was used to increase transport across the cell membrane before its removal inside cells being demonstrated by both its sub-cellular relocation and a significant increase in fluorescence response after an incubation time. Chapter 5 presents the development of an alternative modular 'click-S_NAr-click' approach towards subcellular localised fluorescent probes, and through this new

method a related series of ER, mitochondria and lysosome targeting probes were synthesized more effectively and efficiently. There then follows a future work section, an experimental chapter, relevant references and two appendices.

Table of Contents

Acknowledgements

Firstly, I would like to express my sincere gratitude to my supervisor Prof. Mike Watkinson for his support, help, encouragement and understanding. In these four years, with his valuable guidance and advice, I have overcome many challenges and more importantly, I have learned a lot from him, especially the way to think about research, the attitude towards problems. Mike is not only my supervisor in my study but also a mentor of my life, I have learned to be as tough as him when facing difficulties. Also, I am really grateful to my supervisor Dr. Chris Jones for taking care of me after Mike moved to Keele and supporting me to continue the project. With his expertise in organic chemistry, he helped a lot in organic synthesis. Many thanks to my second supervisor Dr. Rachel Crespo-Otero for her help in DFT calculations, it is totally a new area and I have learned much knowledge under her patient supervision. It is a great honour working with my three supervisors.

Also I would like to show my appreciation to my colleagues and collaborators. Dr. Giuseppe Trigiante, Dr. Hemanth Tummala in The Blizard Institute who helped me a lot on the tests *in cellulo*, and I have learned many skills of biological experiments from them. And it is a great pleasure working with the members in Mike's group and Chris' group.

On a personal note, I want to take this opportunity to thank my girlfriend, Lei. We met in London and have fallen in love soon after we met. Staying far away from home, we stick together and have been through a lot towards the same goal. We share our happiness in success, encourage each other in frustration, and I will never forget so many beautiful moments here. And in particular, to my parents for their support and love, even in their hard time, they still support me to finish my study. Love you.

I am grateful to China Scholarship Council for the financial support and Queen Mary University of London for providing this nice environment to study and do research.

List of abbreviations

Ac	Acetic/acetate
AIE	Aggregation induced emission
ATP	Adenosine triphosphate
Boc	*tert*-Butyloxycarbonyl
CASSCF	Complete active space self-consistent field
CUAAC	Copper(I)-catalyzed alkyne-azide cycloaddition
DBU	1,8-Diazabicyclo(5.4.0)undec-7-ene
DCM	Dichloromethane
DFT	Density functional theory
DIBAL-H	Diisobutyl aluminium hydride
DIC	Differential interference contrast microscopy
DIPEA	*N*,*N*-Diisopropylethylamine
DMF	*N*,*N*-Dimethylformamide
DMSO	Dimethyl sulfoxide
DNA	Deoxyribonucleic acid
DPA	di-2-Picolylamine
DPEN	*N*,*N*-di-(2-Picolyl)ethylenediamine
DPPA	Diphenyl phosphoryl azide
EDTA	Ethylenediaminetetraacetic acid
EGTA	Ethylene glycol-bis(β-aminoethyl ether)-N,N,N',N'-tetraacetic acid
ER	Endoplasmic reticulum
ESIPT	Excited state intramolecular proton transfer

Et	Ethyl
FRET	Förster resonance energy transfer
GFP	Green fluorescent protein
HEPES	4-(2-Hydroxyethyl)-1-piperazineethanesulfonic acid
HOMO	The highest occupied molecular orbital
HRMS	High-resolution mass spectrometry
ICT	Intramolecular charge transfer
IR	Infrared
LUMO	The lowest un-occupied molecular orbital
K_a	Acid dissociation constant
K_d	Dissociation constant
Lyso	Lysosome
Me	Methyl
Mito	Mitochondrion
MTs	Metallothioneins
NBD	Nitrobenzoxadiazole
NMM	*N*-Methylmorpholine
NMP	*N*-Methyl-2-pyrrolidone
NMR	Nuclear magnetic resonance
OPM	One-photon excitation microscopy
PBS	Phosphate-buffered saline
PET	Photoinduced electron transfer
Petrol	Petroleum ether

PMA	Phosphomolybdic acid
RFP	Red fluorescent protein
RIM	Restriction of intramolecular motion
RNA	Ribonucleic acid
S_NAr	Nucleophilic aromatic substitution
SNOC	*S*-Nitrosocysteine
t-Bu	*tert*-Butyl
t-BuONO	*tert*-Butyl nitrite
TDDFT	Time-dependent density functional theory
TFA	Trifluoroacetic acid
THF	Tetrahydrofuran
TLC	Thin-layer chromatography
$TMSN_3$	Trimethylsilyl azide
TP	Two-photon
TPM	Two-photon excitation microscopy
TPP	Triphenylphosphonium salt
TPEA	*N*,*N*,*N*'-tri(Pyridin-2-ylmethyl)-ethane-1,2-diamine
TPEN	*N*,*N*,*N*',*N*'-tetrakis(2-Pyridinylmethyl)-1,2-ethanediamine
Trans	Transmission
UPR	Unfolded protein response
UV-Vis	Ultraviolet-visible spectroscopy

Chapter 1 Introduction

1.1 The role of Zn^{2+} in the human body

Zn^{2+} is the second most abundant d-block metal ion in the human body with the total amount being about 2 g which is mostly bound to proteins. It is estimated to exist in over three thousand proteins and is widely used for catalytic, regulatory, and structural roles. Zinc plays an important part in a wide range of biological processes, such as brain function and pathology, immune function, gene transcription, and mammalian reproduction. Due to this, it is unsurprising that problems with zinc homeostasis are associated with many diseases, including Alzheimer's disease,[1] prostate cancer,[2] type 2 diabetes,[3] and immune dysfunction and infection.[4] Whilst the majority of zinc is found in bound forms, there exists a pool of 'mobile' or 'free' zinc, which initiates transient signals that stimulate various physiological processes, though its concentration in the cytosol is only in the picomolar range.[5] The thiol-rich metallothioneins (MTs) and zinc transporters are normally involved in the processes to maintain cellular zinc homeostasis.[5] MTs acting as Zn^{2+} buffers, can bind a large amount of Zn^{2+} and release it under oxidative stress due to the antioxidant role it plays. There are mainly two families of zinc transporters, ZIP and ZNT, which control the import and export of cytosolic zinc to intracellular organelles or extracellular space (Figure 1.1).[6] Mobile Zn^{2+} is associated with the regulation of gene expression, insulin secretion, and is also considered as a signalling ion for intra- and intercellular communication, such as neurotransmission.[7] Therefore, effective methods are required to image mobile Zn^{2+} at the cellular or subcellular level in order to understand these processes.[8]

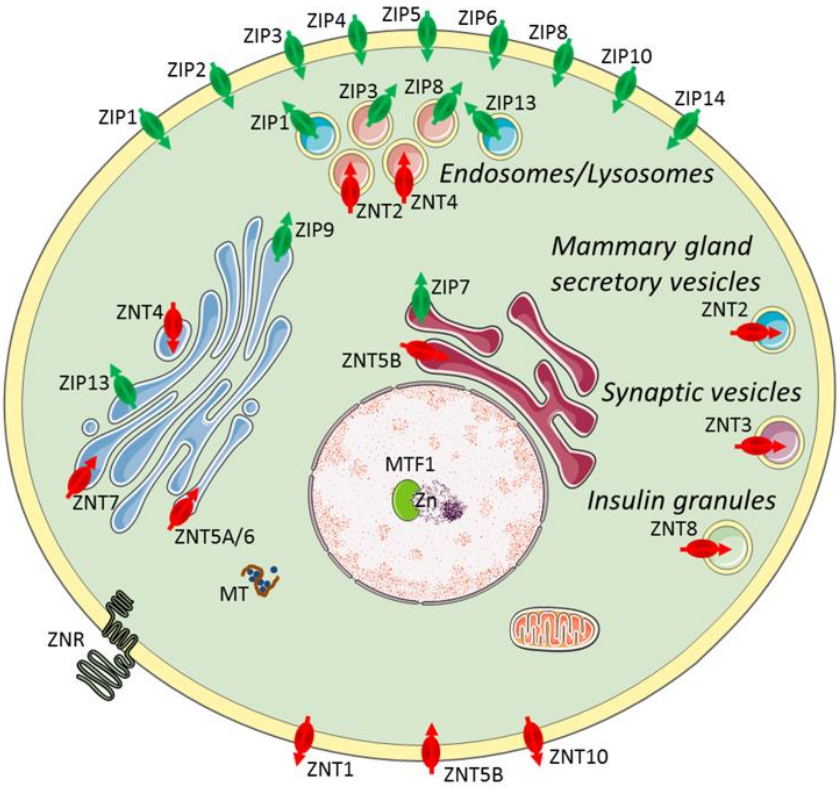

Figure 1.1 Zinc transporters (ZIP importers and ZNT exporters) and metallothioneins (MTs) to control cellular and subcellular zinc homeostasis, adapted from ref. 6.

1.2 Fluorescent chemosensors to image Zn^{2+}

Since Zn^{2+} has a d^{10} configuration, it is redox inert in biology and is rendered spectroscopically silent for most of the commonly used photo-spectroscopic techniques.[9] As a result, the development of fluorescent chemosensors has become popular for non-invasive real-time Zn^{2+} imaging. A typical fluorescent chemosensor contains a fluorophore (the signal source), a spacer and a receptor (the recognition site). A change in the fluorescence intensity or wavelength occurs due to analyte binding, which leads to signal output. Notably, in the biological environment, fluorescent chemosensors are involved in a competitive exchange equilibrium with endogenous ligands and proteins and thus detect changes of mobile Zn^{2+} pools rather than total cellular zinc levels. Therefore, high sensitivity with low detection limit, high specificity and selectivity to distinguish Zn^{2+} from competing metal ions are preferred.

There are three main types of fluorescent sensors for biological zinc imaging: small molecule probes, protein-based biosensors and peptide targeting fluorescent sensors. Protein-based biosensors and peptide targeting fluorescent sensors can localise to specific organelles by introducing genetically encoded site-directing proteins and selecting specific amino acid sequences which have high affinity for the particular targets.[8] However, they are not without some limitations. The genetically encoded protein-based sensors cannot be transfected into all cell lines, have a small range of excitation and emission wavelengths available as well as low photochemical stability and brightness. The peptide-based sensors are sensitive to proteases *in vivo* and cell internalization can be difficult, except for specific peptide sequences. In contrast, small molecule fluorescent probes can display high sensitivity and selectivity, low toxicity, and good photophysical properties. However, the failure to control the small molecule probes' cellular or subcellular location can limit their utility somewhat.

1.3 Mechanism of Zn^{2+} sensing

The change of fluorescence intensity, fluorescence lifetime, or a shift of fluorescence wavelength can all be measured and are useful attributes of fluorescent chemosensors. There are a variety of fluorescence mechanisms that can be used in the design of chemosensors, such as Förster resonance energy transfer (FRET), photoinduced electron transfer (PET) (sometimes also termed chelation enhanced fluorescence (CHEF)), intermolecular charge transfer (ICT) and excited state intramolecular proton transfer (ESIPT), which have been widely applied for Zn^{2+} imaging in living systems.

1.3.1 The PET mechanism

PET sensors commonly adopt the fluorophore-spacer-receptor scaffold. The fluorophore is usually connected via a spacer to a receptor, which contains a relatively high-energy non-bonding electron pair, such as on an sp^3 hybridised nitrogen atom. In the unbound state, the

high-energy non-bonding electron pair can transfer an electron to the excited state of the fluorophore, which quenches the fluorescence response (Figure 1.2). When this electron pair is coordinated with a cation, the redox potential of the receptor is raised and the HOMO of the receptor becomes lower in energy than that of the fluorophore. Thus, the PET process from the receptor to the fluorophore is blocked and the fluorescence is switched on. The spacer holds the fluorophore and receptor close enough to allow electron transfer and is generally less than a three-carbon linker, which guarantees the maximum efficiency of PET. Most of the effective PET type probes undergo a fluorescence "switch on" response to Zn^{2+}.

There are a number of PET probes that have already been used to image zinc in living cells. As an example, the structures of two probes utilising a PET mechanism are shown in Figure 1.3. Probe **1**, with the typical DPA (di-2-picolylamine) Zn^{2+} ligand[10] and a Bodipy fluorophore, exhibited a selective fluorescence enhancement (7 fold) upon Zn^{2+} binding with a low pK_a value of 2.1 ± 0.1, low dissociation constant and high quantum yield of the zinc-bound species (Table 1). It has been successfully applied to image intracellular Zn^{2+} changes in PC12 cells (Figure 1.4). Compound **2** is another PET-based probe with a dimethoxylcoumarin fluorophore and cyclen as the receptor, which displays a similar switch on fluorescence response (4.4-fold enhancement) on binding to Zn^{2+}.[11] Once **2** passively diffused into cells, some or all the pendant esters are cleaved by cellular esterase, which produced a probe with carboxylate residues which is retained in cells.

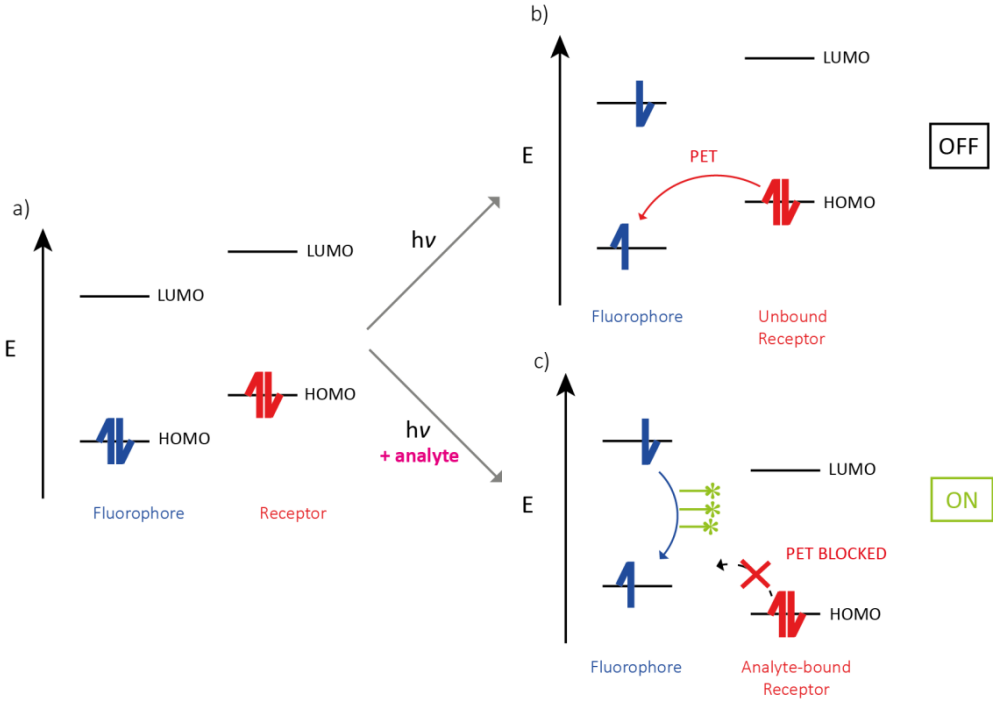

Figure 1.2 Orbital energy diagram to demonstrate the 'off' and 'on' states of a generic fluorescent chemosensor utilising the PET mechanism.

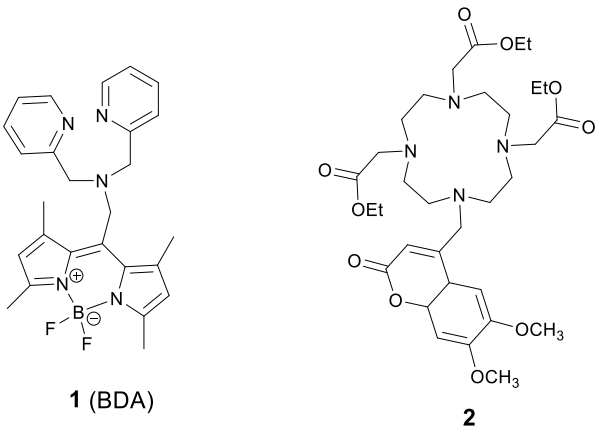

Figure 1.3 Two examples of probes based on a PET mechanism for zinc sensing in living cells.

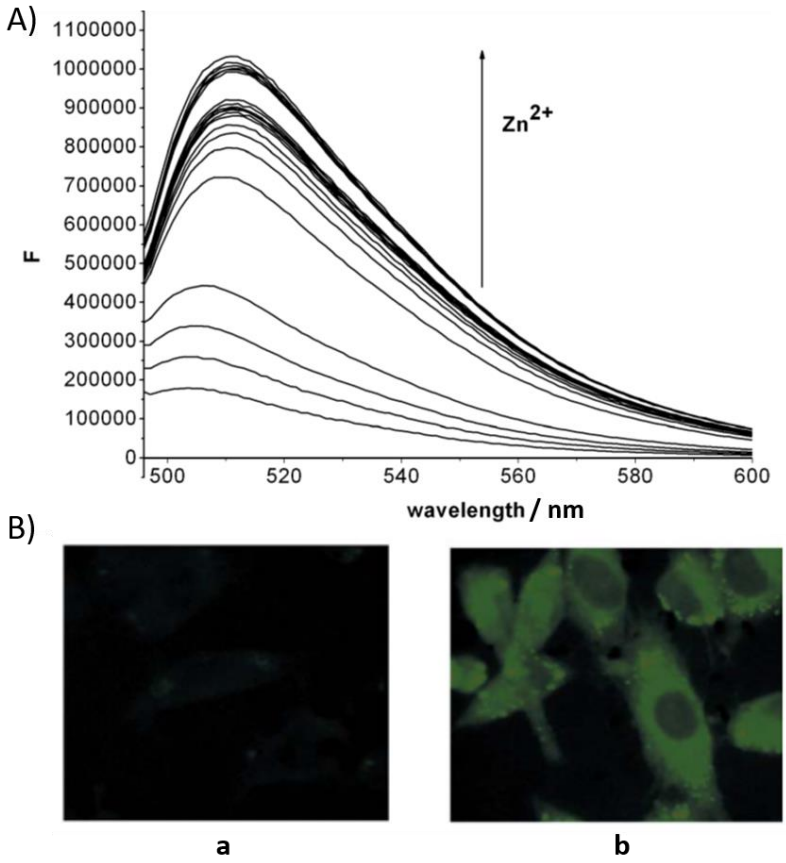

Figure 1.4 A) The fluorescence spectrum of **1** (BDA) with addition of Zn^{2+} in tris–HCl buffer solution (20 mM, pH 7.4, 100 mM NaCl), F is the fluorescence intensity; B) fluorescence images of PC12 cells loaded with **1** (10 μM, a) and with subsequent addition of Zn^{2+} (50 μM, b). Adapted from ref. 10

1.3.2 The ICT mechanism

Probes based on ICT mechanisms are often made up of a fluorophore and receptor with no spacer, which form a conjugated system with an electron-rich and an electron-deficient region. If the charge distribution in the molecule is altered there is normally an apparent change in fluorescence emission that can be observed. When a receptor (playing the role of an electron donor within the fluorophore) interacts with a cation, it decreases the electron-donating character of the receptor and a blue shift of the emission spectrum is expected. In the same way, if a cation receptor plays the role of an electron receptor, the interaction between the cation and the receptor would further strengthen the push-pull effects, then a

red shift in emission would be found. This behaviour often gives ICT probes a ratiometric response, i.e. the emission ratio at the two different wavelengths can be attributed to cation concentration, and these probes can potentially quantify zinc in the sample, such as solutions, cells or tissues. ICT mechanisms are also often extremely solvent dependent, since polarity plays an important part in stabilising the electronic states of the molecule.

Compounds **3** and **4** are two examples of ICT based probes that have been used to image zinc in cellular environments. **3** (SBD-TPEA) is a visible light excited ratiometric probe with TPEA (*N*,*N*,*N*'-tri(pyridin-2-ylmethyl)-ethane-1,2-diamine) as the Zn^{2+} chelator and ICT donor linked directly to the sulfamoylbenzoxadiazole fluorophore.[12] When excited at 460 nm, **3** displayed an emission band centred at 585 nm, and a 40 nm hypochromic emission shift was observed upon Zn^{2+} binding (See Figure 1.5B). With good photophysical properties, **3** was utilised for *in cellulo* and *in vivo* ratiometric Zn^{2+} imaging in HepG2 cells and live zebrafish larvae, respectively. Probe **4** is based on benzothiazole-terpyridine conjugate, which showed high selectivity to Zn^{2+}.[13] Upon the addition of Zn^{2+}, it showed a 42 nm emission blueshift, accompanied by a strong fluorescence enhancement at 500 nm and when studied by microscopy in HeLa cells, the probe was observed separately in the red and green channel in the absence or presence of exogenous Zn^{2+} (see Figure 1.6).

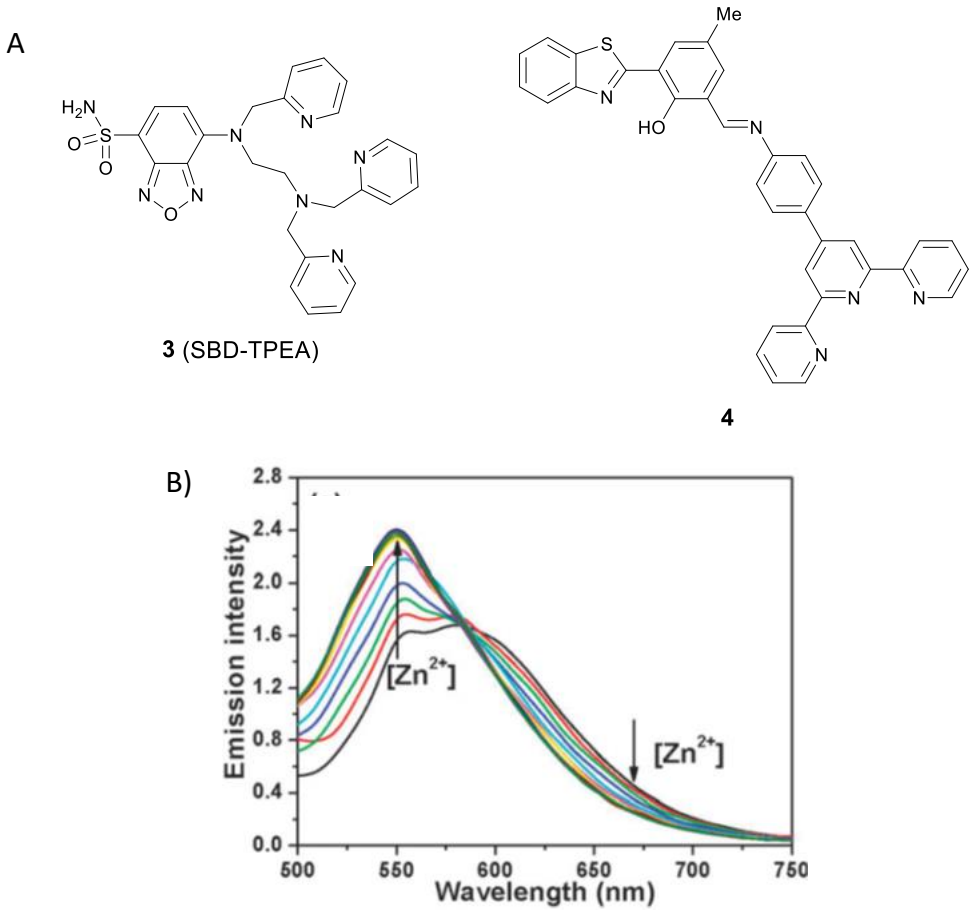

Figure 1.5 A) Structures of ICT-based fluorescent probes, **3** (SBD-TPEA) and **4**; B) the fluorescence spectrum of **3** (3 μM, λ_{ex} = 460 nm) with the addition of aliquots of Zn^{2+} in HEPES buffer (50 mM, 0.1 M KNO_3, pH 7.2, containing 0.15% DMSO). Adapted from ref. 12

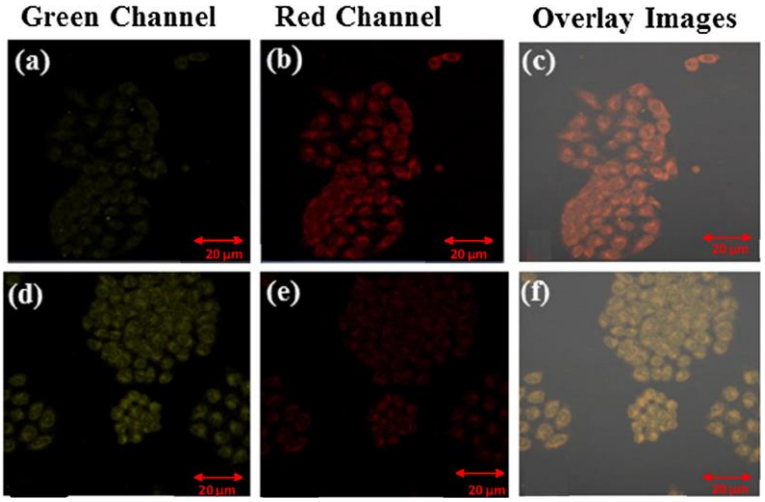

Figure 1.6 Fluorescence images of HeLa cells with probe **4** (10 μM, a-c) and with subsequent addition of zinc perchlorate (10 μM, d-f). Adapted from ref. 13

1.3.3 The FRET mechanism

Förster resonance energy transfer (FRET) is defined as a distance-dependent energy transfer from an excited-state fluorophore (donor) to a ground-state fluorophore (acceptor), exciting the acceptor which then exhibits its fluorescence. The fluorophores of the FRET pair must have an appropriate extent of spectral overlap between the emission of the donor fluorophore and the absorption spectra of the acceptor. Upon binding the analyte, the distance between the FRET pair can be altered, thereby altering/arresting the FRET mechanism, which allows for ratiometric quantification of the analyte in live cells. This type of mechanism is generally utilised when employing two fluorescent proteins for a FRET-based sensor. Alternatively, in the case of small molecule probes, it is possible to disrupt the degree of overlap between the FRET pair of fluorophores by altering the emission of the donor fluorophore upon a binding event.

Some fluorescent probes based on the FRET mechanism have been successfully applied for Zn^{2+} imaging in cells. In probe **5**, the rhodamine spirolactam is a non-fluorescent fluorophore, and upon binding with Zn^{2+}, the ring-opening reaction of the spirolactam was triggered, generating the long-wavelength rhodamine fluorophore which acts as the energy acceptor.[14] Fluorescein is the energy donor since its emission is well-matched with the absorption spectrum of rhodamine, excited at its absorption wavelength (λ_{ex} = 485 nm). On addition of Zn^{2+}, the fluoroscein fluorescence is decreased while the emission of rhodamine is increased (Figure 1.7B). The probe showed excellent selectivity for Zn^{2+} over competing cations, even Cd^{2+}, which is a common problem of the di(2-picolyl)amine ligand and preliminary experiments in HeLa cells demonstrated that it could be used for ratiometric Zn^{2+} imaging (Figure 1.7C).

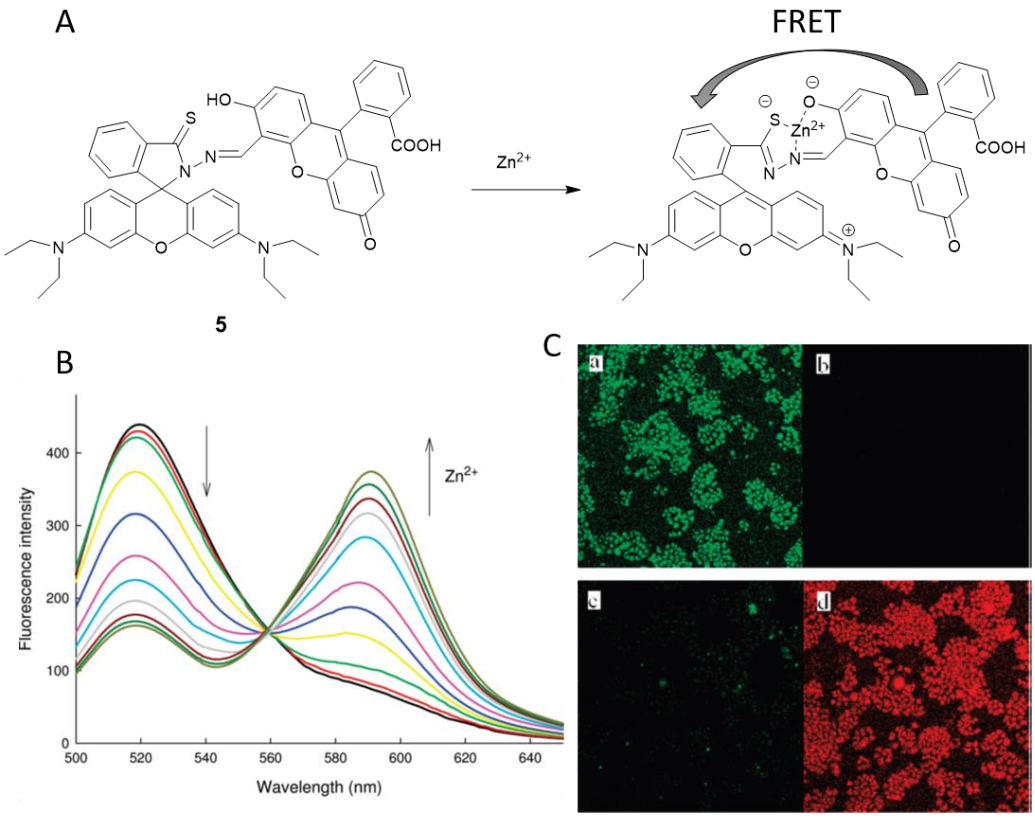

Figure 1.7 A) Structure of **5** and its complex with Zn^{2+}; B) The fluorescence emission spectra of **5** (10 µM) in the presence of different concentrations of Zn^{2+} in buffered (0.1 M HEPES, pH = 7.2) 50% aqueous acetonitrile solution (H_2O/CH_3CN = 1:1, v/v), λ_{ex} = 485 nm; C) The images of Hela cells incubated by probe **5** (10 µM, a,b) and then further treated with 10 µM $Zn(NO_3)_2$ and 20 µM pyrithione (c,d). λ_{em} = 515 ± 10 nm and λ_{em} = 590 ± 10 nm respectively. Adapted from ref. 14

1.3.4 The ESIPT mechanism

Excited state intramolecular proton transfer (ESIPT) is a process whereby photoexcited molecules relax through tautomerization by transfer of protons. In general, molecules incorporating an intramolecular hydrogen bonding interaction between a hydrogen bond donor and a hydrogen bond acceptor can exhibit ESIPT fluorescence. Due to its unique four-level photochemical process, shown in Figure 1.8, probes based on an ESIPT mechanism usually display a large Stokes shift (~200 nm) and ability for ratiometric sensing.[15] However, because they are very sensitive to local surroundings, particularly the presence of polar and hydrogen bond donating solvents which can inhibit the ESIPT process, many ESIPT-based

probes require a large amount of organic solvents to be operationally effective, which limits their use in living systems. Consequently among the ESIPT-based probes reported for Zn^{2+} imaging, there are few reports of their application in cells, however, probe **6**, developed from the thymolphthalein fluorophore, with hydroxyl and amino groups providing Zn^{2+} coordination sites displays a good 'switch on' fluorescence response since the ESIPT process was quenched upon binding with Zn^{2+} (Figure 1.9) and it was successfully utilized to image Zn^{2+} in A549 cells.[16]

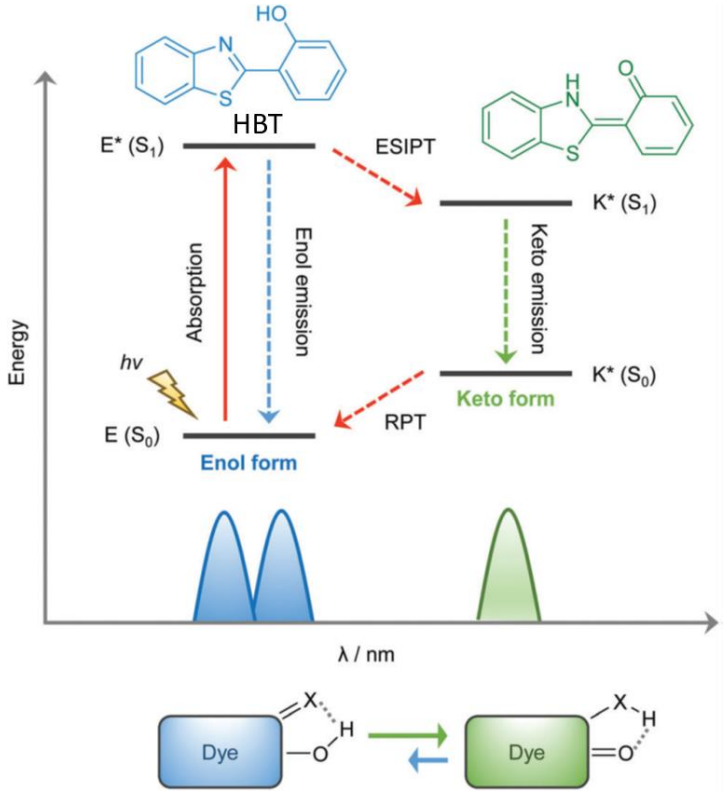

Figure 1.8 Orbital energy diagram description of the ESIPT process. Adapted from ref. 15

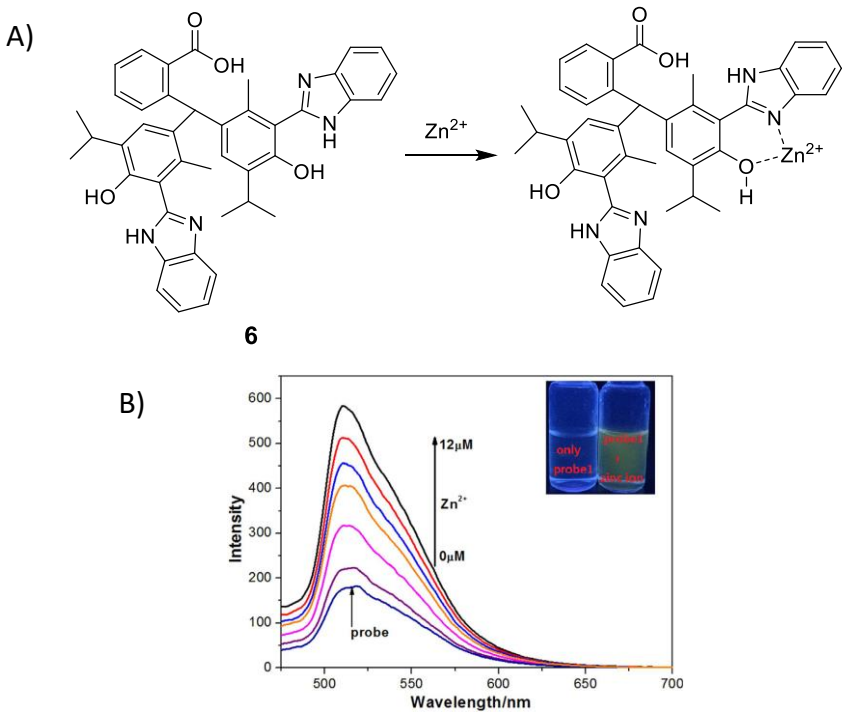

Figure 1.9 A) The structure of probe **6** and its complex with Zn^{2+}; B) fluorescence spectrum of probe **6** (2 μM) in the presence of different concentrations of Zn^{2+} in EtOH. Adapted from ref. 16

1.3.5 The restriction of intramolecular motion (RIM) mechanism

The restriction of intramolecular motion (RIM) mechanism is proposed to explain the aggregation induced emission (AIE) phenomenon, which is observed in certain organic fluorescent dyes that show higher photoluminescence efficiency in the aggregated state than in solution. Since the fluorescence of most organic fluorophores are quenched when aggregated, the luminogens displaying the AIE phenomenon are very limited, among these, tetraphenylethene, tetraphenylsilole, triphenylamine derivatives are widely studied.[17] This type of molecule usually have freely rotating groups, which provide a pathway for relaxation of a photochemical excited state and is the reason for their low quantum yield in solution. However, when aggregated or crystallised, the rotational processes are restricted, thus they become emissive and display high quantum yields.

Based on this mechanism, AIE fluorophores have been applied for Zn^{2+} imaging showing an excellent turn-on fluorescence response, for example, Ning *et al.* reported the ratiometric probe **7** (8AQ) containing a bis-naphthylamide connected by an isobutylene unit.[18] Upon Zn^{2+} binding, the fluorescence showed a bathochromic shift of 106 nm (the solution colour changed from blue to yellow-green), accompanied by a strong fluorescence increase. In HepG2 cells, it displayed ratiometric fluorescence response towards exogenous Zn^{2+} (Figure 1.10).

In addition to these classical AIE systems, it has been noted that many cases of fluorescence quenching in small molecule probes have been automatically ascribed to PET processes without compelling experimental proof. However, with the advent of time-dependent density functional theory (TD-DFT) and complete active space self-consistent field (CASSCF) calculations, the potential energy surfaces of the lowest-lying excited states can now be studied, and it has been found the fluorescence quenching in some systems, which were believed to be originated by PET, should be revised to a dark-state quenching mechanism[19], which is specified to elaborate RIM mechanisms.[20] Therefore, the fluorescence quenching of some Zn^{2+} probes is probably caused by non-radiative decay due to intramolecular motions. After binding with Zn^{2+}, these intramolecular rotations are considerably restricted, which reduces this decay through nonradiative pathways and increases the fluorescence emission.

A

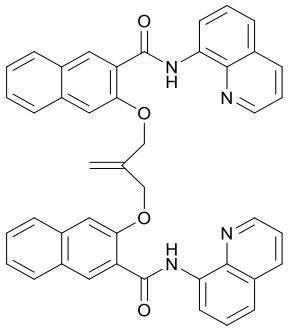

7 (8AQ)

B)

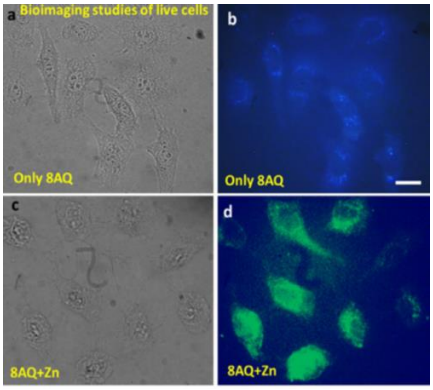

Figure 1.10 A) The structure of probe **7** (8AQ); B) fluorescence microscopy images of **7** in HepG2 cells.

Table 1.1 The photophysical properties of probes **1**-**6**.

Probe	Solvent	max λ_{ex} / nm		max λ_{em} / nm		ε [a] / M^{-1} cm^{-1}		Φ [b]		K_d [c]	LOD [d]
		no Zn^{2+}	with Zn^{2+}	no Zn^{2+}	with Zn^{2+}	no Zn^{2+}	with Zn^{2+}	no Zn^{2+}	with Zn^{2+}		
1	Tris-HCl buffer	491	491	509	511	1.95×10^4	1.80×10^4	0.077	0.875	1.0 ± 0.1 nM	N/A
2	PIPES buffer	345	345	448	448	9.20	9.20	N/A	> 0.26	< 1 μM	N/A
3	HEPES buffer	456	386	585	545	4.46×10^3	$3{,}29 \times 10^3$	N/A	N/A	2.1 ± 0.27 nM	0.5 nM
4	HEPES buffer	467	376	542	500	N/A	N/A	N/A	N/A	1.00 μM	35 nM
5	H_2O/CH_3CN (1:1)	490	560	518	590	N/A	N/A	N/A	N/A	N/A	40 nM
6	EtOH	278	278	510	510	N/A	N/A	N/A	N/A	N/A	25 μM
7	Tris-HCl buffer	333	382	430	536	N/A	N/A	N/A	N/A	20 nM	2.6 nM

[a] Molar extinction coefficient; [b] fluorescence quantum yield; [c] dissociation constant; [d] the limit of detection for Zn^{2+}.

1.4 Subcellular localised small molecule fluorescent Zn^{2+} probes

As discussed earlier, the failure to control the subcellular location of small molecule fluorescent probes has limited their utility somewhat, however, in the last two decades, there have been considerable efforts to overcome this problem. At the subcellular level, organelles require zinc for their normal function and the dysfunction of zinc homeostasis results in pathological processes, such as cellular stress, and these can induce cell apoptosis. Therefore, the development of Zn^{2+} probes capable of predictable and reliable subcellular localisation is required for biological applications.

1.4.1 Plasma membrane targeting

1.4.1.1 Plasma membrane and the role of Zn^{2+} in its function

The plasma membrane, also known as the cell membrane, is mainly formed by a lipid bilayer to protect cells from their external environment. The membrane controls the import and export of substances and the selective uptake of ions and organic molecules. Membrane transporters, a kind of membrane protein, play an important role in these processes. As shown in Figure 1.1, ZIP 1-6, ZIP8, ZIP10 and ZIP14 are zinc transporters that control zinc uptake, while ZNT1, ZNT5B and ZNT10 are responsible for zinc efflux through the membrane. Some data has suggested that when zinc is present in sufficiently high concentration it can act as a stabilizer of the cell membrane.[21] It has also been reported that zinc deficiency in membranes causes a defect in calcium channels, which impairs the uptake of Ca^{2+}.[22]

1.4.1.2 Plasma membrane localised Zn^{2+} probes

There are a few small molecule fluorescent probes reported to image Zn^{2+} in the cell membrane. Due to the phospholipid bilayer nature of the membrane, a highly hydrophobic group is normally used as a membrane targeting unit. In 2011, Yamamoto *et al.*, reported that cholesterol could be applied as a cell membrane targeting unit.[23] With fluorescein as the fluorophore and an o-aminophenol-*N*,*N*,*O*-triacetic acid-based zinc-chelating moiety, probe **8** (LF-Chol) showed good cell membrane localisation and fluorescence response when Zn^{2+} was added or removed (Figure 1.11).

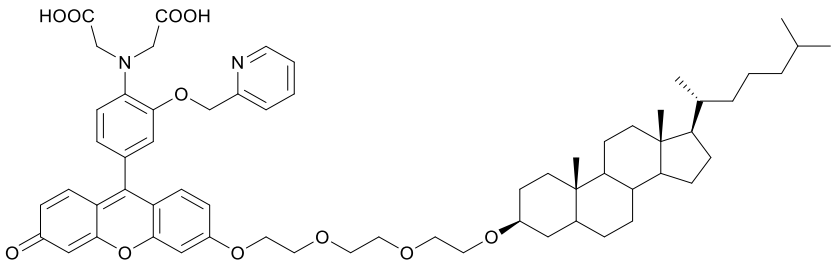

8 (LF-Chol)

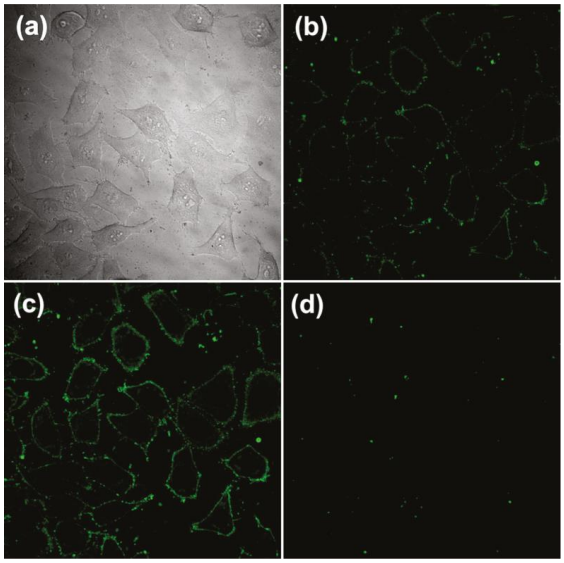

Figure 1.11 The structure of **8** (LF-Chol) and (b) its fluorescence response in cells; (c) fluorescence response in the presence of 20 μM Zn^{2+} and (d) response after the subsequent addition of 100 μM EDTA. Adapted from ref. 23

Besides cholesterol, long alkyl chains have also been widely used for membrane targeting. Rutter and Li *et al.,* reported the fluorescent probe **9** (ZIMIR, Figure 1.12) in which a pair of dodecyl alkyl chains were used as the membrane targeting unit as a Zn^{2+} indicator to image dynamic insulin release.[24] The probe was quenched based on the PET mechanism and displayed a robust fluorescence increase after binding with Zn^{2+}. **9** showed low toxicity and membrane labelling in a wide range of cell lines. Using this probe, the authors demonstrated exocytotic activity at subcellular resolution from pancreatic β cells in intact islets and found that the sites of Zn^{2+}/insulin release are mainly in small groups of adjacent β cells. Similar results were observed by Watkinson *et al.* with the plasma membrane targeting Zn^{2+} probe **10**.[25] The di-dodecylamide motif as the membrane targeting unit was introduced through a one-pot modular 'click-S_NAr-click' approach, which was proven to be more efficient in the synthesis. Probe **10** showed a significant switch on fluorescence response to Zn^{2+} due to aggregation phenomena, and *in cellulo* experiments in mouse pancreatic islets demonstrated its localisation to the exterior of the plasma membrane. This probe was subsequently used to

measure dynamic insulin secretion by Hodson *et al.* since zinc is co-released from insulin-containing granules.[26]

Similarly, Cho *et al.,* synthesized the two-photon (TP) probe, **11** (FZn-mem), to image near-membrane Zn^{2+} by introducing a long alkyl chain to 2-amino-7-(3-oxo-1-dodecen-1'-yl)-9.9-dimethylfluorene (ADF), a two-photon fluorophore with a large TP cross section.[27] With the same ligand as **9**, **11** was shown to be highly selective for Zn^{2+} over competing cations, and its dissociation constant K_d was determined to be 20 ± 0.4 nM and 19 ± 0.2 nM by one-photon and two-photon spectroscopy, respectively. After TP excitation by 820 nm femtosecond laser pulses, the fluorescence of **11** could be collected in the emission wavelength range of 450-600 nm, and near-membrane Zn^{2+} could be detected in living cells and tissue at a depth of 110 µm.

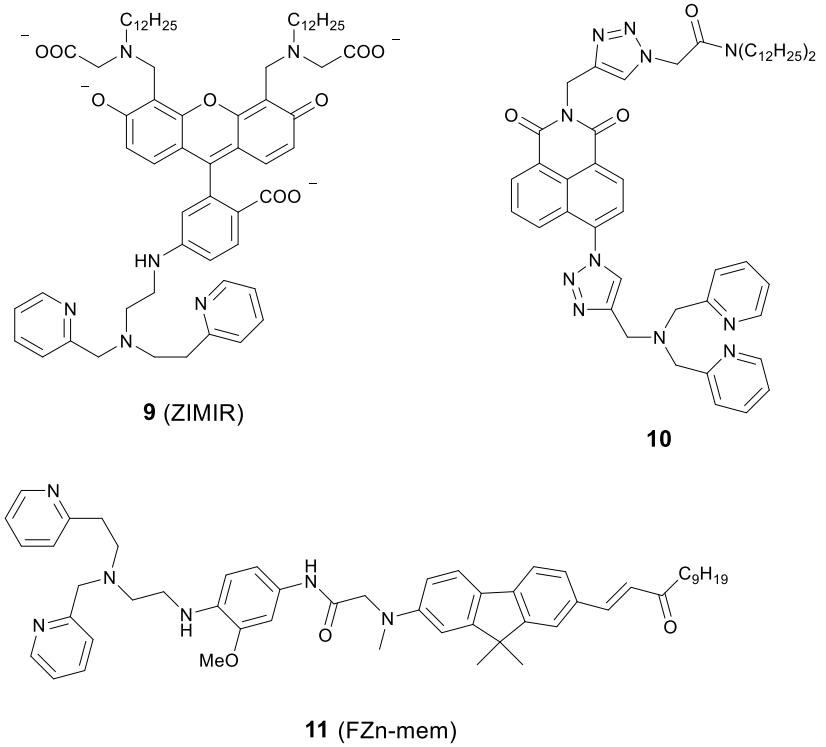

9 (ZIMIR)

10

11 (FZn-mem)

Figure 1.12 Plasma membrane localised Zn^{2+} probes with long alkyl chain as their targeting unit.

Table 1.2 The photophysical properties of probes **8**-**21**.

Probe	Solvent	max λ_{ex} / nm		max λ_{em} / nm		ε [a] / M^{-1} cm^{-1}		Φ [b]		K_d [c]
		no Zn^{2+}	with Zn^{2+}	no Zn^{2+}	with Zn^{2+}	no Zn^{2+}	with Zn^{2+}	no Zn^{2+}	with Zn^{2+}	
8	HEPES buffer	470	470	517	517	N/A	N/A	< 0.005	0.18	126 nM
9	HEPES buffer	493	493	515	515	7.3×10^4	N/A	0.0032	0.225	0.45 μM
10	HEPES buffer	347	347	420	443	N/A	N/A	N/A	N/A	N/A
11	MOPS/DPPC (1:1)	400	415	506	520	1.64×10^4	N/A	0.19	N/A	20 ± 0.4 nM
12	MOPS buffer	545	N/A	575	575	N/A	N/A	N/A	N/A	65 ± 10 nM
13	PIPES buffer	497	490	522	517	3.3×10^4	4.2×10^4	0.36	0.80	1.5 ± 0.2 μM
14	PIPES buffer	569	573	629	631	2.84×10^4	3.67×10^4	0.0355	0.5025	3.25 ± 0.12 nM
15	MOPS buffer	388	375	500	493	1.87×10^4	2.31×10^4	0.15	0.92	3.1 nM
16	HEPES buffer	413	395	536	536	1.85×10^4	2.10×10^4	0.0048	0.33	1.4 nM
17	MOPS buffer	392	N/A	559	N/A	1.32×10^4	N/A	0.023	N/A	17 ± 2 nM
18	HEPES buffer	453	391	625 [d]	542 [d]	6.2×10^3	4.2×10^3	N/A	0.03	8.2 ± 0.2 nM
19	HEPES buffer	420	370	550	504	N/A	N/A	0.11	0.22	0.45 ± 0.01 nM
20	CH_3CN	347 [e]	363 [e]	633	633	81×10^3 [e]	67×10^3 [e]	0.28 [g]	0.29 [h]	9.1 μM
		602 [f]	602 [f]			23×10^3 [f]	21×10^3 [f]			
21	PIPES buffer	510	510	535	529	N/A	N/A	< 0.001	0.75 ± 0.03	0.6 ± 0.03 nM

[a] Molar extinction coefficient; [b] fluorescence quantum yield, and for the cases of two-photon probes, only one-photon excited quantum yield is recorded here; [c] dissociation constant; [d] λ_{ex} = 466 nm; [e] the parameters of donor; [f] the parameters of acceptor; [g] λ_{ex} = 565 nm; [h] λ_{ex} = 400 nm.

1.4.2 Mitochondria targeting

1.4.2.1 The mitochondrion and the role of Zn^{2+} in its function

The mitochondrion is an important organelle in eukaryotic organisms. It generates most of the chemical energy supply of adenosine triphosphate (ATP) in all cells, and takes part in many biological processes, such as signalling, the cell cycle, cell growth and cell death.[28] Mitochondria are involved in intracellular Zn^{2+} storage in yeast and as a co-factor for a wide range of enzymatic reactions and Zn^{2+} is closely related to the mitochondrial respiratory chain.[29] It was also reported that zinc can reduce mitochondrial damage under stress conditions, which can protect cells from oxidatively-induced apoptosis.[30] In contrast, mitochondrial dysfunction may cause rapid Zn^{2+} entry, which is one of the major contributors to neuronal injury.[31] Therefore, to better-understand these processes, mitochondria localised zinc imaging is in demand.

1.4.2.2 Mitochondria localised Zn^{2+} probes

The first example of mitochondrial fluorescent Zn^{2+} probe was reported by Gee *et al.,* in 2003.[32] Probe **12** (RhodZin-3, Figure 1.13) displayed a 75-fold fluorescence increase after

binding Zn^{2+} and good selectivity over competing cations. The ester form was loaded into cells due to its membrane permeability and it showed co-localisation with a mitochondrial marker MitoTracker Green and Zn^{2+} response in cortical neurons.

In 2006, Lippard *et al*., synthesized a series of probes and found **13** (ZS5), displaying green fluorescence, could localise to mitochondria.[33] This strategy is perhaps not so effective since this was the only probe to display mitochondrial localisation within a larger series of structurally similar probes synthesized. Moreover, another probe **14** (ZBR4), a red fluorescent probe, was subsequently found to spontaneously accumulate in mitochondria in 2014 by the same group. However, the localisation was again serendipitous as this was the only probe in another large family of probes that failed to localise to the endoplasmic reticulum (ER) and accumulate in the mitochondria.[34]

Delocalised lipophilic cations, such as the triphenylphosphonium salt (TPP), are known as effective mitochondrial targeting groups, since they can cross hydrophobic membranes and accumulate in the mitochondria in living cells. By introducing this group, Kim and Cho *et al.,* obtained a mitochondria-targeting two-photon probe **15** (SZn-Mito) for Zn^{2+} imaging (Figure 1.14).[35] The probe showed a 7-fold increase of two-photon excited fluorescence after being bound with Zn^{2+} and was able to detect zinc in living tissues to a depth of 100-200 μm through two-photon microscopy. Just one year later, the same group developed a similar mitochondria targeting probe **16** (SZn2-Mito) which had a 70-fold two-photon excited fluorescence increase in response to Zn^{2+} and displayed similar properties.[36] Besides these, another two-photon Zn^{2+} probe **17** (FZn-Mito) was synthesized with a different fluorophore, but had similar mitochondria targeting behaviour and two-photon emission response to Zn^{2+}.[37]

In 2012, Guo *et al.,* synthesized the ratiometric probe **18** (Mito-ST) which was capable of imaging zinc ions in the mitochondria.[38] With Zn^{2+} associated, the probe showed a blue shift in both excitation and emission wavelength. Interestingly, they observed the concentration of Zn^{2+} in mitochondria started to increase immediately upon H_2O_2 (10 mM) stimulation and increased to 1.6 nM (from 0.6 nM) with the ratiometric imaging result based on the method reported by Tsien *et al.*[39] However, the Zn^{2+} release stimulated by *S*-nitrosocysteine (SNOC,10 mM), a precursor of the NO radical, experienced a lag phase, and the concentration was much higher (76 nM) compared to that stimulated by H_2O_2. In the same year, Jiang *et al.,* reported the quinoline-based ratiometric probe **19** (DQZn2) with similar properties.[40] The emission of the probe showed a 46 nm blueshift, with about a 5-fold change of the emission intensity ratio after binding with Zn^{2+}, which allowed the concentration of mitochondrial free Zn^{2+} to be quantitatively measured in NIH3T3 cells.

The mitochondria localised Zn^{2+} probe **20** utilising a FRET mechanism was reported by Zhu *et al.*[41] The FRET donor fluorophore displayed a bathochromic shift of emission when coordinated with Zn^{2+}. The spectral overlap between the emission of the donor and the absorption of the acceptor increased upon Zn^{2+} binding, which enhanced the FRET efficiency. In HeLa cells, when the probe was excited at 405 nm, red fluorescence with emission wavelength 580-680 nm could be observed after addition of $ZnCl_2$.

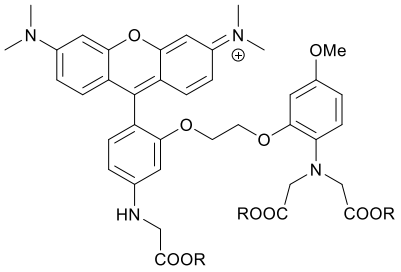

12 RhodZin-3, R = K
RhodZin-3-AM, R =

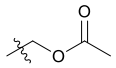

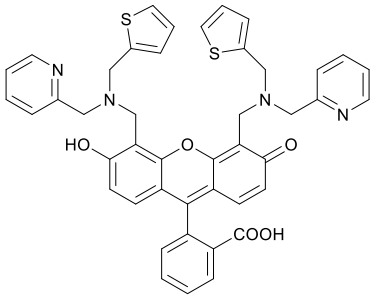

13 ZS5

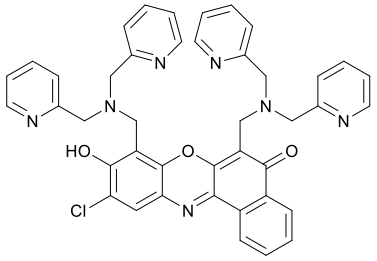

14 ZBR4

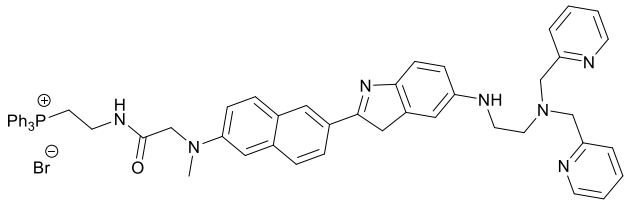

15 SZn-Mito

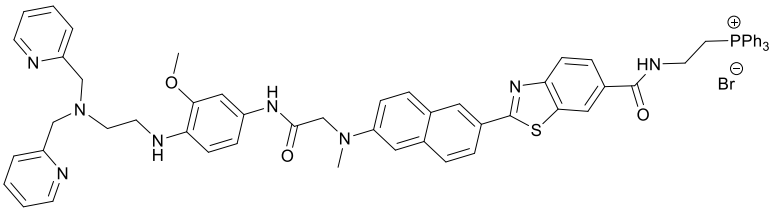

16 SZn2-Mito

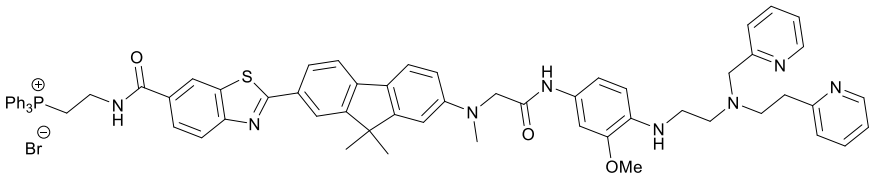

17 FZn-Mito

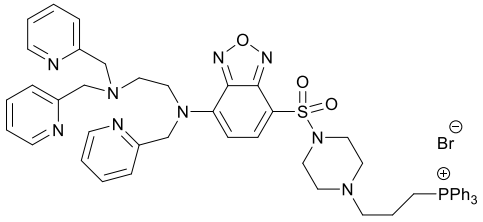

18 Mito-ST

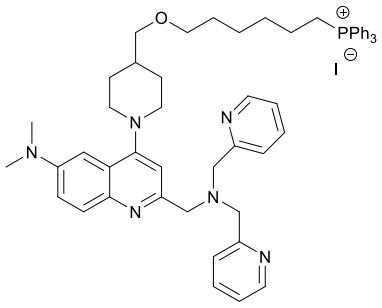

19 DQZn2

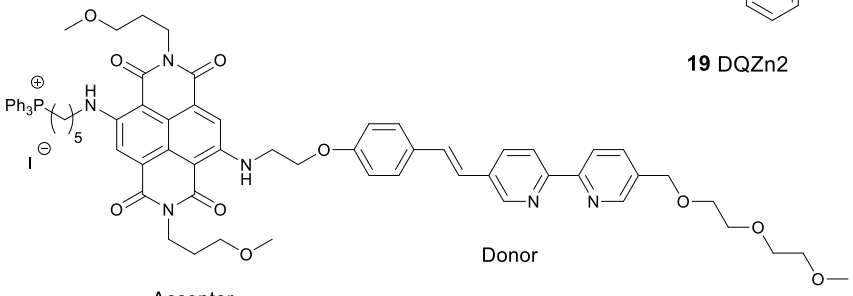

Acceptor Donor

20

Figure 1.13 The structures of mitochondria localised fluorescent probes **12**-**20**.

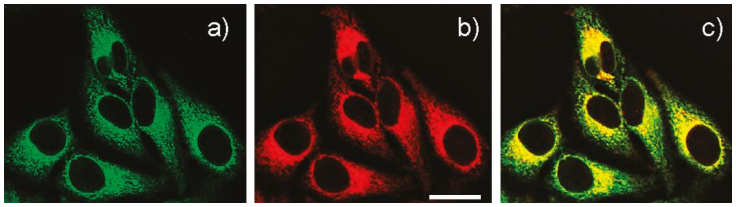

Figure 1.14 (a) TPM and (b) OPM images of HeLa cells co-labelled with (a) **15** (0.5 µM) and (b) Mitotracker Red FM (1 µM) for 30 min; (c) Colocalised image. Adapted from ref. 35

In 2014, a reaction-based fluorescent probe **21** (DA-ZP1-TPP) was reported to investigate mobile Zn^{2+} in mitochondria.[42] As shown in Figure 1.15, the phenolic oxygen atoms of the xanthene ring in the fluorescein moiety was protected with an acetyl group, which rendered it non-fluorescent in metal-free media. In the presence of Zn^{2+}, the ester group was hydrolysed, and the PET mechanism quenched by Zn^{2+} association, giving a strong fluorescence response (more than a 140-fold increase). Interestingly, using this probe, the authors found that tumorigenic epithelial prostate cells could not accumulate mobile Zn^{2+} in their mitochondria, compared to that of healthy epithelial prostate cells, which could.

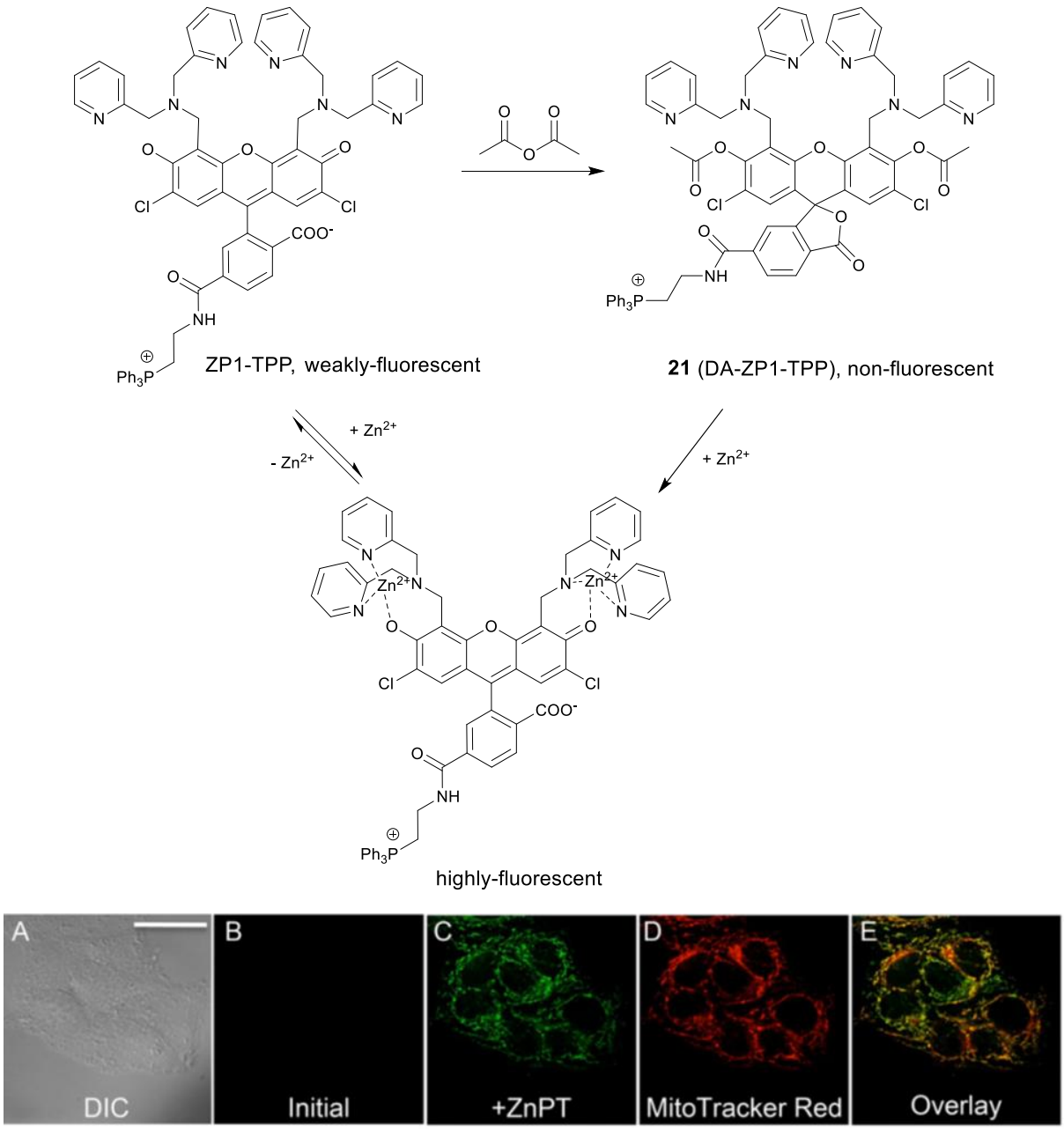

Figure 1.15 The structure of the reaction-based probe **21** (DA-ZP1-TPP). Its fluorescence response to Zn^{2+} and co-localisation with Mito-tracker red in HeLa cells. Adapted from ref. 42

1.4.3 Lysosome targeting

1.4.3.1 The lysosome and the role of Zn^{2+} in its function

The lysosome acts as the waste disposal system in cells by digesting unwanted materials in the cytoplasm. Zn^{2+} homeostasis in the lysosome is regulated by zinc transporters, ZIP3, ZIP8 and ZNT2, and its dysregulation is associated with a wide range of pathological processes at

the cellular level. For example, oxidative stress induced by H_2O_2 causes Zn^{2+} accumulation in the lysosome in hippocampal neurons, which eventually undergo lysosomal membrane permeabilization (LMP) and this may be the mechanism of oxidative neuronal death.[43] It was also reported that lysosome-related organelles in intestinal cells of *C. elegans* (gut granules) are the major site of zinc storage, which promotes detoxification and subsequent mobilization, regulating cellular and organismal zinc metabolism.[44] Therefore, it is vital to develop fluorescent probes to image Zn^{2+} in the lysosomal space to help understand these kinds of biological processes.

1.4.3.2 Lysosome localised Zn^{2+} probes

In 2009, Guo *et al.,* synthesized the intramolecular charge transfer (ICT) based probe **22** (NBD-TPEA, Figure 1.16).[45] The probe demonstrated a good selectivity for Zn^{2+}, a large Stokes shift, and was also applied for *in vivo* Zn^{2+} imaging in zebrafish larva. However, subcellular experiments showed it to not only accumulate in the lysosome but also in the Golgi apparatus, which limits its application in lysosomal Zn^{2+} imaging.

The basic ethylenediamine group has been reported to accumulate in the lysosome since it can be protonated by the acid environment in lysosomal space (pH = 4.5 - 5.5). The basic dimethylethylamino moiety has therefore been introduced as a lysosome targeting group in the ratiometric probe **23** (DQZn4) based on quinoline and showed good targeting behaviour.[46] It performed well in the acidic pH environment, showing a significant turn-on fluorescence response and 47 nm blueshift of emission wavelength on binding Zn^{2+}. With these desirable properties *in vitro*, it was successfully utilised for imaging lysosomal Zn^{2+} changes in NIH 3T3 cells.

Another group that has been frequently used for targeting the lysosome is the morpholine unit. One example is the two-photon probe **24** based on a naphthalimide dye with an *N*,*N*-di-

(2-picolyl)ethylenediamine (DPEN) Zn^{2+} ligand, which can image intracellular Zn^{2+} in the lysosome and mouse brain tissues under two-photon excited microscopy.[47] Unlike the other subcellular targeting probes, in this case organelle differentiation relied on a concentration gradient of the probe intracellularly. Probe **24** showed a strong fluorescence switch on response to Zn^{2+} in the lysosomal pH range (pH = 4.5 - 5.5) but the intensity increase was much smaller at cytosolic pH range (pH = 7.2 - 7.4), therefore it was able to detect lysosomal Zn^{2+} specifically.

Using the same targeting unit, Peng *et al.*, reported a ratiometric probe **25** (LysoZn-1) to image lysosomal Zn^{2+} (Figure 1.17).[48] The authors introduced an electron donor 4-ethoxylphenyl to the *meso*-position of a styryl-Bodipy-DPA scaffold, which distinguished Zn^{2+} from Cd^{2+} very well. They explained this using Hard-Soft Acid-Base theory, which was supported by Gaussian calculations. Probe **25** exhibited a significant fluorescence increase and ratiometric ($F_{578\ nm}/F_{680\ nm}$) changes upon Zn^{2+} binding and had a good response to Zn^{2+} in the lysosomal pH range. Using **25** it was observed that lysosomal Zn^{2+} concentration increased upon H_2O_2 stimulation in neuronal stem cells and a similar phenomenon was observed by Uvdal *et al.* with a PET based lysosome localised probe **26** (Lys-NBD-TPEA)[49] in which morpholine was again utilised as the targeting unit.

Based on a FRET mechanism, two fluorescent Zn^{2+} probes **27** were prepared by Zhu *et al.* with different aliphatic amino groups as the lysosome targeting units.[50] A Zn^{2+}-sensitive arylvinylbipyridyl fluorophore was selected as the FRET donor, and through the efficient intramolecular FRET process, its broad emission band was transformed into a strong, narrow emission band of the acceptor Bodipy, which is preferable for multi-colour imaging. With a 2:1 stoichiometry between **27** and Zn^{2+}, the molar absorptivity of the donor was increased upon Zn^{2+} coordination, leading to the enhancement of acceptor emission. The lysosome

localisation was confirmed by confocal microscopy and with the high resolution of structured illumination microscopy (SIM), they found **27b** localised to the interior of lysosomes in HeLa cells, rather than anchoring at the lysosomal membranes (Figure 1.18).

Sessler *et al.* synthesized a series of probes **28** (LysoDPP-C2-C4), which were designed based on AND logic to detect both Zn^{2+} and the acidic pH of the lysosome.[51] The morpholine moiety served not only as a lysosome targeting unit but also as a pH-responsive marker, since the nitrogen in the morpholine moiety was protonated at low pH and the PET was quenched, which increased the fluorescence of the diketopyrrolopyrrole (DPP) fluorophore in the same way as the PET quenching upon Zn^{2+} binding. The experiments *in cellulo* showed **28c** was the most effective probe in terms of the initial fluorescence and the fluorescence response to Zn^{2+}. When incubated with **28c**, the cancerous prostate cell lines PC3 and DU145 showed no change in fluorescence intensity, while the normal human prostate epithelial cell line RWPE1 displayed a significant increase on the addition of exogenous Zn^{2+}. The authors also demonstrated that the probe was capable of imaging the prostate *in vivo* nude mice models and discriminate between cancerous and normal prostate tissue through histological studies.

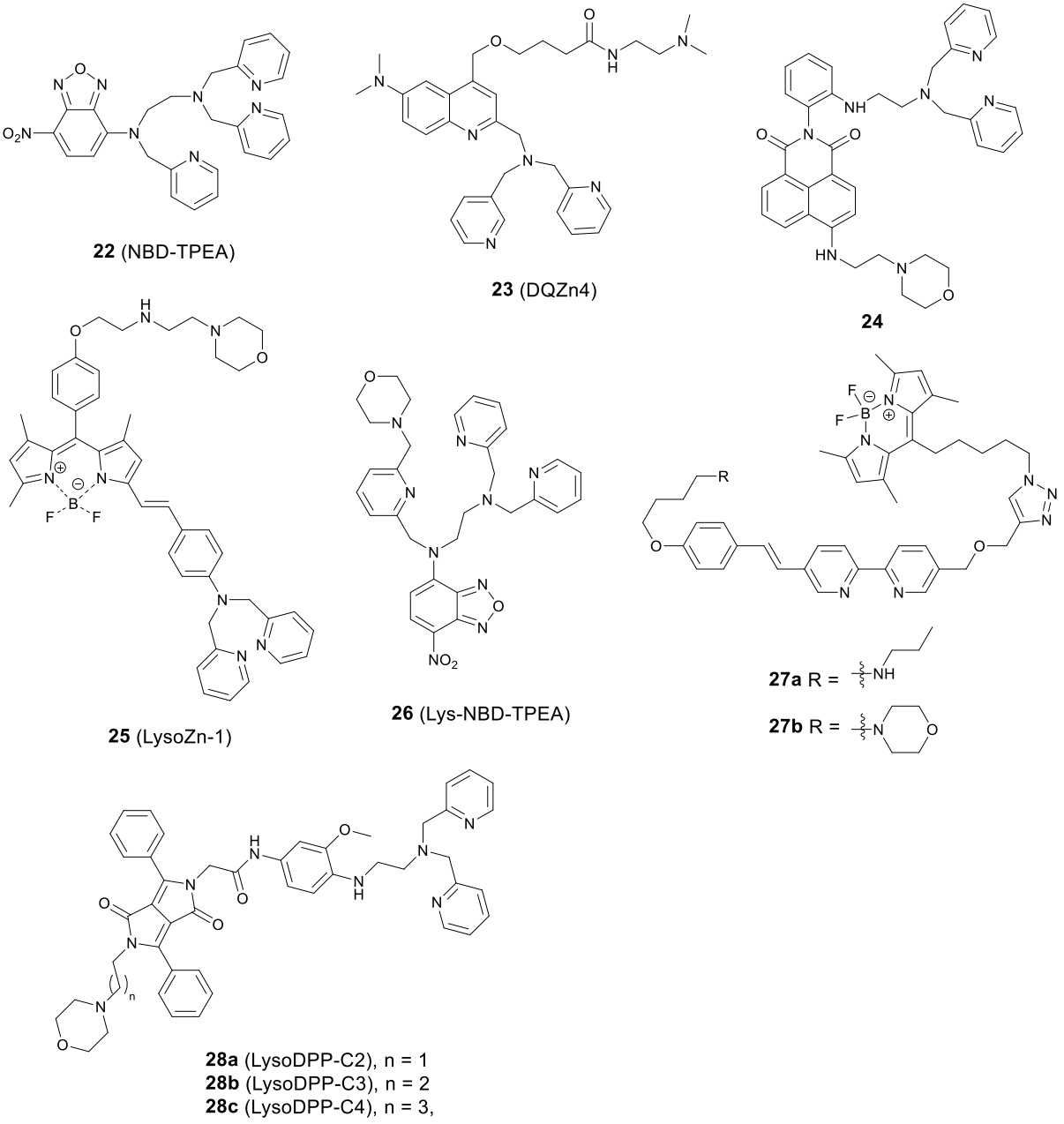

Figure 1.16 The structures of lysosome localised fluorescent probes **22**-**28**.

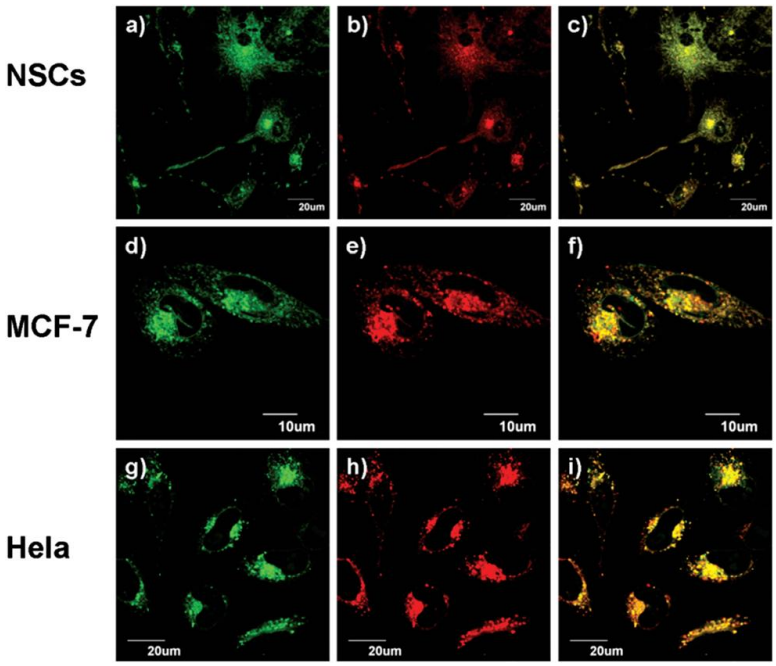

Figure 1.17 **25** (LysoZn-1) co-localises to lysosomes in neural stem cells (NSCs, a–c), MCF-7 (d–f) and Hela (g–i) cells. Cells were stained with LysoSensor Green (1 µM) (a, d and g), and **25** (1 µM)(b, e and h), (c, f and i) Overlap of these two channels. Adapted from ref. 48

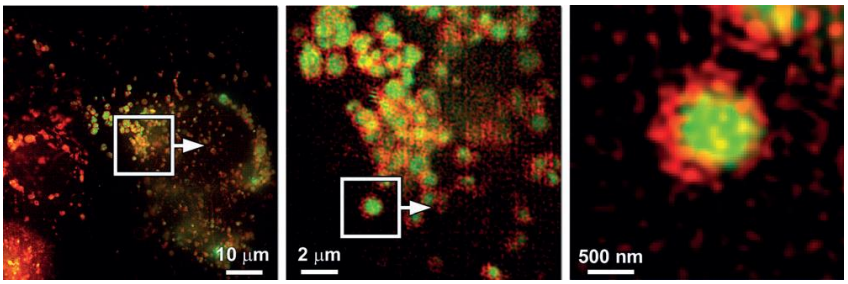

Figure 1.18 SIM images to show the localisation of compound **27b** (green) compared to that of the lysosome-associated membrane protein (LAMP) fused to the fluorescent protein FusionRed (red). Adapted from ref. 50

Table 1.3 The photophysical properties of probes **22**-**37**.

Probe	Solvent	max λ_{ex} / nm		max λ_{em} / nm		ε [a] / M^{-1} cm^{-1}		Φ [b]		K_d [c]	LOD [d]
		no Zn^{2+}	with Zn^{2+}	no Zn^{2+}	with Zn^{2+}	no Zn^{2+}	with Zn^{2+}	no Zn^{2+}	with Zn^{2+}		
22	HEPES buffer	496	469	550	534	2.10×10^4	1.40×10^4	0.003	0.046	1.0 ± 0.1 nM	N/A
23 [e]	MES buffer	285	261	542	495	4.30×10^3	1.66×10^3	0.11	0.17	16 ± 1.1 nM	N/A
24 [f]	MES buffer	435	444	528	536	1.55×10^4	1.81×10^4	0.03	0.23	8.5 µM	0.18 µM
25	EtOH/tris-HCl (9:1)	597	568	647	578	N/A	N/A	N/A	0.23	68 ± 4 µM [g] 123 ± 6 µM [h]	0.48 µM
26	MES buffer [i]	500	490	536	536	N/A	N/A	N/A	N/A	N/A	0.477 µM
27a	HEPES buffer /	350	365	504	504	N/A	N/A	0.25	0.24	1 nM [2]	N/A
27b	CH_3CN (1:1)	350	359	504	504	N/A	N/A	0.32	0.33	0.17 nM [2]	N/A
28a	HEPES buffer	456	454	515	515	N/A	N/A	0.0027	0.0482	1.54 nM	N/A
28b	HEPES buffer	454	451	509	515	N/A	N/A	0.0064	0.2606	2.57 nM	N/A
28c	HEPES buffer	453	453	512	517	N/A	N/A	0.0077	0.3283	1.91 nM	N/A
29a	PIPES buffer	478	530	625	628	1.93×10^4	2.64×10^4	0.067	0.41	0.69 nM	N/A
29b	PIPES buffer	480	524	630	630	1.69×10^4	2.56×10^4	0.069	0.22	0.70 nM	N/A
29c	PIPES buffer	480	535	623	628	1.33×10^4	1.93×10^4	0.342	0.60	< 0.001 nM	N/A
30	EtOH	406	N/A	490	N/A	N/A	N/A	< 0.01	0.12	5.5 nM	5.8 nM
31	PIPES buffer	515	507	530	525	7.95×10^4	8.40×10^4	0.39	0.87	0.7 ± 0.1 nM	N/A
32a	PIPES buffer	499	496	519	514	2.72×10^4	1.60×10^4	0.004	0.73	[j]	N/A
32b	PIPES buffer	498	492	515	515	6.41×10^4	4.00×10^4	0.012	0.51	[k]	N/A
33	HEPES buffer	302	360	532	532	420	4680	0.015	0.055	1.8 ± 0.1 pM	0.042 pM
35	MOPS buffer	384	388	518	518	2.89×10^4	N/A	0.12 [l]	0.93 [l]	1.7 nM [l]	N/A
37	HEPES buffer	453	442	546	536	N/A	N/A	N/A	0.19	4 nM	57 nM

[a] Molar extinction coefficient; [b] fluorescence quantum yield; [c] dissociation constant; [d] the limit of detection; [e] all results shown here were recorded at lysosomal pH 5.2; [f] all results shown here were recorded at lysosomal pH 5.0; [g] calculated from turn on fluorescence emission at wavelength 578 nm; [h] calculated from the ratio of $F_{578\ nm}/F_{680\ nm}$; [i] the pH of the buffer is 5.0; [j] K_{d1} = 3.5 ± 0.1 mM, K_{d2} = 150 ± 100 µM; [k] K_{d1} = 220 ± 30 µM, K_{d2} = 160 ± 80 µM, K_{d3} = 9 ± 6 µM; [l] the results were obtained in solution EtOH:MOPS buffer (1:1, v/v).

1.4.4 Endoplasmic reticulum (ER) targeting

1.4.4.1 The ER and the role of Zn^{2+} in its function

The endoplasmic reticulum (ER), an organelle in eukaryotic cells, serves a number of important cellular roles, such as protein synthesis and transport, protein folding, carbohydrate metabolism, lipid and steroid synthesis.[52] Proteins synthesized in the ER are normally properly folded and transported to the Golgi apparatus. However, when there are changes to ER function, resulting from factors such as ageing, genetic mutations, or the environment, unfolded or misfolded proteins are synthesized and accumulate in the ER, causing ER stress, which activates the unfolded protein response (UPR).[53]

It is known the ER acts as an intracellular store for biological mediators, including zinc, which it requires for normal function. For example, it has been found that zinc can be released from thapsigargin- and inositol 1,4,5-trisphosphate (IP3)-sensitive ER storage in cortical neurons.[54] ZIP7, ZIP9, ZIP13 and ZNT5-7 are the transporters to regulate Zn^{2+} inside the ER and the

depletion of zinc transporters and zinc deficiency can cause ER stress and upregulate the UPR,[55,56] which results in a wide range of diseases, such as inflammation,[57] diabetes[58] and neurodegenerative disorders, including Parkinson's and Alzheimer's diseases.[59] However, the role of 'free' or 'mobile' zinc in these processes is little understood due to the lack of suitable molecular tools to image this subcellular region that exist.

1.4.4.2 ER localised Zn^{2+} probe

Reports of ER localised small molecule Zn^{2+} probes are very limited, and all of them were found to accumulate in the ER adventitiously. In 2013, Lippard *et al.,* reported a series of benzoresorufin based red-emitting fluorescent probes **29** (the ZBR family, Figure 1.19) for labile Zn^{2+}.[60] The probes displayed a broad absorption band and a bathochromic shift after binding with Zn^{2+}, while the emission showed up to 8.4-fold increase with addition of Zn^{2+}. *In cellulo* studies revealed all probes accumulated in the ER in a variety of cell lines (Figure 1.20), as the Pearson's correlation coefficient with ER tracker was much higher than the other organelle tracker dyes. Interestingly, with **29a**, the authors observed the depletion of labile zinc in the ER of neural stem cells under ER stress induced by peroxynitrite.

The conveniently prepared small molecular fluorescent probe **30** included benzothiazole as the fluorophore and an *o*-hydroxyl Schiff base as the Zn^{2+} receptor.[61] Upon binding Zn^{2+}, the PET process was blocked, and the fluorescence response had a 65-fold increase with a slight red shift, with a Job's plot showing a 2:1 binding stoichiometry between **30** and Zn^{2+}. In human liver hepatocellular carcinoma cells, **30** was able to detect intracellular endogenous Zn^{2+} and its subcellular localisation was found to be the ER with a Pearson's correlation coefficient of 0.88 compared to ER tacker Red. Moreover, **30** was applied to investigate Zn^{2+} in plant tissues where it was shown that Zn^{2+} mainly accumulates in vascular tissue and epidermal cells in the cotyledons when treated with exogenous Zn^{2+}.

Given the ongoing need to develop an effective and reliable strategy for targeting ER localised probes a sensible strategy, based on the previous experience of targeting other organelles, would be to identify methods to incorporate an ER targeting unit in the probe design. Glibenclamide is one option since the commercial ER tracker red and ER tracker green both have glibenclamide group, however, a number of recent reports have appeared in which the methyl sulfonamide group has been used as a targeting unit to visualize hydrogen peroxide,[62] methylglyoxal,[63] hypochlorite[64] and hydrogen sulfide[65] in the ER.

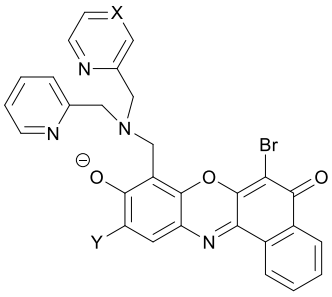

29a (ZBR1), X = N, Y = H
29b (ZBR2), X = N, Y = Cl
29c (ZBR3), X = CH, Y = H

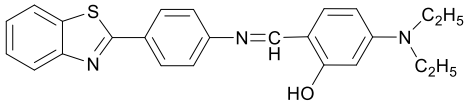

30

Figure 1.19 The structures of ER localised fluorescent probes **29** and **30**.

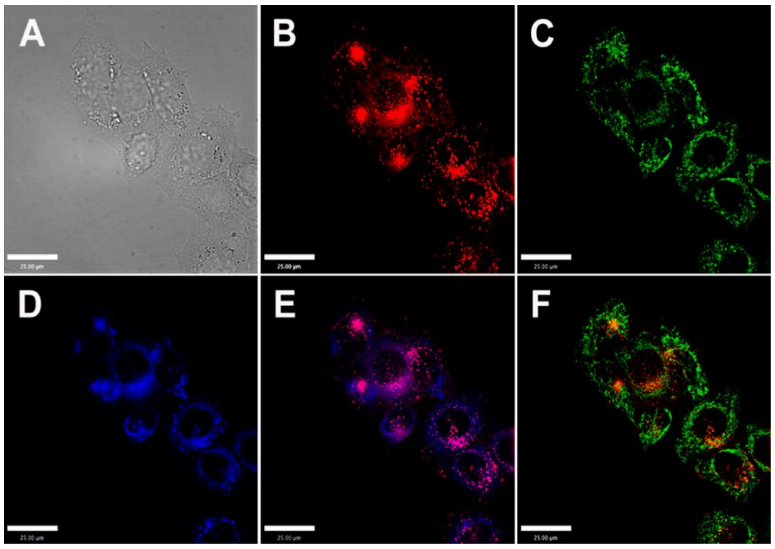

Figure 1.20 Co-localisation analysis of **29a** (ZBR1) with organelle-specific markers in HeLa cells (A) Bright-field image; (B) **29a** (5 µM); (C) Mito-Tracker Green (0.2 µM); (D) ER-Tracker (1 µM); (E) Overlay of **29a** and ER-Tracker; (F) Overlay of **29a** and Mito-Tracker Green. Scale bar = 25 µm. Adapted from ref. 60

1.4.5 Golgi apparatus targeting

1.4.5.1 The Golgi apparatus and the role of Zn^{2+} in its function

The Golgi apparatus works as a central station in cells, receiving secretory cargoes exported from the ER packing proteins into membrane-bound vesicles and sending them to their intra- and extra-cellular destinations. Zn^{2+} is integral to these processes for a variety of proteins, functioning in catalytic, regulatory, and structural roles. For example, it was found that zinc takes part in the interaction between the two main Golgi proteins GRASP55 and Golgin45, maintaining the normal morphology of the Golgi apparatus;[66] Zn^{2+} also coordinates with insulin monomers in the trans-Golgi network to package it into secretory granules, which are then released from pancreatic β-cells.[67] To regulate Zn^{2+} homeostasis in the Golgi apparatus, transporters ZNT4-7 and ZIP7, ZIP9, ZIP11, ZIP13 were responsible for Zn^{2+} import and export, respectively. The breakdown of Zn^{2+} homeostasis in the Golgi apparatus is likely to be associated with a range of human disorders, such as cancer and neuronal, liver, kidney and eye diseases[68] and the development of effective methods for its detection and monitoring are required.

1.4.5.2 Golgi apparatus localised Zn^{2+} probe

The first probe to localise in the Golgi apparatus was reported in 2000 by Lippard and Tsien *et al.,*[69] With fluorescein as the signalling unit, probe **31** (Zinpyr-1, Figure 1.21) has a large extinction coefficient, high quantum yield, and good membrane permeability. Experiments in Cos-7 cells showed it colocalised well with a galactosyl transferase-enhanced cyan fluorescent protein fusion (GT-ECFP), confirming **31** stains the Golgi apparatus. Some years later, Lippard *et al.,* presented two cell-trappable fluorescent Zn^{2+} probes: a carboxylic ester probe **32a** (QZ2E) and its carboxylic acid analogue **32b** (QZ2A).[70] The probes were poorly emissive but had a significant increase in emission after binding with Zn^{2+} (120-fold for **32a**, 30-fold for

32b). Interestingly, the authors found the **32b** was cell membrane-impermeable due to its carboxylic acid moieties, but **32a** was membrane permeable and mainly localised to the Golgi apparatus; after 18 hours' incubation time, the ester was hydrolysed to produce **32b**, which was trapped inside cells.

Guo *et al.,* modified the 8-sulfonamidoquinoline based commercial probe Zinquin to produce a new fluorescent probe **33** (BPSQ) to image Zn^{2+} with a 1:1 binding stoichiometry, which was better at discriminating mobile Zn^{2+}.[71] Colocalisation experiments showed it to accumulate preferentially in the Golgi apparatus.

Following the previous experience on mitochondria targeting Zn^{2+} probes,[35,36] Kim *et al.,* reported a Golgi-localised two-photon probe **35** (SZnC), which had a strong two-photon excited fluorescence enhancement in response to Zn^{2+} for real-time monitoring of Golgi Zn^{2+} changes (Figure 1.22).[72] According to theoretical predictions for Golgi apparatus staining, the lipophilicity value (log*P* value) should be within the range of 3-5.[73] The log*P* values were calculated through measuring the probe's partitioning ratio between *n*-octanol and buffer, and the value of **35** was found to be 2.9 ± 0.1, which is reasonably matched to the theoretical range whereas it was determined to be 2.5 ± 0.1 for the control compound **34** (SZn), which experiment proved to be non-Golgi targeting. However, the log*P* values of another control probe **36** was 3.1 ± 0.1 and this was spread over the entire cell except the nucleus. The authors attributed the Golgi localisation of **35** to the weakly basic pyridyl group, which **36** does not possess. Therefore, both the lipophilicity and pyridyl moiety of **35** appear to contribute to its accumulation in the Golgi apparatus and the probe was applied for imaging Zn^{2+} in rat hippocampal tissue and could be observed at a depth of more than 100 μm with two-photon microscopy.

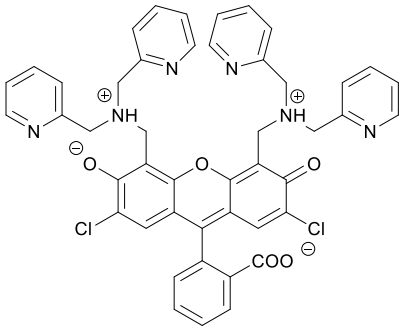

31 (Zinpyr-1)

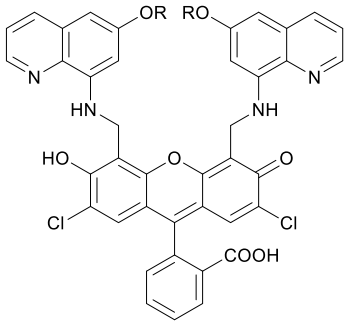

32a (QZ2E), R = CH_2CO_2Et
32b (QZ2A), R = CH_2COOH

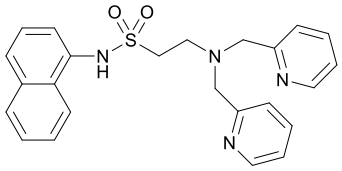

33 (BPSQ)

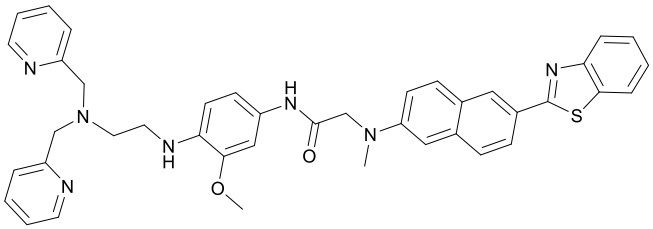

34 (SZn)

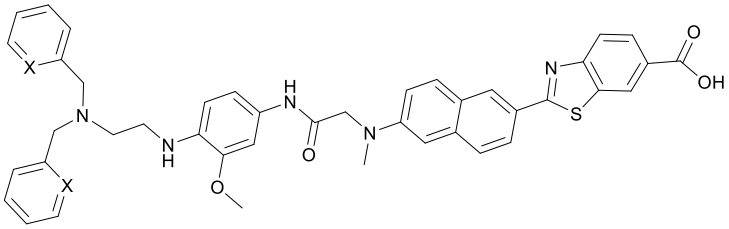

35 (SZnC), X = N
36 X = CH

Figure 1.21 The structures of Golgi apparatus localised fluorescent probes **31**-**36**.

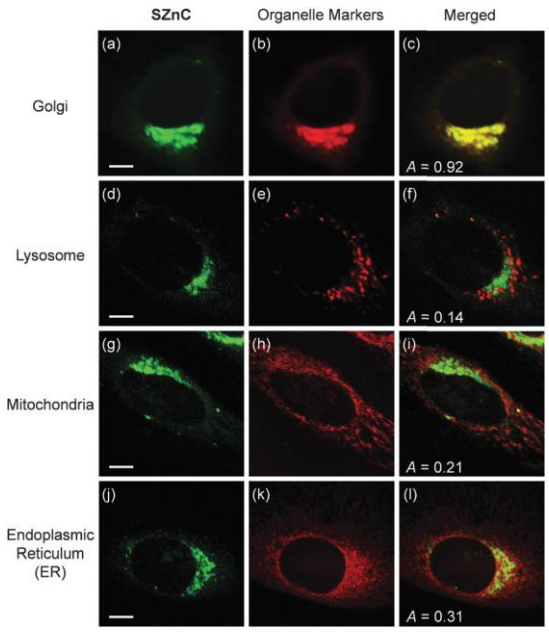

Figure 1.22 The colocalisation of probe **35** (SZnC) (2 µM) and organelle markers (BODIPY TR ceramide and lysosome, mitochondria, ER marker red) in HeLa cells. Adapted from ref. 72

It appears that all of the probes described above were found to reside in the Golgi apparatus adventitiously, therefore a Golgi targeting unit is still required in order to develop reliable Golgi apparatus localised Zn^{2+} probes. Ceramide may be an option for Golgi apparatus targeting since it has been employed in commercial stains for the Golgi apparatus such as NBD-ceramide and Bodipy-ceramide. However, it requires multi-step synthesis (see Appendix 8.1) and also co-localises to the plasma membrane, which limits its application somewhat. More recently cysteine has been reported as a Golgi apparatus targeting unit,[74,75] since galactosyltransferase and protein kinase D were found to anchor to the Golgi region via their cysteine residues or cysteine rich domains[76,77] and this may find utility.

1.4.6 Nucleus targeting

1.4.6.1 The nucleus and the role of Zn^{2+} in its function

The nucleus, as the control centre of the cell, maintains the integrity of genes and controls the activities of the cell by regulating gene expression. In eukaryotic cells, there is a double membrane which encloses the organelle from the cytoplasm. This nuclear membrane is impermeable to large molecules, and the nuclear pores are the channels for large molecules which must be actively transported by carrier proteins, while also allowing free movement of small molecules and ions. Among these, ZNT9 and ZIP7 were found to be responsible for zinc influx and efflux.[78] About 30-40% of total intracellular zinc is found in the nucleus, which plays an important role in the regulation of cell proliferation. It stabilises the structures of DNA, RNA, and is involved in DNA and protein synthesis.[79] Nuclear hormone receptors use zinc finger domains to bind DNA, and zinc deficiency impairs this behaviour, which also has effects on metabolic processes related to growth.[79] Some zinc-dependent proteins have been found in the nucleus functioning as transporters.[80] It is therefore necessary to image Zn^{2+} in the nucleus to better understand zinc influx and distribution and its related biological processes.

1.4.6.2 Nucleus localised Zn^{2+} probe

Nucleus localised Zn^{2+} probes have been realised by genetically encoded sensors[81] or small molecule fusion protein tags,[82] however there are no small molecule Zn^{2+} probes showing specific nucleus targeting, though the commercial probes Newport Green[83] and Zinquin[84] have been reported to display entire cell distribution, including the nucleus. A fluorescent probe based on naphthalimide, **37** (Naph-BPEA), reported by Guo *et al.,*[85] displayed a 4-fold fluorescence enhancement and blue shift of the ICT absorption band on Zn^{2+} binding. The intracellular distribution of the probe was studied in HeLa and HepG2 cells and when the cells were stained with **37**, only cytosolic fluorescence was observed. However, when exogenous Zn^{2+} was added, the entire cell became fluorescent, including the nucleus, which was confirmed with the Hoechst stain, a commercial DNA dye (Figure 1.23). It demonstrated the ability of the probe to penetrate the nuclear envelope, but the nuclear fluorescence response was small due to the low nuclear concentration of mobile or free Zn^{2+}. The authors speculated that incorporation of the 4-amino-1,8-naphthalimide moiety to be the reason for its nuclear envelope penetrability through positive and negative control experiments. Furthermore, the *in vivo* Zn^{2+} imaging in zebrafish larva was also performed.

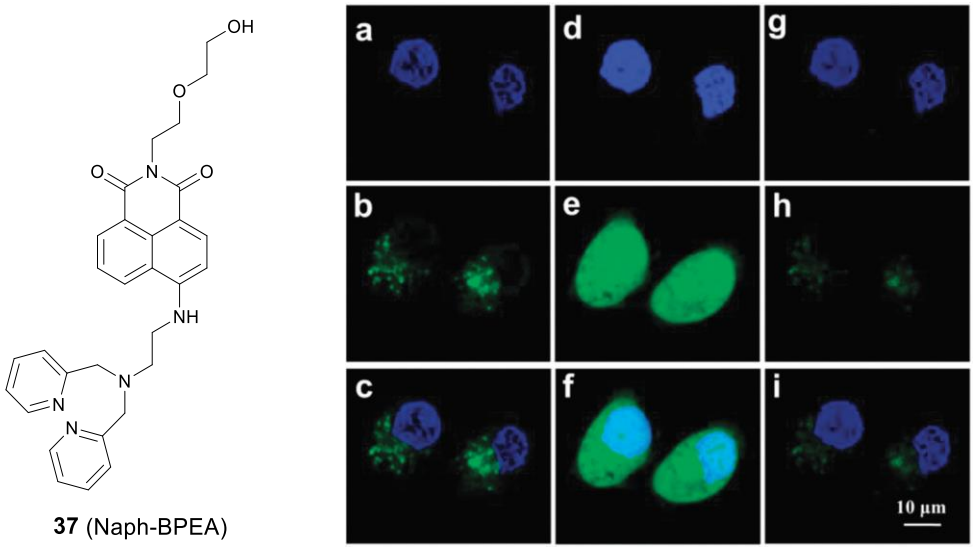

37 (Naph-BPEA)

Figure 1.23 The structure of **37** (Naph-BPEA) and confocal fluorescence images of HeLa cells co-stained with Hoechst 33 342 (5 µg/mL, blue) and **37** (5 µM, green). (a-c): images of the co-stained cells; (d-f): images of the co-stained cells followed by Zn^{2+}-pyrithione incubation; (g-i): images of cells which were subsequently treated by TPEN. Adapted from ref. 85

1.5 Overall aims of the project

In light of these findings, this project aims to develop a series of cellular or subcellular localised fluorescent Zn^{2+} probes. Based on the previous development of Zn^{2+} probes in the Watkinson group,[25] the main aim was to overcome the difficulties of the control of small molecule fluorescent probes' localisation *in cellulo* by introducing specific cell or specific organelle targeting units through the reported 'click-S_NAr-click' strategy, which utilises the copper(I)-catalysed azide-alkyne cycloaddition (CuAAC) reaction. In particular at the subcellular level, a reliable strategy to develop ER and Golgi apparatus targeting Zn^{2+} probes is required to study the Zn^{2+}-associated biological processes in these subcellular regions.

Chapter 2 A biotin-tagged fluorescent probe to visualise mobile Zn^{2+} in cancer cells

2.1 Introduction

Cancer causes millions of deaths every year and is a major burden of disease around the world. There is evidence that zinc is important in cancer development.[86] This is perhaps unsurprising as zinc is necessary for the human superoxide dismutase enzyme system to function, and cancer cells are highly dependent on superoxide dismutase for protecting themselves from the damage induced by reactive oxygen species, since the superoxide anion radical, O_2^-, is actively produced in cancer cells.[87] Zinc is also a growth factor in cell proliferation,[88] which is attenuated in the absence of zinc.[89] However, it is found that the alterations of mobile zinc concentration in malignant cells are tissue specific. For example, zinc concentration increases by about 72% in breast cancer tissue,[90] while it decreases by 75% in malignant prostate tissue[91] compared to their non-cancerous counterparts. These differences have been explained by changes in the expression of zinc transporters, which directly influence the Zn^{2+} cellular influx and efflux. In prostate cancer, the low Zn^{2+} concentration is due to the downregulation of the zinc transporter ZIP1,[91] whilst ZIP6,[92] ZIP7[93] and ZIP10[94] have been proposed to be important in the elevated levels in breast cancer. Though there is an increasing understanding of these processes, it is still unclear whether these changes are a cause or an effect of tumour growth. Furthermore, it is not clear whether zinc itself or zinc transporters are associated with cancer-related events.[86] However, the difficulty of imaging *in vivo* represents a significant barrier to understanding its role in cancer. Therefore, the development of an effective way to detect mobile zinc specifically in tumour cells would allow us to achieve a better understanding of its role in the mechanism of cancer initiation, progression, and potentially, its prevention.

Biotin is a vitamin that is essential to cancer cells, and the sodium-dependent multivitamin transporter (SMVT) is overexpressed in many cancers, including breast, lung, ovarian, mastocytoma and renal,[95,96] meaning that cancer cells take up more biotin than normal cells. Based on this, some biotin tagged cancer drugs have been developed and have shown good targeting ability.[97–100] Therefore by incorporating a biotin tag into a zinc probe, using the previously reported methodology,[25] a small molecule probe that could detect zinc specifically was targeted, and the results are discussed in this chapter.

2.2 Probe design and synthesis

The cyclam ligand has previously been shown to be an effective receptor unit for mobile zinc,[101,102] and was therefore chosen in this study. The synthetic route to the target probe, **47**, is shown in Schemes 2.1 and 2.2. Biotin azide, **43**, was prepared from D-(+)-biotin by adapting literature procedures.[103,104] The fluorophore and ligand were introduced via alkynes **38** and **40**, which were synthesized using the procedure reported previously.[25,101,102] After double click reactions, the Boc-protected **46** was isolated in moderate yield and was de-protected under standard conditions[25] to give probe **47**.

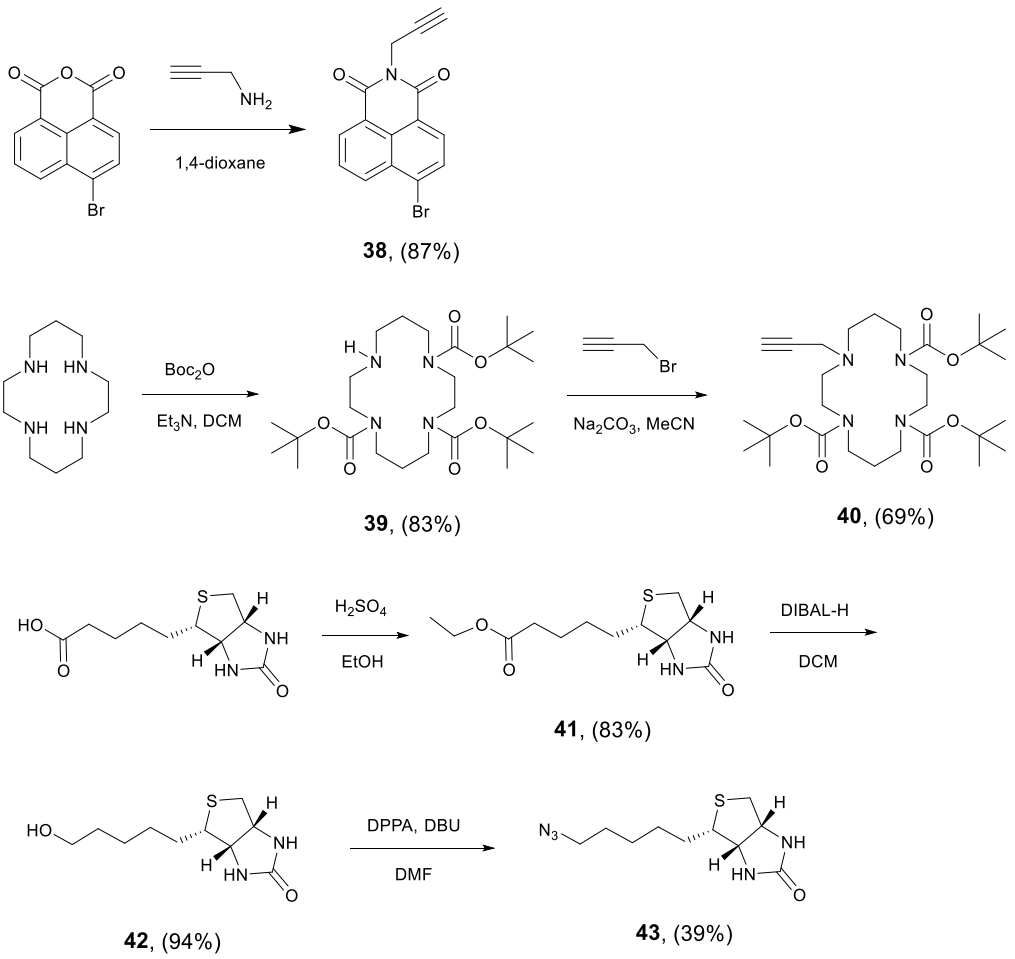

Scheme 2.1 The synthetic routes to precursors **38**, **40** and **43**.

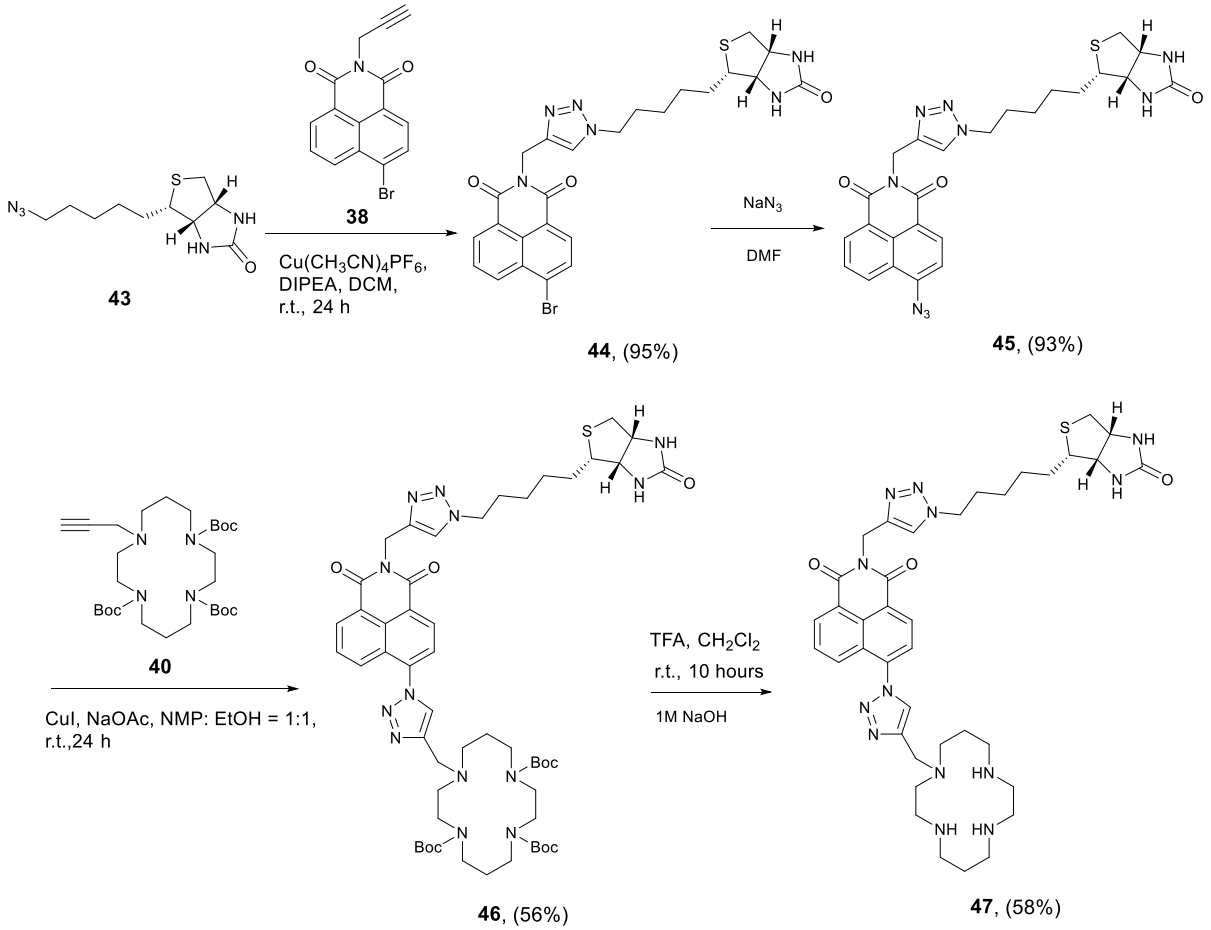

Scheme 2.2 The synthetic route to probe **47**.

2.3 Photophysical properties

The absorption spectra of probe **47** and its complex with different equivalents Zn^{2+} is shown in Figure 2.1, which shows there is no blue shift or red shift after binding with Zn^{2+}. The fluorescence of **47** is switched on by adding Zn^{2+} as shown in Figure 2.2, upon addition of Zn^{2+}, the fluorescence intensity increased gradually with an approximately 5-fold maximum increase. The Job's plot clearly showed the expected 1:1 Zn^{2+}:**47** binding stoichiometry (see Figure 2.3).

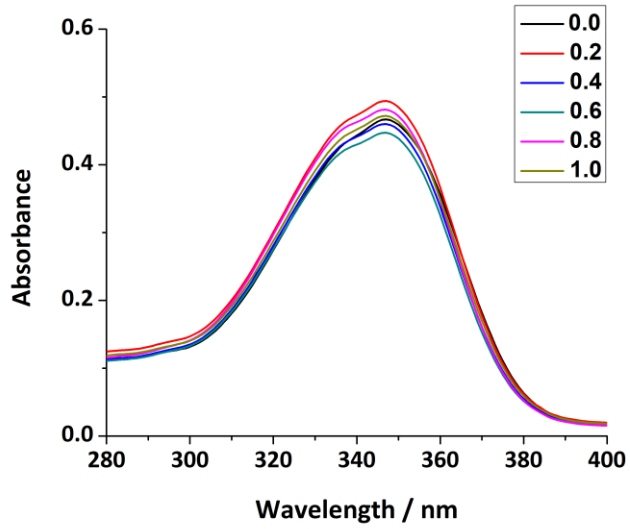

Figure 2.1 The UV-Vis spectra of probe **47** (50 µM) with different equivalents of Zn^{2+} in 0.1 mM HEPES buffer at pH 7.4.

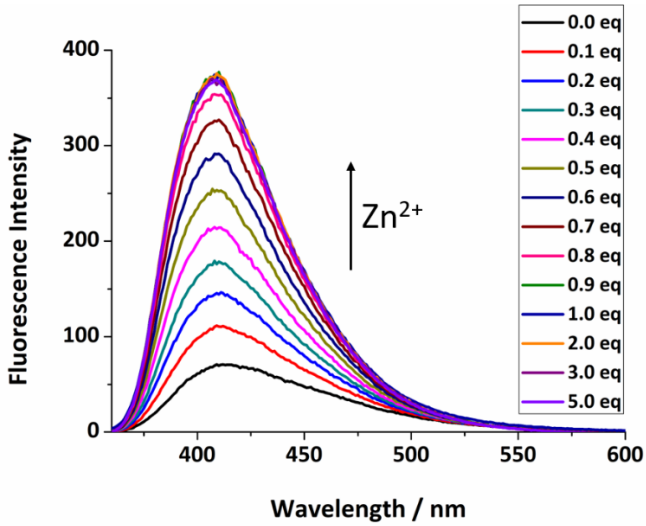

Figure 2.2 The fluorescence switch-on response of probe **47** (50 µM) to different equivalents Zn^{2+} in 0.1 mM HEPES buffer at pH 7.4. (λ_{ex} = 346 nm, slit widths: 5/5 nm)

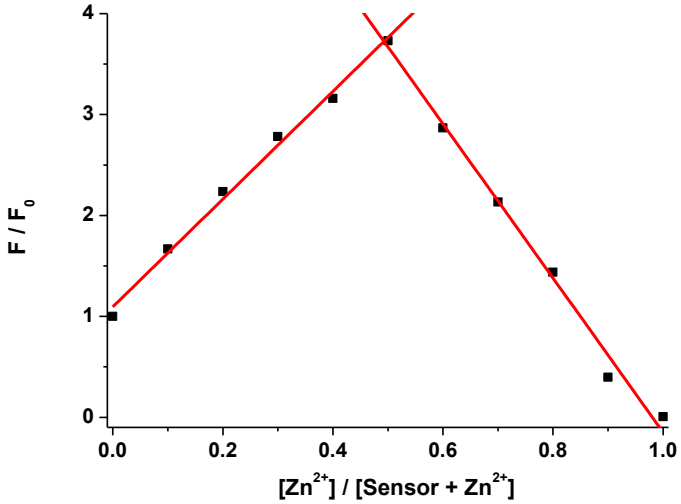

Figure 2.3 The Job's plot to determine the stoichiometry of the complex formed between probe **47** and Zn^{2+}.

As the binding stoichiometry is 1:1, the dissociation constant with Zn^{2+} was then measured through non-linear curve fitting (Figure 2.4) using Equation 2.1, in which the values *CM* and *CL* are the concentrations of Zn^{2+} and probe respectively, *F* is the observed fluorescence intensity, *F(0)* is the observed fluorescence of the probe alone (i.e. *CM* = 0) in absence of chelating agent, and *F(max)* is the observed fluorescence of the probe in presence of excess Zn^{2+} (5 equivalents). The K_d was determined to be 1.88×10^{-8} M. The quantum yield of **47** was determined by Equation 7.2, and was found to be 0.02, while this increased to 0.05 after binding to 1 equivalent of Zn^{2+} (Figure 2.5). Although this is rather modest, it is in line with previous measurements,[101,102] and it has shown such probes to be tractable in biological milieu.

$$\frac{F}{F(0)} = 1 + \left(\frac{F(\max)}{2F(0)} - 0.5\right) \times \left\{1 + \frac{CM}{CL} + \frac{Kd}{CL} - \left[\left(1 + \frac{CM}{CL} + \frac{Kd}{CL}\right)^2 - \frac{4CM}{CL}\right]^{0.5}\right\} \quad \text{(Equation 2.1)}$$

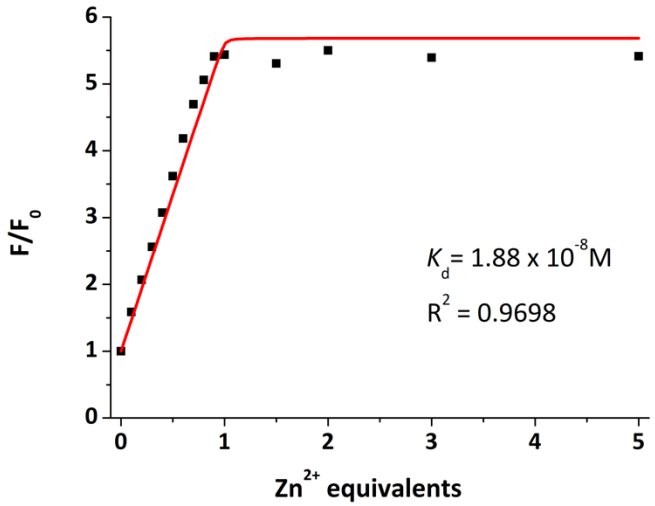

Figure 2.4 The non-linear curve fitting of the fluorescence intensity of **47** against different equivalents Zn^{2+}.

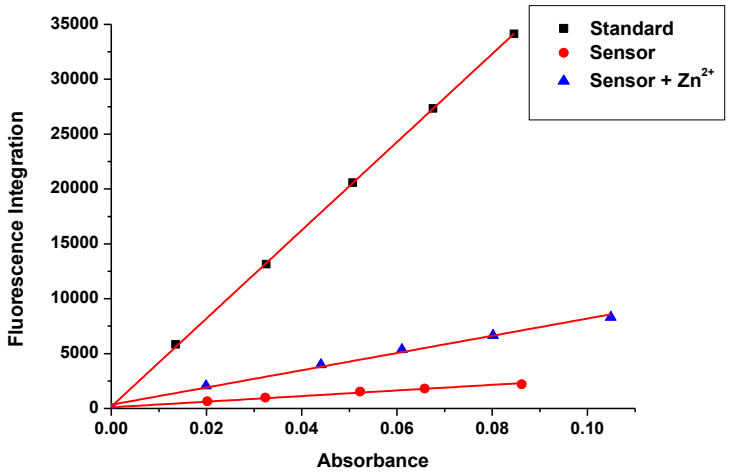

Figure 2.5 Linear plots for standard sample, **47**, and **47** + Zn^{2+} to obtain quantum yields. Anthracene (Φ = 0.27 in ethanol) was used as standard sample. (λ_{ex} = 346 nm, λ_{em} = 414 nm, slit widths: 5/5 nm).

The pH-dependent fluorescence response was measured, as it is known that although cancer cells maintain their pH near to neutrality, the cytoplasm is more alkaline than that of normal cells while the environment outside cancer cells is more acidic.[105] As shown in Figure 2.6, probe **47** showed a good switch-on response to 1 equivalent Zn^{2+} in the range of pH 5.5-10.5, indicating that it should be able to detect Zn^{2+} in most cancer cells. The apparent pK_a of **47**

was measured by integrating the fluorescence intensity of emission spectra against pH (Figure 2.7). Through non-linear curve fitting (Equation 7.5), the four apparent pK_as of **47** are: pK_{a1} = 1.64 ± 0.14, pK_{a2} = 4.18 ± 0.23, pK_{a3} = 9.24 ± 0.31, pK_{a4} = 11.18 ± 0.18.

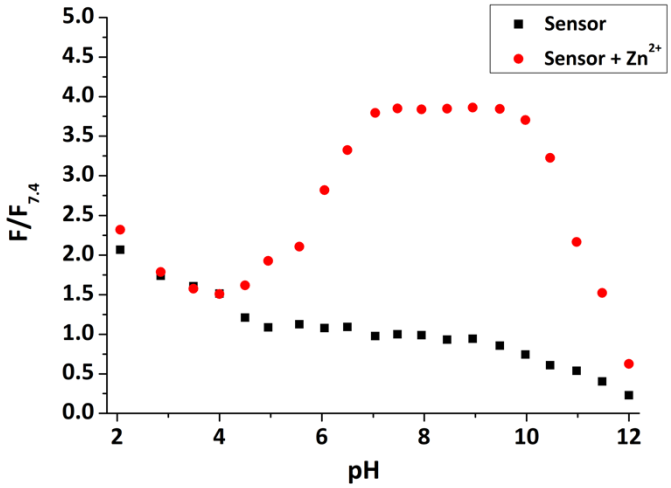

Figure 2.6 The pH profile of **47** (50 μM) and **47** with 1 equivalent Zn^{2+} in HEPES buffer (0.1 mM).

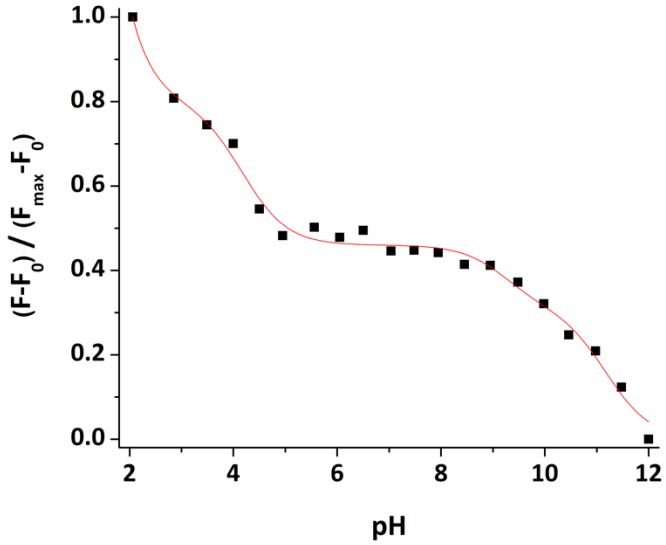

Figure 2.7 Normalized integrated fluorescence emission *vs* pH, the nonlinear curve fitting used to determine the apparent pK_a values of **47**.

The selectivity of probe **47** to Zn^{2+} over other competing metal ions was also investigated. As shown in Figure 2.8, besides Zn^{2+}, the fluorescence is not switched on after the addition of

other metal ions, with the exception of Cd^{2+}, which shows a similar response and is in line with previous findings.[101,102] However, as its concentration in tissues is negligible, this is not an issue for cellular imaging. Whilst Fe^{3+}, Co^{2+} and Cu^{2+} induce significant quenching[106] of the fluorescence of **47**, they almost exclusively exist in bound forms in biology, rather than as the free cations tested here. The cations Na^{+}, K^{+}, Ca^{2+}, and Mg^{2+}, which are the main metal ions in cells, showed no effect on the fluorescence intensity of **47**, meaning that it should have good selectivity for Zn^{2+} and can potentially be applied *in cellulo*. The water-solubility of **47** is also an attractive feature for cell imaging as it does not require the addition of co-organic solvents to solubilise the probe.

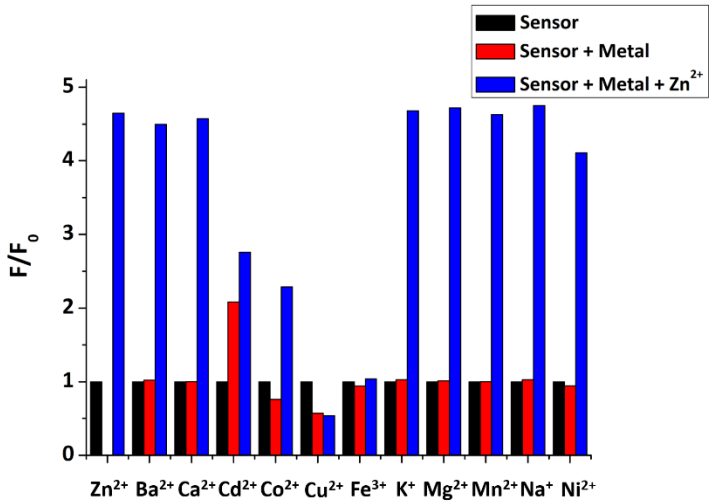

Figure 2.8 Metal ion selectivity of **47** in 0.1 mM HEPES buffer at pH 7.4. Average normalized fluorescence intensities for **47** (50 µM) (black bars), after addition of 5 equivalents of various metal ions (red bars), followed by addition of 1 equivalent $ZnCl_2$ (blue bars).

2.4 DFT calculations

DFT and TDDFT calculations were undertaken to understand the binding behaviour of **47** with Zn^{2+} and their excited states. The optimised structure of probe **47** with 1 equivalent of Zn^{2+} (Figure 2.9) shows the bottom triazole nitrogen is involved in binding with Zn^{2+} in addition to

the cyclam nitrogen donors, which is consistent with previous observations in closely related analogues.[101,107]

The calculated vertical excitations are in good agreement with the experimental values. The deviations from the experimental values are due to the lack of explicit consideration of vibrational effects and the solvent molecules in calculations. In line with the experimental measurements, the predicted emission energy for the Zn^{2+} complex is very similar to that obtained for probe **47** (see Table 2.1).

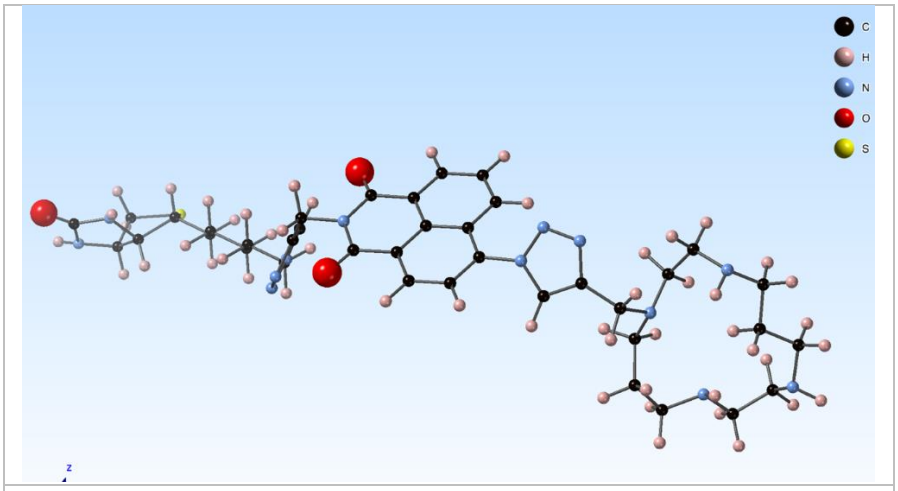

Probe **47**

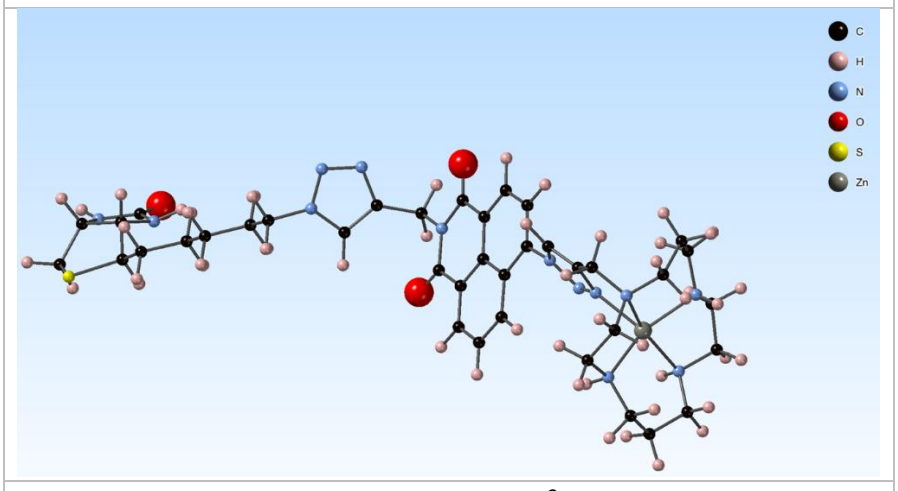

Complex with Zn^{2+}

Figure 2.9 The optimized structures of probe **47** and its complex with Zn^{2+}.

Table 2.1. Comparison of the experimental data with the calculated result of vertical electronic excitation energies (eV) and the emission from S_1 to ground state of **47** and its Zn^{2+} complex.

	Electronic transition	Energy (eV)	Wavelength (nm)	Oscillator strength (f)	Experimental data
Probe **47**					
Absorption	$S_0 \rightarrow S_1$	3.88	320	0.5493	3.58 eV/346 nm
	$S_0 \rightarrow S_2$	4.27	290	0.0438	
	$S_0 \rightarrow S_3$	4.37	284	0.0001	
	$S_0 \rightarrow S_4$	4.39	282	0.0002	
	$S_0 \rightarrow S_5$	4.67	265	0.0004	
	$S_0 \rightarrow S_6$	4.72	262	0.0011	
Emission	$S_1 \rightarrow S_0$	3.18	390	0.7172	3.01 eV/412 nm
Complex of **47** with Zn^{2+}					
Absorption	$S_0 \rightarrow S_1$	3.95	314	0.5023	3.58 eV/346 nm
	$S_0 \rightarrow S_2$	4.26	291	0.0521	
	$S_0 \rightarrow S_3$	4.34	286	0.0003	
	$S_0 \rightarrow S_4$	4.62	268	0.0002	
	$S_0 \rightarrow S_5$	4.94	251	0.0319	
	$S_0 \rightarrow S_6$	5.29	234	0.0055	
Emission	$S_1 \rightarrow S_0$	3.22	385	0.6672	3.01 eV/412 nm

The S_1-S_0 electron density plots (Figure 2.10) show that the electron transition is localised on naphthalimide moiety and the vicinal triazole for both **47** and its complex with Zn^{2+}. These calculations show that cyclam does not contribute to the process. The formation of the complex has a minor impact on the electronic densities. There is a slight decrease of the electron density on the nitrogen from the triazole involved in the complex formation, and the oscillator strength is not significantly affected. Consequently, this does not justify the enhancement of emission observed experimentally. Based on these results, the mechanism of fluorescence enhancement seems to be consistent with the restriction of the intramolecular rotations after complexation with Zn^{2+}. When bound with Zn^{2+}, the stabilisation of the complex hampers large amplitude vibrations in the vicinity of the

fluorophore, reducing the possibility of relaxation through non-radiative pathways and increasing the quantum yield of emission. The still small quantum yield can be associated with other nonradiative mechanisms that are not affected by complexation with Zn^{2+} including intramolecular rotations and energy transfer involving the second triazole and biotin.

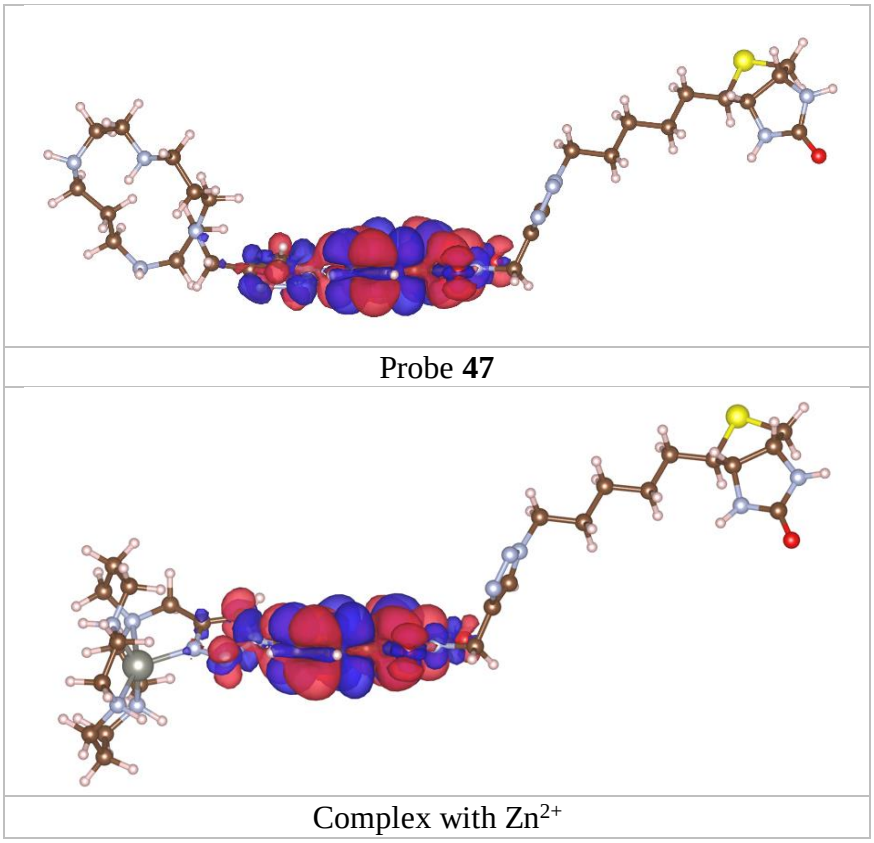

Figure 2.10 S_1-S_0 electron density map for probe **47** and its complex with Zn^{2+} (S_1 minima). Red represents positive densities and blue negative values.

2.5 *In cellulo* tests

With the promising properties confirmed in solutions, the innate toxicity of **47** was then measured. The MCF-7 breast cancer and N-TERT keratinocyte cell lines were incubated in cell medium solution containing different concentrations of **47** for 24 hours. Then the solution was washed away, and AlamarBlue was added as an indicator of cell viability.[108] From these experiments (Table 2.2), it can be concluded that the probe has no toxicity to either cell type since the viability of cells does not decrease as the concentration of **47** increases.

Fluorescence microscopy was used to detect mobile Zn^{2+} in MCF-7 and N-TERT keratinocytes cells and the results are shown in Figure 2.11. For MCF-7 breast cancer cells, when there was no probe, the fluorescence of the cells was very weak, resulting from their background autofluorescence. After incubation with a 100 μM solution of **47** for 2 hours, the fluorescence increased considerably, and the Zn^{2+} in cytoplasm can be visualised clearly, but there was no response from the nucleus. On the addition of zinc pyrithione, a membrane permeable zinc source,[109] the fluorescence response of the cells became stronger, and a fluorescence response was observed from the whole cell, including the nucleus. Therefore, it is assumed that this probe is also permeable to the nucleus, but that the concentration of nuclear mobile zinc in MCF-7 cells is very low. When TPEN, a well-known zinc chelator,[110] was added to remove Zn^{2+} inside cells, the fluorescence of the cells decreased markedly as expected. Pleasingly, as hypothesized, for the normal control N-TERT keratinocytes cells, no strong fluorescence response was observed even after the addition of zinc pyrithione, supporting the selective localisation of **47** in the cancer cells.

Table 2.2 The fluorescence reading of AlamarBlue indicating cell viability.

	MCF-7						N-TERT					
Concentration (μM)	0	10	30	50	70	100	0	10	30	50	70	100
Fluorescence reading	5255	5037	5050	5335	5454	5239	7631	7606	7517	7053	6874	8911
	5207	4920	4990	4922	5519	5133	7753	7324	7233	7349	9130	8404
	5197	4809	4422	5151	5268	5453	8800	6909	7214	7347	7110	8226
	5317	5207	4620	4902	5177	5340	7924	7515	7195	7189	7928	7999
	5558	5490	4861	5262	5001	5493	7017	7583	7896	7567	8536	8227
Average	5260	5055	4824	5112	5230	5344	7769	7474	7321	7295	7858	8286
Cell viability percent	100%	96%	92%	97%	99%	102%	100%	96%	94%	94%	101%	107%

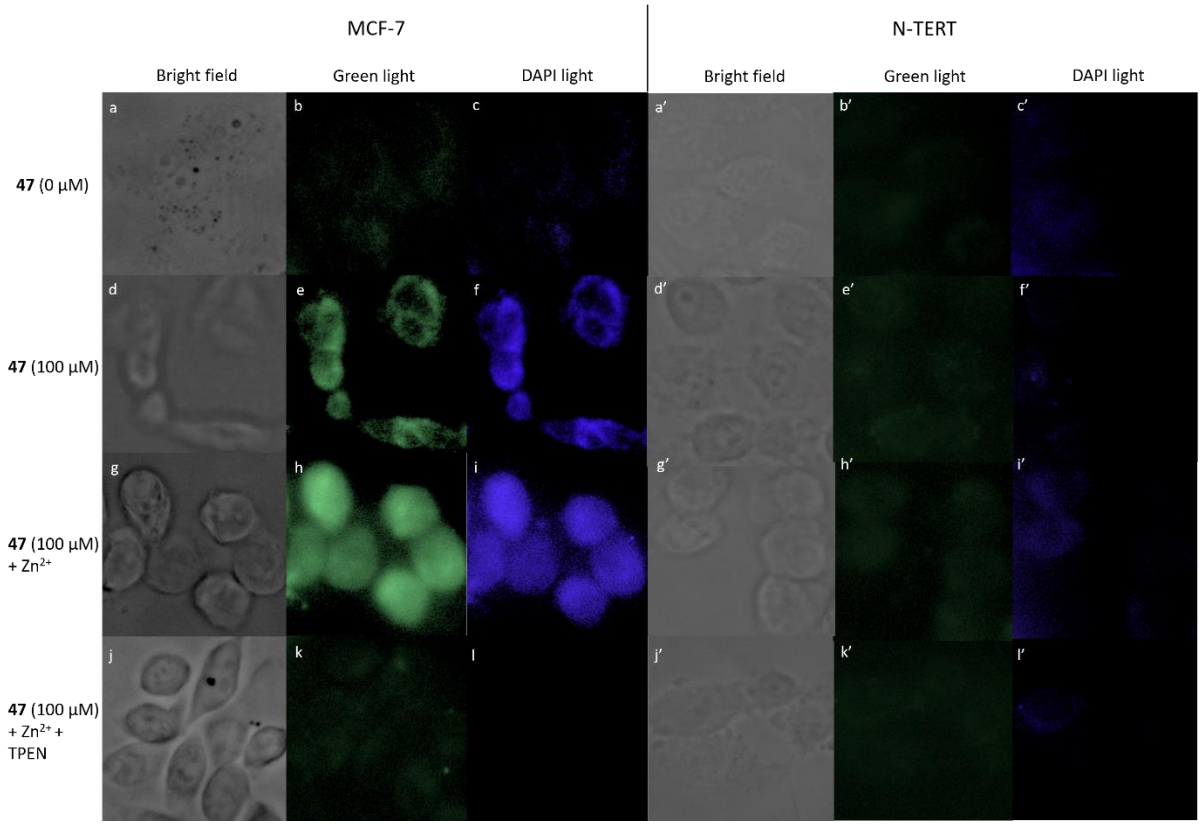

Figure 2.11 Fluorescence microscopy images of MCF-7 cells (a-l) and N-TERT cells (a'-l') treated with no probe (a-c and a'-c'), 100 μM probe **47** (d-f and d'-f'), probe **47** (100 μM) with saturated zinc pyrithione (g-i and g'-i'), and probe **47** (100 μM) after loading the cells with zinc pyrithione, then TPEN (2 μM) was added (j-l and j'-l').

2.6 Summary

In conclusion, the biotin tagged fluorescent probe **47** was developed using a double click reaction. It is water-soluble, and has high selectivity, low toxicity, shows good fluorescence response and a low dissociation constant to Zn^{2+}. Testing in cells confirms it can localise selectively in cancer cells, can image mobile Zn^{2+}, and therefore has the potential to help better understand the role of Zn^{2+} in cancer initiation and progression.

Chapter 3 Endoplasmic reticulum targeting fluorescent probes to image mobile Zn^{2+}

3.1 Probe design and synthesis

As discussed earlier (see Section 1.4.4), glibenclamide could be a good option for endoplasmic reticulum (ER) targeting unit. Glibenclamide, an antidiabetic drug, is employed in the commercial dyes ER tracker red and ER tracker green because it binds and inhibits ATP-sensitive K^+ channels that are abundant on the ER membrane.[111,112] There is also a report of the use of glibenclamide as the targeting group in a small molecule chemical probe which was shown to selectively accumulate in the ER and image glutathione.[113] Therefore a synthetic route was developed towards a 'clickable' variant of glibenclamide **53** which was prepared through six steps in moderate yield (Scheme 3.1). The CuAAC reaction with alkyne **38** proceeded, as expected, in good yield (Scheme 3.2), however, when installing the Zn^{2+} binding unit **54**, the second 'click' reaction to give compound **57** failed completely, despite a range of Cu(I) sources being tested. Given the success of the first 'click' reaction, it was decided to investigate the development of a 'reverse' methodology in which the metal-binding unit was first installed into anhydride **58** before the addition of the targeting unit via a second 'click' process was attempted (see Scheme 3.3). Although the first 'click' reaction again worked well, the second 'click' reaction to incorporate the glibenclamide azide completely failed.

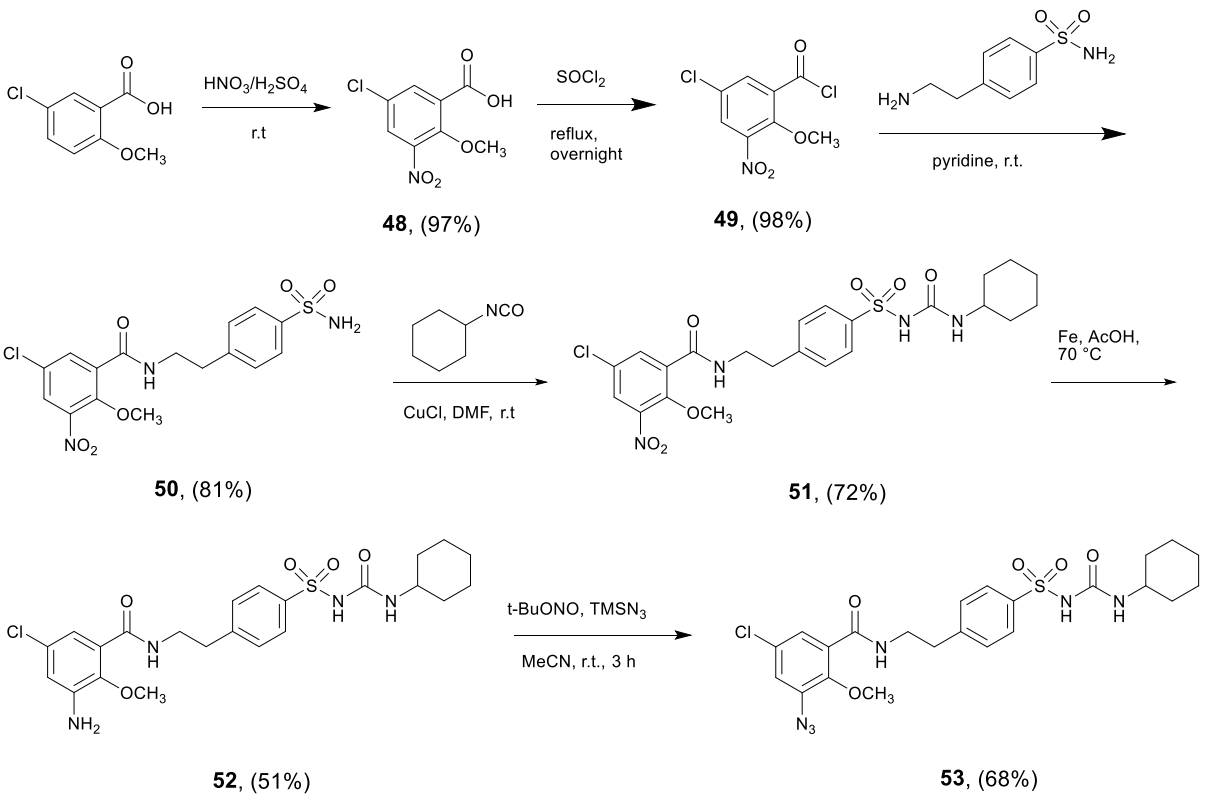

Scheme 3.1 The synthetic route towards glibenclamide azide **53**.

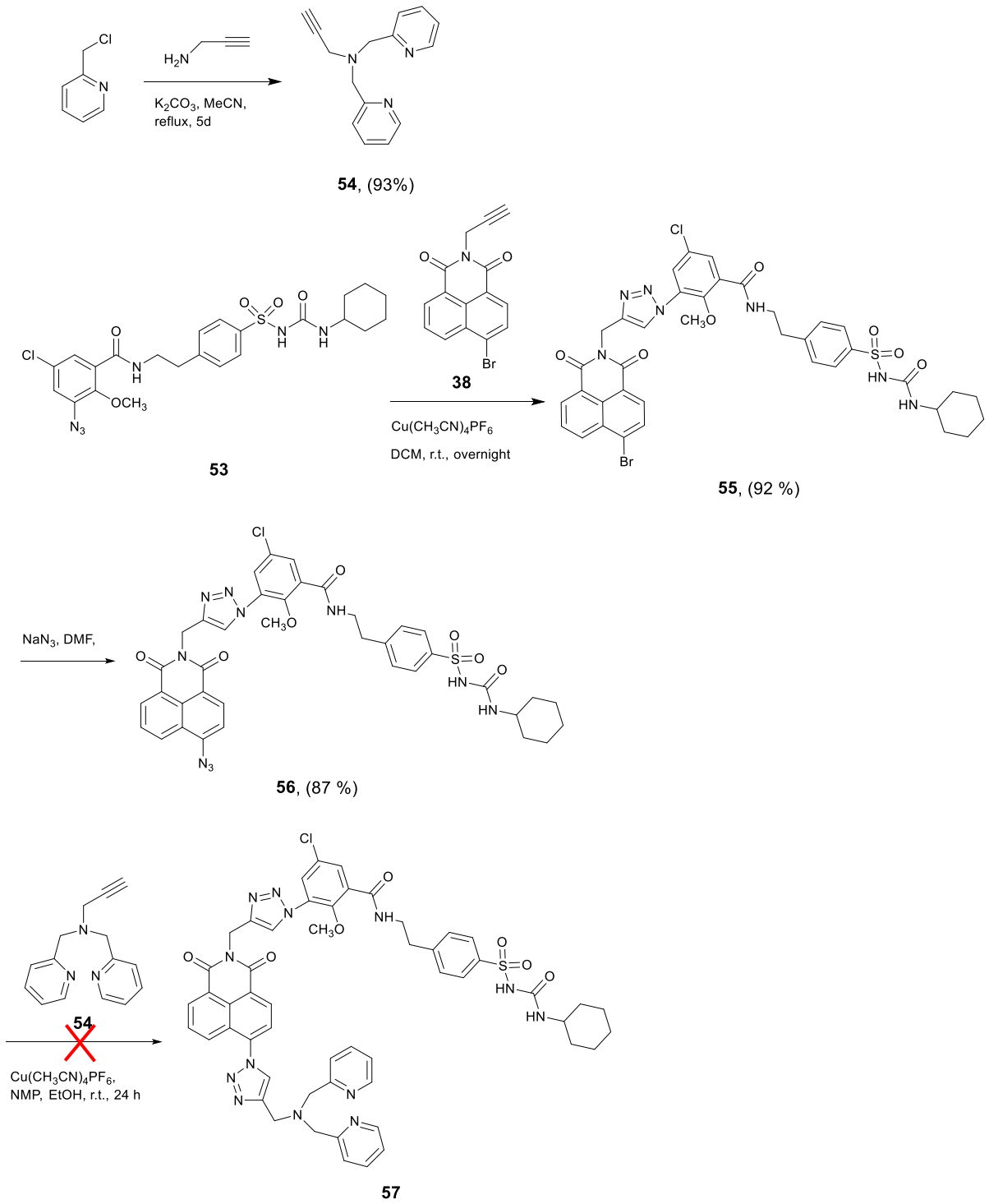

Scheme 3.2 The modular click reaction method for 'top to bottom' click.

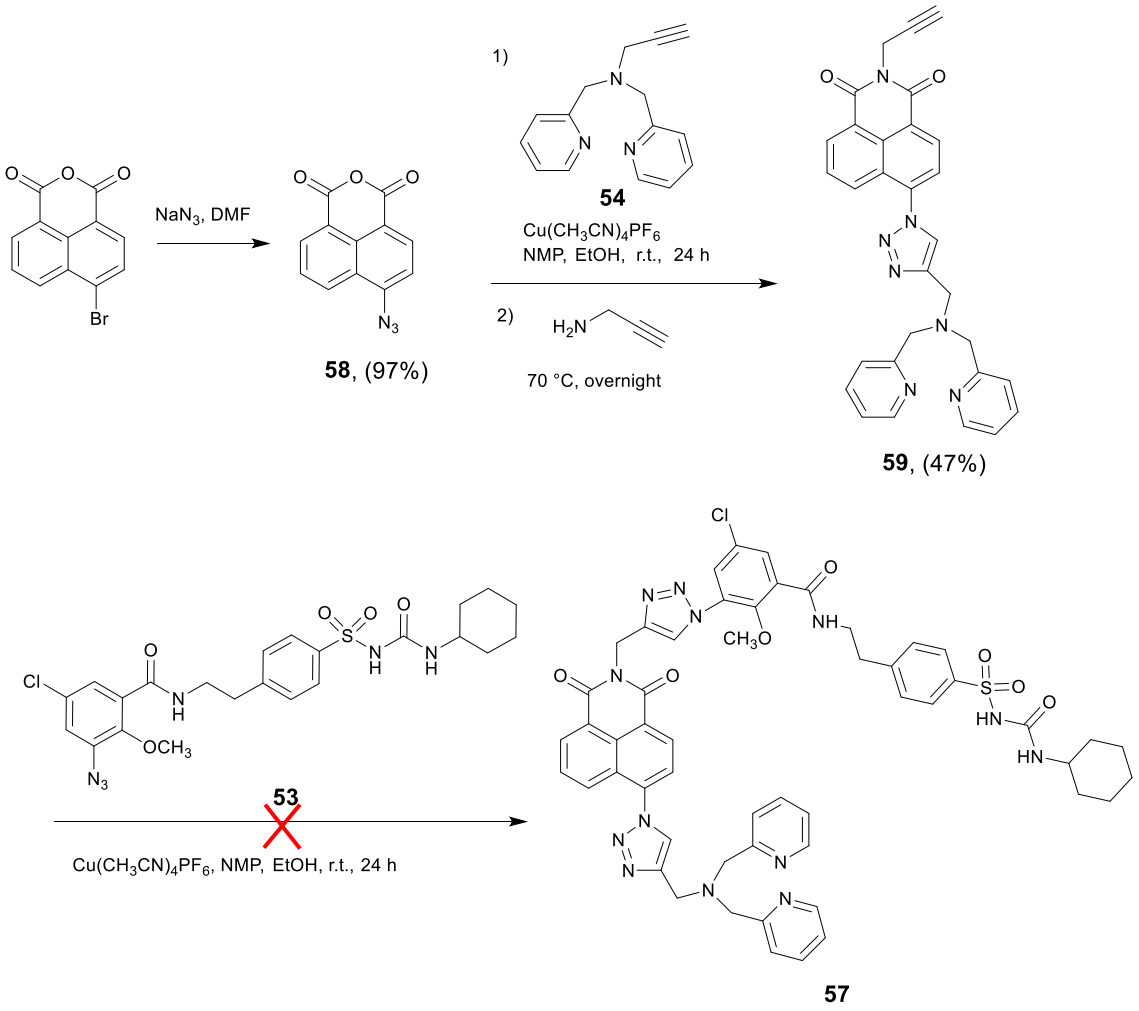

Scheme 3.3 The modular click reaction for 'bottom to top' click.

At this point, it was decided to review the synthetic strategy as a number of recent reports have revealed that the cyclohexyl sulfonylurea moiety of glibenclamide is an important element in binding with ATP-sensitive K^+ channels.[26,114,115] Therefore an alternative route in which this ER targeting unit was directly incorporated into the naphthalimide was designed, which also makes the synthesis route shorter and easier.

The new synthetic route started from 4-(2-aminoethyl)benzenesulfonamide to give ER-targeting group **62** through the route depicted (see Scheme 3.4) and this was directly introduced into the fluorophore through reaction with commercially available 4-bromo-1,8-naphthalic anhydride (Scheme 3.5). This was then conveniently converted to azide **64** using

standard conditions for such S_NAr reactions, which then underwent smooth and high yielding 'click' reactions with alkynes **54** or **40** to yield probes **65** and **67**, the latter after deprotection of **66** with TFA.

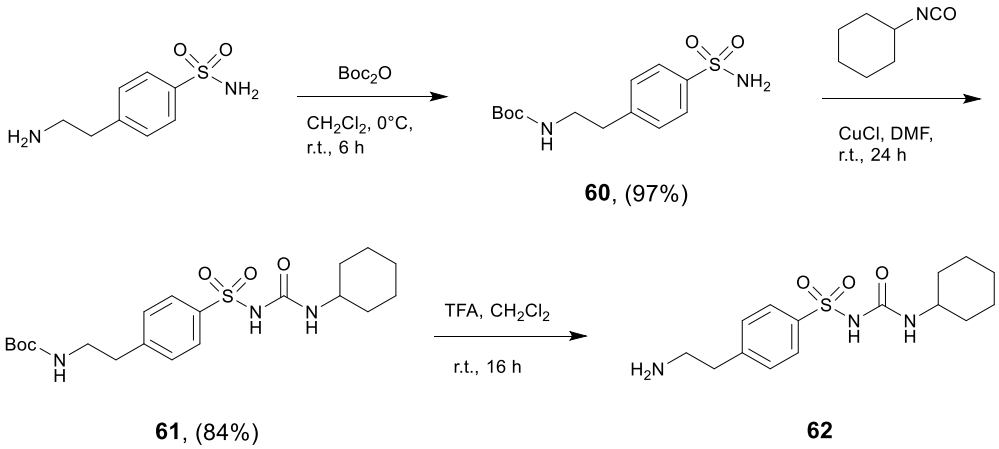

Scheme 3.4 The synthetic route to obtain sulfonylurea unit **62**.

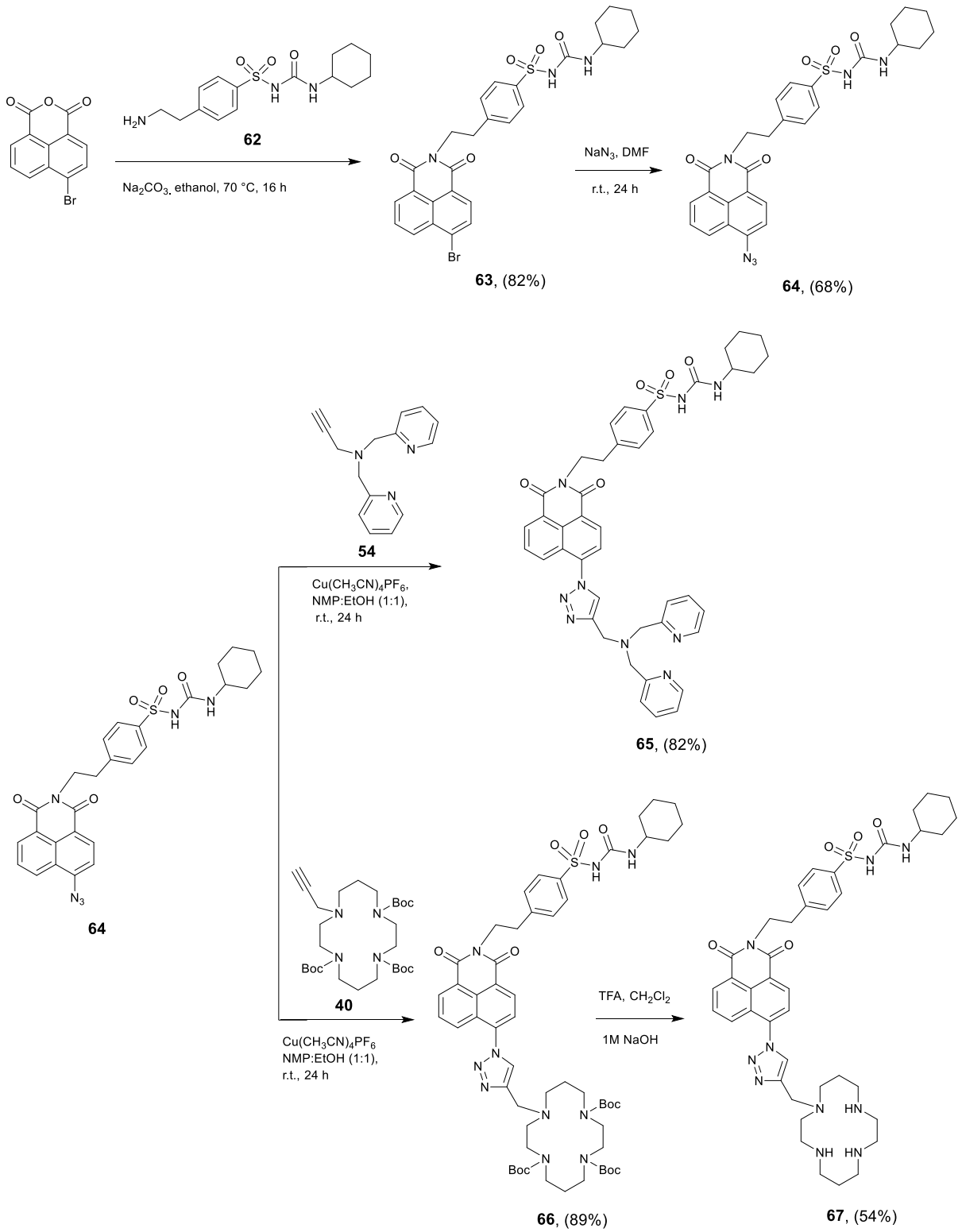

Scheme 3.5 The successful synthetic route to probes **65** and **67** incorporating cyclohexyl sulfonylurea as the ER targeting unit.

Another probe, **70**, with the same ER-targeting unit but a different Zn^{2+} ligand was also prepared as shown in Scheme 3.6. The carboxyl ester should be hydrolysed by esterase

enzymes in cells after which it has been reported to have Zn^{2+} binding ability.[116–118] However, it proved to be cytotoxic (shown in Figure 3.16c) and was not taken forward to *in cellulo* studies. All products were satisfactorily characterised by ^{1}H, ^{13}C NMR and IR spectroscopies as well as high-resolution mass spectrometry.

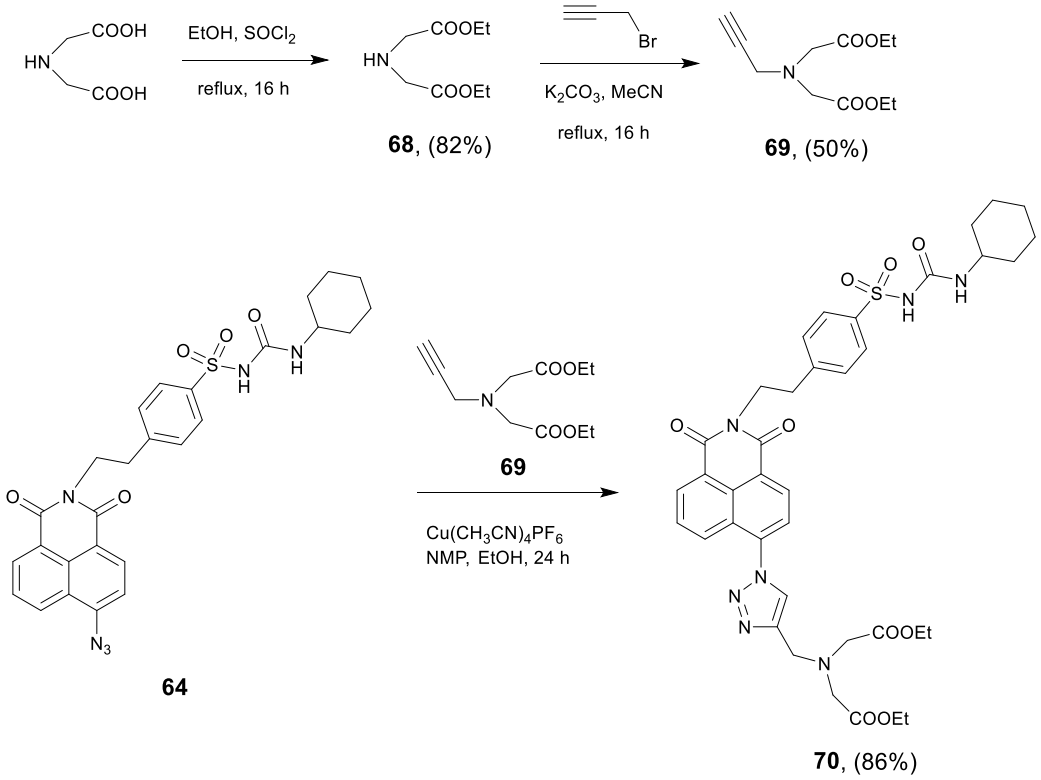

Scheme 3.6 The synthetic route toward **70**.

3.2 Photophysical properties in solution

Fluorescence titrations with Zn^{2+} were first undertaken to show that both probes **65** and **67** have a switch-on response to Zn^{2+}. From Figure 3.2, it can clearly be seen that with increasing Zn^{2+} equivalents, the fluorescence intensity of probes **65** and **67** increased gradually with about 16-fold and 4-fold maximal increase, respectively. Subsequent treatment with TPEN resulted in the expected decrease in fluorescence with that of **65** being completely quenched while that of **67** was partly quenched (Figure 3.3). The Job's plot (Figure 3.4) revealed the expected 1:1 binding stoichiometry with Zn^{2+}.

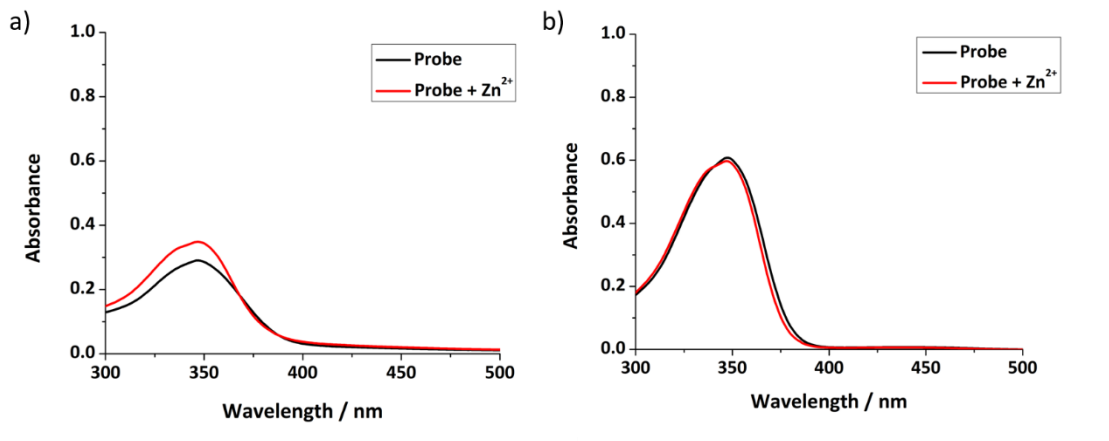

Figure 3.1 The UV-Vis spectra of a) **65** (50 µM) and b) **67** (50 µM), and their complexes with 1 equivalent of Zn^{2+} in 0.1 mM HEPES buffer at pH 7.4.

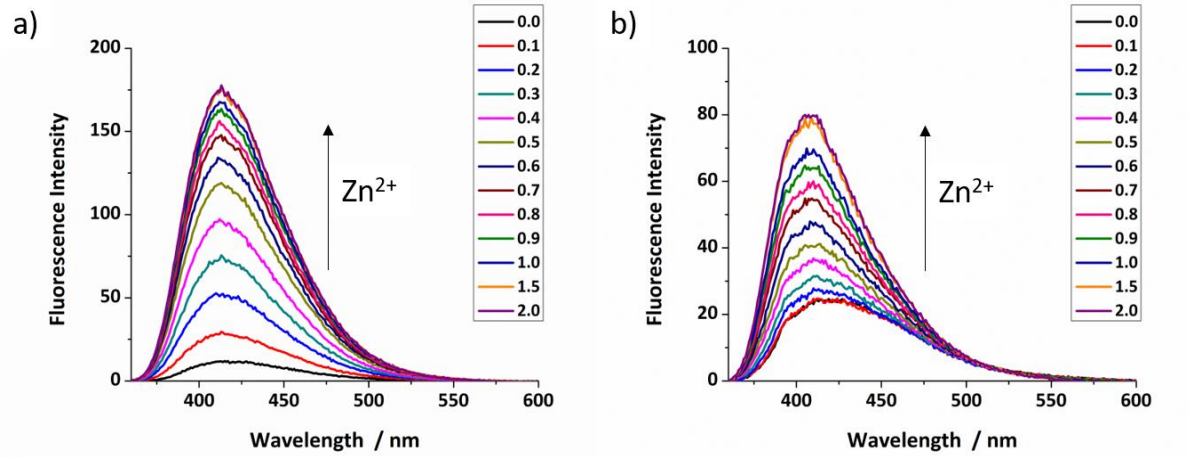

Figure 3.2 The fluorescence response of a) **65** (10 µM) and b) **67** (10 µM) to different equivalents of Zn^{2+} in 0.1 mM HEPES buffer at pH 7.4 (λ_{ex} = 346 nm, slit widths: 5/5 nm).

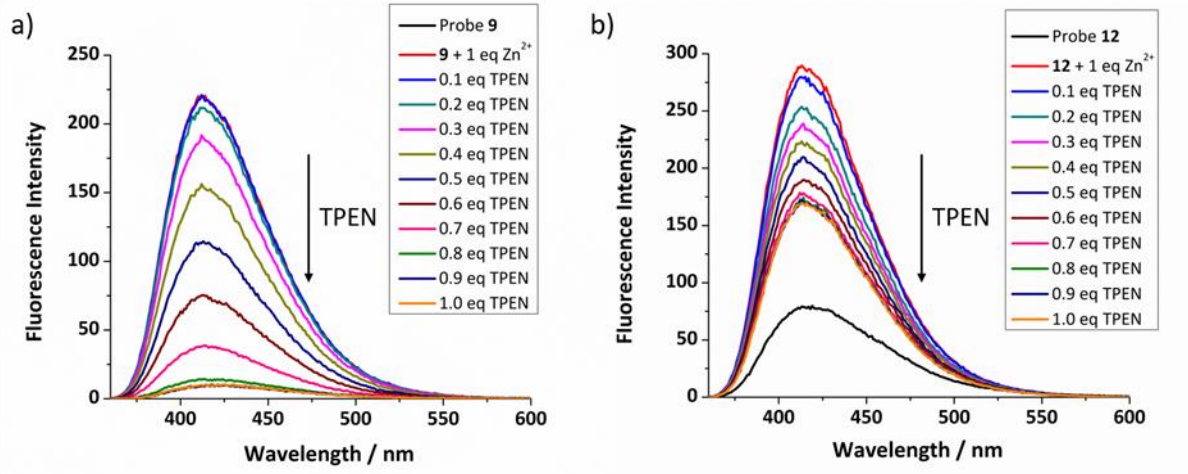

Figure 3.3 The fluorescence response of a) **65** (50 µM) and b) **67** (50 µM) with 1 equivalent Zn^{2+} to different equivalents of TPEN in 0.1 mM HEPES buffer at pH 7.4. (λ_{ex} = 346 nm, slit widths: 5/5 nm).

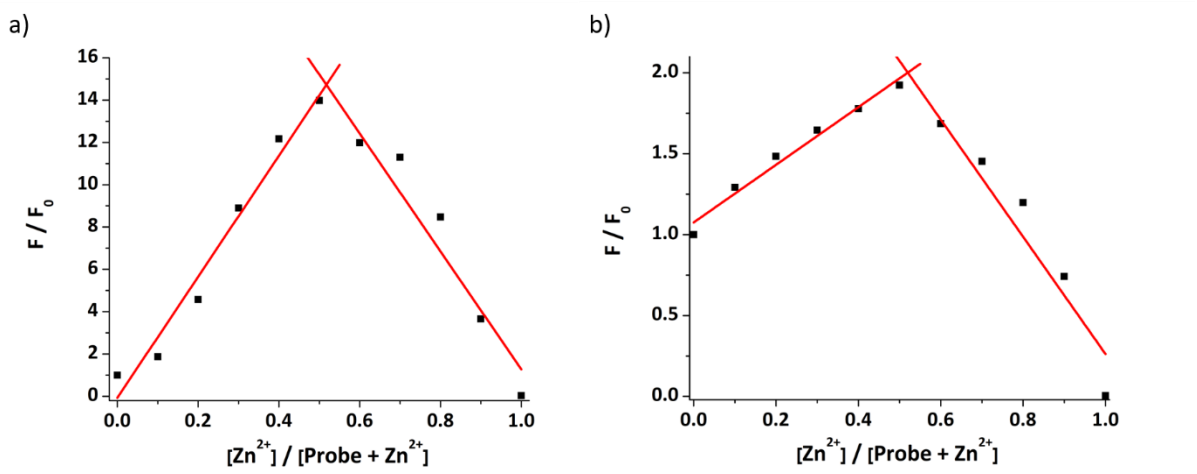

Figure 3.4 The Job's plot to determine the stoichiometry of the complex formed between a) **65** and Zn^{2+}, b) **67** and Zn^{2+}. The total amount of [Probe + Zn^{2+}] is 50 µM, (λ_{ex} = 346 nm, λ_{em} = 414 nm).

The dissociation constants K_d for probes **65** and **67** were obtained through non-linear curve fitting using reported methods[119,120] at a number of probe concentrations (Figure 3.5, Table 3.1). However, because of the very low K_d values for these compounds and to mimic the buffered nature of mobile zinc *in cellulo*, EGTA (ethylene glycol-bis(β-aminoethyl ether)-*N*,*N*,*N*',*N*'-tetraacetic acid) was used as a competitive chelator and the K_d values again calculated at three different concentrations (Figure 3.6) with optimal fit being observed at 0.01 µM in all cases (Table 3.2) revealing the dissociation constant of **65** to be 3.5 nM and 4.7 nM for **67**. The detection limits of **65** and **67** (Figure 3.7) were also estimated to be 47 pM and 0.71 nM, respectively.

[Probe]	Probe **65**	Probe **67**
50 µM	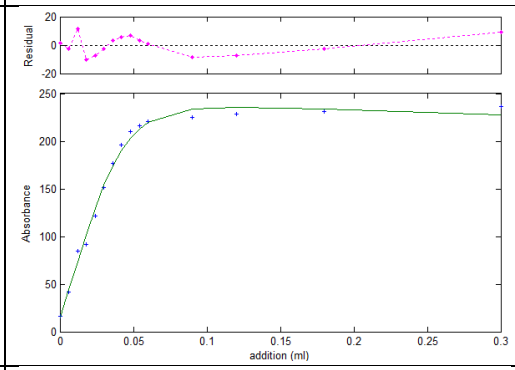	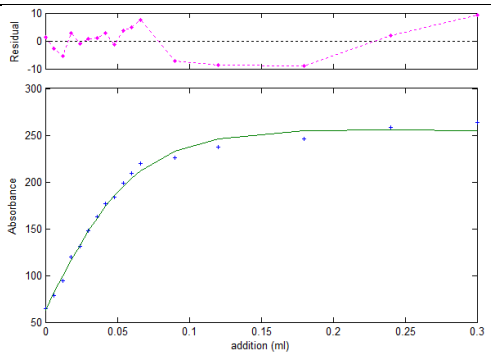
10 µM	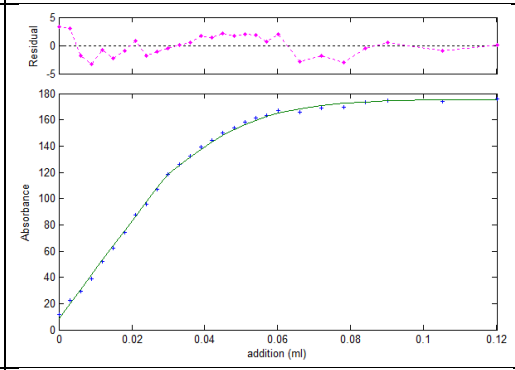	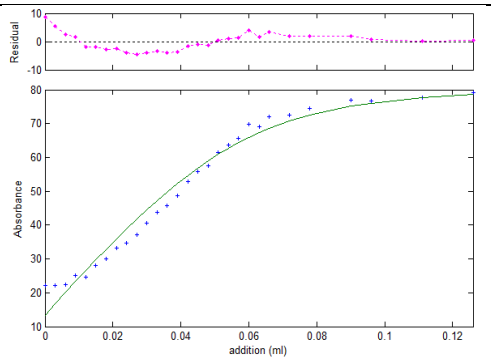
1 µM	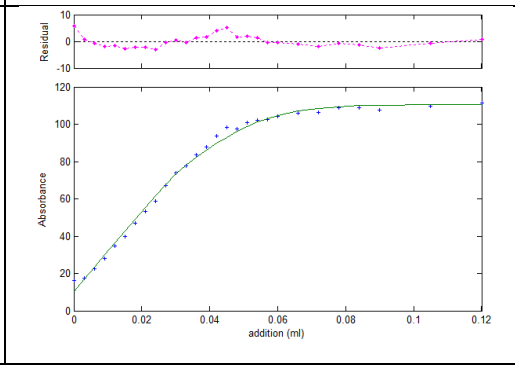	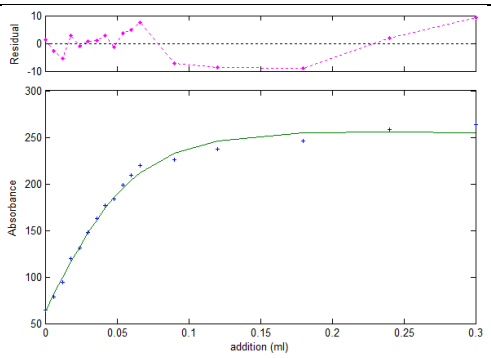

Figure 3.5 The non-linear curve fitting of the fluorescence intensity as a function of [Zn^{2+}] of **65** and **67** at different concentrations to determine K_d (Blue = measured data, Green = fit). Residuals at each datapoint are shown in pink. For all complexes, 0.06 mL addition of Zn^{2+} solutions represent a 1:1 ratio of probe and Zn^{2+}. (λ_{ex} = 346 nm, λ_{em} = 414 nm (probe **65**), λ_{em} = 406 nm (probe **67**)). Fits for probe **65** incorporate fitting of an ML_2 species at low abundance (see Table 3.1). Non-linear regression was carried out using Reactlab Equilibria software.

Table 3.1 Summary of apparent K_d calculated for probes **65** and **67** using the free Zn^{2+} method as a function of concentration.

K_d	[Probe] = 50 µM	[Probe] = 10 µM	[Probe] = 1 µM
65[i]	1.0×10^{-7} M	3.0×10^{-10} M	2.8×10^{-10} M
67	1.0×10^{-5} M	1.1×10^{-6} M	4.5×10^{-8} M

[i]The best fit for probe **65** by this method was obtained by also allowing for the presence of a second species of the form ML_2. In all cases, the second stepwise association constant K_2 was 1-2 orders of magnitude smaller than K_1 indicative of strongly negative cooperativity, and this species was only observed in the presence of a large excess of probe in the early parts of the

titration. No improvement in fitting was observed by including any other stoichiometries in the fitting for probe **67**.

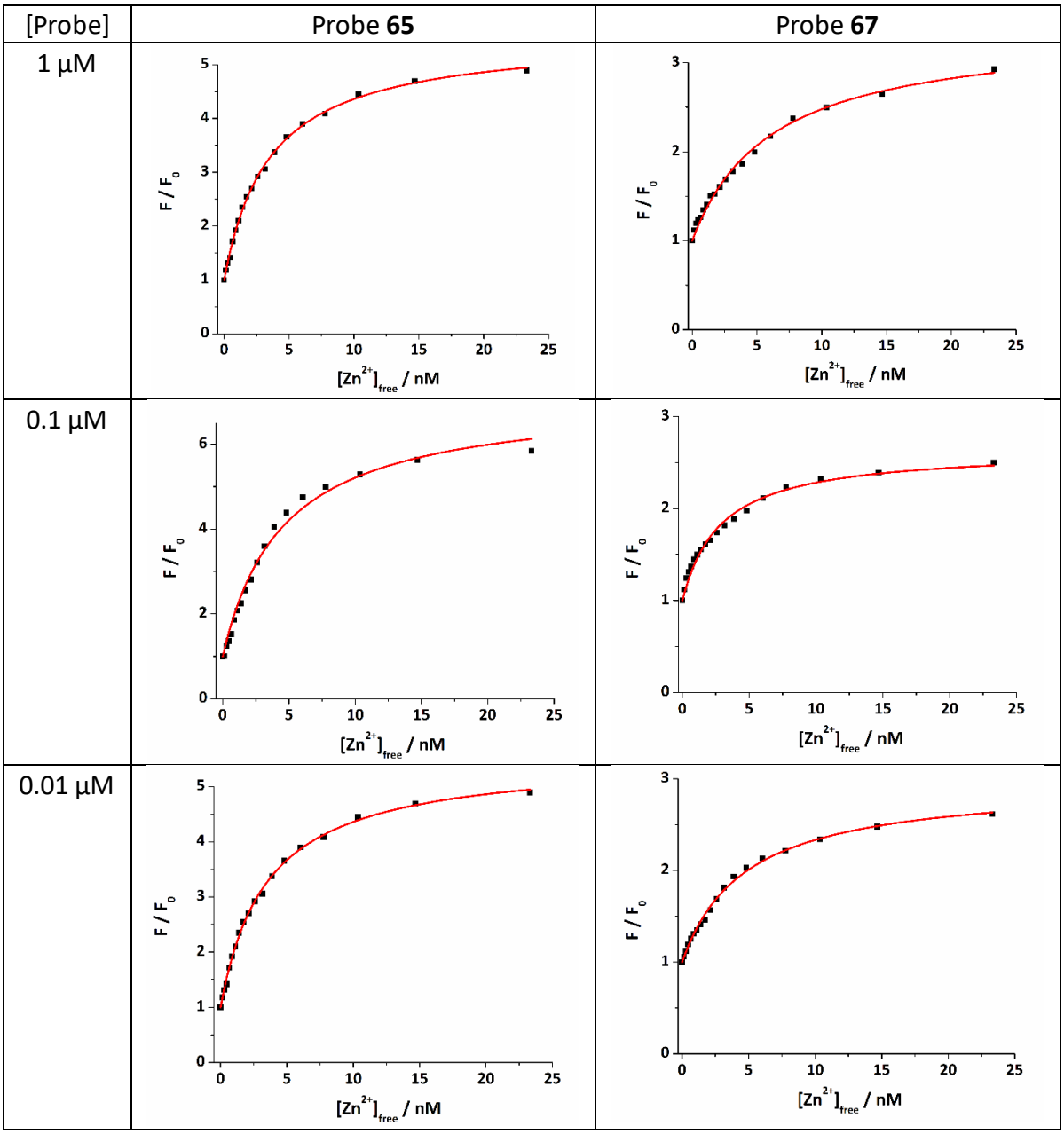

Figure 3.6 The non-linear curve fitting of the fluorescence intensity of **65** and **67** at different concentrations against different equivalents of Zn^{2+} to determine K_d applying Equation 7.1. (λ_{ex} = 346 nm, λ_{em} = 414 nm).

Table 3.2 Summary of K_d values for probes **65** and **67**.

	[Probe] = 1 µM		[Probe] = 0.1 µM		[Probe] = 0.01 µM	
	K_d	R^2	K_d	R^2	K_d	R^2
65	4.70 ± 0.49 nM	0.9825	4.54 ± 0.38 nM	0.9883	3.50 ± 0.10 nM	0.9985
67	6.11 ± 0.41 nM	0.9926	2.87 ± 0.22 nM	0.9871	4.73 ± 0.20 nM	0.9968

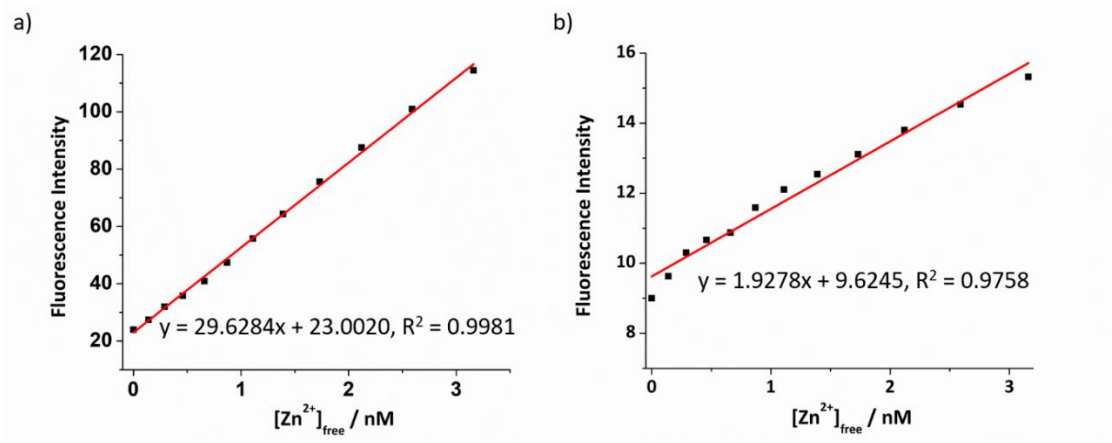

Figure 3.7 Fluorescence response of a) **65** (1 μM) and b) **67** (1 μM) against $[Zn^{2+}]_{free}$ in HEPES buffer solution (50 mM, pH 7.2, 0.1 M KCl).. (λ_{ex} = 346 nm, λ_{em} = 414 nm)

The quantum yields of both probes were measured using anthracene as the standard. It was found that the quantum yield of **65** was 0.041, which increased to 0.25 after binding with 1 eq. of Zn^{2+}. In line with the results seen in Chapter 2 (see Section 2.3) and previous reports,[102,121] the quantum yield of **67** was much lower, 0.013 and only increased to 0.041 for the complex with 1 equivalent of Zn^{2+} (Figure 3.8).

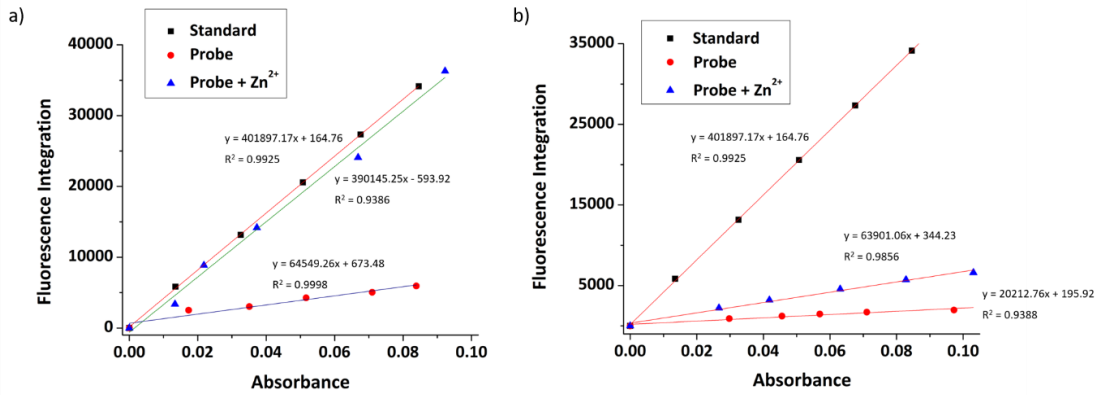

Figure 3.8 Linear plots for a) standard sample, **65**, and **65** + Zn^{2+}, b) standard sample, **67**, and **67** + Zn^{2+} to obtain quantum yields. Anthracene (Φ = 0.27 in ethanol) was used as standard sample. (λ_{ex} = 346 nm, λ_{em} = 414 nm, slit widths: 5/5 nm).

The pH-dependent fluorescence response of both probes was tested to confirm that they have fluorescence responses to Zn^{2+} in the biologically relevant pH range. Figure 3.9a shows that **65** has a good switch on fluorescence response to Zn^{2+} over a wide pH range of 3.0-10.0,

and the fluorescence of both probe and complex is increased in an acidic environment. In contrast, **67** (Figure 3.9b) shows a poor response in acid conditions, presumably due to the basic nature of the polyamine ligand, but works well in the pH range 6.0-12.0; given that the reported pH of the ER is the same as the cytoplasm, which is about 7.2,[122] both probes should have a response to mobile Zn^{2+} *in cellulo*. Through non-linear curve fitting applied with the Equation 7.4 and Equation 7.5, the pK_a values of both probes could be obtained, which are pK_{a1} = 0.81 ± 0.19, pK_{a2} = 4.34 ± 0.11, pK_{a3} = 6.83 ± 0.53, pK_{a4} = 11.63 ± 0.41 for **65**, and pK_{a1} = 3.20 ± 0.14, pK_{a2} = 8.07 ± 0.11, pK_{a3} = 11.07 ± 0.58 for **67** (Figure 3.10). These values are comparable to those reported for related compounds.[121]

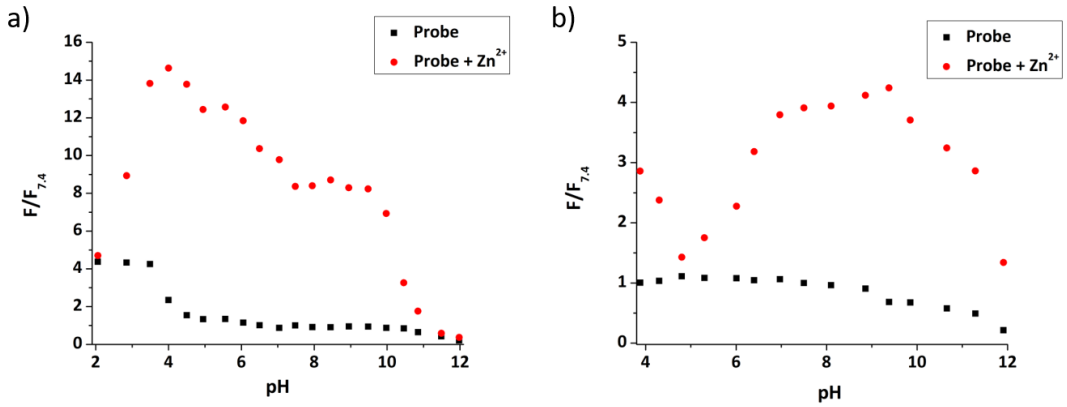

Figure 3.9 The pH profile of a) **65** (50 µM, black dots) and b) **67** (50 µM, black dots) and their complex with 1 equivalent of Zn^{2+} (red dots).

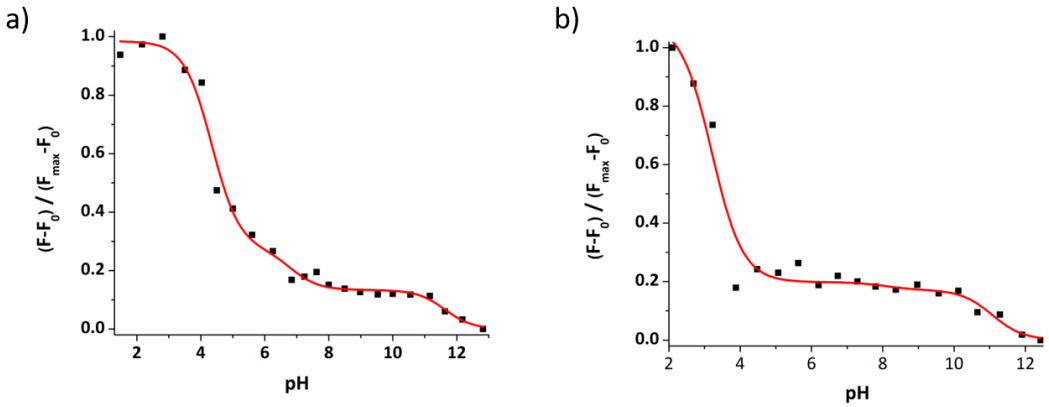

Figure 3.10 Normalized integrated fluorescence emission of a) **65** (50 µM) and b) **67** (50 µM) vs pH, the nonlinear curve fitting used to determine the apparent pK_a values.

The selectivity of the two probes over a range of other competing cations was also investigated. As shown in Figure 3.11a, beside Zn^{2+}, the fluorescence of **65** was not switched on obviously after addition of 5 equivalents of other cations, except for the stereoelectronic isostere Cd^{2+}, which is a common issue for many Zn^{2+} probes,[123] but is not a problem in biological milieu due to its negligibly low concentration. Subsequent addition of Zn^{2+} resulted in recovery of a fluorescence response in most cases, however for Co^{2+}, Cu^{2+} and Ni^{2+} fluorescence was not recovered, but as they mostly exist in bound forms in biology, rather than the free cations tested here this is unconcerning. For **67**, results were similar, as shown in Figure 3.11b, with only Cu^{2+}, Fe^{2+} and Fe^{3+} continuing to quench fluorescence after the addition of Zn^{2+}. Importantly, the metal ions Na^{+}, K^{+}, Ca^{2+} and Mg^{2+}, which are abundant in cells, show no effect on either probe. Overall these results indicate that they should show a selective response to 'mobile' Zn^{2+} *in cellulo*.

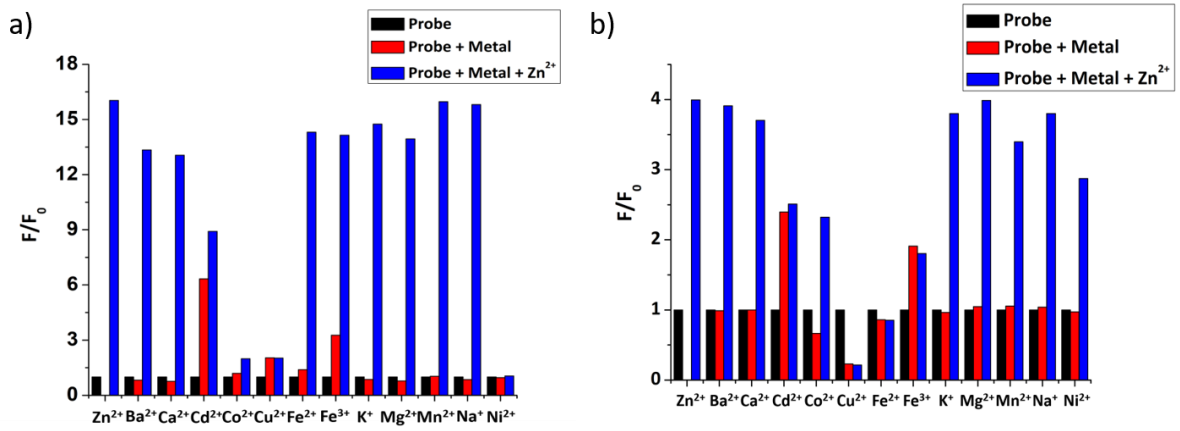

Figure 3.11 Metal ion selectivity of a) **65** and b) **67** in 0.1 mM HEPES buffer at pH 7.4. Average normalized fluorescence intensities for probes (50 µM) (black bars), after addition of 5 equivalents of various cations (red bars), followed by addition of 1 equivalent of $ZnCl_2$ (blue bars).

3.3 DFT calculations

DFT and TDDFT calculations were undertaken to understand the binding behaviour of **65** and **67** with Zn^{2+} and their excited states. The optimised structure of probe **65** with 1 equivalent

of Zn^{2+} (Figure 3.12) shows the Zn^{2+} is bound to the nitrogen in ligand DPEN and a nitrogen atom of the triazole. For **67** (Figure 3.13), the triazole nitrogen is involved in binding with Zn^{2+} in addition to the cyclam nitrogen donors, which is consistent with previous observations in closely related analogues.[101,107]

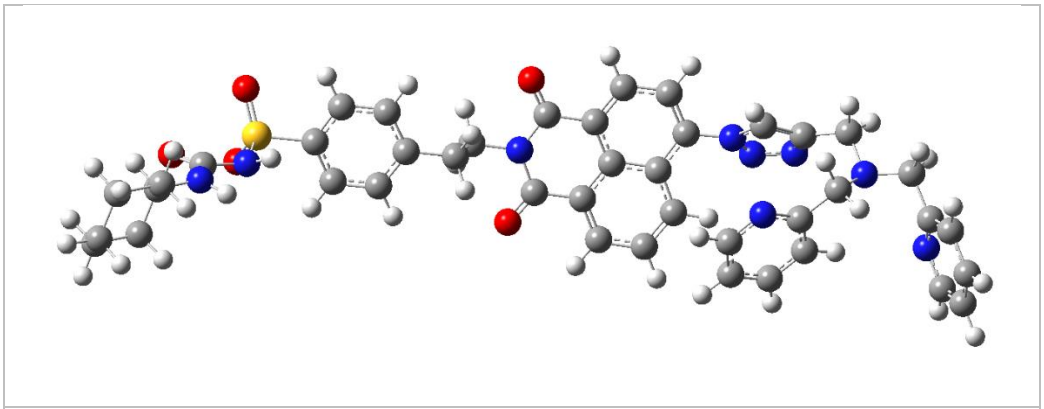

Probe **65**

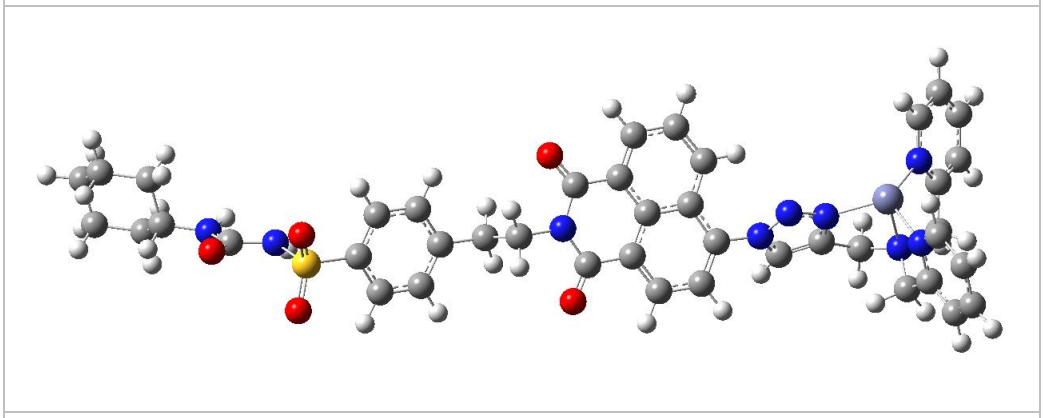

Complex with Zn^{2+}

Figure 3.12 The optimised structures of **65** and its complex with Zn^{2+}.

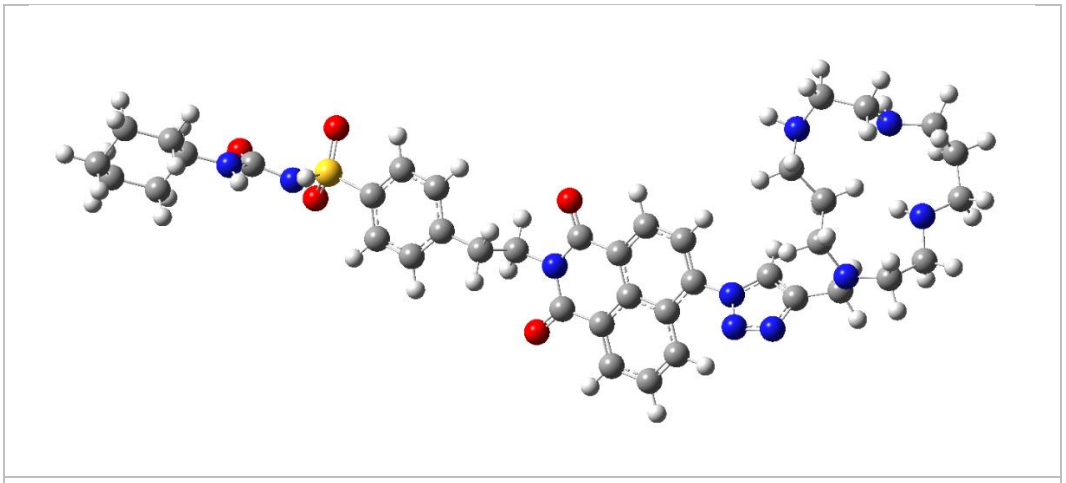

Probe **67**

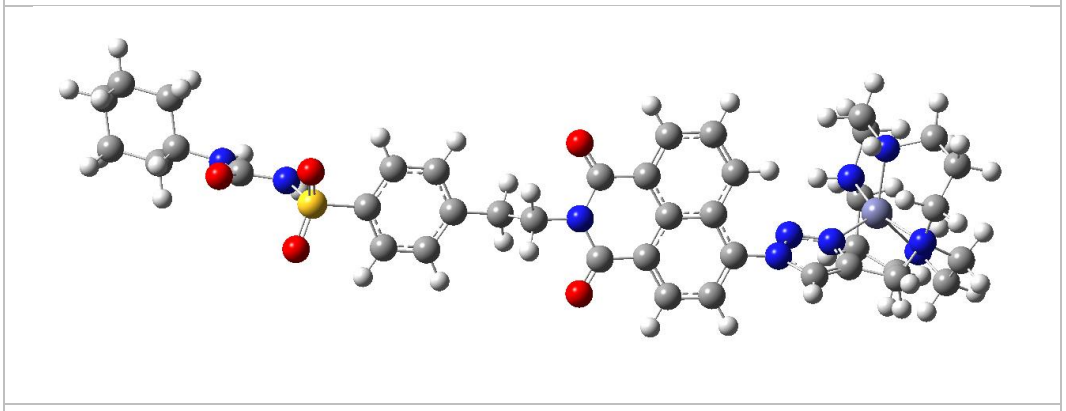

Complex with Zn^{2+}

Figure 3.13 The optimised structures of **67** and its complex with Zn^{2+}.

The calculated vertical excitations and emissions are in relatively good agreement with experimental data (see Table 3.3 and 3.4). The excited state calculations also show that positions of the absorption maxima and the emission energies are not significantly affected by the formation of the complexes with Zn^{2+}, as observed experimentally. This behaviour can be understood by visualising the S_1-S_0 electron density plots (Figure 3.14 for **65**, Figure 3.15 for **67**). The electronic transition is localised on the naphthalimide moiety and the vicinal triazole, and that there is no major difference between probes and their complexes with Zn^{2+}; only a slight decrease of electron density on the nitrogen from the triazole is observed when it is involved in complex formation, and the oscillator strength is not significantly affected. These calculations indicate that the enhancement of emissive behaviour of the complexes

should be related to a reduced decay through nonradiative pathways after complexation with Zn^{2+} in contrast with the typical PET mechanism. The role of alternative mechanisms to PET in enhancing the fluorescence of organometallic complexes has been recently highlighted (see also Section 1.3.5).[19,124] The formation of the complex hinders large amplitude vibrations in the vicinity of the fluorophore hampering access to nonradiative mechanisms and increasing the quantum yield of the emission. The restriction of intramolecular rotations can also hinder the access to low energy conical intersections associated with ultrafast decay to the ground state. Tang *et al*., have recently shown how the restriction of intramolecular motions in a Zn^{2+} complex can hamper the access to a dark state enhancing the fluorescence response.[125]

Table 3.3. Comparison of the experimental data with the calculated result of vertical electronic excitation energies (eV) and the emission from S_1 to ground state of **65** and its Zn^{2+} complex.

	Electronic transition	Energy (eV)	Wavelength (nm)	Oscillator strength (f)	Experimental data
65					
Absorption	$S_0 \rightarrow S_1$	3.84	322	0.5747	3.58 eV/346 nm
	$S_0 \rightarrow S_2$	4.27	290	0.0384	
	$S_0 \rightarrow S_3$	4.39	282	0.0002	
	$S_0 \rightarrow S_4$	4.71	263	0.0041	
	$S_0 \rightarrow S_5$	4.72	262	0.0043	
	$S_0 \rightarrow S_6$	4.90	253	0.0043	
Emission	$S_1 \rightarrow S_0$	3.19	388	0.7145	3.01 eV/412 nm
Complex of **65** with Zn^{2+}					
Absorption	$S_0 \rightarrow S_1$	3.95	314	0.5437	3.58 eV/346 nm
	$S_0 \rightarrow S_2$	4.26	291	0.0501	
	$S_0 \rightarrow S_3$	4.33	286	0.0006	
	$S_0 \rightarrow S_4$	4.68	265	0.0082	
	$S_0 \rightarrow S_5$	4.93	252	0.0328	
	$S_0 \rightarrow S_6$	5.33	233	0.0138	
Emission	$S_1 \rightarrow S_0$	3.18	390	0.7059	3.01 eV/412 nm

Table 3.4. Comparison of the experimental data with the calculated result of vertical electronic excitation energies (eV) and the emission from S_1 to ground state of **67** and its Zn^{2+} complex.

	Electronic transition	Energy (eV)	Wavelength (nm)	Oscillator strength (f)	Experimental data
67					
Absorption	$S_0 \rightarrow S_1$	3.87	320	0.5642	3.58 eV/346 nm
	$S_0 \rightarrow S_2$	4.06	305	0.0021	
	$S_0 \rightarrow S_3$	4.27	290	0.0424	
	$S_0 \rightarrow S_4$	4.39	283	0.0010	
	$S_0 \rightarrow S_5$	4.68	265	0.0000	
	$S_0 \rightarrow S_6$	4.73	262	0.0064	
Emission	$S_1 \rightarrow S_0$	3.18	390	0.7329	3.01 eV/412 nm
Complex of **67** with Zn^{2+}					
Absorption	$S_0 \rightarrow S_1$	3.97	312	0.5188	3.58 eV/346 nm
	$S_0 \rightarrow S_2$	4.27	290	0.0534	
	$S_0 \rightarrow S_3$	4.33	286	0.0008	
	$S_0 \rightarrow S_4$	4.69	264	0.0045	
	$S_0 \rightarrow S_5$	4.93	251	0.0310	
	$S_0 \rightarrow S_6$	5.41	229	0.0126	
Emission	$S_1 \rightarrow S_0$	3.20	387	0.6879	3.01 eV/412 nm

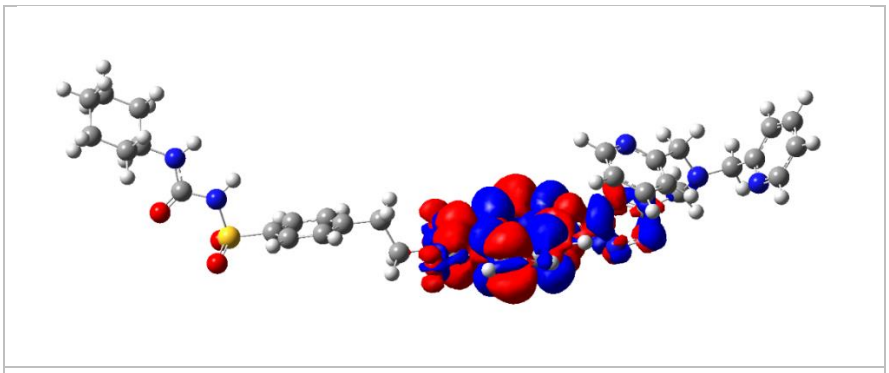

Probe **65**

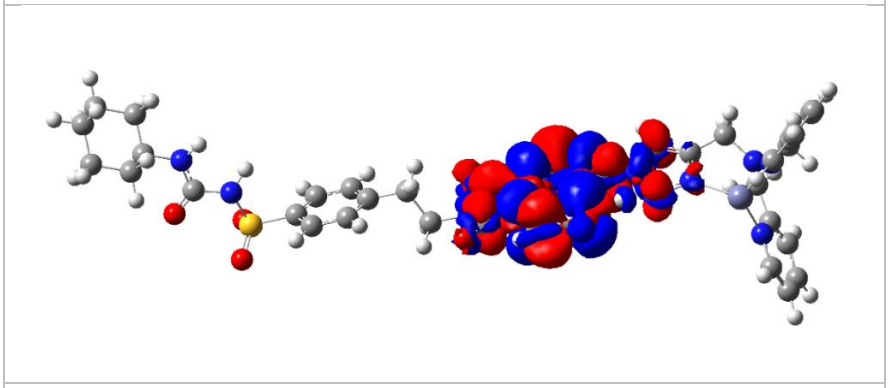

Complex with Zn^{2+}

Figure 3.14 S_1-S_0 electron density map for probe **65** and its complex with Zn^{2+} (S_1 minima). Red represents positive densities and blue negative values.

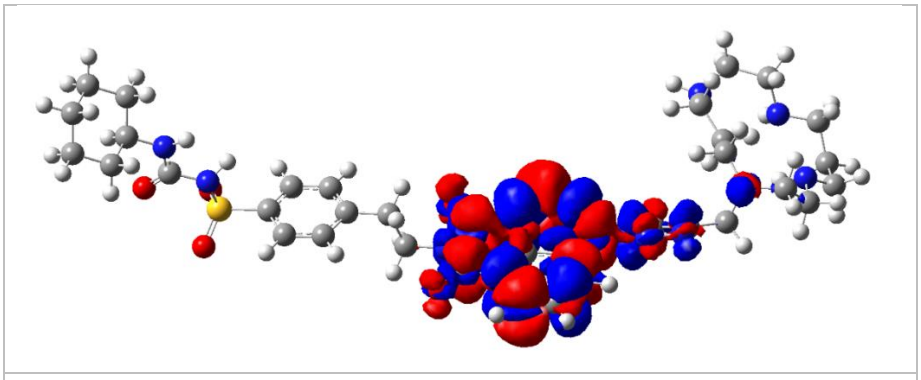

Probe **67**

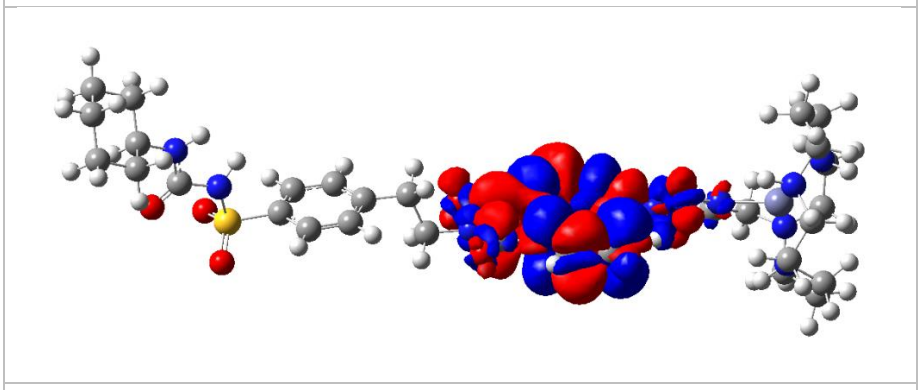

Complex with Zn^{2+}

Figure 3.15 S_1-S_0 electron density map for probe **67** and its complex with Zn^{2+} (S_1 minima). Red represents positive densities and blue negative values.

3.4 *In cellulo* tests

3.4.1 Cell viability of probes

Encouraged by the promising properties of **65** and **67** *in vitro*, their suitability for imaging Zn^{2+} in cells was assessed. Firstly, the innate toxicity of the probes was measured by AlamarBlue assays with HeLa cells (Figure 3.16). The cell viabilities were over 90% after 24 h incubation with both **65** and **67** in a concentration range 10-50 μM compared to the control group, demonstrating both have very low cytotoxicity. In contrast, the viability of cells incubated with **70** decreased significantly with concentration increasing, confirming it is toxic.

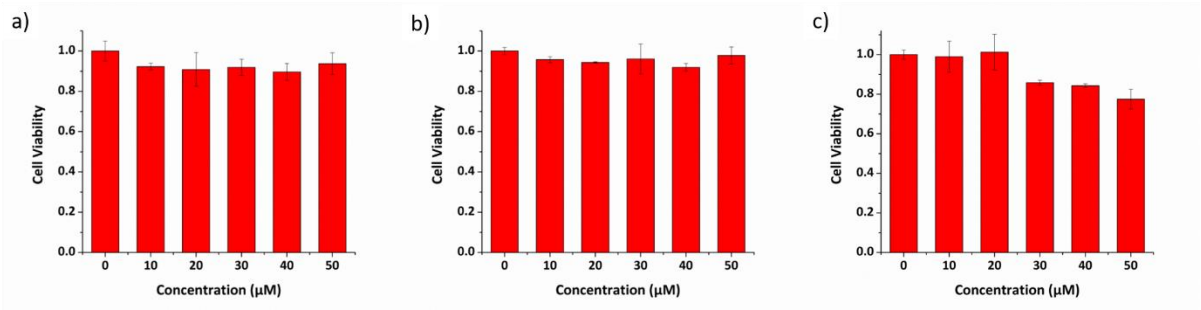

Figure 3.16 The HeLa cell viability against probe a) **65**, b) **67** and c) **70** at different concentrations.

3.4.2 ER-targeting ability

The targeting behaviour of **65** and **67** was then studied using co-staining assays. HeLa cells were co-incubated with **65** and ER-tracker red, as shown in Figure 3.17, the fluorescence of **65** from the green channel overlays well with that of ER-tracker red, which was obtained from the red channel, giving an excellent Pearson's correlation coefficient of 0.92. The negative controls of **65** co-incubated with Mito-tracker red and Lyso-tracker red did not reveal a good overlay and Pearson's correlation coefficients were 0.52 and 0.58, respectively. Similar results were observed for **67** (see Figure 3.18) with Pearson's coefficients of 0.85, 0.52, 0.45 being measured for the ER, mitochondria and lysosome respectively.

To confirm the probes have ER-targeting ability in different cell types, a human breast cancer cell line MCF-7, a sweat gland tissue cell line EC23 and a human liver cancer cell line HepG2 were used to study the ER-targeting behaviour. The results (see Figure 3.19 to 3.21 for probe **65**, Figure 3.22 to 3.24 for probe **67**) show that probe localisation is similar to that observed in HeLa cells demonstrating the general applicability of the probes. Based on these data, it can be concluded that both **65** and **67** show excellent, and general, ER-targeting capability.

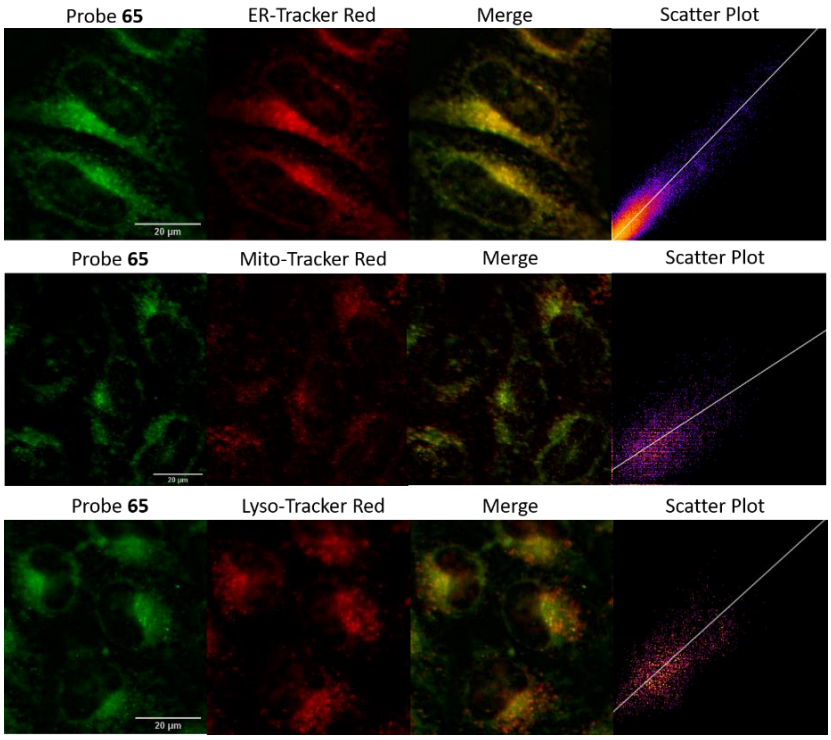

Figure 3.17 The colocalisation images of HeLa cells incubated with **65** (20 µM, GFP filter: λ_{ex} = 470/30 nm, λ_{em} = 530/50 nm) and commercial red organelle tracker dyes (RFP filter: λ_{ex} = 530/40 nm, λ_{em} = 605/55 nm). (Scale bars = 20 µm).

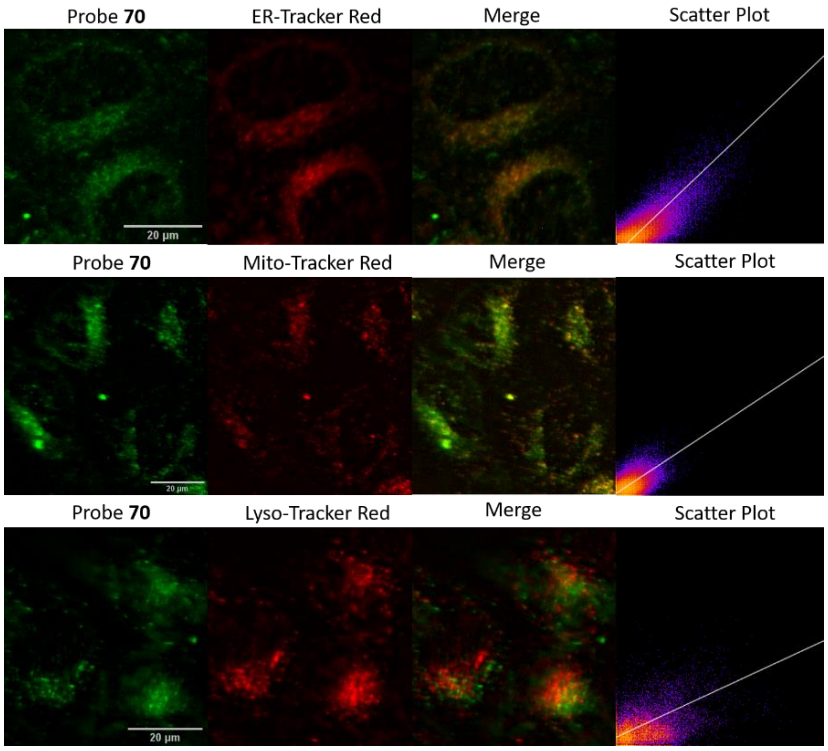

Figure 3.18 The colocalisation images of HeLa cells incubated with probe **67** (20 µM, GFP filter: λ_{ex} = 470/30 nm, λ_{em} = 530/50 nm) and organelle tracker red dyes (RFP filter: λ_{ex} = 530/40 nm, λ_{em} = 605/55 nm). (Scale bars = 20 µm).

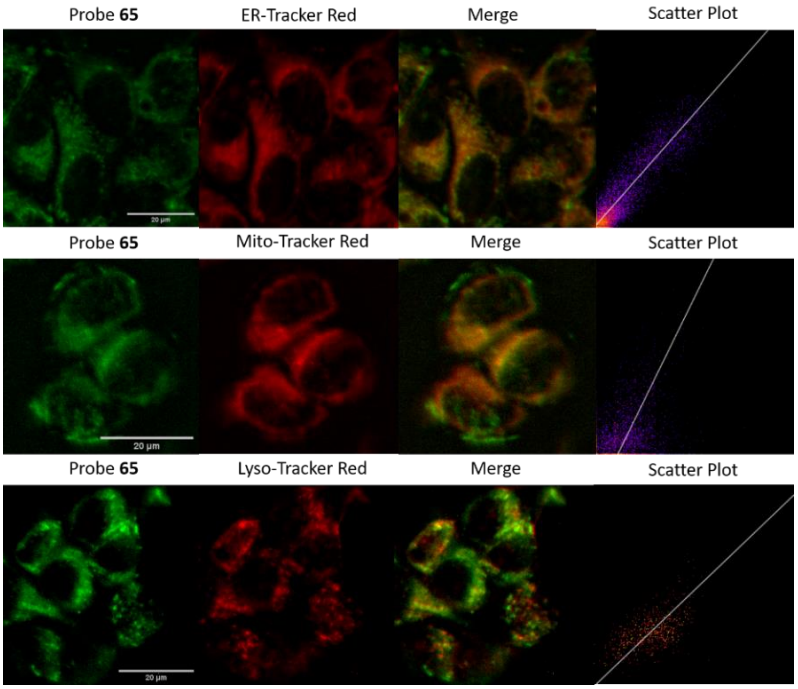

Figure 3.19 The colocalisation images of MCF-7 cells incubated with probe **65** (20 µM, GFP filter: λ_{ex} = 470/30 nm, λ_{em} = 530/50 nm) and organelle tracker red dyes (RFP filter: λ_{ex} = 530/40 nm, λ_{em} = 605/55 nm). (Scale bars = 20 µm). Pearson's correlation coefficients were 0.87, 0.43 and 0.49 compared to ER-tracker red, Mito-tracker red and Lyso-tracker red, respectively.

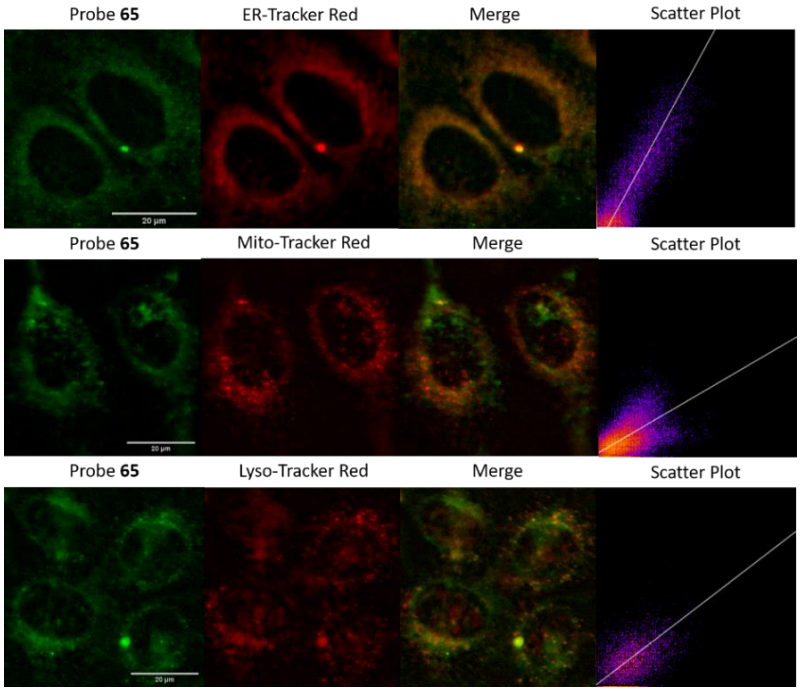

Figure 3.20 The colocalisation images of EC23 cells incubated with probe **65** (20 µM, GFP filter: λ_{ex} = 470/30 nm, λ_{em} = 530/50 nm) and organelle tracker red dyes (RFP filter: λ_{ex} = 530/40 nm, λ_{em} = 605/55 nm). (Scale bars = 20 µm). Pearson's correlation coefficients were 0.88, 0.48 and 0.44 compared to ER-tracker red, Mito-tracker red and Lyso-tracker red, respectively.

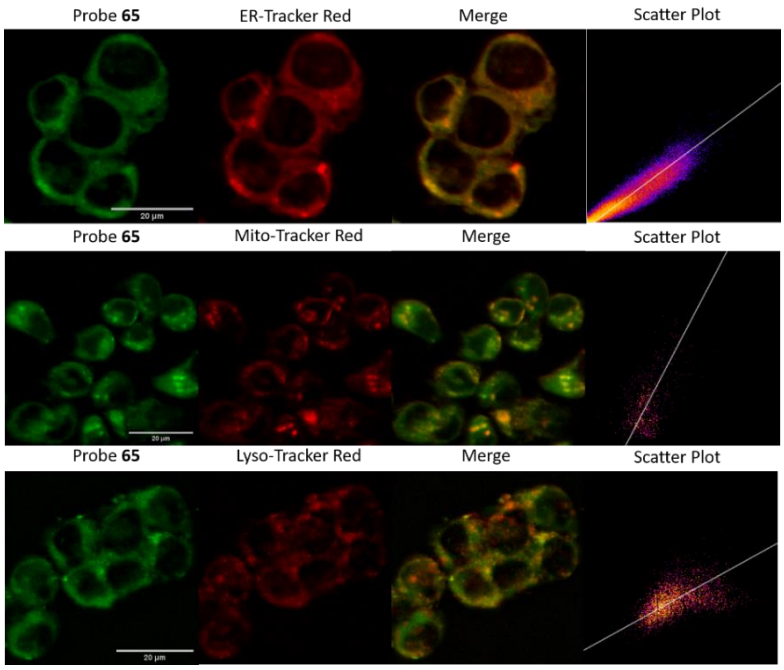

Figure 3.21 The colocalisation images of HepG2 cells incubated with probe **65** (20 µM, GFP filter: λ_{ex} = 470/30 nm, λ_{em} = 530/50 nm) and organelle tracker red dyes (RFP filter: λ_{ex} = 530/40 nm, λ_{em} = 605/55 nm). (Scale bars = 20 µm). Pearson's correlation coefficients were 0.91, 0.64 and 0.46 compared to ER-tracker red, Mito-tracker red and Lyso-tracker red, respectively.

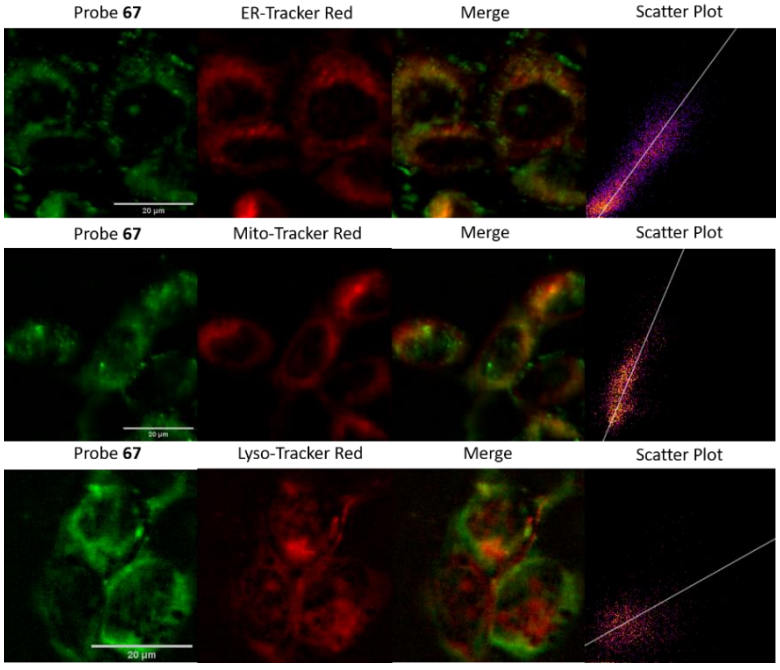

Figure 3.22 The colocalisation images of MCF-7 cells incubated with probe **67** (20 µM, GFP filter: λ_{ex} = 470/30 nm, λ_{em} = 530/50 nm) and organelle tracker red dyes (RFP filter: λ_{ex} = 530/40 nm, λ_{em} = 605/55 nm). (Scale bars = 20 µm). Pearson's correlation coefficients were 0.82, 0.54 and 0.38 compared to ER-tracker red, Mito-tracker red and Lyso-tracker red, respectively.

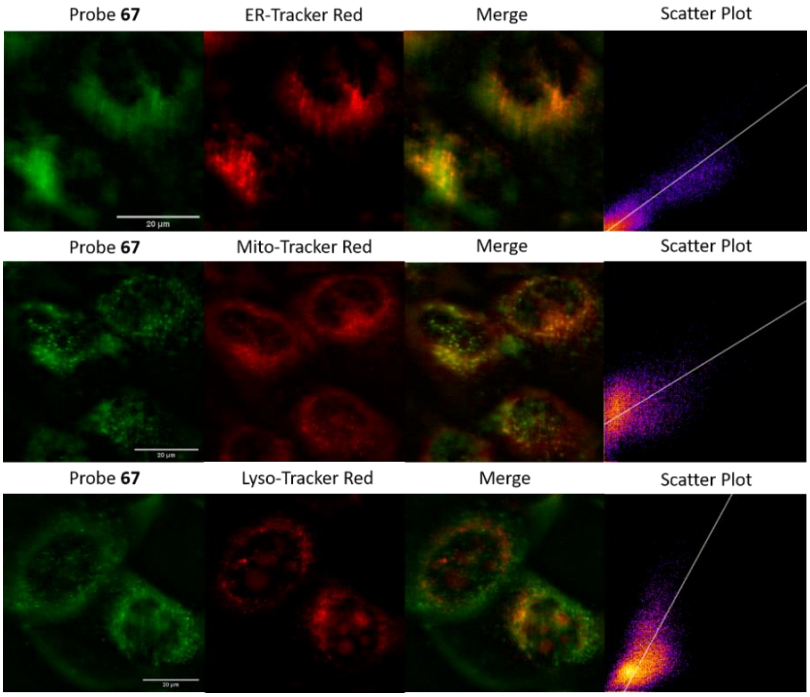

Figure 3.23 The colocalisation images of EC23 cells incubated with probe **67** (20 µM, GFP filter: λ_{ex} = 470/30 nm, λ_{em} = 530/50 nm) and organelle tracker red dyes (RFP filter: λ_{ex} = 530/40 nm, λ_{em} = 605/55 nm). (Scale bars = 20 µm). Pearson's correlation coefficients were 0.87, 0.48 and 0.53 compared to ER-tracker red, Mito-tracker red and Lyso-tracker red, respectively.

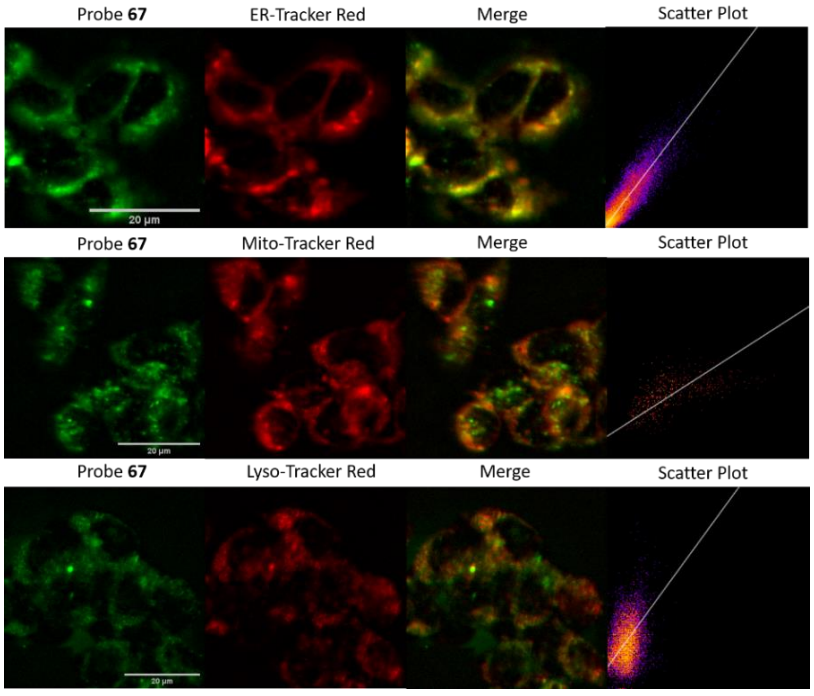

Figure 3.24 The colocalisation images of HepG2 cells incubated with probe **67** (20 µM, GFP filter: λ_{ex} = 470/30 nm, λ_{em} = 530/50 nm) and organelle tracker red dyes (RFP filter: λ_{ex} = 530/40 nm, λ_{em} = 605/55 nm). (Scale bars = 20 µm). Pearson's correlation coefficients were 0.88, 0.51 and 0.36 compared to ER-tracker red, Mito-tracker red and Lyso-tracker red, respectively.

3.4.3 Zn^{2+} fluorescence response in cells

As **65** and **67** can localise to the ER, their fluorescence response to 'mobile' Zn^{2+} *in cellulo* was tested to demonstrate that they have the ability to image Zn^{2+} in the ER. As shown in Figure 3.25, the fluorescence response of probe **65** in HeLa cells could be clearly observed in the ER. Upon the addition of zinc pyrithione, the fluorescence intensity increased considerably; the addition of TPEN, resulted in almost complete quenching of fluorescence, as expected from *in vitro* control experiments. Similar results were observed in other cell lines and also for **67** (Figure 3.26 to 3.32) demonstrating that both probes are tractable in their ability to image mobile Zn^{2+} *in cellulo*. The fluorescence intensity read from these images (Figure 3.33) clearly reveals these changes. For example, in HeLa cells the intensity of the fluorescence response increases 3.6 times after the addition of zinc pyrithione and decreases by 30% on addition of TPEN compared to that observed for **65** alone.

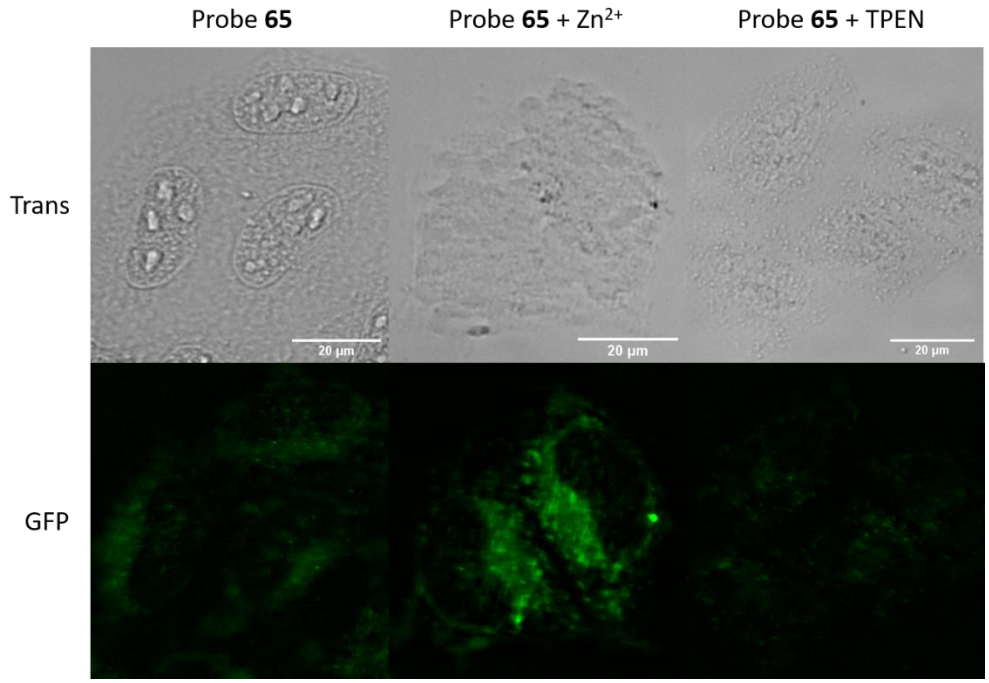

Figure 3.25 Fluorescence microscopy images of HeLa cells treated with **65** (20 µM), **65** (20 µM) with zinc pyrithione (100 µM), and **65** (20 µM) with TPEN (100 µM). (Scale bars = 20 µm).

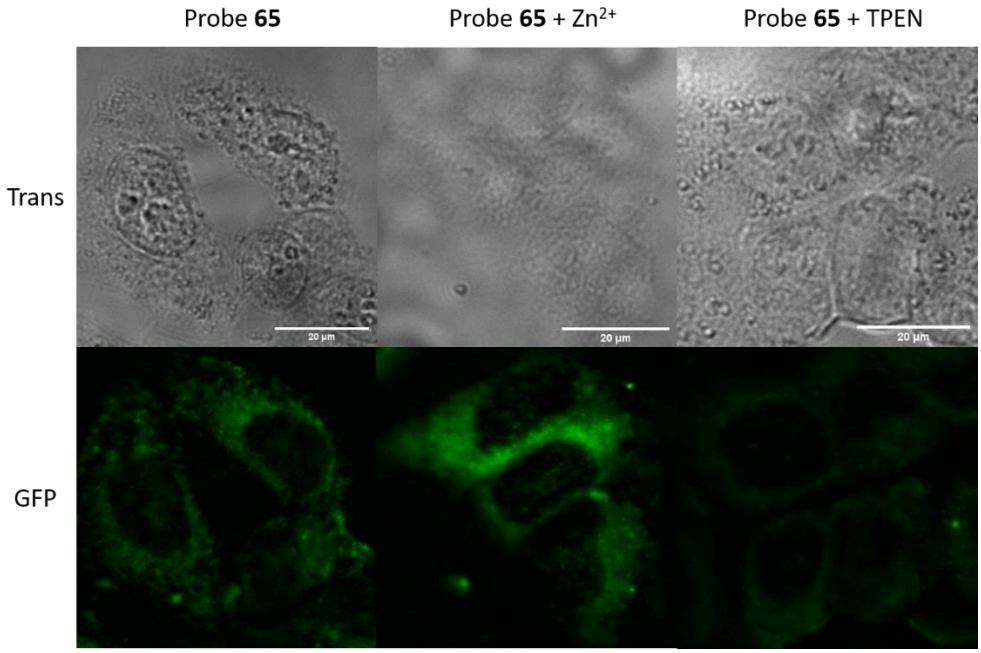

Figure 3.26 Fluorescence microscopy images of MCF-7 cells treated with **65** (20 µM), **65** (20 µM) with zinc pyrithione (100 µM), and **65** (20 µM) with TPEN (100 µM). (Scale bars = 20 µm).

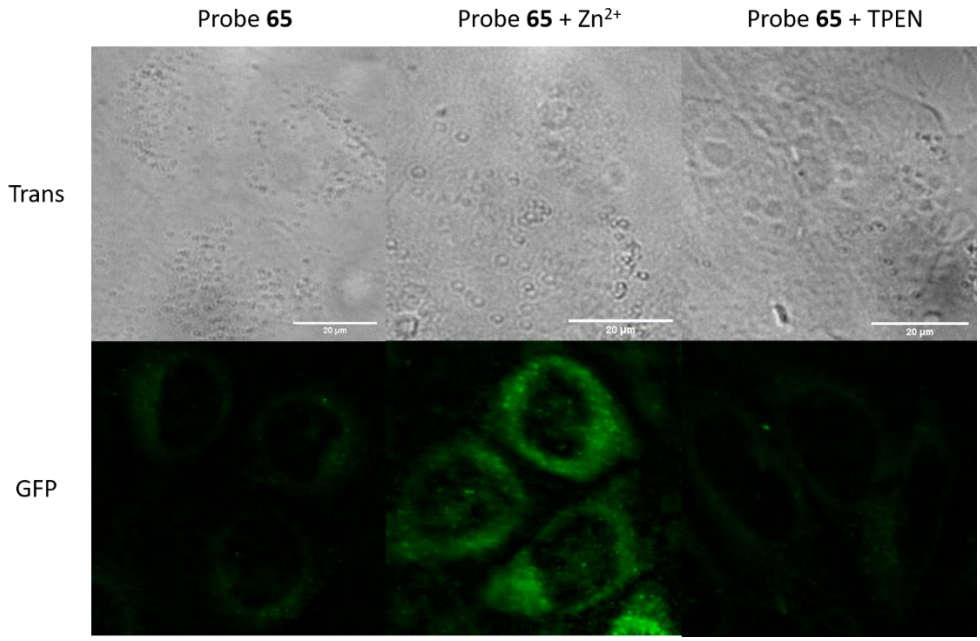

Figure 3.27 Fluorescence microscopy images of EC23 cells treated with **65** (20 µM), **65** (20 µM) with zinc pyrithione (100 µM), and **65** (20 µM) with TPEN (100 µM). (Scale bars = 20 µm).

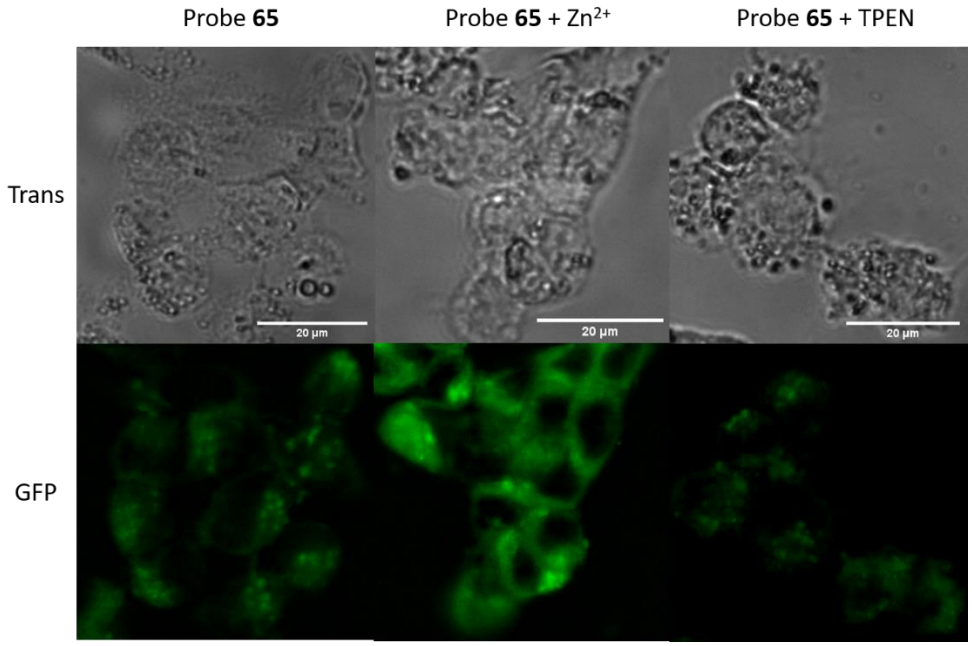

Figure 3.28 Fluorescence microscopy images of HepG2 cells treated with **65** (20 µM), **65** (20 µM) with zinc pyrithione (100 µM), and **65** (20 µM) with TPEN (100 µM). (Scale bars = 20 µm).

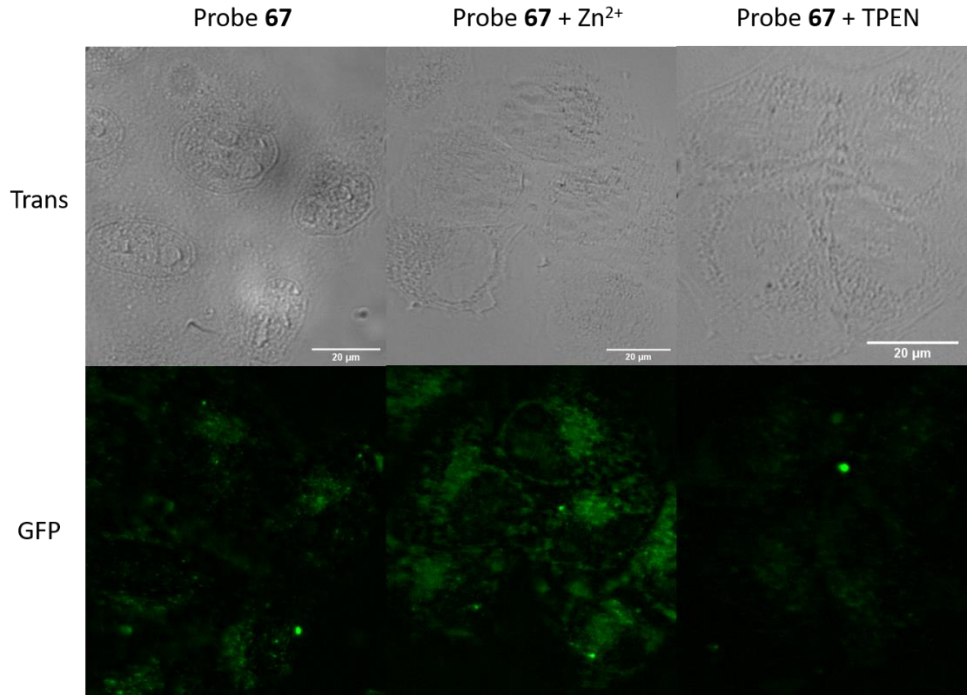

Figure 3.29 Fluorescence microscopy images of HeLa cells treated with **67** (20 µM), **67** (20 µM) with zinc pyrithione (100 µM), and **67** (20 µM) with TPEN (100 µM). (Scale bars = 20 µm).

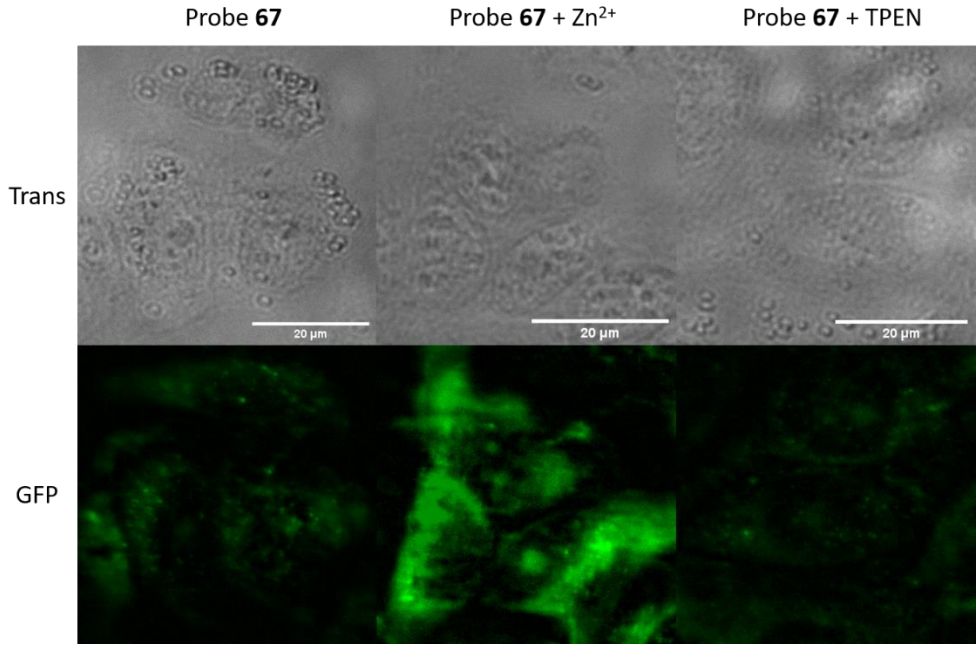

Figure 3.30 Fluorescence microscopy images of MCF-7 cells treated with **67** (20 µM), **67** (20 µM) with zinc pyrithione (100 µM), and **67** (20 µM) with TPEN (100 µM). (Scale bars = 20 µm).

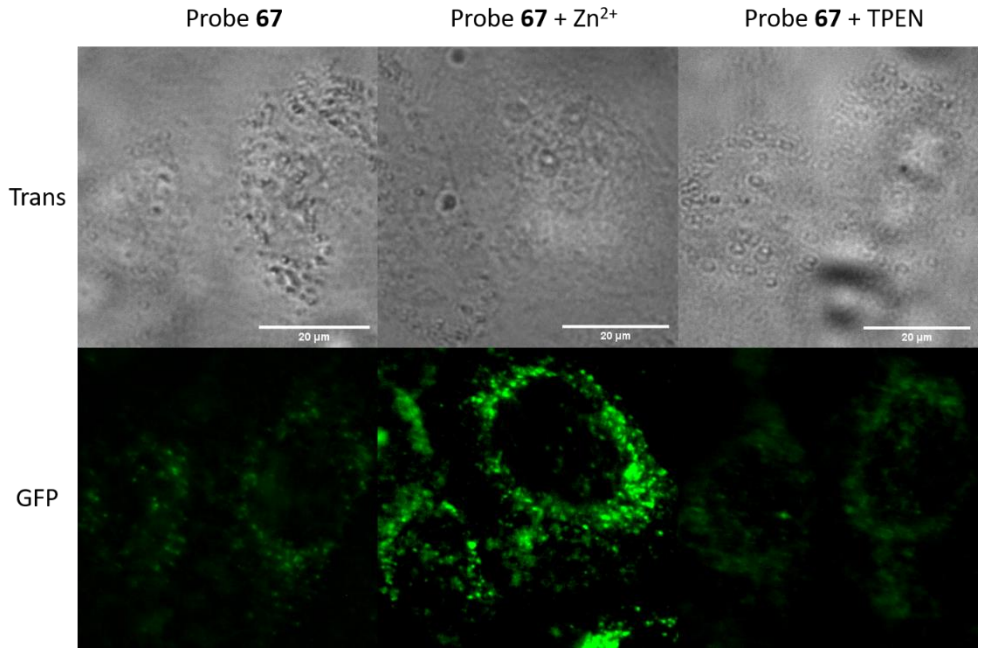

Figure 3.31 Fluorescence microscopy images of EC23 cells treated with **67** (20 µM), **67** (20 µM) with zinc pyrithione (100 µM), and **67** (20 µM) with TPEN (100 µM). (Scale bars = 20 µm).

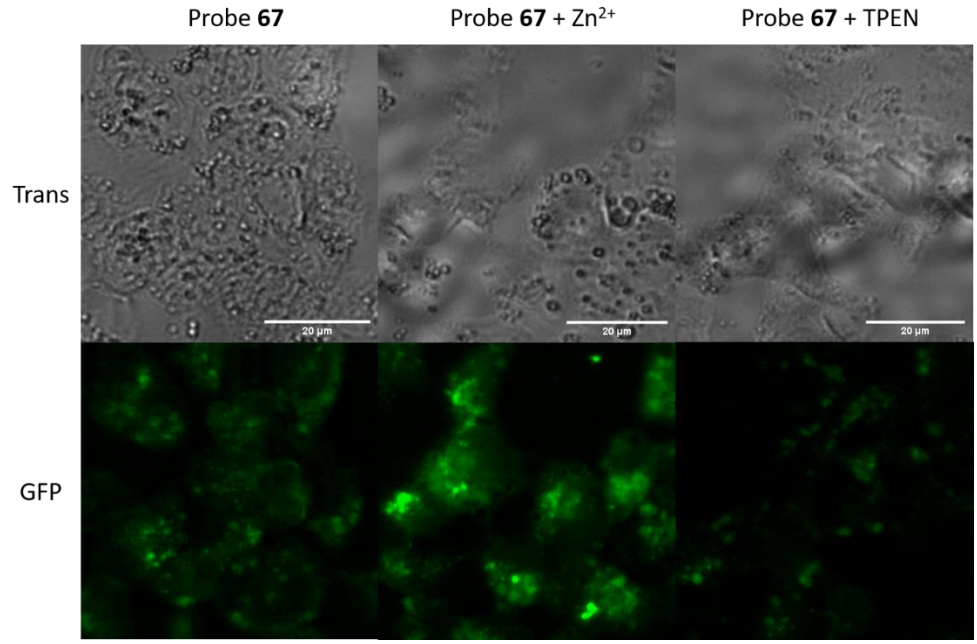

Figure 3.32 Fluorescence microscopy images of HepG2 cells treated with **67** (20 μM), **67** (20 μM) with zinc pyrithione (100 μM), and **67** (20 μM) with TPEN (100 μM). (Scale bars = 20 μm).

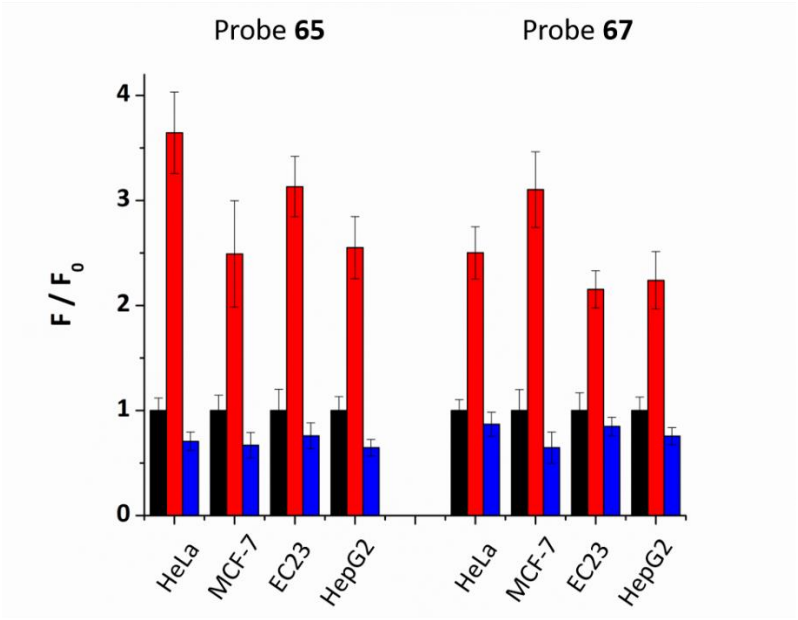

Figure 3.33 The fluorescence intensity (F) in different cell lines in the presence of zinc pyrithione (red bars) or TPEN (blue bars) relative to the intensity of the probe alone (F_0, black bars, normalised to 1).

3.4.4 Fluorescence changes under ER stress

As **65** shows excellent ER-localisation and Zn^{2+} response, attempts were made to explore whether it could be applied to monitor changes in mobile Zn^{2+} levels. It has been reported

that ER stress can be induced by tunicamycin and thapsigargin, with tunicamycin causing unfolded protein accumulation and thapsigargin reducing Ca^{2+} levels.[126] As shown in Figure 3.34, the fluorescence intensity of **65** in HepG2 cells decreased significantly after treatment with both ER stress inducers, indicating that the mobile Zn^{2+} level in the ER was significantly depleted under ER stress within 1 hour. As a control, no fluorescence intensity change was observed in the absence of inducers (Figure 3.35).

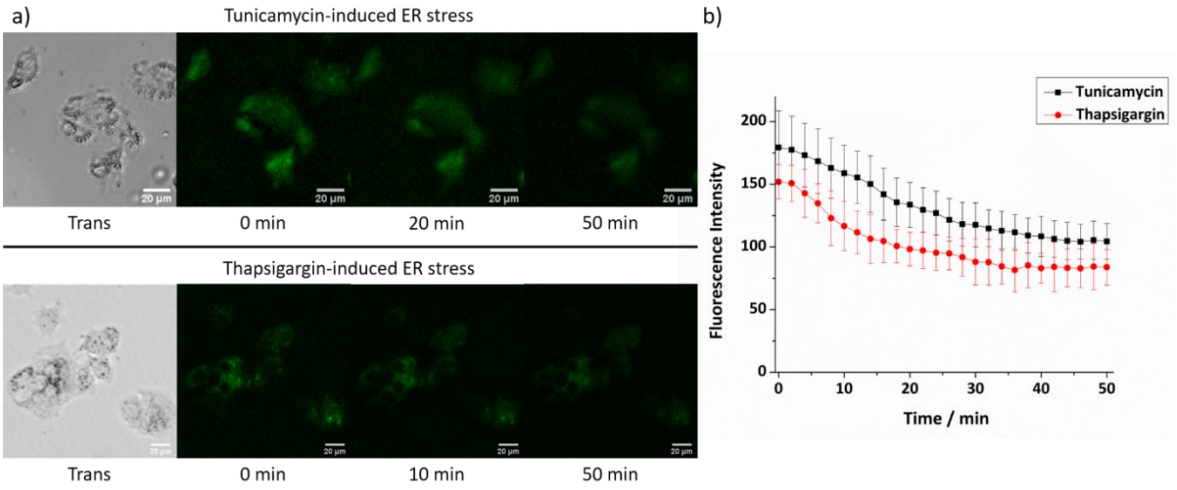

Figure 3.34 a) Fluorescence microscopy images and b) fluorescence intensity changes of probe **65** (20 µM) in HepG2 cells at ER stress state induced by tunicamycin (5 µg/mL) or thapsigargin (1 µM). (Scale bars = 20 µm).

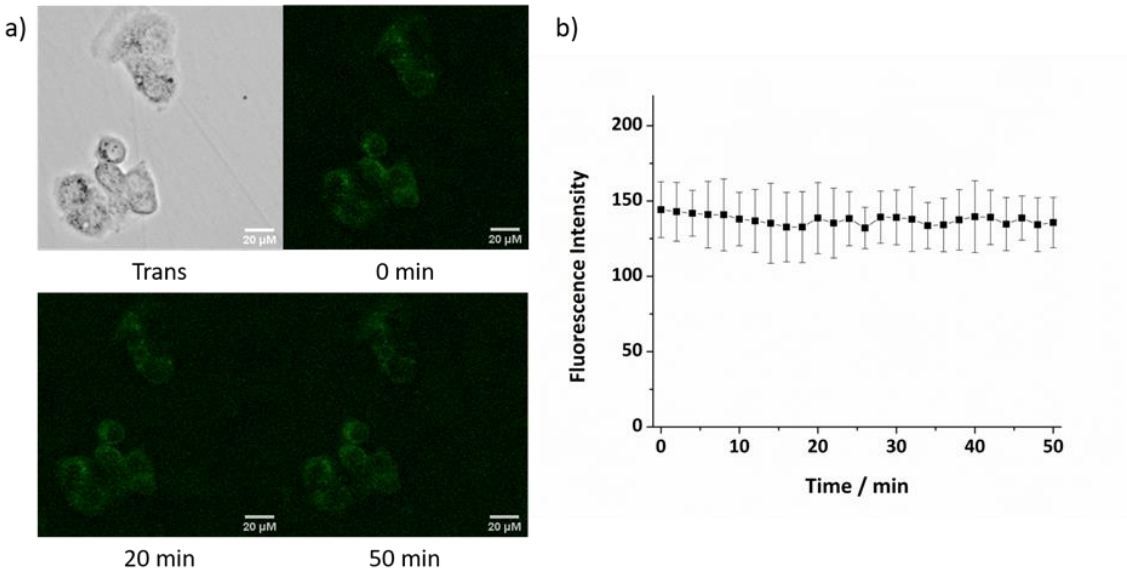

Figure 3.35 a) Fluorescence microscopy images and b) fluorescence intensity changes of probe **65** (20 µM) in HepG2 cells against time. (Scale bars = 20 µM).

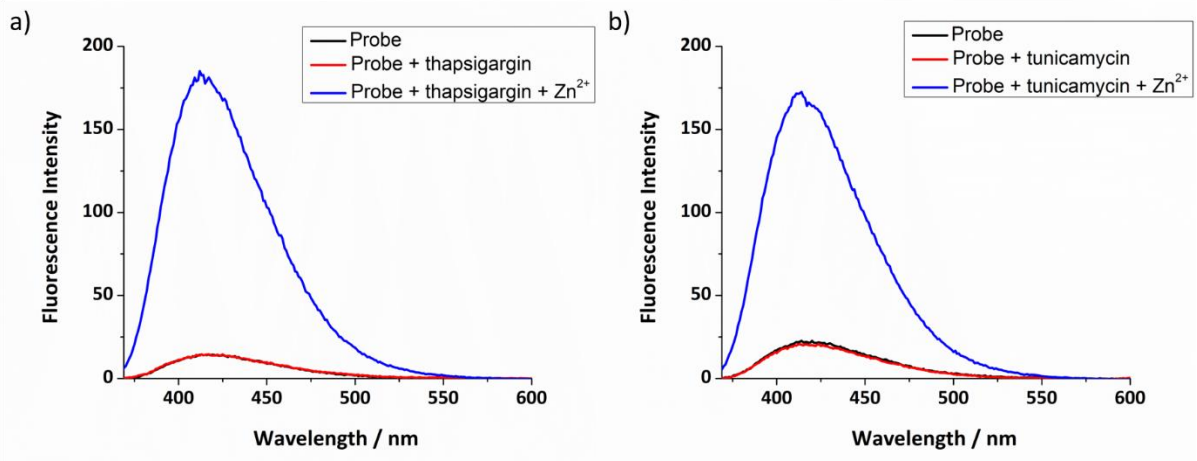

Figure 3.36 Fluorescence spectra of probe **65** (20 µM) and after addition of ER stress inducers (1 equivalent), subsequent addition of $ZnCl_2$ (1 equivalent), to show ER stress inducers do not affect fluorescence of probe **65** and its response to Zn^{2+}.

3.5 Summary

In conclusion, the ER localised fluorescent probes **65** and **67** have been developed to image mobile Zn^{2+} in the ER through the introduction of a simple sulfonylurea targeting group. They show a good fluorescence response to Zn^{2+}, high selectivity over biologically relevant competing cations, and can be used to detect Zn^{2+} over a wide range of pH *in vitro*. Their low toxicity, ER-targeting and ability to image mobile Zn^{2+} in different cell lines should allow them to be applied in imaging Zn^{2+} related biological processes in the ER. The fluorescence intensity of **65** was also shown to decrease under ER stress inducers, indicating that mobile Zn^{2+} levels are reduced. The ER localised probes may therefore provide a platform to understand the mechanisms cells use to respond to dysfunction of zinc homeostasis in the ER, and to develop a better understanding of the role of Zn^{2+} in the initiation and progression of related diseases.

Chapter 4 Golgi apparatus targeting fluorescent probes to image mobile Zn^{2+}

4.1 Probe design and synthesis

As described in Chapter 1 (see section 1.4.5), cysteine may be used as a targeting unit for the Golgi apparatus due to its propensity to accumulate in this organelle. However, cysteine as a targeting vector has its limitations in small molecule probes since it is rather hydrophilic,[127] and consequently not membrane permeable in some cases. Such poor membrane permeability has been classically addressed through the use of an ethyl ester protected carboxylic acid in the commercial probe Zinquin, which undergoes esterase catalysed cleavage *in cellulo*,[128] and this strategy has also been utilised to load cells with small molecule zinc probes.[42] To overcome the poor membrane permeability of cysteine, a trityl protecting group was used to increase the hydrophobicity of the probe in this work. Following passive diffusion into cells, the acid-labile trityl group is removed intracellularly releasing the free cysteine, which then anchors the probe to the Golgi apparatus (Figure 4.1).

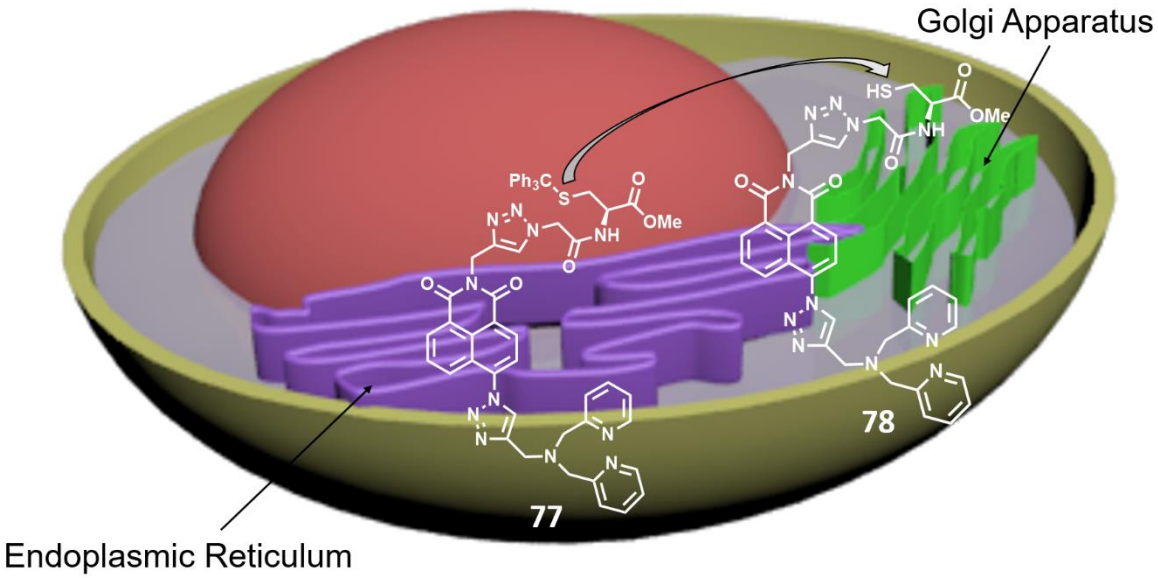

Figure 4.1 The structure of the trityl protected Zn^{2+} probe, **77**, and subsequent targeting of **78** to the Golgi apparatus after deprotection.

The synthetic route to both trityl protected probe **77** and its deprotected analogue **78** is shown in Scheme 4.1. Firstly, the cysteine thiol group was protected with a trityl group, as reported,[129] to give **72**. Following protection of the carboxylic acid as its methyl ester to give **73**,[130] a 'click' azide group was then introduced to give amide **74**. The trityl protected probe **77** was then readily obtained by stepwise double 'click' reactions following the originally reported procedures.[121] Although the deprotected probe **78** was ultimately ineffective *in cellulo*, as expected, it was also isolated for further characterisation and testing *in vitro*. All products were satisfactorily characterized by ^{1}H, ^{13}C NMR and IR spectroscopies, as well as high-resolution mass spectrometry.

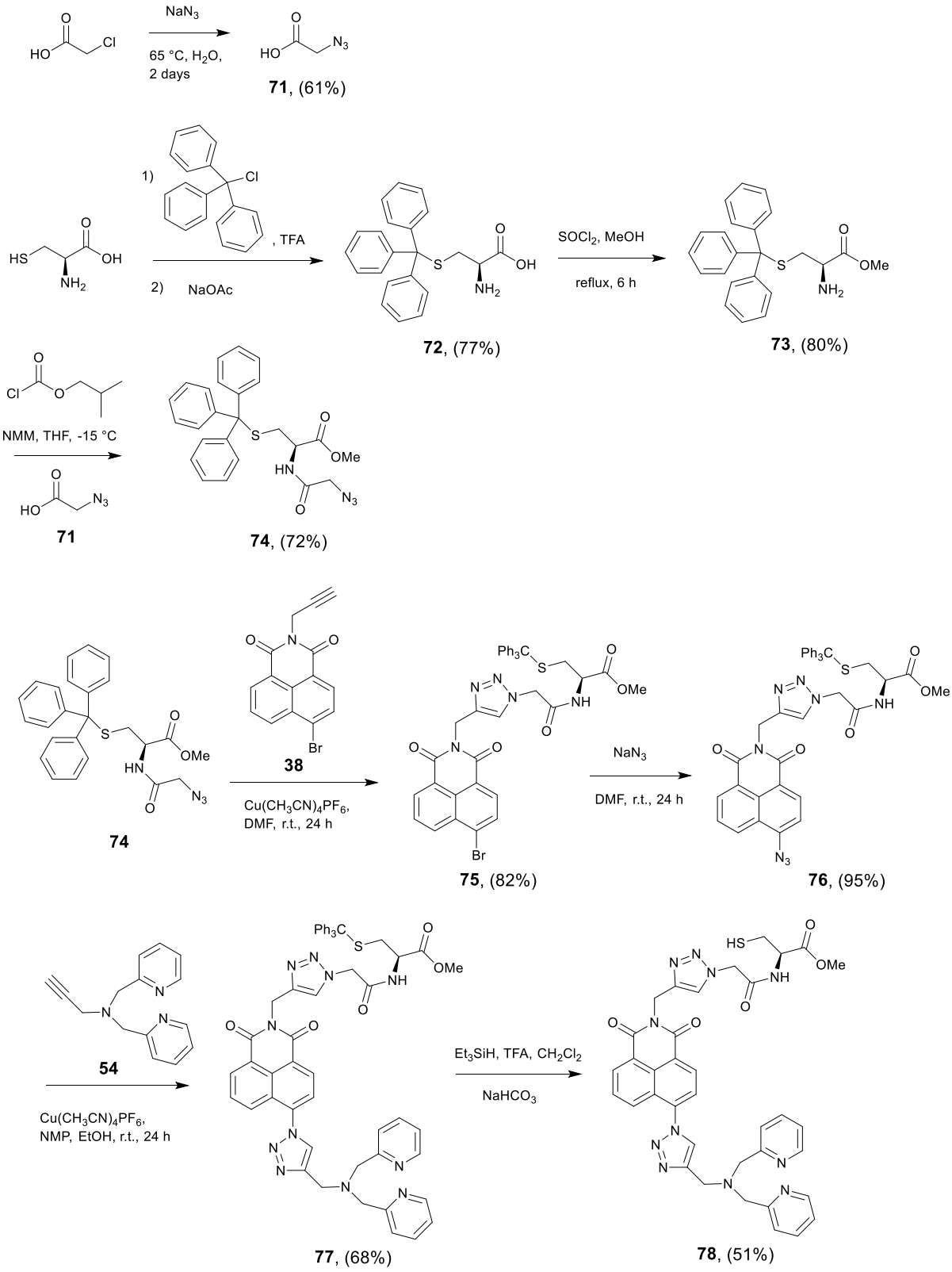

Scheme 4.1 The synthetic route towards **77** and **78**.

4.2 Photophysical studies

Fluorescence Zn^{2+} titration of probe **77** (Figure 4.3a) shows it has a modest switch on response to Zn^{2+} with a dissociation constant of 3.28 nM (Figure 4.4 and Table 4.1), which is consistent with previous values observed in related probes with this zinc-binding motif and fluorophore. A titration of probe **77** with different equivalents of Zn^{2+} by ^{1}H NMR spectroscopy (Figure 4.5 to 4.7) was performed to further demonstrate the Zn^{2+} association. As expected, the ligand DPEN and the bottom triazole (protons $H_{a\text{-}g}$) are clearly involved in Zn^{2+} binding. In addition, a number of other proton signals (protons $H_{h\text{-}l}$ and $H_{m\text{-}t}$) display changes to their chemical shifts with increasing equivalents of Zn^{2+}, however this is comparable to the behaviour seen previously by us in related systems,[131] (see also Section 5.3) which is attributed to global changes due to Zn^{2+} binding to DPEN. The de-protected probe **78** displays a similar switch on fluorescence response to Zn^{2+} (Figure 4.3b) and its dissociation constant was similarly determined to be 3.30 nM (Figure 4.4 and Table 4.1). However, it was unable to perform a titration by ^{1}H NMR spectroscopy in this case due to poor solubility.

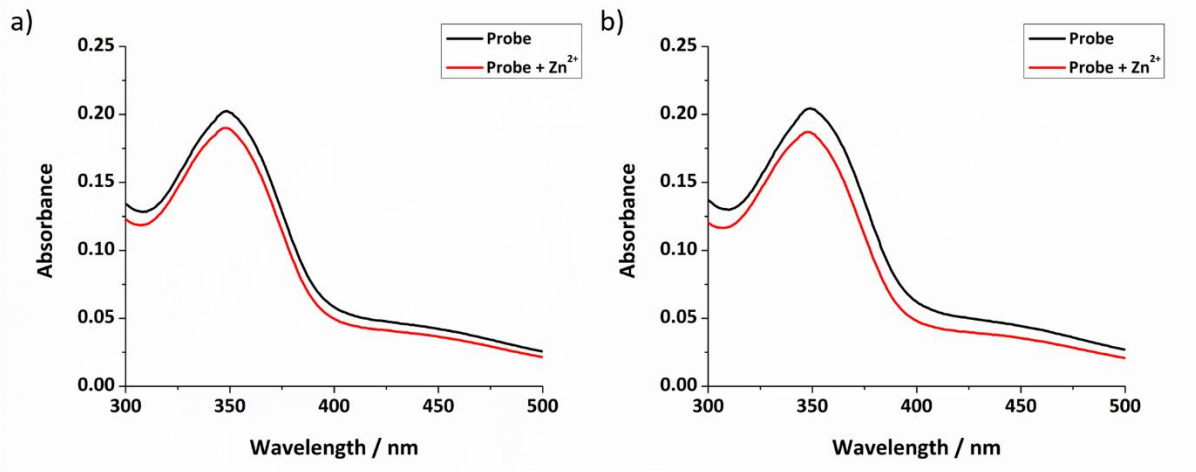

Figure 4.2 The UV-Vis spectra of a) **77** (20 µM) or b) **78** (20 µM) and when saturated with Zn^{2+} in 0.1 mM HEPES buffer at pH 7.4.

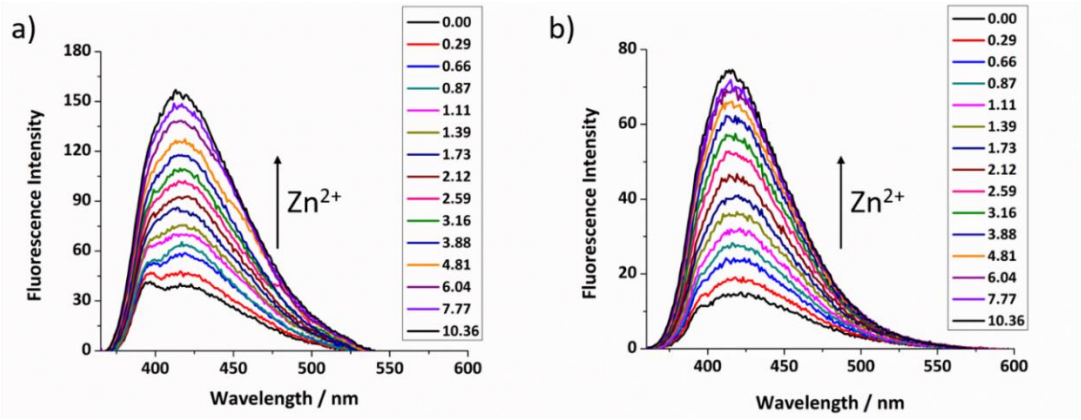

Figure 4.3 The fluorescence spectra of a) **77** (1 µM) and b) **78** (1 µM) at different concentrations of free Zn^{2+} (nM) in HEPES buffer solution (50 mM, pH 7.2, 0.1 M KCl). (λ_{ex} = 346 nm).

[Probe]	Probe **77**	Probe **78**
1 µM	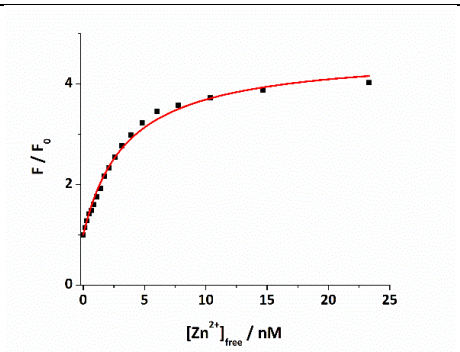	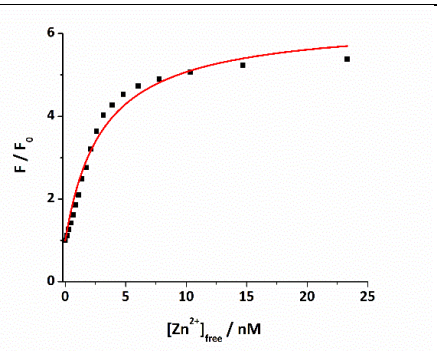
0.1 µM	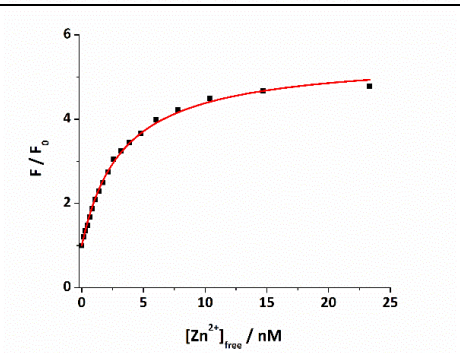	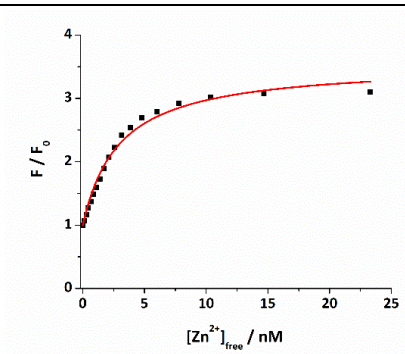
0.01 µM	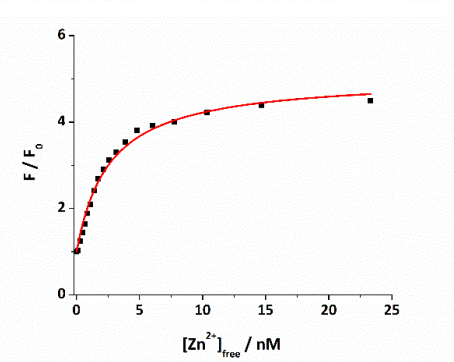	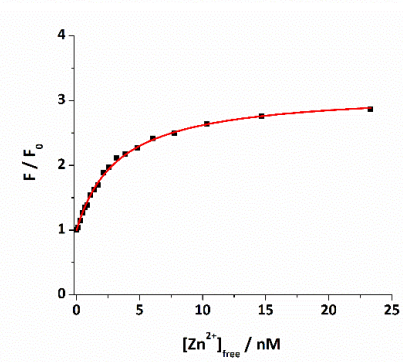

Figure 4.4 The non-linear curve fitting of the fluorescence intensity of **77** and **78** at different concentrations against different concentration of free Zn^{2+} to determine K_d applying Equation 7.1. (λ_{ex} = 346 nm, λ_{em} = 414 nm).

Table 4.1 The summary of K_d values for probes **77** and **78**.

	[probe] = 1 μM		[probe] = 0.1 μM		[probe] = 0.01 μM	
	K_d	R^2	K_d	R^2	K_d	R^2
77	3.52 ± 0.22 nM	0.9926	3.28 ± 0.12 nM	0.9972	2.59 ± 0.19 nM	0.9897
78	3.06 ± 0.35 nM	0.9760	2.96 ± 0.25 nM	0.9865	3.30 ± 0.13 nM	0.9971

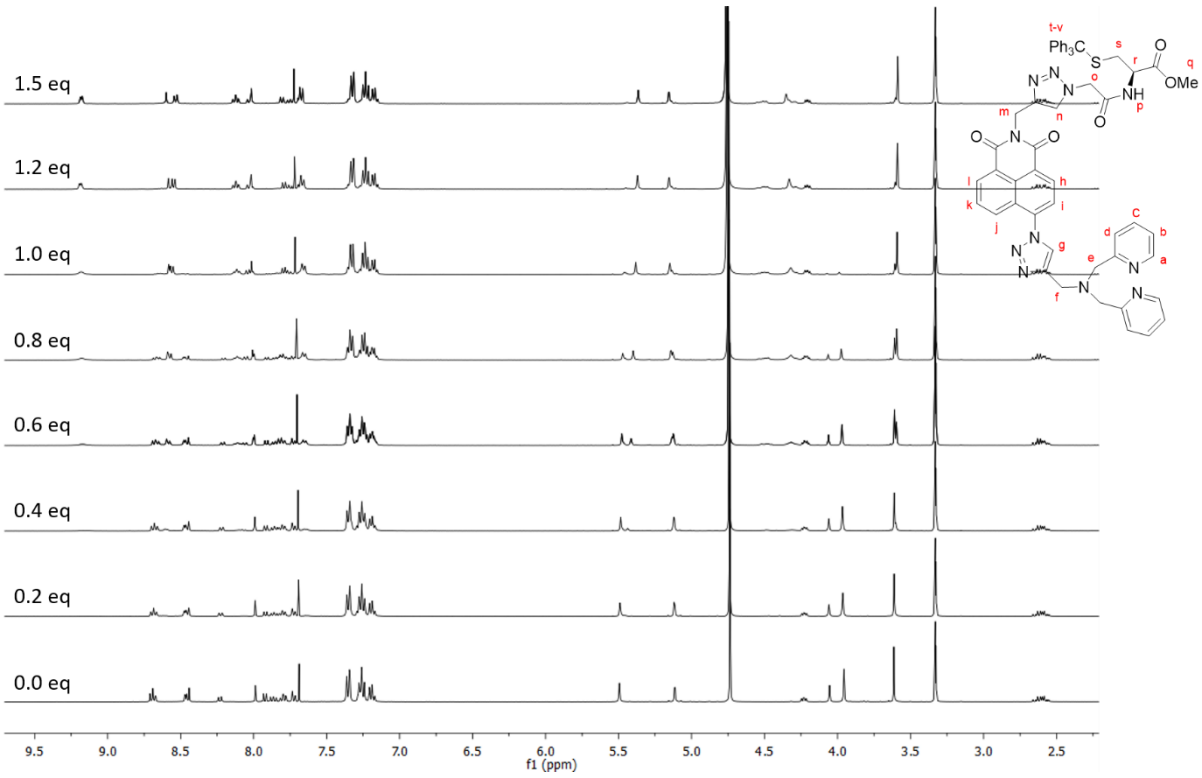

Figure 4.5 ^{1}H NMR titration spectra (whole range) of probe **77** (5 mM) with different equivalents of $ZnCl_2$ in CD_3OD.

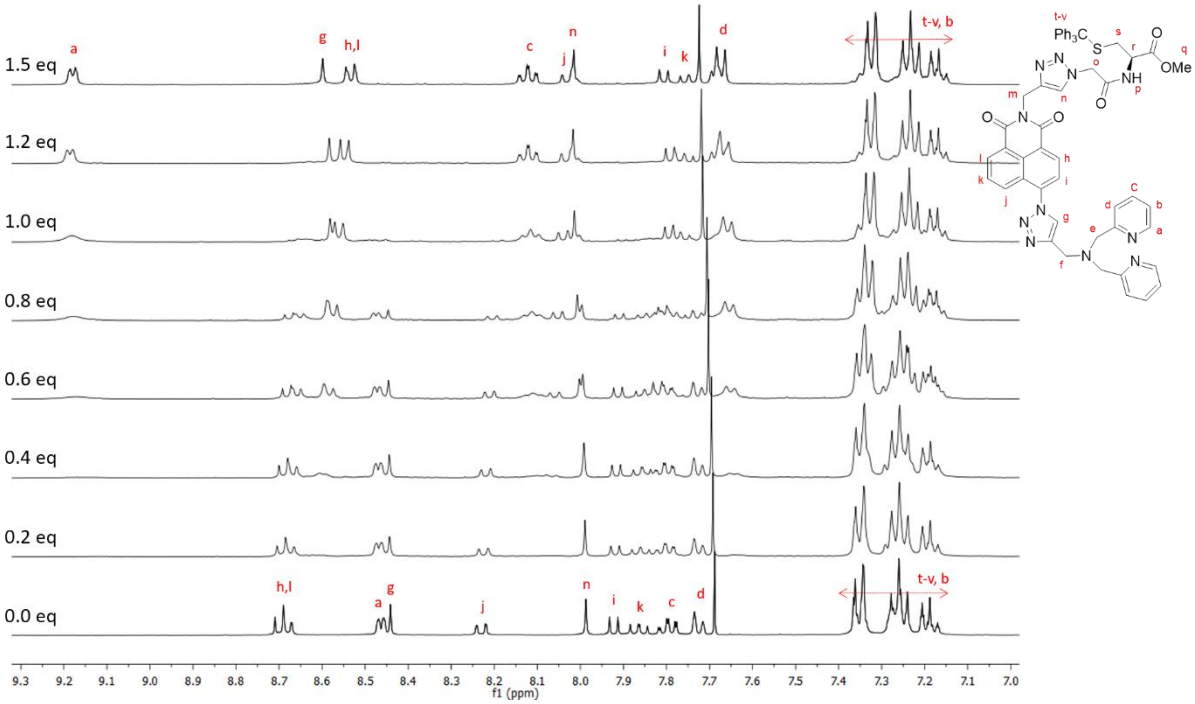

Figure 4.6 ^{1}H NMR titration spectra (aromatic range) of probe **77** (5 mM) with different equivalents of $ZnCl_2$ in CD_3OD.

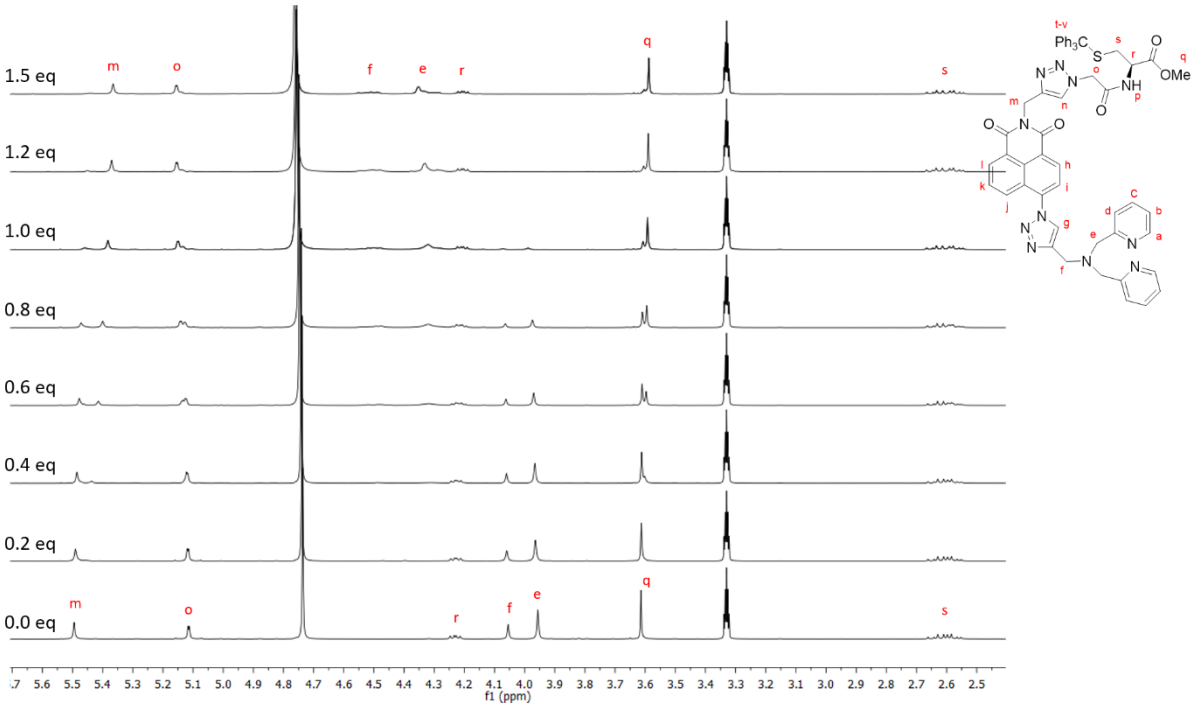

Figure 4.7 ^{1}H NMR titration spectra (range 2.50 - 5.60 ppm) of probe **77** (5 mM) with different equivalents of $ZnCl_2$ in CD_3OD.

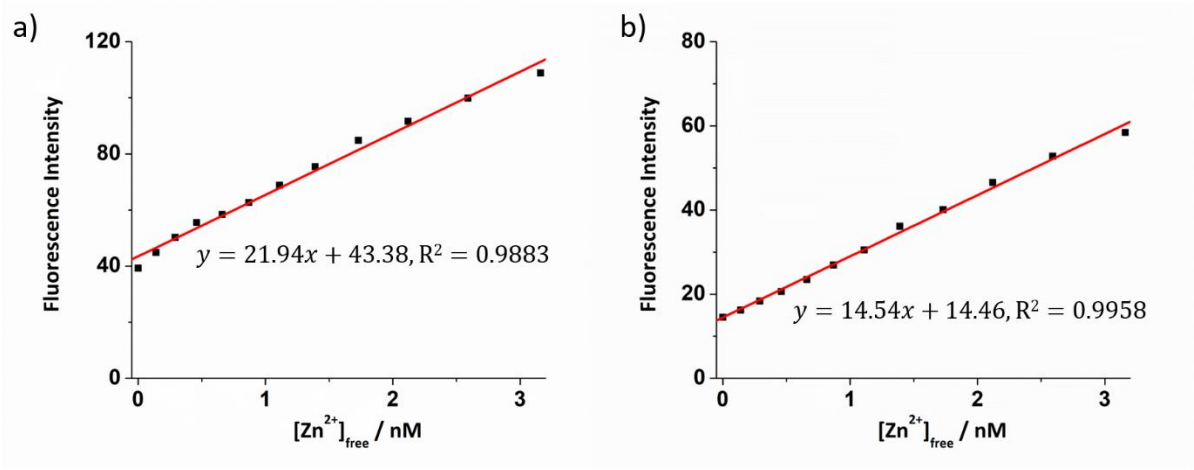

Figure 4.8 Fluorescence response of a) **77** (1 µM) and b) **78** (1 µM) against $[Zn^{2+}]_{free}$ in HEPES buffer solution (50 mM, pH 7.2, 0.1 M KCl).. (λ_{ex} = 346 nm, λ_{em} = 414 nm, slit widths: 5/5 nm).

The fluorescence quantum yield of probe **77** was measured and was determined to be 0.0014, while its complex with one equivalent Zn^{2+} only increased to 0.0073 (Figure 4.9a), which is much lower than that of the similar probes in the last chapter. This is likely to be due to the large amplitude vibrations of the trityl group, which increases non-radiative decay pathways. It is therefore unsurprising that when the trityl protecting group was removed, the quantum yield increased significantly and the quantum yield of probe **78** reached 0.046 and that of its complex with 1 equivalent of Zn^{2+} became 0.092 (Figure 4.9b). Given that the quantum yield ratio between **78** and **77** is 33 it was anticipated that if **77** proved to be cell membrane permeable and could be converted to **78** *in cellulo* that this feature could prove to be experimentally useful since a significant increase in fluorescence output after deprotection of **77** and consequent Golgi apparatus localisation of **78** should result.

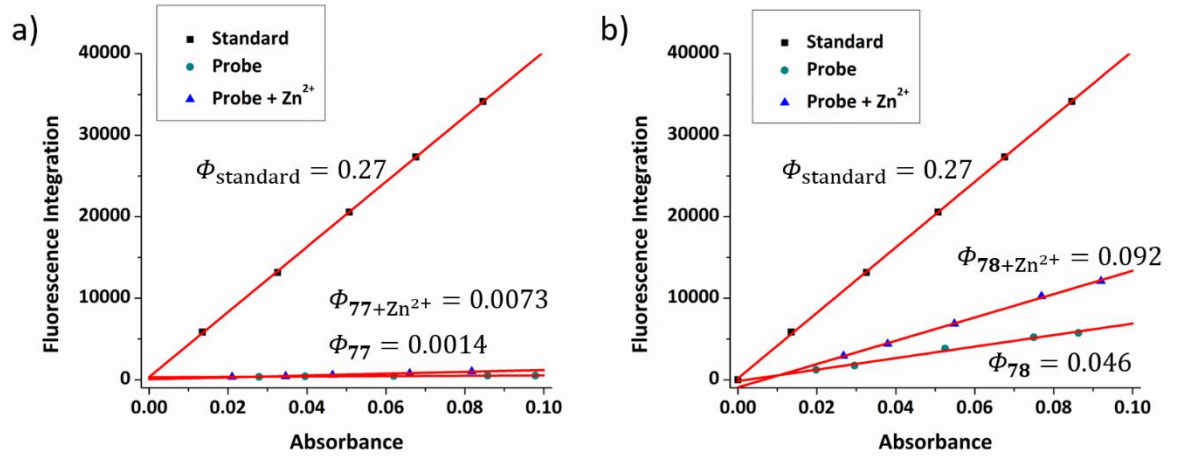

Figure 4.9 Linear plots for **77**, **78** and their Zn^{2+} complexes to obtain quantum yield values. Anthracene (Φ = 0.27 in ethanol) was used as a standard sample. (λ_{ex} = 346 nm, λ_{em} = 414 nm, slit widths: 5/5 nm).

The fluorescence of probe **77** and **78** at different pH values was measured. Through non-linear curve fitting (Figure 4.10) of the fluorescence emission integration against pH based on Equation 7.4, three pK_a values of each probe were determined: for **77** pK_{a1} = 3.95 ± 0.18, pK_{a2} = 7.24 ± 0.17 and pK_{a3} = 9.31 ± 0.35 whilst for **78** they were pK_{a1} = 4.24 ± 0.17, pK_{a2} = 6.13 ± 0.18 and pK_{a3} = 8.39 ± 0.34. After addition of Zn^{2+}, the fluorescence intensity increased in the pH range of 3.0-11.0 (Figure 4.11), which more than covers the biologically relevant range and suggests that the probe should perform well in the cellular environment.

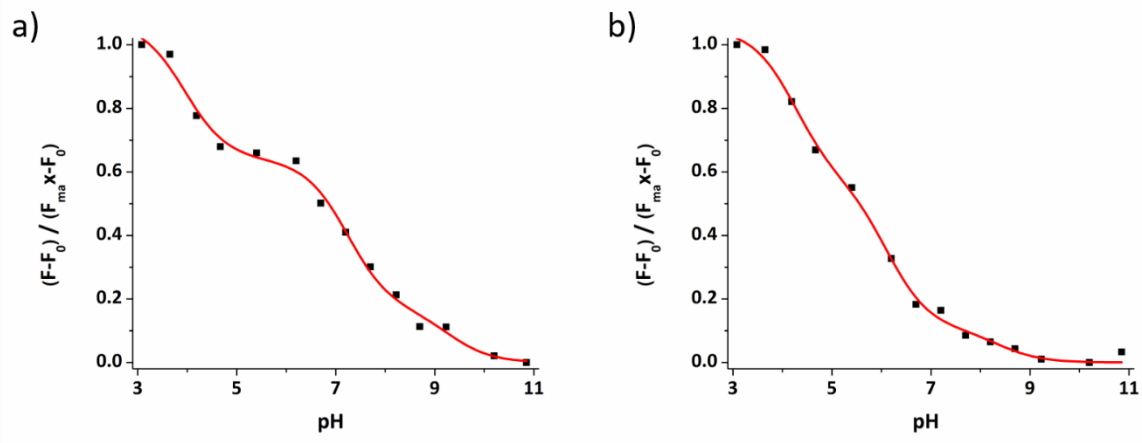

Figure 4.10 Normalized integrated fluorescence emission of a) **77** (10 µM) and b) **78** (10 µM) vs pH, the nonlinear curve fitting used to determine the apparent pK_a values.

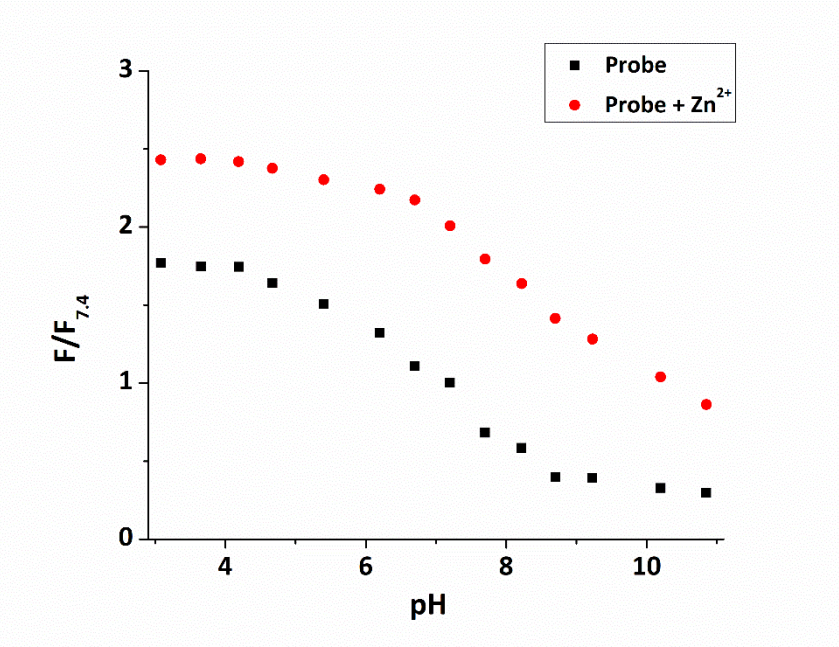

Figure 4.11 The pH profile of **77** (10 μM, black dots) and its complex with saturated Zn^{2+} (red dots). *F* is the fluorescence intensity observed, $F_{7.4}$ is the fluorescence intensity observed at pH 7.4. (λ_{ex} = 346 nm, λ_{em} = 414 nm, slit widths: 5/5 nm).

To specifically study the fluorescent stability of **77**, time-dependent fluorescence measurements were undertaken at a range of cellularly relevant pH.[132] The probe was stirred in PBS buffer solution at a range of different pH values and its fluorescence response measured after 1, 6, 12 and 24 hours (Figure 4.12). The fluorescence at pH 6.0 (the pH of the trans-Golgi) was higher than that at 7.2 (the pH of cytoplasm and endoplasmic reticulum) presumably due to the more acidic nature of the solutions, but all of them remained at the same level after 24 hours, indicating the probe to be stable at the relevant cellular pH values for prolonged periods. Furthermore, as no obvious fluorescence increase was observed with time under the acidic conditions, it also suggests that there is no *S*-trityl deprotection in solution at these pH values, indicating that any deprotection that may occur *in cellulo* is likely to be metabolic, rather than protic, in nature.

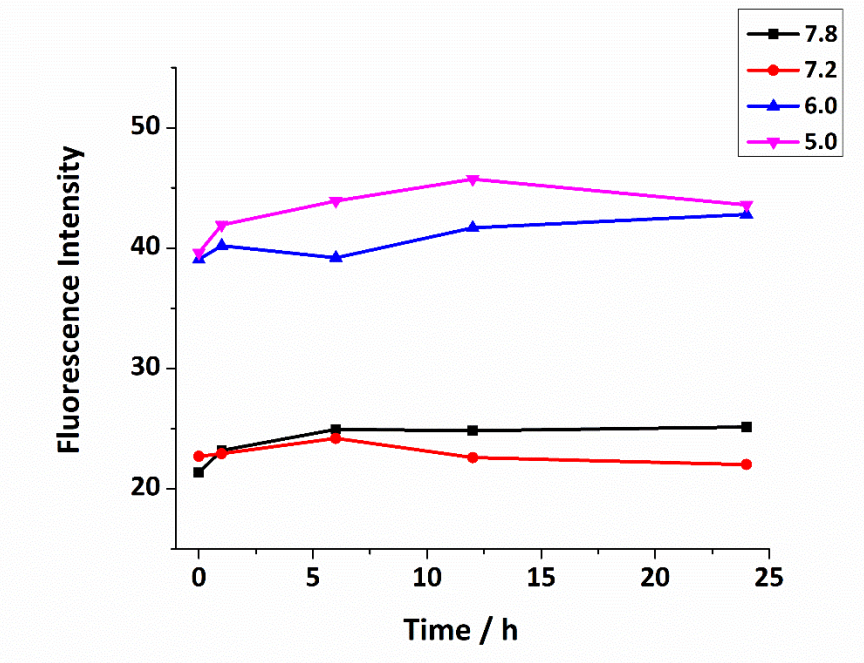

Figure 4.12 The time-dependent fluorescence intensity of **77** (10 μM) stirred in PBS buffer solution at different pH.

The selectivity of the probe was investigated in the presence of a range of other cations. As shown in Figure 4.13a, the addition of a variety of cations has little or no effect on the fluorescence response of **77**, even Cd^{2+}. After subsequent addition of Zn^{2+}, the probe **77** was still quenched in the presence of Co^{2+}, Cu^{2+} and Ni^{2+}, but this is not concerning as these cations are not abundant in free forms in biological environments. Probe **78** (Figure 4.13b) shows broadly the similar selective properties to **77**. For the majority of cations tested, particularly the physiologically relevant cations (Na^{+}, K^{+}, Mg^{2+}, Ca^{2+}), both probes displayed nearly complete recovery after addition of Zn^{2+}, meaning it has the potential to be applied *in cellulo* to image Zn^{2+}.

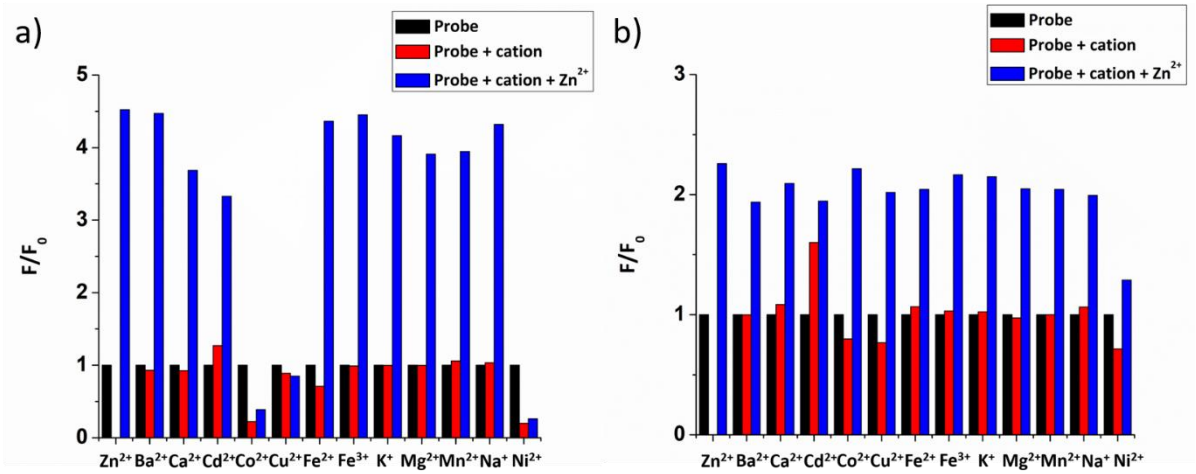

Figure 4.13 Metal ion selectivity of a) **77** and b) **78** in 0.1 mM HEPES buffer solution at pH 7.4. Average normalized fluorescence intensities for probe (10 μM) (black bars), after addition of 5 equivalents of various cations (red bars), followed by addition of $ZnCl_2$ (blue bars).

4.3 DFT calculations

DFT calculations were carried out to study the association between probe and Zn^{2+} *in silico* (Figure 4.14 and Figure 4.15). The calculated optimized structures supported the bottom triazole groups being involved in Zn^{2+} binding in addition to the DPEN ligands, which was also observed by ^1H NMR titrations.

In order to establish the excitation and emission profiles of the probe, TDDFT simulations were again undertaken. The calculated absorption energy from ground state S_0 to excited state S_1, and the emission energy from S_1 to S_0 were in agreement with the experimental data (Table 4.2 and Table 4.3). The S_1-S_0 electron density transition map (Figure 4.16 to Figure 4.17) shows the electron changes mainly occur at the naphthalimide moiety and the vicinal triazole. After binding with Zn^{2+}, there is only a slight decrease of electron density on the triazole, and the oscillator strength is not significantly affected compared to the free probe. Therefore, the emission increase of the complex again appears to be related to a reduced decay through nonradiative pathways after binding with Zn^{2+}. The stabilization of the complex hinders large amplitude vibrations in the vicinity of the fluorophore, which hampers access to nonradiative

mechanisms and increases the quantum yield of fluorescence. The restriction of intramolecular rotations can also hinder the access to low energy conical intersections associated with ultrafast decay to the ground state.

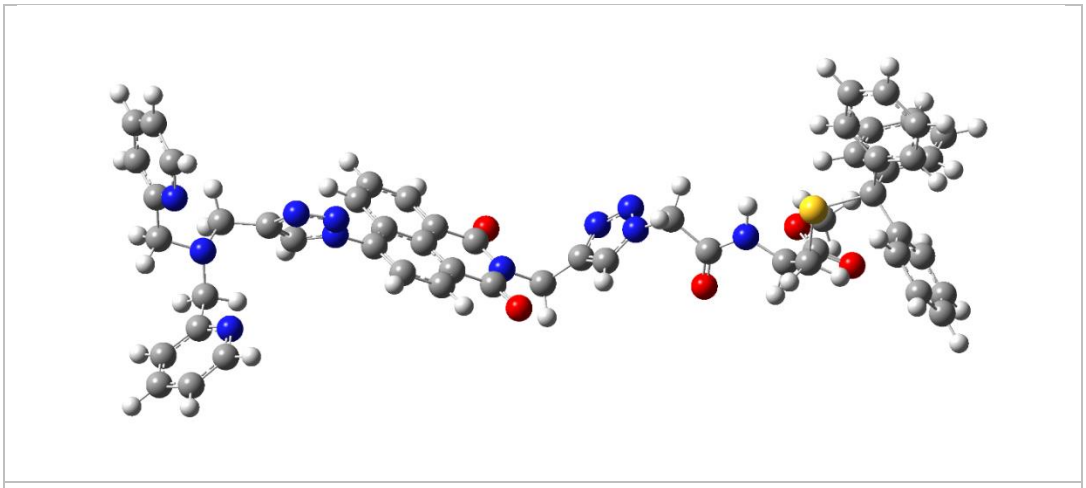

Probe **77**

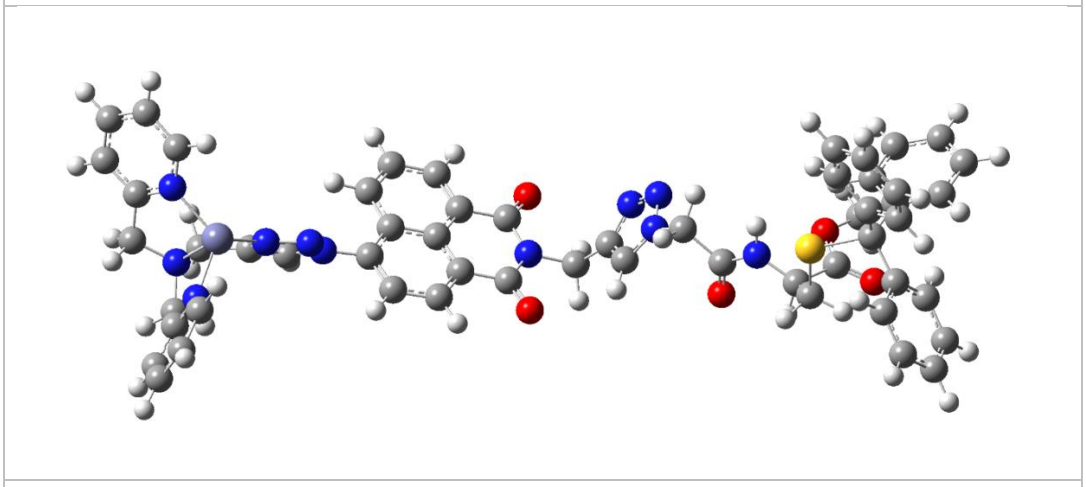

Complex with Zn^{2+}

Figure 4.14 The optimised structures of **77** and its complex with Zn^{2+}.

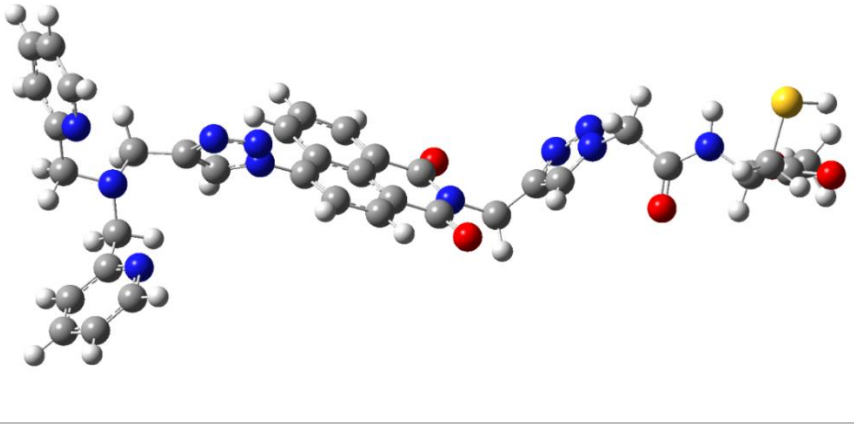

Probe **78**

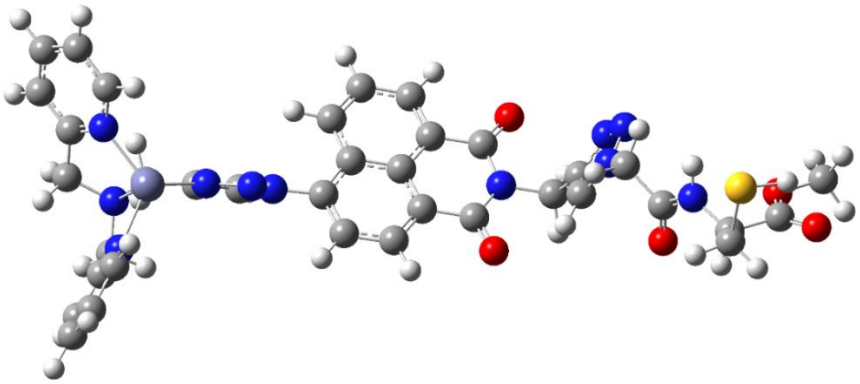

Complex with Zn^{2+}

Figure 4.15 The optimized structures of **78** and its complex with Zn^{2+}.

Table 4.2. Comparison of the experimental data with the calculated result of vertical electronic excitation energies (eV) and the emission from S_1 to ground state of **77** and its Zn^{2+} complex.

	Electronic transition	Energy (eV)	Wavelength (nm)	Oscillator strength (f)	Experimental data
77					
Absorption	$S_0 \rightarrow S_1$	3.90	318	0.5434	3.58 eV/346 nm
	$S_0 \rightarrow S_2$	4.26	291	0.0480	
	$S_0 \rightarrow S_3$	4.38	283	0.0003	
	$S_0 \rightarrow S_4$	4.66	266	0.0007	
	$S_0 \rightarrow S_5$	4.84	256	0.0190	
	$S_0 \rightarrow S_6$	4.93	251	0.0200	
Emission	$S_1 \rightarrow S_0$	3.14	395	0.7226	2.99 eV/414 nm
Complex of **77** with Zn^{2+}					
Absorption	$S_0 \rightarrow S_1$	3.96	313	0.5070	3.58 eV/346 nm
	$S_0 \rightarrow S_2$	4.26	291	0.0552	
	$S_0 \rightarrow S_3$	4.33	286	0.0003	
	$S_0 \rightarrow S_4$	4.60	270	0.0003	
	$S_0 \rightarrow S_5$	4.94	251	0.0327	
	$S_0 \rightarrow S_6$	5.29	234	0.0027	
Emission	$S_1 \rightarrow S_0$	3.23	384	0.6630	2.99 eV/414 nm

Table 4.3. Comparison of the experimental data with the calculated result of vertical electronic excitation energies (eV) and the emission from S_1 to ground state of **78** and its Zn^{2+} complex.

	Electronic transition	Energy (eV)	Wavelength (nm)	Oscillator strength (f)	Experimental data
78					
Absorption	$S_0 \rightarrow S_1$	3.89	319	0.5438	3.58 eV/346 nm
	$S_0 \rightarrow S_2$	4.26	291	0.0476	
	$S_0 \rightarrow S_3$	4.38	283	0.0003	
	$S_0 \rightarrow S_4$	4.67	265	0.0007	
	$S_0 \rightarrow S_5$	4.84	256	0.0175	
	$S_0 \rightarrow S_6$	4.92	252	0.0226	
Emission	$S_1 \rightarrow S_0$	3.14	395	0.7241	2.99 eV/414 nm
Complex of **78** with Zn^{2+}					
Absorption	$S_0 \rightarrow S_1$	3.96	313	0.4989	3.58 eV/346 nm
	$S_0 \rightarrow S_2$	4.25	291	0.0554	
	$S_0 \rightarrow S_3$	4.33	286	0.0001	
	$S_0 \rightarrow S_4$	4.61	269	0.0002	
	$S_0 \rightarrow S_5$	4.90	253	0.0320	
	$S_0 \rightarrow S_6$	5.27	235	0.0065	
Emission	$S_1 \rightarrow S_0$	3.21	386	0.6742	2.99 eV/414 nm

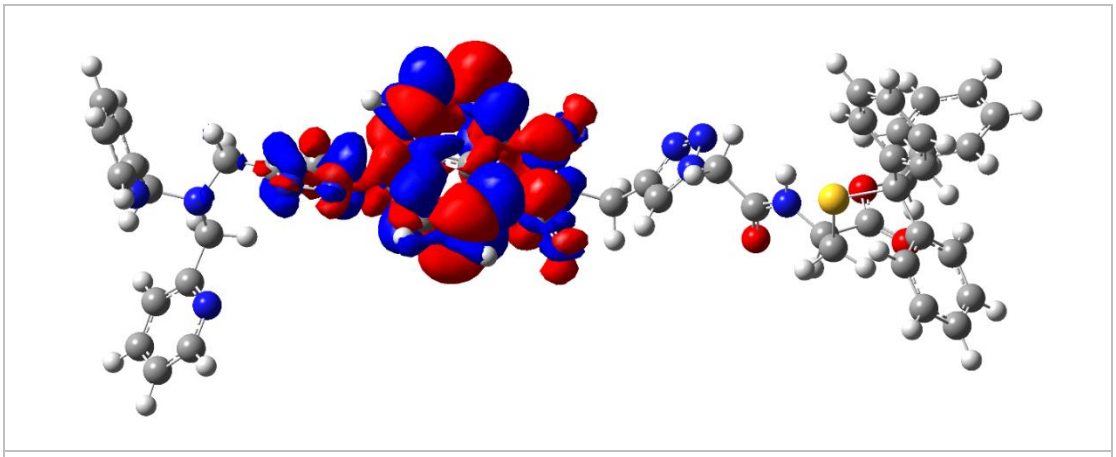

Probe **77**

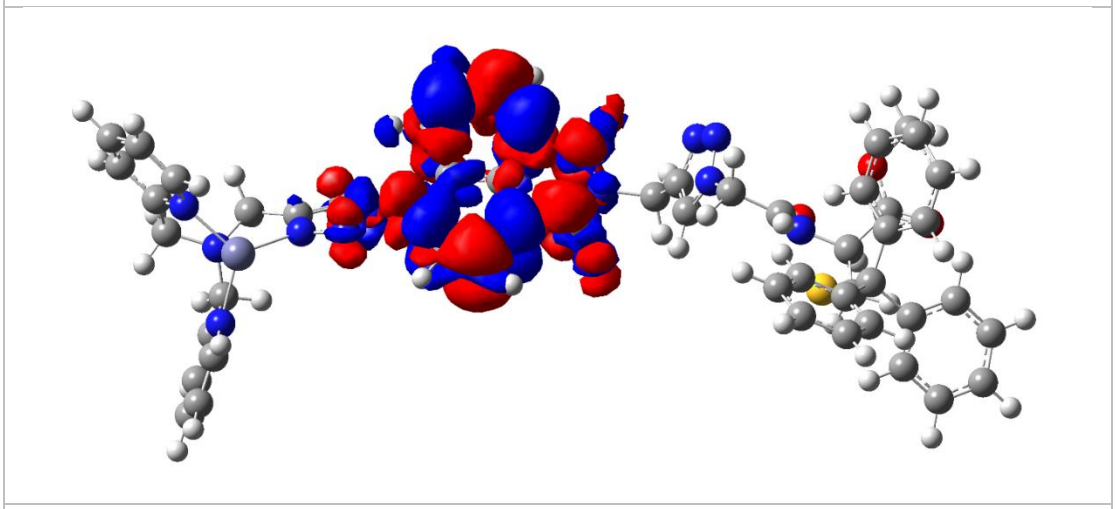

Complex with Zn^{2+}

Figure 4.16. S_1-S_0 electron density map for probe **77** and its complex with Zn^{2+} (S_1 minima). Red represents positive densities and blue negative values.

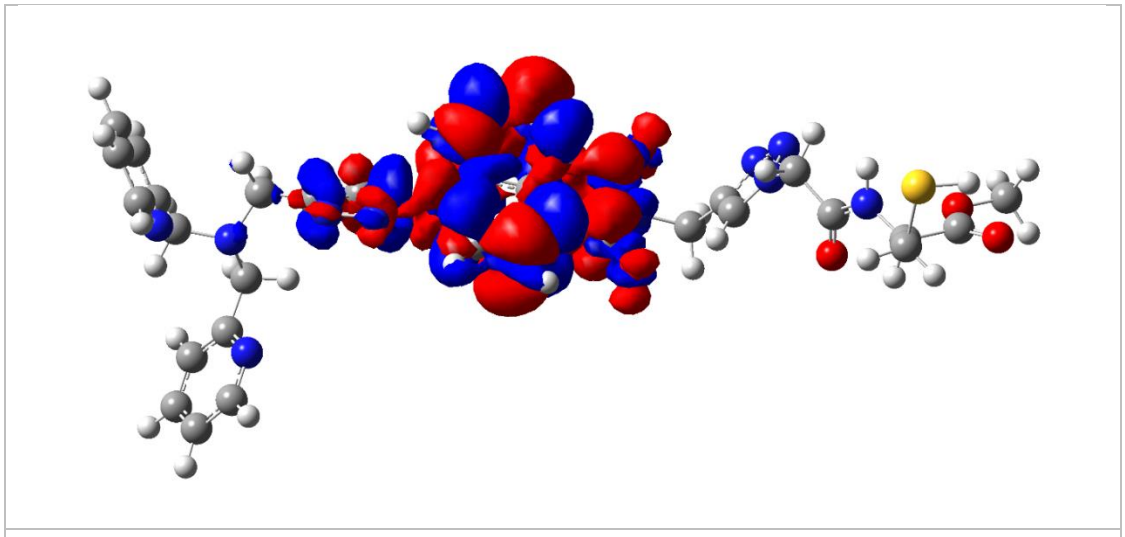

Probe **78**

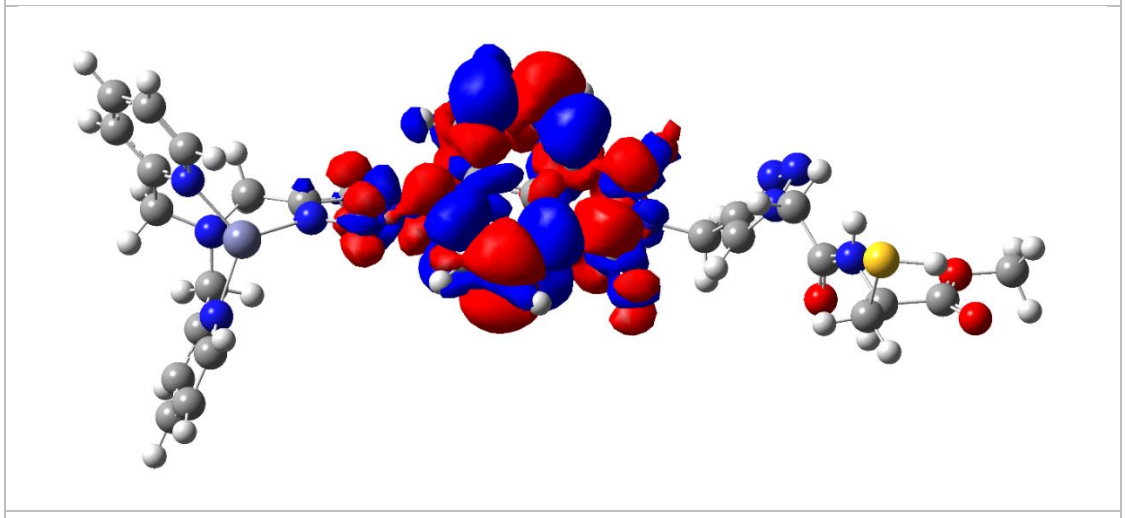

Complex with Zn^{2+}

Figure 4.17. S_1-S_0 electron density map for probe **78** and its complex with Zn^{2+} (S_1 minima). Red represents positive densities and blue negative values.

4.4 *In cellulo* tests

4.4.1 Cell toxicity and permeability of probes

As the probes showed promising photophysical properties in solution, their application in cells was also assessed. Firstly, the toxicity of **77** and **78** was measured through the AlamarBlue cell viability assay, and after 24 hours' incubation with both probes, the viability of HeLa cells (Figure 4.18) did not show any obvious decrease even with probe concentrations up to 50 µM, indicating that they are not cytotoxic. However, initial fluorescence microscopy tests of the

probes in HeLa cells (Figure 4.19) showed that the cells incubated with **78** do not display any intracellular fluorescence, indicating that **78**, as expected due to its hydrophilic nature, is not membrane permeable. In contrast, cells incubated with **77** clearly showed evidence of probe internalization. Therefore, further cell experiments only focused on probe **77**.

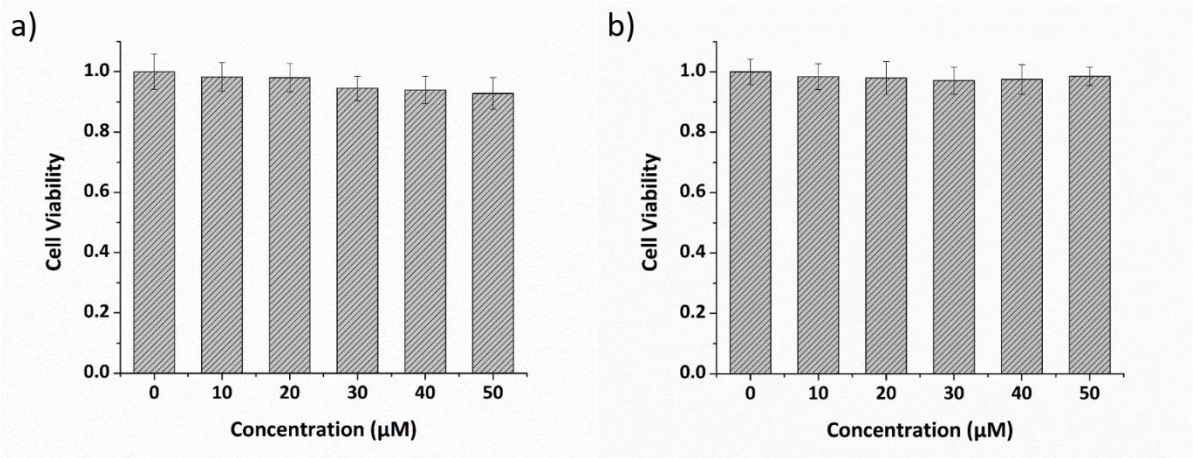

Figure 4.18 The HeLa cell viability against probe a) **77** and b) **78** at different concentrations.

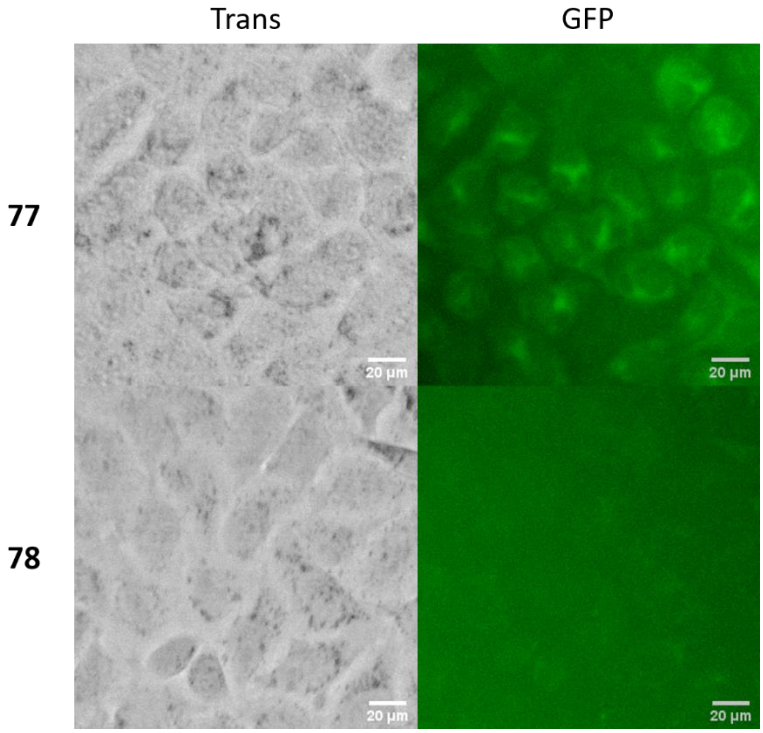

Figure 4.19 Fluorescence microscopy images of HeLa cells after 10 minutes' treatment with probes **77** and **78** (10 μM) without any processing clearly showing internalisation of **77** and not **78**. (GFP filter: λ_{ex} = 470/30 nm, λ_{em} = 530/50 nm, scale bars = 20 μm).

4.4.2 Subcellular localisation

To test the Golgi apparatus targeting ability of **77**, HeLa cells were incubated in its presence for 1 hour and were then co-incubated with different organelle tracker dyes for a certain time period (normally 15-30 minutes). This revealed that the fluorescence response of **77** was almost exclusively only observed in the endoplasmic reticulum (ER) rather than the Golgi apparatus (Figure 4.20) and was of relatively low intensity. It was speculated that this was because the trityl protecting group was not removed in this time period *in cellulo* and that a longer incubation time was required to facilitate this and subsequent re-localisation into the Golgi apparatus. Indeed, this proved to be the case and when the incubation time was extended to 24 hours the fluorescent response showed a significant increase in intensity, with excellent co-localisation with Bodipy TR ceramide observed, a commercial Golgi tracker red reagent, with no evidence of ER fluorescence as had been the case for the shorter incubation periods. The same result was also observed in the MCF-7 cell line (Figure 4.21), suggesting this behaviour to be generic to some extent.

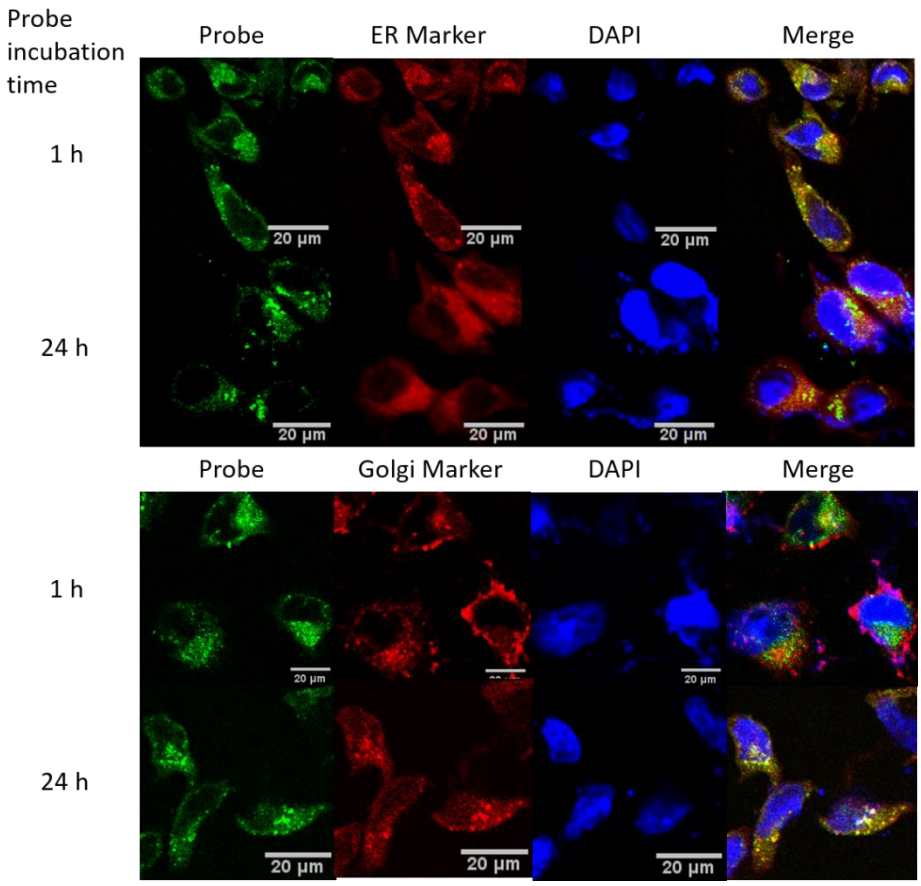

Figure 4.20 Confocal microscopy images of HeLa cells after treatment with **77** (10 µM, λ_{ex} = 488 nm, λ_{em} = 509 nm) for 1 h or 24 h, compared to ER marker or Golgi marker (λ_{ex} = 594 nm, λ_{em} = 620 nm). (Scale bars = 20 µm).

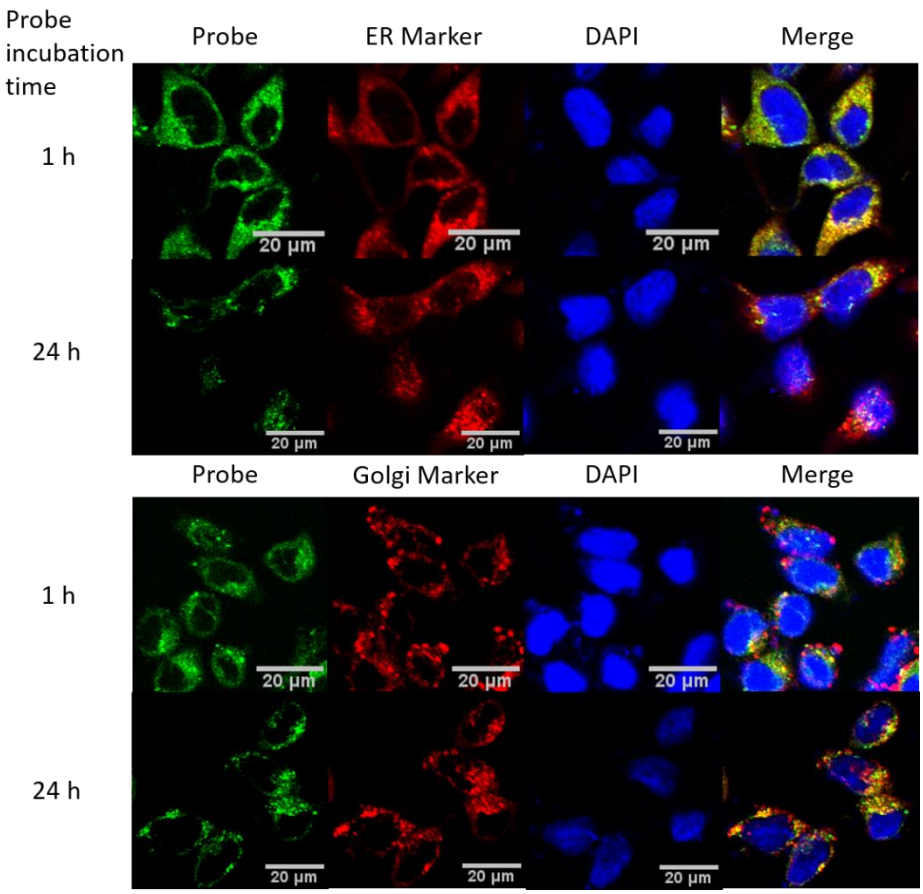

Figure 4.21 Confocal microscopy images of MCF-7 cells after treatment with **77** (10 µM, λ_{ex} = 488 nm, λ_{em} = 509 nm) for 1 h or 24 h, compared to ER marker or Golgi marker (λ_{ex} = 594 nm, λ_{em} = 620 nm). (Scale bars = 20 µm).

The Pearson's correlation coefficient was measured by comparing probe **77** (GFP channel) after 24 hours of incubation to different organelle trackers (RFP channel). In HeLa cells (Figure 4.22), the fluorescence of **77** showed excellent correlation with that of Bodipy TR ceramide, giving a Pearson's coefficient of 0.92. The values of negative control groups were much lower, with values of 0.42, 0.38 and 0.59 when compared to commercial ER, Mito and Lyso tracker red dyes respectively. Similar results were obtained in the breast cancer cell line MCF-7 (Figure 4.23) and a sweat gland tissue cell line EC23 (Figure 4.24), revealing the probe's general Golgi-targeting capability.

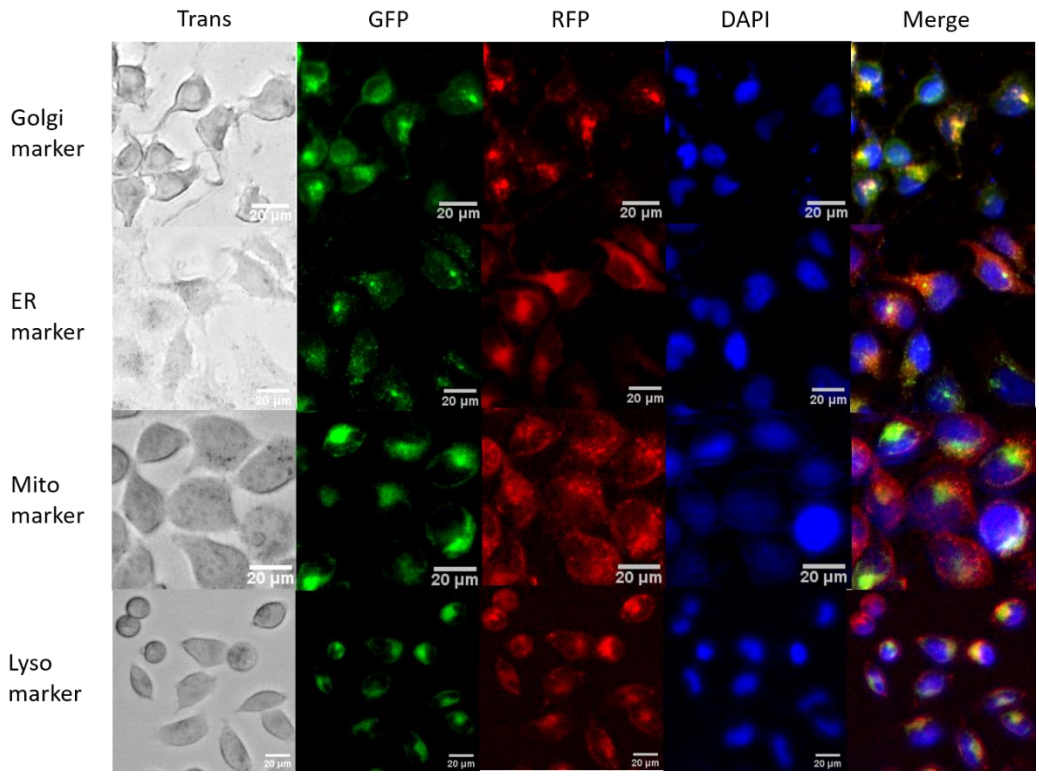

Figure 4.22 The colocalisation images of HeLa cells incubated with probe **77** (10 μM, GFP filter: λ_{ex} = 470/30 nm, λ_{em} = 530/50 nm) and organelle tracker red dyes (RFP filter: λ_{ex} = 530/40 nm, λ_{em} = 605/55 nm). (Scale bars = 20 μm).

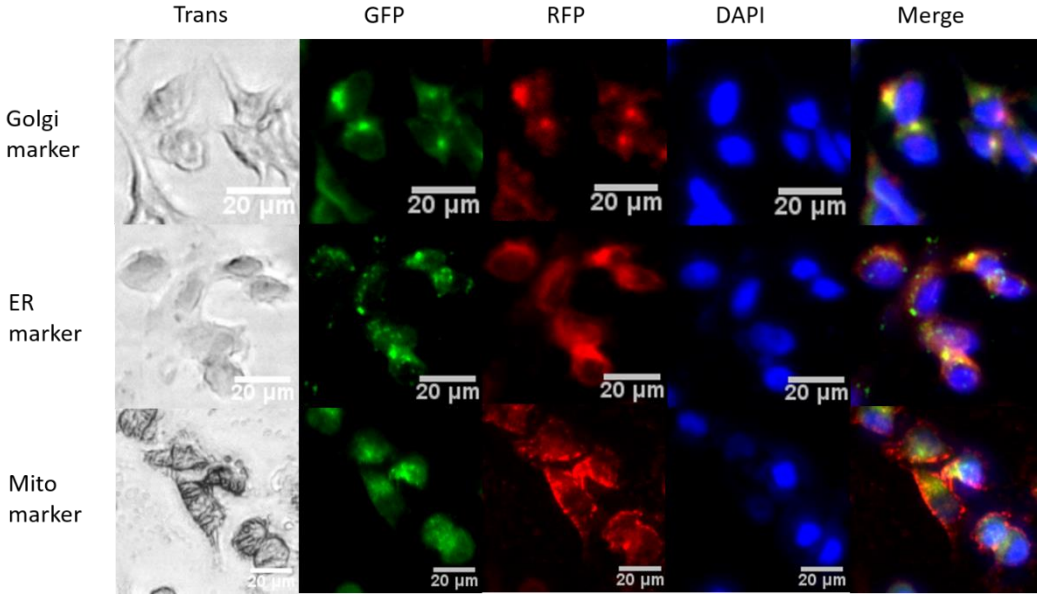

Figure 4.23 The colocalisation images of MCF-7 cells incubated with probe **77** (10 μM, GFP filter: λ_{ex} = 470/30 nm, λ_{em} = 530/50 nm) and organelle tracker red dyes (RFP filter: λ_{ex} = 530/40 nm, λ_{em} = 605/55 nm). (Scale bars = 20 μm). Pearson's correlation coefficients were 0.86, 0.54 and 0.34 compared to Golgi-tracker red, ER-tracker red and Mito-tracker red, respectively.

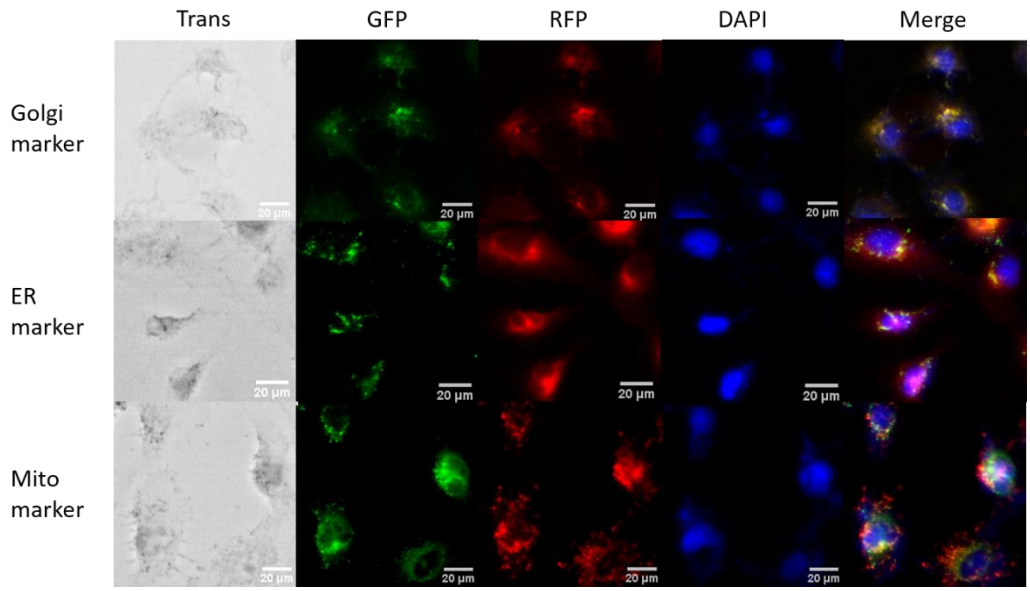

Figure 4.24 The colocalisation images of EC23 cells incubated with probe **77** (10 μM, GFP filter: λ_{ex} = 470/30 nm, λ_{em} = 530/50 nm) and organelle tracker red dyes (RFP filter: λ_{ex} = 530/40 nm, λ_{em} = 605/55 nm). (Scale bars = 20 μm). Pearson's correlation coefficients were 0.92, 0.52 and 0.60 compared to Golgi-tracker red, ER-tracker red and Mito-tracker red, respectively.

4.4.3 Zn^{2+} response in cells

The response of probe **77** in cells was recorded to demonstrate its ability to respond to variation in Zn^{2+} levels in the Golgi apparatus. As shown in Figure 4.25, the fluorescence of **77** in HeLa cells increased significantly after the addition of zinc pyrithione indicating it has a switch on fluorescence response to Zn^{2+} *in cellulo*. When TPEN was added, the fluorescence was almost completely quenched. Similar results were also observed in MCF-7 (Figure 4.26) and EC23 cell lines (Figure 4.27), and the fluorescence intensity read from the images is shown in Figure 4.28.

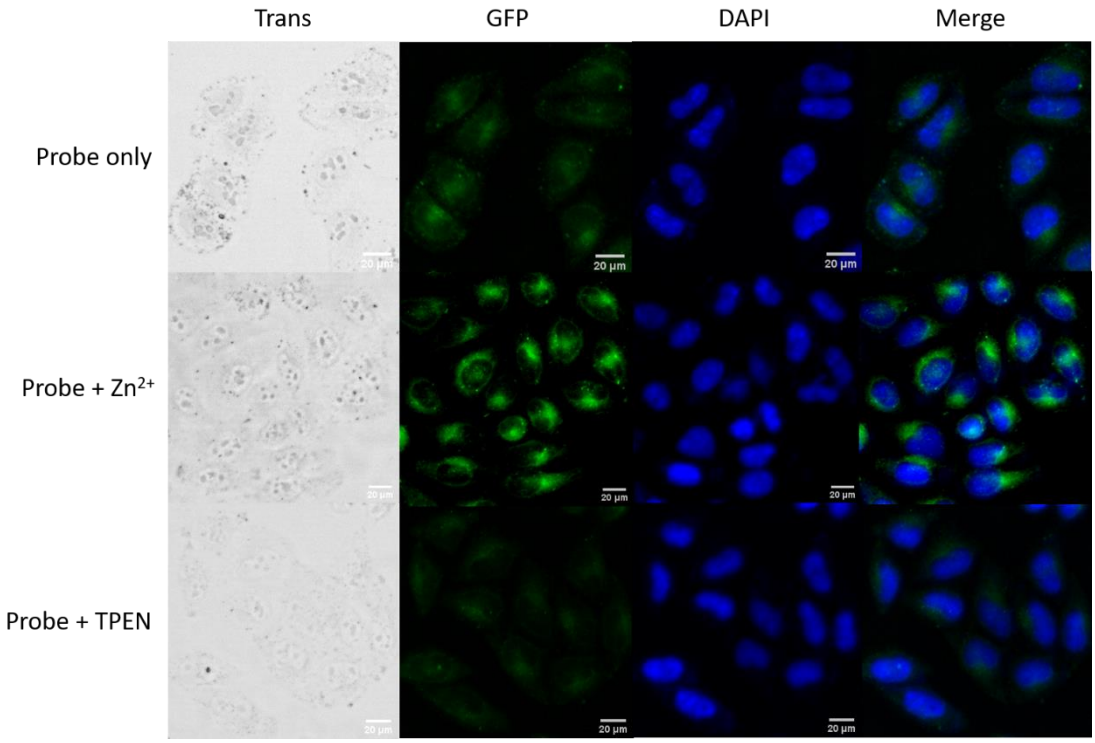

Figure 4.25 Fluorescence microscopy images of HeLa cells treated with **77** (10 µM), **77** (10 µM) with zinc pyrithione (50 µM), and **77** (10 µM) with TPEN (50 µM). (Scale bars = 20 µm, GFP filter: λ_{ex} = 470/30 nm, λ_{em} = 530/50 nm).

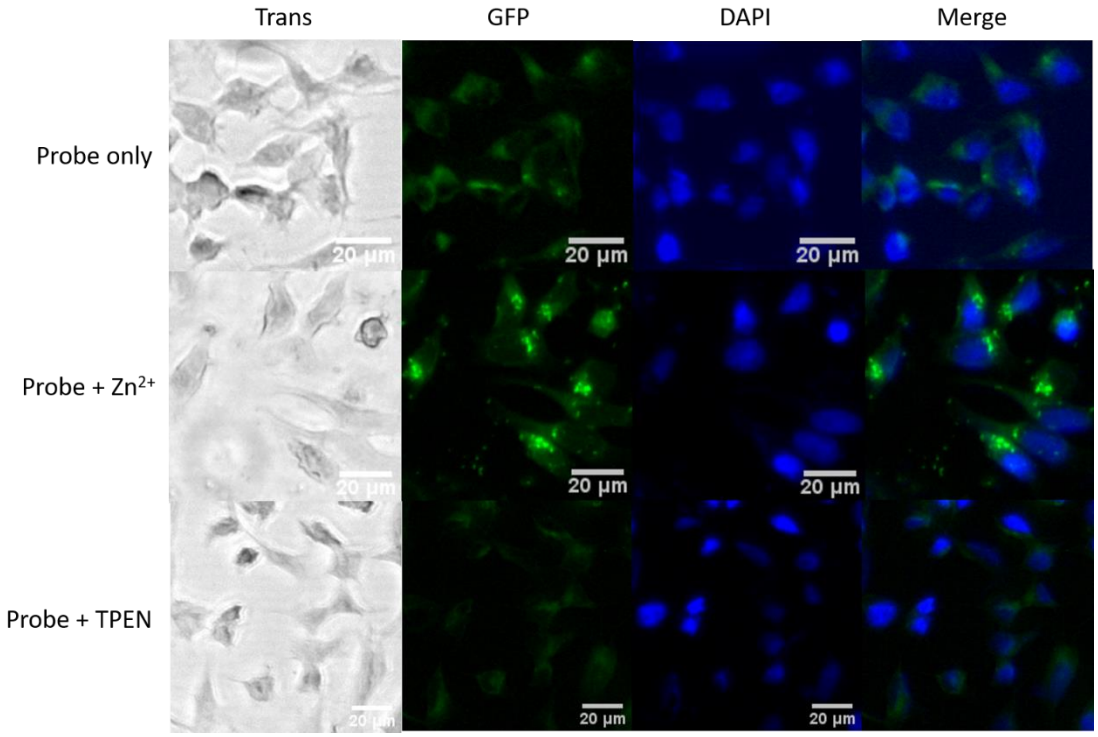

Figure 4.26 Fluorescence microscopy images of MCF-7 cells treated with **77** (10 µM), **77** (10 µM) with zinc pyrithione (50 µM), and **77** (10 µM) with TPEN (50 µM). (Scale bars = 20 µm, GFP filter: λ_{ex} = 470/30 nm, λ_{em} = 530/50 nm).

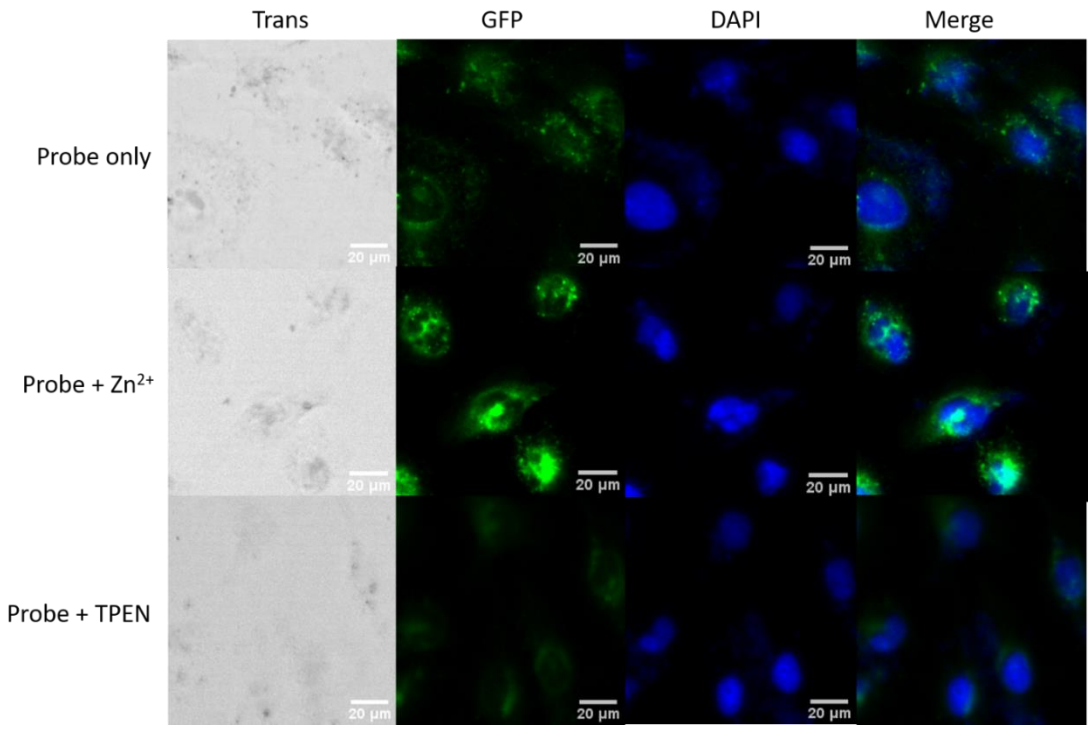

Figure 4.27 Fluorescence microscopy images of EC23 cells treated with **77** (10 μM), **77** (10 μM) with zinc pyrithione (50 μM), and **77** (10 μM) with TPEN (50 μM). (Scale bars = 20 μm, GFP filter: λ_{ex} = 470/30 nm, λ_{em} = 530/50 nm).

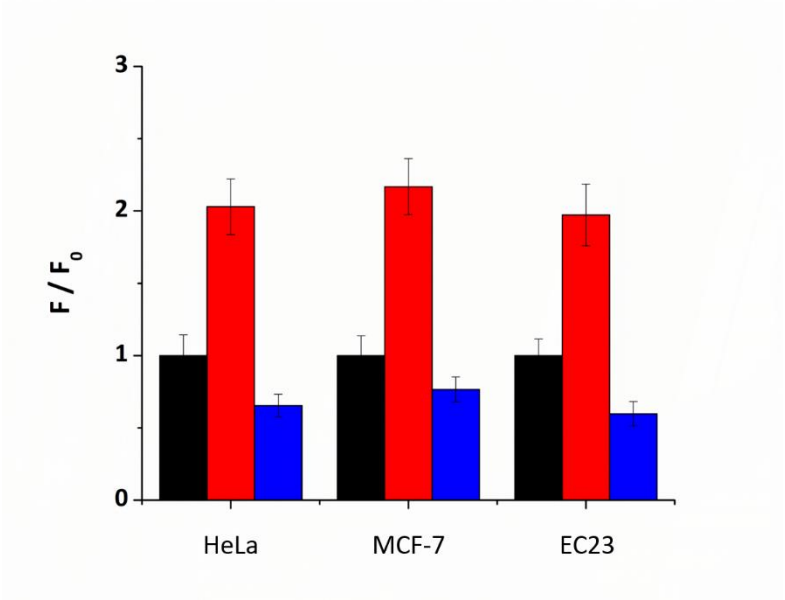

Figure 4.28 The fluorescence intensity (F) of **77** in different cell lines with zinc pyrithione (red bars) or TPEN (blue bars) relative to the intensity of the probe alone (F_0, black bars, normalised to 1).

4.4.4 Zn^{2+} level changes during oxidative stress

Given that **77** is able to image Zn^{2+} in the Golgi apparatus in three cell lines and respond to variations in its levels induced by the addition of zinc pyrithione or TPEN, it was applied to monitor mobile Zn^{2+} changes in the Golgi apparatus during changes to redox status, as this has not been investigated widely due to the lack of an effective tool to do so. MCF-7 cells, after 24 hours' incubation with **77**, were first treated with H_2O_2 to induce oxidative stress and the intensity of the fluorescence response in the cells monitored against time (Figure 4.29a). The fluorescence response was observed to be significantly reduced after the addition of H_2O_2 with levels stabilising after approximately 30 mins. Then glutamine, was added to reverse oxidative status, and the fluorescence intensity then remained stable. In contrast, when glutamine was first introduced and H_2O_2 subsequently added the fluorescence remained largely stable with only a small decrease of its intensity (Figure 4.29b). The reasons for the reduced fluorescence response observed in Figure 4.29a may, in part, be due to the known antioxidant role zinc plays since it is a cofactor of the superoxide dismutase enzyme, which regulates the detoxification of reactive oxygen species, protecting cells against the oxidative stress.[3] However, it has also been reported that the concentration of mobile Zn^{2+} increases in the mitochondria[38] and lysosome[48] under oxidative stress induced by H_2O_2. Metallothionein, which is mainly localised to the membrane of the Golgi apparatus,[133] is known to play an important role in the regulation of Zn^{2+} homeostasis, as well as providing protection against oxidative stress in cells.[134] It is therefore assumed that under oxidative stress, Zn^{2+} is transported from the Golgi apparatus to the mitochondria and lysosome to function. In contrast, if glutamine was first added, the addition of H_2O_2 should not cause high levels of oxidative stress, therefore zinc levels would not be reduced and therefore no significant fluorescence decrease would be expected, as observed. Similar results were also observed in

HeLa cells, (Figure 4.30), indicating that this process is likely to be general among different cell lines. Finally, an *in vitro* control experiment was undertaken to exclude the effect of H_2O_2 and glutamine themselves on the fluorescence response of the probe, which showed there was no difference in response when the two reagents were added separately in the presence of zinc (Figure 4.31 and Figure 4.32). Therefore, it appears reasonable to propose that there is a lowering of the concentration of mobile Zn^{2+} in the Golgi apparatus in response to oxidative stress.

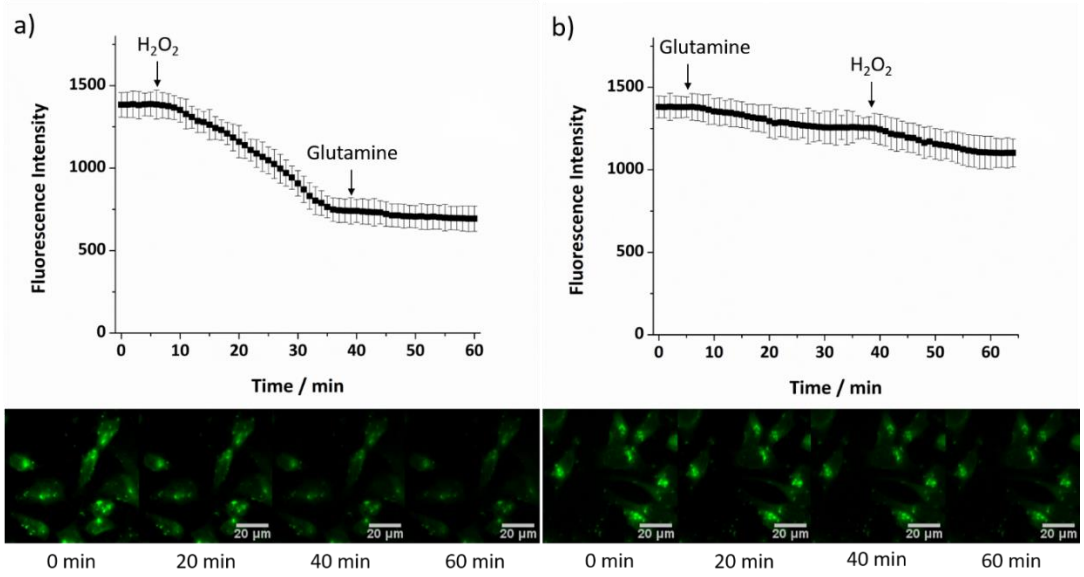

Figure 4.29 Fluorescence intensity of **77** (10 µM) in MCF-7 cells treated with a) H_2O_2 (200 µM) and then glutamine (200 µM) or b) glutamine (200 µM) and then H_2O_2 (200 µM) and the cell images taken at different times. (Scale bars = 20 µm).

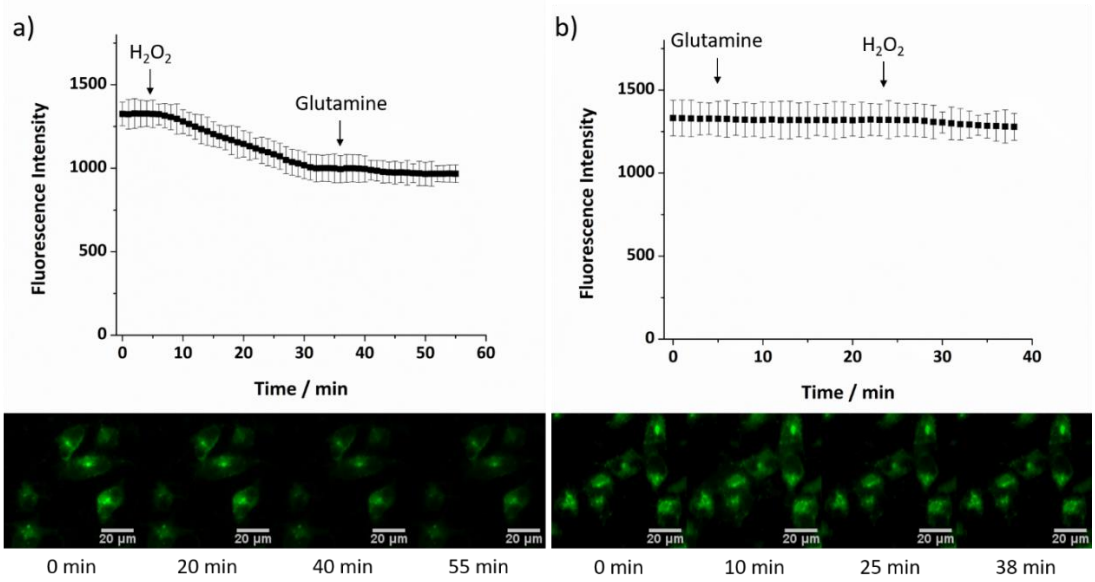

Figure 4.30 Fluorescence intensity of **77** (10 µM) in HeLa cells treated with a) H_2O_2 (200 µM) and then glutamine (200 µM) or b) glutamine (200 µM) and then H_2O_2 (200 µM) and the cell images taken at different times. (Scale bars = 20 µm).

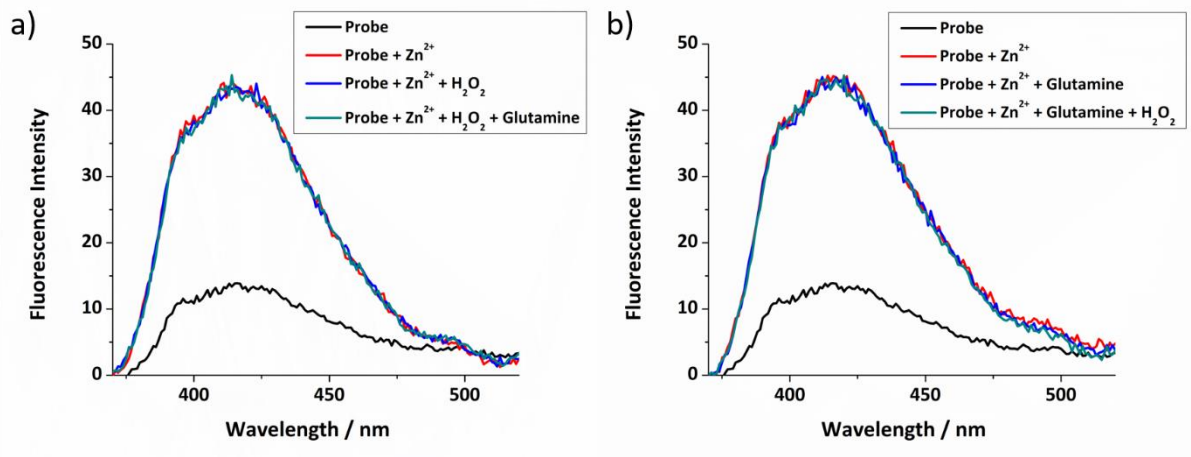

Figure 4.31 Fluorescence spectra of **77** (10 µM) and with subsequent addition of excess $ZnCl_2$, H_2O_2 (100 µM) and glutamine (100 µM) in PBS buffer.

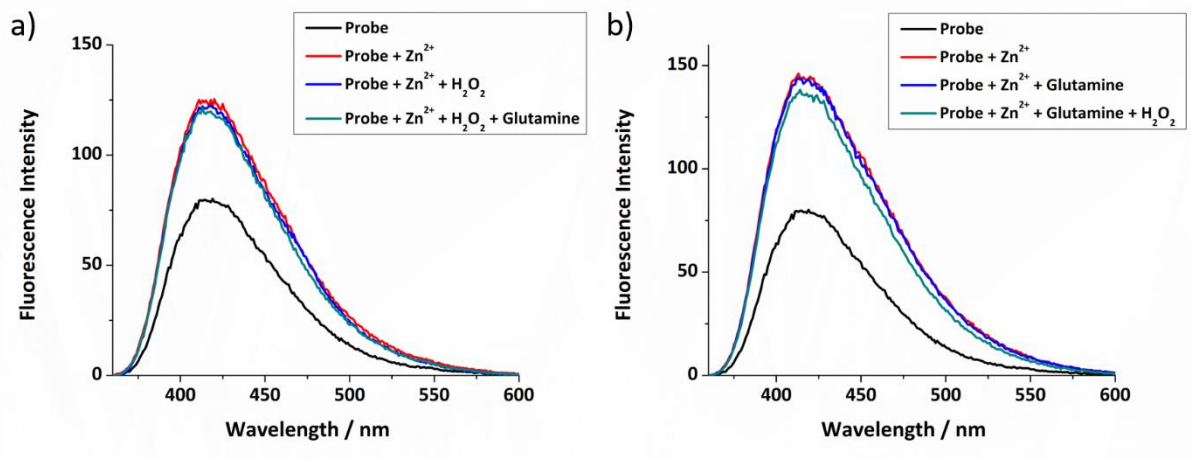

Figure 4.32 Fluorescence spectra of **78** (10 µM) and with subsequent addition of excess $ZnCl_2$, H_2O_2 (100 µM) and glutamine (100 µM) in PBS buffer.

4.5 Summary

In summary, a Golgi apparatus targeted Zn^{2+} probe **77** was successfully synthesized that is able to undergo passive membrane diffusion as a result of the lipophilic nature of the *S*-trityl protecting group. It is apparent that initial probe localisation *in cellulo* occurs in the ER, however, after 24 hours the fluorescence response increases significantly, presumably due to *S*-trityl group deprotection forming **78**, which displays a quantum yield that is 33-fold higher than **77**, and the probe consequently becomes anchored to the Golgi apparatus. The probe shows excellent specificity for targeting of the Golgi apparatus and the ability to image mobile Zn^{2+} in different cell lines. This allowed it to be applied in the monitoring of changes to mobile Zn^{2+} levels in the Golgi apparatus in response to oxidative stress induced by H_2O_2, which indicated that the concentration of mobile Zn^{2+} decreases. This suggests that the probe may provide an effective tool to probe changes to mobile Zn^{2+} that occur in the Golgi apparatus in response to cellular stress in a number of diseases states.

Chapter 5 An alternative modular 'click-S_NAr-click' approach to develop subcellular localised fluorescent probes to image mobile Zn^{2+}

5.1 Probe design and synthesis

Previously a modular 'click' synthetic methodology to produce an array of fluorescent probes for imaging of zinc at specific cellular targets was described in Chapter 2 to Chapter 4. However, this methodology, based on a 'top to bottom' double click process (i.e. first incorporate the targeting unit through a click reaction and then to introduce the Zn^{2+} binding ligand through a second click reaction) can be hampered somewhat by the final synthetic step, which can be a slow, moderately low yielding reaction and can also lead to the unwanted formation of an aniline by-product that is difficult to remove. This is unattractive if the targeting unit is either expensive or requires complex multi-step synthesis. Therefore, an alternative approach to ameliorate these issues was sought utilising a modular strategy involving a 'bottom to top' double click reaction methodology (i.e. first incorporate the Zn^{2+} binding ligand through a click reaction and perform a click reaction in the last step to introduce the targeting unit), which would have the advantage that high value organelle targeting vectors could be introduced in the last synthetic step, which is generally fast and high yielding. Using this strategy, endoplasmic reticulum (ER), mitochondria and lysosome targeting probes were successfully prepared.

The precursors **80**,[135] **82**,[25] **84**[25] were all synthesized according to reported procedures (Scheme 5.1). The conversion of azide **58**, to alkyne **59**, using the same procedure as reported in Chapter 3 (see Section 3.1), was performed in a one-pot reaction because the intermediate formed after the 'click' reaction could not be readily extracted from the aqueous layer. It proved expedient to simply follow this step by the direct addition of propargylamine to the reaction mixture to give **59** in a moderate yield. With alkyne **59** and the range of different

organelle targeting azides **80**, **82** and **84** in hand, the top 'click' reactions were performed successfully in moderate to good yields to produce the different organelle targeting probes **85**-**87**. As a control, the non-targeting probe **90** was also prepared as reported in 93% yield (Scheme 5.2).[102] All products were satisfactorily characterized by ^{1}H, ^{13}C NMR and IR spectroscopies as well as high-resolution mass spectrometry.

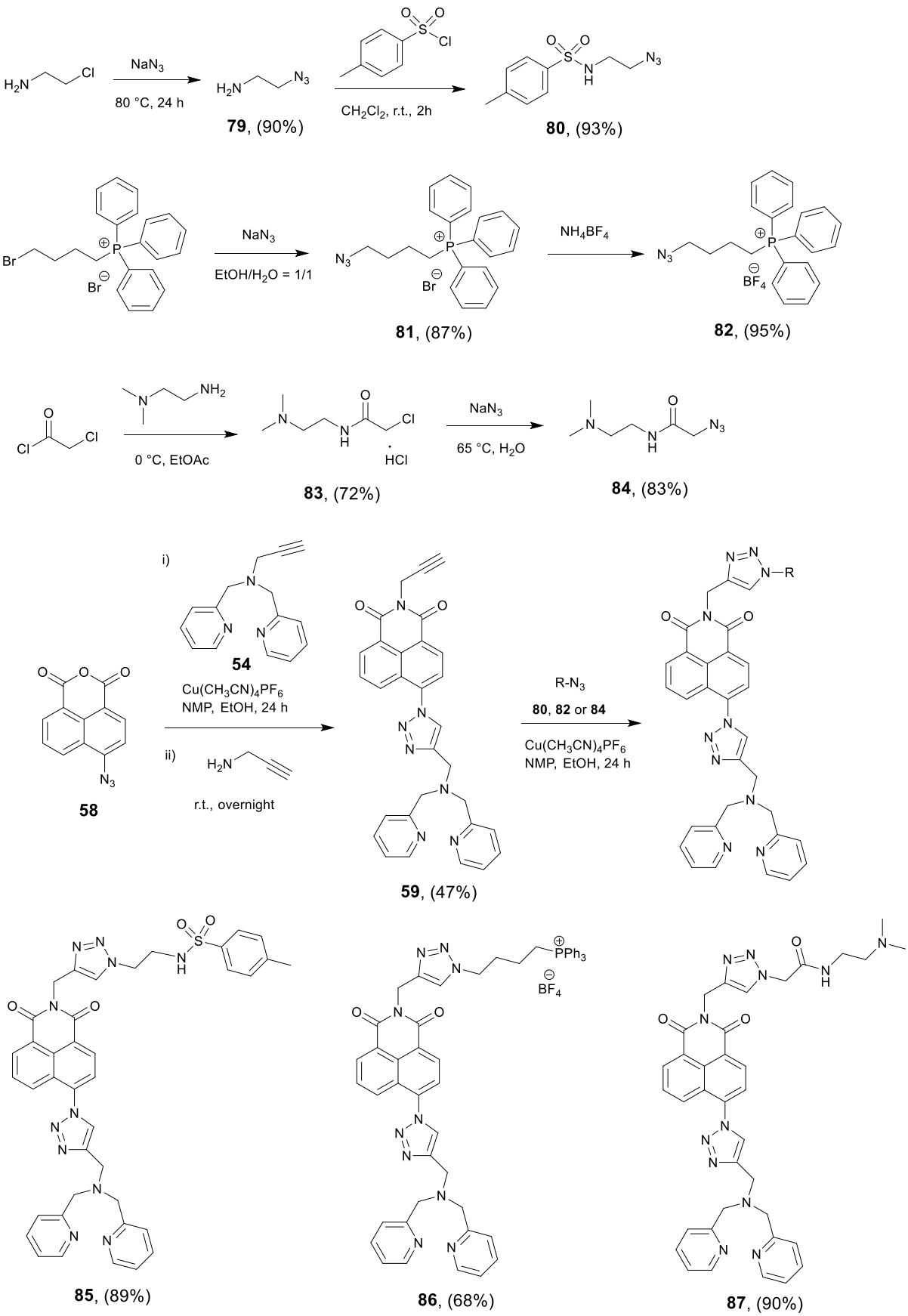

Scheme 5.1 The new 'bottom to top' modular synthetic route towards the sub-cellular targeting Zn^{2+} probes: ER probe (**85**), mitochondria probe (**86**) and lysosome probe (**87**).

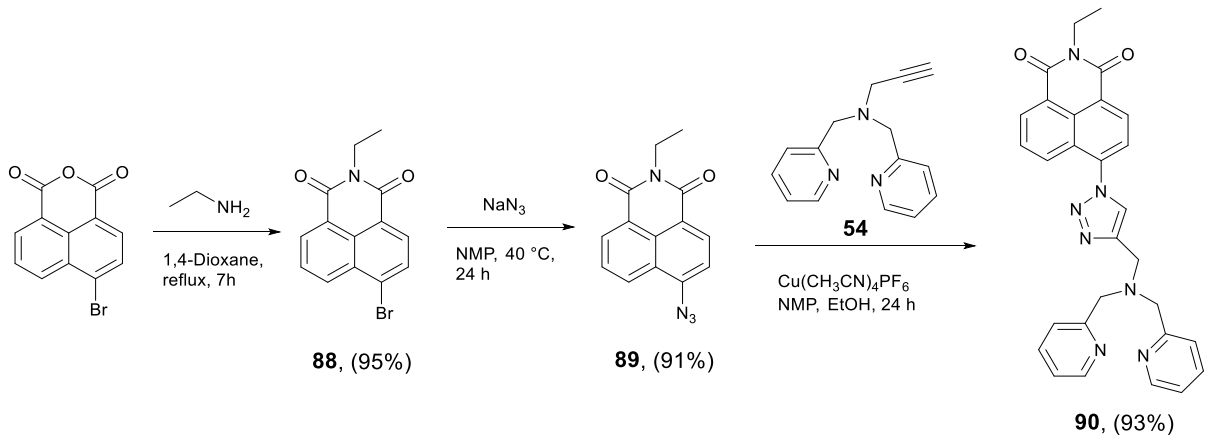

Scheme 5.2 The synthesis of the non-targeting control probe **90**.

5.2 Photophysical properties

Fluorescence titrations of the different probes with Zn^{2+} were undertaken to show their Zn^{2+} response. As shown in Figure 5.2, the addition of Zn^{2+} results in the fluorescence intensity of all probes increasing gradually, until a maximal more than 10-fold increase was observed. The Job's plots of the probes (Figure 5.3) revealed the expected 1:1 binding stoichiometry with Zn^{2+}. Dissociation constants, K_d, were evaluated from non-linear curve fitting analysis (Figure 5.4) of the data obtained from the fluorescence titrations of different concentration probes in a competitive system with EGTA and the results given in Table 5.1. The best fitting for all probes was observed at 0.01 µM and K_d values were determined to be 2.83 ± 0.11 nM for **85**, 3.44 ± 0.22 nM for **86**, 3.68 ± 0.26 nM for **87** and 3.24 ± 0.20 nM for **90**, which are consistent and comparable to reported values for this chelate.[35,136] The detection limit was determined to be 48 pM for **85**, 99 pM for **86**, 51 pM for **87** and 47 pM for **90** (Figure 5.5).

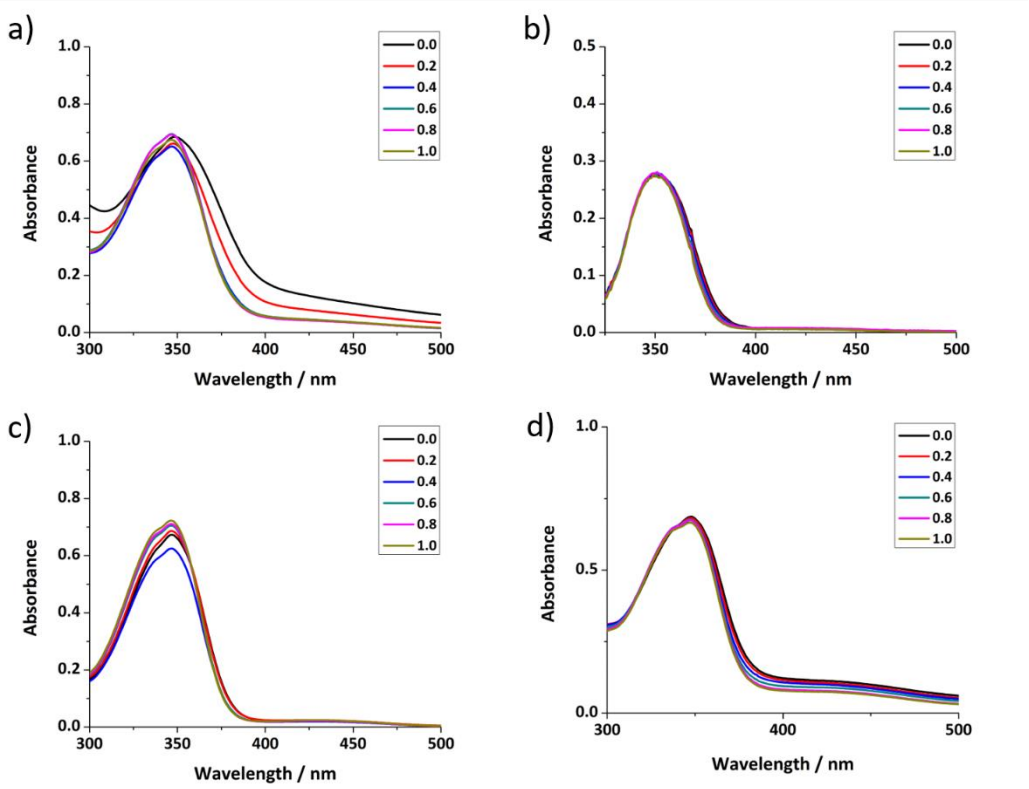

Figure 5.1 The UV-Vis spectra of 50 µM a) **85**, b) **86**, c) **87** and d) **90** and their complexes with different equivalents of Zn^{2+} in 0.1 mM HEPES buffer at pH 7.4.

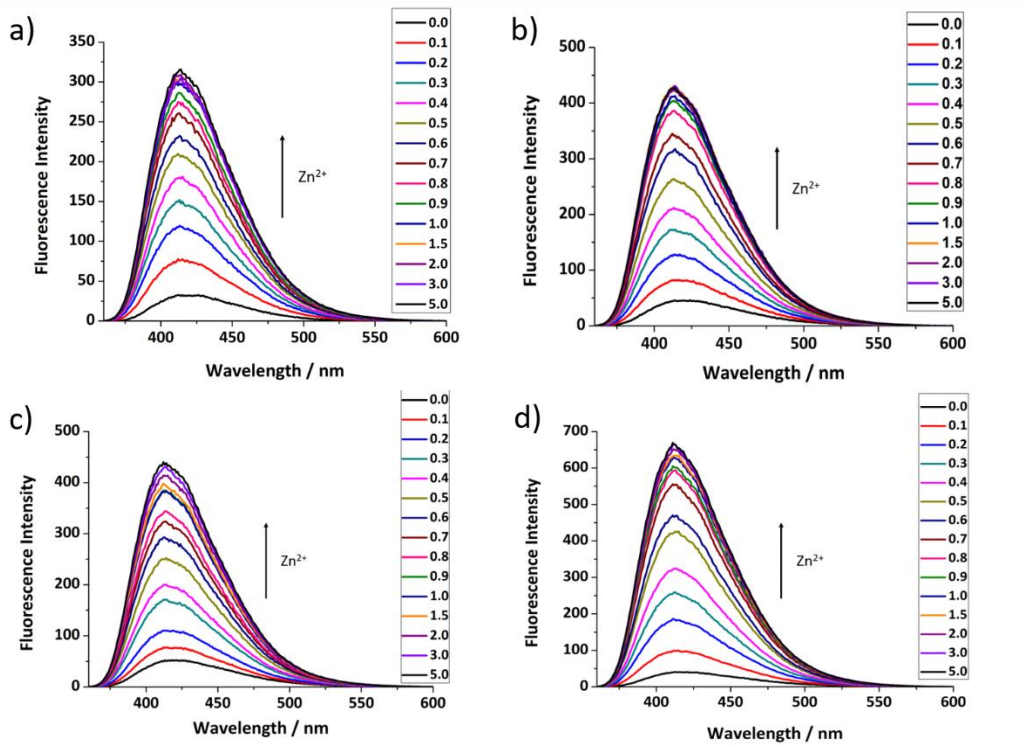

Figure 5.2 The fluorescence response of 50 µM a) **85**, b) **86**, c) **87** and d) **90** to different equivalents of Zn^{2+} in 0.1 mM HEPES buffer at pH 7.4. (λ_{ex} = 346 nm, slit widths: 5/2.5 nm).

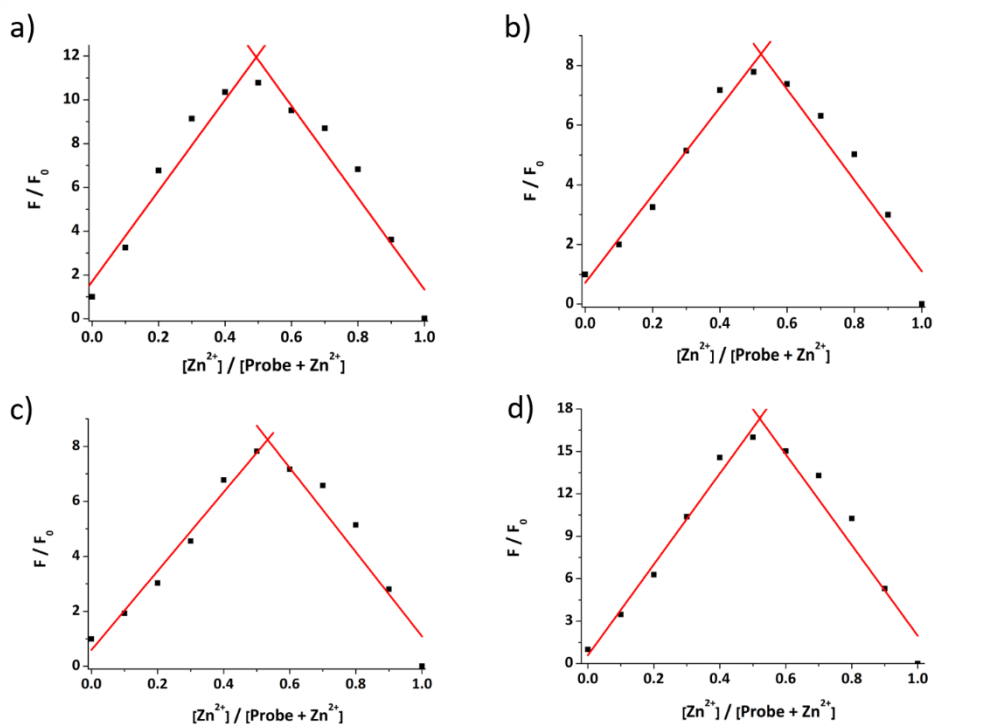

Figure 5.3 The Job's plot to determine the stoichiometry of the complex formed between probes a) **85**, b) **86**, c) **87** and d) **90** and Zn^{2+}. The total amount of [Probe + Zn^{2+}] was 100 µM. (λ_{ex} = 346 nm, λ_{em} = 414 nm, slit widths: 5/2.5 nm).

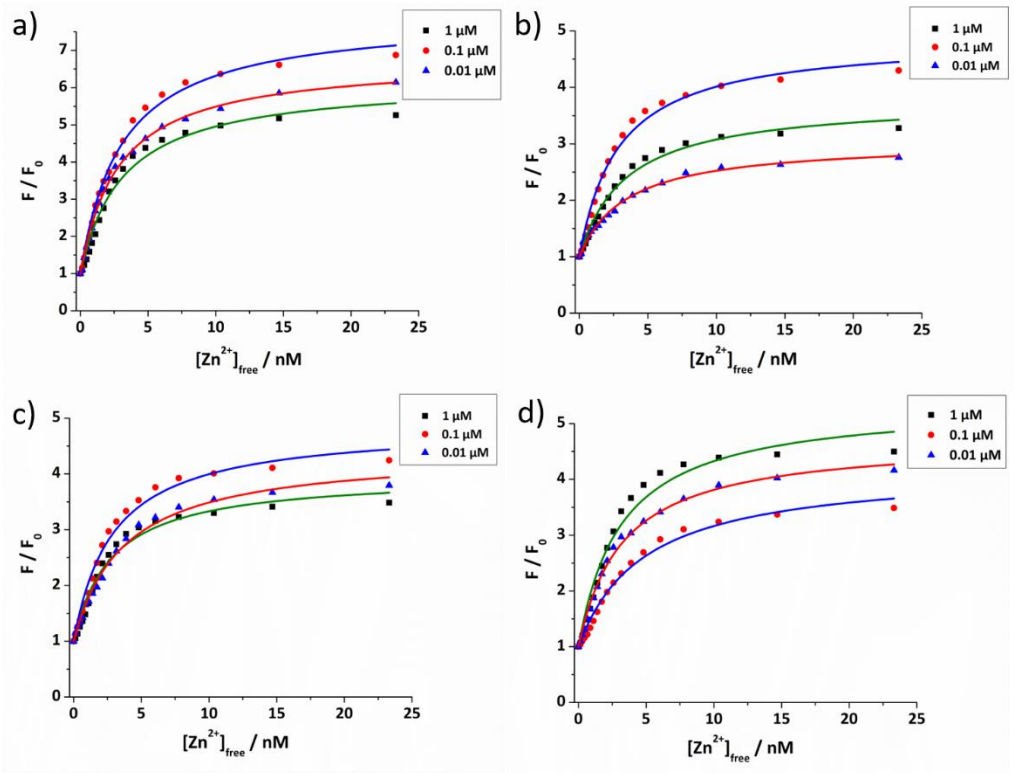

Figure 5.4 The non-linear curve fitting of the fluorescence intensity of probes a) **85**, b) **86**, c) **87** and d) **90** at different concentrations against $[Zn^{2+}]_{free}$ in HEPES buffer solution (50 mM, pH 7.2, 0.1 M KCl). (λ_{ex} = 346 nm, λ_{em} = 414 nm).

Table 5.1 The summary of K_d for probes **85**-**87** and **90**.

	[probe] = 1 µM		[probe] = 0.1 µM		[probe] = 0.01 µM	
	K_d	R^2	K_d	R^2	K_d	R^2
85	3.16 ± 0.34 nM	0.9789	3.05 ± 0.18 nM	0.9931	2.83 ± 0.11 nM	0.9968
86	3.38 ± 0.29 nM	0.9866	2.87 ± 0.23 nM	0.9878	3.44 ± 0.22 nM	0.9919
87	2.78 ± 0.34 nM	0.9734	2.91 ± 0.26 nM	0.9845	3.68 ± 0.26 nM	0.9911
90	3.15 ± 0.40 nM	0.9719	4.81 ± 0.47 nM	0.9850	3.24 ± 0.20 nM	0.9932

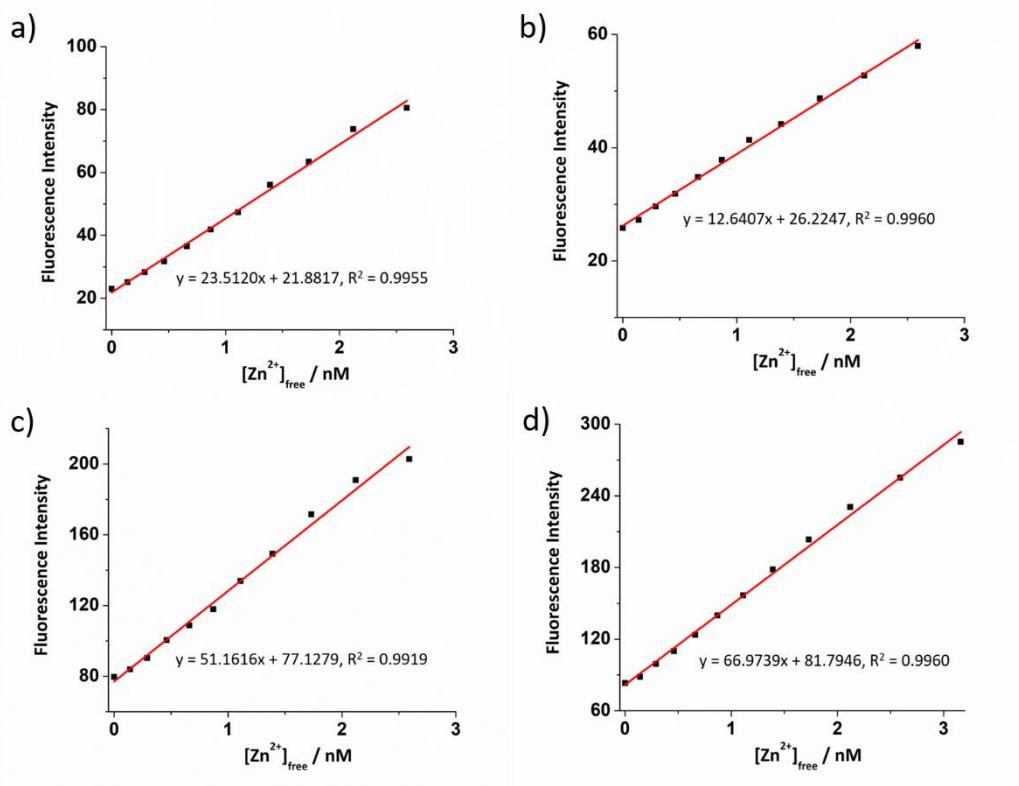

Figure 5.5 Fluorescence response of 1 µM probes a) **85**, b) **86**, c) **87** and d) **90** against $[Zn^{2+}]_{free}$ in HEPES buffer solution (50 mM, pH 7.2, 0.1 M KCl). (λ_{ex} = 346 nm, λ_{em} = 414 nm, slit widths: 5/5 nm).

The fluorescence quantum yield was again measured using anthracene as a standard and linear plots of probes and their complexes with one equivalent of Zn^{2+} are shown in Figure 5.6. The calculated quantum yields are listed in Table 5.2 and show that the targeting units reduce the probes' quantum yields significantly, compared to that of **90**, with no targeting unit, presumably due to the increased access to non-radiative pathways that are available in the larger molecular structures.

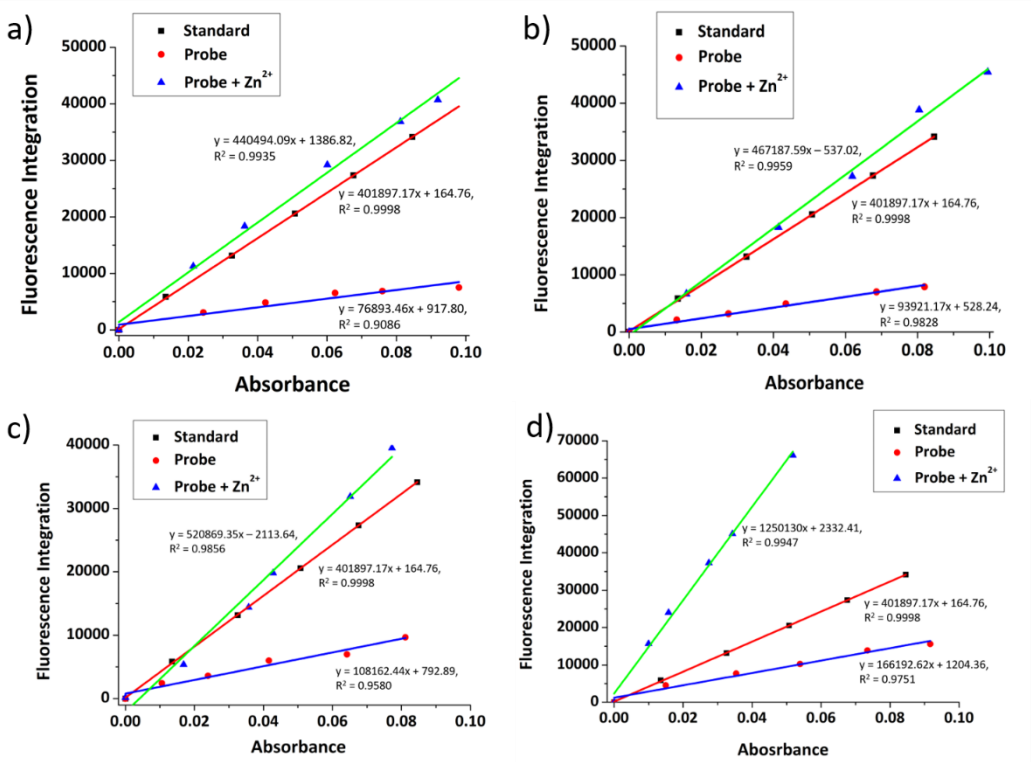

Figure 5.6 Linear plots for standard sample, probes a) **85**, b) **86**, c) **87** and d) **90**, and their complexes with 1 equivalent Zn^{2+} to obtain quantum yields. (λ_{ex} = 346 nm, slit widths: 5/5 nm).

Table 5.2 The quantum yield of probes and their complex with 1 equivalent Zn^{2+}.

Probe	Φ_{probe}	$\Phi_{complex}$
85	0.05	0.28
86	0.06	0.30
87	0.07	0.34
90	0.11	0.81

The pH-dependent fluorescence response was measured to show that all probes have fluorescence responses to Zn^{2+} in the biologically relevant pH range. As shown in Figure 5.7a, probe **85** shows a good switch on response to Zn^{2+} over a wide pH range 3.0-10.0, the same results were broadly observed for the other probes (Figure 5.7), as expected due to the identical metal-chelating motif. The fluorescence intensity of all probes increased in an acidic environment, however, compared to the other three probes, **85** and its complex were significantly brighter. Sessler *et al.* explained this behaviour based on a PET mechanism,[51] however, Veale and Gunnlaugasson have previously suggested that this is unlikely because

the PET quenching from groups connected via the imide moiety is normally prevented.[137] It therefore seems more likely that the differences in emission observed at different pH values are due to the presence of different species formed by the protonation of the tertiary amine or by the deprotonation of coordinated water. Given the range of pH observed in different organelles and the cytoplasm (i.e. the pH is about 7.2 in ER and cytoplasm, 8 in the mitochondria and around 5 in the lysosome), all probes should display a response to mobile Zn^{2+} *in cellulo*. By integrating the intensity of the fluorescence emission spectra against pH (Figure 5.8) for different probes, their apparent pK_a values were determined through non-linear curve fitting applying Equation 7.5.

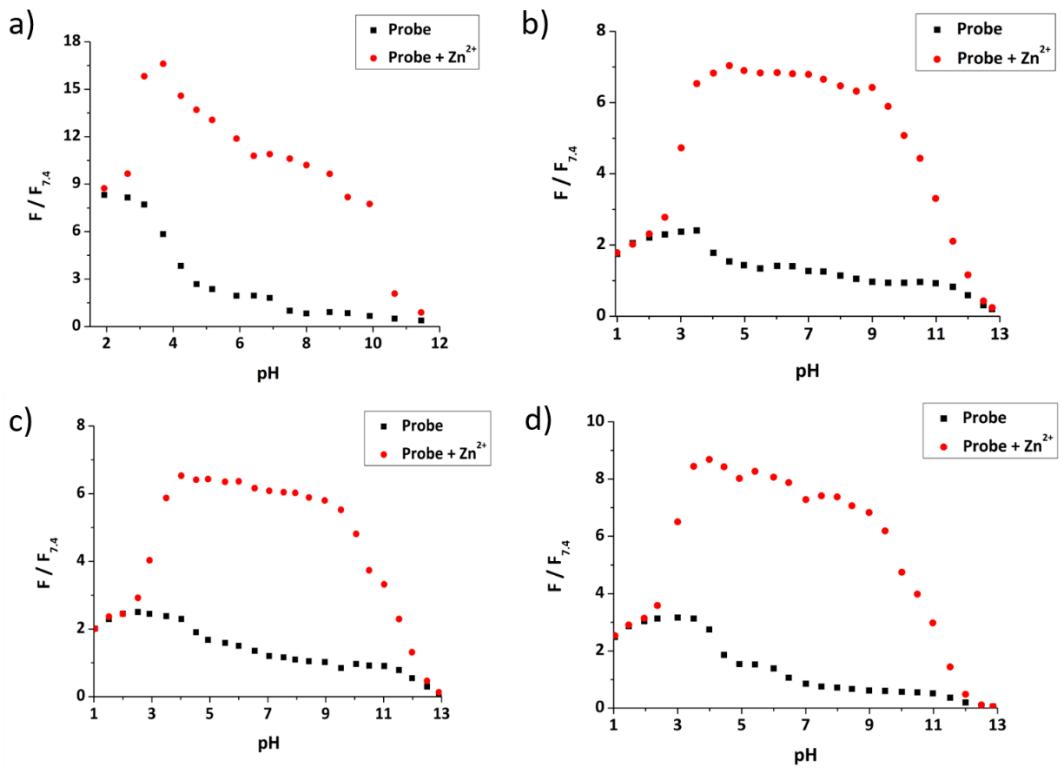

Figure 5.7 The pH profiles of probes a) **85**, b) **86**, c) **87** and d) **90** (50 µM, black dots) and their complexes with 1 equivalent of Zn^{2+} (red dots). (λ_{ex} = 346 nm, λ_{em} = 414 nm, slit widths: 5/2.5 nm).

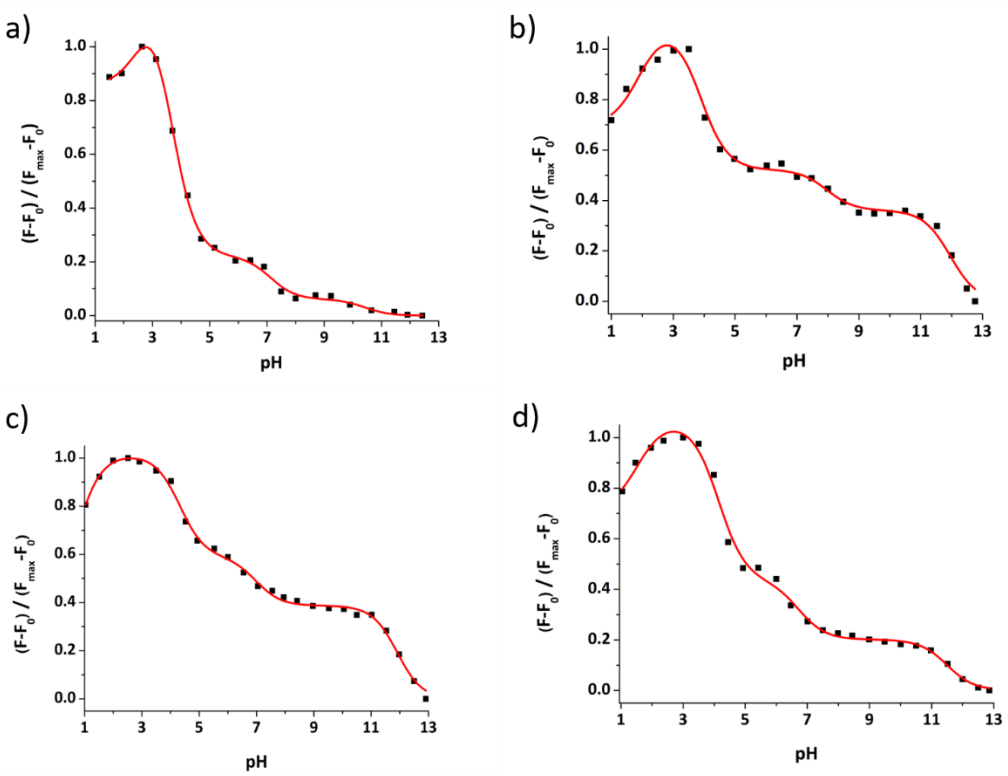

Figure 5.8 Normalized integrated fluorescence emission of probes (50 µM) vs pH, the nonlinear curve fitting used to determine the apparent pK_a values. The determined pK_a values are: a) **85**, pK_{a1} = 2.65 ± 0.26, pK_{a2} = 3.62 ± 0.09, pK_{a3} = 7.13 ± 0.17, pK_{a4} = 10.42 ± 0.41, R^2 = 99.83%; b) **86**, pK_{a1} = 1.91 ± 0.27, pK_{a2} = 3.88 ± 0.13, pK_{a3} = 7.97 ± 0.32, pK_{a4} = 11.95 ± 0.12, R^2 = 98.57%; c) **87**, : pK_{a1} = 0.70 ± 0.38, pK_{a2} = 4.33 ± 0.08, pK_{a3} = 6.99 ± 0.15, pK_{a4} = 11.91 ± 0.06, R^2 = 99.64%; d) **90**, pK_{a1} = 1.53 ± 0.29, pK_{a2} = 4.14 ± 0.10, pK_{a3} = 6.73 ± 0.21, pK_{a4} = 11.50 ± 0.17, R^2 = 99.39%.

The selectivity of probes was investigated in the presence of a range of other biologically relevant cations. From Figure 5.9, it can be seen that all probes display similar behaviour, which is to be expected given they contain the same metal binding motif. The fluorescence did not show an obvious increase after addition of 5 equivalents of other cations, except, as previously, for the stereoelectronic isostere Cd^{2+}. Subsequent addition of 1 equivalent of Zn^{2+} resulted in recovery of a fluorescence response for most cations, except for Co^{2+}, Cu^{2+} and Ni^{2+} for which fluorescence again remained quenched. Therefore, the results above suggest that all probes should have a selective response to mobile Zn^{2+} *in cellulo*.

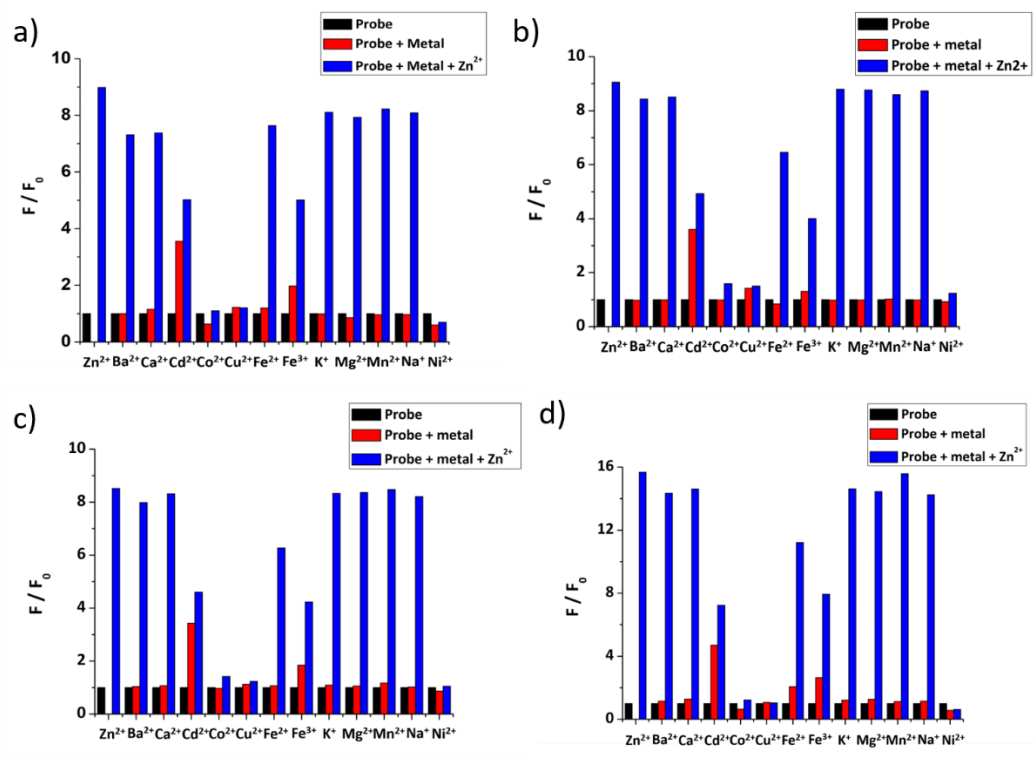

Figure 5.9 Metal ion selectivity of probes a) **85**, b) **86**, c) **87** and d) **90** in 0.1 mM HEPES buffer solution at pH 7.4. Average normalized fluorescence intensities for probes (50 µM) (black bars), after addition of 5 equivalents of various cations (red bars), followed by addition of 1 equivalent of $ZnCl_2$ (blue bars).

5.3 NMR titration of **90** with Zn^{2+}

In order to study the binding behaviour between **90** and Zn^{2+}, a ^1H NMR titration with different equivalents of Zn^{2+} was performed (see Figure 5.10). From Figure 5.11 and Figure 5.12, it can be seen that protons H_{c-g} are largely unaffected, while H_{l-n}, H_h and $H_{i,j}$ have significant downfield shifts after binding with Zn^{2+}. This indicates that the DPEN ligand and the triazole are involved in metal binding. This result is consistent with the behaviour observed by single crystal X-ray diffraction in related structures[101,107] as well as the DFT calculations.

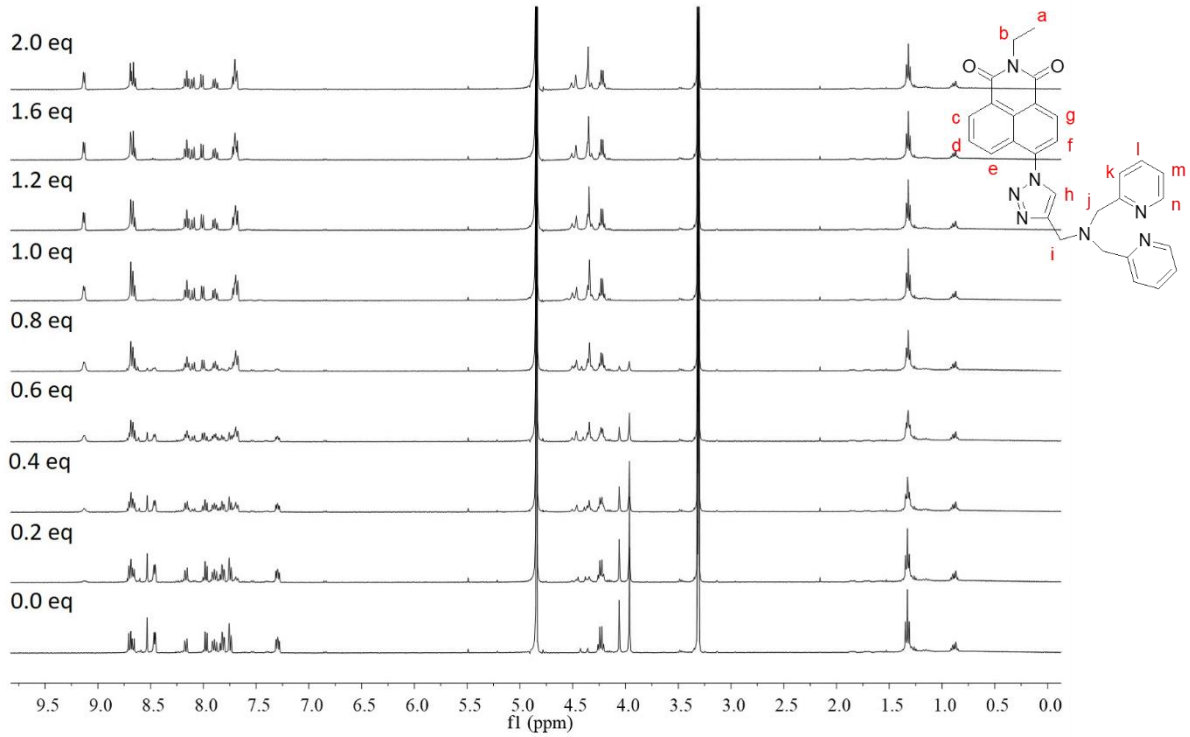

Figure 5.10 ^{1}H NMR titration spectra (whole range) of probe **90** (5 mM) with different equivalents $ZnCl_2$ in CD_3OD.

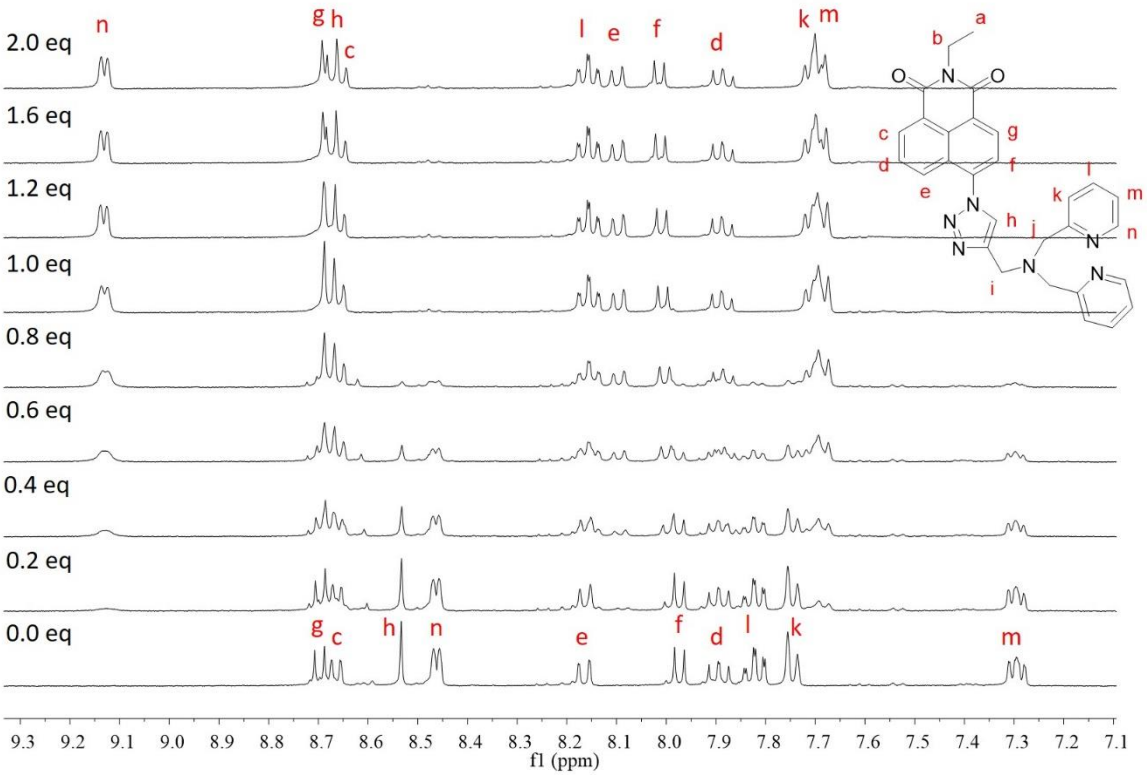

Figure 5.11 The aromatic region of the ^{1}H NMR spectra of probe **90** (5 mM) with different equivalents of $ZnCl_2$ in CD_3OD.

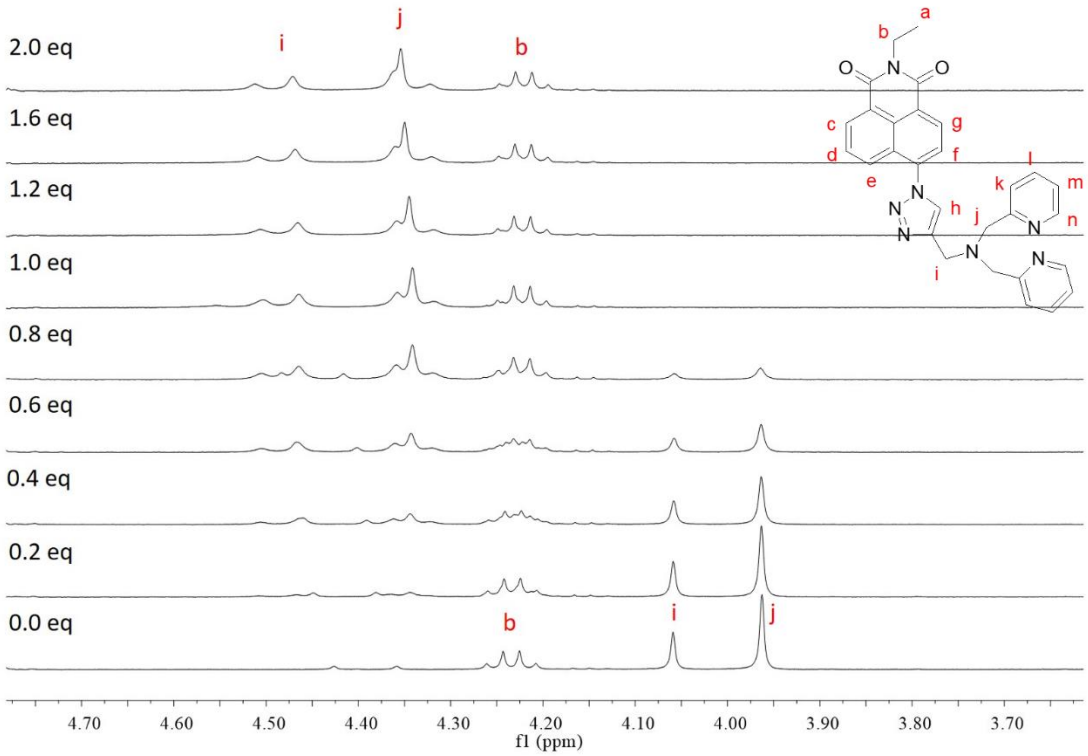

Figure 5.12 ^{1}H NMR titration spectra (range 3.70 - 4.70 ppm) of probe **90** (5 mM) with different equivalents $ZnCl_2$ in CD_3OD.

5.4 DFT calculations

In addition to the ^{1}H NMR spectroscopic titration, DFT calculations were also undertaken to study the association between the probes and Zn^{2+}. The optimised structures of the complexes of probes with 1 equivalent Zn^{2+} (Figure 5.13 to 5.16) also show the nitrogen atoms in the triazoles adjacent to the DPEN ligand are involved in binding with Zn^{2+}, in addition to those of the DPEN ligands.

TDDFT studies were also undertaken to understand the excitation and emission profiles of probes. The results of calculated absorption energy from ground state S_0 to the excited state S_1, and the emission energy were in agreement with the experimental data (Table 5.3 to 5.6). There was also nearly no difference among the different probes, showing that the targeting groups have negligible effects on the Zn^{2+} association and photophysical properties, other than quantum yields, which is consistent with the experimental data above.

In keeping with the previous chapters, the S_1-S_0 electron density transition (Figure 5.17 to 5.20) of all probes is mainly localised on the naphthalimide moiety and the vicinal triazole, and there is only a slight decrease of electron density on the triazole when it is involved in complex formation and the oscillator strength is not significantly affected. Therefore, the enhancement of emissive behaviour of the complexes should again be related to a reduced decay through nonradiative pathways after complexation with Zn^{2+}. The stabilisation of the complex hinders large amplitude vibrations in the vicinity of the fluorophore hampering the access to nonradiative mechanisms and increasing the quantum yield of emission. The restriction of intramolecular rotations can also hinder the access to low energy conical intersections associated with ultrafast decay to the ground state.

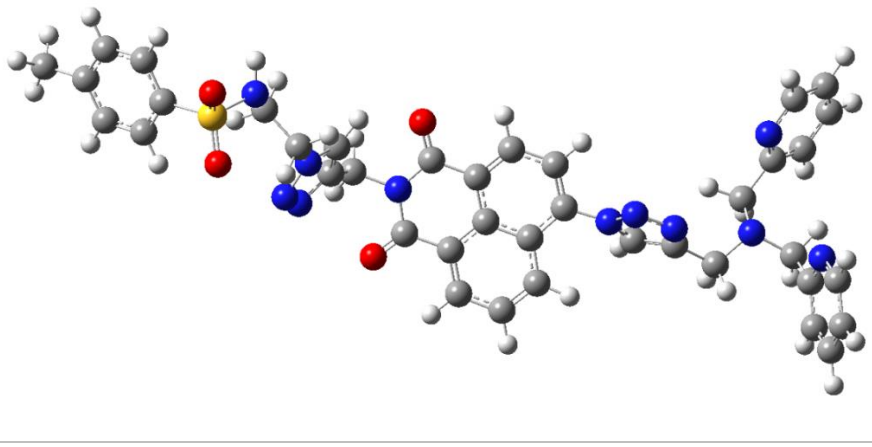

Probe **85**

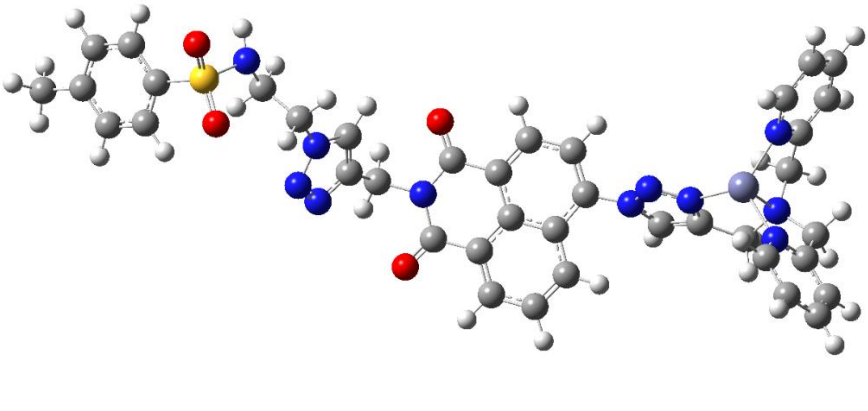

Complex with Zn^{2+}

Figure 5.13 The optimised structures of **85** and its complex with Zn^{2+}.

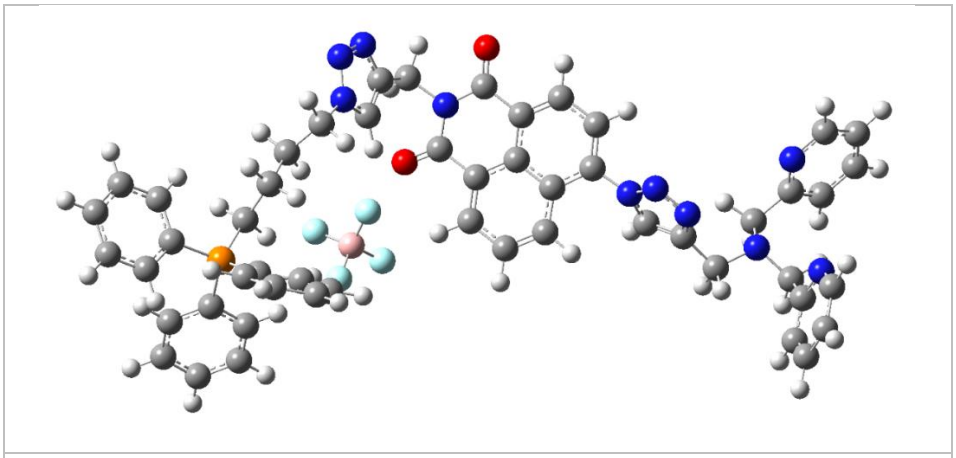

Probe **86**

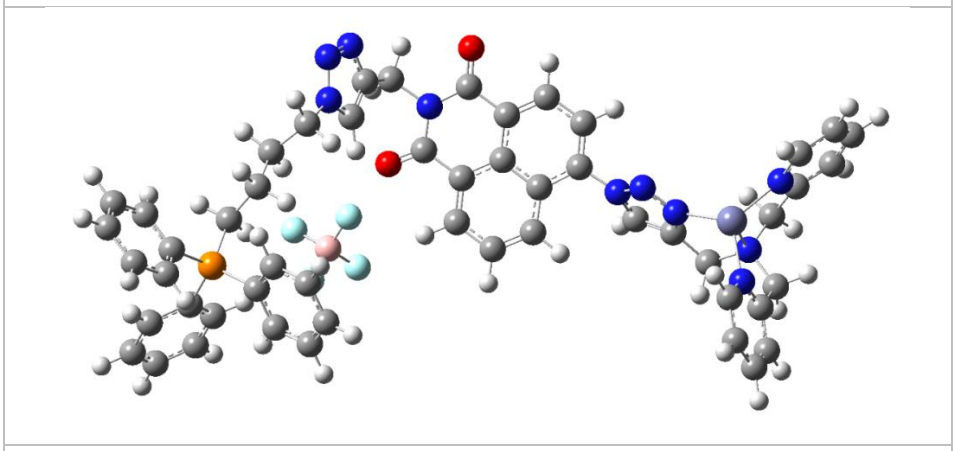

Complex with Zn^{2+}

Figure 5.14 The optimised structures of **86** and its complex with Zn^{2+}.

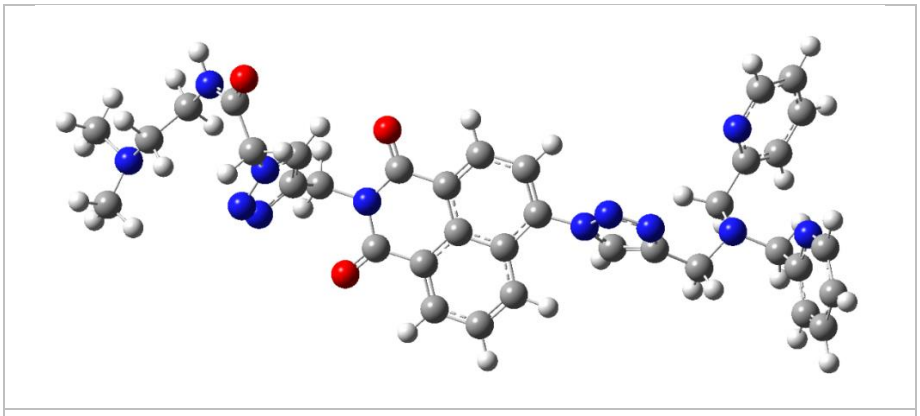

Probe **87**

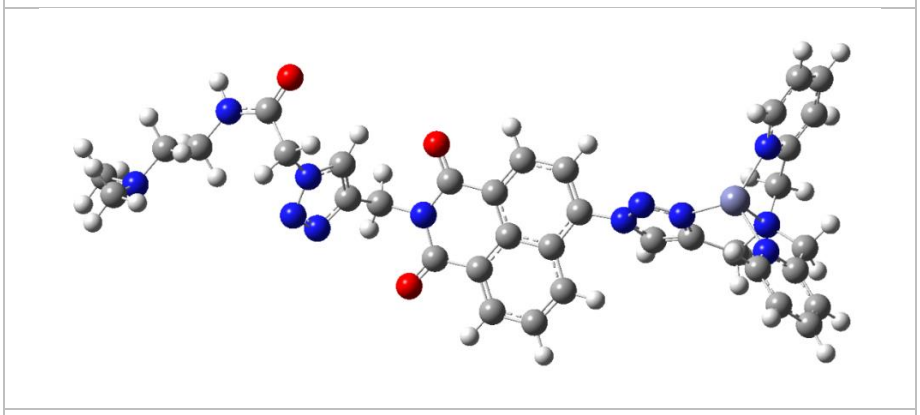

Complex with Zn^{2+}

Figure 5.15 The optimised structures of **87** and its complex with Zn^{2+}.

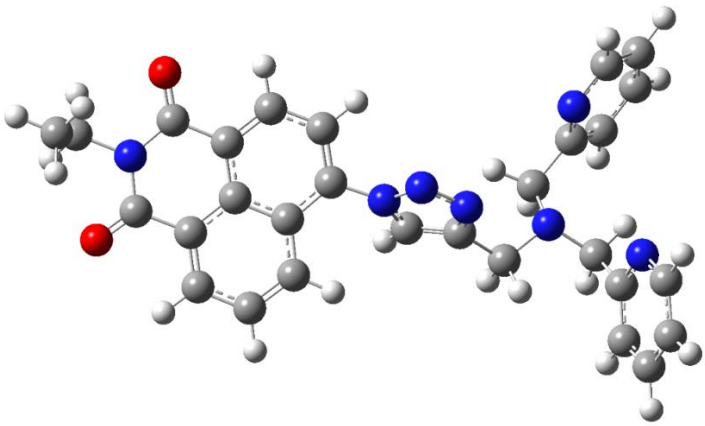

Probe **90**

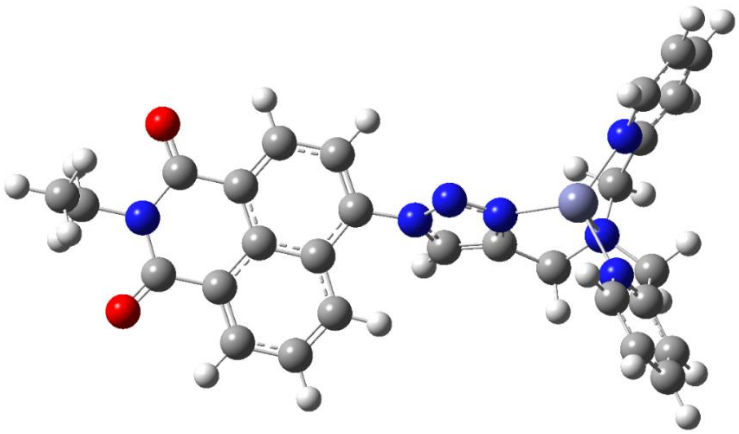

Complex with Zn^{2+}

Figure 5.16 The optimised structures of **90** and its complex with Zn^{2+}.

Table 5.3. Comparison of the experimental data with the calculated result of vertical electronic excitation energies (eV) and the emission from S_1 to ground state of **85** and its Zn^{2+} complex.

	Electronic transition	Energy (eV)	Wavelength (nm)	Oscillator strength (f)	Experimental data
85					
Absorption	$S_0 \rightarrow S_1$	3.90	318	0.5443	3.58 eV/346 nm
	$S_0 \rightarrow S_2$	4.26	291	0.0483	
	$S_0 \rightarrow S_3$	4.38	283	0.0002	
	$S_0 \rightarrow S_4$	4.68	265	0.0010	
	$S_0 \rightarrow S_5$	4.84	256	0.0201	
	$S_0 \rightarrow S_6$	4.93	251	0.0190	
Emission	$S_1 \rightarrow S_0$	3.14	395	0.7240	3.01 eV/412 nm
Complex of **85** with Zn^{2+}					
Absorption	$S_0 \rightarrow S_1$	3.96	313	0.5015	3.58 eV/346 nm
	$S_0 \rightarrow S_2$	4.25	291	0.0557	
	$S_0 \rightarrow S_3$	4.33	286	0.0002	
	$S_0 \rightarrow S_4$	4.62	268	0.0004	
	$S_0 \rightarrow S_5$	4.94	251	0.0329	
	$S_0 \rightarrow S_6$	5.31	234	0.0055	
Emission	$S_1 \rightarrow S_0$	3.21	386	0.6748	3.01 eV/412 nm

Table 5.4. Comparison of the experimental data with the calculated result of vertical electronic excitation energies (eV) and the emission from S_1 to ground state of **86** and its Zn^{2+} complex.

	Electronic transition	Energy (eV)	Wavelength (nm)	Oscillator strength (f)	Experimental data
86					
Absorption	$S_0 \rightarrow S_1$	3.89	318	0.5149	3.58 eV/346 nm
	$S_0 \rightarrow S_2$	4.25	292	0.0493	
	$S_0 \rightarrow S_3$	4.38	283	0.0009	
	$S_0 \rightarrow S_4$	4.73	262	0.0034	
	$S_0 \rightarrow S_5$	4.84	256	0.0302	
	$S_0 \rightarrow S_6$	4.89	253	0.0049	
Emission	$S_1 \rightarrow S_0$	3.14	394	0.7137	3.01 eV/412 nm
Complex of **86** with Zn^{2+}					
Absorption	$S_0 \rightarrow S_1$	3.95	314	0.4796	3.58 eV/346 nm
	$S_0 \rightarrow S_2$	4.25	292	0.0530	
	$S_0 \rightarrow S_3$	4.33	286	0.0019	
	$S_0 \rightarrow S_4$	4.68	265	0.0003	
	$S_0 \rightarrow S_5$	4.84	256	0.0273	
	$S_0 \rightarrow S_6$	5.13	242	0.0178	
Emission	$S_1 \rightarrow S_0$	3.26	381	0.6351	3.01 eV/412 nm

Table 5.5. Comparison of the experimental data with the calculated result of vertical electronic excitation energies (eV) and the emission from S_1 to ground state of **87** and its Zn^{2+} complex.

	Electronic transition	Energy (eV)	Wavelength (nm)	Oscillator strength (f)	Experimental data
87					
Absorption	$S_0 \rightarrow S_1$	3.89	319	0.5481	3.58 eV/346 nm
	$S_0 \rightarrow S_2$	4.26	291	0.0479	
	$S_0 \rightarrow S_3$	4.39	282	0.0001	
	$S_0 \rightarrow S_4$	4.70	264	0.0022	
	$S_0 \rightarrow S_5$	4.83	257	0.0142	
	$S_0 \rightarrow S_6$	4.90	253	0.0012	
Emission	$S_1 \rightarrow S_0$	3.14	394	0.7241	3.01 eV/412 nm
Complex of **87** with Zn^{2+}					
Absorption	$S_0 \rightarrow S_1$	3.94	314	0.5169	3.58 eV/346 nm
	$S_0 \rightarrow S_2$	4.25	292	0.0543	
	$S_0 \rightarrow S_3$	4.34	286	0.0002	
	$S_0 \rightarrow S_4$	4.64	267	0.0008	
	$S_0 \rightarrow S_5$	4.95	250	0.0329	
	$S_0 \rightarrow S_6$	4.97	249	0.0015	
Emission	$S_1 \rightarrow S_0$	3.22	385	0.6710	3.01 eV/412 nm

Table 5.6. Comparison of the experimental data with the calculated result of vertical electronic excitation energies (eV) and the emission from S_1 to ground state of **90** and its Zn^{2+} complex.

	Electronic transition	Energy (eV)	Wavelength (nm)	Oscillator strength (f)	Experimental data
90					
Absorption	$S_0 \rightarrow S_1$	3.92	316	0.4960	3.58 eV/346 nm
	$S_0 \rightarrow S_2$	4.27	290	0.0445	
	$S_0 \rightarrow S_3$	4.35	285	0.0004	
	$S_0 \rightarrow S_4$	4.69	264	0.0085	
	$S_0 \rightarrow S_5$	4.88	254	0.0251	
	$S_0 \rightarrow S_6$	4.96	250	0.0138	
Emission	$S_1 \rightarrow S_0$	3.15	393	0.7005	3.01 eV/412 nm
Complex of **90** with Zn^{2+}					
Absorption	$S_0 \rightarrow S_1$	3.99	311	0.4455	3.58 eV/346 nm
	$S_0 \rightarrow S_2$	4.26	291	0.0518	
	$S_0 \rightarrow S_3$	4.30	289	0.0009	
	$S_0 \rightarrow S_4$	4.65	267	0.0072	
	$S_0 \rightarrow S_5$	4.94	251	0.0369	
	$S_0 \rightarrow S_6$	5.41	229	0.0385	
Emission	$S_1 \rightarrow S_0$	3.21	386	0.6601	3.01 eV/412 nm

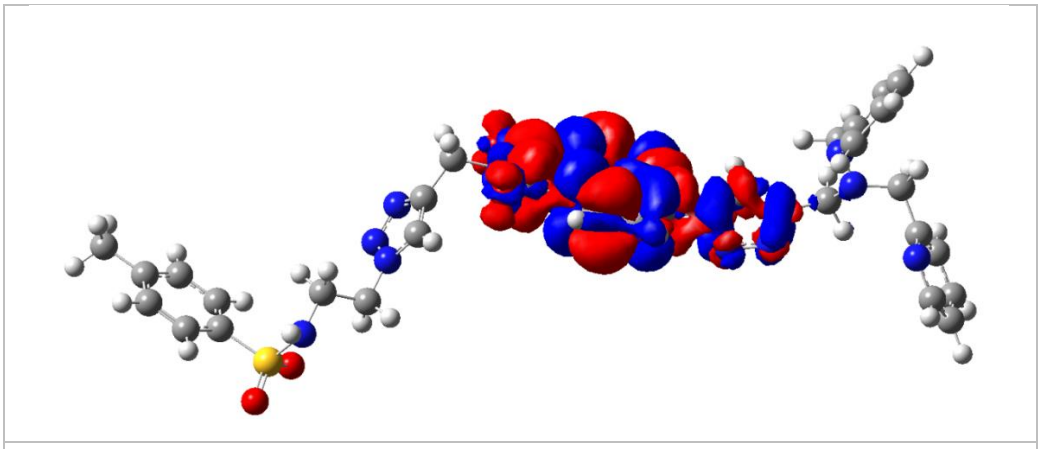

Probe **85**

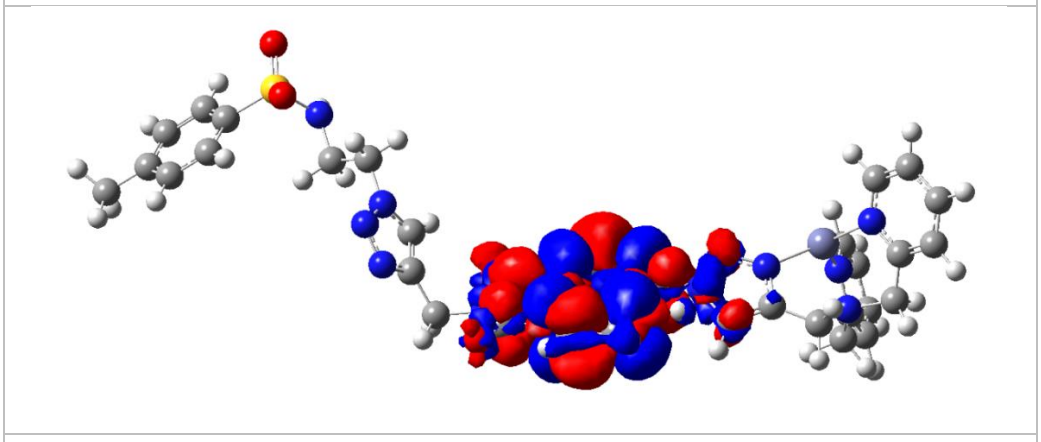

Complex with Zn^{2+}

Figure 5.17 S_1-S_0 electron density map for probe **85** and its complex with Zn^{2+} (S_1 minima). Red represents positive densities and blue negative values.

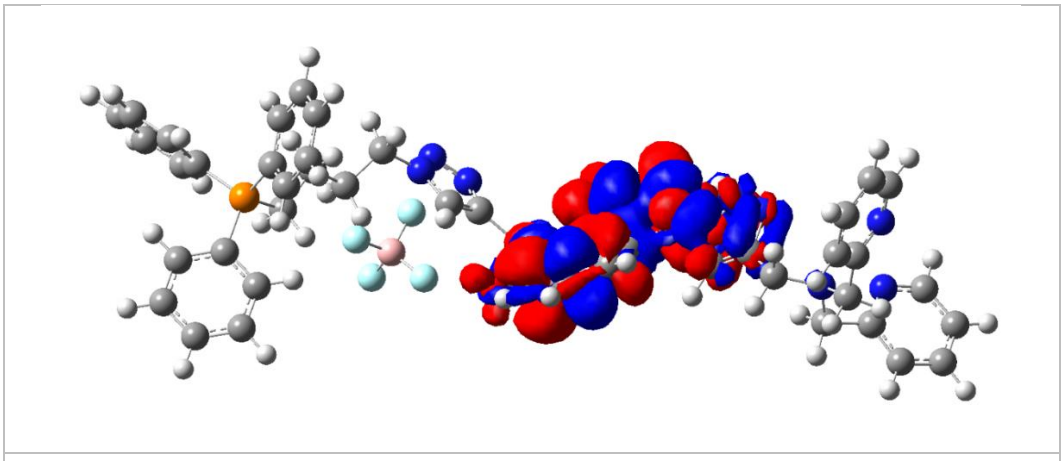

Probe **86**

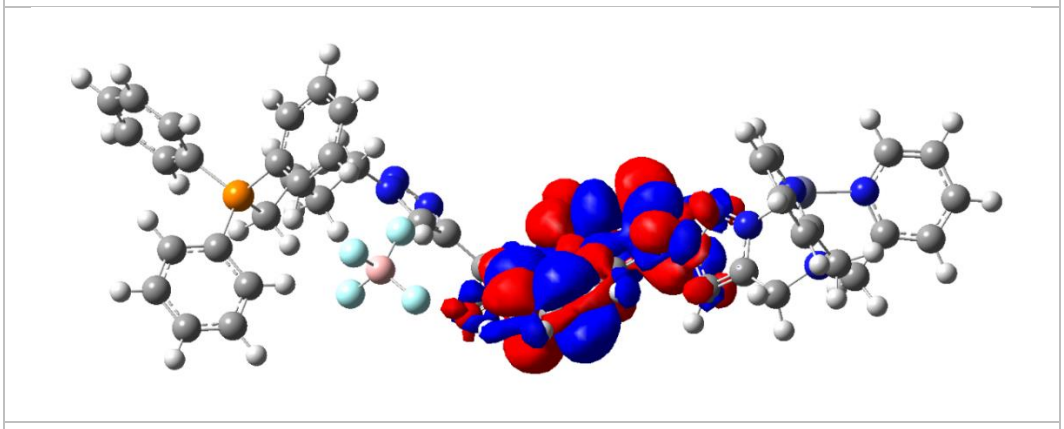

Complex with Zn^{2+}

Figure 5.18 S_1-S_0 electron density map for probe **86** and its complex with Zn^{2+} (S_1 minima). Red represents positive densities and blue negative values.

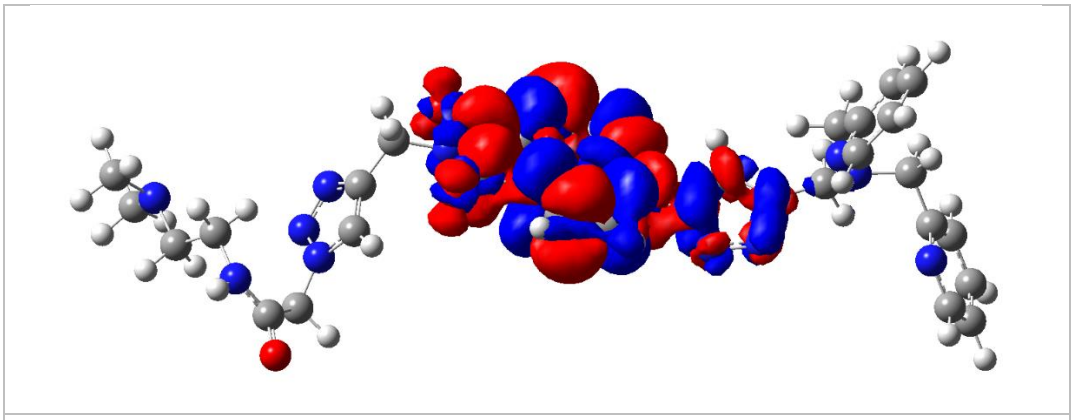

Probe **87**

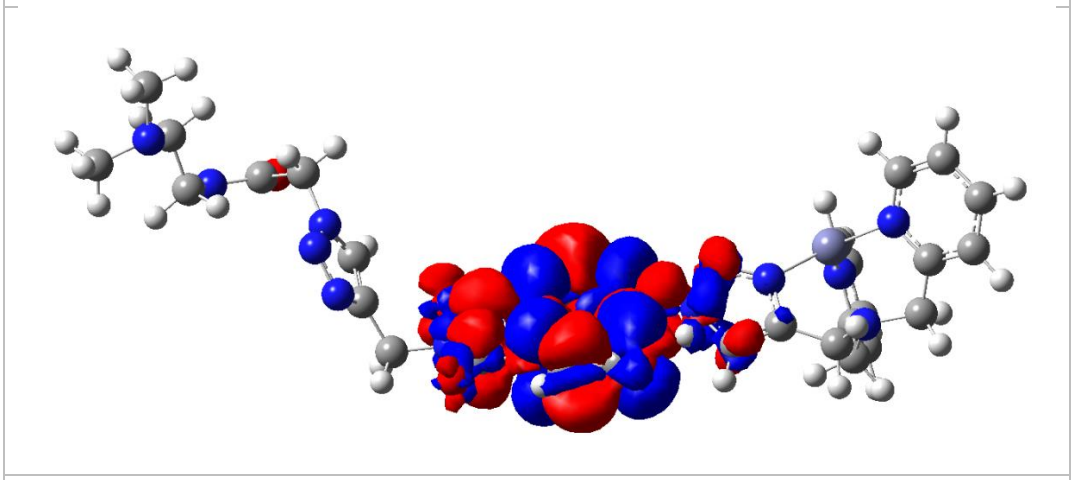

Complex with Zn^{2+}

Figure 5.19 S_1-S_0 electron density map for probe **87** and its complex with Zn^{2+} (S_1 minima). Red represents positive densities and blue negative values.

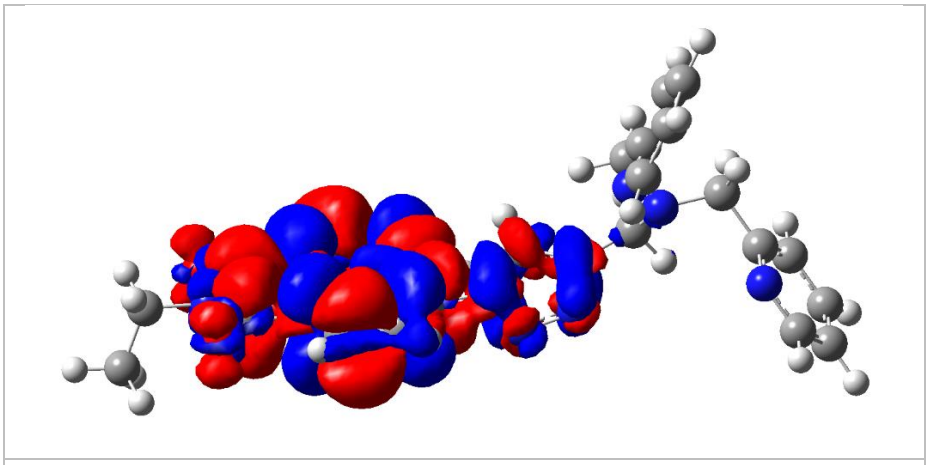

Probe **90**

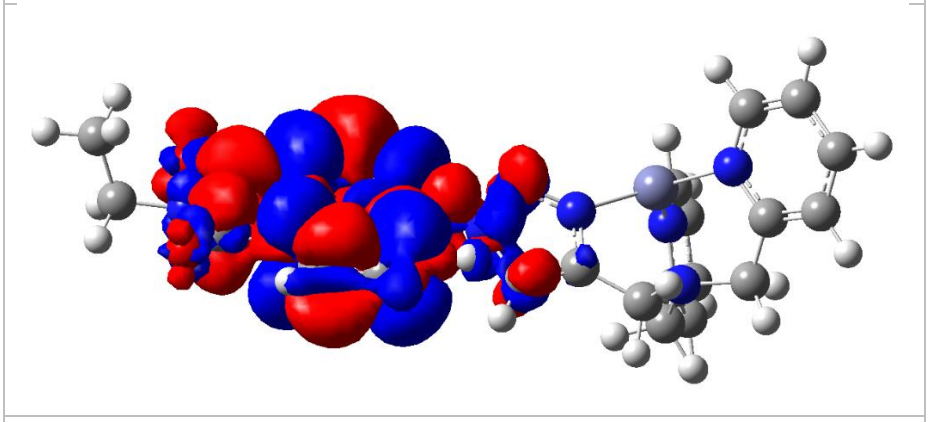

Complex with Zn^{2+}

Figure 5.20 S_1-S_0 electron density map for probe **90** and its complex with Zn^{2+} (S_1 minima). Red represents positive densities and blue negative values.

5.5 *In cellulo* tests

5.5.1 Cell toxicity of probes

As all probes show excellent photophysical properties *in vitro*, their suitability for imaging Zn^{2+} *in cellulo* was assessed. Firstly, the innate toxicity of all probes was again measured through an AlamarBlue cell viability assay. After 24 hours' incubation with probes, the HeLa cells' viability (Figure 5.21) did not show an obvious decrease with increasing probe concentration from 0 to 50 µM, indicating that the probes have no toxicity to cells.

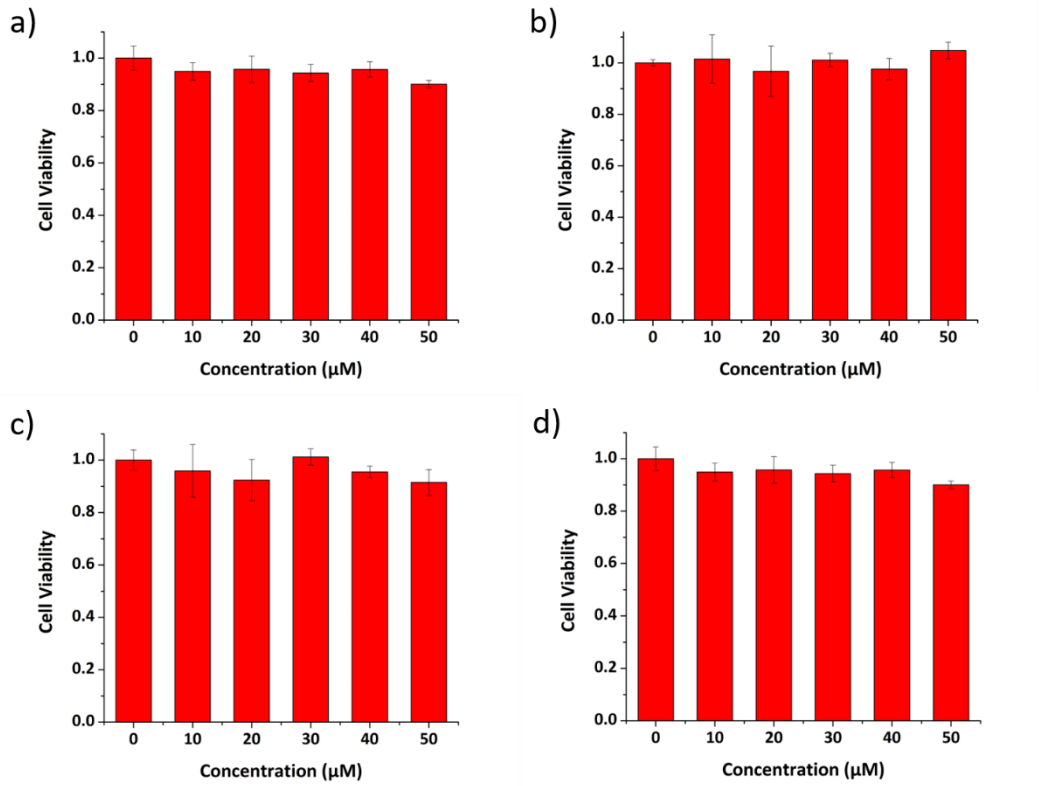

Figure 5.21 The HeLa cell viability against probes a) **85**, b) **86**, c) **87** and d) **90** at different concentrations.

5.5.2 Subcellular localisation studies

Co-localisation experiments were undertaken to confirm the probes' subcellular targeting ability. HeLa cells were co-incubated with probes and organelle tracking dyes, as shown in Figure 5.22, probe **85** displays excellent co-localisation with ER-tracker red with a Pearson's correlation coefficient of 0.88, and its dispersion in the ER and other organelles compares well with recent reports.[63] Probes **86** and **87** also displayed good co-localisation with Mito-tracker red and Lyso-tracker red (Pearson's coefficients of 0.93 and 0.86 respectively, see Figure 5.23 and 5.24). In contrast, control probe **90**, which has no targeting group, was widely distributed in all three organelles (Figure 5.25). Therefore, it can be concluded that probes **85**-**87**, which incorporate different organelle targeting groups, have the expected organelle localisation ability.

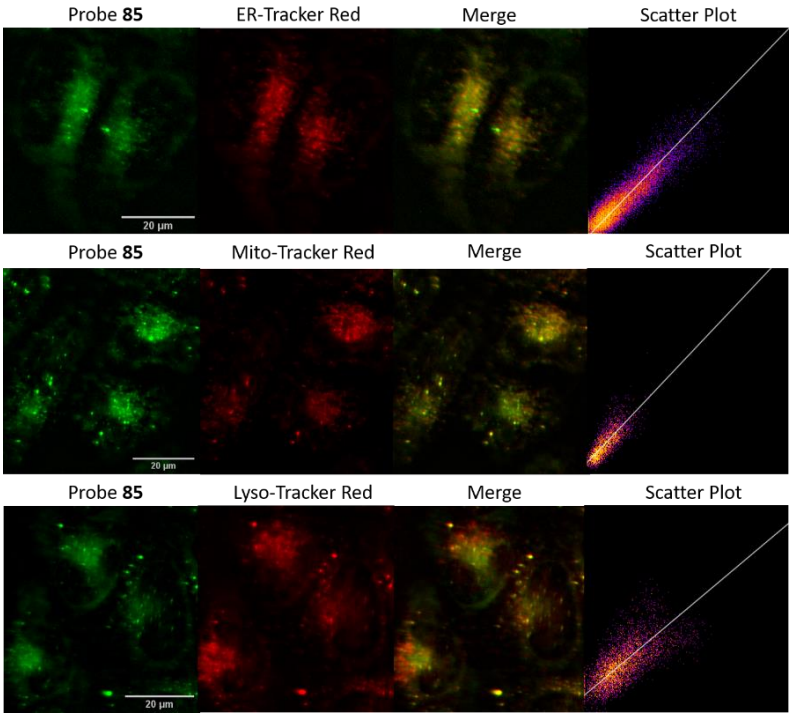

Figure 5.22 The colocalization images of HeLa cells incubated with probe **85** (20 μM, GFP filter: λ_{ex} = 470/30 nm, λ_{em} = 530/50 nm) and organelle tracker red dyes (RFP filter: λ_{ex} = 530/40 nm, λ_{em} = 605/55 nm). (Scale bars = 20 μm). Pearson's correlation coefficients were 0.88, 0.73 and 0.50 compared to ER-tracker red, Mito-tracker red and Lyso-tracker red, respectively.

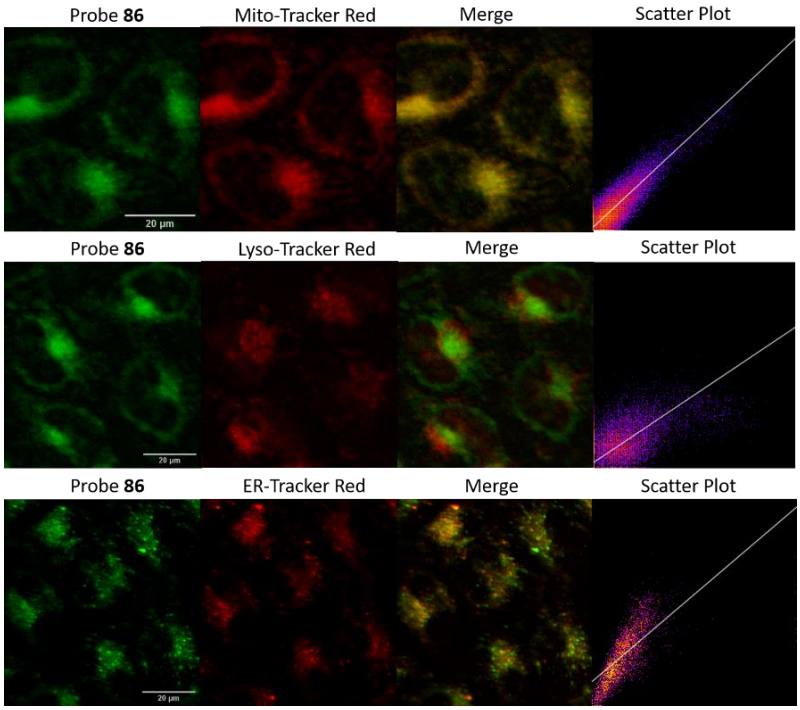

Figure 5.23 The colocalization images of HeLa cells incubated with probe **86** (20 μM, GFP filter: λ_{ex} = 470/30 nm, λ_{em} = 530/50 nm) and organelle tracker red dyes (RFP filter: λ_{ex} = 530/40 nm, λ_{em} = 605/55 nm). (Scale bars = 20 μm). Pearson's correlation coefficients were 0.93, 0.41 and 0.68 compared to Mito-tracker red, Lyso-tracker red and ER-tracker red, respectively.

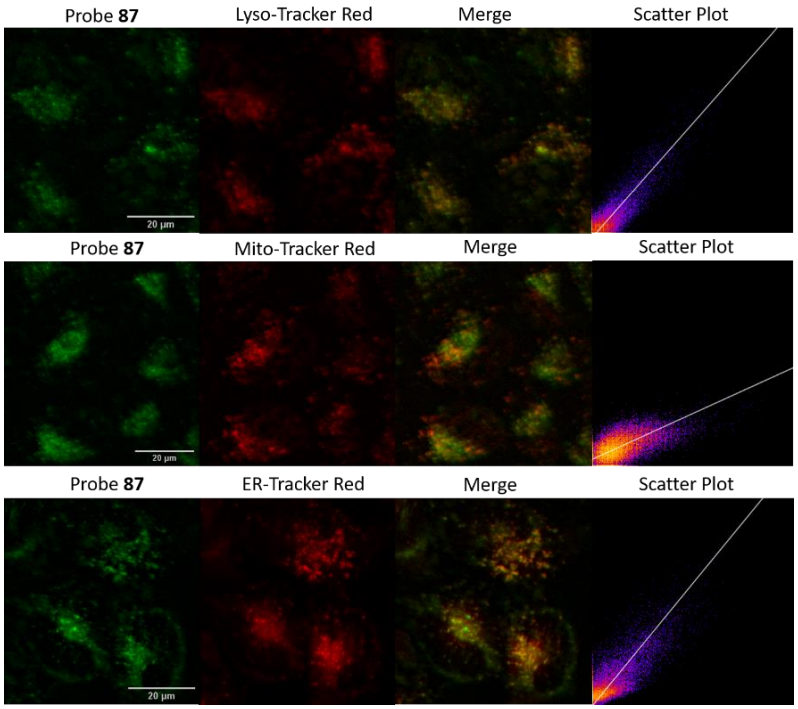

Figure 5.24 The colocalization images of HeLa cells incubated with probe **87** (20 µM, GFP filter: λ_{ex} = 470/30 nm, λ_{em} = 530/50 nm) and organelle tracker red dyes (RFP filter: λ_{ex} = 530/40 nm, λ_{em} = 605/55 nm). (Scale bars = 20 µm). Pearson's correlation coefficients were 0.86, 0.47 and 0.71 compared to Lyso-tracker red, Mito-tracker red and ER-tracker red, respectively.

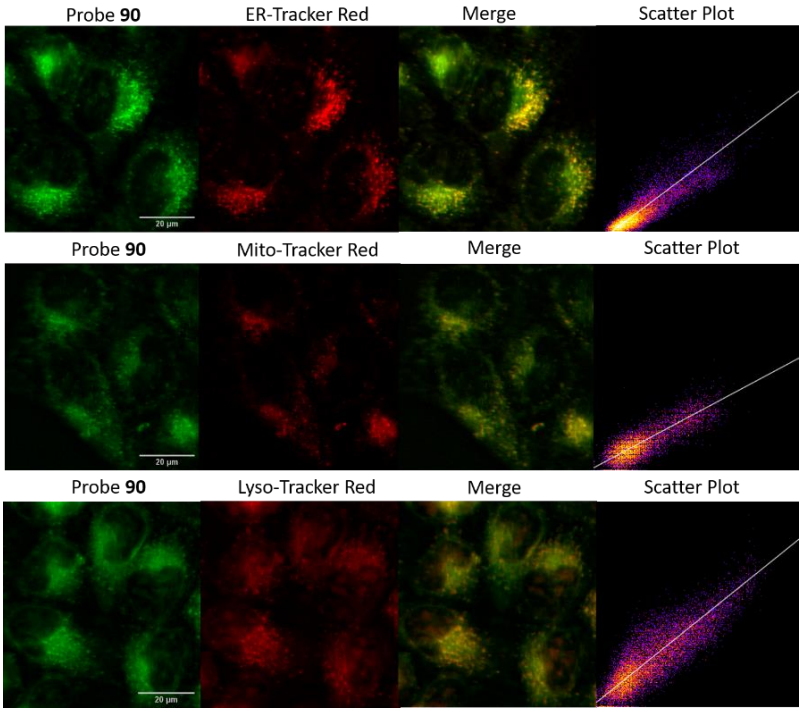

Figure 5.25 The colocalization images of HeLa cells incubated with probe **90** (20 µM, GFP filter: λ_{ex} = 470/30 nm, λ_{em} = 530/50 nm) and organelle tracker red dyes (RFP filter: λ_{ex} = 530/40 nm, λ_{em} = 605/55 nm). (Scale bars = 20 µm). Pearson's correlation coefficients were 0.85, 0.78 and 0.81 compared to ER-tracker red, Mito-tracker red and Lyso-tracker red, respectively.

5.5.3 Zn^{2+} fluorescence response in cells

As all probes displayed organelle targeting behaviour, their fluorescence response to increased levels of cellular Zn^{2+} was measured. As shown in Figure 5.26, the fluorescence of probe **85** in the ER can be observed, and after the addition of zinc pyrithione the fluorescence intensity increased considerably. The addition of TPEN, as expected caused almost complete quenching of the fluorescence. Similar results were obtained for the other probes (Figure 5.27 to 5.29), indicating that all probes display a clear fluorescence response to mobile Zn^{2+} in cells and the fluorescence intensity read from the cells for each probe is shown in Figure 5.30.

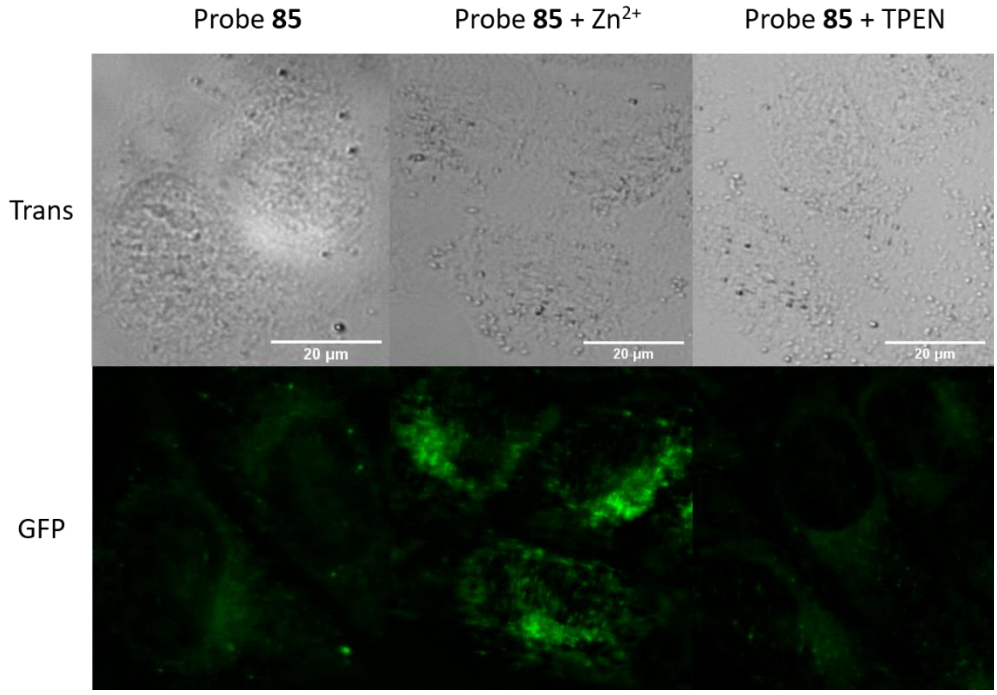

Figure 5.26 Fluorescence microscopy images of HeLa cells treated with **85** (20 µM), **85** (20 µM) with zinc pyrithione (100 µM), and **85** (20 µM) with TPEN (100 µM). (Scale bars = 20 µm).

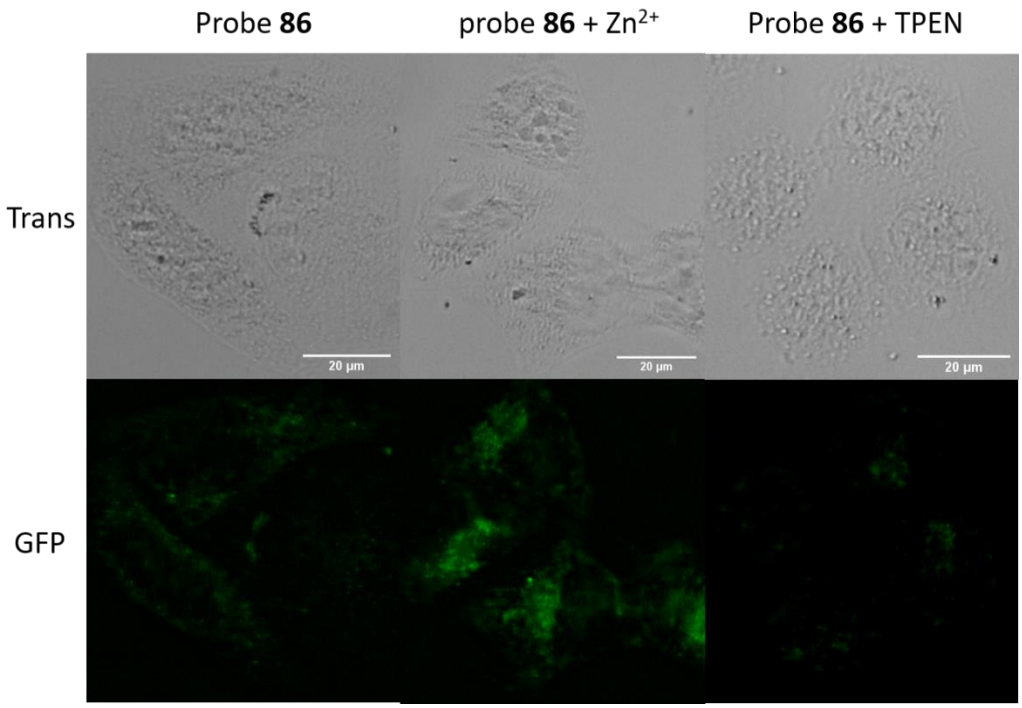

Figure 5.27 Fluorescence microscopy images of HeLa cells treated with **86** (20 µM), **86** (20 µM) with zinc pyrithione (100 µM), and **86** (20 µM) with TPEN (100 µM). (Scale bars = 20 µm).

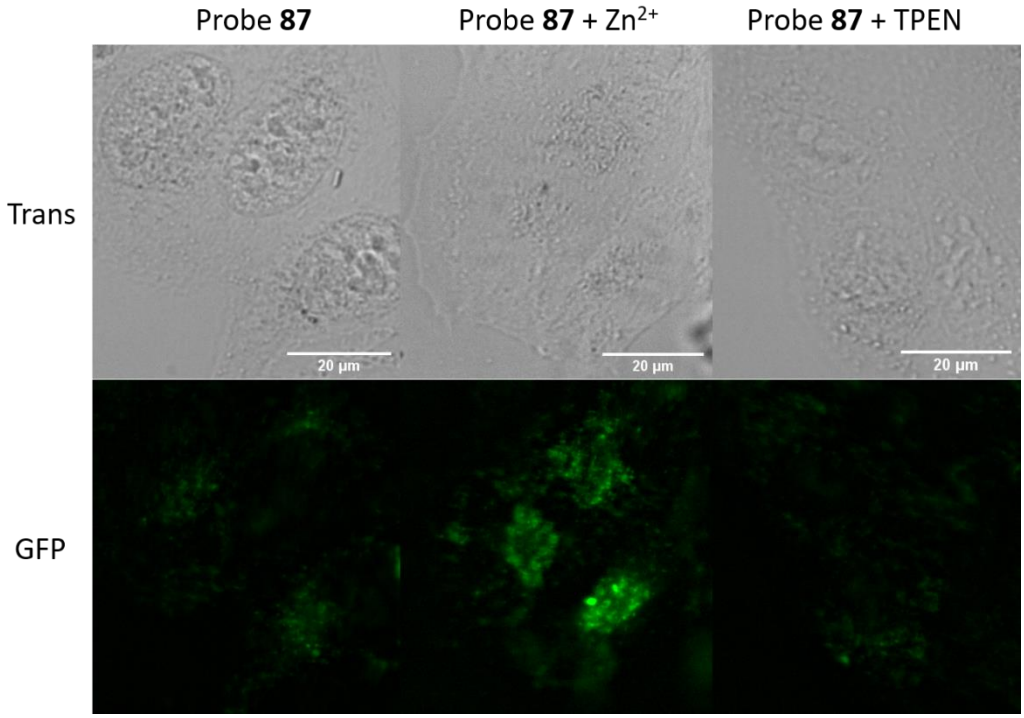

Figure 5.28 Fluorescence microscopy images of HeLa cells treated with **87** (20 µM), **87** (20 µM) with zinc pyrithione (100 µM), and **87** (20 µM) with TPEN (100 µM). (Scale bars = 20 µm).

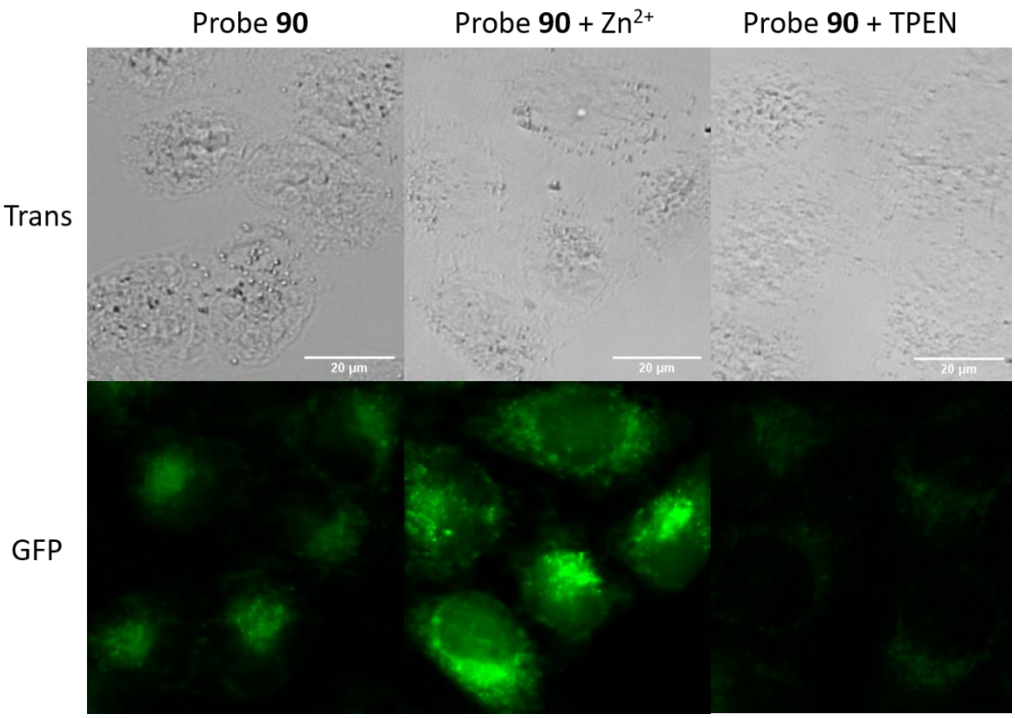

Figure 5.29 Fluorescence microscopy images of HeLa cells treated with **90** (20 µM), **90** (20 µM) with zinc pyrithione (100 µM), and **90** (20 µM) with TPEN (100 µM). (Scale bars = 20 µm).

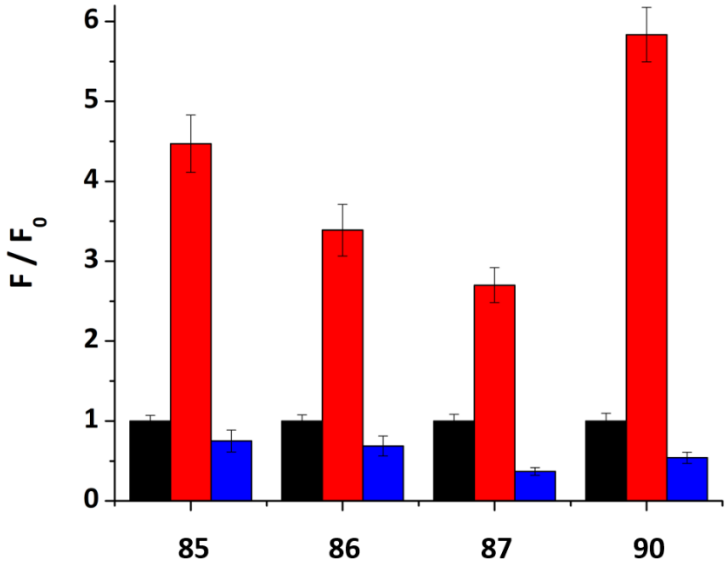

Figure 5.30 The fluorescence intensity (F) of probes in HeLa cells with zinc pyrithione (red bars) or TPEN (blue bars) relative to the intensity of the probe alone (F_0, black bars, normalised to 1).

5.6 Summary

In conclusion, a new modular 'bottom to top' click approach has been developed to synthesize subcellular localised probes by incorporating organelle targeting vectors in the last step click reaction, which is an effective and efficient method to prepare an array of different organelle targeting Zn^{2+} probes. Three probes **85**-**87** have been successfully prepared through this approach, and have been proven to localise in the ER, mitochondria and lysosome, and all display a good fluorescence response to Zn^{2+} *in vitro* and *in cellulo*. It is believed that these probes have significant potential to be applied in the imaging of mobile Zn^{2+} related biological processes in these organelles and that through this method, other sub-cellular targeting mobile Zn^{2+} probes can be developed to satisfy the imaging demands of other specific cellular locations.

Chapter 6 Conclusions and future work

6.1 Conclusions

In conclusion, a series of cellular or subcellular localised Zn^{2+} probes have been successfully prepared through the incorporation of specific targeting units. Their Zn^{2+} binding behaviours were explored by fluorescence and ^{1}H NMR spectroscopic titrations, and all probes showed high sensitivity and selectivity to Zn^{2+} both in solution and *in cellulo*. The probes also showed good accumulation in the targeted cellular location as designed. At the cellular level, a biotin tagged Zn^{2+} probe **47** was synthesized and showed high accumulation in breast cancer cells rather than in normal tissue N-TERT cells. At the subcellular level, the originally designed endoplasmic reticulum (ER) targeting probes **65** and **67** incorporating a sulfonylurea targeting group, Golgi apparatus targeting probe **78** incorporating a cysteine targeting residue, which was deprotected from the membrane permeable probe **77** inside cells, showed their accumulation in the organelles expected, and good response to Zn^{2+} in various cell lines. Probes **65** and **77** were also applied to monitor Zn^{2+} level changes during biological processes, in the ER and Golgi apparatus under oxidative stress. In addition, an alternative modular 'click-S_NAr-click' approach was developed to make the subcellular localised probe synthesis more efficient and effective, and based on this strategy, the ER, mitochondria and lysosome targeting probes **85**-**87** were obtained. With these probes available, the mobile Zn^{2+} in different organelles could be studied and related biological processes monitored to help better understand the role Zn^{2+} plays in them.

6.2 Future work

In future, some further work could be undertaken to extend the project further and some suggestions for the design of new probes will be discussed below.

6.2.1 Nucleus targeting Zn^{2+} probe

As an obvious extension of the current suite of probes, and as discussed in Section 1.4.6, it is necessary to develop a probe to image Zn^{2+} in the nucleus specifically, though the concentration of mobile Zn^{2+} in this organelle is very low. It is reported that the pyrrole-imidazole (Py-Im) polyamides have some programmable sequence recognition properties, which can bind the minor groove of DNA with high affinity.[138] Normally, they are used to modulate gene expression in cells.[139,140] However, in this case, the non-fluorescent motif, which can bind to DNA could be introduced in probe **91** as a nucleus targeting group through a click reaction.

A further interesting challenge would be to develop ratiometric probes to quantify mobile Zn^{2+} concentration in the nucleus. Besides the usually used mechanisms, such as ICT and FRET, it may be possible simply to incorporate a fluorescent nucleus targeting dye into a conventional Zn^{2+} probe. However, to prevent the spectral crosstalk between two channels, the nucleus stain must have an excitation and emission profile far away from that of the naphthalimide fluorophore. Therefore, a commercially available nuclear dye such as TO-PRO-3 iodide, which has red fluorescence with λ_{ex} = 642 nm, λ_{em} = 661 nm is a possible nucleus targeting unit which could be incorporated as shown in probe **92**.

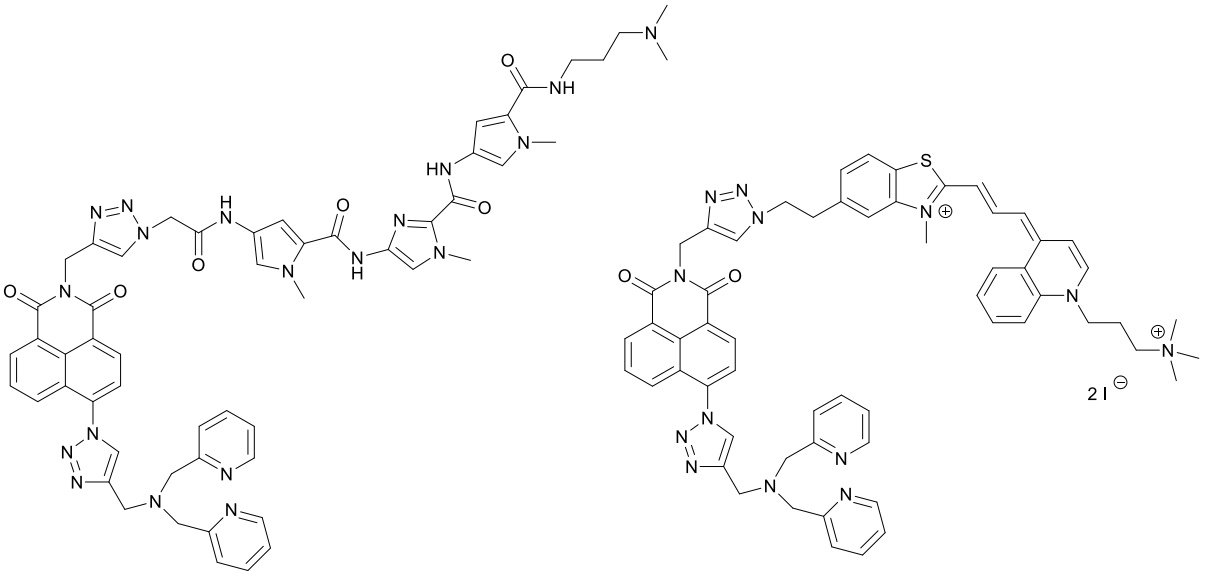

91 **92**

Figure 6.1 The structures of two proposed nucleus targeting Zn^{2+} probes, **91** and **92**.

6.2.2 Zn^{2+} probes to study metabolic processes

It is known that spatiotemporal zinc fluctuations in response to intra- or extracellular environmental changes are related to many biological processes[82] and tools to study the role Zn^{2+} plays in these are still required. Though the probes prepared in this thesis showed the expected subcellular organelle accumulation, to study the specific biological process, especially a specific protein involved process, protein-based sensors using genetically encoded targeting sequences may be better to control the cellular localisation, but as discussed, they have their limitations mainly in brightness and photostability. To overcome the disadvantages of the protein-based or peptide-based sensors, hybrid probes, such as SNAP-tag and HaloTag, the self-labelling protein tags based on O-6-methylguanine-DNA methyltransferase and haloalkane dehalogenase respectively, may provide a new strategy, as they have already been widely used as biomarkers. Protein tags are peptide sequences that can be genetically fused to any protein of interest and further specifically to tag with a suitable ligand, such as fluorescent dye by a covalent bond and Lippard *et al.* have reported a series

of organelle targeted small molecule-protein hybrid zinc probes based on SNAP-tag[141] and HaloTag.[82] Probes **93** and **94** are designed for SNAP-tag and HaloTag, respectively, which can be fused to the protein of interest to study the Zn^{2+} functions in the protein related processes.

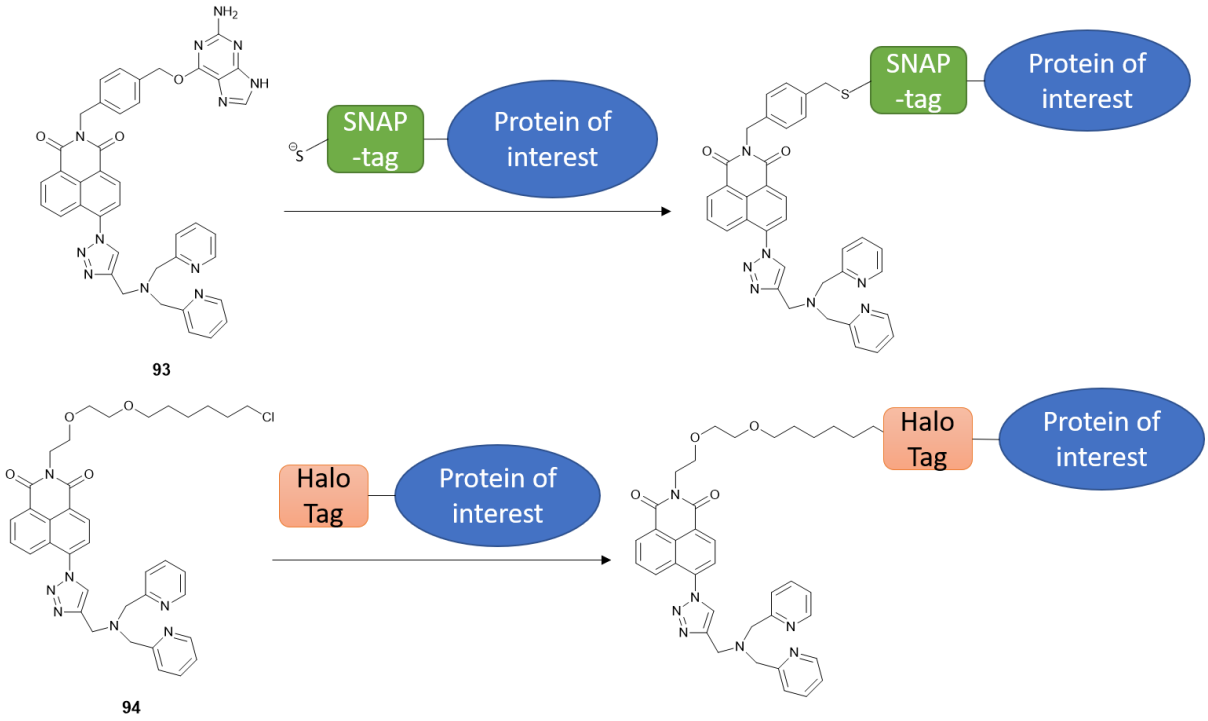

Figure 6.2 Proposed hybrid Zn^{2+} probes **93** and **94** capable of utilising SNAP-tag and HaloTag.

6.2.3 Probes with other fluorophores

In recent years, probes with longer wavelength excitation and emission profiles, such as the near-infrared range (650 – 900 nm), have found increasing application *in vivo*, since the longer wavelength light allows for deeper tissue penetration and less autofluorescence from surrounding tissues. Although previous studies have demonstrated zinc imaging systems that have a two-photon profile, problems with photostability have largely limited their applications to single photon excitation[25] and consequently due to the short wavelength of excitation and emission, the naphthalimide may need to be replaced by another fluorophore. Furthermore, with the fast development of high spatiotemporal resolution fluorescent microscope, such as total internal reflection fluorescence microscope and super-resolution

microscope, probes able to provide real-time information about the locations, dynamics and interactions of individual molecules in living cells are highly desired. However, many fluorescent proteins and synthetic dyes are not suitable for these new techniques due to their low brightness and photostability under high photon intensity microscopy, including the naphthalimide probes prepared in this thesis. To find applications in biological labelling, probes must have good membrane permeability, suitable wavelength excitation and emission, high photostability, a good signal-noise ratio as well as specific targeting ability. Therefore modification of fluorophores, such as Rhodamine and Bodipy may be good options as they are widely used in cells imaging, can be readily structurally modified to obtain the long wavelength excitation and emission profiles desired and by modification of their substitutions, it may be possible to develop analogous modular routes towards a series of organelle targeted probes with probes like **95** and **96**.

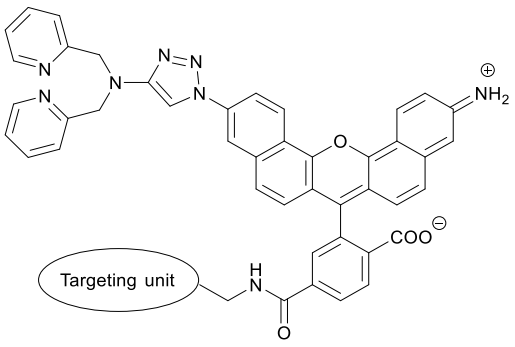

95

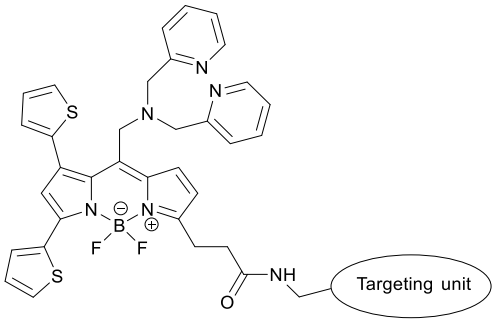

96

Figure 6.3 Proposed Zn^{2+} probes **95** and **96** based on Rhodamine and Bodipy derivatives.

Chapter 7 Experimental

7.1 General experimental information

Unless otherwise stated, reactions were carried out using commercially available reagents, used as supplied from Sigma Aldrich, Alfa Aesar, or Tokyo Chemical Industry (TCI), in combination with solvents from Honeywell Solvents. ER-tracker red, Mito-tracker red and Lyso-tracker red were purchased from Enzo Life Sciences. Bodipy TR ceramide purchased from Thermo Fisher was used as a control Golgi tracker dye. DAPI (4',6-diamidino-2-phenylindole) was purchased from Thermo Fisher for DNA stain to show nucleus. The HeLa, MCF-7 and HepG2 cell lines used for fluorescence imaging were provided from American Type Culture Collection (ATCC Middlesex, UK), and the EC23 cell line was provided by Prof. Michael P. Philpott of Barts and The London School of Medicine and Dentistry, Queen Mary University of London. Anhydrous DCM and DMF were purified from an MBRAUN MB SPS-800 solvent purification system. "H_2O" refers to deionized water.

For synthesis requiring anhydrous conditions, reactions were carried out under a nitrogen atmosphere using oven-dried glassware. Solvents were removed *in vacuo* using a Heidolph Hei-VAP Value G1 rotary evaporator with a water and dry ice bath condenser. Analytical thin layer chromatography was carried out on Merck Kiesel gel 60 aluminium-backed silica plates, with visualisation using short-wave ultraviolet light (254 nm) or staining with $KMnO_4$ or phosphomolybdic acid (PMA) stain. Column chromatography was carried out using BDH (40-60 μm) silica gel.

Infrared spectra were obtained on a Bruker Tensor 37 FTIR spectrometer in the range 4000-600 cm^{-1}. UV-Vis spectra were obtained on a PerkinElmer Lambda 35 UV/Vis spectrometer. Fluorescence spectra were measured on an Agilent Cary eclipse fluorescence spectrophotometer with a 1 cm path length cell. The fluorescence microscope images were

obtained from a Logos CELENA S digital imaging system. Confocal microscopy images were taken by Leica TCS SP5 Confocal microscope. ^{1}H NMR spectra were recorded at 400 MHz on a Bruker Avance I or Bruker Avance III spectrometer. Chemical shifts are reported in δ (ppm), quoted to the nearest 0.01 ppm and referenced to the residual solvent peak used as the internal standard: $CHCl_3$ (7.26 ppm), MeOH (3.31 ppm), DMSO (2.50 ppm) and CH_3CN (1.94 ppm). Coupling constants (J) are measured in Hertz (Hz) and reported to 1 d.p. Peak multiplicities for resonances are noted as standard abbreviations: s, singlet; d, doublet; dd, double doublet; dt, doublet of triplets, t, triplet; q, quartet; m, unresolved multiplet; bs, broad singlet. ^{13}C NMR spectra were recorded at 101 MHz on a Bruker Avance III spectrometer. Chemical shifts (δ) are quoted to the nearest 0.1 ppm, with reference to the given solvent $CDCl_3$ (77.2 ppm), MeOD (49.0 ppm), DMSO (39.5 ppm) and CD_3CN (118.3 ppm) as the internal standard. High resolution mass spectrometry was carried out by the Waters Synapt G2Si HDMS, while some spectra were provided by the EPSRC National Mass Spectrometry Service, University of Wales. Molecular ions are reported for ^{35}Cl and ^{79}Br isotopes. Melting points were measured on a Stuart SMP3 melting point apparatus and are uncorrected.

Unless noted otherwise, the solution for all photophysical tests was a 0.1 mM HEPES (⩾99.5%) buffer (pH 7.4) made up from a DMSO stock solution to dissolve probes with a 1% total DMSO concentration. $ZnCl_2$ was used as the Zn^{2+} source to simulate the chloride-rich biological environment. The medium used to incubate HeLa, MCF-7 and HepG2 cells was Dulbecco's Modified Eagle Medium (DMEM), supplemented with 10% heat-deactivated fetal bovine serum (FBS). The medium used for EC23 cells was DMEM/F12 1:1 supplemented with 10% heat-deactivated FBS and RM^{+} (Rheinwald Media: transferrin 5 μg/mL, hydrocortisone 0.4 μg/mL, cholera toxin 10^{-10} M, epidermal growth factor 10 ng/mL (AbD Serotec, Oxford, UK), insulin 5 μg/ml, liothyronine 2×10^{-11} M, adenine 1.8×10^{-4} M). In all medium, 1% (v/v)

penicillin streptomycin was added as antibiotics. Unless noted otherwise, all cells were incubated at 37 °C in a 5% CO_2/ 95% air incubator. AlamarBlue™ was used to check cells' viability according to the manufacturer's instructions. For ER stress or oxidative stress studies, the alive cells after probes' treatment were washed with phosphate-buffered saline (PBS) and then the cells were cultured in PBS for imaging under microscopy. All the images of cells were processed by ImageJ software, and the fluorescence intensity in cells was read directly from ImageJ before processing.

7.2 General procedures

7.2.1 Fluorescence titration to determine dissociation constant K_d

To determine the dissociation constant K_d, a series of HEPES (4-(2-hydroxyethyl)-1-piperazineethanesulfonic acid) buffer solutions (50 mM, pH 7.2, 0.1 M KCl) containing various amounts of $ZnCl_2$ (0 ~ 9.0 mM) and 10 mM of EGTA (ethylene glycol-bis(2-aminoethylether)-*N*,*N*,*N'*,*N'*-tetraacetic acid) were prepared. The $[Zn^{2+}]_{free}$ was calculated followed the reported methods.[37,142,143]

The calculated $[Zn^{2+}]_{free}$ concentration of each solution is:

$[Zn^{2+}]_{total}$ (mM)	0.0	0.5	1.0	1.5	2.0	2.5	3.0	3.5
$[Zn^{2+}]_{free}$ (nM)	0.00	0.14	0.29	0.46	0.66	0.87	1.11	1.39
$[Zn^{2+}]_{total}$ (mM)	4.0	4.5	5.0	6.0	7.0	8.0	9.0	
$[Zn^{2+}]_{free}$ (nM)	1.73	2.12	2.59	3.88	6.04	10.36	23.31	

To determine the apparent dissociation constants for probes, the fluorescence titration curves at concentrations 1 μM, 0.1 μM and 0.01 μM were obtained and fitted to Equation 7.1.[37,136] *F* is the observed fluorescence intensity, F_0 is the observed fluorescence of the probe alone. Non-linear curve fitting analysis was used to determine F_{max}/F_0 and K_d.

$$\frac{F}{F_0} = 1 + \left(\frac{F_{max}}{F_0} - 1\right)\frac{[Zn^{2+}]_{free}}{K_d + [Zn^{2+}]_{free}} \quad \text{(Equation 7.1)}$$

7.2.2 Quantum yield *Φ* measurement

Based on the absorption wavelength of probes studied in this thesis, anthracene (*Φ* = 0.27 in ethanol) was chosen as a standard sample. In order to minimise the re-absorption effects, the absorbance of all samples should be below 0.1 at the excitation wavelength. For standard sample, each probe and its complex, UV-Vis and fluorescence spectra of five solutions with increasing concentrations were recorded, and the linear plots of integrated fluorescence intensity against absorbance were obtained. The gradient for each sample is proportional to the sample's fluorescence quantum yield, which can be calculated through Equation 7.2 by comparing to the known quantum yield of the standard compound. Where the subscripts *ST* and *X* denote standard and test respectively, *Φ* is the fluorescence quantum yield, *Grad* the gradient from the plot of integrated fluorescence intensity *vs* absorbance, and *η* the refractive index of the solvent.

$$\Phi_X = \Phi_{ST}\left(\frac{Grad_X}{Grad_{ST}}\right)\left(\frac{\eta_X}{\eta_{ST}}\right)^2 \quad \text{(Equation 7.2)}$$

7.2.3 Detection limit (LOD) measurement

To determine the detection limit, the fluorescence spectrum of the probe only was measured 20 times and the standard deviation of this blank measurement was obtained as σ. The slope K was obtained from linear fitting of the fluorescence Zn^{2+} titration data and the detection limit was then calculated through Equation 7.3.

$$LOD = \frac{3\sigma}{K} \quad \text{(Equation 7.3)}$$

7.2.4 The apparent pK_a values calculation

The fluorescence spectra were recorded at different pH, the integrated fluorescence intensity against pH was plotted and through non-linear curve fitting with the Equation 7.4 or Equation 7.5, three or four pK_a values were obtained, respectively. F_{max} is the maximum normalized emission integration (F_{max} = 1), F_0 is the minimum normalized emission integration obtained, and ΔF_{1max}, ΔF_{2max}, ΔF_{3max} and ΔF_{4max} are the maximum fluorescence integration changes associated with the corresponding pK_a values.

$$\frac{F - F_0}{F_{max} - F_0} = \frac{\Delta F_{1max}}{(1 + 10^{(pH - pK_{a1})})} + \frac{\Delta F_{2max}}{(1 + 10^{(pH - pK_{a2})})} + \frac{\Delta F_{3max}}{(1 + 10^{(pH - pK_{a3})})} \quad \text{(Equation 7.4)}$$

$$\frac{F - F_0}{F_{max} - F_0} = \frac{\Delta F_{1max}}{(1 + 10^{(pH - pK_{a1})})} + \frac{\Delta F_{2max}}{(1 + 10^{(pH - pK_{a2})})} + \frac{\Delta F_{3max}}{(1 + 10^{(pH - pK_{a3})})} + \frac{\Delta F_{4max}}{(1 + 10^{(pH - pK_{a4})})} \quad \text{(Euqation 7.5)}$$

7.2.5 The AlamarBlue assay to determine cell viability

The cells were cultured in 96-well plate and treated with various concentration of probes (0 ~ 50 μM) in the medium at 37 °C in a 5% CO_2/ 95% air incubator for 24 hours. After culture medium was removed, the cells were washed with PBS for three times, and further incubated with 10% (v/v) AlamarBlue assay in the medium for a certain time (normally 1 ~ 2 hours) until the colour changed to pink. Then the fluorescence was obtained by microplate fluorometer using 560/590 nm ($\lambda_{ex}/\lambda_{em}$) filter settings. The fluorescence intensity is proportional to cell viability.

7.2.6 The subcellular localisation studies

The subcellular localisation of probes was studied by co-localisation experiments. The cells were cultured on 11 mm circular coverslips in 12-well plate and then treated with probes for a certain time (normally 1 hour unless noted otherwise) at 37 °C in a 5% CO_2/95% air incubator.

After that, all cells were washed with PBS three times, and then Bodipy TR ceramide, ER-tracker red, Mito-tracker red and Lyso-tracker red were added in different groups respectively for a certain time following the protocol. Again, the cells were washed with PBS for three times and fixed with 4% paraformaldehyde for 20 minutes. Then the cells were treated with DAPI, followed by three times washing. After the cover slips were mounted on the microscope slides, the probes' subcellular localisation in cells can be investigated under microscope. The Pearson's correlation coefficient was obtained through the comparison of the fluorescence of probes and that of the organelle markers in the same area of interest by ImageJ software.

7.2.7 Zn^{2+} response in cells

For Zn^{2+} response experiments, the cells were cultured on 11 mm circular coverslips in 12-well plate and then treated with probes for a certain time (normally 1 hour unless noted otherwise) at 37 °C in a 5% CO_2/ 95% air incubator unless noted otherwise, and then washed with PBS for three times. Zinc pyrithione and TPEN were added to different groups respectively for 15 minutes incubation, while no treatment needed for the control group. After all treatments, the cells were washed with PBS buffer three times and following with the DAPI treatment. After washing, the cover slips were mounted on the microscope slides, and the fluorescence of cells was investigated by microscope. The fluorescence intensity of the area of interest was read by ImageJ software before processing.

7.2.8 DFT and TDDFT calculations

To understand the binding behaviour of the probes with Zn^{2+} and its fundamental electronic structure, DFT and TDDFT studies were performed. The structure of probes and their complexes with Zn^{2+} were optimised using B3LYP functional and 6-31G* basis set in Gaussian 09. The calculation of excited states and structures of the S_1 minima were obtained at

CAMB3LYP/6-31G* level of theory. All calculations considered H_2O as solvent using a continuum model (PCM). All calculations were performed on Queen Mary's Apocrita HPC facility, supported by QMUL Research-IT.

7.3 Experimental data

6-Bromo-2-(prop-2-yn-1-yl)-1*H*-benzo[*de*]isoquinoline-1,3(2*H*)-dione (**38**)

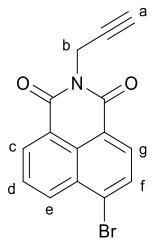

4-Bromo-1,8-naphthalic anhydride (1.0 g, 3.6 mmol) was dissolved in 1,4-dioxane (30 mL) and to this was added propargylamine (0.28 mL, 4.3 mmol). The yellow-brown suspension was stirred at room temperature for 1 h, and then heated to 70 °C overnight to give a dark brown solution. Then the mixture was cooled to room temperature and slowly poured into ice-cold H_2O (120 mL). The resulting precipitate was collected by filtration and washed with H_2O (30 mL) and dried *in vacuo* to give **38** as a light brown solid (0.98 g, 87%). ^{1}H NMR (400 MHz, $CDCl_3$) δ_H 8.73 (dd, 1H, *J* = 7.3, 0.9, H_c), 8.64 (dd, 1H, *J* = 8.4, 0.9, H_e), 8.49 (d, 1H, *J* = 7.9, H_g), 8.09 (d, *J* = 7.9, H_f), 7.90 (dd, 1H, *J* = 8.4, 7.3, H_d), 4.98 (d, 2H, *J* = 2.5 , H_b), 2.22 (t, 1H, *J* = 2.4, H_a). ^{13}C NMR (101 MHz, $CDCl_3$) δ 162.8 (×2), 133.7, 132.5, 131.6, 131.2, 130.8, 130.7, 129.0, 128.2, 122.8, 121.9, 78.3, 70.7, 29.6. All other spectroscopic data were consistent with those previously reported.[25]

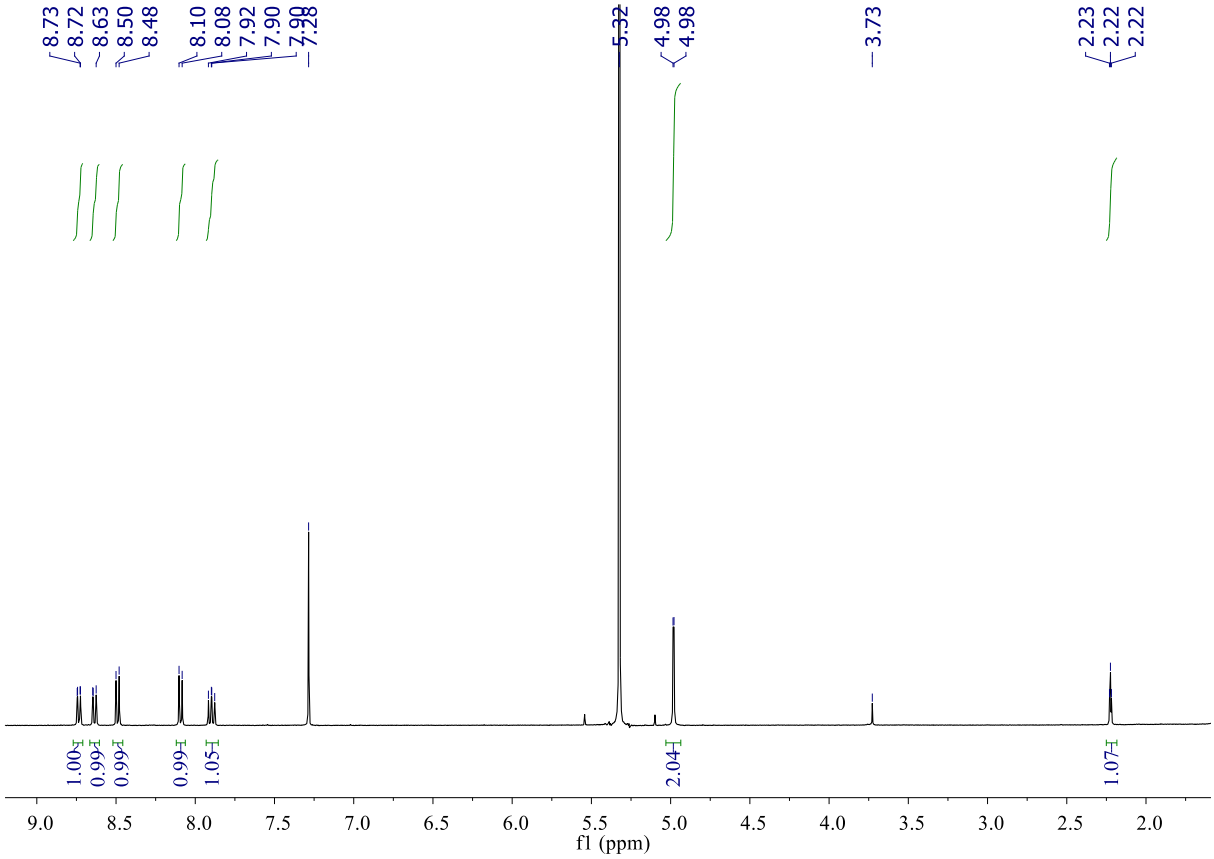
8.73
8.72
8.63
8.50
8.48
8.10
8.08
7.92
7.90
7.28
5.32
4.98
4.98
3.73
2.23
2.22
2.22
1.00
0.99
0.99
0.99
1.05
2.04
1.07
f1 (ppm)

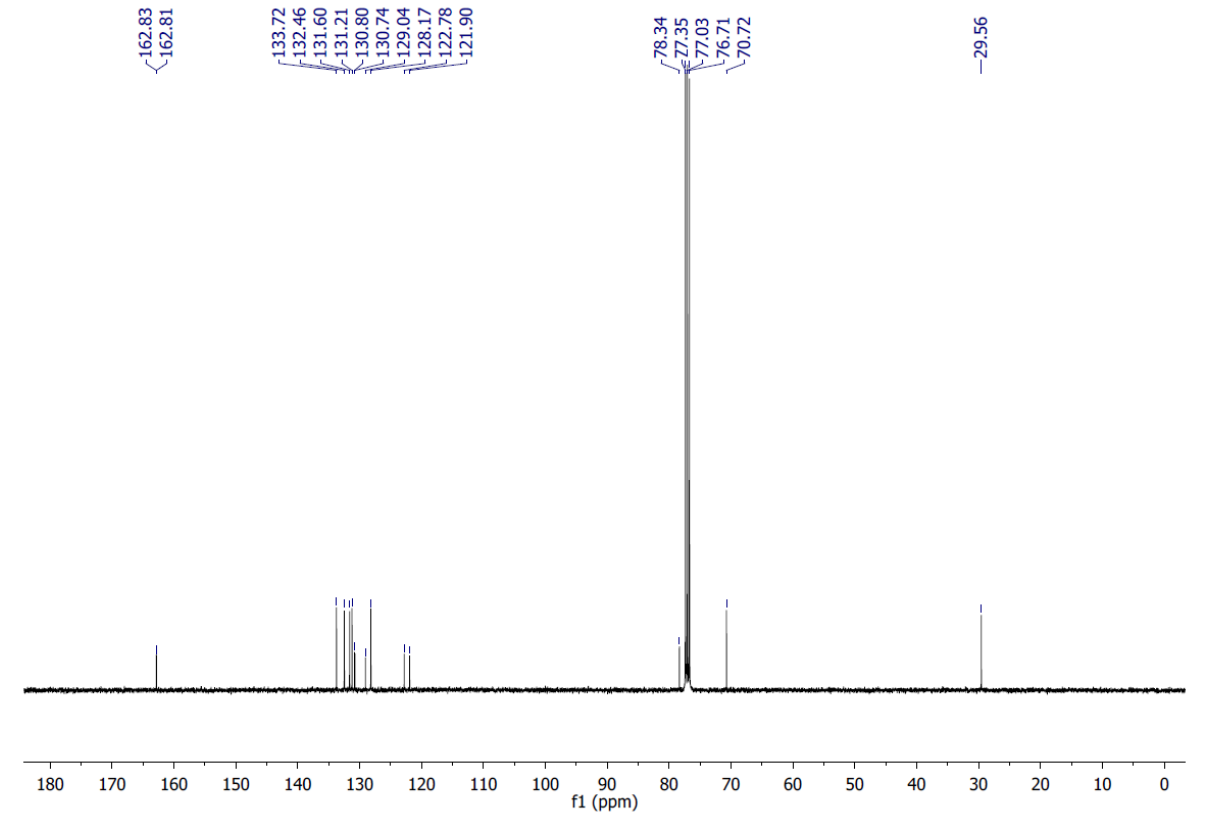
162.83
162.81
133.72
132.46
131.60
131.21
130.80
130.74
129.04
128.17
122.78
121.90
78.34
77.35
77.03
76.71
70.72
29.56
f1 (ppm)

Tri-*tert*-butyl 1,4,8,11-tetraazacyclotetradecane-1,4,8-tricarboxylate **(39)**

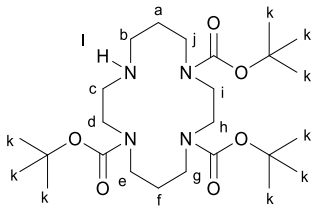

Under an atmosphere of nitrogen, 1,4,8,11-tetraazacyclotetradecane (cyclam, 1.0 g, 5.0 mmol) was dissolved in dry DCM (200 mL). The colourless solution was stirred at room temperature and Et_3N (3.5 mL, 25 mmol) was added, followed was added dropwise by a solution of Boc_2O (2.0 g, 9.2 mmol) in anhydrous DCM (60 mL). The reaction was then cooled to -15 °C and a further portion of Boc_2O (1.3 g, 6.0 mmol) in anhydrous DCM (40 mL) was added. The mixture was stirred overnight allowing warming to room temperature over this time. The reaction mixture was washed with 0.25 M Na_2CO_3 (5 × 20 mL), dried over $MgSO_4$, and concentrated *in vacuo.* The resulting crude material was purified by column chromatography (eluent: DCM/MeOH 20:1) to give **39** as a viscous, colourless oil (2.1 g, 83%). ^{1}H NMR (400 MHz, $CDCl_3$) δ_H 3.41-3.30 (m, 12H, $H_{d\text{-}e,\ g\text{-}j}$), 2.80 (t, 2H, J = 5.6, H_c), 2.63 (t, 2H, J = 5.6, H_b), 2.02-1.88 (m, 2H, H_f), 1.76-1.68 (m, 2H, H_a), 1.47 (s, 27H, H_k). All other spectroscopic data were consistent with those previously reported.[144]

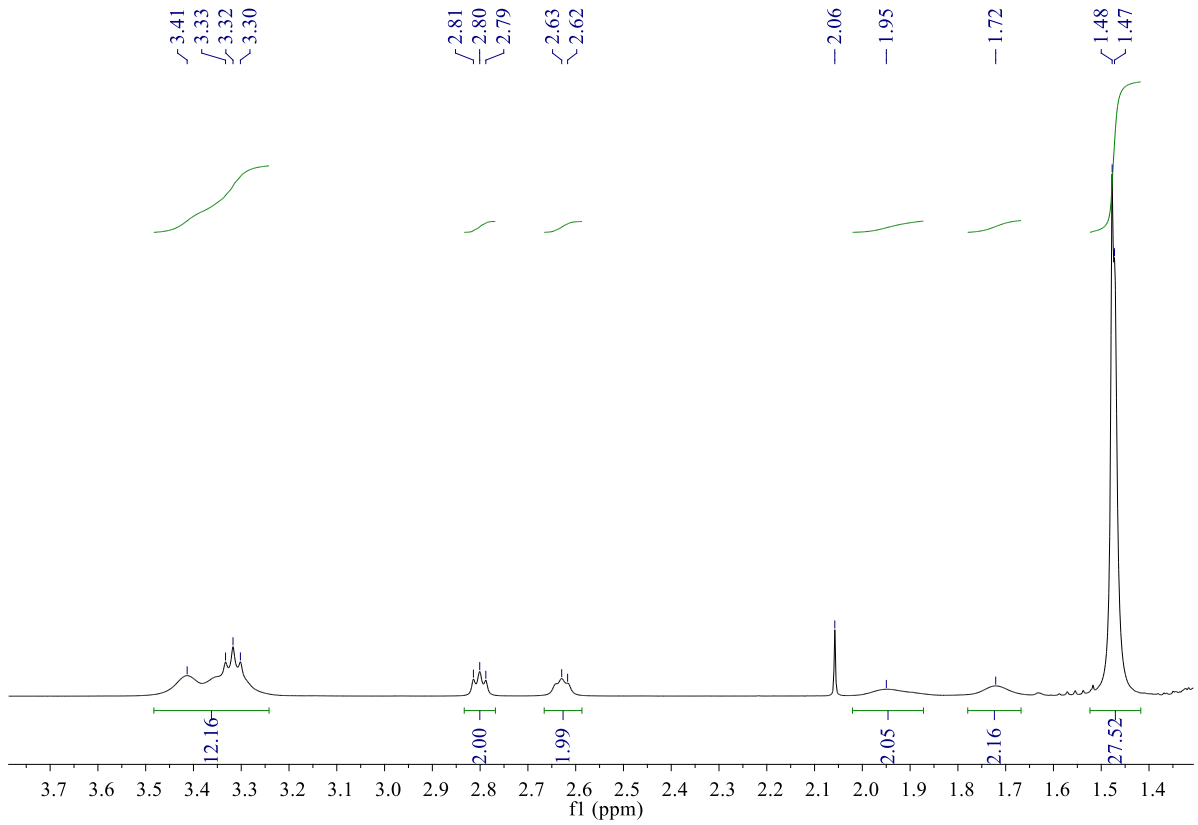
3.41
3.33
3.32
3.30
2.81
2.80
2.79
2.63
2.62
2.06
1.95
1.72
1.48
1.47
12.16
2.00
1.99
2.05
2.16
27.52
3.7 3.6 3.5 3.4 3.3 3.2 3.1 3.0 2.9 2.8 2.7 2.6 2.5 2.4 2.3 2.2 2.1 2.0 1.9 1.8 1.7 1.6 1.5 1.4
f1 (ppm)

Tri-*tert*-butyl 11-(prop-2-yn-1-yl)-1,4,8,11-tetraazacyclotetradecane-1,4,8-tricarboxylate (**40**)

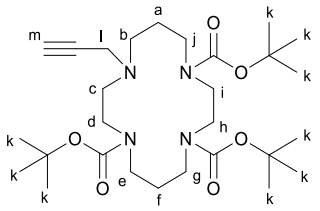

Tri-Boc protected cyclam **39** (488 mg, 0.975 mmol) was dissolved in MeCN (12.5 mL) and to this was added Na_2CO_3 (207 mg, 1.95 mmol) followed by propargyl bromide (80 % wt. in toluene, 96.0 µL, 1.07 mmol). The mixture was heated to reflux and stirred overnight. Then the reaction was cooled to room temperature, filtered to remove insoluble salts, and concentrated *in vacuo*. The resulting crude material was purified by column chromatography (eluent: Petrol/EtOAc 2:1), to give **40** as a viscous, colourless oil. (363 mg, 69%). ^{1}H NMR (400 MHz, $CDCl_3$) δ_H 3.42 (bs, 2H, H_l), 3.38-3.26 (m, 12H, $H_{d\text{-}e,\ g\text{-}j}$), 2.72-2.68 (m, 2H, H_c), 2.53 (t, 2H, J = 5.8, H_b), 2.18 (bs, 1H, H_m), 1.96-1.86 (m, 2H, H_f), 1.74-1.68 (m, 2H, H_a), 1.48 (s, 27H, H_k). All other spectroscopic data were consistent with those previously reported.[101]

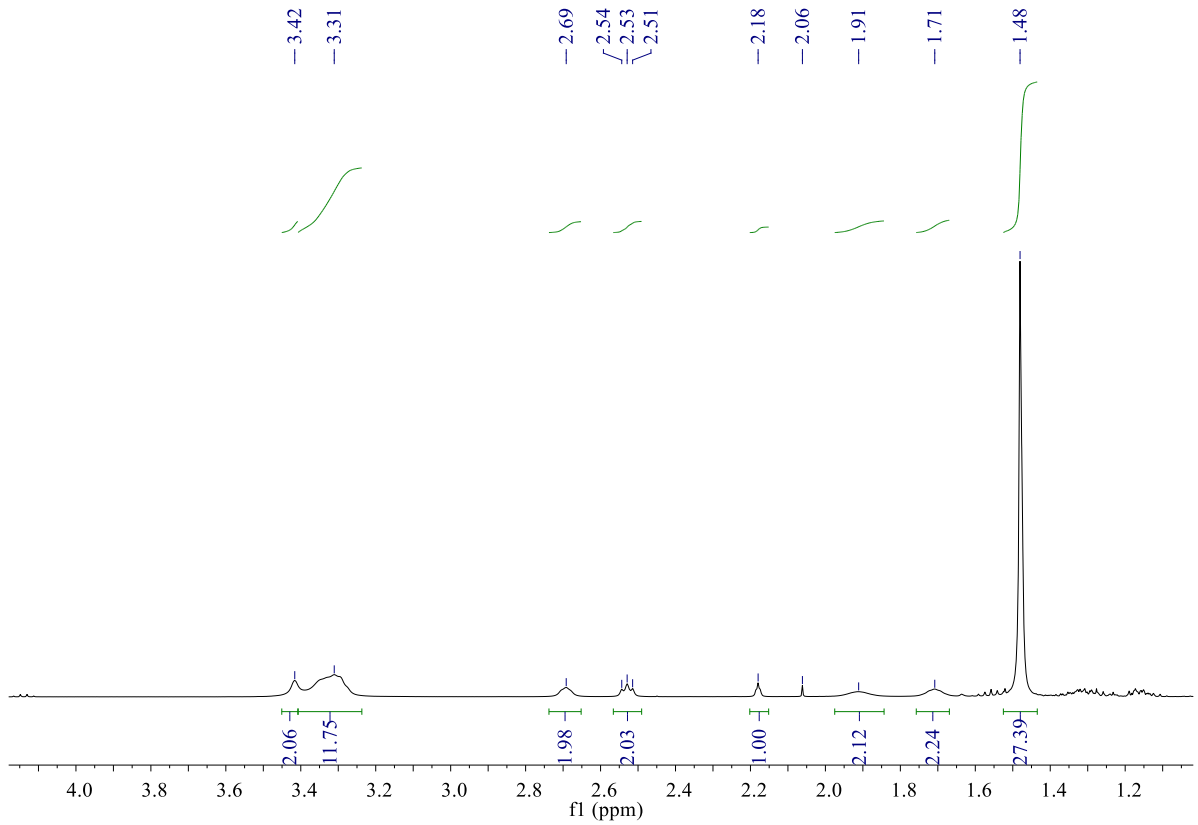
3.42
3.31
2.69
2.54
2.53
2.51
2.18
2.06
1.91
1.71
1.48
2.06
11.75
1.98
2.03
1.00
2.12
2.24
27.39
4.0
3.8
3.6
3.4
3.2
3.0
2.8
2.6
2.4
2.2
2.0
1.8
1.6
1.4
1.2
f1 (ppm)

Ethyl 5-((3a*S*,4*S*,6a*R*)-2-oxohexahydro-1*H*-thieno[3,4-*d*]imidazol-4-yl)pentanoate (**41**)

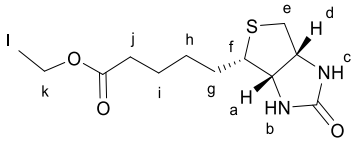

D-(+)-biotin (500 mg, 2.00 mmol) was dissolved in absolute EtOH (20 mL) and to this was added concentrated H_2SO_4 (3 drops). The flask was covered and heated to reflux with stirring overnight. After that, the reaction was cooled to room temperature, and concentrated *in vacuo*, the residue was diluted with DCM (50 mL) and the organic phase washed with 0.25 M Na_2CO_3 (3 × 50 mL) and H_2O (2 × 50 mL). The organic layer was dried over $MgSO_4$, filtered and concentrated *in vacuo* to give **41** as a white solid (461 mg, 83%). ^{1}H NMR (400 MHz, $CDCl_3$) δ_H 5.53 (s, 1H, H_c), 5.14 (s, 1H, H_b), 4.59-4.51 (m, 1H, H_d), 4.39-4.31 (m, 1H, H_a), 4.15 (q, 2H, J = 7.1, H_k), 3.22-3.17 (m, 1H, H_f), 2.95 (dd, 1H, J = 12.8, 5.0, H_e), 2.77 (d, 1H, J = 12.8, H_e), 2.35 (t, 2H, J = 7.5, H_j), 1.79-1.64 (m, 4H, $H_{g,i}$), 1.55-1.43 (m, 2H, H_h), 1.28 (t, 3H, J = 7.1, H_l). ^{13}C NMR (101 MHz, $CDCl_3$) δ 173.7, 163.6, 62.0, 60.3, 60.1, 55.4, 40.6, 34.0, 28.4, 28.3, 24.8, 14.3. All other spectroscopic data were consistent with those previously reported.[103]

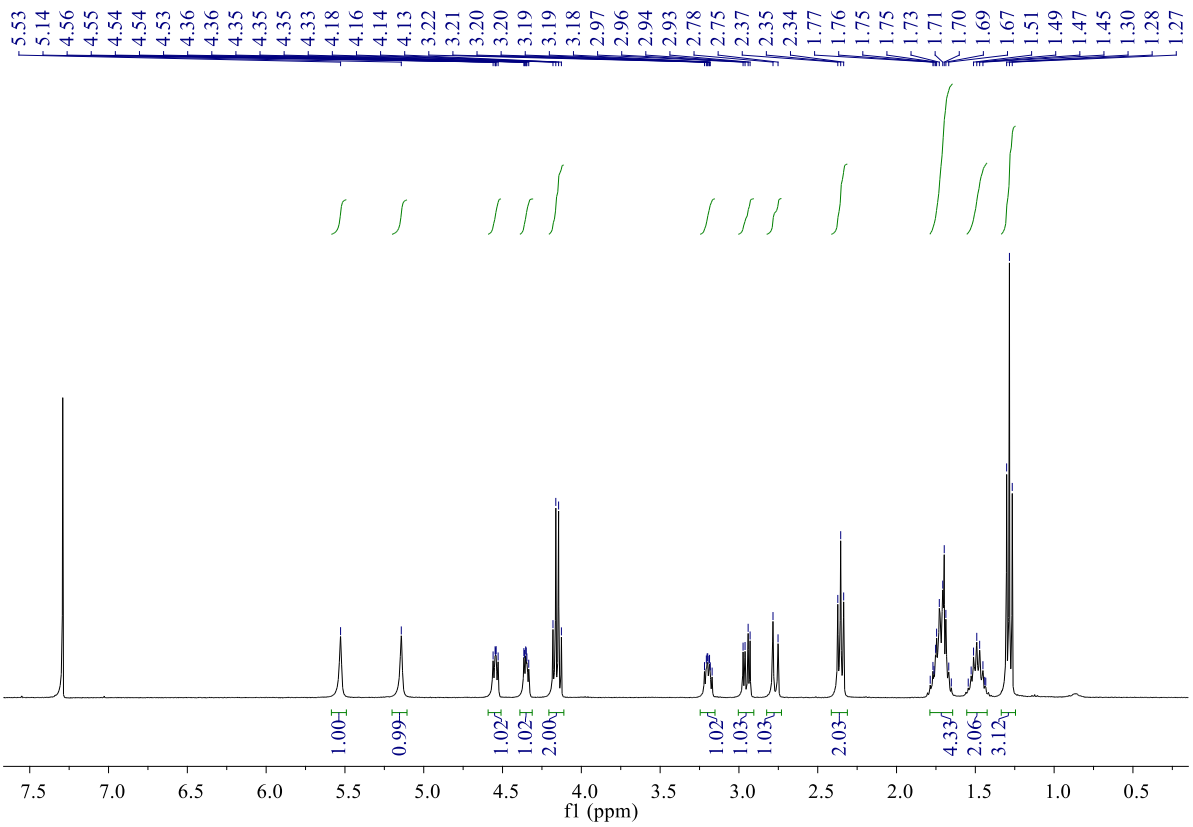
5.53
5.14
4.56
4.55
4.54
4.54
4.53
4.36
4.36
4.35
4.35
4.35
4.33
4.18
4.16
4.14
4.13
3.22
3.21
3.20
3.20
3.19
3.19
3.18
2.97
2.96
2.94
2.93
2.78
2.75
2.37
2.35
2.34
1.77
1.76
1.75
1.75
1.73
1.71
1.70
1.69
1.67
1.51
1.49
1.47
1.45
1.30
1.28
1.27
1.00
0.99
1.02
1.02
2.00
1.02
1.03
1.03
2.03
4.33
2.06
3.12
7.5
7.0
6.5
6.0
5.5
5.0
4.5
4.0
3.5
3.0
2.5
2.0
1.5
1.0
0.5
f1 (ppm)

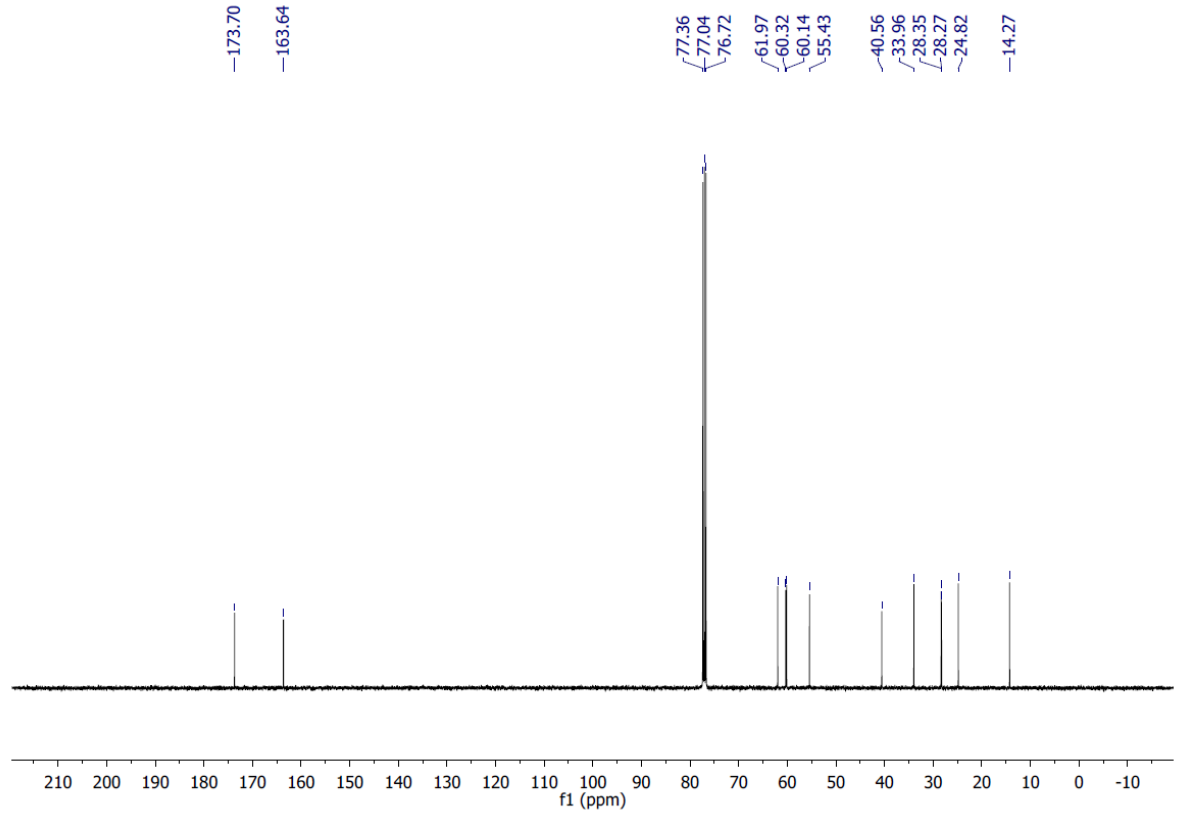
173.70
163.64
77.36
77.04
76.72
61.97
60.32
60.14
55.43
40.56
33.96
28.35
28.27
24.82
14.27
210
200
190
180
170
160
150
140
130
120
110
100
90
80
70
60
50
40
30
20
10
0
-10
f1 (ppm)

(3a*S*,4*S*,6a*R*)-4-(5-Hydroxypentyl)tetrahydro-1*H*-thieno[3,4-*d*]imidazol-2(3*H*)-one (**42**)

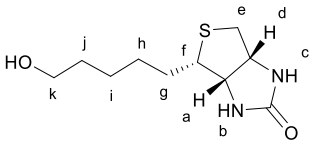

Under a nitrogen atmosphere, **41** (100 mg, 0.370 mmol) was dissolved in anhydrous DCM (10 mL) and the solution was cooled to -78 °C. DIBAL-H (1.0 M in hexanes, 1.3 mL, 1.3 mmol, 3.5 eq.) was added dropwise over a period of 15 minutes and the solution was stirred at -78 °C for 30 min. After this time, the reaction was warmed to room temperature and stirred for a further 2 h. The reaction was then cooled to -78 °C and quenched by the dropwise addition of MeOH (3 mL) followed by MeOH: H_2O (6 mL: 3 mL). The mixture was concentrated *in vacuo* and the crude material was transferred to a cellulose thimble and purified by Soxhlet extraction by EtOH for 3 days. The solvent was removed *in vacuo* to give **42** as a white solid (80 mg, 94%). ^{1}H NMR (400 MHz, CD_3OD): δ_H 4.51-4.47 (m, 1H, H_d), 4.32-4.29 (m, 1H, H_a), 3.55 (t, 2H, J = 6.5 Hz, H_k), 3.24-3.19 (m, 1H, H_f), 2.93 (dd, 1H, J = 12.8, 5.0, H_e), 2.70 (d, 1H, J = 12.8, H_e), 1.75-1.40 (m, 8H, $H_{g\text{-}j}$). ^{13}C NMR (100 MHz, CD_3OD): δ_C 166.3, 63.6, 63.0, 61.8, 57.4, 41.2, 33.6, 30.3, 30.0, 27.1. All other spectroscopic data were consistent with those previously reported.[103]

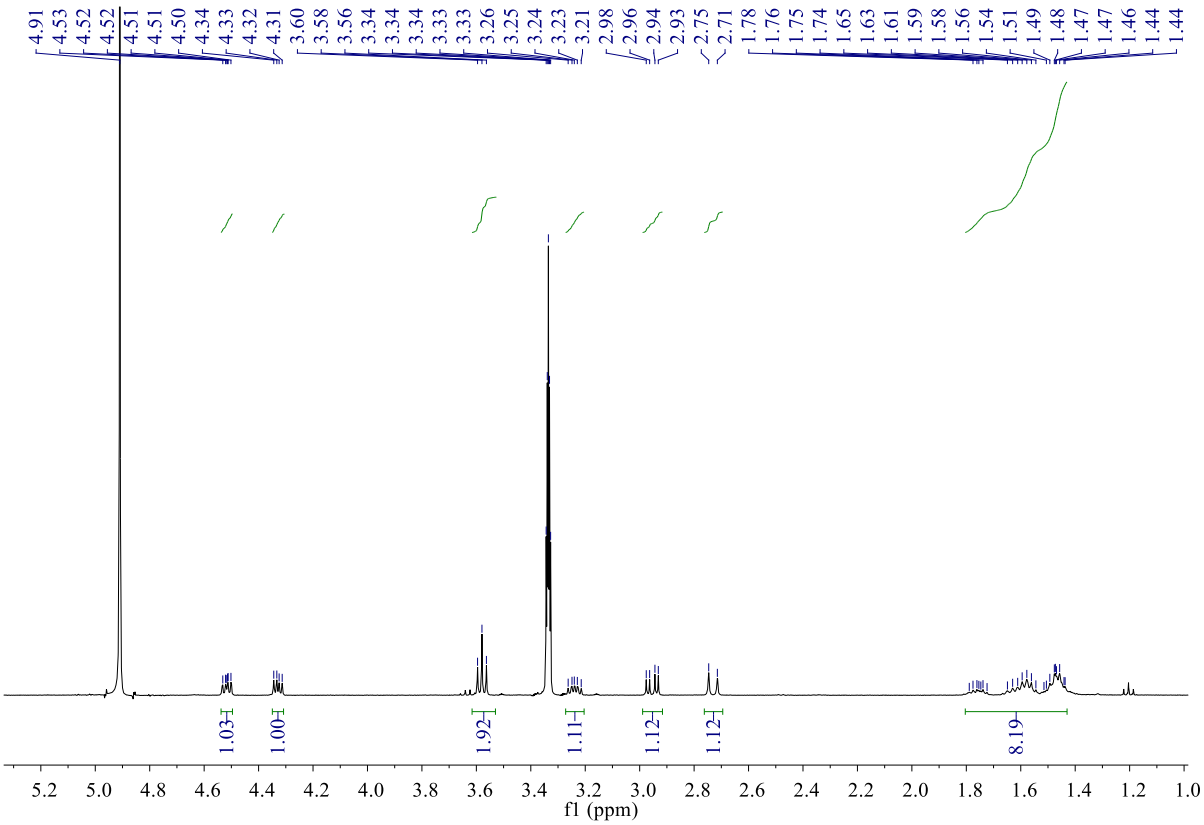
4.91 4.53 4.52 4.52 4.51 4.51 4.50 4.34 4.33 4.32 4.31 3.60 3.58 3.56 3.34 3.34 3.34 3.33 3.33 3.26 3.25 3.24 3.23 3.21 2.98 2.96 2.94 2.93 2.75 2.71 1.78 1.76 1.75 1.74 1.65 1.63 1.61 1.59 1.58 1.56 1.54 1.51 1.49 1.48 1.47 1.47 1.46 1.44 1.44
1.03 1.00 1.92 1.11 1.12 1.12 8.19
5.2 5.0 4.8 4.6 4.4 4.2 4.0 3.8 3.6 3.4 3.2 3.0 2.8 2.6 2.4 2.2 2.0 1.8 1.6 1.4 1.2 1.0
f1 (ppm)

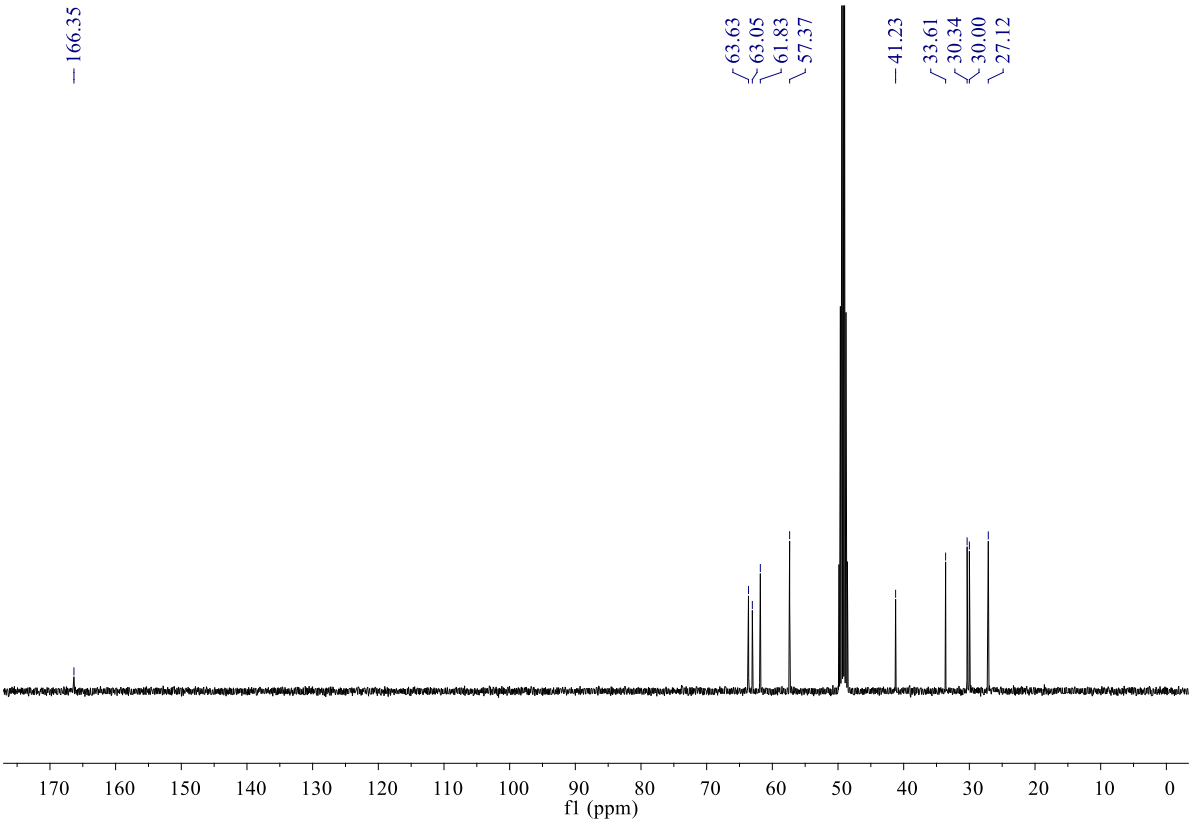
166.35
63.63 63.05 61.83 57.37
41.23 33.61 30.34 30.00 27.12
170 160 150 140 130 120 110 100 90 80 70 60 50 40 30 20 10 0
f1 (ppm)

(3a*S*,4*S*,6a*R*)-4-(5-Azidopentyl)tetrahydro-1*H*-thieno[3,4-*d*]imidazol-2(3*H*)-one (**43**)

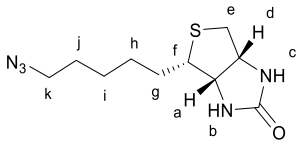

Under an atmosphere of nitrogen, biotinol **42** (240 mg, 1.04 mmol) was dissolved in anhydrous DMF (10.4 mL) and the colourless solution was cooled to 0 °C. DPPA (0.448 mL, 2.08 mmol) was added followed by DBU (0.310 mL, 2.08 mmol). The solution was stirred at 0 °C for 15 min, then heated to 65 °C, covered and stirred for 18 h. Then the reaction was cooled to room temperature and the resulting red-orange solution was diluted with H_2O (200 mL), extracted with EtOAc (2 × 100 mL). The combined organic phase was washed with brine (2 × 100 mL) and saturated $NaHCO_3$ (2 × 100 mL), dried over $MgSO_4$, filtered and concentrated *in vacuo* to give a pale-yellow solid residue. This crude material was purified by flash chromatography (eluent: DCM/MeOH 20:1) to give **43** as a white solid (104 mg, 39%). ^{1}H NMR (400 MHz, $CDCl_3$) δ_H 5.13 (s, 1H, H_c), 4.90 (s, 1H, H_b), 4.56-4.48 (m, 1H, H_d), 4.35-4.29 (m, 1H, H_a), 3.28 (t, 2H, J = 6.8, H_k), 3.19-3.15 (m, 1H, H_f), 2.94 (dd, 1H, J = 12.8, 5.1, H_e), 2.74 (d, 1H, J = 12.8, H_e), 1.72-1.40 (m, 8H, $H_{e\text{-}h}$). ^{13}C NMR: (100 MHz, $CDCl_3$): δ_C 164.0, 62.2, 60.2, 55.7, 51.5, 40.7, 28.7, 26.7. All other spectroscopic data were consistent with those previously reported.[145]

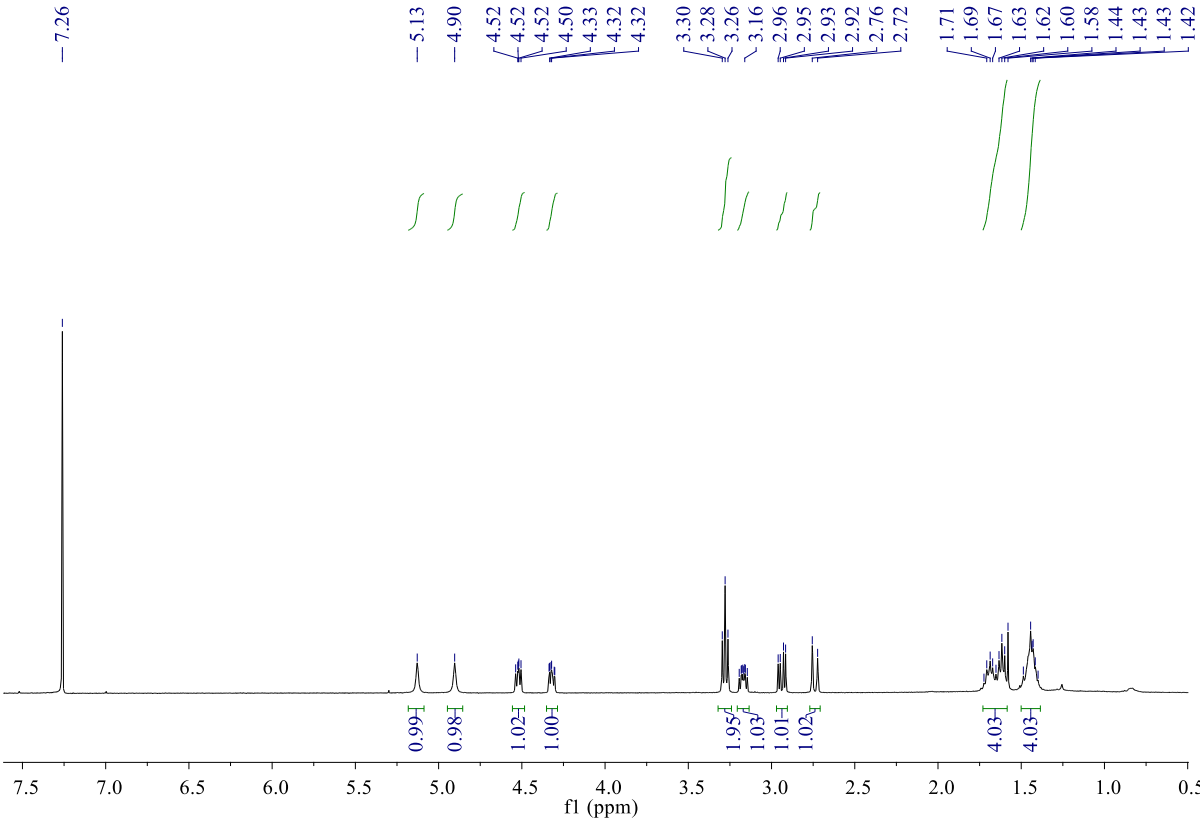
7.26
5.13
4.90
4.52
4.52
4.52
4.50
4.33
4.32
4.32
3.30
3.28
3.26
3.16
2.96
2.95
2.93
2.92
2.76
2.72
1.71
1.69
1.67
1.63
1.62
1.60
1.58
1.44
1.43
1.43
1.42
0.99
0.98
1.02
1.00
1.95
1.03
1.01
1.02
4.03
4.03
7.5
7.0
6.5
6.0
5.5
5.0
4.5
4.0
3.5
3.0
2.5
2.0
1.5
1.0
f1 (ppm)

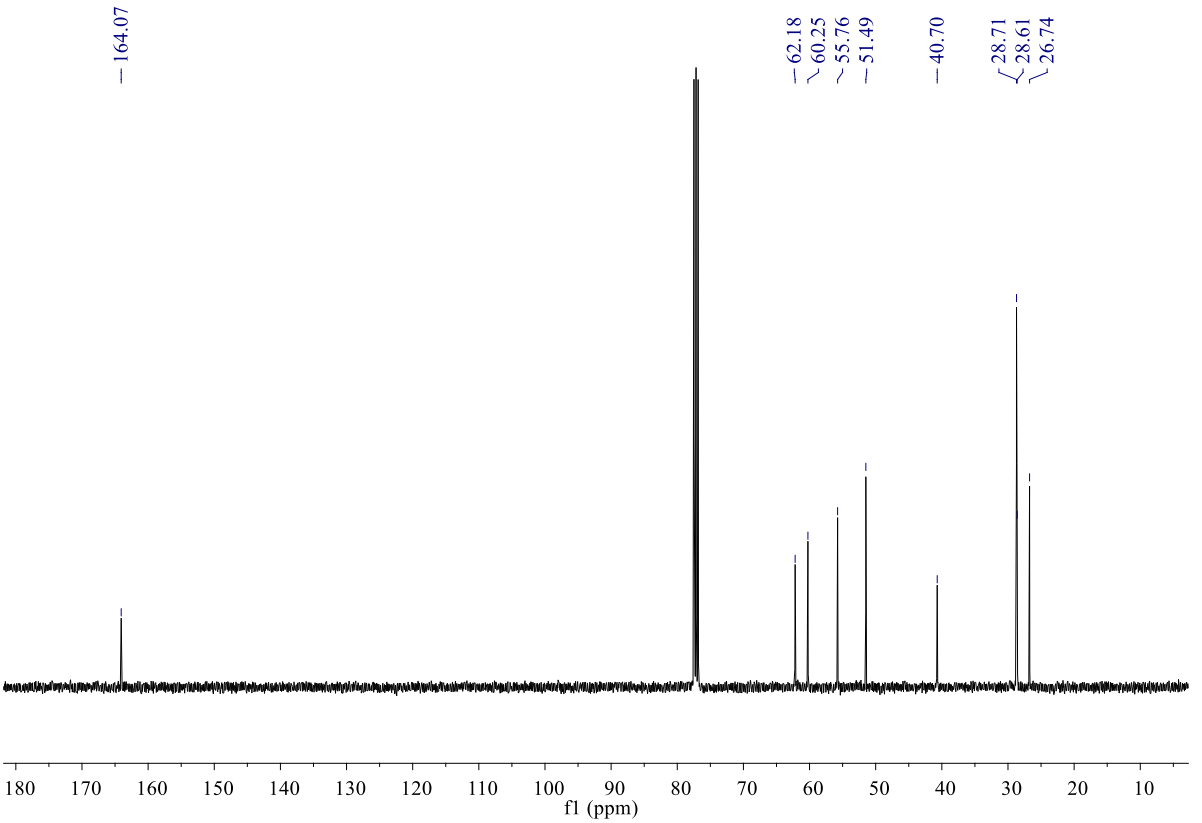
164.07
62.18
60.25
55.76
51.49
40.70
28.71
28.61
26.74
180
170
160
150
140
130
120
110
100
90
80
70
60
50
40
30
20
10
f1 (ppm)

6-Bromo-2-((1-(5-((3a*S*,4*S*,6a*R*)-2-oxohexahydro-1*H*-thieno[3,4-*d*]imidazol-4-yl)pentyl)-1*H*-1,2,3-triazol-4-yl)methyl)-1*H*-benzo[*de*]isoquinoline-1,3(2*H*)-dione (**44**)

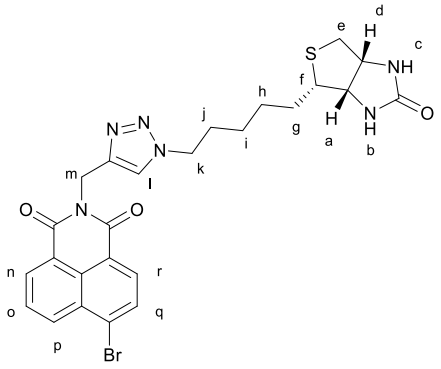

Biotin azide **43** (25 mg, 0.10 mmol), and **38** (31 mg, 0.10 mmol) were dissolved in anhydrous DCM (0.50 mL) under a nitrogen atmosphere. To this solution, tetrakis(acetonitrile)copper(I) hexafluorophosphate (7.5 mg, 0.020 mmol), DIPEA (10 µL, 0.057 mmol) was added and the flask was covered with aluminium foil and stirred at room temperature for 48 h. Then the yellow solution was washed with a saturated solution of EDTA in 17% NH_4OH (5 mL), and the aqueous layer was extracted with DCM (3 × 15 mL). The combined organic layers were dried over $MgSO_4$, filtered and concentrated *in vacuo* to give **44** as a white solid (54 mg, 95%, M.p. 104-107 °C). ^{1}H NMR (400 MHz, $CDCl_3$) δ_H 8.67 (d, 1H, *J* = 6.8, H_n), 8.57 (d, 1H, *J* = 8.4, H_p), 8.43 (d, 1H, *J* = 8.0, H_r), 8.04 (d, 1H, *J* = 8.0, H_q), 7.88-7.81 (m, 1H, H_o), 7.66 (s, 1H, H_l), 5.49 (s, 2H, H_m), 5.29 (s, 1H, H_c), 4.76 (s, 1H, H_b), 4.54-4.50 (m, 1H, H_d), 4.36-4.28 (m, 3H, H_a and H_k), 3.12-3.06 (m, 1H, H_f), 2.89 (dd, 1H, *J* = 13.0, 5.0, H_e), 2.70 (d, 1H, *J* = 13.0, H_e), 1.88-1.35 (m, 8H, $H_{g\text{-}j}$). ^{13}C NMR (101 MHz, $CDCl_3$) δ_C 163.9, 163.4 (overlapping signal), 143.2, 133.6, 132.3, 131.5, 131.1, 130.6, 129.0, 128.1, 123.4, 122.7, 121.8, 61.9, 60.0, 55.4, 54.2, 50.1, 42.3, 40.2, 35.1, 29.8, 28.3, 26.1. IR: (υ_{max}/cm^{-1}) 3231, 2934, 2680, 1698, 1657, 1463, 1343, 1235, 1046, 951. HR-ESI MS (*m/z*) $[M+H]^+$ calcd for $C_{25}H_{26}BrN_6O_3S$ 569.0965, found 569.0962.

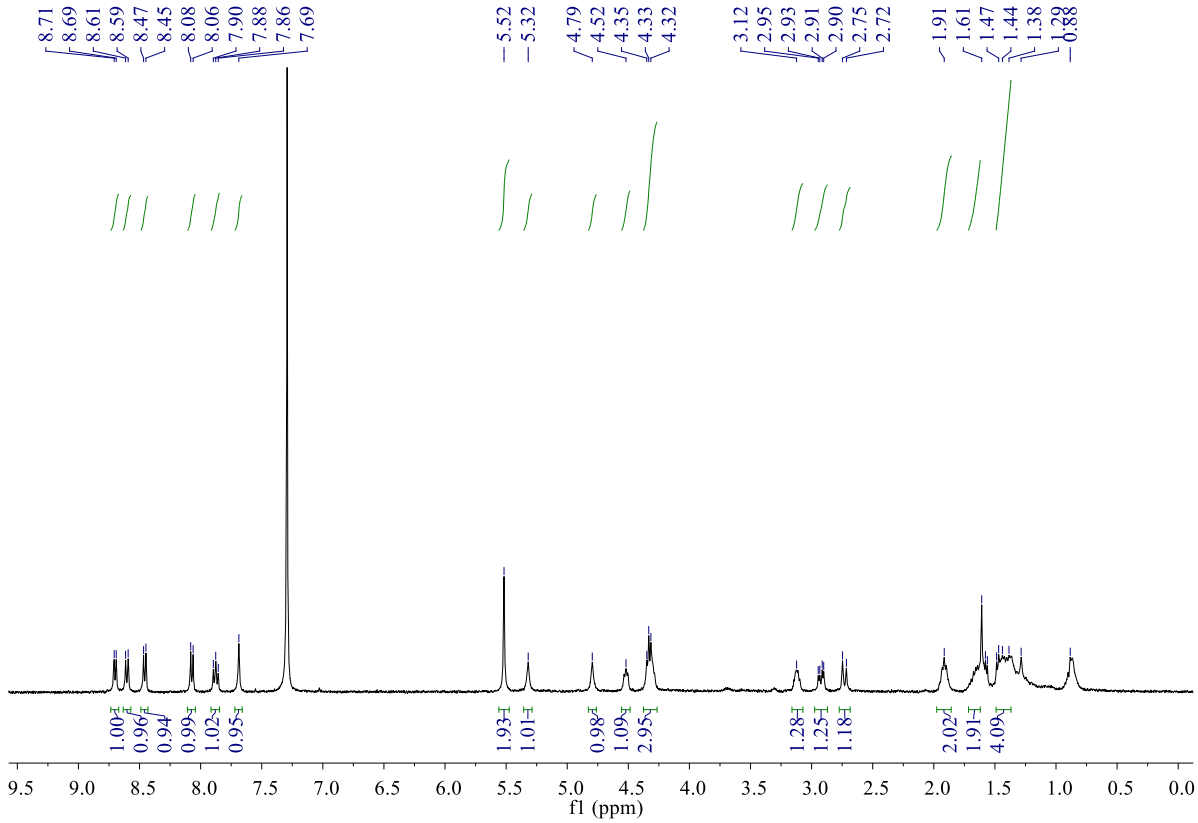
8.71
8.69
8.61
8.59
8.47
8.45
8.08
8.06
7.90
7.88
7.86
7.69
5.52
5.32
4.79
4.52
4.35
4.33
4.32
3.12
2.95
2.93
2.91
2.90
2.75
2.72
1.91
1.61
1.47
1.44
1.38
1.29
0.88
1.00
0.96
0.94
0.99
1.02
0.95
1.93
1.01
0.98
1.09
2.95
1.28
1.25
1.18
2.02
1.91
4.09
9.5 9.0 8.5 8.0 7.5 7.0 6.5 6.0 5.5 5.0 4.5 4.0 3.5 3.0 2.5 2.0 1.5 1.0 0.5 0.0
f1 (ppm)

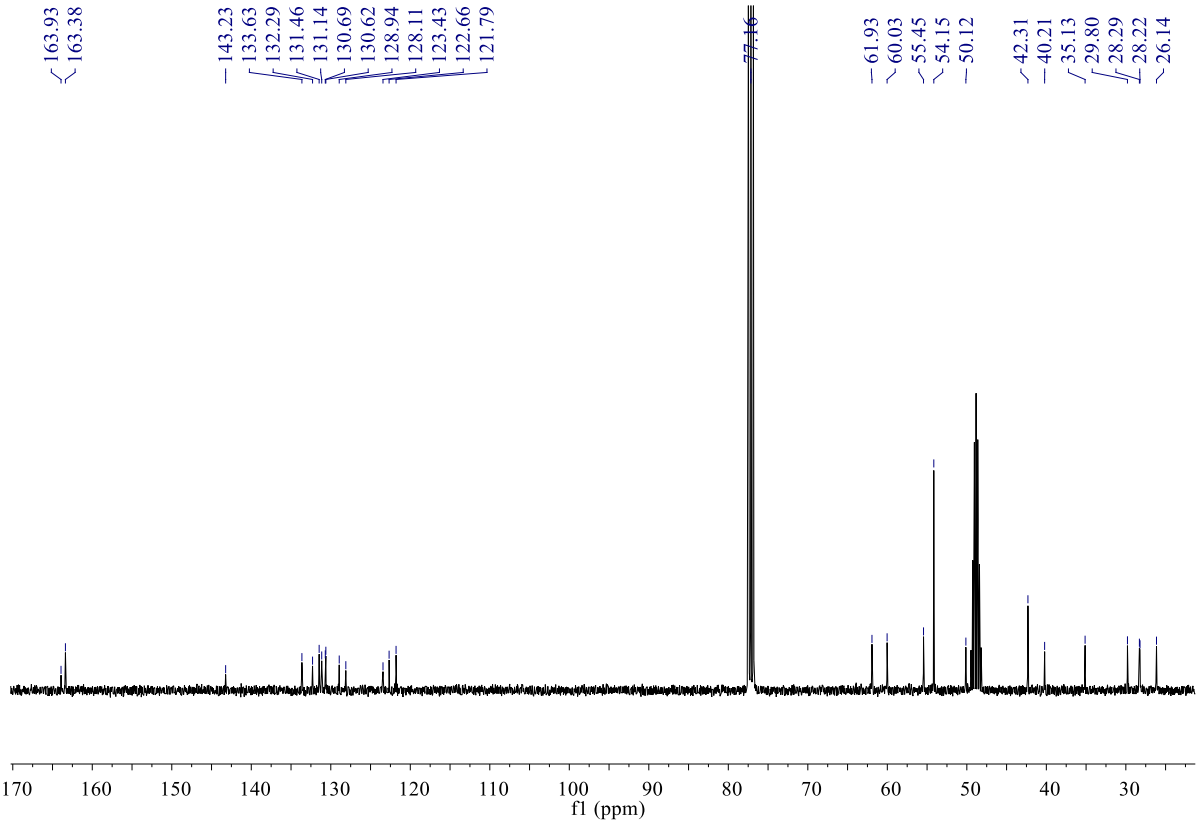
163.93
163.38
143.23
133.63
132.29
131.46
131.14
130.69
130.62
128.94
128.11
123.43
122.66
121.79
77.16
61.93
60.03
55.45
54.15
50.12
42.31
40.21
35.13
29.80
28.29
28.22
26.14
170 160 150 140 130 120 110 100 90 80 70 60 50 40 30
f1 (ppm)

6-Azido-2-((1-(5-((3a*S*,4*S*,6a*R*)-2-oxohexahydro-1*H*-thieno[3,4-*d*]imidazol-4-yl)pentyl)-1*H*-1,2,3-triazol-4-yl)methyl)-1*H*-benzo[*de*]isoquinoline-1,3(2*H*)-dione (**45**)

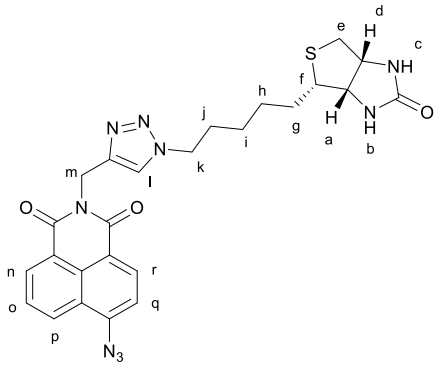

Bromide **44** (38 mg, 0.067 mmol) and NaN_3 (6.5 mg, 0.10 mmol) were combined in DMF (2.0 mL) and the mixture was stirred at room temperature for 3 days. Then the mixture was diluted with water (20 mL) and extracted with EtOAc (3 × 15 mL). The organic layers were combined and washed with brine (2 × 30 mL), dried over $MgSO_4$, concentrated *in vacuo* to give **45** as a yellow solid (33 mg, 93%, M.p. 154-157 °C). ^{1}H NMR (400 MHz, $CDCl_3$) δ_H 8.68 (d, 1H, *J* = 7.4, H_n), 8.63 (d, 1H, *J* = 8.0, H_r), 8.47 (d, 1H, *J* = 8.6, H_p), 7.80-7.73 (m, 1H, H_o), 7.66 (s, 1H, H_l), 7.50 (d, 1H, J = 8.0, H_q), 5.51 (s, 2H, H_m), 4.95 (s, 1H, H_c), 4.62 (s, 1H, H_b), 4.54-4.49 (m, 1H, H_d), 4.35-4.28 (m, 3H, H_a and H_k), 3.16-3.09 (m, 1H, H_f), 2.93 (dd, 1H, *J* = 12.9, 5.0, H_e), 2.72 (d, 1H, *J* = 12.9, H_e), 1.93-1.37 (m, 8H, $H_{g\text{-}j}$). ^{13}C NMR (101 MHz, $CDCl_3$) δ_C 168.0, 167.8, 167.3, 147.9, 136.4, 136.0, 133.1, 133.0, 130.8, 128.2, 127.5, 126.1, 122.3, 118.7, 65.9, 64.0, 59.5, 54.1, 44.2, 39.0, 33.8, 33.5, 32.3, 32.2, 30.1. IR: (υ_{max}/cm^{-1}) 3083, 2098, 1733, 1649, 1494, 1374, 1268, 1082, 1017, 809, 658. HR-ESI MS (*m/z*) $[M+H]^+$ calcd for $C_{25}H_{26}N_9O_3S$ 532.1847, found 532.1869.

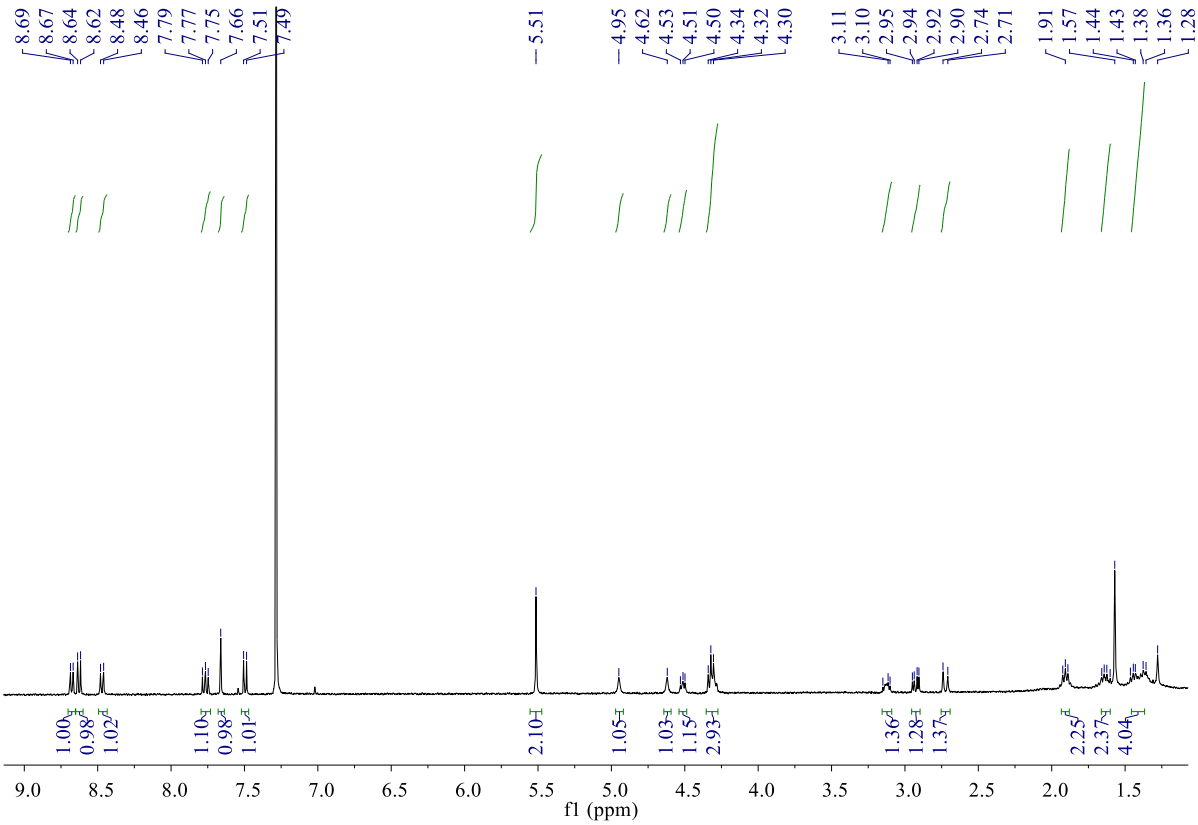
8.69
8.67
8.64
8.62
8.48
8.46
7.79
7.77
7.75
7.66
7.51
7.49
5.51
4.95
4.62
4.53
4.51
4.50
4.34
4.32
4.30
3.11
3.10
2.95
2.94
2.92
2.90
2.74
2.71
1.91
1.57
1.44
1.43
1.38
1.36
1.28
1.00
0.98
1.02
1.10
0.98
1.01
2.10
1.05
1.03
1.15
2.93
1.36
1.28
1.37
2.25
2.37
4.04
9.0
8.5
8.0
7.5
7.0
6.5
6.0
5.5
5.0
4.5
4.0
3.5
3.0
2.5
2.0
1.5
f1 (ppm)

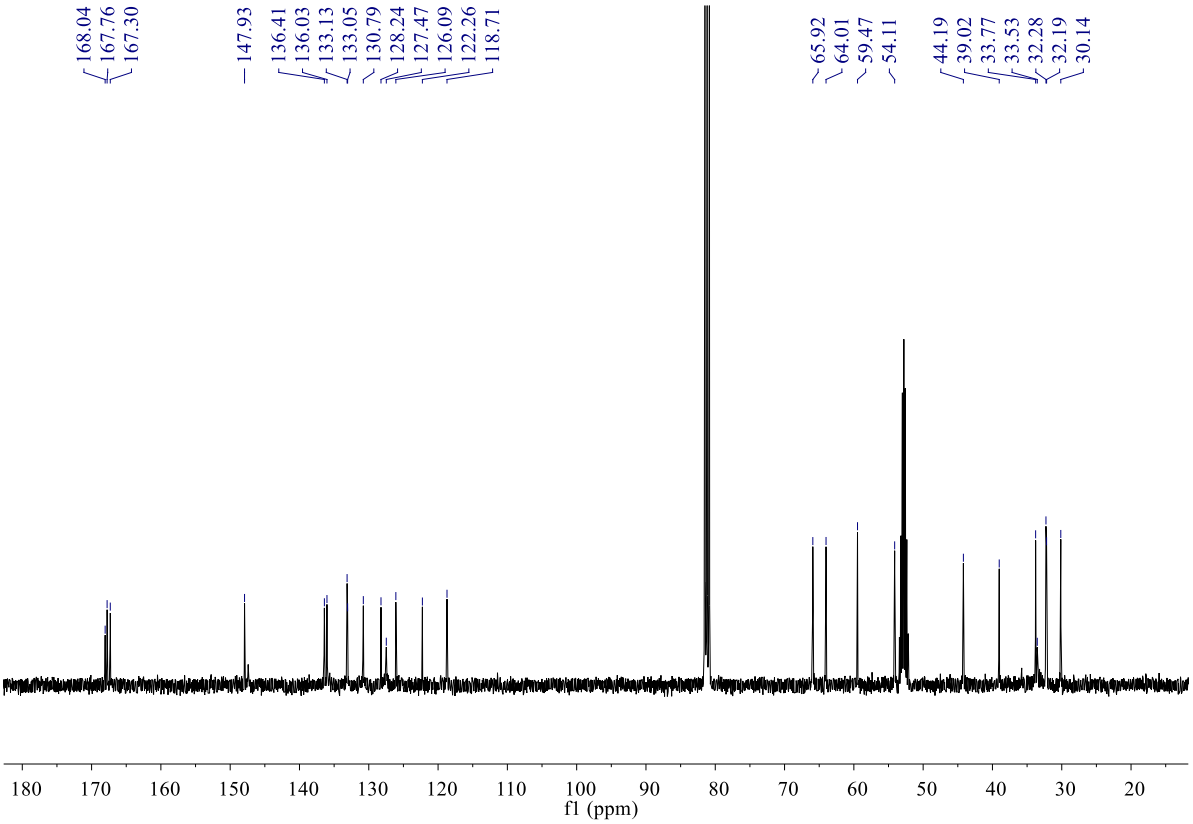
168.04
167.76
167.30
147.93
136.41
136.03
133.13
133.05
130.79
128.24
127.47
126.09
122.26
118.71
65.92
64.01
59.47
54.11
44.19
39.02
33.77
33.53
32.28
32.19
30.14
180
170
160
150
140
130
120
110
100
90
80
70
60
50
40
30
20
f1 (ppm)

Tri-*tert*-butyl 11-((1-(1,3-dioxo-2-((1-(5-((3a*S*,4*S*,6a*R*)-2-oxohexahydro-1*H*-thieno[3,4-*d*]imidazol-4-yl)pentyl)-1*H*-1,2,3-triazol-4-yl)methyl)-2,3-dihydro-1*H*-benzo[*de*]isoquinolin-6-yl)-1*H*-1,2,3-triazol-4-yl)methyl)-1,4,8,11-tetraazacyclotetradecane-1,4,8-tricarboxylate (**46**)

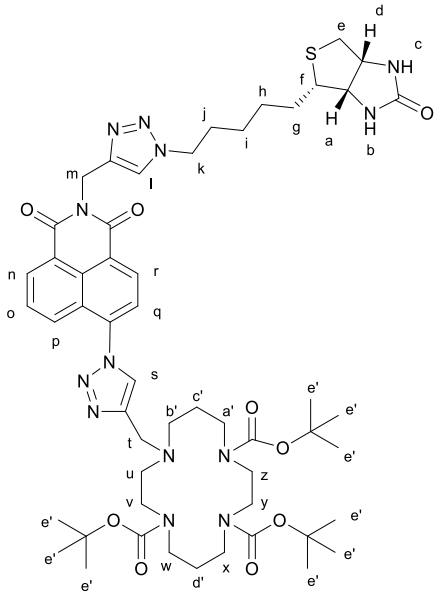

The azide **45** (32 mg, 0.060 mmol) and acetylene **40** (33 mg, 0.060 mmol) were dissolved in NMP (1.0 mL), followed by CuI (2.3 mg, 0.012 mmol), NaOAc (1.0 mg, 0.012 mmol), and EtOH (1.0 mL). The mixture was stirred at room temperature for 3 days under a nitrogen atmosphere. After that time a saturated solution of EDTA in 17 % NH_3 H_2O (5 mL) was added and the yellow precipitate was collected by filtration, washed with water and dried *in vacuo*. The crude product was dissolved in DCM (2.0 mL) and poured into petroleum ether (20 mL) to give **46** as a yellow powder (36 mg, 56%, M.p. 148-153 °C). ^{1}H NMR (400 MHz, $CDCl_3$) δ_H 8.71 (d, 2H, *J* = 7.1, H_n and H_r), 8.27 (d, 1H, *J* = 7.6, H_p), 8.04 (s, 1H, H_s), 7.90-7.83 (m, 2H, H_o and H_q), 7.70 (s, 1H, H_l), 5.50 (s, 2H, H_m), 5.41 (s, 1H, H_c), 4.97 (s, 1H, H_b), 4.45-4.40 (m, 1H, H_d), 4.31 (t, 2H, *J* = 4.1, H_k), 4.25-4.20 (m, 1H, H_a), 3.96 (s, 2H, H_t), 3.42-3.30 (m, 12H, $H_{v\text{-}a'}$), 3.10-3.05 (m, 1H, H_f), 2.87 (dd, 1H, *J* = 12.9, 4.9, H_e), 2.73 (t, 2H, *J* = 5.4, H_u), 2.67 (d, 1H, *J* = 12.9, H_e), 2.58 (t, 2H, *J* = 5.6, $H_{c'}$), 1.94-1.86 (m, 4H, $H_{g,j}$), 1.83-1.75 (m, 4H, $H_{b',d'}$), 1.65-1.61 (m, 4H, $H_{h,i}$), 1.42 (s, 27H, $H_{e'}$). ^{13}C NMR (101 MHz, $CDCl_3$) δ_C 163.5, 162.9, 143.1, 138.4, 132.4,

131.0, 129.9, 129.1, 128.6, 126.5, 123.6, 122.8, 79.7, 61.8, 60.0, 55.6, 50.2, 47.3, 40.6, 35.4, 29.9, 28.4, 27.9, 26.4. (overlapping signals). IR: (υ_{max}/cm^{-1}) 3016, 2970, 1741, 1729, 1435, 1366, 1229, 1217. HR-ESI MS (*m/z*) $[M + H]^+$ calcd for $C_{53}H_{76}N_{13}O_9S$ 1070.5604, found 1070.5606.

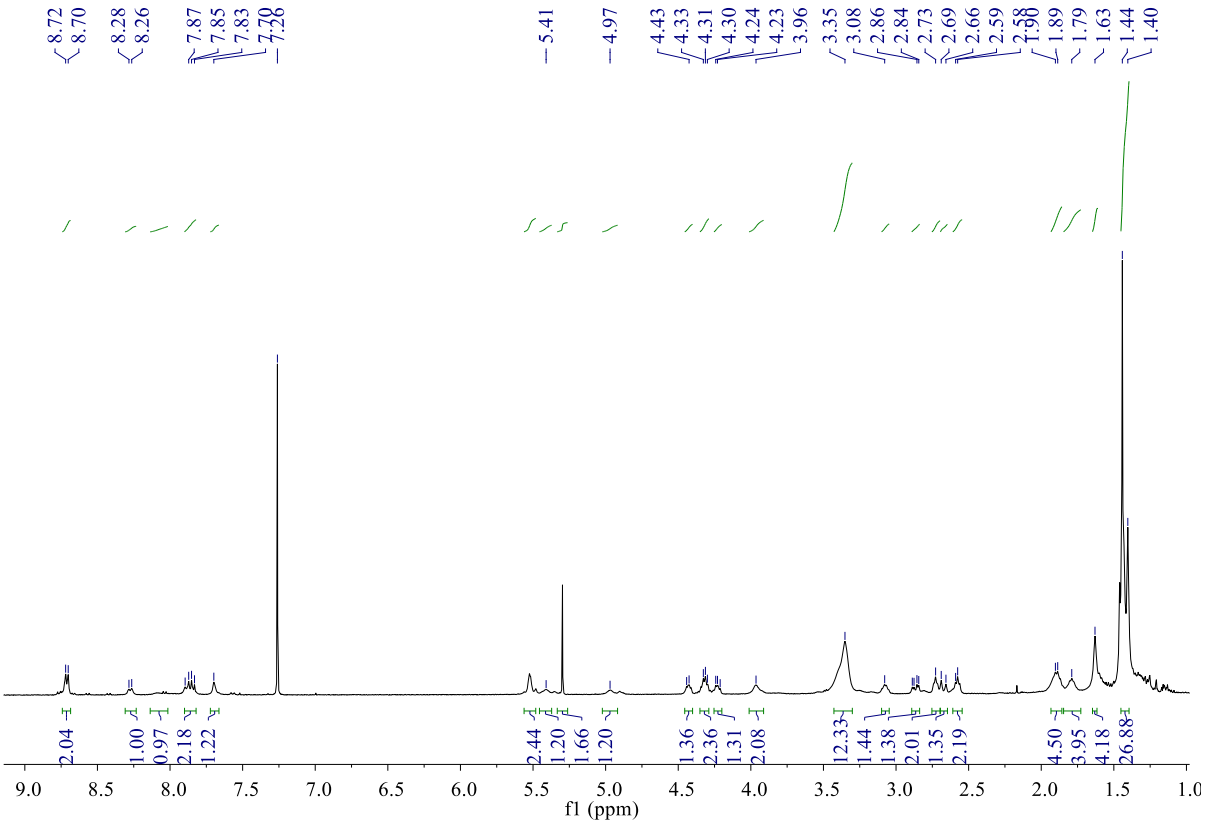
8.72
8.70
8.28
8.26
7.87
7.85
7.83
7.70
7.26
5.41
4.97
4.43
4.33
4.31
4.30
4.24
4.23
3.96
3.35
3.08
2.86
2.84
2.73
2.69
2.66
2.59
2.58
1.90
1.89
1.79
1.63
1.44
1.40
2.04
1.00
0.97
2.18
1.22
2.44
1.20
1.66
1.20
1.36
2.36
1.31
2.08
12.33
1.44
1.38
2.01
1.35
2.19
4.50
3.95
4.18
26.88
f1 (ppm)

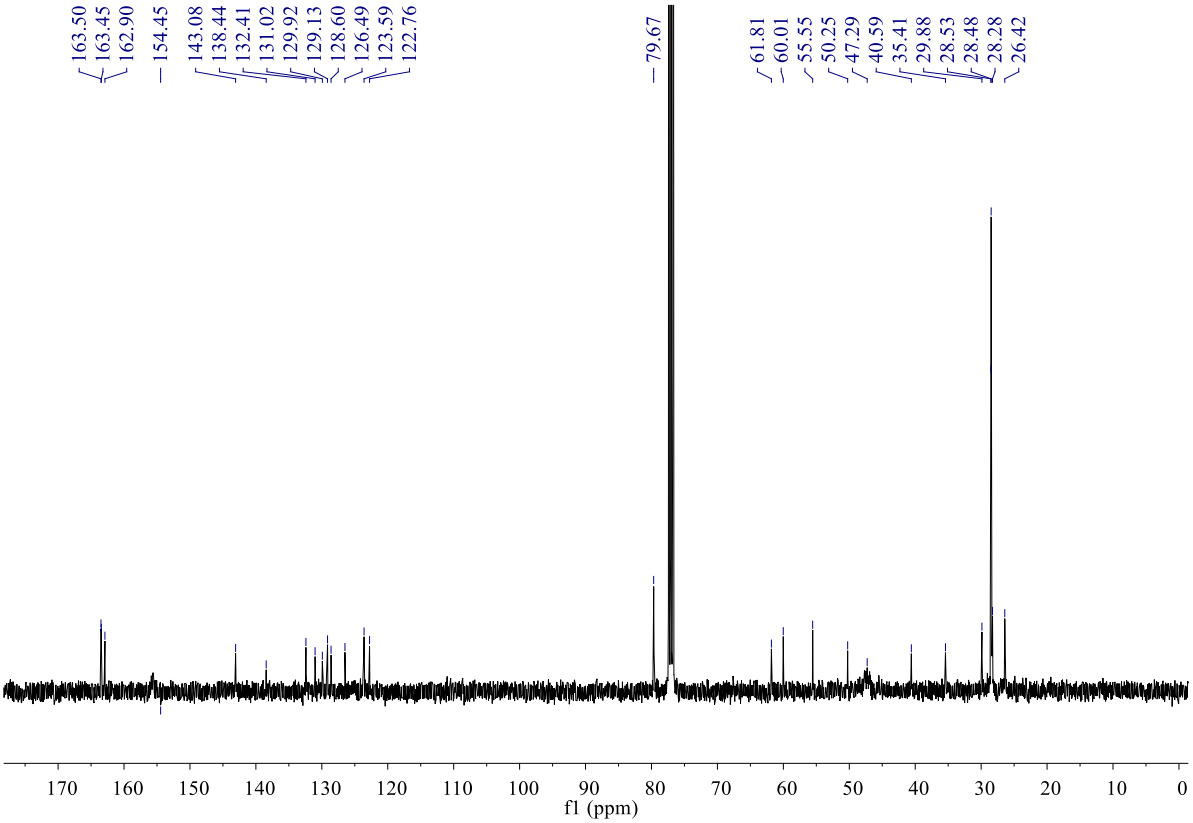
163.50
163.45
162.90
154.45
143.08
138.44
132.41
131.02
129.92
129.13
128.60
126.49
123.59
122.76
79.67
61.81
60.01
55.55
50.25
47.29
40.59
35.41
29.88
28.53
28.48
28.28
26.42
f1 (ppm)

6-(4-((1,4,8,11-tetraazacyclotetradecan-1-yl)methyl)-1*H*-1,2,3-triazol-1-yl)-2-((1-(5-((3a*S*,4*S*,6a*R*)-2-oxohexahydro-1*H*-thieno[3,4-*d*]imidazol-4-yl)pentyl)-1*H*-1,2,3-triazol-4-yl)methyl)-1*H*-benzo[de]isoquinoline-1,3(2*H*)-dione (**47**)

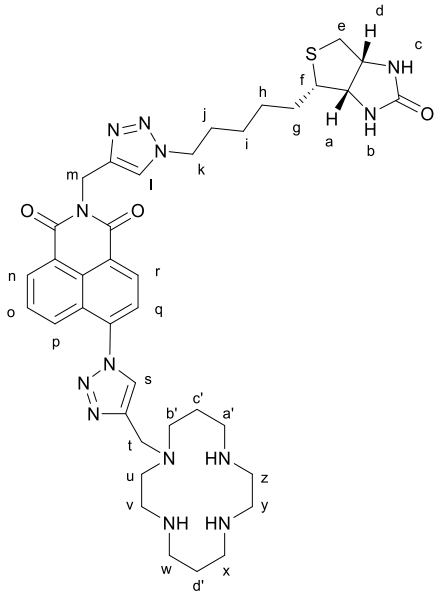

The tri-Boc protected compound **46** (31 mg, 0.029 mmol) was dissolved in a solution of 20% TFA in DCM (1.2 mL) and stirred for 10 h at room temperature. Then the solvent was removed *in vacuo* and the residue was dissolved in chloroform (10 mL) and washed with 1M aqueous NaOH solution (2.0 mL). The aqueous layer was extracted with chloroform (3 × 10 mL) and the organic layers were combined, dried over $MgSO_4$, filtered and concentrated *in vacuo* to give **47** as a brown solid (13 mg, 58 %, M.p. 197-201 °C). ^{1}H NMR (400 MHz, CD_3OD) δ_H 8.66 (d, 1H, *J* = 7.8, H_n), 8.63 (d, 1H, *J* = 7.3, H_r), 8.56 (s, 1H, H_s), 8.25 (d, 1H, *J* = 8.6, H_p), 8.05 (s, 1H, H_l), 7.99 (d, 1H, *J* = 7.3, H_q), 7.89- 7.83 (m, 1H, H_o), 5.45 (s, 2H, H_m), 4.48-4.43 (m, 1H, H_d), 4.41 (t, 2H, *J* = 6.9, H_k), 4.27-4.22 (m, 1H, H_a), 4.01 (s, 2H, H_t), 3.29-3.23 (m, 4H, $H_{v,y}$), 3.21-3.16 (m, 4H, $H_{w,x}$), 3.16-3.09 (m, 1H, H_f), 3.05-3.01 (m, 4H, $H_{z,a'}$), 2.97-2.92 (m, 4H, $H_{u,c'}$), 2.87 (dd, 1H, *J* = 12.8, 5.8, H_e), 2.64 (d, 1H, *J* = 12.8, H_e), 2.18-2.11 (m, 2H, $H_{d'}$), 1.95-1.89 (m, 2H, $H_{b'}$), 1.70-1.33 (m, 8H, H_{g-j}). ^{13}C NMR (101 MHz, CD_3OD) δ_C 164.6, 164.1 (×2), 146.3, 144.6, 139.4, 133.2, 131.9, 130.7, 130.0, 129.7, 127.5, 127.5, 125.4, 125.2, 124.9, 123.9, 63.4, 61.6, 57.0, 55.4,

54.0, 51.3, 51.1, 50.5, 49.5, 49.3, 49.1, 48.1, 46.8, 46.3, 41.0, 36.3, 31.0, 29.6, 27.4, 26.5, 24.6. IR: (υ_{max}/cm^{-1}) 2921, 2851, 1662, 1587, 1427, 1233, 1199, 952, 785. HR-ESI MS (*m/z*) $[M+H]^+$ calcd for $C_{38}H_{52}N_{13}O_3S$ 770.4031, found 770.4024.

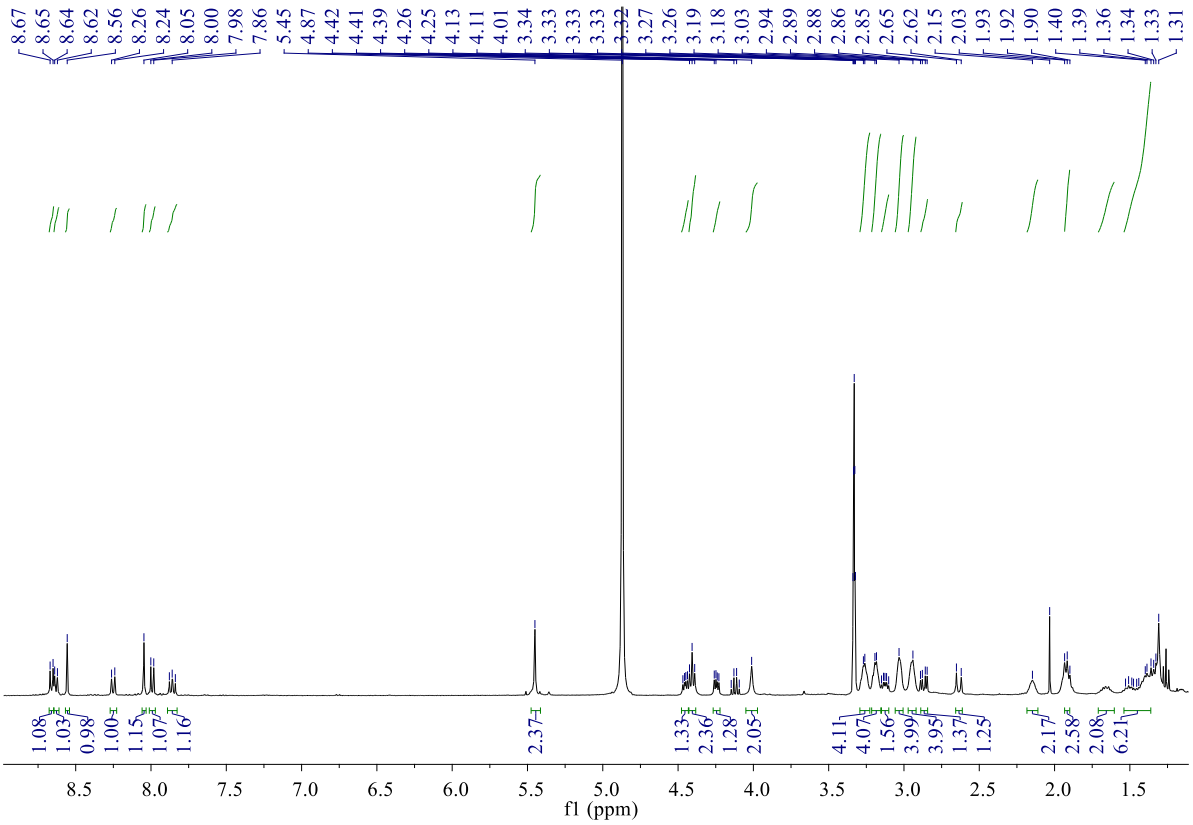
8.67 8.65 8.64 8.62 8.56 8.26 8.24 8.05 8.00 7.98 7.86 5.45 4.87 4.42 4.41 4.39 4.26 4.25 4.13 4.11 4.01 3.34 3.33 3.33 3.33 3.32 3.27 3.26 3.19 3.18 3.03 2.94 2.89 2.88 2.86 2.85 2.65 2.62 2.15 2.03 1.93 1.92 1.90 1.40 1.39 1.36 1.34 1.33 1.31
1.08 1.03 0.98 1.00 1.15 1.07 1.16 2.37 1.33 2.36 1.28 2.05 4.11 4.07 1.56 3.99 3.95 1.37 1.25 2.17 2.58 2.08 6.21
8.5 8.0 7.5 7.0 6.5 6.0 5.5 5.0 4.5 4.0 3.5 3.0 2.5 2.0 1.5
f1 (ppm)

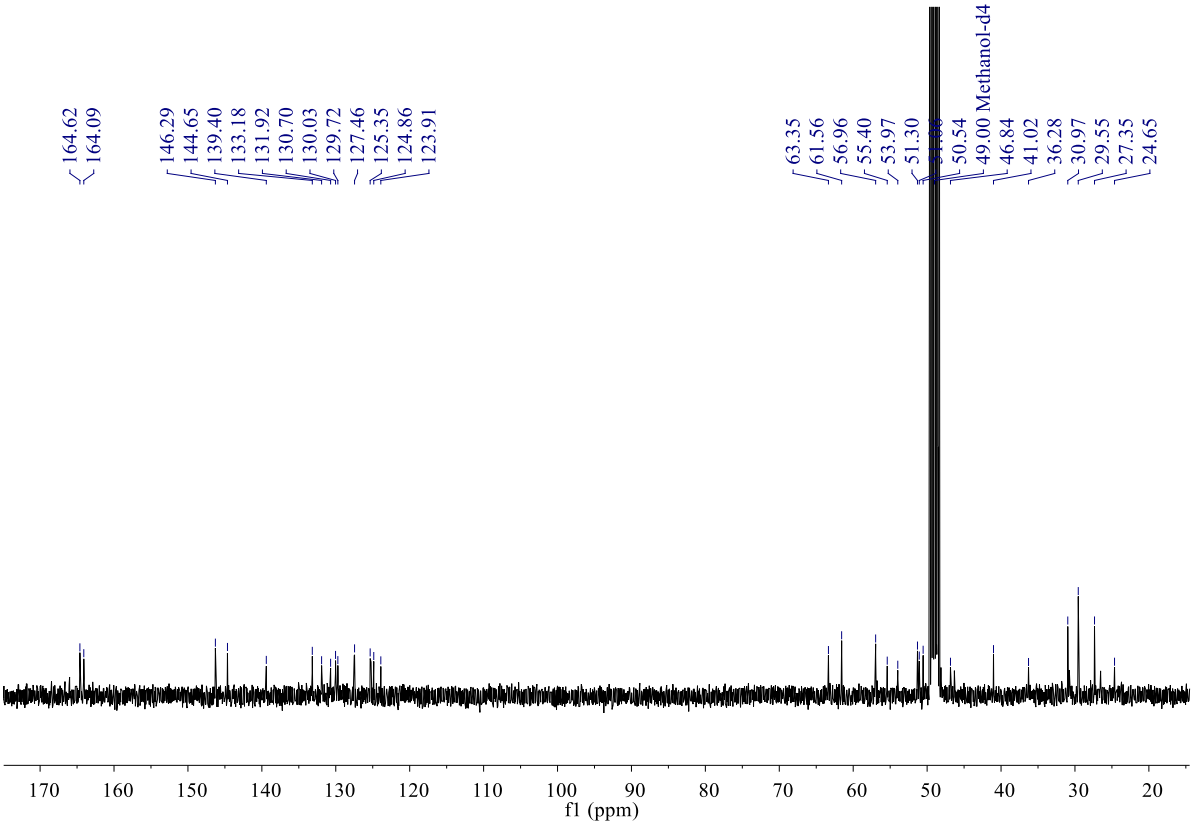
164.62 164.09 146.29 144.65 139.40 133.18 131.92 130.70 130.03 129.72 127.46 125.35 124.86 123.91 63.35 61.56 56.96 55.40 53.97 51.30 50.54 49.00 Methanol-d4 46.84 41.02 36.28 30.97 29.55 27.35 24.65
170 160 150 140 130 120 110 100 90 80 70 60 50 40 30 20
f1 (ppm)

5-Chloro-2-methoxy-3-nitrobenzoic acid (**48**)

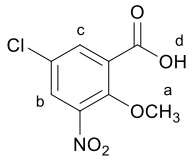

5-Chloro-2-methoxybenzoic acid (1.08 g, 5.80 mmol) and concentrated sulfuric acid (3.8 mL) were mixed in a 50 mL round bottom flask in ice-salt water bath. The mixture of 0.9 mL concentrated sulfuric acid and 0.4 mL nitric acid was added dropwise to the flask over 30 min while the temperature was kept below 5 °C. Then the cooling bath was removed and the reaction was stirred for another 5 h at room temperature. When the starting material was completely consumed, the reaction was quenched by pouring into ice water. The precipitate can be collected by filtration and washed by water (100 mL). The product was dried *in vacuo* to obtain **48** (1.30 g, 97%, M.p. 171-174 °C) as a pale yellow solid. ^{1}H NMR (400 MHz, DMSO-d_6) δ 8.55-8.47 (bs, 1H, H_d), 8.35-8.21 (bs, 1H, H_b), 8.09-8.76 (bs, 1H, H_c), 3.89 (s, 3H, H_a). ^{13}C NMR (101 MHz, DMSO-d_6) δ 164.4, 150.3, 145.6, 134.4, 129.7, 127.8, 127.3, 64.0. IR: (υ_{max}/cm^{-1}) 3080, 1709, 1533, 1361, 1293, 1248, 1167, 979, 900, 693. HR-NSI MS (*m/z*) $[M+H]^+$ calcd for $C_8H_6ClNO_5$ 229.9862, found 229.9863.

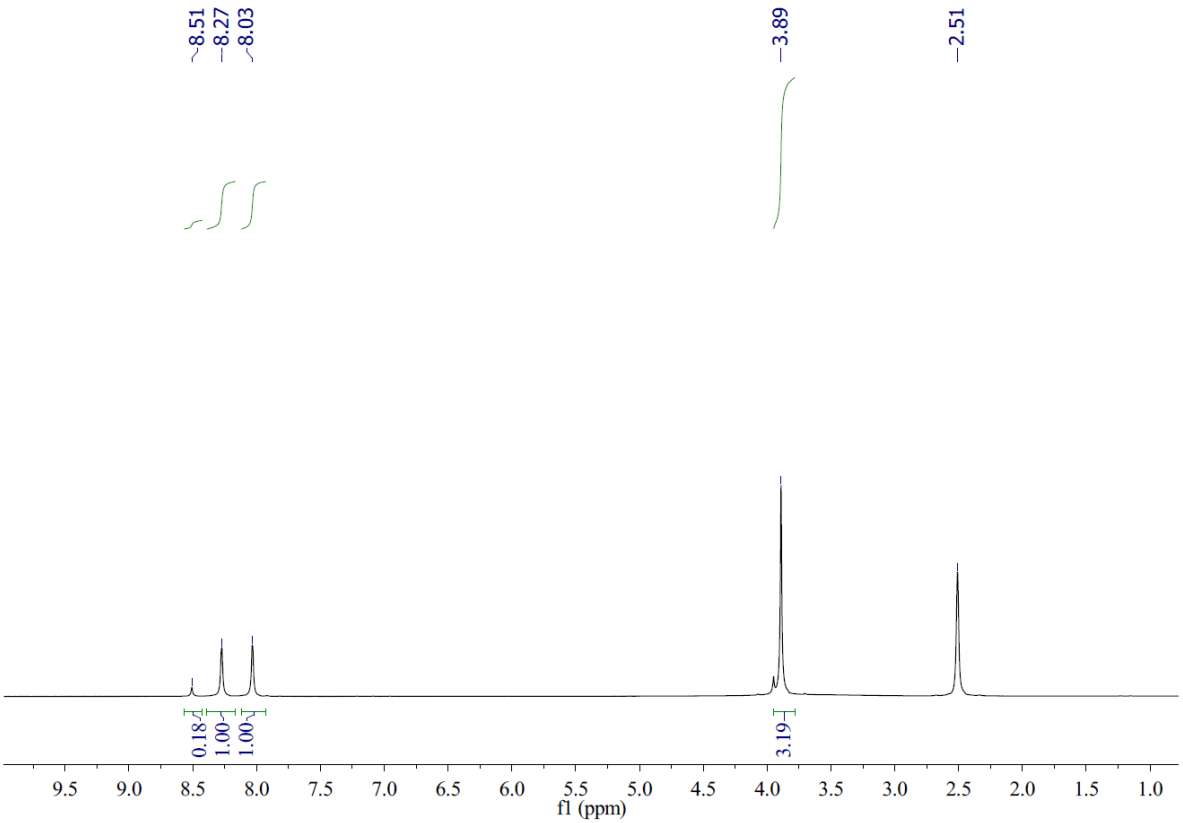
8.51
8.27
8.03
3.89
2.51
0.18
1.00
1.00
3.19
9.5 9.0 8.5 8.0 7.5 7.0 6.5 6.0 5.5 5.0 4.5 4.0 3.5 3.0 2.5 2.0 1.5 1.0
f1 (ppm)

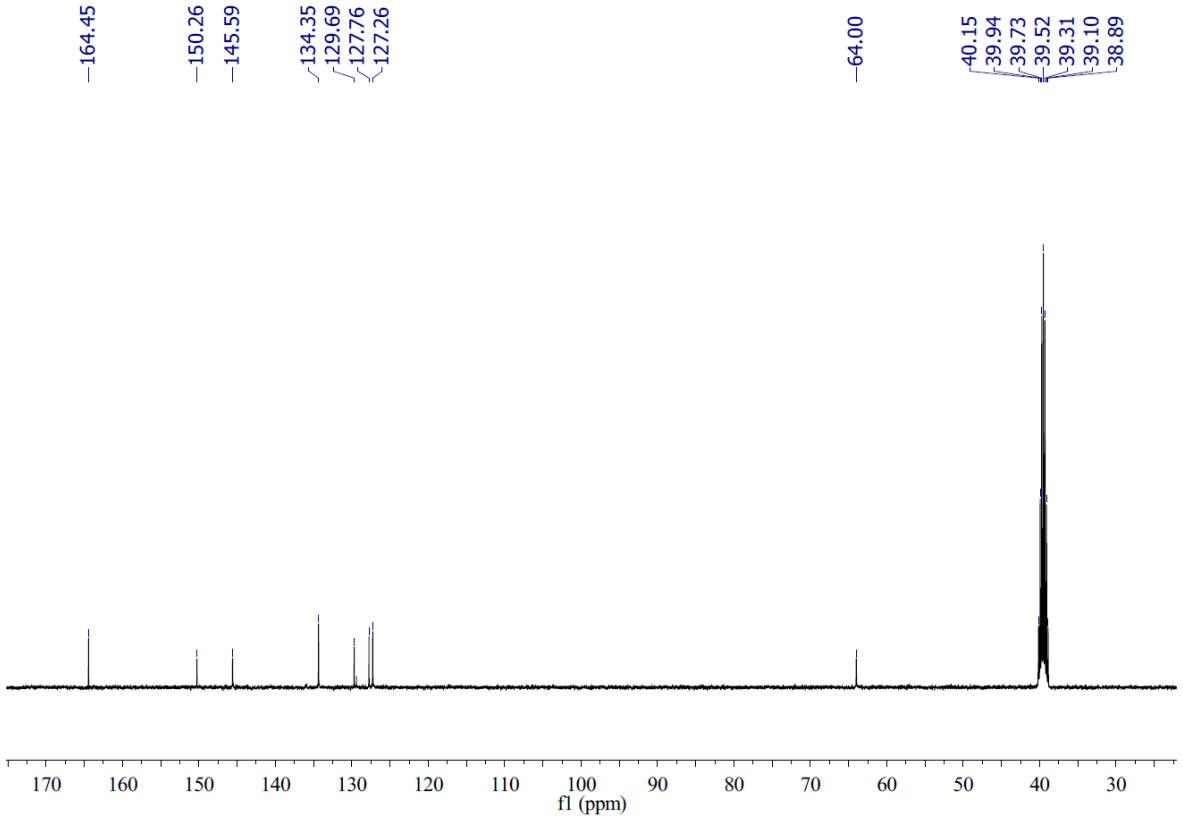
164.45
150.26
145.59
134.35
129.69
127.76
127.26
64.00
40.15
39.94
39.73
39.52
39.31
39.10
38.89
170 160 150 140 130 120 110 100 90 80 70 60 50 40 30
f1 (ppm)

5-Chloro-2-methoxy-3-nitrobenzoyl chloride **(49)**

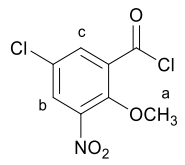

Compound **48** (1.16 g, 5.0 mmol) was dissolved in thionyl chloride (2.0 mL), and the mixture was heated to reflux for 6 hours. When the starting material was consumed confirmed by TLC, the reaction mixture was cooled down and evaporated under reduced pressure to obtain the **49** (1.23 g, 98.4 %) as a red oil. ^{1}H NMR (400 MHz, $CDCl_3$) δ 8.16 (d, 1H, *J* = 2.6, H_b), 8.01 (d, 1H, *J* = 2.6, H_c), 4.01 (s, 3H, H_a). ^{13}C NMR (101 MHz, $CDCl_3$) δ 162.9, 151.6, 145.5, 136.3, 131.9, 130.2, 129.5, 65.0. IR: (υ_{max}/cm^{-1}) 3081, 1785, 1753, 1534, 1342, 1219, 960, 887, 782. EI MS (*m/z*) $[M]^+$ calcd for $C_8H_5Cl_2NO_4$ 249.0, found 248.9.

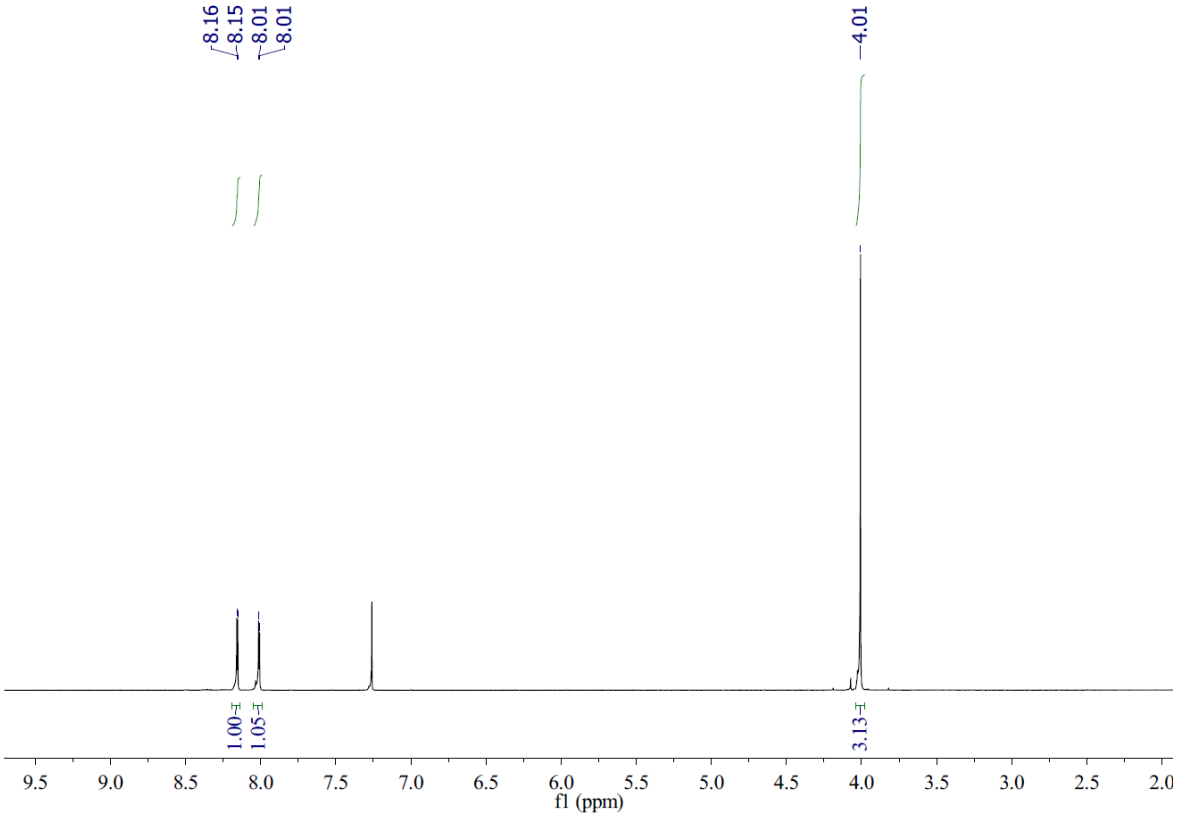
8.16
8.15
8.01
8.01
4.01
1.00
1.05
3.13
9.5 9.0 8.5 8.0 7.5 7.0 6.5 6.0 5.5 5.0 4.5 4.0 3.5 3.0 2.5 2.0
f1 (ppm)

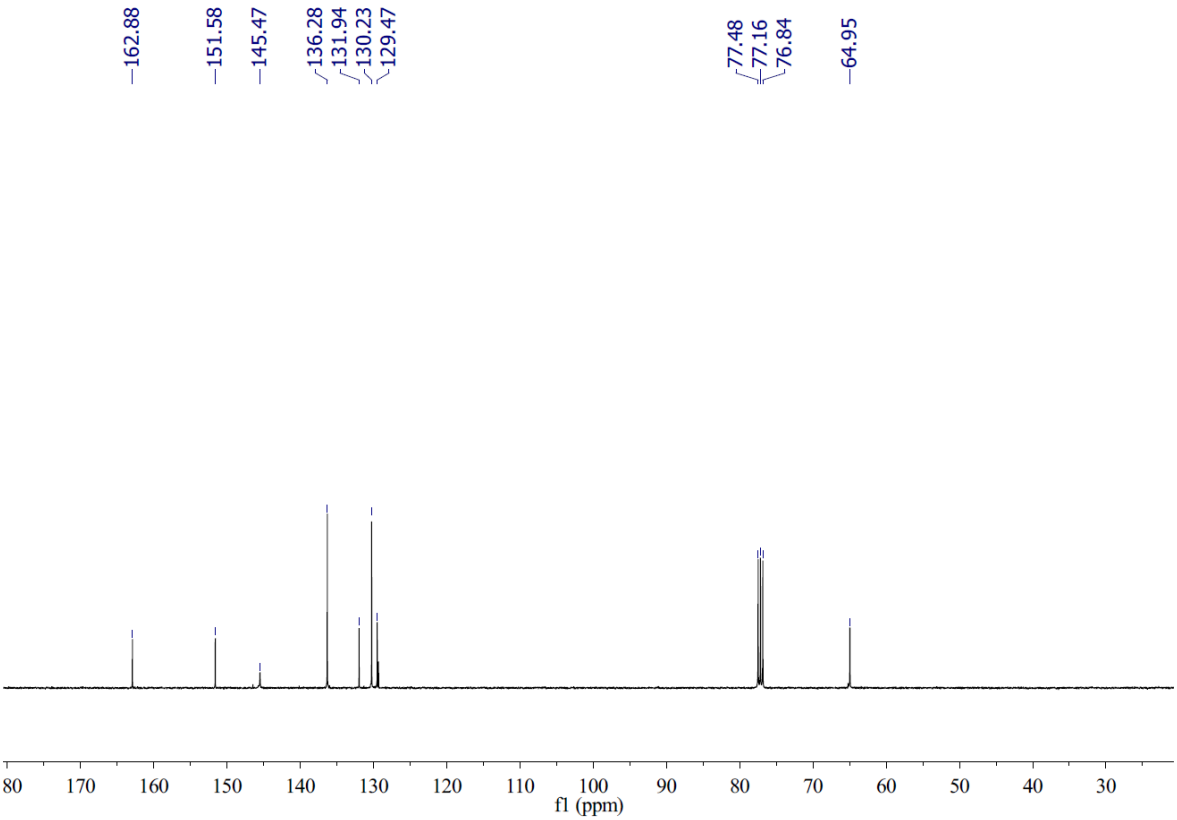
162.88
151.58
145.47
136.28
131.94
130.23
129.47
77.48
77.16
76.84
64.95
80 170 160 150 140 130 120 110 100 90 80 70 60 50 40 30
f1 (ppm)

5-Chloro-2-methoxy-3-nitro-*N*-(4-sulfamoylphenethyl)benzamide (**50**)

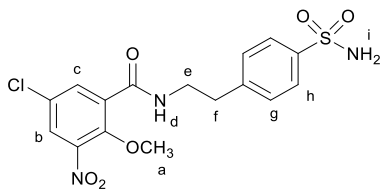

The benzoyl chloride **49** (720 mg, 2.88 mmol) was added slowly to a stirred solution of 4-(2-aminoethyl)benzenesulfonamide (576 mg, 2.88 mmol) in dry pyridine (15 mL). The resultant mixture was stirred overnight at room temperature. Pyridine was removed *in vacuo* and absolute ethanol (10 mL) was added to the residue. The precipitate was collected by filtration and dried *in vacuo* to obtain the **50** (963 mg, 81%, M.p. 208-212 °C) as a white solid. ^{1}H NMR (400 MHz, DMSO-d_6) δ 8.70-8.65 (m, 1H, H_d), 8.11 (d, 1H, J = 2.6, H_b), 7.75 (d, 2H, J = 8.1, H_h), 7.70 (d, 1H, J = 2.6, H_c), 7.45 (d, 2H, J = 8.1, H_g), 7.28 (s, 2H, H_i), 3.69 (s, 3H, H_a), 3.58-3.51 (m, 2H, H_e), 2.96-2.90 (m, 2H, H_f). ^{13}C NMR (101 MHz, DMSO-d_6) δ 163.4, 148.4, 144.5, 143.4, 142.2, 134.0, 132.9, 129.2, 127.5, 125.7, 125.4, 63.2, 40.3, 34.4. IR: (υ_{max}/cm^{-1}) 3152, 1600, 1540, 1453, 1331, 1156, 968, 807, 693. HR-NSI MS (*m/z*) $[M+H]^+$ calcd for $C_{16}H_{17}ClN_3O_6S$ 414.0521, found 414.0519.

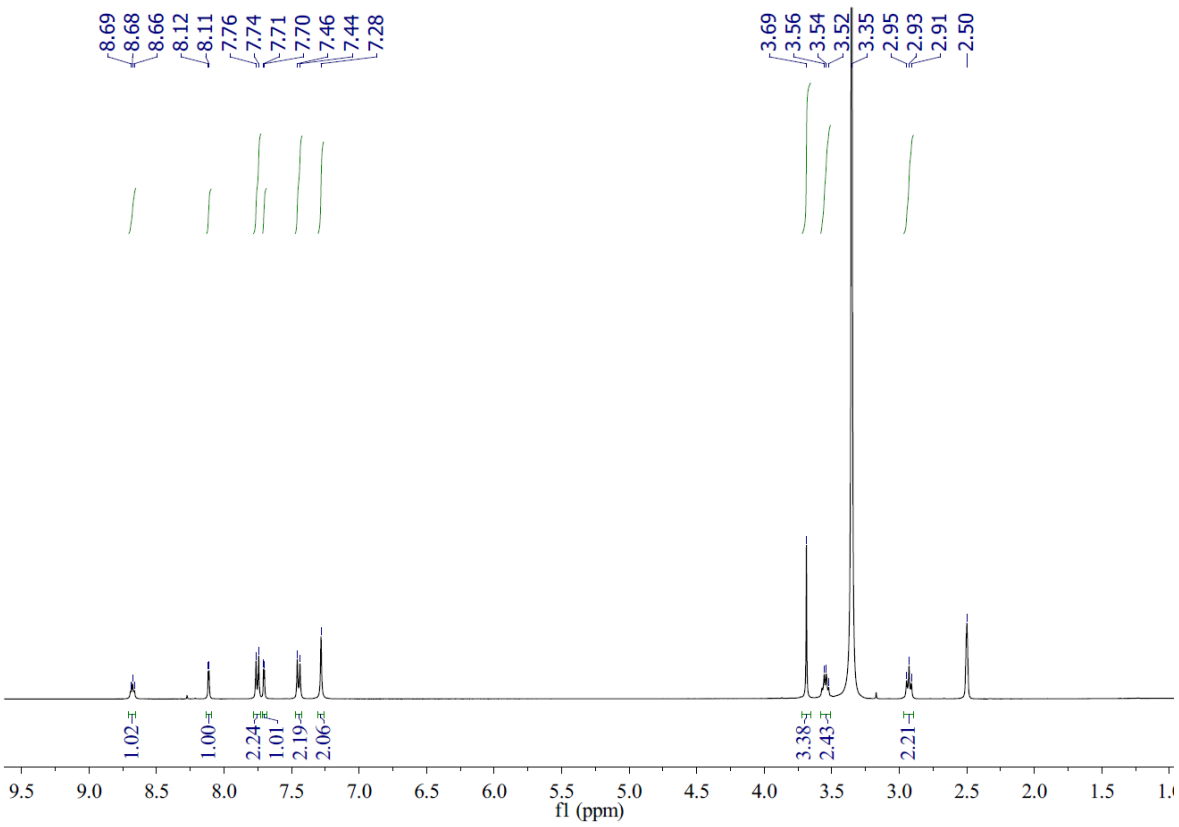
8.69
8.68
8.66
8.12
8.11
7.76
7.74
7.71
7.70
7.46
7.44
7.28
3.69
3.56
3.54
3.52
3.35
2.95
2.93
2.91
2.50
1.02
1.00
2.24
1.01
2.19
2.06
3.38
2.43
2.21
f1 (ppm)

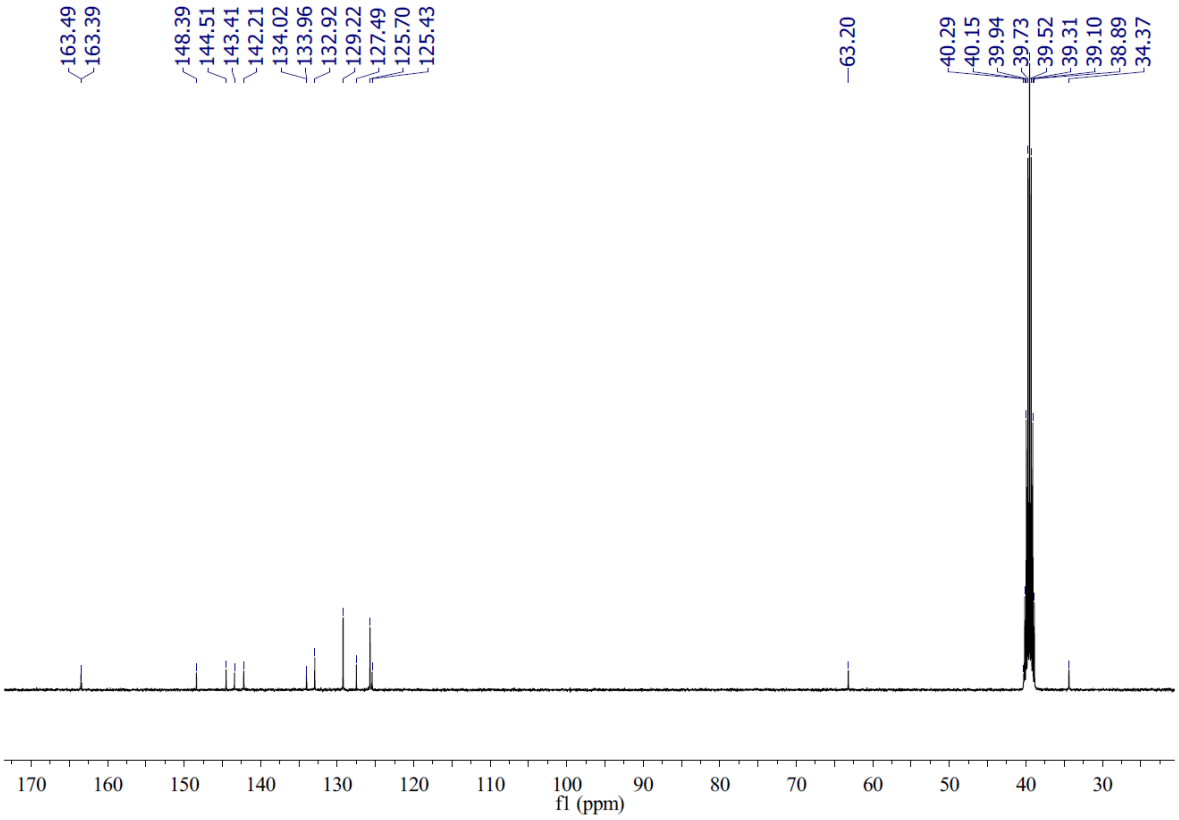
163.49
163.39
148.39
144.51
143.41
142.21
134.02
133.96
132.92
129.22
127.49
125.70
125.43
63.20
40.29
40.15
39.94
39.73
39.52
39.31
39.10
38.89
34.37
f1 (ppm)

5-Chloro-*N*-(4-(*N*-(cyclohexylcarbamoyl)sulfamoyl)phenethyl)-2-methoxy-3-nitrobenzamide (**51**)

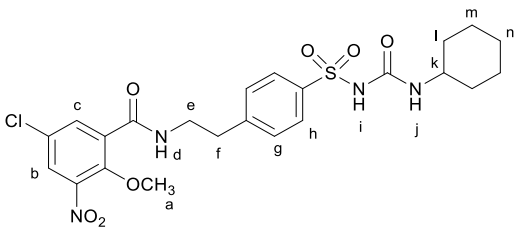

To a stirred solution of sulfonylamine **50** (207 mg, 0.500 mmol) and CuCl (2.5 mg, 0.025 mmol) in DMF (2.0 mL) under N_2 atmosphere, cyclohexyl isocyanate (0.1 mL, 0.750 mmol) was added dropwise. The reaction was stirred at room temperature for 24 hours. The resulting mixture was filtered off and the filtrate was poured slowly into ice cold water (50 mL), acidified with concentrated HCl (0.1 mL) and the precipitate formed was collected by filtration, washed with H_2O, dried *in vacuo* to obtain the **51** (194 mg, 72%, M.p. 221-225 °C) as a white solid. ^{1}H NMR (400 MHz, $CDCl_3$) δ 8.22 (d, 1H, *J* = 2.8, H_b), 7.90 (d, 1H, *J* = 2.8, H_c), 7.85 (d, 2H, *J* = 8.3, H_h), 7.68-7.60 (bs, 1H, H_i), 7.44 (d, 2H, *J* = 8.3, H_g), 6.44 (d, 1H, *J* = 7.7, H_j), 3.84-3.76 (m, 2H, H_e), 3.76 (s, 3H, H_a), 3.63-3.54 (m, 1H, H_k), 3.07 (t, 2H, *J* = 7.1, H_f), 1.88-1.18 (m, 10H, $H_{l\text{-}n}$). ^{13}C NMR (101 MHz, $CDCl_3$) δ 162.8, 149.9, 149.1, 144.9, 144.6, 135.8, 130.9, 130.3, 129.7, 128.4, 127.9, 64.2, 49.5, 41.1, 35.2, 33.9, 25.1, 24.8. IR: (υ_{max}/cm^{-1}) 3293, 2930, 2854, 1645, 1535, 1449, 1342, 1250, 1163, 1087, 1030, 904, 661. HR-NSI MS (*m/z*) $[M+H]^+$ calcd for $C_{23}H_{28}ClN_4O_7S$ 539.1362, found 539.1357.

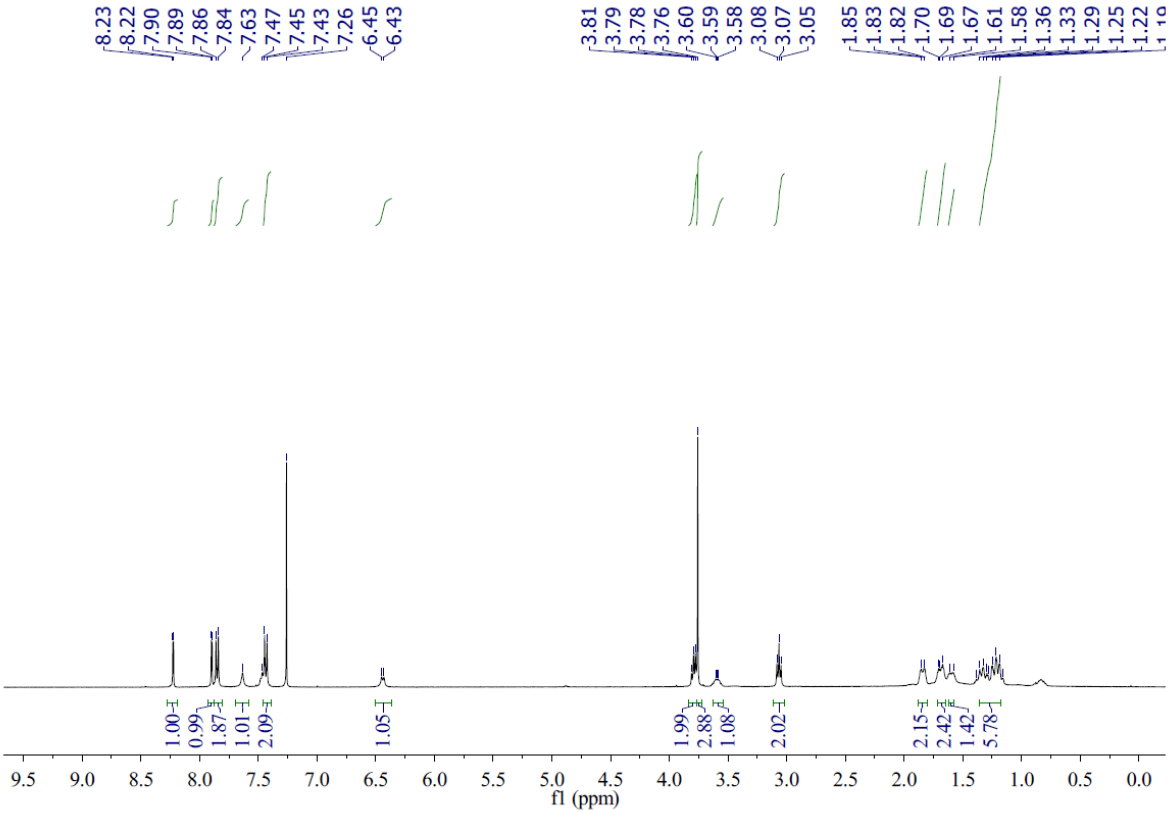
8.23
8.22
7.90
7.89
7.86
7.84
7.63
7.47
7.45
7.43
7.26
6.45
6.43
3.81
3.79
3.78
3.76
3.60
3.59
3.58
3.08
3.07
3.05
1.85
1.83
1.82
1.70
1.69
1.67
1.61
1.58
1.36
1.33
1.29
1.25
1.22
1.00
0.99
1.87
1.01
2.09
1.05
1.99
2.88
1.08
2.02
2.15
2.42
1.42
5.78
f1 (ppm)

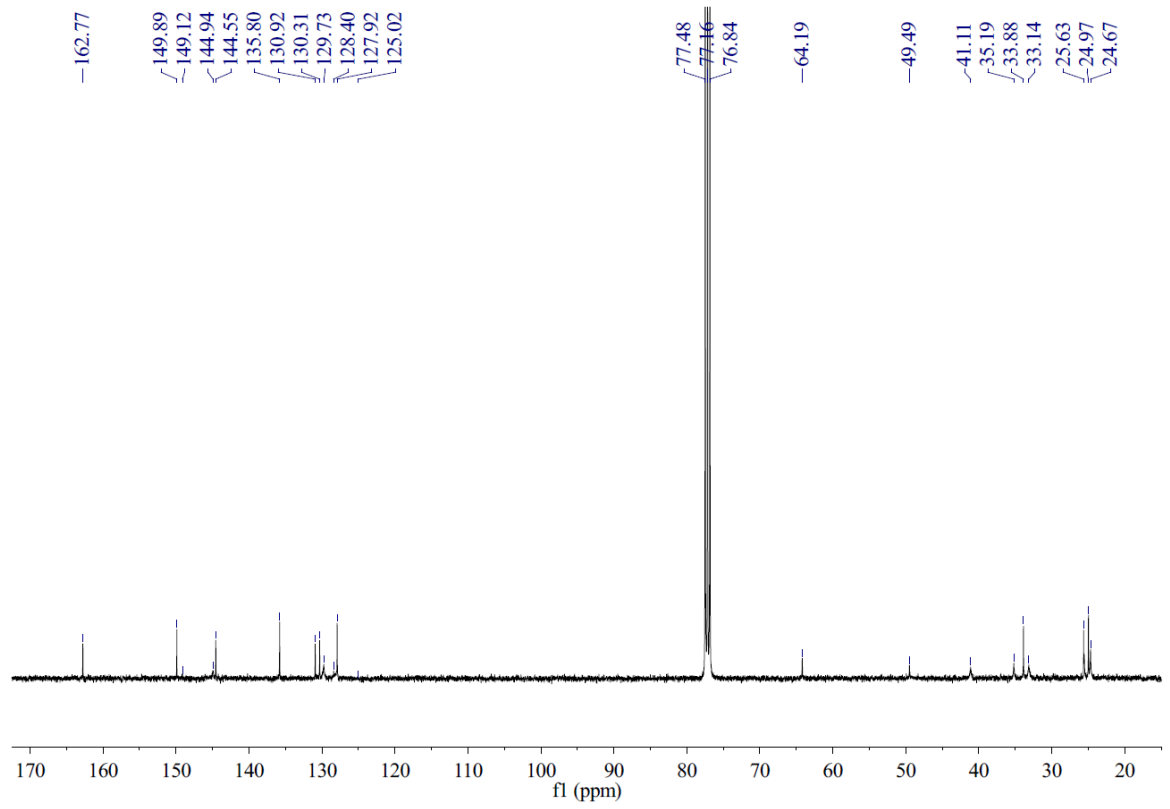
162.77
149.89
149.12
144.94
144.55
135.80
130.92
130.31
129.73
128.40
127.92
125.02
77.48
77.16
76.84
64.19
49.49
41.11
35.19
33.88
33.14
25.63
24.97
24.67
f1 (ppm)

3-Amino-5-chloro-*N*-(4-(*N*-(cyclohexylcarbamoyl)sulfamoyl)phenethyl)-2-methoxybenzamide (**52**)

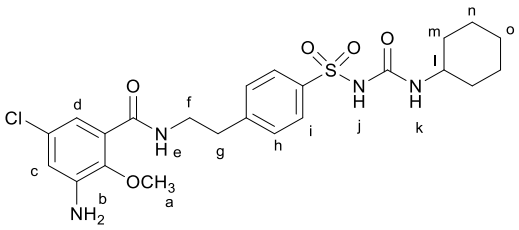

The compound **51** (568 mg, 1.05 mmol) was dissolved in acetic acid (9.0 mL) and heated to 70 °C under N_2 atmosphere. Fe powder (177 mg, 3.16 mmol) was added in this solution and the reaction mixture was stirred at 70 °C for 30 minutes. Then the mixture was cooled to room temperature and concentrated under reduced pressure. The residue was dissolved in ethyl acetate (30 mL) and washed with saturated $NaHCO_3$ (30 mL × 3). The organic layer was dried over $MgSO_4$ and the solution was concentrated *in vacuo*. The product was purified by silica gel chromatography (2% methanol in dichloromethane) to give **52** (260 mg, 51%, M.p. 101-104 °C) as a white solid. ^{1}H NMR (400 MHz, $CDCl_3$) δ 7.85 (d, 2H, *J* = 8.4, H_i), 7.75-7.68 (m, 1H, H_j), 7.41 (d, 2H, *J* = 8.4, H_h), 7.29 (d, 1H, *J* = 2.6, H_c), 6.80 (d, 1H, *J* = 2.6, H_d), 6.42 (d, 1H, *J* = 7.9, H_j), 3.80-3.73 (m, 2H, H_f), 3.60-3.54 (m, 1H, H_l), 3.48 (s, 3H, H_a), 3.08-3.01 (m, 2H, H_g), 1.82-1.15 (m, 10H, H_{m-o}). ^{13}C NMR (101 MHz, CD_3OD) δ 166.5, 151.5, 145.5, 143.3, 143.0, 138.3, 129.5, 129.3, 128.4, 127.5, 117.0, 116.5, 59.6, 48.8, 40.1, 34.6, 32.4, 25.1, 24.4. IR: (υ_{max}/cm^{-1}) 3459, 3016, 2970, 1757, 1714, 1426, 1367, 1216, 1092, 900. HR-ESI MS (*m/z*) $[M+H]^+$ calcd for $C_{23}H_{30}ClN_4O_5S$ 509.1620, found 509.1613.

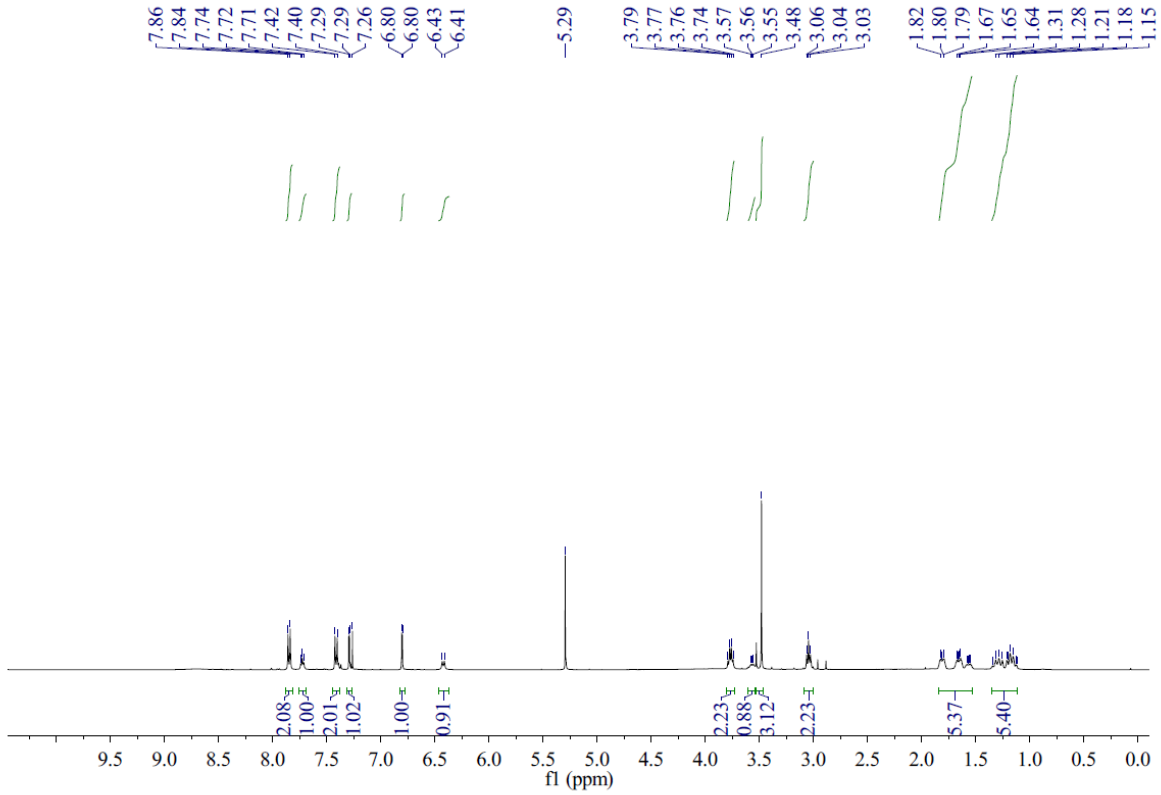
7.86
7.84
7.74
7.72
7.71
7.42
7.40
7.29
7.29
7.26
6.80
6.80
6.43
6.41
5.29
3.79
3.77
3.76
3.74
3.57
3.56
3.55
3.48
3.06
3.04
3.03
1.82
1.80
1.79
1.67
1.65
1.64
1.31
1.28
1.21
1.18
1.15
2.08
1.00
2.01
1.02
1.00
0.91
2.23
0.88
3.12
2.23
5.37
5.40
9.5 9.0 8.5 8.0 7.5 7.0 6.5 6.0 5.5 5.0 4.5 4.0 3.5 3.0 2.5 2.0 1.5 1.0 0.5 0.0
f1 (ppm)

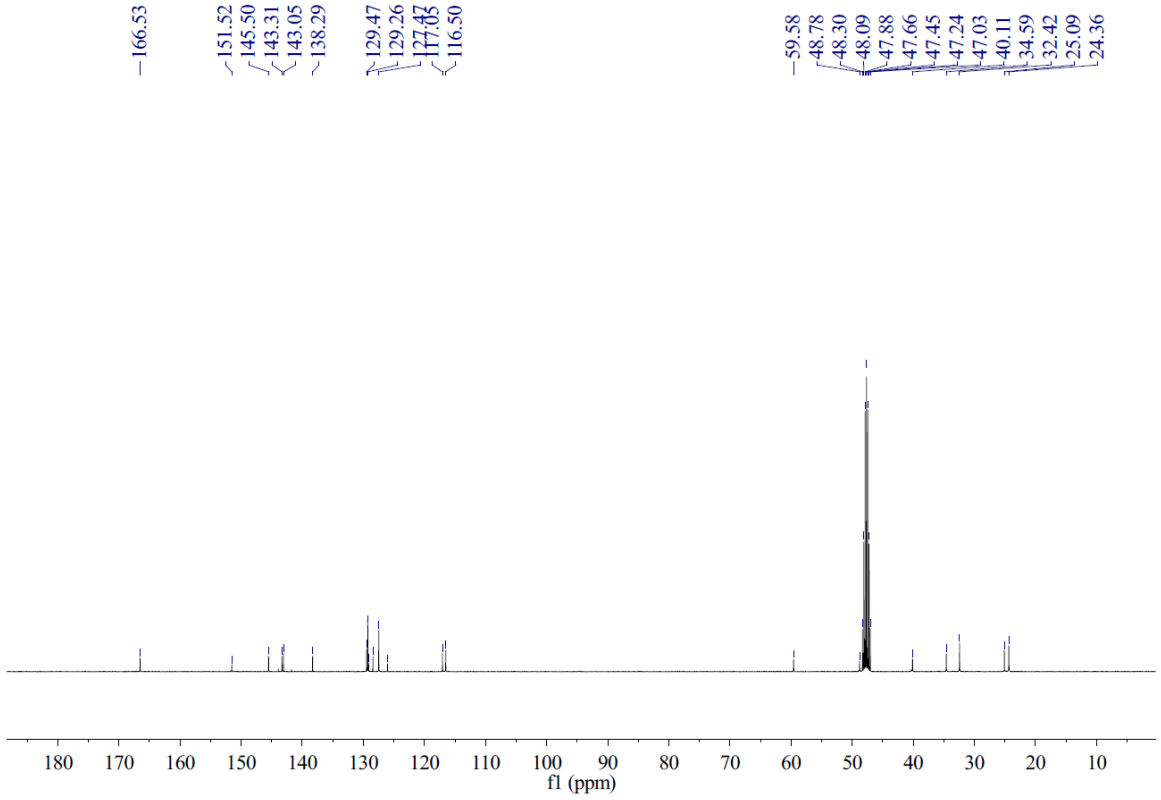
166.53
151.52
145.50
143.31
143.05
138.29
129.47
129.26
117.47
117.05
116.50
59.58
48.78
48.30
48.09
47.88
47.66
47.45
47.24
47.03
40.11
34.59
32.42
25.09
24.36
180 170 160 150 140 130 120 110 100 90 80 70 60 50 40 30 20 10
f1 (ppm)

3-Azido-5-chloro-*N*-(4-(*N*-(cyclohexylcarbamoyl)sulfamoyl)phenethyl)-2-methoxybenzamide (**53**)

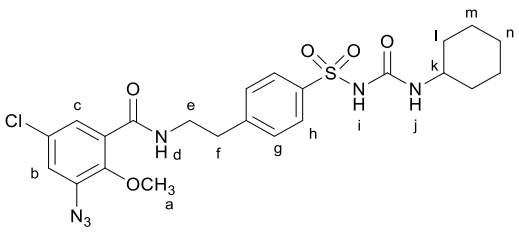

The compound **52** (127 mg, 0.250 mmol) was dissolved in acetonitrile (3.0 mL) and cooled in an ice-water bath. To this solution was added dropwise t-BuONO (50 µL, 0.38 mmol) and $TMSN_3$ (38 µL, 0.30 mmol). After stirring for 30 min, the ice-water bath was removed and the mixture was stirred for 6 hours at room temperature. Then the solvent was evaporated under reduced pressure and the residue was washed with petroleum ether and water, dried *in vacuo* to obtain the **53** (91 mg, 68%, M.p. 191-194 °C) as a pale yellow solid. ^{1}H NMR (400 MHz, $CDCl_3$) δ 8.65 (bs, 1H, H_i), 7.85 (d, 2H, J = 8.3, H_h), 7.78 (d, 1H, J = 2.4, H_c), 7.41 (d, 2H, J = 8.3, H_g), 7.16 (d, 1H, J = 2.4, H_b), 6.42 (d, 1H, J = 7.7, H_j), 3.82-3.70 (m, 2H, H_e), 3.63 (s, 3H, H_a), 3.61-3.52 (m, 1H, H_k), 3.08-3.00 (m, 2H, H_f), 1.83-1.16 (m, 10H, $H_{l\text{-}n}$). ^{13}C NMR (101 MHz, CD_3OD and $CDCl_3$) δ 166.0, 149.6, 146.3, 139.4, 136.1, 131.2, 130.8, 130.3, 128.6, 127.2, 126.8, 123.7, 62.9, 54.4, 41.4, 35.7, 33.6, 26.2, 25.4. IR: (υ_{max}/cm^{-1}) 2930, 2111, 1739, 1631, 1533, 1445, 1345, 1169, 983, 900, 691. HR-ESI MS (*m/z*) $[M+H]^+$ calcd for $C_{23}H_{28}ClN_6O_5S$ 535.1525, found 535.1520.

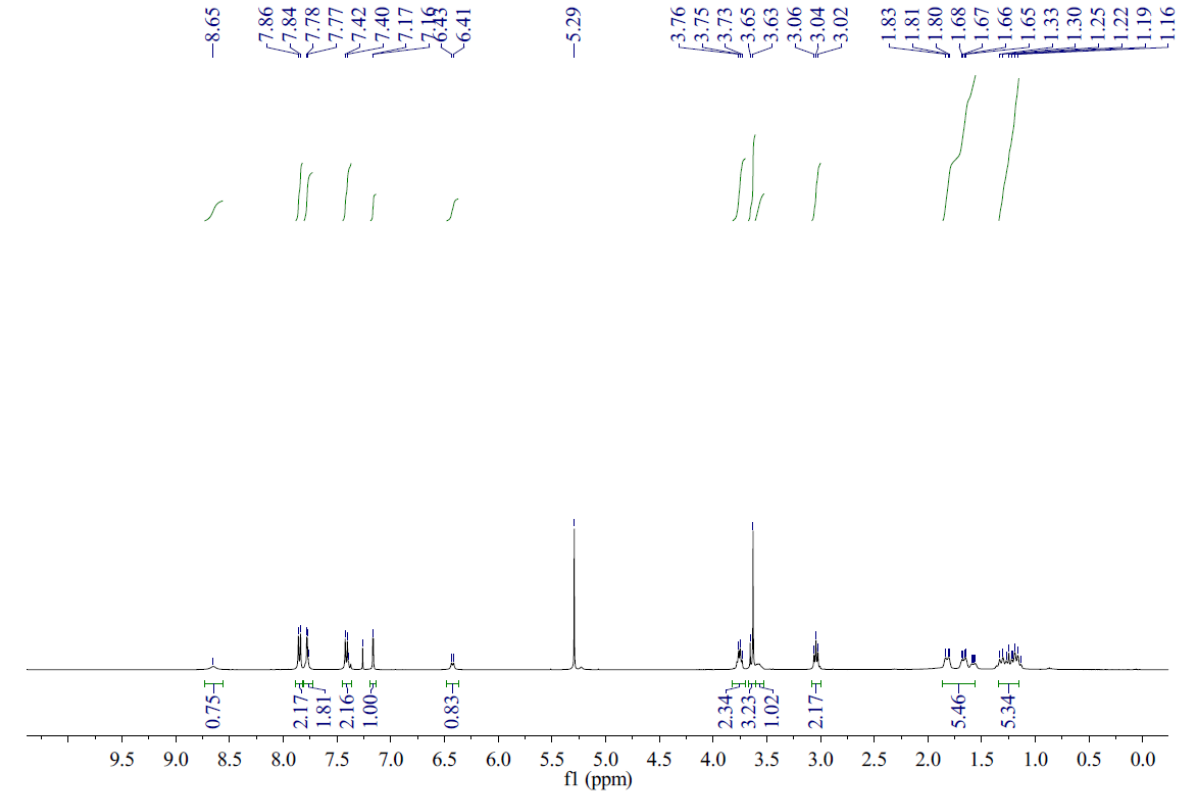
8.65
7.86
7.84
7.78
7.77
7.42
7.40
7.17
7.16
6.43
6.41
5.29
3.76
3.75
3.73
3.65
3.63
3.06
3.04
3.02
1.83
1.81
1.80
1.68
1.67
1.66
1.65
1.33
1.30
1.25
1.22
1.19
1.16
0.75
2.17
1.81
2.16
1.00
0.83
2.34
3.23
1.02
2.17
5.46
5.34
9.5 9.0 8.5 8.0 7.5 7.0 6.5 6.0 5.5 5.0 4.5 4.0 3.5 3.0 2.5 2.0 1.5 1.0 0.5 0.0
f1 (ppm)

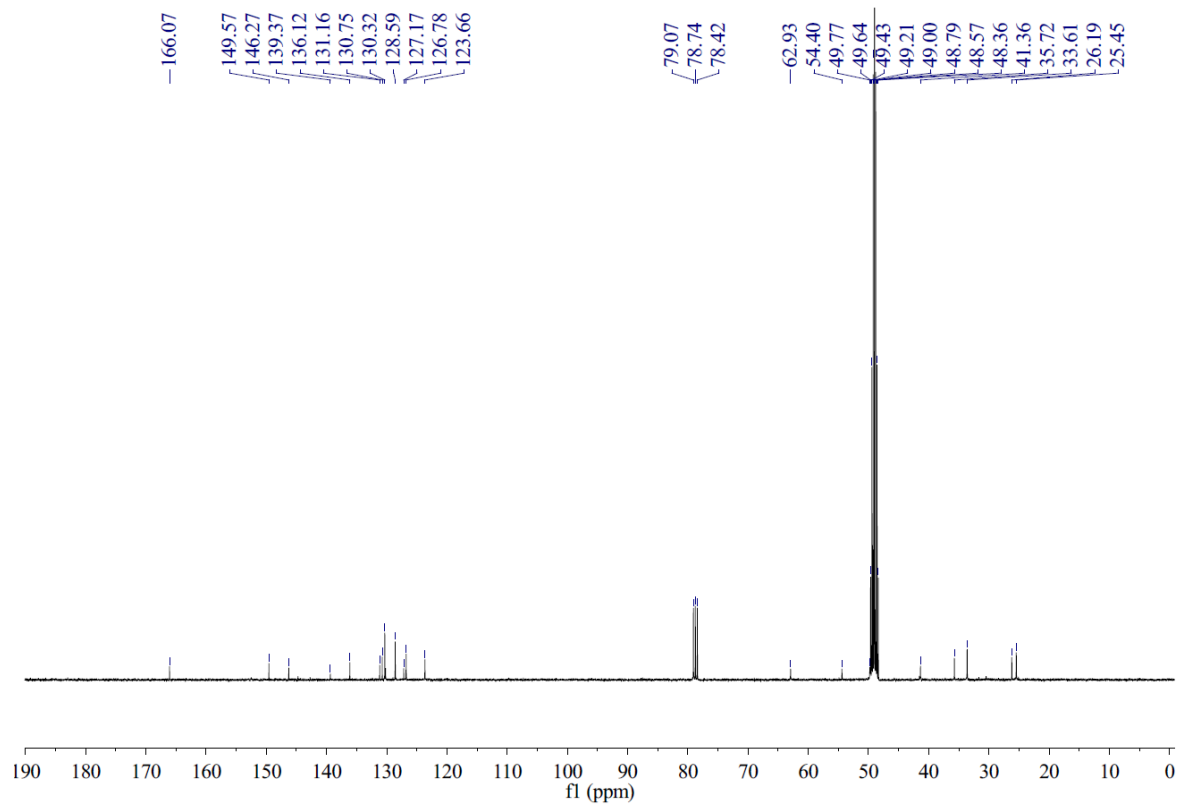
166.07
149.57
146.27
139.37
136.12
131.16
130.75
130.32
128.59
127.17
126.78
123.66
79.07
78.74
78.42
62.93
54.40
49.77
49.64
49.43
49.21
49.00
48.79
48.57
48.36
41.36
35.72
33.61
26.19
25.45
190 180 170 160 150 140 130 120 110 100 90 80 70 60 50 40 30 20 10 0
f1 (ppm)

N,N-bis(Pyridin-2-ylmethyl)prop-2-yn-1-amine (**54**)

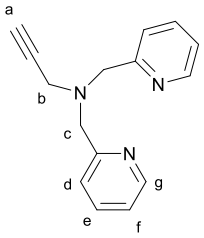

A mixture of propargylamine (1.50 g, 27.3 mmol) and potassium carbonate (22.8 g, 164 mmol) was stirred in acetonitrile (140 mL) for 5 mins. Then 2-picolyl chloride hydrochloride (9.84 g, 60.0 mmol) dissolved in acetonitrile (140 mL) was added. The resulting solution was stirred under reflux for 5 days. After the reaction was complete, the mixture was filtered and the filtration evaporated under reduced pressure. The resulting brown oil was dissolved in distilled water (100 mL) and extracted with dichloromethane (3 × 50 mL). The organic layers were combined and dried over $MgSO_4$. The solvent was evaporated to afford **54** (6.04 g, 93%) as a brown oil. ^{1}H NMR (400 MHz, $CDCl_3$) δ 8.56-8,53 (m, 2H, H_g), 7.65 (td, 2H, J = 7.7, 1.8, H_e), 7.51 (m, 2H, H_d), 7.17-7.13 (m, 2H, H_f), 3.92 (s, 4H, H_c), 3.42 (d, 2H, J = 2.4, H_b), 2.29 (t, 1H, J = 2.4, H_a). ^{13}C NMR (101 MHz, $CDCl_3$) δ 158.8, 149.3, 136.5, 123.2, 122.1, 78.4, 73.6, 59.5, 42.6. All other spectroscopic data were consistent with those previously reported.[146]

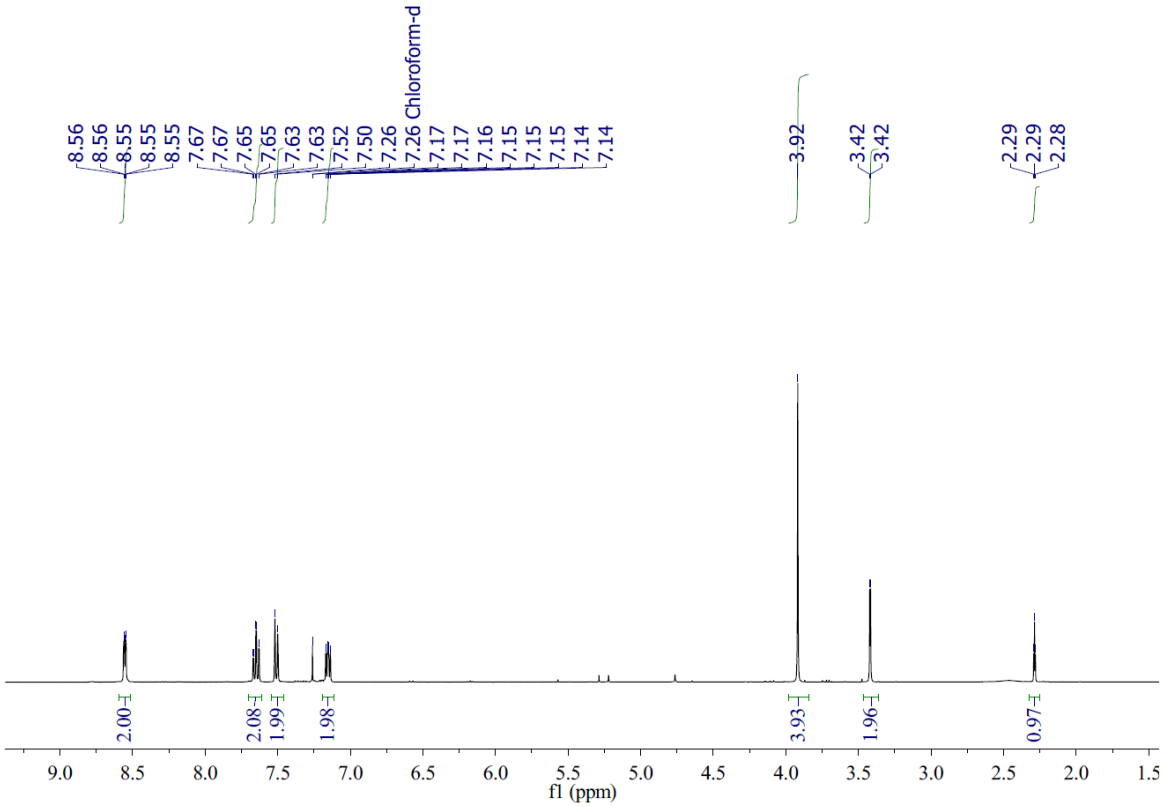
8.56
8.56
8.55
8.55
8.55
7.67
7.67
7.65
7.65
7.63
7.63
7.52
7.50
7.26
Chloroform-d
7.26
7.17
7.17
7.16
7.15
7.15
7.15
7.14
7.14
3.92
3.42
3.42
2.29
2.29
2.28
2.00
2.08
1.99
1.98
3.93
1.96
0.97
9.0
8.5
8.0
7.5
7.0
6.5
6.0
5.5
5.0
4.5
4.0
3.5
3.0
2.5
2.0
1.5
f1 (ppm)

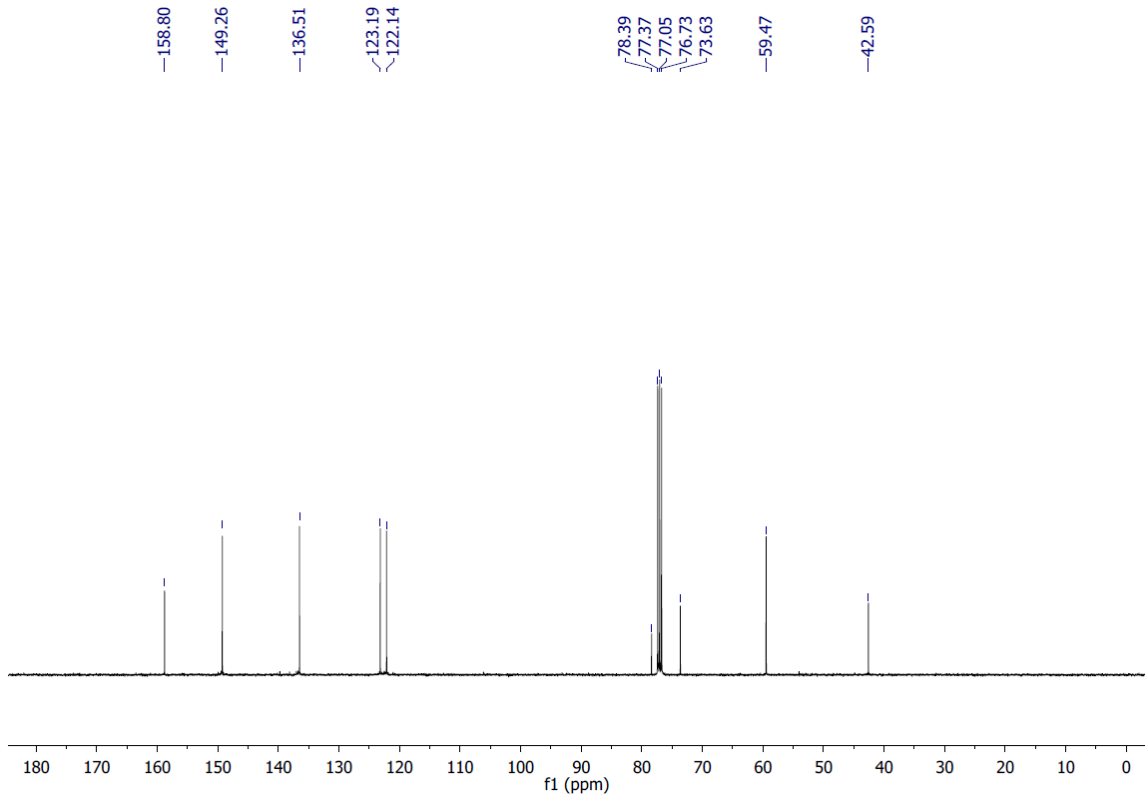
158.80
149.26
136.51
123.19
122.14
78.39
77.37
77.05
76.73
73.63
59.47
42.59
180
170
160
150
140
130
120
110
100
90
80
70
60
50
40
30
20
10
0
f1 (ppm)

3-(4-((6-bromo-1,3-dioxo-1*H*-benzo[*de*]isoquinolin-2(3*H*)-yl)methyl)-1*H*-1,2,3-triazol-1-yl)-5-chloro-*N*-(4-(*N*-(cyclohexylcarbamoyl)sulfamoyl)phenethyl)-2-methoxybenzamide (**55**)

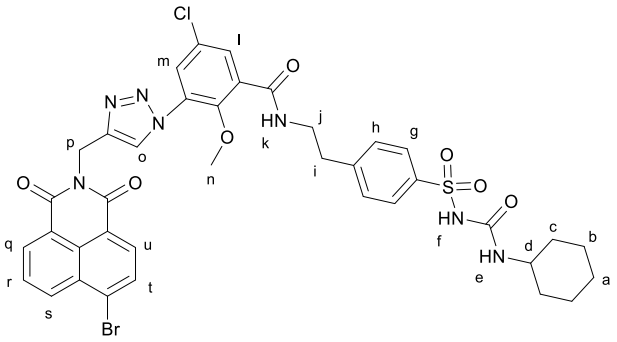

Under a nitrogen atmosphere, the glibenclamide azide **53** (53.5 mg, 0.10 mmol) and alkyne **54** (31.4 mg, 0.10 mmol) were dissolved in anhydrous DCM (5.0 mL), then DIPEA (20 µL, 0.18 mmol) and tetrakis(acetonitrile)copper(I) hexafluorophosphate (7.5 mg, 0.020 mmol) was added to the above solution. The flask was covered with aluminium foil and stirred at room temperature for 48 h. After the reaction complete, the reaction mixture was diluted with DCM (20 mL) and washed with saturated EDTA in 17 % $NH_3 \cdot H_2O$ (10 mL), water (20 mL) and brine (20 mL). The organic layer was dried over $MgSO_4$, filtered and concentrated *in vacuo* to give **55** (78.1 mg, 92%, M.p. 117-120 °C) as a yellow solid. ^{1}H NMR (400 MHz, $CDCl_3$) δ 8.77 (d, 1H, J = 6.5, H_q), 8.62 (d, 1H, J = 8.5, H_s), 8.53 (d, 1H, J = 7.9, H_u), 8.20 (s, 1H, H_o), 8.11 (d, 1H, J = 2.7, H_m), 8.09 (d, 1H, J = 7.9, H_t), 7.95 (d, 2H, J = 8.3, H_g), 7.92-7.86 (m, 1H, H_r), 7.82 (d, 1H, J = 2.7, H_l), 7.57-7.51 (m, 1H, H_k), 7.46 (d, 2H, J = 8.3, H_h), 6.48 (d, 1H, J = 8.0, H_e), 5.63 (s, 2H, H_p), 3.85-3.78 (m, 2H, H_j), 3.63-3.50 (m, 1H, H_d), 3.16 (s, 3H, H_n), 3.06 (t, 2H, J = 6.7, H_i), 1.81-1.17 (m, 10H, $H_{a\text{-}c}$).^{13}C NMR (101 MHz, $CDCl_3$) δ 175.1, 167.5, 163.6, 148.7, 145.1, 144.1, 135.3, 133.8, 132.6, 131.9, 131.8, 131.7, 131.3, 131.0, 130.7, 129.8, 129.0, 128.8, 128.3, 127.5, 125.4, 122.7, 121.8, 62.2, 60.4, 53.5, 35.2, 33.0, 25.3, 24.6, 21.1. IR: (υ_{max}/cm^{-1}) 3142, 1600, 1534, 1483, 1344, 1242, 1169, 1025, 968, 807, 777, 688. HR-NSI MS (*m/z*) $[M+H]^+$ calcd for $C_{38}H_{36}BrClN_7O_7S$ 848.1262, found 848.1263.

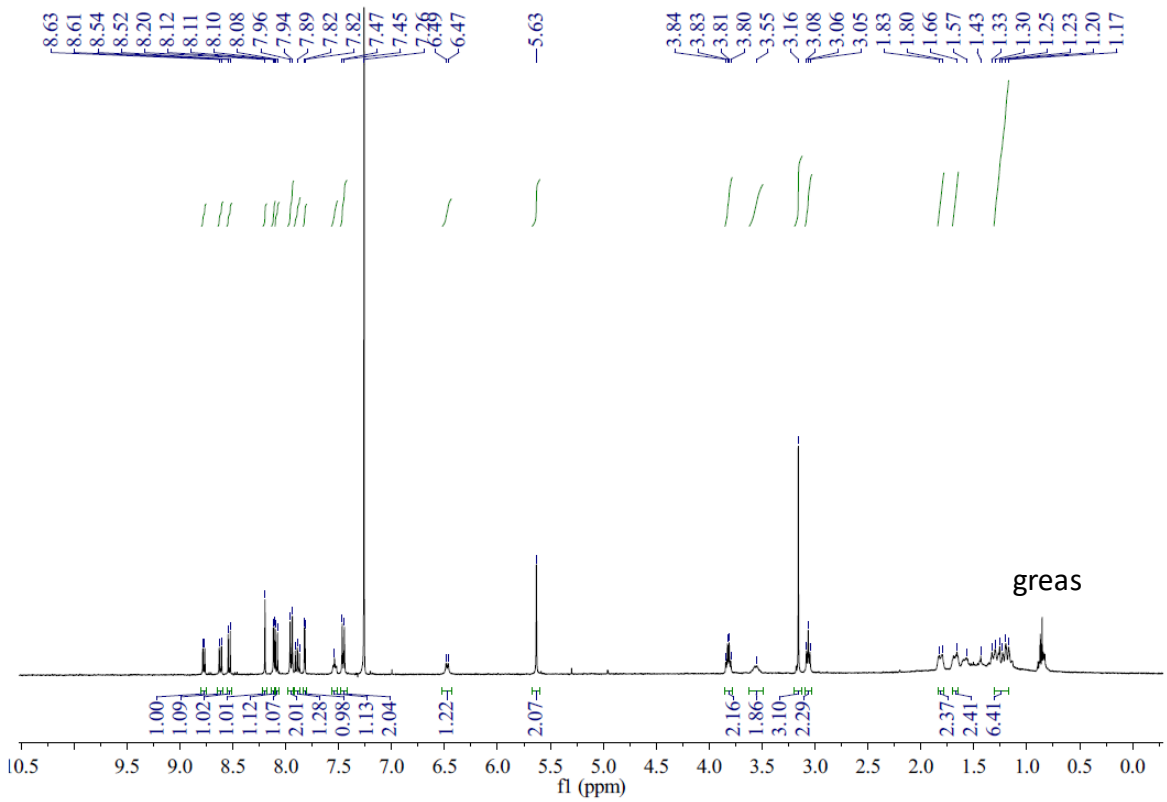
8.63
8.61
8.54
8.52
8.20
8.12
8.11
8.10
8.08
7.96
7.94
7.89
7.82
7.82
7.47
7.45
7.26
6.48
6.47
5.63
3.84
3.83
3.81
3.80
3.55
3.16
3.08
3.06
3.05
1.83
1.80
1.66
1.57
1.43
1.33
1.30
1.25
1.23
1.20
1.17
greas
1.00
1.09
1.02
1.01
1.12
1.07
2.01
1.28
0.98
1.13
2.04
1.22
2.07
2.16
1.86
3.10
2.29
2.37
2.41
6.41
10.5
9.5
9.0
8.5
8.0
7.5
7.0
6.5
6.0
5.5
5.0
4.5
4.0
3.5
3.0
2.5
2.0
1.5
1.0
0.5
0.0
f1 (ppm)

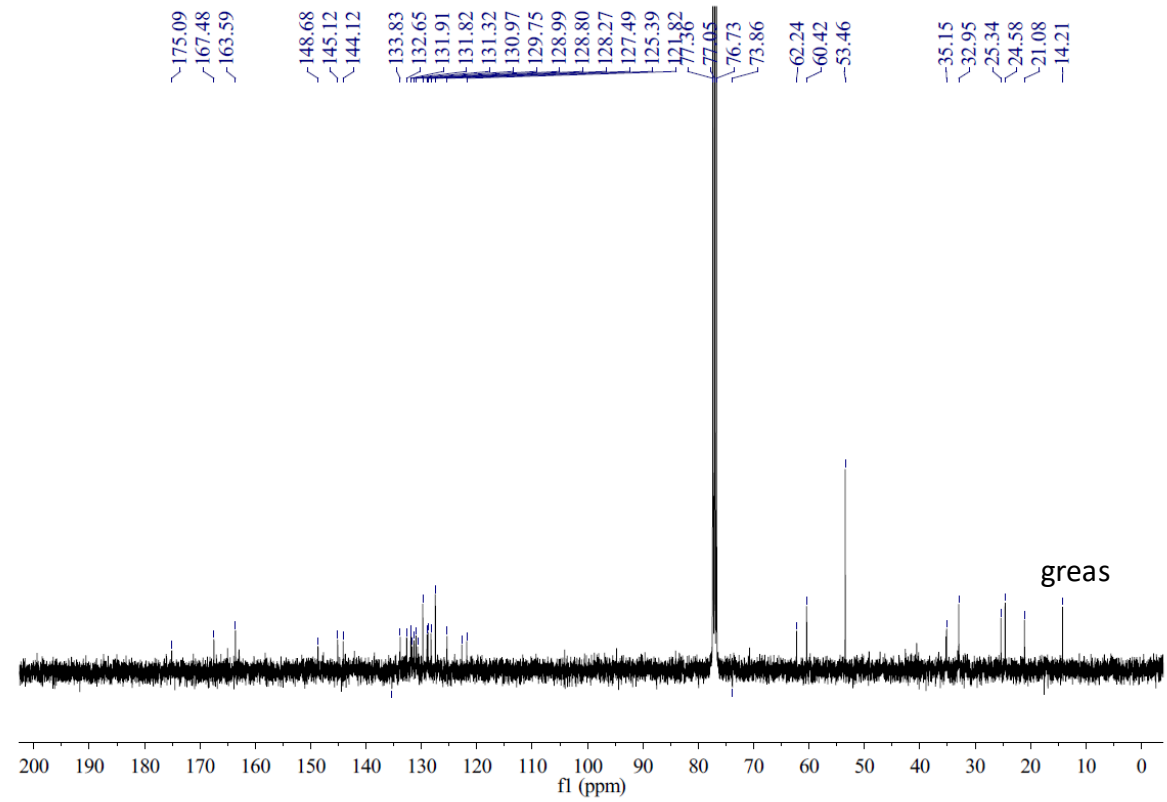
175.09
167.48
163.59
148.68
145.12
144.12
133.83
132.65
131.91
131.82
131.32
130.97
129.75
128.99
128.80
128.27
127.49
125.39
121.82
77.36
77.05
76.73
73.86
62.24
60.42
53.46
35.15
32.95
25.34
24.58
21.08
14.21
greas
200
190
180
170
160
150
140
130
120
110
100
90
80
70
60
50
40
30
20
10
0
f1 (ppm)

3-(4-((6-azido-1,3-dioxo-1*H*-benzo[*de*]isoquinolin-2(3*H*)-yl)methyl)-1*H*-1,2,3-triazol-1-yl)-5-chloro-*N*-(4-(*N*-(cyclohexylcarbamoyl)sulfamoyl)phenethyl)-2-methoxybenzamide (**56**)

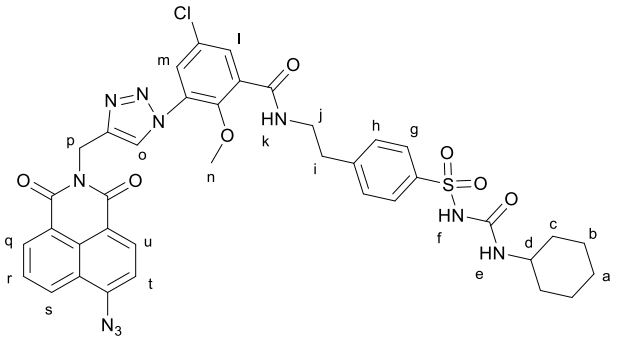

Compound **55** (67.9 mg, 0.08 mmol) was dissolved in DMF (2.0 mL), and sodium azide (6.5 mg, 0.1 mmol) was added in the reaction mixture and it was stirred at room temperature for 24 h. Then the reaction mixture was diluted with water (20 mL) and extracted with EtOAc (3 × 20 mL). The organic layers were combined and washed with brine, dried over $MgSO_4$, and concentrated *in vacuo* to obtain the **56** (56.5 mg, 87 %, M.p. 190-194 °C) as yellow solid. ^{1}H NMR (400 MHz, $CDCl_3$) δ 8.72 (d, 1H, *J* = 7.3, H_q), 8.68 (d, 1H, *J* = 8.0, H_u), 8.47 (d, 1H, *J* = 8.4, H_s), 8.19 (s, 1H, H_o), 8.09 (d, 1H, *J* = 2.7, H_m), 7.94 (d, 2H, *J* = 8.3, H_g), 7.79 (d, 1H, *J* = 2.7, H_l), 7.77-7.74 (m, 1H, H_r), 7.61-7.57 (m, 1H, H_k), 7.50 (d, 1H, *J* = 8.0, H_t), 7.44 (d, 2H, *J* = 8.3, H_h), 6.45 (d, 1H, *J* = 7.6, H_e), 5.61 (s, 2H, H_p), 3.83-3.78 (m, 2H, H_j), 3.57-3.50 (m, 1H, H_d), 3.16 (s, 3H, H_n), 3.07 (t, 2H, *J* = 6.8, H_i), 1.82-1.13 (m, 10H, $H_{a\text{-}c}$). ^{13}C NMR (101 MHz, $CDCl_3$) δ 164.1, 163.7, 163.1, 150.5, 148.8, 145.3, 144.5, 138.6, 133.0, 132.6, 132.0, 131.8, 131.1, 129.9, 129.8, 129.5, 129.1, 128.9, 127.6, 127.2, 125.5, 124.5, 123.1, 122.3, 118.5, 115.0, 62.3, 49.3, 40.6, 35.3 (× 2), 33.1, 25.5, 24.7. IR: (υ_{max}/cm^{-1}) 2930, 2124, 1704, 1663, 1534, 1342, 1242, 1161, 1042, 904, 784, 659. HR-NSI MS (*m/z*) $[M+H]^+$ calcd for $C_{38}H_{36}ClN_{10}O_7S$ 811.2172, found 811.2172.

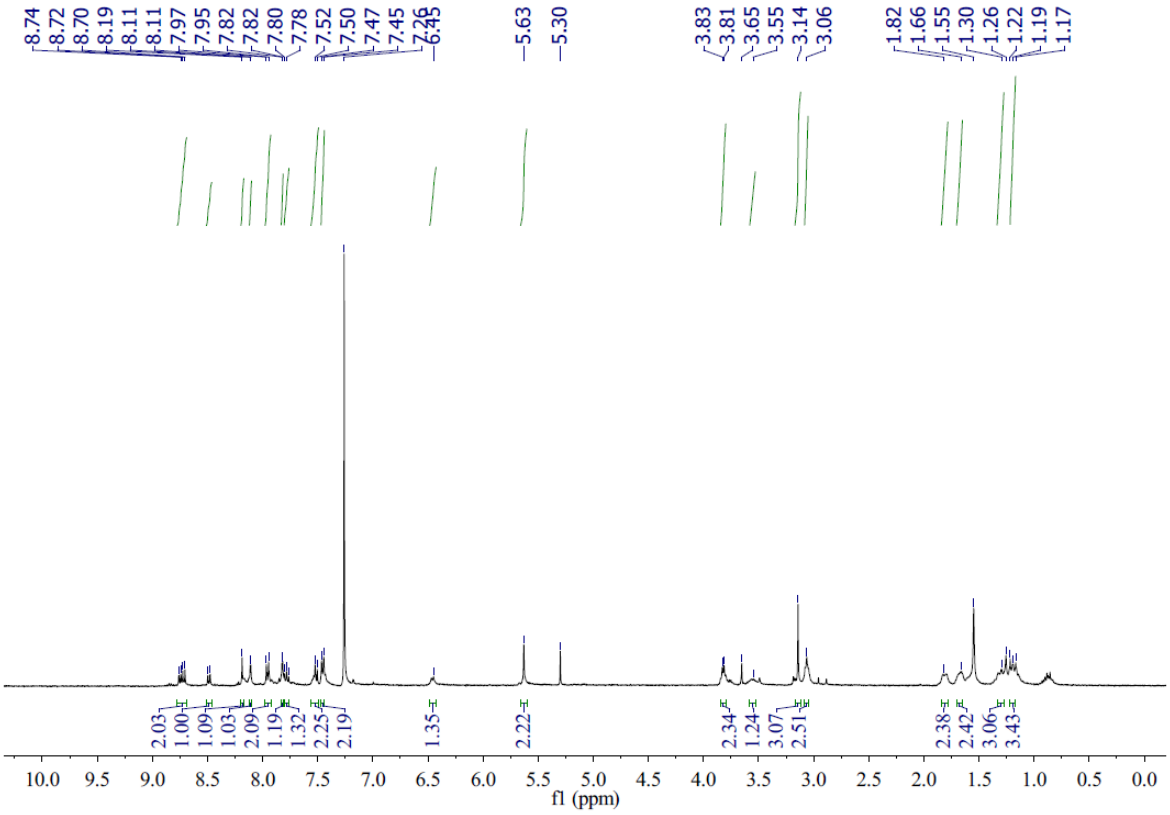
8.74
8.72
8.70
8.19
8.11
8.11
7.97
7.95
7.82
7.82
7.80
7.78
7.52
7.50
7.47
7.45
6.45
5.63
5.30
3.83
3.81
3.65
3.55
3.14
3.06
1.82
1.66
1.55
1.30
1.26
1.22
1.19
1.17
2.03
1.00
1.09
1.03
2.09
1.19
1.32
2.25
2.19
1.35
2.22
2.34
1.24
3.07
2.51
2.38
2.42
3.06
3.43
10.0 9.5 9.0 8.5 8.0 7.5 7.0 6.5 6.0 5.5 5.0 4.5 4.0 3.5 3.0 2.5 2.0 1.5 1.0 0.5 0.0
f1 (ppm)

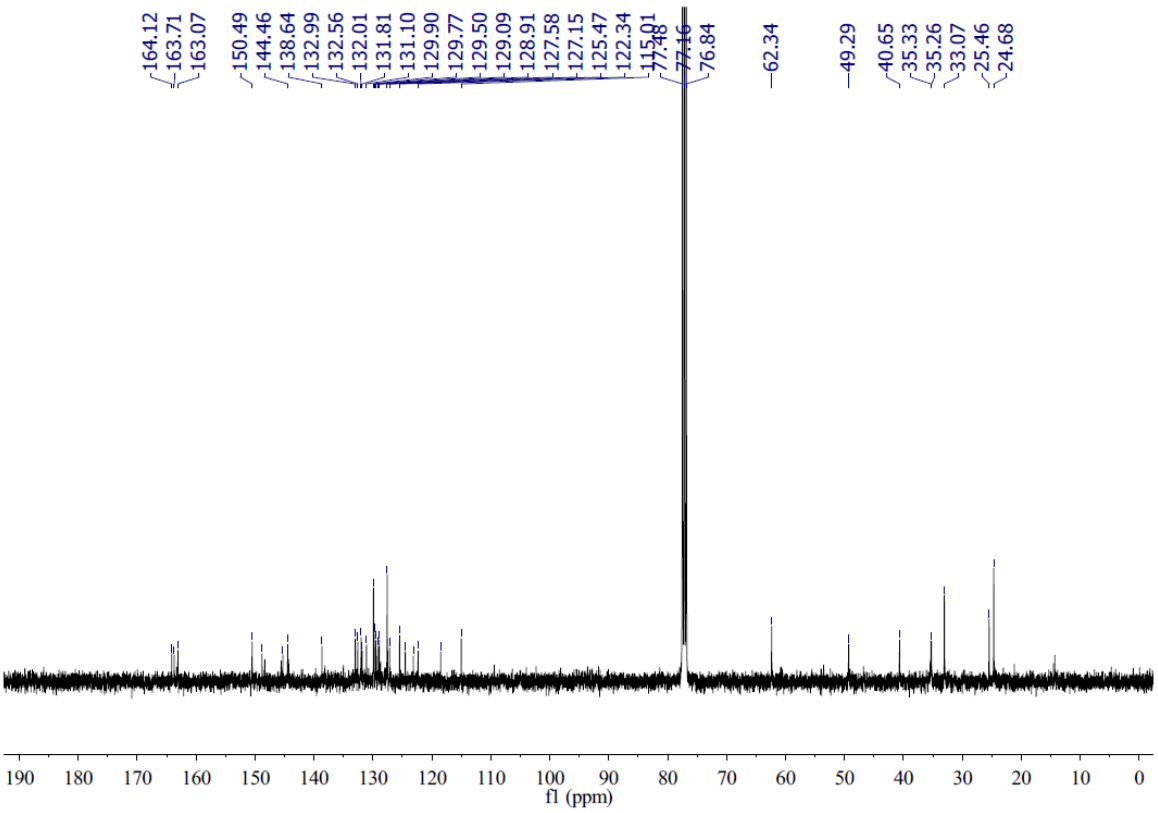
164.12
163.71
163.07
150.49
144.46
138.64
132.99
132.56
132.01
131.81
131.10
129.90
129.77
129.50
129.09
128.91
127.58
127.15
125.47
122.34
77.16
76.84
62.34
49.29
40.65
35.33
35.26
33.07
25.46
24.68
190 180 170 160 150 140 130 120 110 100 90 80 70 60 50 40 30 20 10 0
f1 (ppm)

6-Azido-1*H*,3*H*-benzo[*de*]isochromene-1,3-dione (**58**)

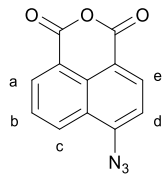

To the solution of 4-bromo-1,8-naphthalic anhydride (500 mg, 1.80 mmol) in DMF (5.0 mL), NaN_3 (175 mg, 2.69 mmol) was added and the mixture was stirred at room temperature for 12 h. After the reaction complete judged by TLC, water (30 mL) was added and the precipitate was collected by filtration, then washed with water (50 mL), dried *under vacuum* to obtain **58** (418 mg, 97 %) as a pale-yellow solid. ^{1}H NMR (400 MHz, $CDCl_3$) δ 8.67 (dd, 1H, *J* = 7.3, 1.1, H_a), 8.62 (d, 1H, *J* = 8.0, H_e), 8.55 (dd, 1H, *J* = 8.5, 1.1, H_c), 7.82 (dd, 1H, *J* = 8.5, 7.3, H_b), 7.53 (d, 1H, *J* = 8.0, H_d). ^{13}C NMR (101 MHz, $CDCl_3$) δ 160.5, 160.0, 145.2, 134.4, 134.0, 131.4, 130.4, 127.3, 124.6, 118.9, 115.1, 114.6. All other spectroscopic data were consistent with those previously reported.[147]

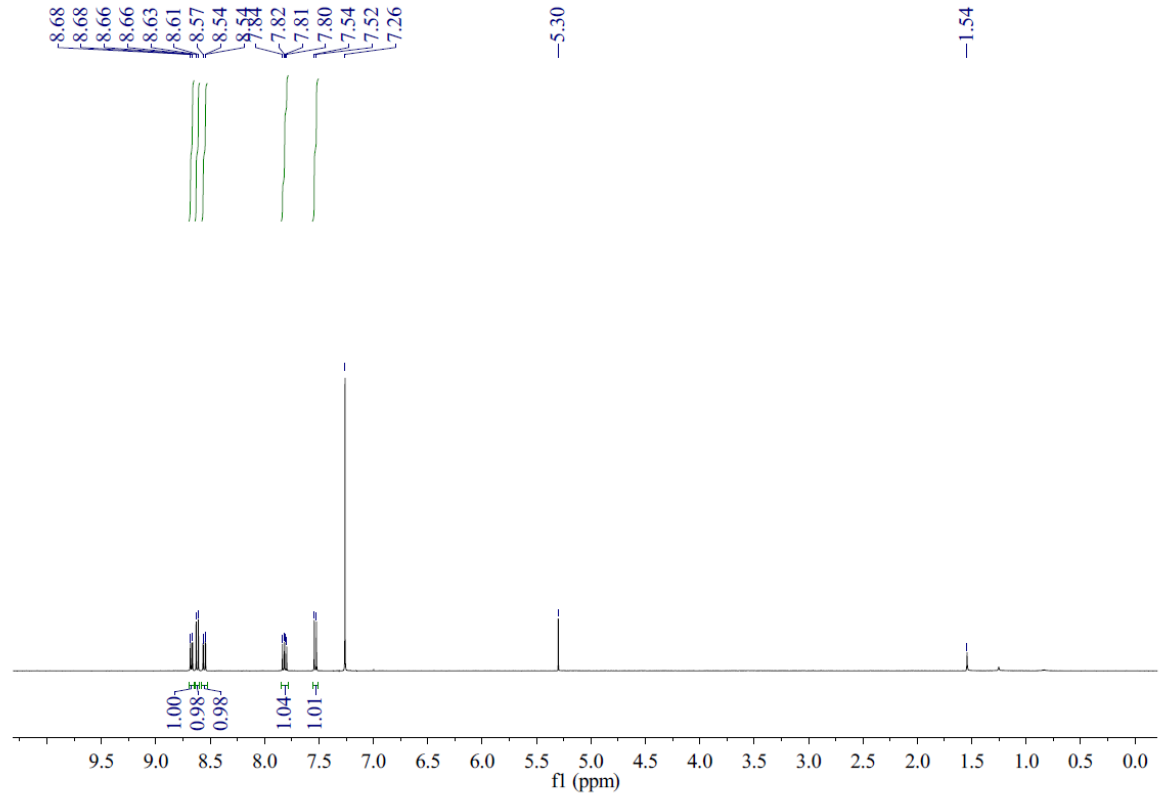
8.68
8.68
8.66
8.66
8.63
8.61
8.57
8.54
7.84
7.82
7.81
7.80
7.54
7.52
7.26
5.30
1.54
1.00
0.98
0.98
1.04
1.01
9.5 9.0 8.5 8.0 7.5 7.0 6.5 6.0 5.5 5.0 4.5 4.0 3.5 3.0 2.5 2.0 1.5 1.0 0.5 0.0
f1 (ppm)

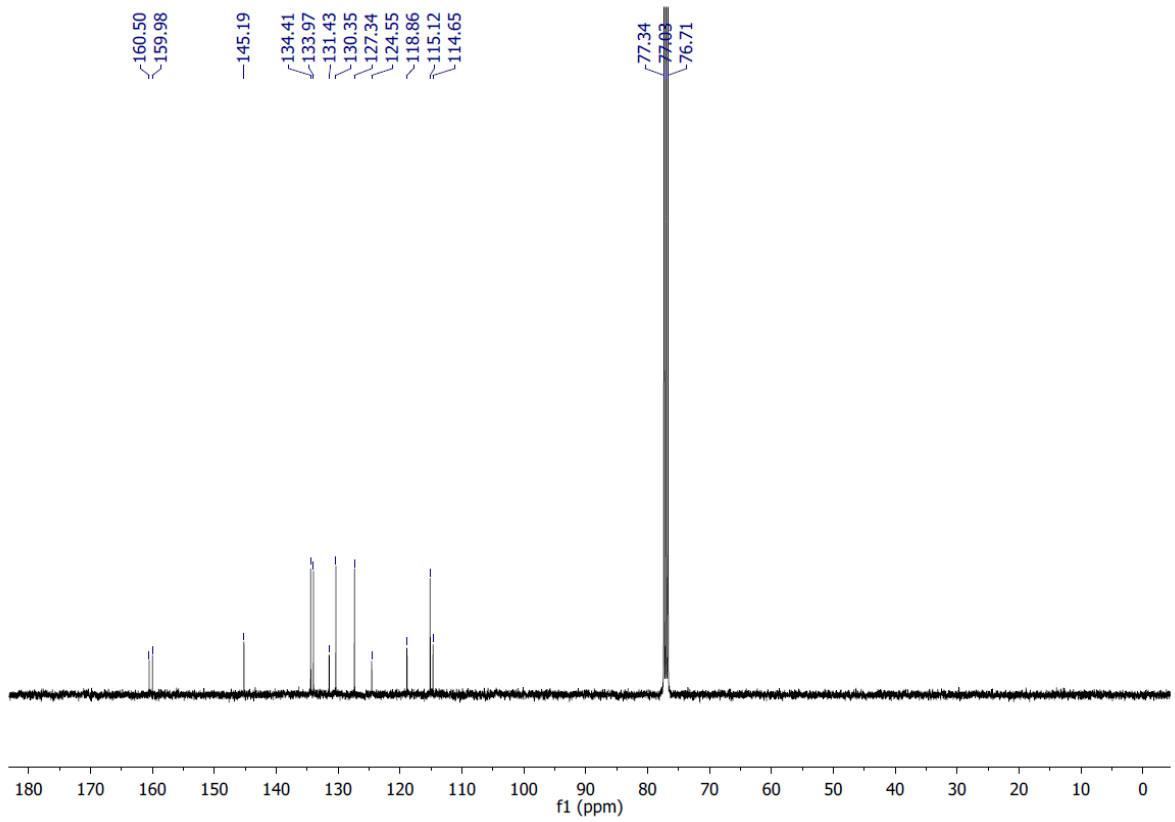
160.50
159.98
145.19
134.41
133.97
131.43
130.35
127.34
124.55
118.86
115.12
114.65
77.34
77.03
76.71
180 170 160 150 140 130 120 110 100 90 80 70 60 50 40 30 20 10 0
f1 (ppm)

6-(4-((bis(pyridin-2-ylmethyl)amino)methyl)-1*H*-1,2,3-triazol-1-yl)-2-(prop-2-yn-1-yl)-1*H*-benzo[*de*]isoquinoline-1,3(2*H*)-dione (**59**)

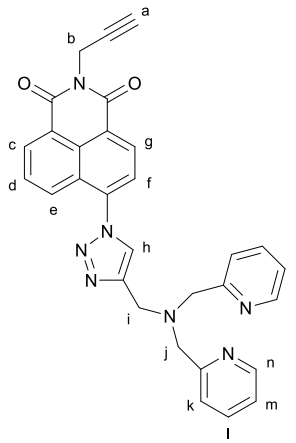

Under nitrogen atmosphere, the azide **58** (23.9 mg, 0.100 mmol), alkyne **54** (23.7 mg, 0.100 mmol), and tetrakis(acetonitrile)copper(I) hexafluorophosphate (10.0 mg, 0.030 mmol), was added in the mixture of NMP (1.0 mL) and EtOH (1.0 mL). The reaction mixture was stirred at room temperature for 24 h, after the starting material finished judged by TLC, the propargylamide (9 µL, 0.140 mmol) was added and the mixture was stirred at room temperature for overnight. After the reaction complete, the saturated EDTA in 10% $NH_3 \cdot H_2O$ (5.0 mL) was added and the precipitate was collected by filtration. The crude product was purified by column chromatography on silica gel (eluent DCM: MeOH = 20:1) to give **59** (24 mg, 47%, M.p. 182-185 °C) as a brown solid. ^{1}H NMR (400 MHz, $CDCl_3$) δ 8.79-8.73 (m, 2H, $H_{c,g}$), 8.57 (d, 2H, J = 4.2, H_n), 8.32 (dd, 1H, J = 8.6, 0.9, H_e), 8.17 (s, 1H, H_h), 7.88-7.82 (m, 2H, $H_{d,f}$), 7.72-7.66 (m, 2H, H_l), 7.63-7.57 (m, 2H, H_k), 7.21-7.15 (m, 2H, H_m), 5.00 (d, 2H, J = 2.4, H_b), 4.09 (s, 2H, H_i), 3.97 (s, 4H, H_j), 2.23 (t, 1H, J = 2.4, H_a). ^{13}C NMR (101 MHz, $CDCl_3$) δ 163.0, 162.5, 159.0, 149.3, 145.1, 138.8, 136.8, 135.8, 132.7, 131.2, 130.3, 129.3, 128.7, 126.6, 125.8, 123.6, 123.5, 122.7, 122.4, 78.3, 71.0, 59.9, 48.6, 29.8. IR: (υ_{max}/cm^{-1}) 1744, 1707, 1665, 1581, 1483, 1378, 1232, 1040, 845, 782, 754. HR-NSI MS (*m/z*) $[M+Na]^+$ calcd for $C_{30}H_{23}N_7O_2Na$ 536.1805, found 536.1796.

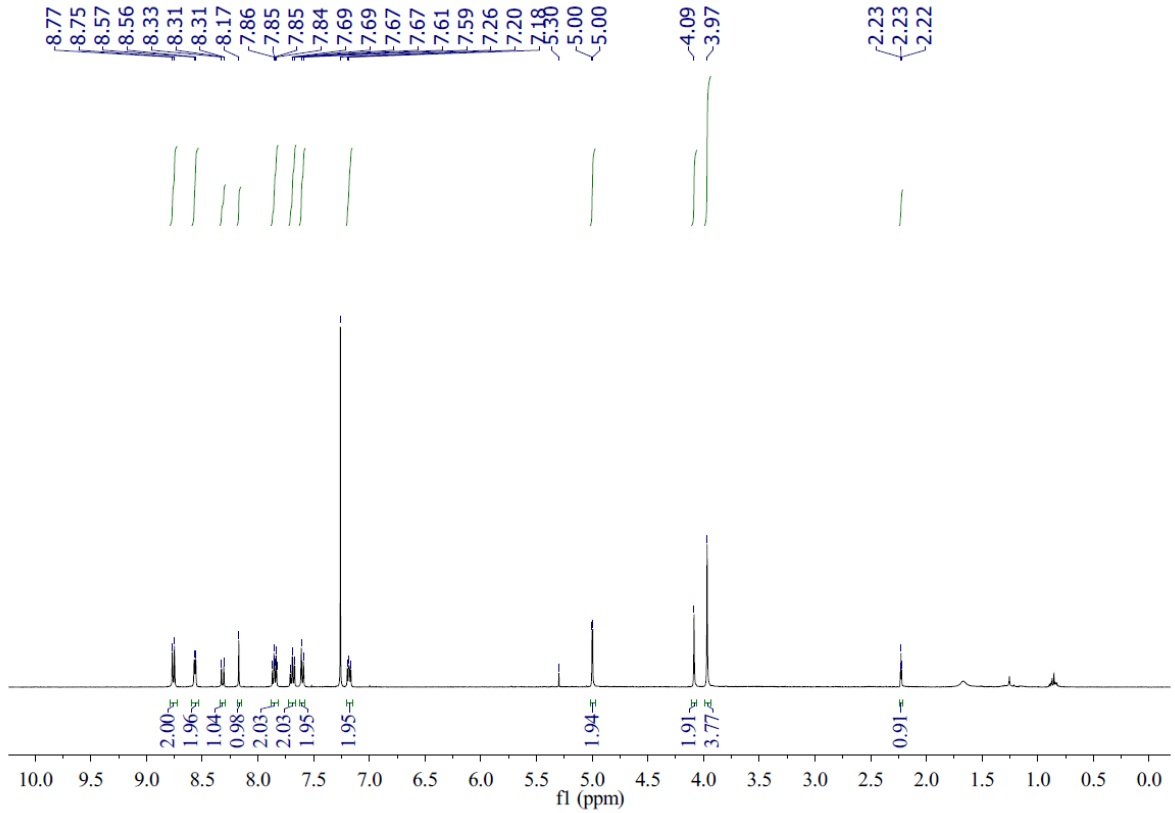
8.77
8.75
8.57
8.56
8.33
8.31
8.31
8.17
7.86
7.85
7.85
7.84
7.69
7.69
7.67
7.67
7.61
7.59
7.26
7.20
5.30
5.00
5.00
4.09
3.97
2.23
2.23
2.22
2.00
1.96
1.04
0.98
2.03
2.03
1.95
1.95
1.94
1.91
3.77
0.91
10.0 9.5 9.0 8.5 8.0 7.5 7.0 6.5 6.0 5.5 5.0 4.5 4.0 3.5 3.0 2.5 2.0 1.5 1.0 0.5 0.0
f1 (ppm)

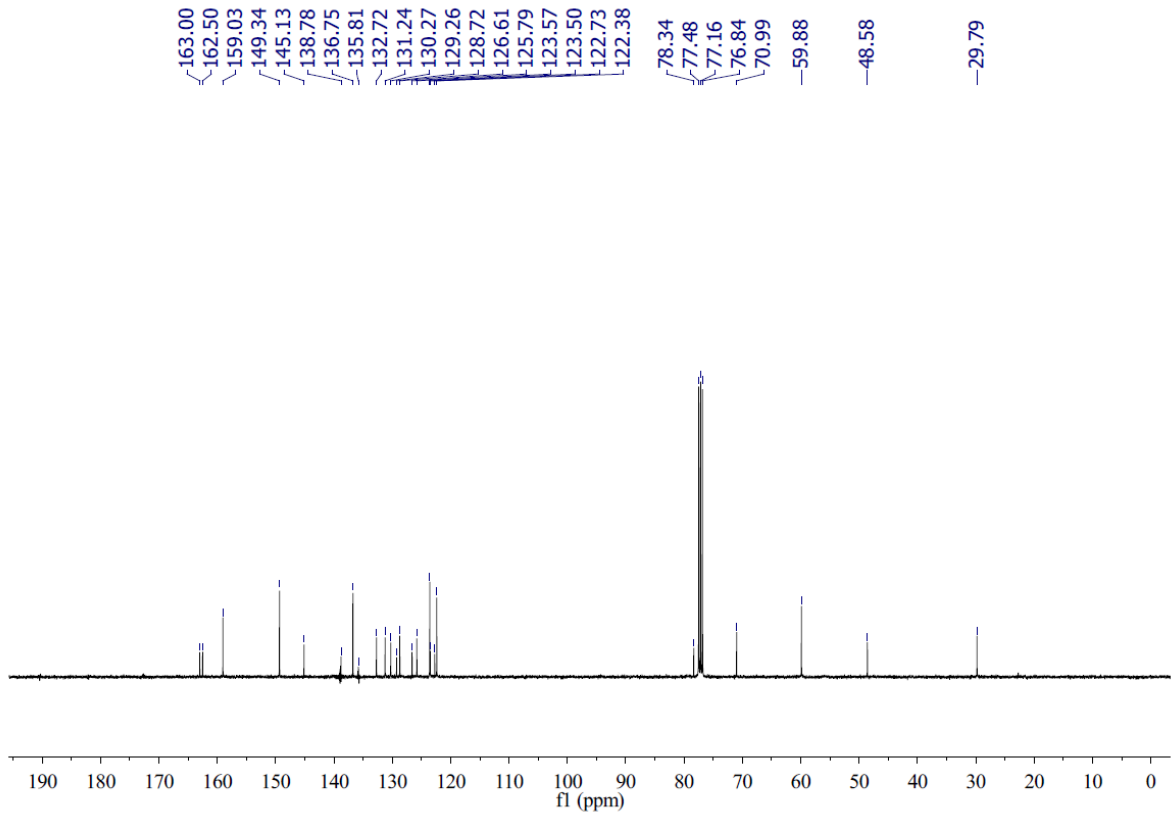
163.00
162.50
159.03
149.34
145.13
138.78
136.75
135.81
132.72
131.24
130.27
129.26
128.72
126.61
125.79
123.57
123.50
122.73
122.38
78.34
77.48
77.16
76.84
70.99
59.88
48.58
29.79
190 180 170 160 150 140 130 120 110 100 90 80 70 60 50 40 30 20 10 0
f1 (ppm)

tert-Butyl (4-sulfamoylphenethyl) carbamate (**60**)

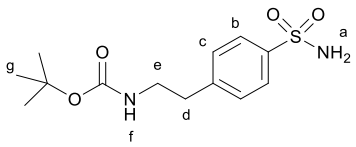

4-(2-Aminoethyl) benzenesulphonamide (0.40 g, 2.0 mmol) was dissolved in CH_2Cl_2 (5.0 mL) and cooled to 0 °C in an ice bath. Di-*tert*-butyl decarbonate (0.44 g, 2.0 mmol) was dissolved in CH_2Cl_2 (5.0 mL) and then added to the above solution slowly. After the completion of the addition, the ice bath was removed and the mixture was stirred at room temperature for 6 hours. The solvent was evaporated *in vacuo* and the residue was diluted with water (20 mL) and extracted with CH_2Cl_2 (20 mL × 2). The organic layers were combined and dried over $MgSO_4$, filtered and dried *under vacuum* to give **60** as a white solid (0.58 g, 97%, M.p. 188-189 °C). ^{1}H NMR (400 MHz, DMSO-d_6) δ 7.75 (d, 2H, J = 8.3, H_b), 7.39 (d, 2H, J = 8.3, H_c), 7.30 (s, 2H, H_a), 6.92 (t, 1H, J = 5.2, H_f), 3.22-3.15 (m, 2H, H_e), 2.82-2.76 (m, 2H, H_d), 1.38 (s, 9H, H_g). ^{13}C NMR (101 MHz, DMSO-d_6) δ 155.5, 143.7, 142.0, 129.1, 125.6, 77.6, 41.1, 35.1, 28.2. IR: (υ_{max}/cm^{-1}) 3384, 3333, 3235, 1660, 1524, 1338, 1307, 1280, 1154, 1094, 906, 683. HR-ESI MS (*m/z*) $[M+NH_4]^+$ calcd for $C_{13}H_{24}N_3O_4S$ 318.1482, found 318.1486.

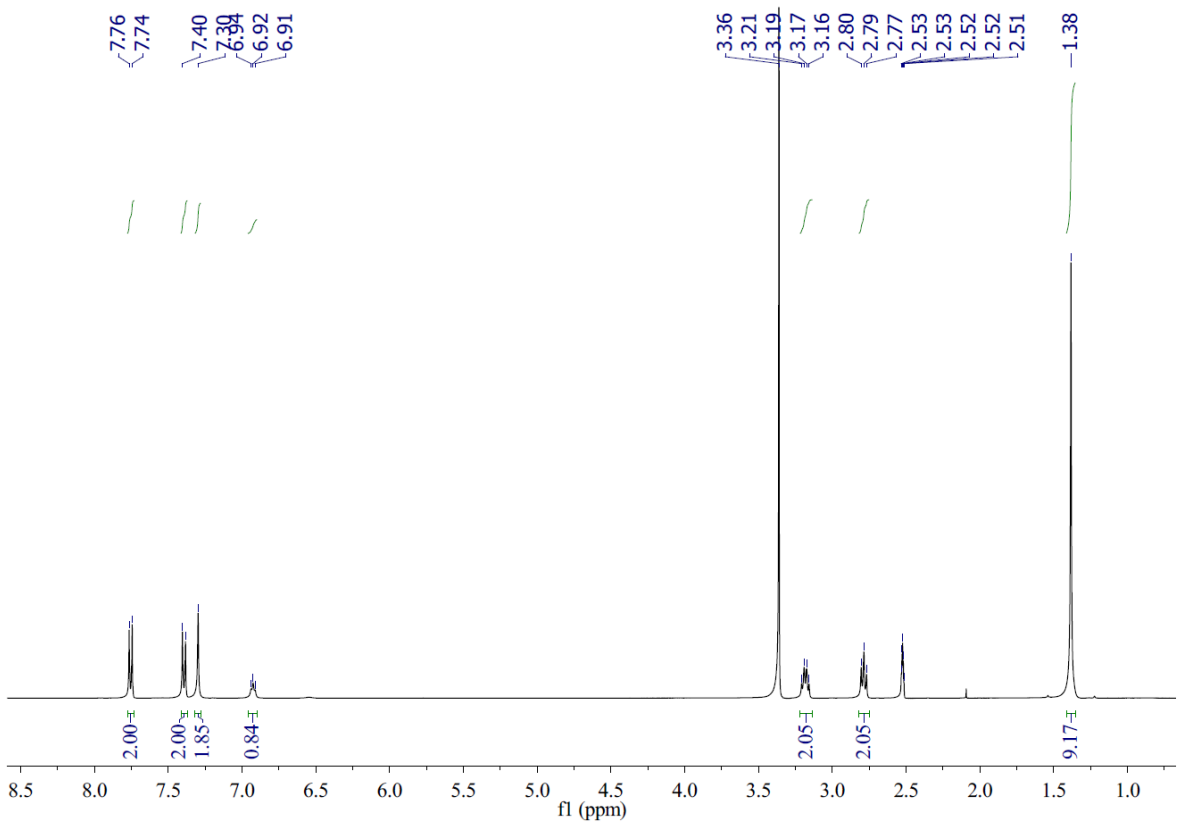
7.76
7.74
7.40
7.30
6.94
6.92
6.91
3.36
3.21
3.19
3.17
3.16
2.80
2.79
2.77
2.53
2.53
2.52
2.52
2.51
1.38
2.00
2.00
1.85
0.84
2.05
2.05
9.17
8.5
8.0
7.5
7.0
6.5
6.0
5.5
5.0
4.5
4.0
3.5
3.0
2.5
2.0
1.5
1.0
f1 (ppm)

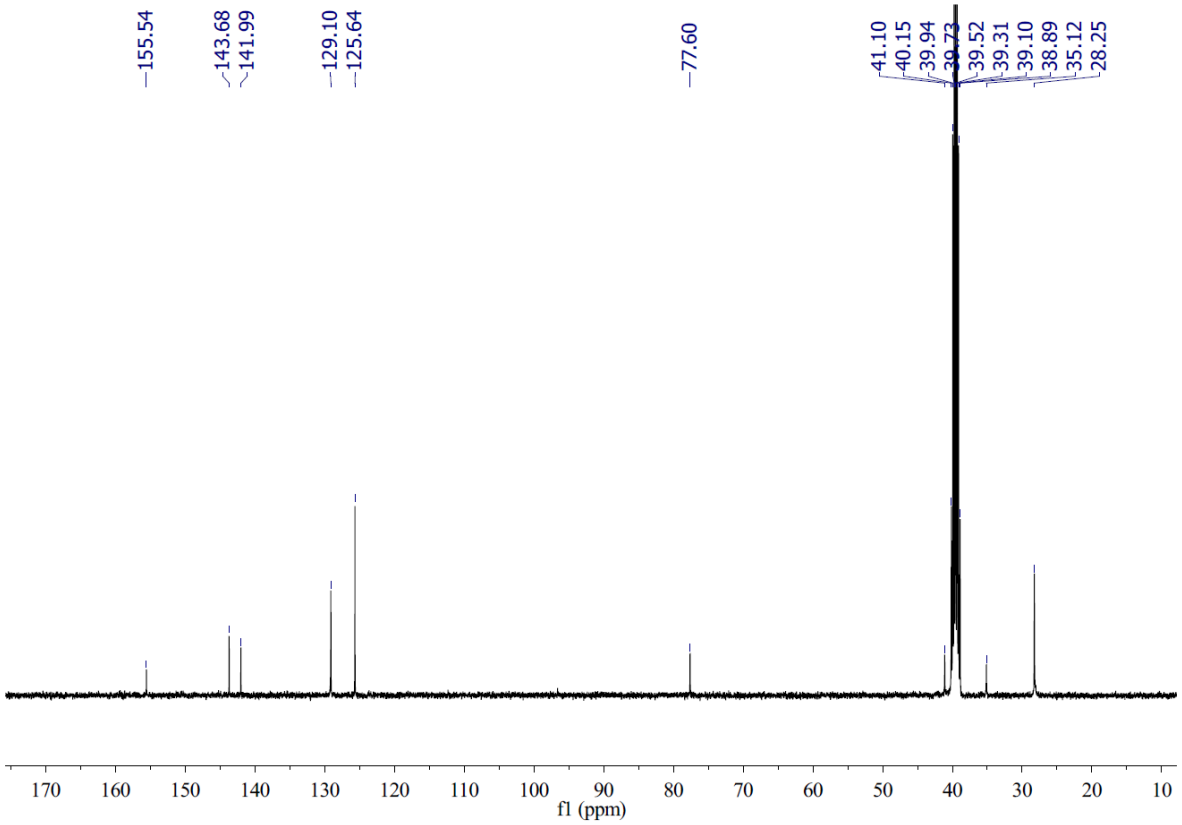
155.54
143.68
141.99
129.10
125.64
77.60
41.10
40.15
39.94
39.73
39.52
39.31
39.10
38.89
35.12
28.25
170
160
150
140
130
120
110
100
90
80
70
60
50
40
30
20
10
f1 (ppm)

tert-Butyl (4-(*N*-(cyclohexylcarbamoyl)sulfamoyl)phenethyl)carbamate **(61)**

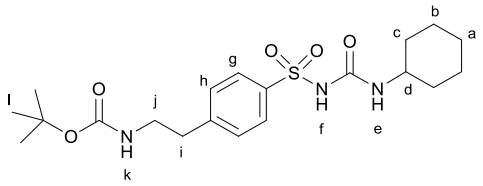

Under a nitrogen atmosphere, **60** (0.15 g, 0.50 mmol) and CuCl (5.0 mg, 0.050 mmol) were dissolved in DMF (2.0 mL), cyclohexyl isocyanate (0.1 mL, 0.75 mmol) was added dropwise and the mixture was stirred for 24 hours at room temperature. The resultant precipitate was filtered off and the filtrate was poured slowly into ice cold water (50 mL). Concentrated HCl (0.1 ml) was added to acidify the resultant mixture and the precipitate was isolated by suction filtration and washed with water (50 mL) to give **61** as a white solid (0.18 g, 84%, M.p. 184-186 °C). ^{1}H NMR (400 MHz, $CDCl_3$) δ 7.95-7.73 (bs, 2H, H_g), 7.42-7.32 (bs, 2H, H_h), 6.56-6.30 (bs, 1H, H_e), 4.66-4.52 (bs, 1H, H_k), 3.66-3.54 (bs, 1H, H_d), 3.43-3.32 (bs, 2H, H_j), 2.96-2.83 (bs, 2H, J = 5.8, H_i), 1.96-1.59 (m, 6H, $H_{a,c}$), 1.43 (s, 9H, H_l), 1.32-1.10 (m, 4H, H_b) ^{13}C NMR (101 MHz, $CDCl_3$) δ 183.4, 155.9, 145.3, 129.6, 127.5, 127.4, 79.5, 49.3, 41.4, 36.1, 33.7, 32.9, 28.4, 25.4, 24.8, 24.6. IR: (υ_{max}/cm^{-1}) 3331, 3271, 2935, 2856, 1690, 1660, 1532, 1435, 1352, 1296, 1250, 1163, 1038, 967, 869, 683. HR-ESI MS (*m/z*) $[M+H]^+$ calcd for $C_{20}H_{32}N_3O_5S$ 426.2057, found 426.2057.

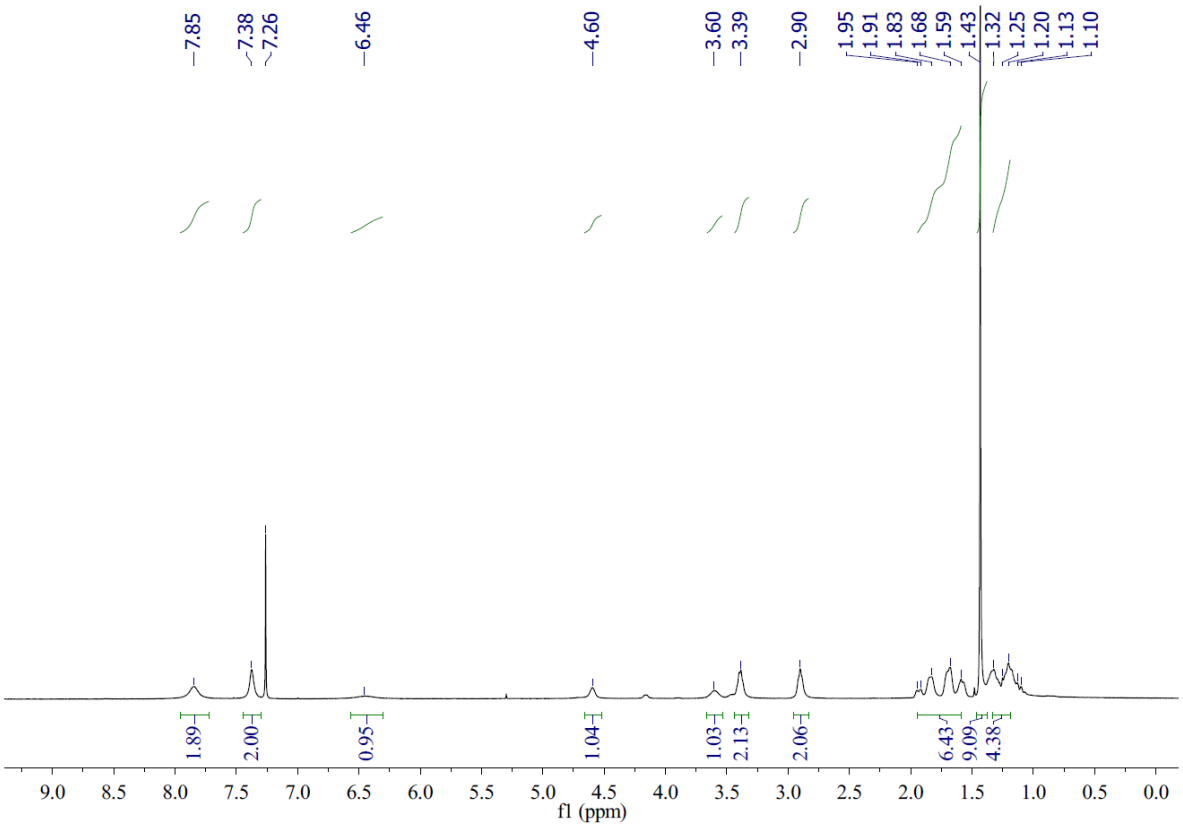
7.85
7.38
7.26
6.46
4.60
3.60
3.39
2.90
1.95
1.91
1.83
1.68
1.59
1.43
1.32
1.25
1.20
1.13
1.10
1.89
2.00
0.95
1.04
1.03
2.13
2.06
6.43
9.09
4.38
9.0 8.5 8.0 7.5 7.0 6.5 6.0 5.5 5.0 4.5 4.0 3.5 3.0 2.5 2.0 1.5 1.0 0.5 0.0
f1 (ppm)

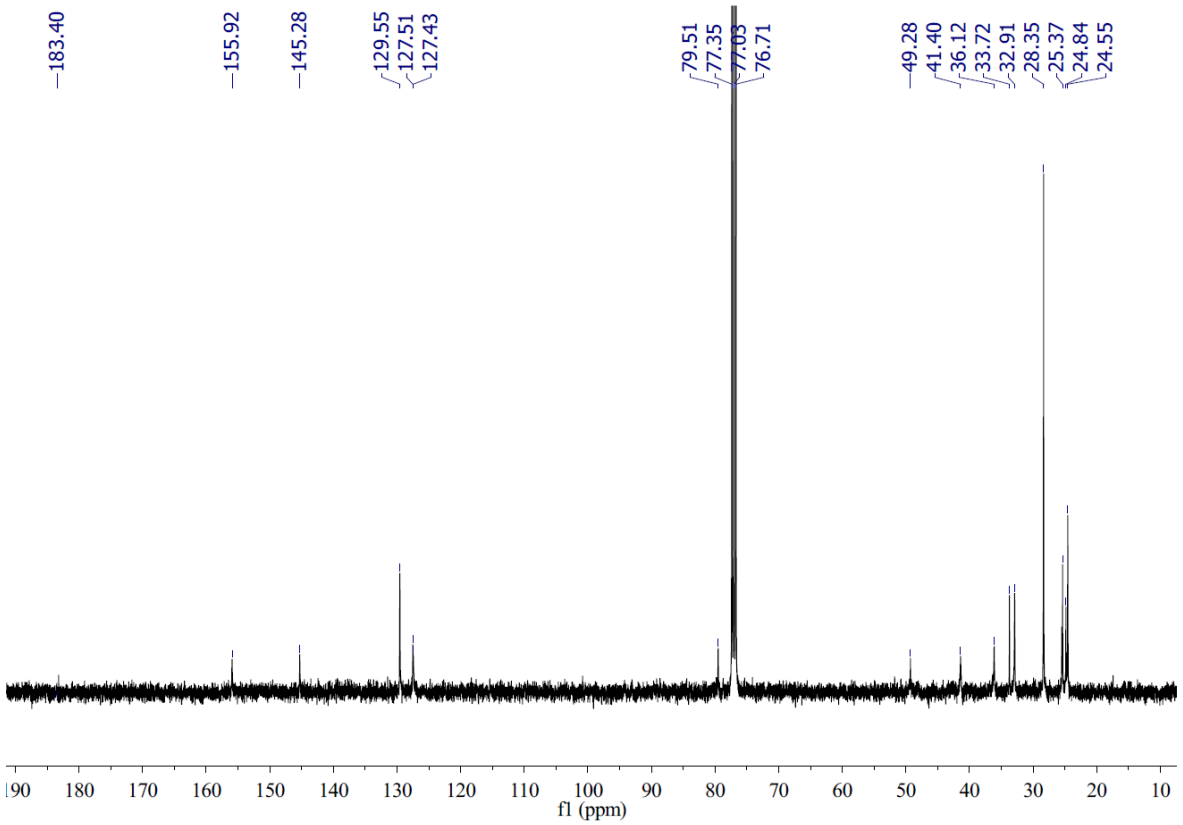
183.40
155.92
145.28
129.55
127.51
127.43
79.51
77.35
77.03
76.71
49.28
41.40
36.12
33.72
32.91
28.35
25.37
24.84
24.55
190 180 170 160 150 140 130 120 110 100 90 80 70 60 50 40 30 20 10
f1 (ppm)

COSY spectrum:

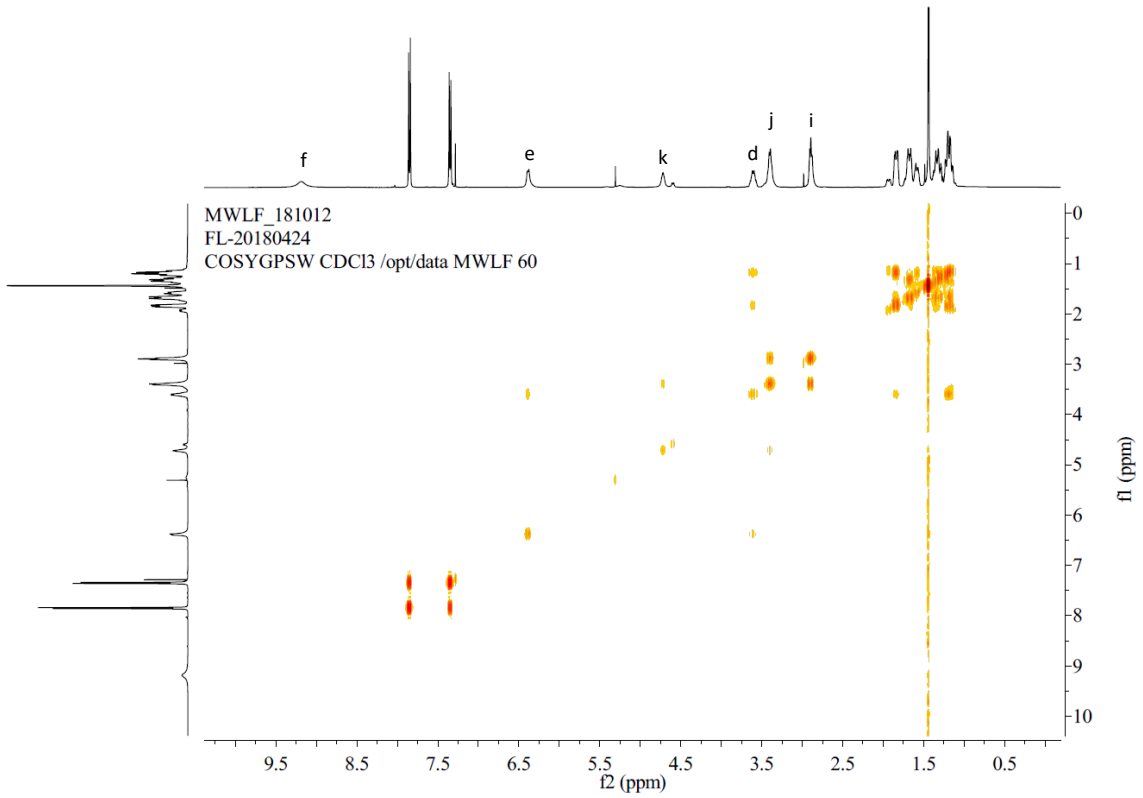

HSQC spectrum:

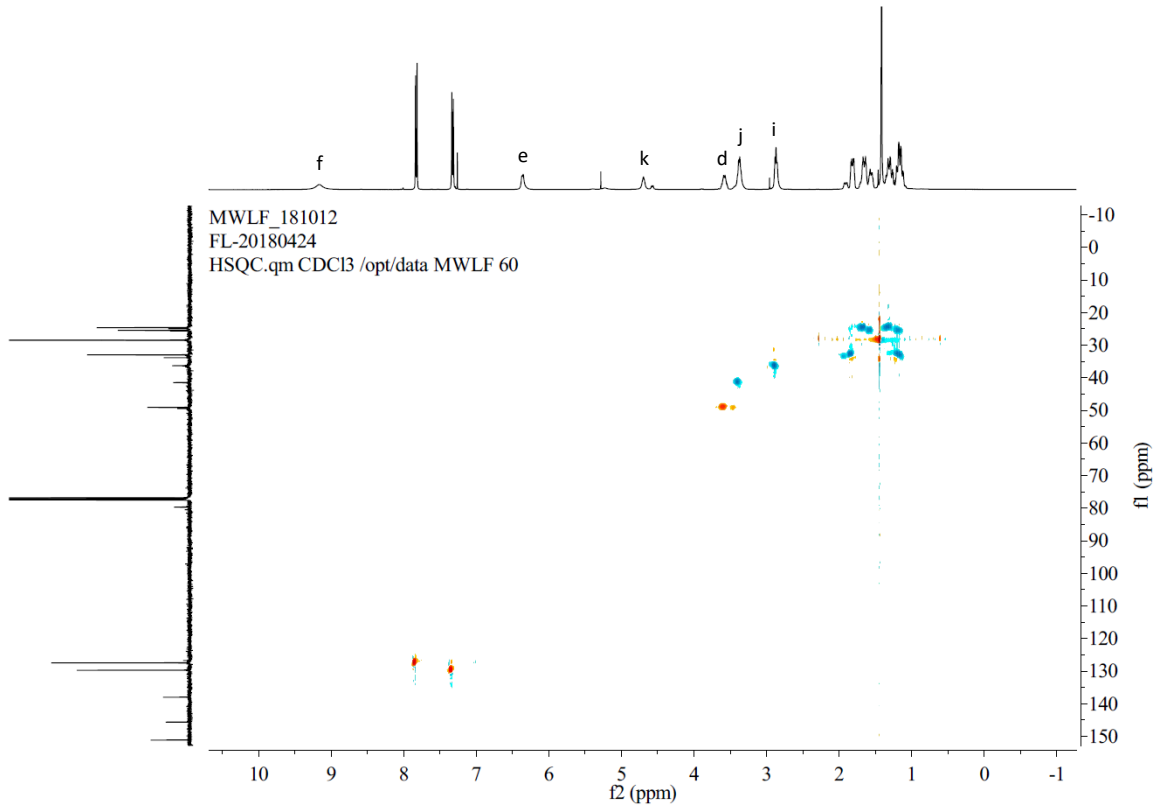

4-(2-Aminoethyl)-*N*-(cyclohexylcarbamoyl)benzenesulfonamide (**62**)

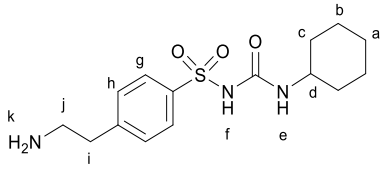

Boc protected **61** (132 mg, 0.310 mmol) was dissolved in DCM (4.0 mL) and trifluoracetic acid (0.4 mL) was added dropwise. The reaction was stirred overnight at room temperature. The solvent was evaporated under reduced pressure and the product was used without purification in the next step. ^{1}H NMR (400 MHz, D_2O) δ 7.95 (d, 2H, J = 8.4, H_g), 7.57 (d, 2H, J = 8.4, H_h), 3.38-3.30 (m, 3H, $H_{j,d}$), 3.17-3.09 (m, 2H, H_i), 1.74-1.51 (m, 6H, $H_{a,c}$), 1.37-1.10 (m, 4H, H_b).

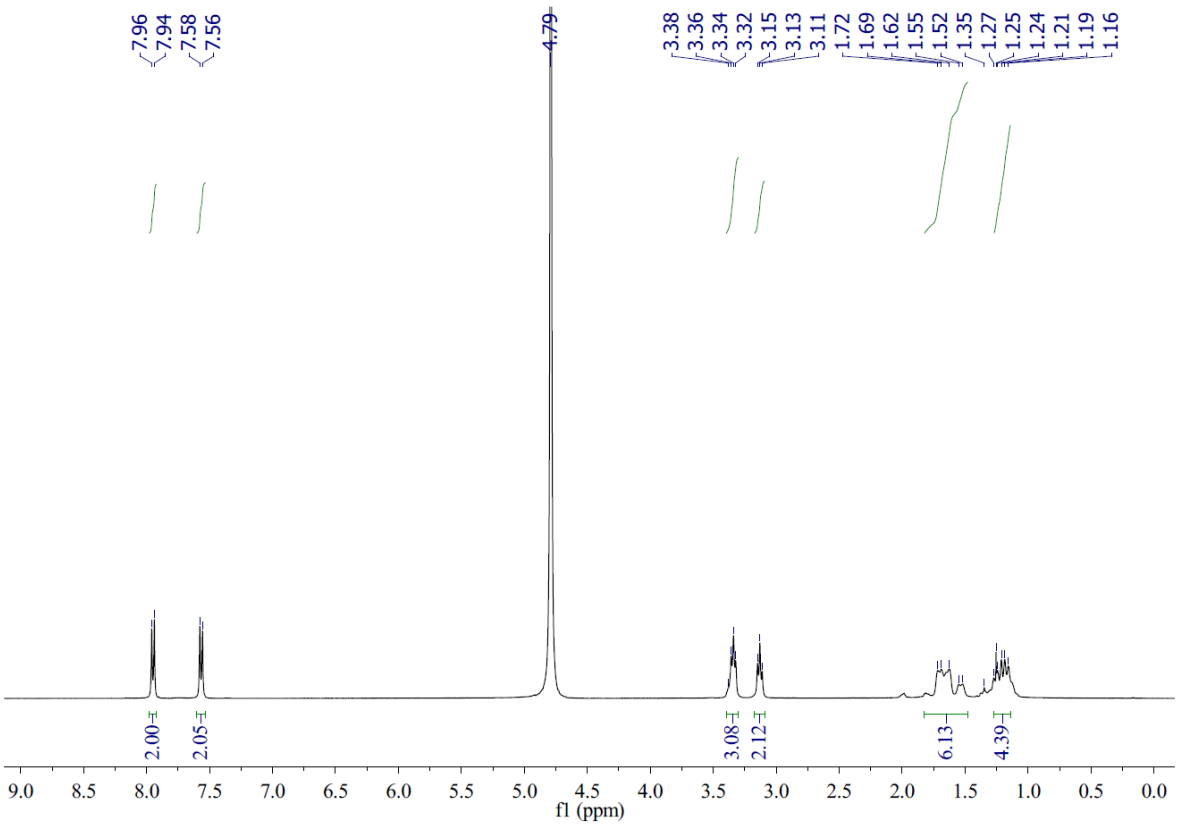
7.96
7.94
7.58
7.56
4.79
3.38
3.36
3.34
3.32
3.15
3.13
3.11
1.72
1.69
1.62
1.55
1.52
1.35
1.27
1.25
1.24
1.21
1.19
1.16
2.00
2.05
3.08
2.12
6.13
4.39
9.0
8.5
8.0
7.5
7.0
6.5
6.0
5.5
5.0
4.5
4.0
3.5
3.0
2.5
2.0
1.5
1.0
0.5
0.0
f1 (ppm)

4-(2-(6-Bromo-1,3-dioxo-1*H*-benzo[*de*]isoquinolin-2(3*H*)-yl)ethyl)-*N*-(cyclohexylcarbamoyl)benzenesulfonamide (**63**)

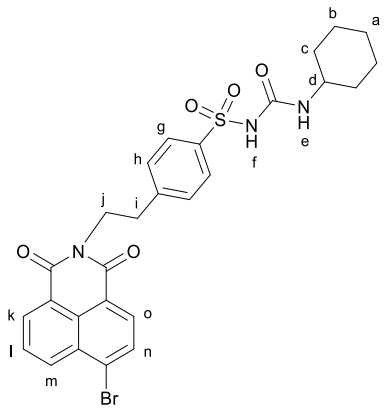

After de-protection, the product **62** was dissolved in ethanol (2.0 mL), then Na_2CO_3 (65.7 mg, 0.620 mmol) was added to the above solution. 4-Bromo-1,8-naphthalic anhydride (85.9 mg, 0.310 mmol) was added and the mixture was refluxed for 6 hours. After the reaction complete, the solvent was evaporated *in vacuo* and the residue was washed with water (30 mL). The precipitate was collected by filtration and dried *in vacuo* to obtain **63** (149 mg, 82%, M.p. 264-268 °C) as a white solid. ^{1}H NMR (400 MHz, DMSO-d_6) δ 8.61-8.53 (m, 2H, $H_{k,m}$), 8.35 (d, 1H, J = 7.9, H_o), 8.23 (d, 1H, J = 7.9, H_n), 8.05-7.97 (m, 1H, H_l), 7.65 (d, 2H, J = 7.9, H_g), 7.25 (d, 2H, J = 7.9, H_h), 5.70-5.58 (bs, 1H, H_e), 4.29-4.18 (m, 2H, H_j), 3.27-3.14 (bs, 1H, H_d), 2.99-2.88 (m, 2H, H_i), 1.72-1.47 (m, 6H, $H_{a,c}$), 1.20-0.99 (m, 4H, H_b). ^{13}C NMR (101 MHz, DMSO-d_6) δ 162.6, 132.6, 131.5, 131.3, 130.9, 129.6, 129.2, 128.7, 128.5, 128.1, 127.8, 127.1, 127.0, 122.5, 121.7, 48.6, 40.9, 33.2, 32.8, 25.2, 24.6. IR: (υ_{max}/cm^{-1}) 3378, 2929, 2854, 1700, 1653, 1590, 1344, 1254, 1231, 1122, 1086, 1007, 880, 779, 655. HR-ESI MS (*m/z*) $[M+H]^+$ calcd for $C_{27}H_{26}BrN_3O_5S$ 584.0849, found 584.0846.

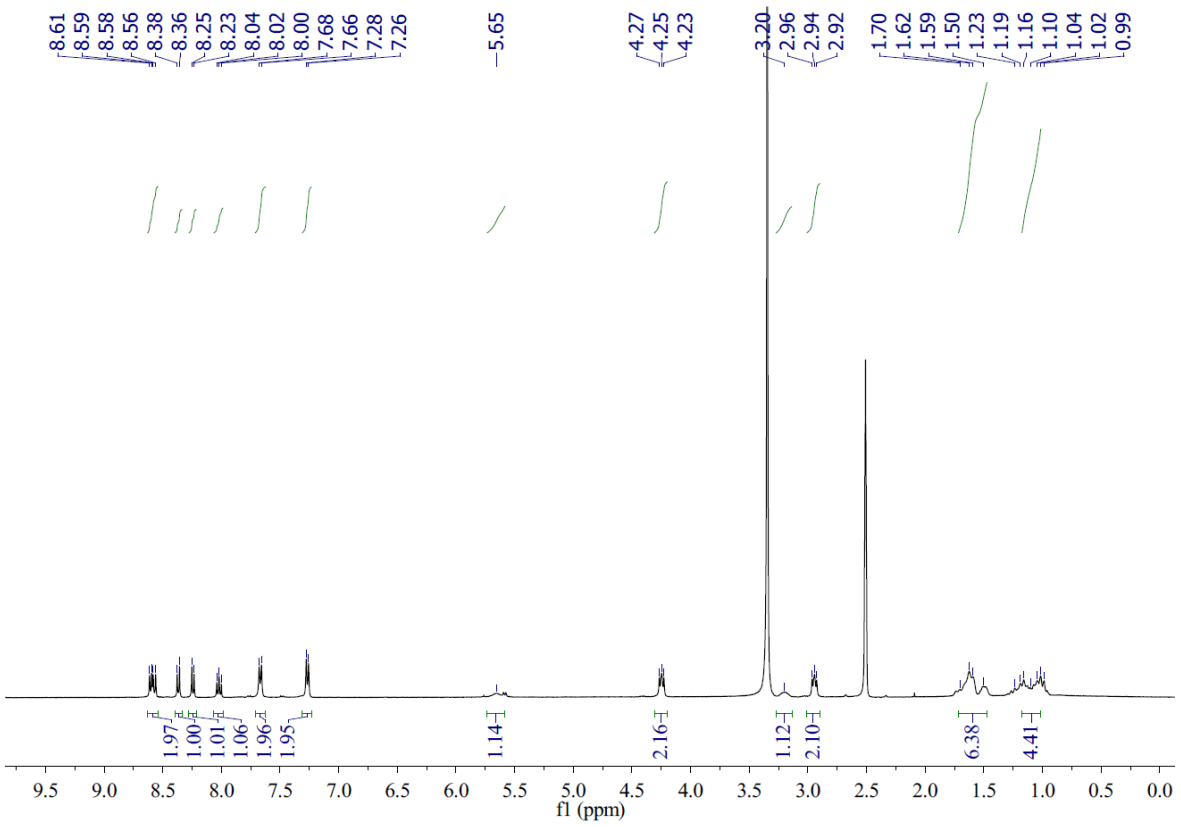
8.61
8.59
8.58
8.56
8.38
8.36
8.25
8.23
8.04
8.02
8.00
7.68
7.66
7.28
7.26
5.65
4.27
4.25
4.23
3.20
2.96
2.94
2.92
1.70
1.62
1.59
1.50
1.23
1.19
1.16
1.10
1.04
1.02
0.99
1.97
1.00
1.01
1.06
1.96
1.95
1.14
2.16
1.12
2.10
6.38
4.41
9.5 9.0 8.5 8.0 7.5 7.0 6.5 6.0 5.5 5.0 4.5 4.0 3.5 3.0 2.5 2.0 1.5 1.0 0.5 0.0
f1 (ppm)

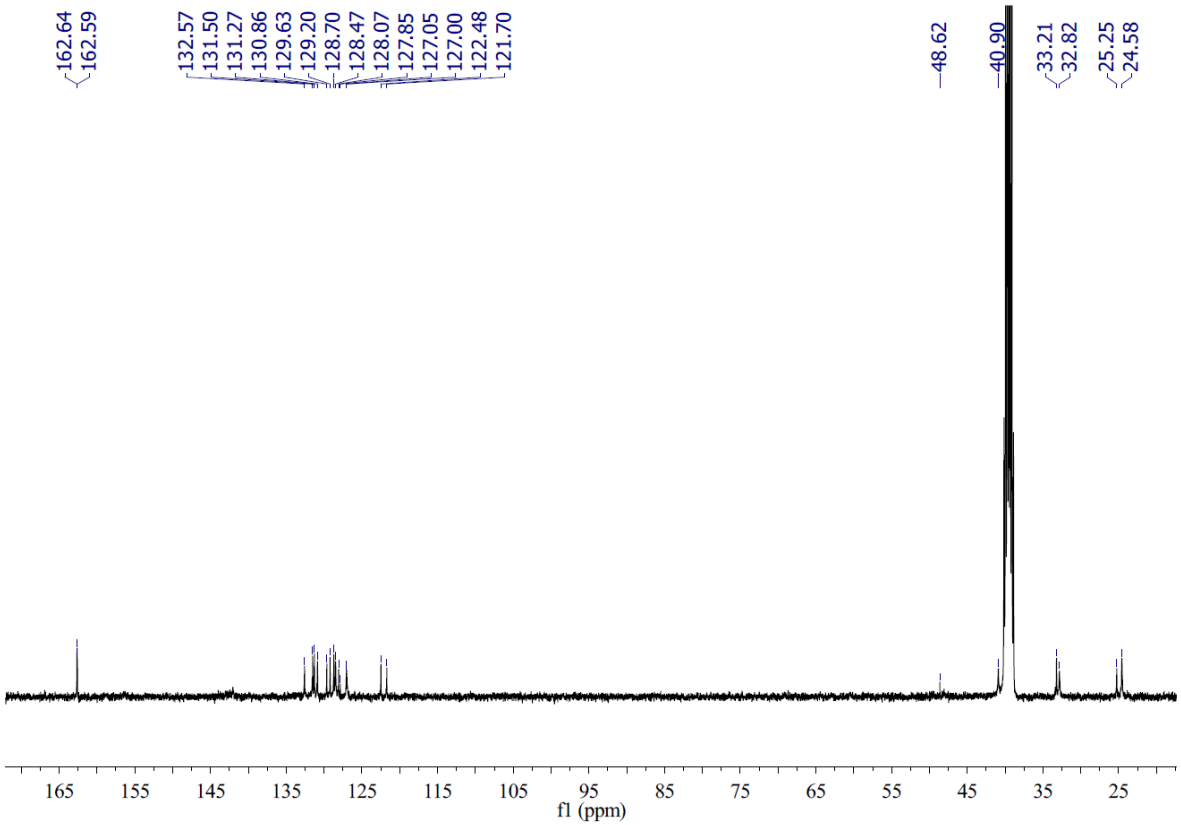
162.64
162.59
132.57
131.50
131.27
130.86
129.63
129.20
128.70
128.47
128.07
127.85
127.05
127.00
122.48
121.70
48.62
40.90
33.21
32.82
25.25
24.58
165 155 145 135 125 115 105 95 85 75 65 55 45 35 25
f1 (ppm)

4-(2-(6-Azido-1,3-dioxo-1*H*-benzo[*de*]isoquinolin-2(3*H*)-yl)ethyl)-*N*-(cyclohexylcarbamoyl)benzenesulfonamide (**64**)

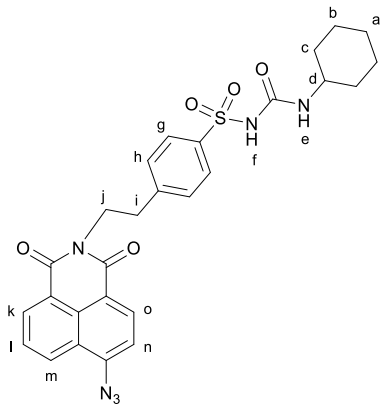

The compound **63** (148 mg, 0.253 mmol) was dissolved in DMF (2.0 mL) and NaN_3 (25 mg, 0.385 mol) was added to the solution. The mixture was stirred for 24 hours under room temperature. The reaction mixture was poured to water (20 mL) and the precipitate was collected by filtration and dried *in vacuo* to obtain **64** (94.0 mg, 68%, M.p. 200-204 °C) as a yellow solid. ^{1}H NMR (400 MHz, DMSO-d_6) δ 8.51 (d, 1H, *J* = 7.3, H_k), 8.46 (d, 1H, *J* = 7.9, H_o), 8.42 (d, 1H, *J* = 8.5, H_m), 7.90- 7.83 (m, 1H, H_l), 7.80 (d, 2H, *J* = 7.9, H_g), 7.74 (d, 1H, *J* = 7.9, H_n), 7.48 (d, 2H, *J* = 7.9, H_h), 6.34-6.26 (bs, 1H, H_e), 4.31-4.21 (m, 2H, H_j), 3.06-2.95 (m, 2H, H_i), 1.68-1.46 (m, 6H, $H_{a,c}$), 1.21-1.06 (m, 4H, H_b). ^{13}C NMR (101 MHz, DMSO-d_6) δ 162.8(d), 156.6, 150.8, 144.3, 142.8, 138.7, 131.6, 129.2, 128.4, 128.2, 127.5, 127.2, 123.4, 121.9, 117.9, 115.9, 48.1, 40.5, 33.4, 32.3, 25.4, 25.0, 24.5, 24.2. IR: (υ_{max}/cm^{-1}) 3299, 2930, 2854, 2123, 1738, 1651, 1591, 1533, 1437, 1353, 1229, 1129, 1087, 843, 780, 690. HR-ESI MS (*m/z*) $[M+H]^+$ calcd for $C_{27}H_{26}N_6O_5S$ 547.1758, found 547.1753.

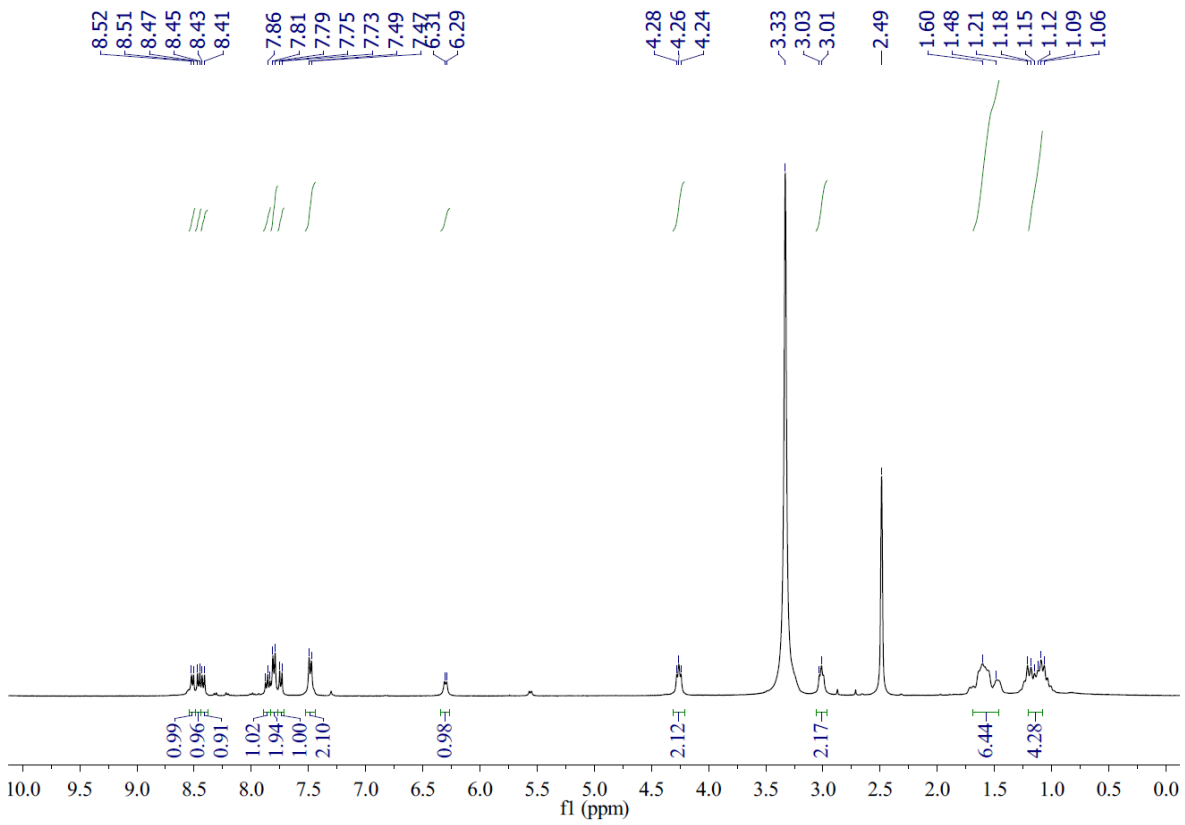
8.52
8.51
8.47
8.45
8.43
8.41
7.86
7.81
7.79
7.75
7.73
7.49
7.47
6.31
6.29
4.28
4.26
4.24
3.33
3.03
3.01
2.49
1.60
1.48
1.21
1.18
1.15
1.12
1.09
1.06
0.99
0.96
0.91
1.02
1.94
1.00
2.10
0.98
2.12
2.17
6.44
4.28
10.0 9.5 9.0 8.5 8.0 7.5 7.0 6.5 6.0 5.5 5.0 4.5 4.0 3.5 3.0 2.5 2.0 1.5 1.0 0.5 0.0
f1 (ppm)

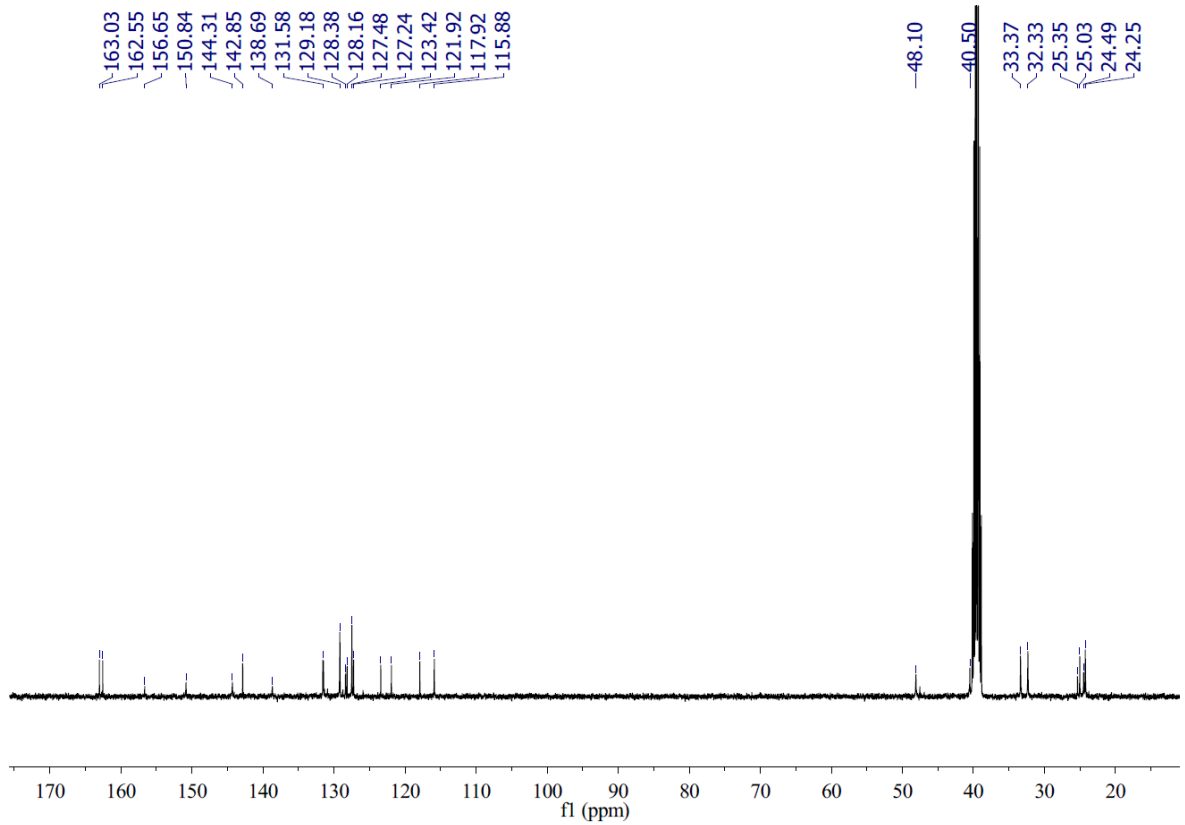
163.03
162.55
156.65
150.84
144.31
142.85
138.69
131.58
129.18
128.38
128.16
127.48
127.24
123.42
121.92
117.92
115.88
48.10
40.50
33.37
32.33
25.35
25.03
24.49
24.25
170 160 150 140 130 120 110 100 90 80 70 60 50 40 30 20
f1 (ppm)

4-(2-(6-(4-((bis(Pyridin-2-ylmethyl)amino)methyl)-1*H*-1,2,3-triazol-1-yl)-1,3-dioxo-1*H*-benzo[*de*]isoquinolin-2(3*H*)-yl)ethyl)-*N*-(cyclohexylcarbamoyl)benzenesulfonamide (**65**)

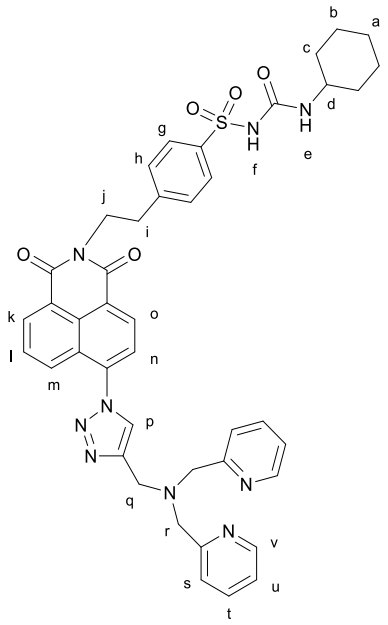

Under an atmosphere of nitrogen, **64** (76.0 mg, 0.150 mmol) and **54** (35.6 mg, 0.150 mmol) were dissolved in NMP (2.0 mL) and tetrakis(acetonitrile)copper(I) hexafluorophosphate (11.2 mg, 0.030 mmol) was added. The mixture was stirred at room temperature for 24 hours. After the reaction finished, saturated EDTA in 17% NH_3:H_2O (20 mL) was poured to the mixture and the precipitate was collected by filtration, and washed with water (30 mL). This crude product was purified by flash chromatography (eluent: DCM/MeOH 20:1) to give **65** as a brown solid (96 mg, 82%, M.p. 148-151 °C). ^{1}H NMR (400 MHz, $CDCl_3$) δ 8.72-8.66 (m, 2H, $H_{k,o}$), 8.56 (d, 2H, J = 4.3, H_v), 8.31 (d, 1H, J = 8.3, H_m), 8.19 (s, 1H, H_p), 7.90-7.82 (m, 4H, $H_{l,n,g}$), 7.69 (td, 2H, J = 7.6, 1.7, H_t), 7.62 (d, 2H, J = 7.8, H_h), 7.53 (d, 2H, J = 8.5, H_s), 7.21-7.15 (m, 2H, H_u), 6.48 (s, 1H, H_e), 4.49-4.41 (m, 2H, H_j), 4.09 (s, 2H, H_q), 3.97 (s, 4H, H_r), 3.58 (bs, 1H, H_d), 3.20-3.10 (m, 2H, H_i), 1.87-1.55 (m, 6H, $H_{a,c}$), 1.32-1.18 (m, 4H, H_b). ^{13}C NMR (101 MHz, $CDCl_3$) δ 163.6, 163.1, 159.0, 149.2, 145.0, 138.6, 136.8, 132.4, 131.0, 130.2, 130.0, 129.2, 128.7, 127.4, 126.5, 125.9, 123.6, 123.5, 122.7, 122.4, 59.9, 49.2, 48.6, 41.4, 34.2, 33.0, 25.5, 24.7.

IR: (υ_{max}/cm^{-1}) 3288, 2926, 2853, 1699, 1654, 1590, 1534, 1433, 1342, 1230, 1157, 1036, 998, 882, 783, 754, 691. HR-ESI MS (*m/z*) $[M+H]^+$ calcd for $C_{42}H_{42}N_9O_5S$ 784.3024, found 784.3017.

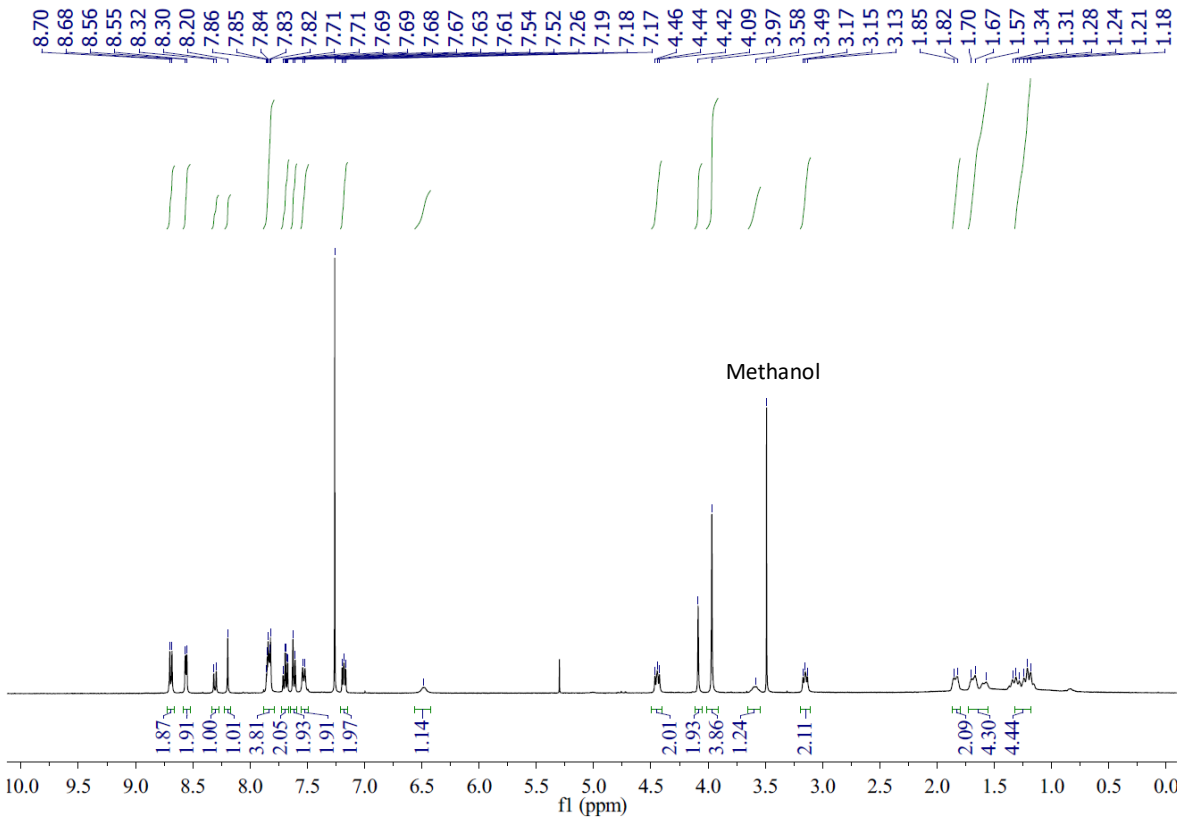
8.70
8.68
8.56
8.55
8.32
8.30
8.20
7.86
7.85
7.84
7.83
7.82
7.71
7.71
7.69
7.69
7.68
7.67
7.63
7.61
7.54
7.52
7.26
7.19
7.18
7.17
4.46
4.44
4.42
4.09
3.97
3.58
3.49
3.17
3.15
3.13
1.85
1.82
1.70
1.67
1.57
1.34
1.31
1.28
1.24
1.21
1.18
Methanol
1.87
1.91
1.00
1.01
3.81
2.05
1.93
1.91
1.97
1.14
2.01
1.93
3.86
1.24
2.11
2.09
4.30
4.44
10.0 9.5 9.0 8.5 8.0 7.5 7.0 6.5 6.0 5.5 5.0 4.5 4.0 3.5 3.0 2.5 2.0 1.5 1.0 0.5 0.0
f1 (ppm)

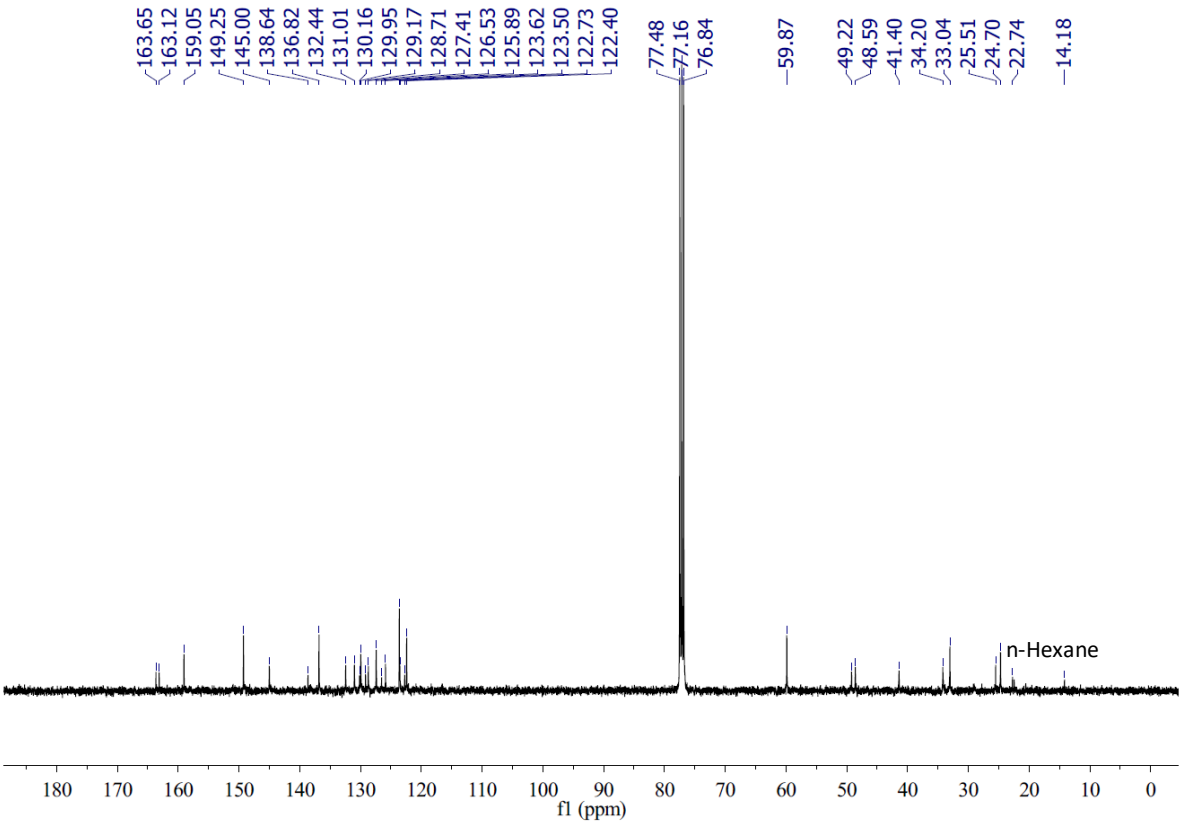
163.65
163.12
159.05
149.25
145.00
138.64
136.82
132.44
131.01
130.16
129.95
129.17
128.71
127.41
126.53
125.89
123.62
123.50
122.73
122.40
77.48
77.16
76.84
59.87
49.22
48.59
41.40
34.20
33.04
25.51
24.70
22.74
14.18
n-Hexane
180 170 160 150 140 130 120 110 100 90 80 70 60 50 40 30 20 10 0
f1 (ppm)

Tri-*tert*-butyl 11-((1-(2-(4-(*N*-(cyclohexylcarbamoyl)sulfamoyl)phenethyl)-1,3-dioxo-2,3-dihydro-1*H*-benzo[*de*]isoquinolin-6-yl)-1*H*-1,2,3-triazol-4-yl)methyl)-1,4,8,11-tetraazacyclotetradecane-1,4,8-tricarboxylate (**66**)

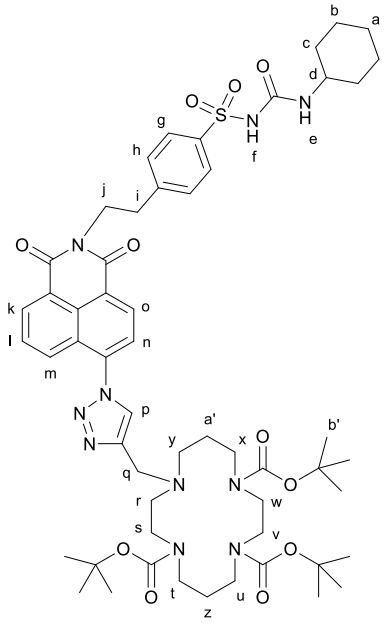

Under an atmosphere of nitrogen, **64** (109 mg, 0.200 mmol) and **40** (108 mg, 0.200 mmol) were dissolved in NMP (2.0 mL) and tetrakis(acetonitrile)copper(I) hexafluorophosphate (14.9 mg, 0.040 mmol) was added. The mixture was stirred at room temperature for 24 hours. After the reaction finished, saturated EDTA in 17% NH_3:H_2O (20 mL) was poured to the mixture and the precipitate was collected by filtration, and washed with water (30 mL). This crude product was purified by flash chromatography (eluent: DCM/MeOH 20:1) to give **66** as a brown solid (193 mg, 89%, M.p. 126-129 °C). ^{1}H NMR (400 MHz, $CDCl_3$) δ 8.68-8.61 (m, 2H, $H_{k,o}$), 8.28 (d, 1H, J = 5.6, H_m), 8.04 (bs, 1H, H_p), 7.94-7.80 (m, 4H, $H_{l,n,g}$), 7.49 (d, 2H, J = 8.2, H_h), 6.36 (d, 1H, J = 7.8, H_e), 4.40 (bs, 2H, H_j), 3.95 (s, 2H, H_q), 3.55 (bs, 1H, H_d), 3.34 (bs, 12H, $H_{s\text{-}x}$), 3.14-3.07 (m, 2H, H_i), 2.72 (bs, 2H, H_r), 2.57 (bs, 2H, H_y), 1.96-1.51 (m, 8H, $H_{c,z,a'}$), 1.50-1.17 (m, 33H, $H_{a,b,b'}$). ^{13}C NMR (101 MHz, $CDCl_3$) δ 163.3(d), 155.7(d), 143.4, 141.0, 138.4, 132.3, 130.9, 130.0, 129.6, 129.5, 129.0, 128.6, 127.6, 126.6, 126.4, 123.6, 123.4, 122.6, 79.7,

53.5, 53.2, 49.1, 48.9, 47.3, 45.6, 41.4, 34.0, 33.9, 33.8, 32.9, 28.5, 25.6, 25.4, 24.9, 24.6. IR: (υ_{max}/cm^{-1}) 2972, 2930, 1740, 1663, 1589, 1411, 1365, 1230, 1157, 1034, 782, 728. HR-ESI MS (*m/z*) $[M+H]^+$ calcd for $C_{55}H_{77}N_{10}O_{11}S$ 1085.5489, found 1085.5474.

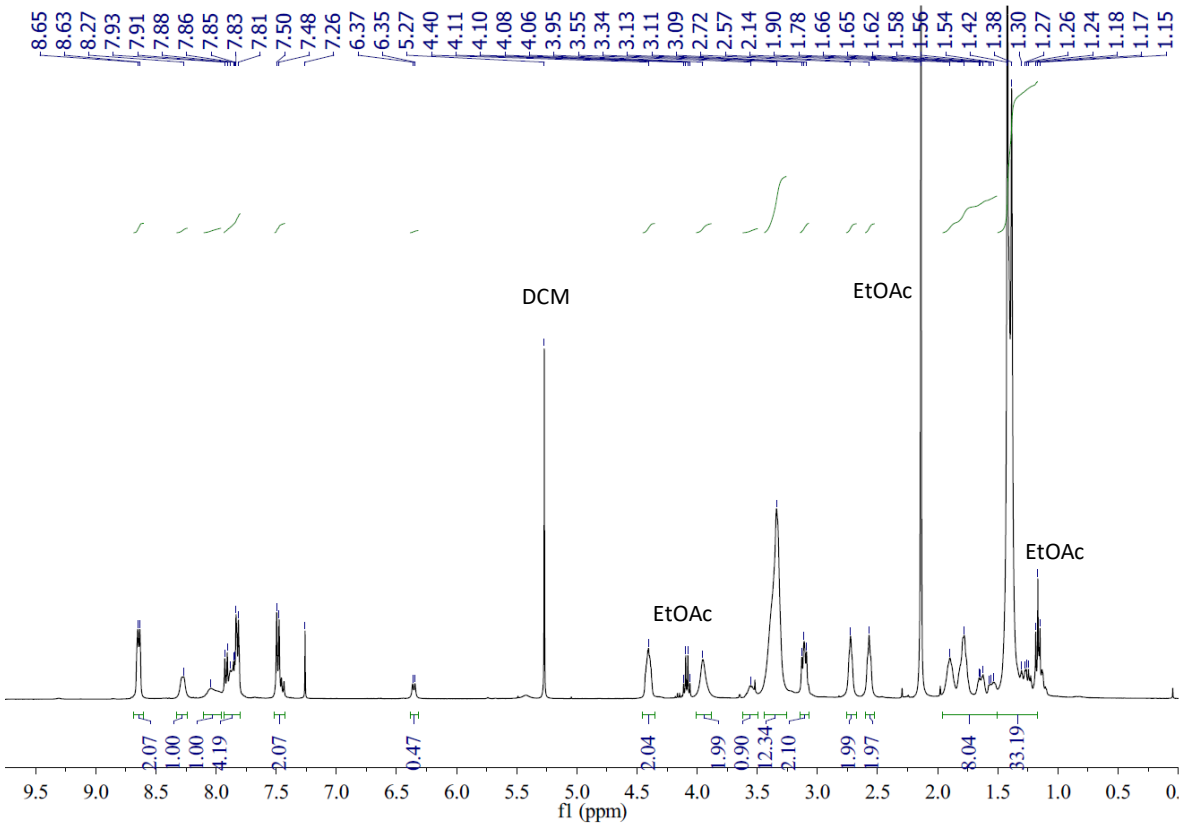
8.65 8.63 8.27 7.93 7.91 7.88 7.86 7.85 7.83 7.81 7.50 7.48 7.26 6.37 6.35 5.27 4.40 4.11 4.10 4.08 4.06 3.95 3.55 3.34 3.13 3.11 3.09 2.72 2.57 2.14 1.90 1.78 1.66 1.65 1.62 1.58 1.56 1.54 1.42 1.38 1.30 1.27 1.26 1.24 1.18 1.17 1.15
DCM
EtOAc
EtOAc
EtOAc
2.07 1.00 1.00 4.19 2.07 0.47 2.04 1.99 0.90 12.34 2.10 1.99 1.97 8.04 33.19
9.5 9.0 8.5 8.0 7.5 7.0 6.5 6.0 5.5 5.0 4.5 4.0 3.5 3.0 2.5 2.0 1.5 1.0 0.5 0.
f1 (ppm)

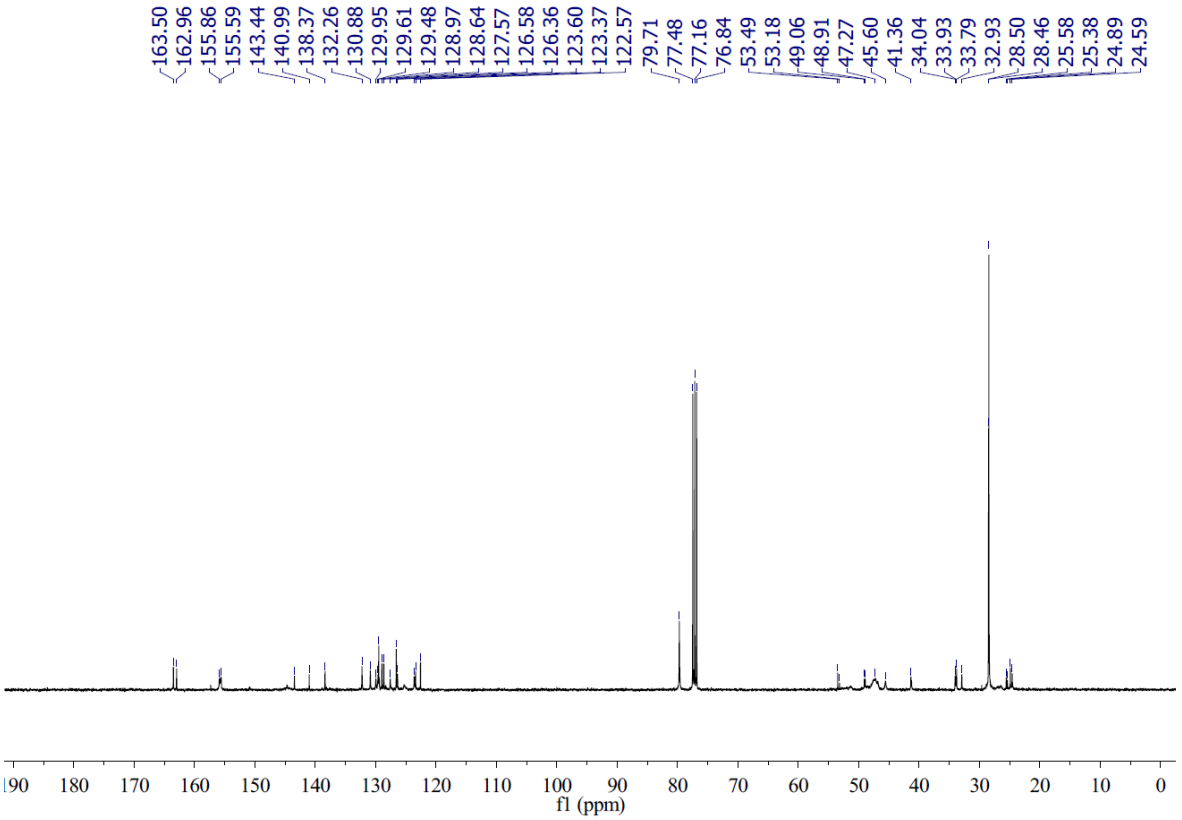
163.50 162.96 155.86 155.59 143.44 140.99 138.37 132.26 130.88 129.95 129.61 129.48 128.97 128.64 127.57 126.58 126.36 123.60 123.37 122.57 79.71 77.48 77.16 76.84 53.49 53.18 49.06 48.91 47.27 45.60 41.36 34.04 33.93 33.79 32.93 28.50 28.46 25.58 25.38 24.89 24.59
190 180 170 160 150 140 130 120 110 100 90 80 70 60 50 40 30 20 10 0
f1 (ppm)

4-(2-(6-(4-((1,4,8,11-Tetraazacyclotetradecan-1-yl)methyl)-1*H*-1,2,3-triazol-1-yl)-1,3-dioxo-1*H*-benzo[de]isoquinolin-2(3*H*)-yl)ethyl)-*N*-(cyclohexylcarbamoyl)benzenesulfonamide (**67**)

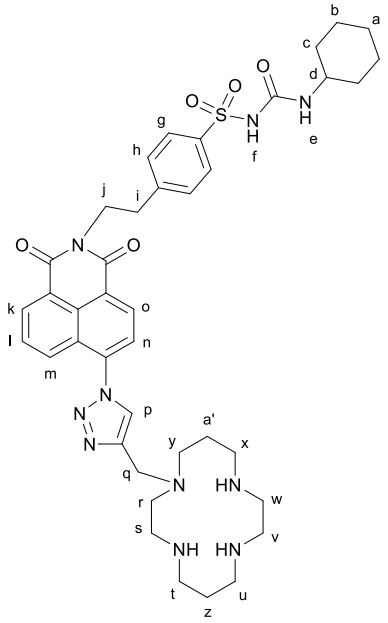

The tri-Boc protected compound **66** (109 mg, 0.100 mmol) was dissolved in a solution of 20% TFA in DCM (2.0 mL) and stirred for 10 h at room temperature. Then the solvent was removed *in vacuo* and the residue was dissolved in chloroform (10 mL) and washed with 1M aqueous NaOH solution (2.0 mL). The aqueous layer was extracted with chloroform (3 × 10 mL) and the organic layers were combined, dried over $MgSO_4$, filtered and concentrated *in vacuo* to give **67** as a brown solid (42 mg, 54 %, M.p. 202-205 °C). ^{1}H NMR (400 MHz, CD_3OD) δ 8.62-8.54 (m, 3H, $H_{k,o,p}$), 8.26 (d, 1H, J = 8.4, H_m), 7.99 (d, 1H, J = 7.8, H_n), 7.89-7.82 (m, 3H, $H_{g,l}$), 7.47 (d, 2H, J = 8.3, H_h), 4.35-4.28 (m, 2H, H_j), 4.03 (bs, 2H, H_q), 3.46-3.37 (m, 4H, $H_{s,v}$), 3.34-3.32 (m,1H H_d), 3.30-3.18 (m, 4H, $H_{t,u}$), 3.13-2.90 (m, 10H, $H_{i,r,w-y}$), 2.19 (bs, 2H, H_z), 1.93 (bs, 2H, $H_{a'}$), 1.79-1.52 (m, 5H, $H_{a,c}$), 1.35-1.13 (m, 5H, $H_{a,b}$). ^{13}C NMR (101 MHz, CD_3OD) δ 164.5(d), 163.1(d), 153.1, 146.4, 139.8, 139.3, 133.1, 131.8, 130.6, 130.0, 129.8, 128.8, 127.4, 125.3, 124.9, 123.9, 119.6, 116.7, 55.5, 54.8, 54.2, 50.7, 50.4, 50.1, 49.8, 48.2, 46.6, 45.9, 42.2, 34.8, 33.8, 26.4(overlapping signals), 25.8, 24.1. IR: (υ_{max}/cm^{-1}) 2929, 2853, 1661, 1587, 1516, 1433,

1347, 1231, 1200, 1121, 864, 782, 719. HR-ESI MS (*m/z*) $[M+H]^+$ calcd for $C_{40}H_{53}N_{10}O_5S$ 785.3916, found 785.3905.

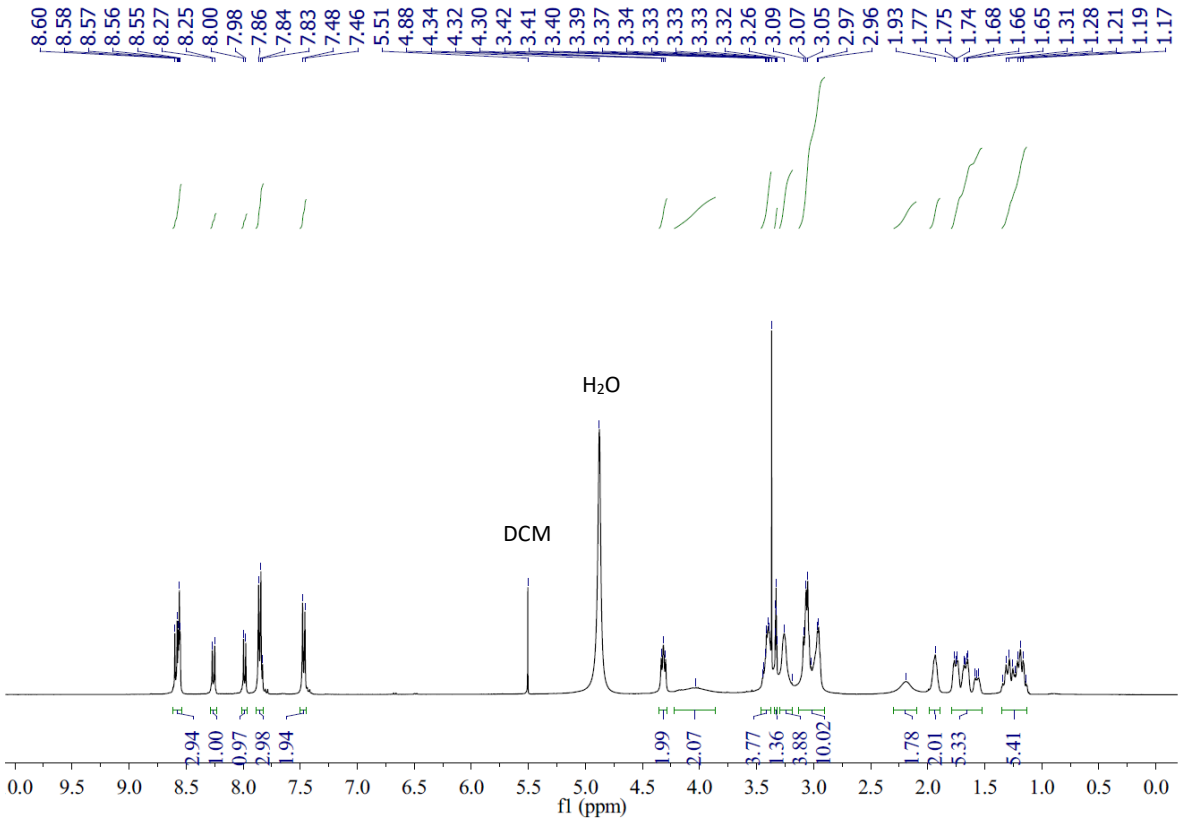
8.60
8.58
8.57
8.56
8.55
8.27
8.25
8.00
7.98
7.86
7.84
7.83
7.48
7.46
5.51
4.88
4.34
4.32
4.30
3.42
3.41
3.40
3.39
3.37
3.34
3.33
3.33
3.33
3.32
3.26
3.09
3.07
3.05
2.97
2.96
1.93
1.77
1.75
1.74
1.68
1.66
1.65
1.31
1.28
1.21
1.19
1.17
H2O
DCM
2.94
1.00
0.97
2.98
1.94
1.99
2.07
3.77
1.36
3.88
10.02
1.78
2.01
5.33
5.41
fl (ppm)

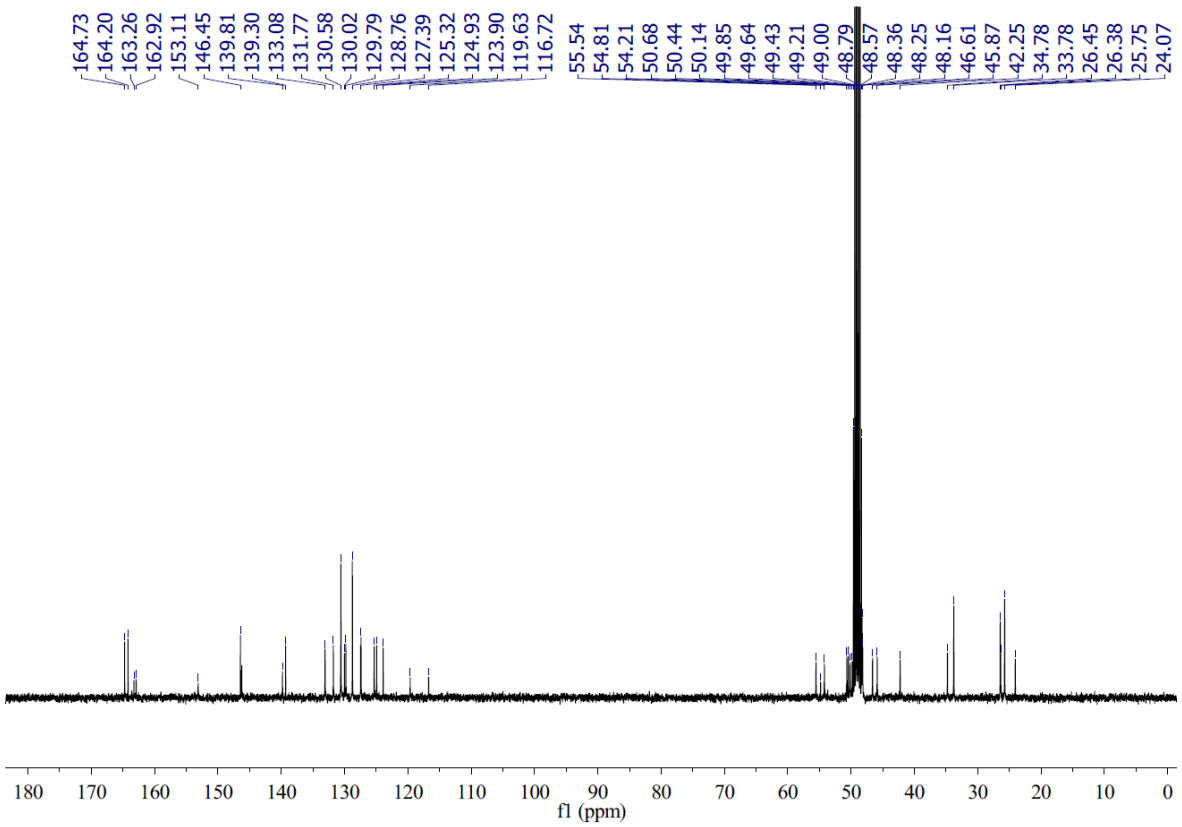
164.73
164.20
163.26
162.92
153.11
146.45
139.81
139.30
133.08
131.77
130.58
130.02
129.79
128.76
127.39
125.32
124.93
123.90
119.63
116.72
55.54
54.81
54.21
50.68
50.44
50.14
49.85
49.64
49.43
49.21
49.00
48.79
48.57
48.36
48.25
48.16
46.61
45.87
42.25
34.78
33.78
26.45
26.38
25.75
24.07
fl (ppm)

Diethyl 2,2'-azanediyldiacetate (**68**)

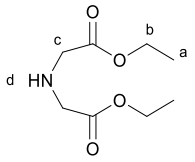

Thionyl chloride (7.26 mL, 100 mmol) was added slowly to stirred absolute ethanol (30 mL) in ice-water bath and the mixture stirred for about 30 mins at room temperature. After the addition of iminodiacetic acid (3.33 g, 25.0 mmol), the reaction mixture was heated at reflux overnight and then the solution was evaporated *in vacuo*. Saturated $NaHCO_3$ solution (20 mL) was added and extracted with CH_2Cl_2 (3 × 30 mL), the organic layers combined, dried over $MgSO_4$, filtered and dried *in vacuo* to give **68** (3.89 g, 82 %) as a colourless oil. ^{1}H NMR (400 MHz, $CDCl_3$) δ 4.08 (q, 4H, J = 7.2, H_b), 3.35 (s, 4H, H_c), 1.98 (s, 1H, H_d), 1.17 (t, 6H, J = 7.2, H_a). ^{13}C NMR (101 MHz, $CDCl_3$) δ 171.6, 60.6, 50.0, 14.0. All other spectroscopic data were consistent with those previously reported.[148]

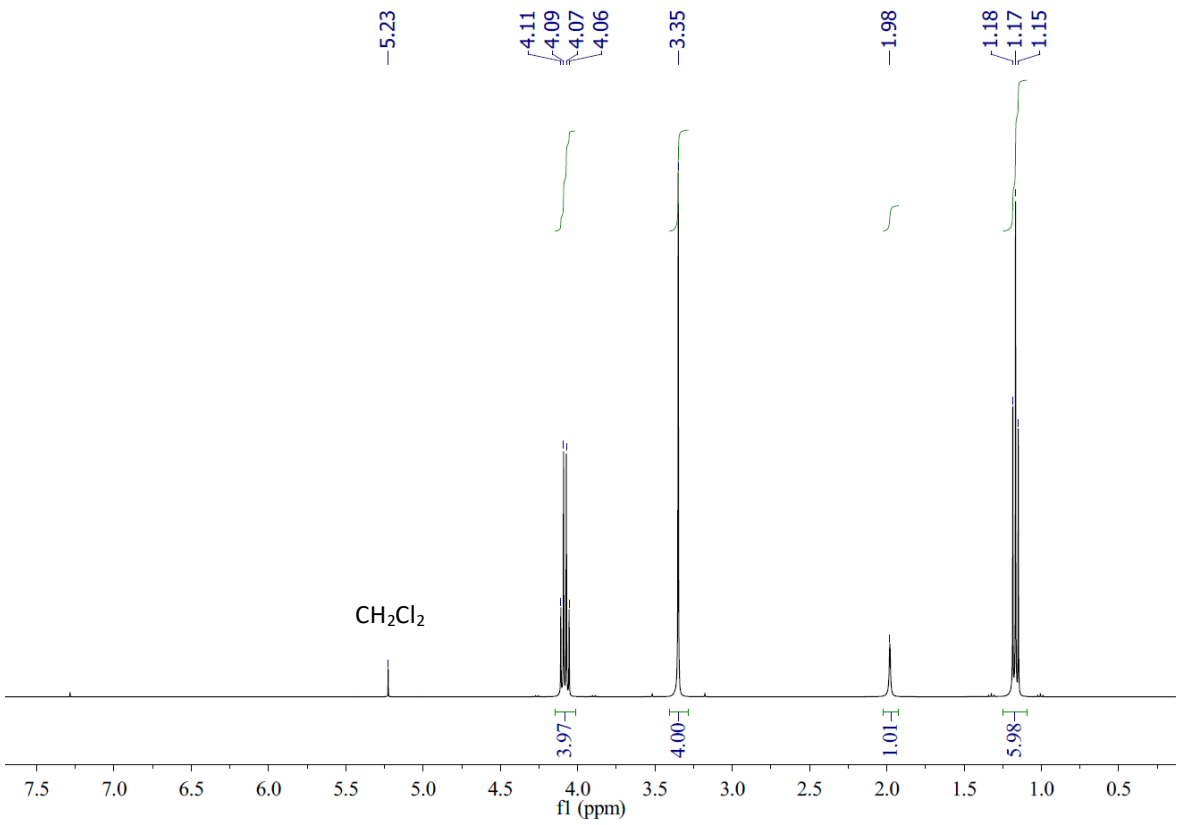
5.23
4.11
4.09
4.07
4.06
3.35
1.98
1.18
1.17
1.15
CH2Cl2
3.97
4.00
1.01
5.98
7.5 7.0 6.5 6.0 5.5 5.0 4.5 4.0 3.5 3.0 2.5 2.0 1.5 1.0 0.5
f1 (ppm)

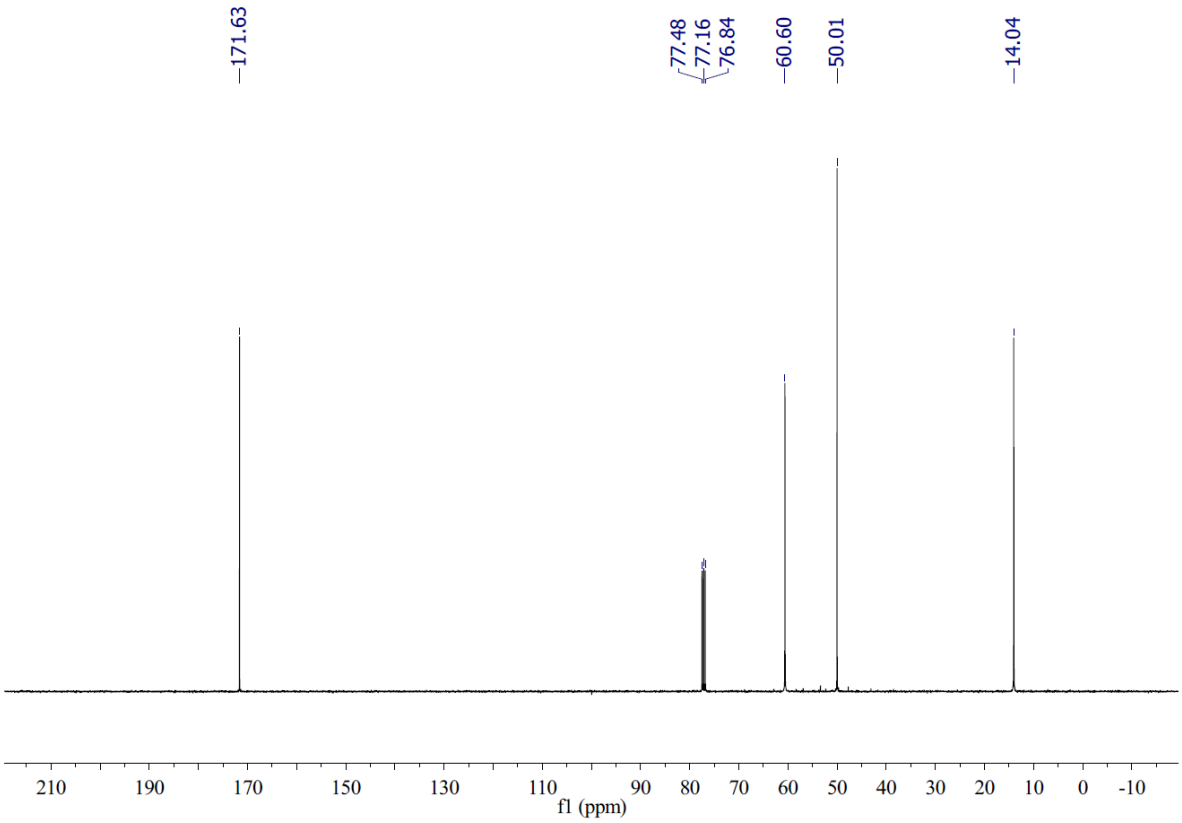
171.63
77.48
77.16
76.84
60.60
50.01
14.04
210 190 170 150 130 110 90 80 70 60 50 40 30 20 10 0 -10
f1 (ppm)

Diethyl 2,2'-(prop-2-yn-1-ylazanediyl)diacetate **(69)**

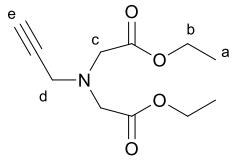

Diethyl iminodiacetate **68** (2.68 g, 14.2 mmol) was dissolved in MeCN (30 mL), then K_2CO_3 (3.92 g, 28.4 mmol) and propargyl bromide (2.52 mL, 17.0 mmol) were added slowly and the mixture heated at reflux for 16 h. After cooling to room temperature, the suspension was filtered and the filtrate evaporated *in vacuo*. The resultant oil was purified by column chromatography (petrol/EtOAc = 20:1 to petrol/EtOAc = 5:1) to obtain **69** as a red oil (1.61 g, 50 %). ^{1}H NMR (400 MHz, $CDCl_3$) δ 4.04 (q, 4H, J = 7.1, H_b), 3.53 (d, 2H, J = 2.4, H_d), 3.40 (s, 4H, H_c), 2.18 (t, 1H, J = 2.4, H_e), 1.13 (t, 6H, J = 7.1, H_a). ^{13}C NMR (101 MHz, $CDCl_3$) δ 170.0, 78.1, 73.6, 60.4, 54.0, 43.0, 13.9. All other spectroscopic data were consistent with those previously reported.[149] There was a by-product **108** obtained in this reaction, which is the reason for its low yield. The spectroscopic data of **108** is shown in Appendix 2.

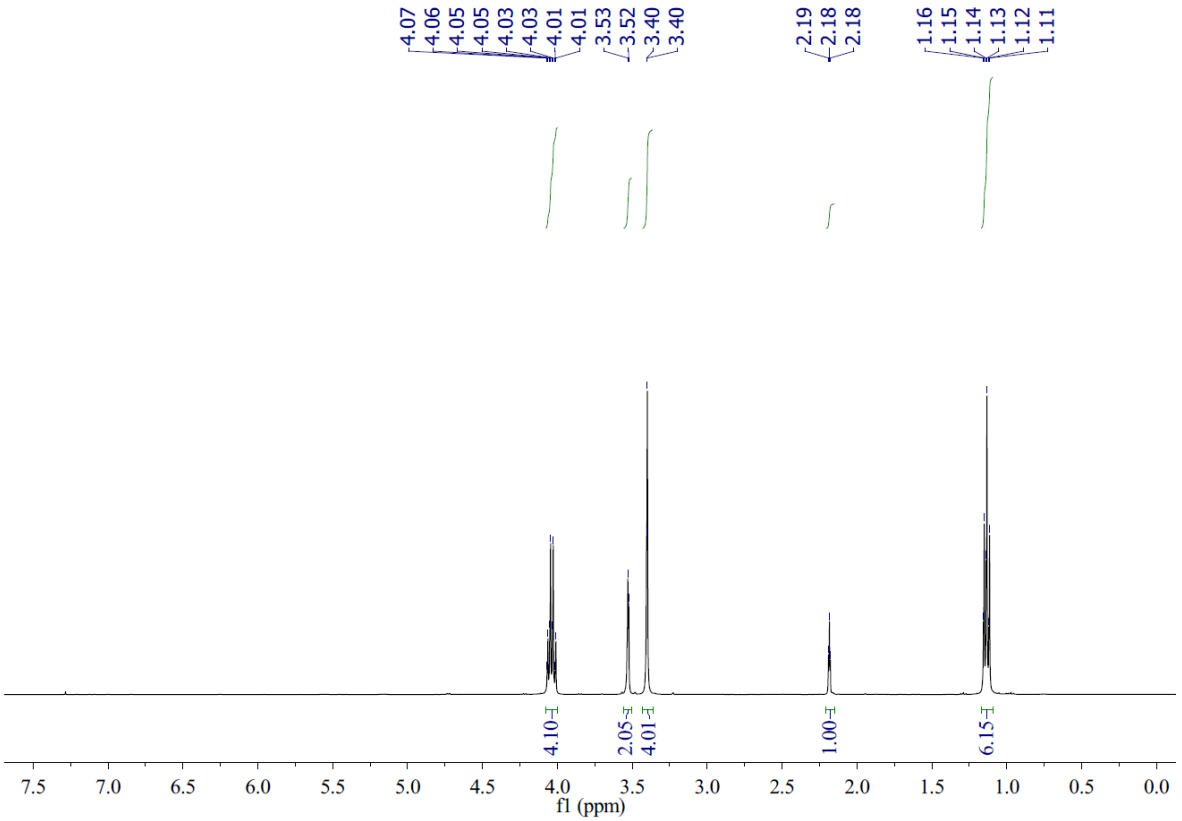
4.07
4.06
4.05
4.05
4.03
4.03
4.01
4.01
3.53
3.52
3.40
3.40
2.19
2.18
2.18
1.16
1.15
1.14
1.13
1.12
1.11
4.10
2.05
4.01
1.00
6.15
7.5 7.0 6.5 6.0 5.5 5.0 4.5 4.0 3.5 3.0 2.5 2.0 1.5 1.0 0.5 0.0
f1 (ppm)

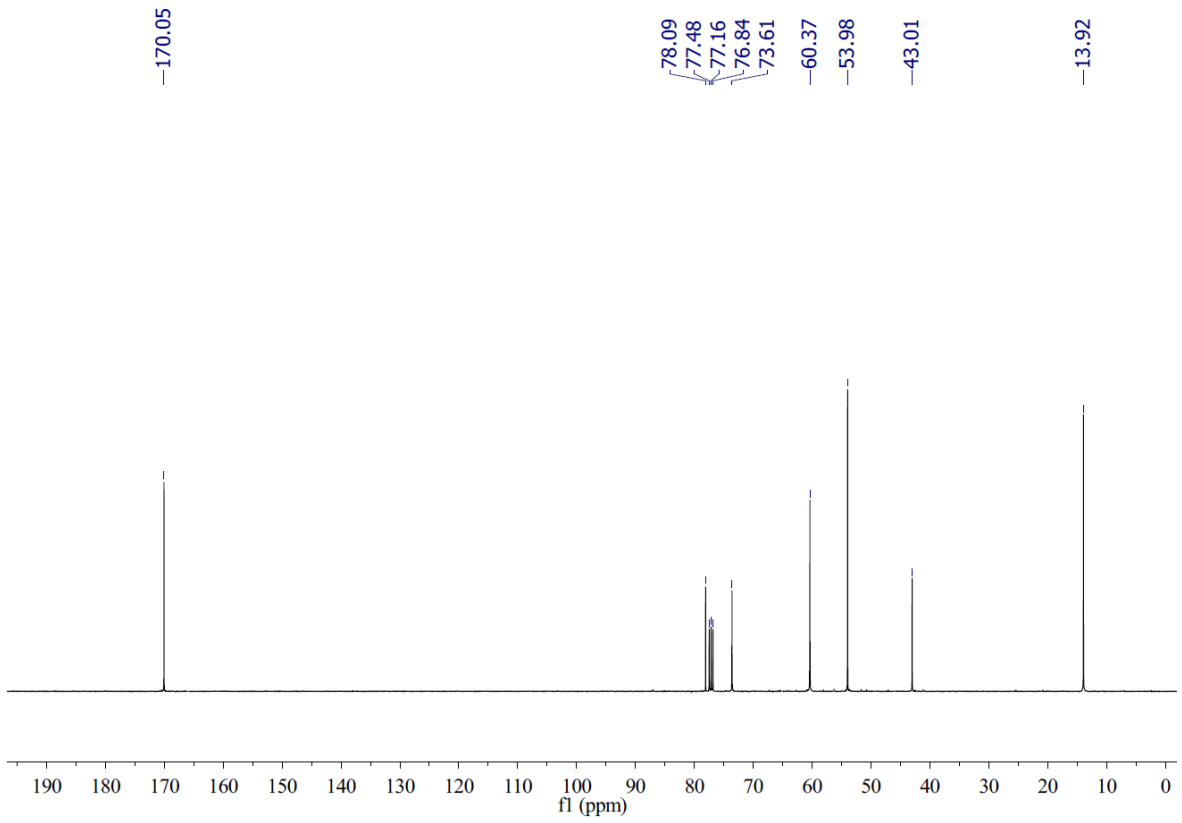
170.05
78.09
77.48
77.16
76.84
73.61
60.37
53.98
43.01
13.92
190 180 170 160 150 140 130 120 110 100 90 80 70 60 50 40 30 20 10 0
f1 (ppm)

Diethyl 2,2'-(((1-(2-(4-(*N*-(cyclohexylcarbamoyl)sulfamoyl)phenethyl)-1,3-dioxo-2,3-dihydro-1*H*-benzo[*de*]isoquinolin-6-yl)-1*H*-1,2,3-triazol-4-yl)methyl)azanediyl)diacetate (**70**)

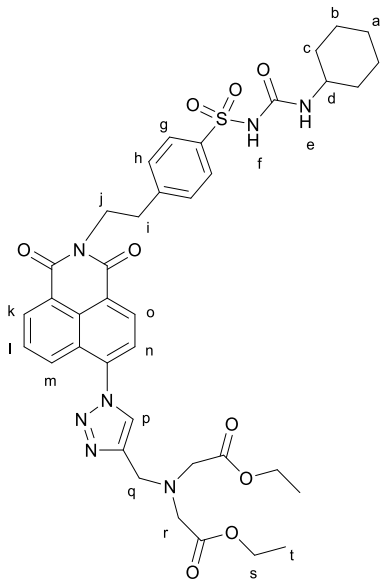

Under an atmosphere of nitrogen, **64** (109 mg, 0.200 mmol) and **69** (45.4 mg, 0.200 mmol) were dissolved in NMP (1.0 mL) and EtOH (1.0 mL), then tetrakis(acetonitrile)copper(I) hexafluorophosphate (14.9 mg, 0.040 mmol) was added. The flask was covered with aluminium foil and the mixture was stirred at room temperature for 24 hours. After the reaction had finished saturated EDTA in 17% NH_3:H_2O (20 mL) was poured into the mixture and the precipitate formed was collected by filtration, and washed with water (30 mL). This crude product was purified by flash chromatography (eluent: DCM/MeOH 20:1) to give **70** as a brown solid (133 mg, 86%, M.p. 164-168 °C). ^{1}H NMR (400 MHz, $CDCl_3$) δ 8.66 (m, 2H), 8.30 (d, 1H, *J* = 8.6), 8.16 (s, 1H), 7.86-7.80 (m, 4H), 7.52 (d, 2H, *J* = 8.3), 6.48 (m, 1H), 4.47-4.40 (m, 2H), 4.24 (s, 2H), 4.18 (q, 4H, *J* = 7.1), 3.69 (s, 4H), 3.66-3.55 (m, 1H), 3.18-3.10 (m, 2H), 1.85-1.56 (m, 6H), 1.35-1.17 (m, 10H).^{13}C NMR (101 MHz, $CDCl_3$) δ 171.2, 163.7, 163.1, 150.7, 146.5, 145.2, 139.3, 138.6, 138.0, 135.6, 132.5, 131.0, 130.0, 129.2, 128.8, 127.4, 126.6, 125.8, 123.7, 123.6, 122.8, 60.9, 55.1, 49.3, 49.2, 41.4, 34.2, 33.0, 25.5, 24.6, 14.4. IR: (υ_{max}/cm^{-1}) 3287,

2930, 2853, 1697, 1656, 1589, 1535, 1433, 1344, 1229, 1157, 1037, 783, 605. HR-NSI MS (*m/z*) $[M+H]^+$ calcd for $C_{38}H_{44}N_7O_9S$ 774.2916, found 774.2907.

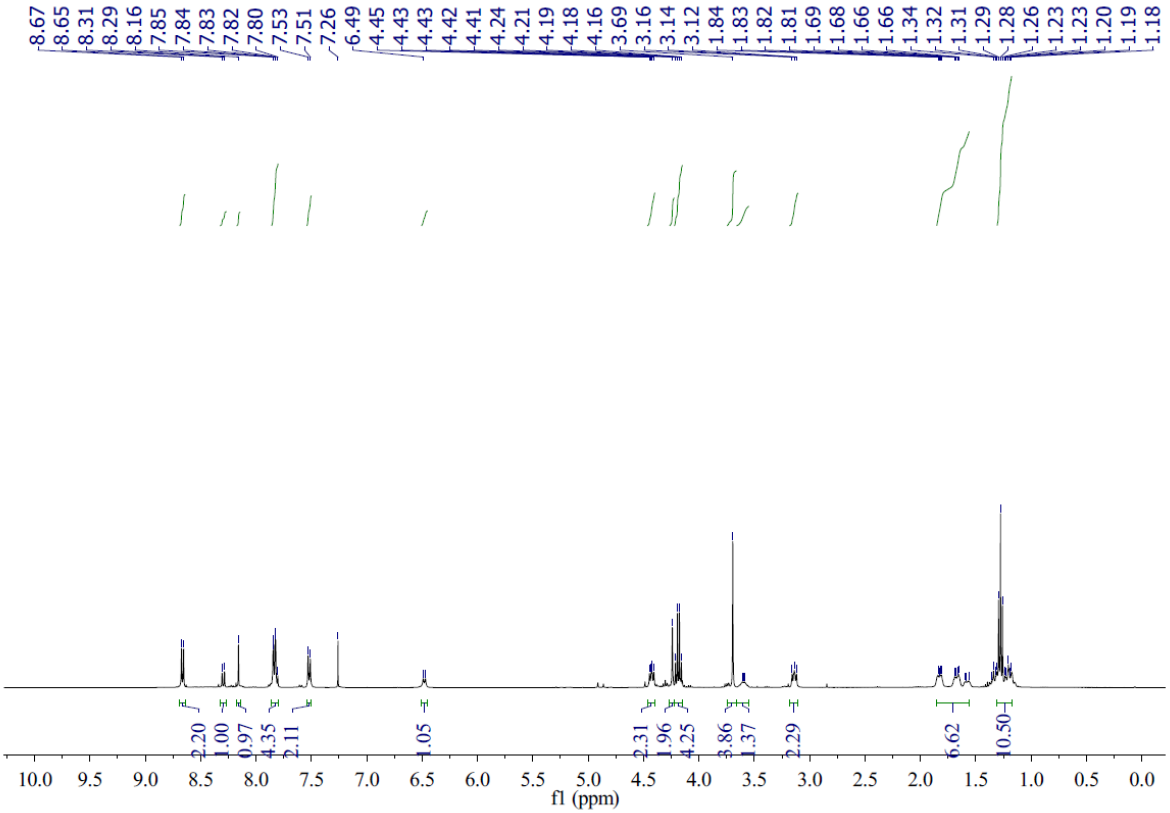
8.67
8.65
8.31
8.29
8.16
7.85
7.84
7.83
7.82
7.80
7.53
7.51
7.26
6.49
4.45
4.43
4.43
4.42
4.41
4.24
4.21
4.19
4.18
4.16
3.69
3.16
3.14
3.12
1.84
1.83
1.82
1.81
1.69
1.68
1.66
1.66
1.34
1.32
1.31
1.29
1.28
1.26
1.23
1.23
1.20
1.19
1.18
2.20
1.00
0.97
4.35
2.11
1.05
2.31
1.96
4.25
3.86
1.37
2.29
6.62
10.50
10.0 9.5 9.0 8.5 8.0 7.5 7.0 6.5 6.0 5.5 5.0 4.5 4.0 3.5 3.0 2.5 2.0 1.5 1.0 0.5 0.0
f1 (ppm)

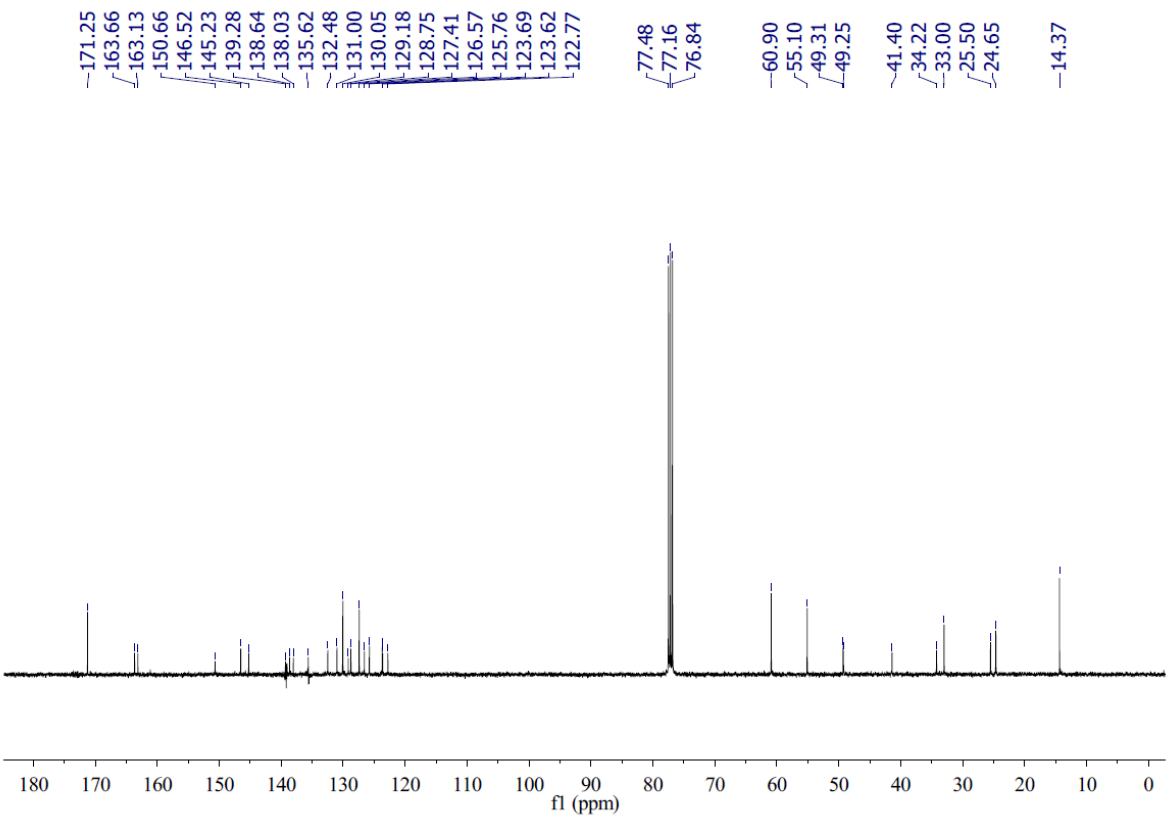
171.25
163.66
163.13
150.66
146.52
145.23
139.28
138.64
138.03
135.62
132.48
131.00
130.05
129.18
128.75
127.41
126.57
125.76
123.69
123.62
122.77
77.48
77.16
76.84
60.90
55.10
49.31
49.25
41.40
34.22
33.00
25.50
24.65
14.37
180 170 160 150 140 130 120 110 100 90 80 70 60 50 40 30 20 10 0
f1 (ppm)

2-Azidoacetic acid (**71**)

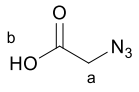

To a solution of 2-chloroethanamine hydrochloride (567 mg, 6.00 mmol) in H_2O (25 mL) was added NaN_3 (1.95 g, 30.0 mmol) at room temperature. After stirring at 65 °C for 48 h, the reaction mixture was acidified with concentrated HCl to pH = 2. Then the aqueous layer was extracted with diethyl ether (3 × 20 mL), the organic layers were combined and washed with brine (10 mL), dried over anhydrous $MgSO_4$, filtered and concentrated *in vacuo* to give **71** (373 mg, 61 %) as a colourless oil. ^{1}H NMR (400 MHz, $CDCl_3$) δ 11.55 (s, 1H, H_b), 3.97 (s, 2H, H_a). ^{13}C NMR (101 MHz, $CDCl_3$) δ 174.8, 50.1. All other spectroscopic data were consistent with those previously reported.[150]

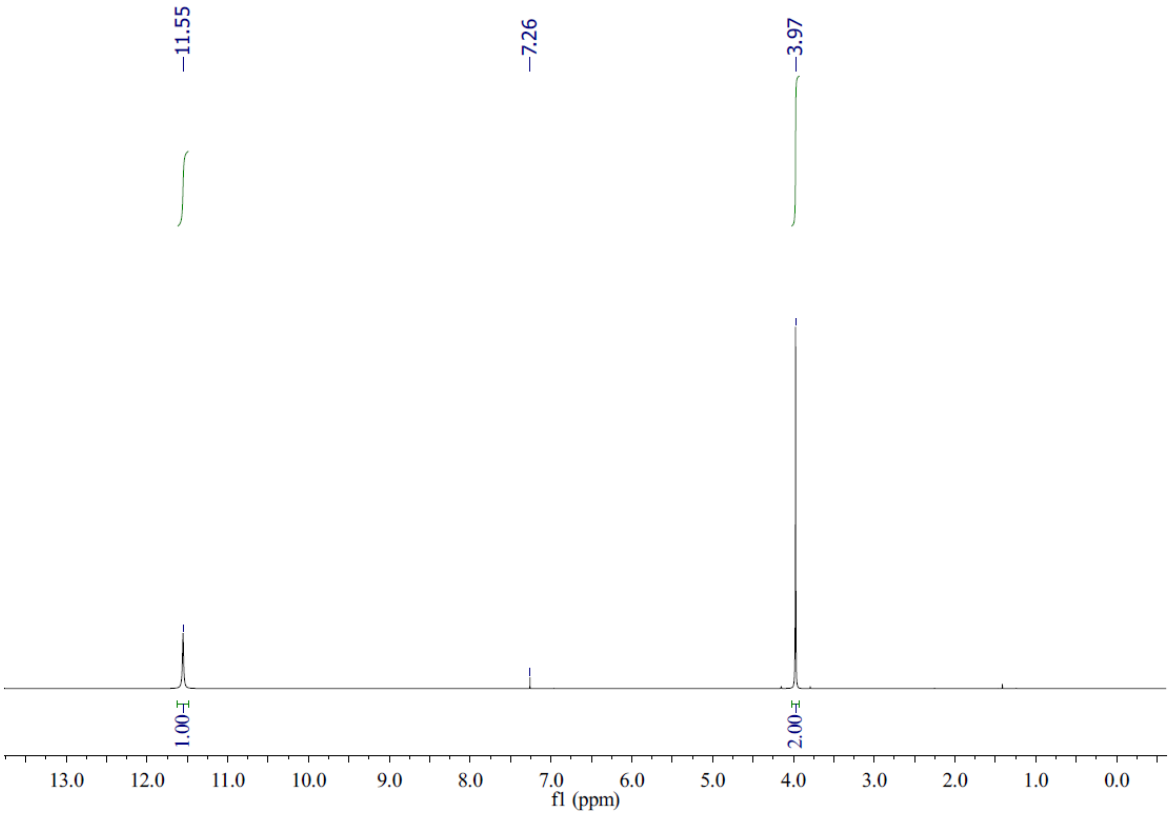
11.55
7.26
3.97
1.00
2.00
13.0
12.0
11.0
10.0
9.0
8.0
7.0
6.0
5.0
4.0
3.0
2.0
1.0
0.0
f1 (ppm)

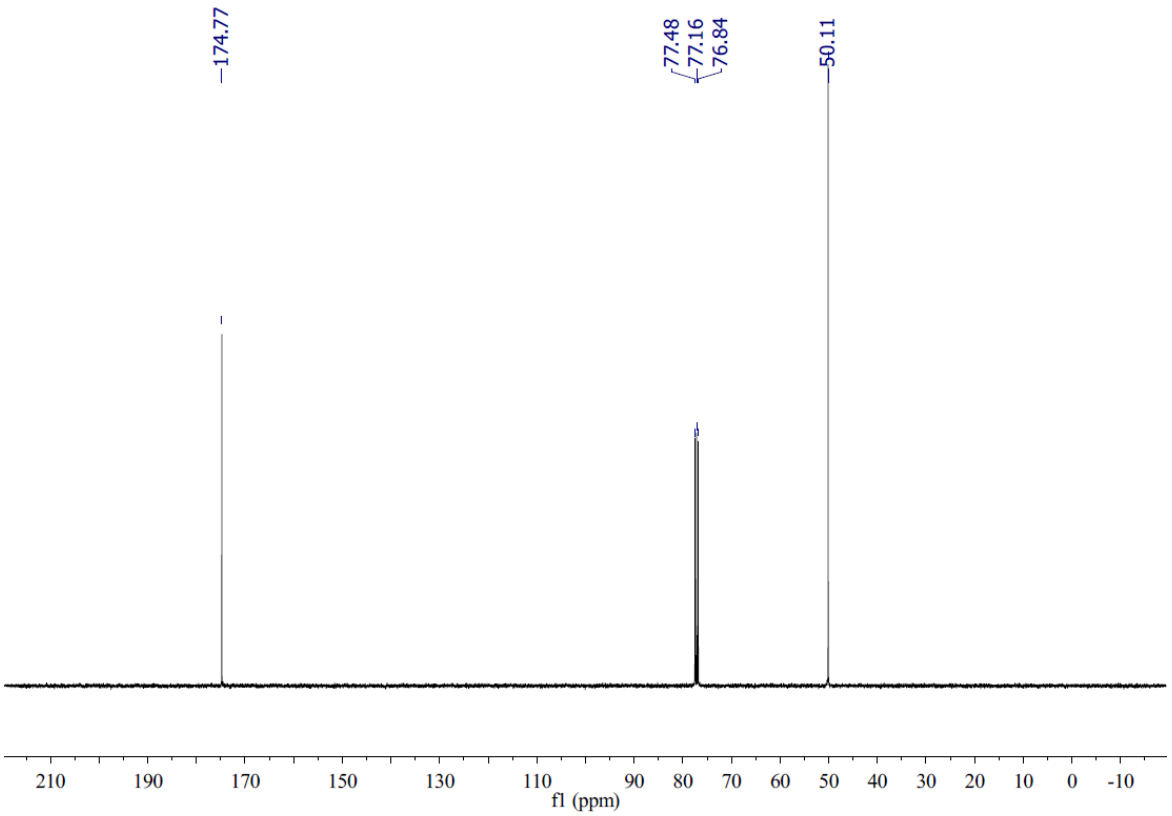
174.77
77.48
77.16
76.84
50.11
210
190
170
150
130
110
90
80
70
60
50
40
30
20
10
0
-10
f1 (ppm)

S-Trityl-L-cysteine (**72**)

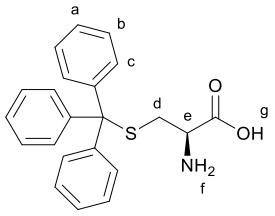

To a solution of L-cysteine (363 mg, 3.00 mmol) in TFA (6.0 mL), trityl chloride (836 mg, 3.00 mmol) was added and the reaction mixture was stirred at room temperature for 30 minutes. Then the excess TFA was removed *in vacuo* and diethyl ether (10 mL) was added. Then aqueous NaOAc (1 M) was added to bring the pH near to neutrality and at this point a white precipitate was formed. The precipitate was collected by filtration and washed with cold water (20 mL), ethanol (6.0 mL) and dried *in vacuo* to give **72** (840 mg, 77%, M.p. 143-146 °C) as a white solid. ^{1}H NMR (400 MHz, DMSO-d_6) δ 7.39 – 7.17 (m, 15H, $H_{a\text{-}c}$), 2.93 (dd, 1H, J = 9.2, 4.3, H_e), 2.58 (dd, 1H, J = 12.5, 4.3, H_d), 2.40 (dd, 1H, J = 12.5, 9.2, H_d). ^{13}C NMR (101 MHz, DMSO-d_6) δ 144.2, 129.1, 128.0, 126.7, 66.0, 53.4, 33.6. All other spectroscopic data were consistent with those previously reported.[129]

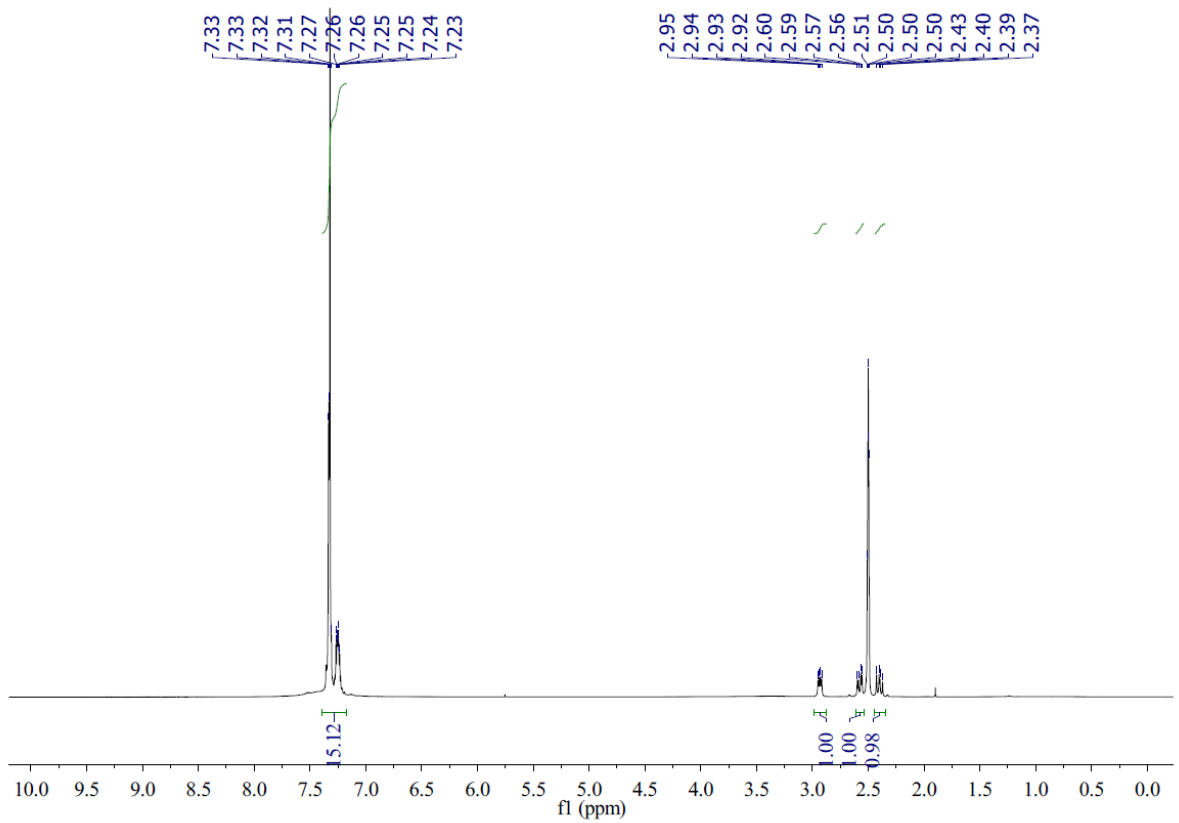
7.33
7.33
7.32
7.31
7.27
7.26
7.26
7.25
7.25
7.24
7.23
2.95
2.94
2.93
2.92
2.60
2.59
2.57
2.56
2.51
2.50
2.50
2.50
2.43
2.40
2.39
2.37
5.12
1.00
1.00
0.98
f1 (ppm)

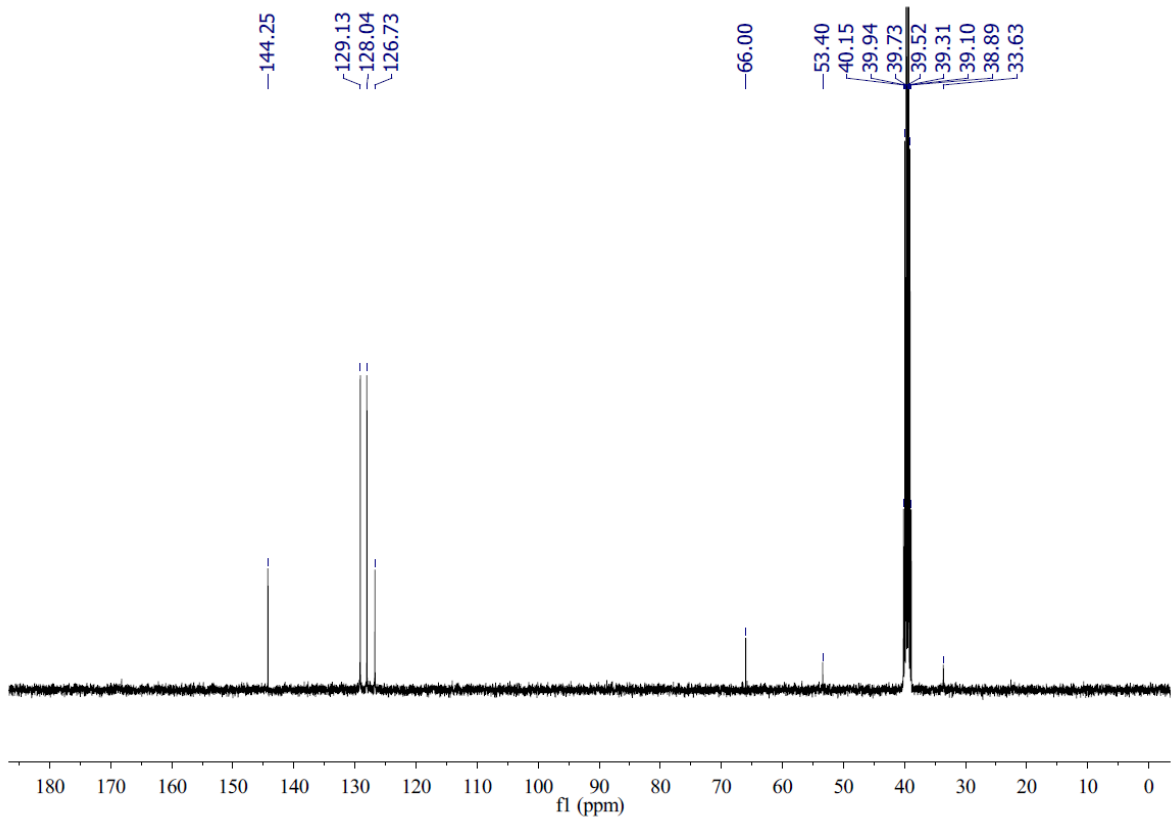
144.25
129.13
128.04
126.73
66.00
53.40
40.15
39.94
39.73
39.52
39.31
39.10
38.89
33.63
f1 (ppm)

Methyl *S*-trityl-L-cysteinate (**73**)

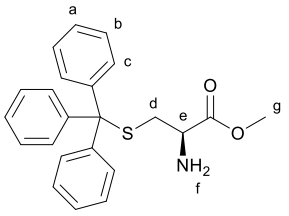

To a stirred solution of **72** (233 mg, 0.650 mmol) in methanol (10 mL), thionyl chloride (0.36 mL, 5.00 mmol) was added in drops at 0 °C. The solution was allowed to warm to room temperature and then refluxed for 5 hours. The solvent was removed *in vacuo* and the crude product was extracted with ethyl acetate (15 mL), which was washed with saturated $NaHCO_3$ (3 × 20 mL). The organic layer was dried over anhydrous $MgSO_4$, filtered and concentrated *in vacuo* to obtain **73** (196 mg, 80%) as a pale-yellow gum. ^{1}H NMR (400 MHz, $CDCl_3$) δ 7.35-7.07 (m, 15H, $H_{a\text{-}c}$), 3.52 (s, 3H, H_g), 3.11 (dd, 1H, J = 7.4, 4.7, H_e), 2.51 (dd, 1H, J = 12.5, 4.7, H_d), 2.40 (dd, 1H, J = 12.5, 7.4, H_d), 2.18-2.02 (bs, 2H, H_f). ^{13}C NMR (101 MHz, $CDCl_3$) δ 173.8, 144.5, 129.6, 128.0, 126.8, 66.9, 53.6, 52.2, 36.6. All other spectroscopic data were consistent with those previously reported.[130]

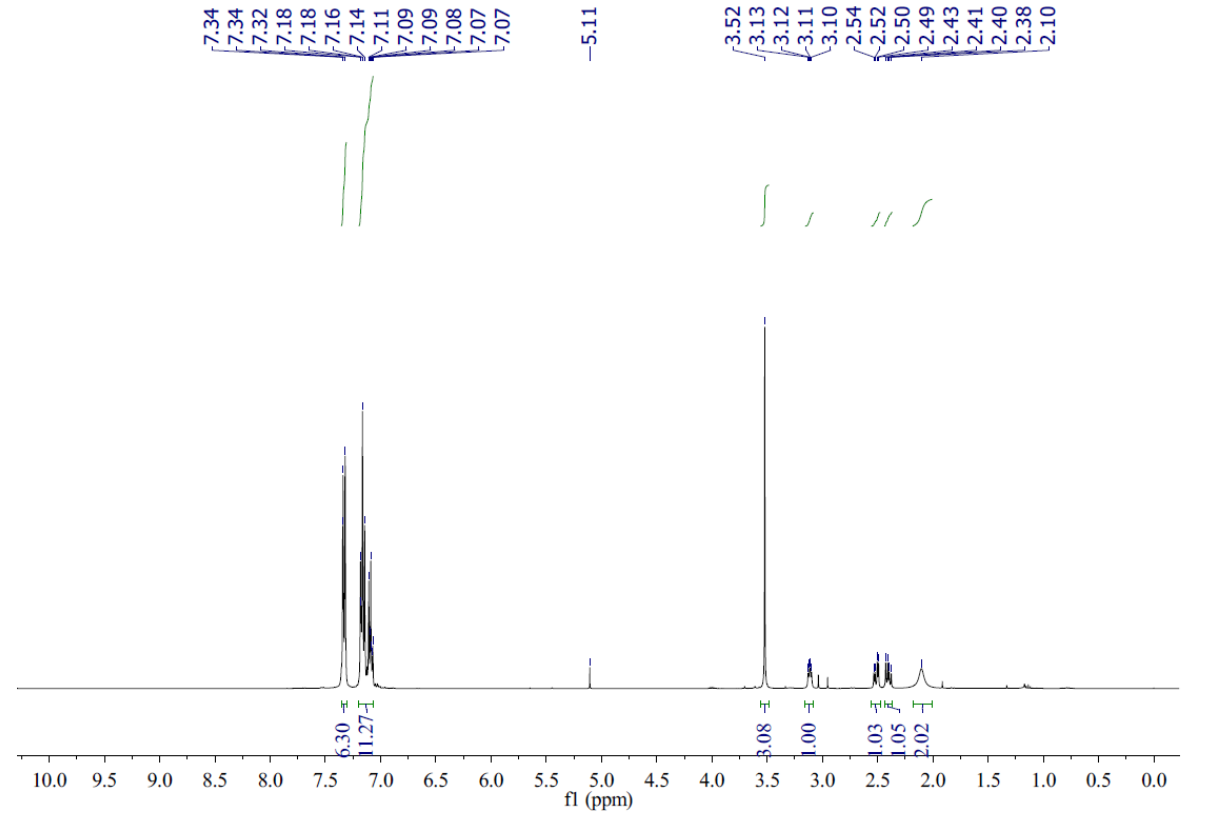
7.34
7.34
7.32
7.18
7.18
7.16
7.14
7.11
7.09
7.09
7.08
7.07
7.07
5.11
3.52
3.13
3.12
3.11
3.10
2.54
2.52
2.50
2.49
2.43
2.41
2.40
2.38
2.10
6.30
11.27
3.08
1.00
1.03
1.05
2.02
10.0 9.5 9.0 8.5 8.0 7.5 7.0 6.5 6.0 5.5 5.0 4.5 4.0 3.5 3.0 2.5 2.0 1.5 1.0 0.5 0.0
f1 (ppm)

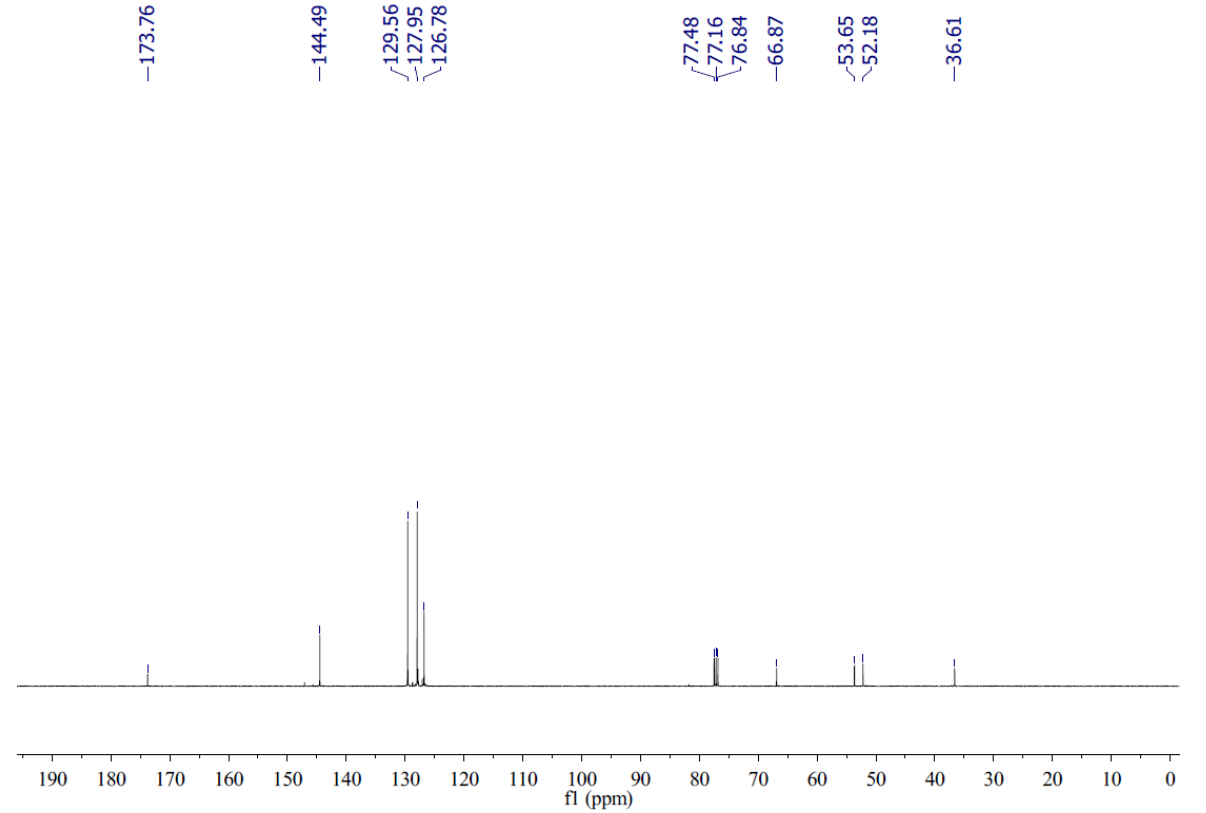
173.76
144.49
129.56
127.95
126.78
77.48
77.16
76.84
66.87
53.65
52.18
36.61
190 180 170 160 150 140 130 120 110 100 90 80 70 60 50 40 30 20 10 0
f1 (ppm)

Methyl *N*-(2-azidoacetyl)-*S*-trityl-L-cysteinate (**74**)

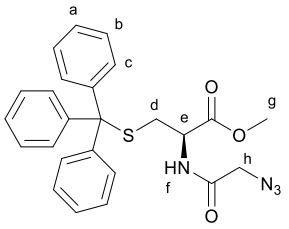

To a stirred solution of 2-azidoacetic acid **71** (260 mg, 2.57 mmol) and *N*-methylmorpholine (314 µL, 2.80 mmol) in THF (10 mL) was added isobutyl chloroformate (364 µL, 2.80 mmol) at -15 °C. The mixture was stirred at the same temperature for 30 min, then **73** (970 mg, 2.57 mmol) was added to the mixture. Stirring was continued for 1 hour at -15 °C and then the cooling bath was removed. The reaction was allowed to warm up to room temperature and stirring was continued overnight. The solvent was removed *in vacuo* and the residue dissolved in EtOAc (30 mL) which was washed with saturated $NaHCO_3$ (30 mL) and water (30 mL), dried over $MgSO_4$ and concentrated *in vacuo* to give **74** (854 mg, 72%, M.p. 115-117 °C) as a white solid. ^{1}H NMR (400 MHz, $CDCl_3$) δ 7.45-7.23 (m, 15H, $H_{a\text{-}c}$), 6.77 (d, 1H, J = 7.9, H_f), 4.64 – 4.57 (m, 1H, H_e), 3.97 (s, 2H, H_h), 3.75 (s, 3H, H_g), 2.78 – 2.62 (m, 2H, H_d). ^{13}C NMR (101 MHz, $CDCl_3$) δ 170.4, 166.4, 144.3, 129.6, 128.1, 127.1, 67.2, 52.9, 52.5, 51.2, 33.7. IR: (υ_{max}/cm^{-1}) 3056, 2105, 1742, 1667, 1521, 1442, 1207, 742, 698. HR-ESI MS (*m/z*) [M-H]$^-$ calcd for $C_{25}H_{23}N_4O_3S$ 459.1479, found 459.1491.

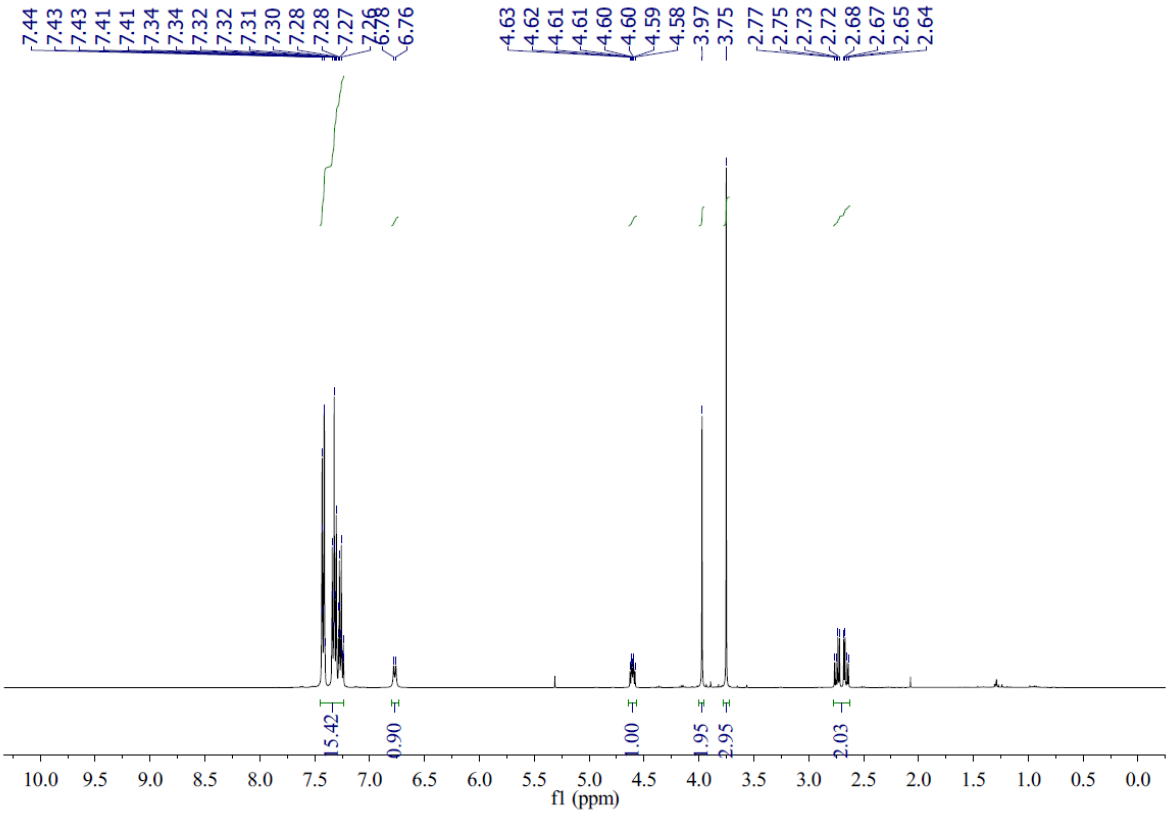
7.44
7.43
7.43
7.41
7.41
7.34
7.34
7.32
7.32
7.31
7.30
7.28
7.28
7.27
6.78
6.76
4.63
4.62
4.61
4.61
4.60
4.60
4.59
4.58
3.97
3.75
2.77
2.75
2.73
2.72
2.68
2.67
2.65
2.64
15.42
0.90
1.00
1.95
2.95
2.03
10.0 9.5 9.0 8.5 8.0 7.5 7.0 6.5 6.0 5.5 5.0 4.5 4.0 3.5 3.0 2.5 2.0 1.5 1.0 0.5 0.0
f1 (ppm)

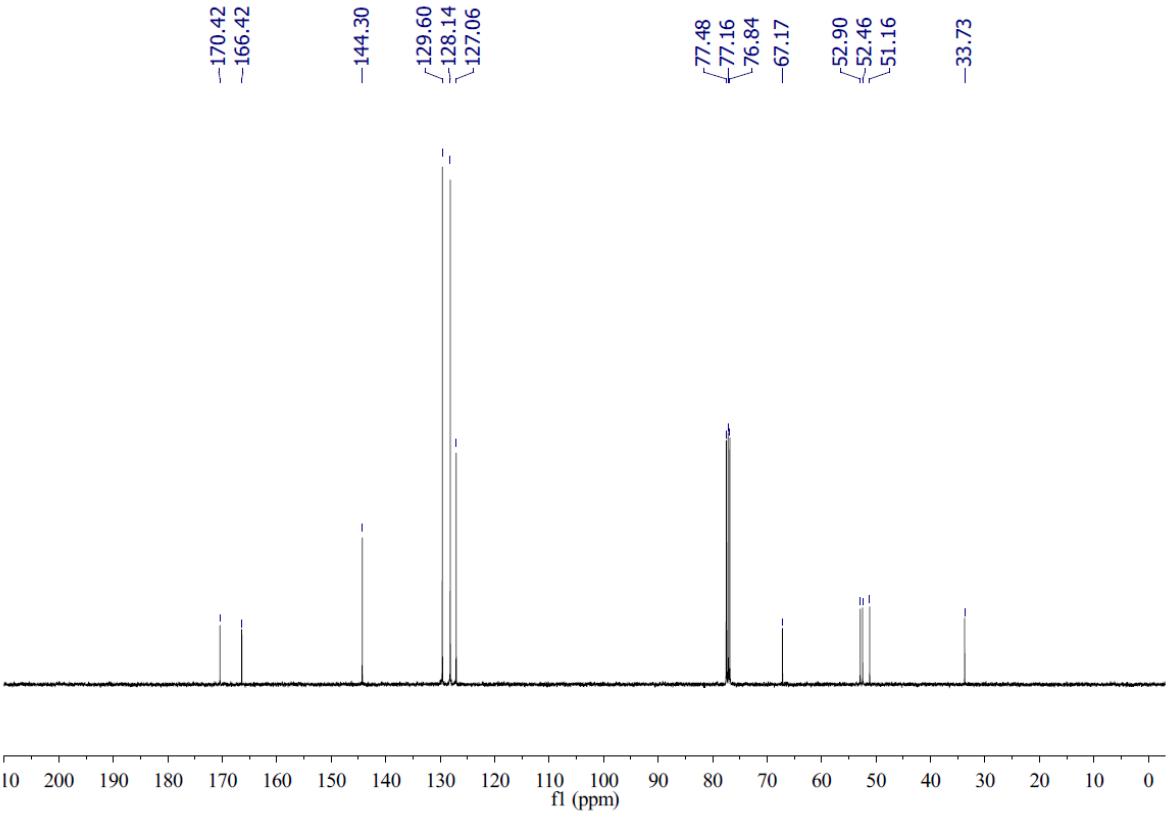
170.42
166.42
144.30
129.60
128.14
127.06
77.48
77.16
76.84
67.17
52.90
52.46
51.16
33.73
210 200 190 180 170 160 150 140 130 120 110 100 90 80 70 60 50 40 30 20 10 0
f1 (ppm)

Methyl *N*-(2-(4-((6-bromo-1,3-dioxo-1*H*-benzo[*de*]isoquinolin-2(3*H*)-yl)methyl)-1*H*-1,2,3-triazol-1-yl)acetyl)-*S*-trityl-L-cysteinate (**75**)

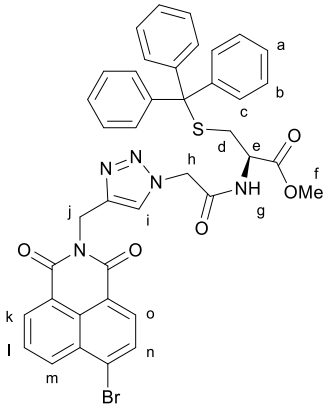

Under an atmosphere of nitrogen, **74** (138 mg, 0.300 mmol) and **38** (94.2 mg, 0.300 mmol) were dissolved in DMF (2.0 mL) and tetrakis(acetonitrile)copper(I) hexafluorophosphate (22.4 mg, 0.060 mmol) was added. The mixture was stirred at room temperature for 24 hours. After the reaction was complete, saturated EDTA in 17% NH_3:H_2O (20 mL) was poured into the reaction mixture and the precipitate that formed was collected by filtration, and washed with water (30 mL), dried *in vacuo*. This crude product was purified by flash chromatography (eluent: DCM/MeOH = 50:1) to give **75** as a brown solid (160 mg, 68%, M.p. 133-136 °C). ^{1}H NMR (400 MHz, $CDCl_3$) δ 8.68 (dd, 1H, *J* = 7.3, 1.1, H_k), 8.59 (dd, 1H, *J* = 8.5, 1.1, H_m), 8.43 (d, 1H, *J* = 7.9, H_o), 8.04 (d, 1H, *J* = 7.9, H_n), 7.88 – 7.84 (m, 1H, H_l), 7.83 (s, 1H, H_i), 7.39 – 7.21 (m, 15H, $H_{a\text{-}c}$), 6.25 (d, 1H, *J* = 7.6, H_g), 5.51 (s, 2H, H_j), 4.97 (m, 2H, H_h), 4.47 – 4.41 (m, 1H, H_e), 3.64 (s, 3H, H_f), 2.69 – 2.59 (m, 2H, H_d). ^{13}C NMR (101 MHz, $CDCl_3$) δ 170.1, 164.7, 163.4 (×2), 144.2, 144.1, 133.6, 132.5, 131.6, 131.2, 130.8, 130.6, 129.6, 129.2, 128.2, 127.1, 125.1, 123.0, 122.2, 67.2, 52.9, 52.6, 51.7, 35.3, 33.4. IR: (υ_{max}/cm^{-1}) 3055, 1744, 1702, 1662, 1588, 1432, 1342, 1234, 1177, 1046, 782, 699. HR-ESI MS (*m/z*) $[M+H]^+$ calcd for $C_{40}H_{33}BrN_5O_5S$ 774.1385, found 774.1404.

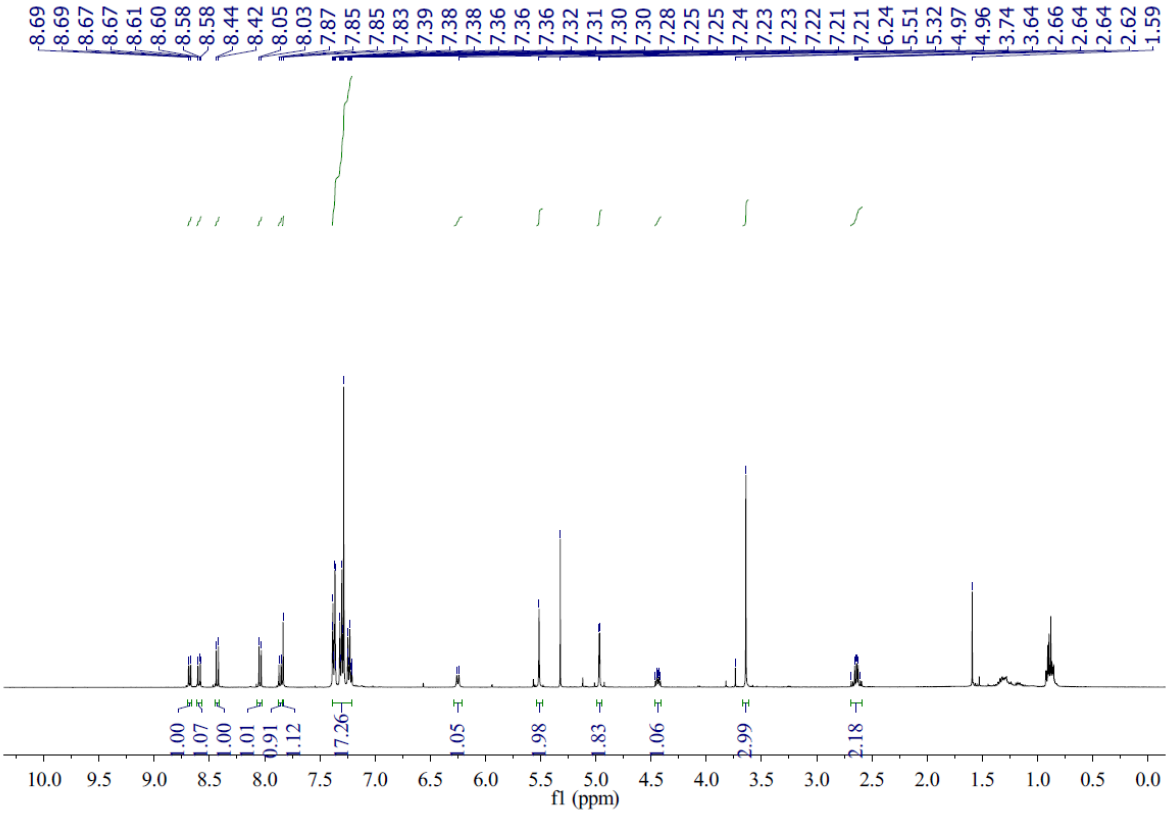
8.69 8.69 8.67 8.67 8.61 8.60 8.58 8.58 8.44 8.42 8.05 8.03 7.87 7.85 7.85 7.83 7.39 7.38 7.38 7.36 7.36 7.36 7.32 7.31 7.30 7.30 7.28 7.25 7.25 7.24 7.23 7.23 7.22 7.21 7.21 6.24 5.51 5.32 4.97 4.96 3.74 3.64 2.66 2.64 2.64 2.62 1.59
1.00 1.07 1.00 1.01 0.91 1.12 17.26 1.05 1.98 1.83 1.06 2.99 2.18
10.0 9.5 9.0 8.5 8.0 7.5 7.0 6.5 6.0 5.5 5.0 4.5 4.0 3.5 3.0 2.5 2.0 1.5 1.0 0.5 0.0
f1 (ppm)

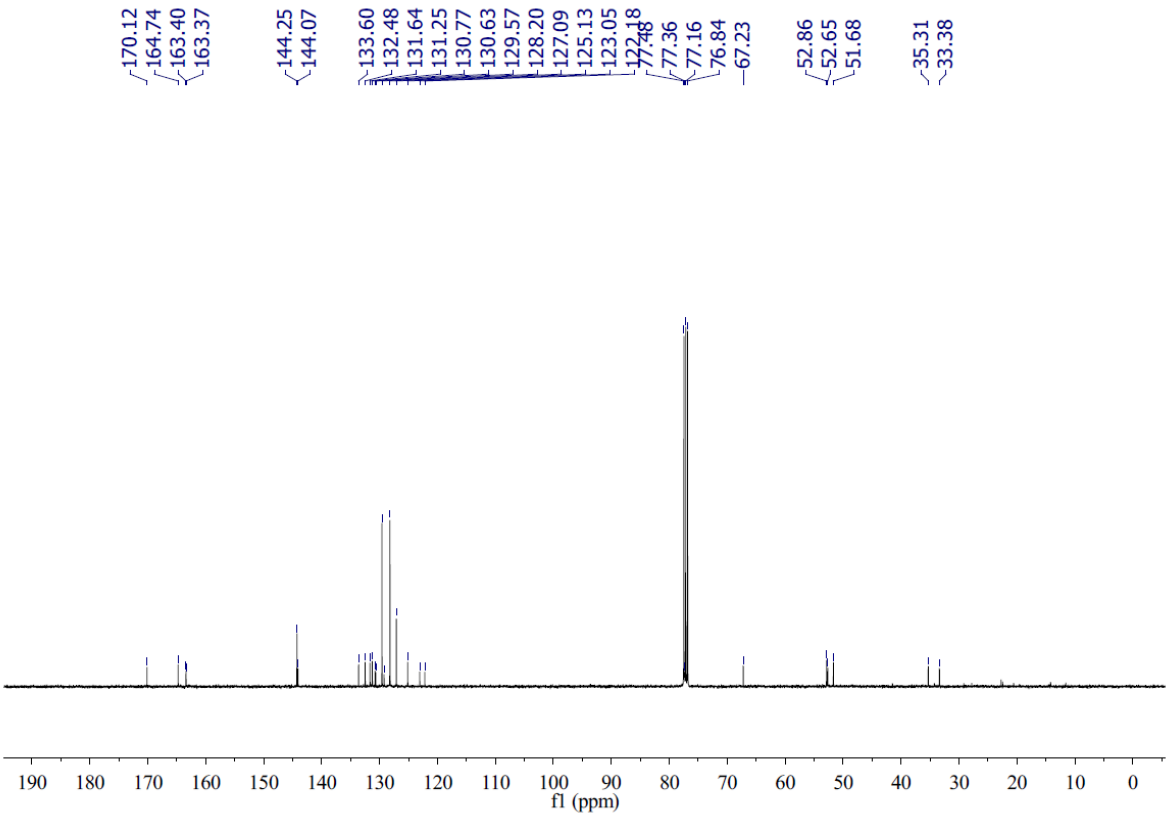
170.12 164.74 163.40 163.37 144.25 144.07 133.60 132.48 131.64 131.25 130.77 130.63 129.57 128.20 127.09 125.13 123.05 122.18 77.48 77.36 77.16 76.84 67.23 52.86 52.65 51.68 35.31 33.38
190 180 170 160 150 140 130 120 110 100 90 80 70 60 50 40 30 20 10 0
f1 (ppm)

Methyl *N*-(2-(4-((6-azido-1,3-dioxo-1*H*-benzo[*de*]isoquinolin-2(3*H*)-yl)methyl)-1*H*-1,2,3-triazol-1-yl)acetyl)-*S*-trityl-L-cysteinate (**76**)

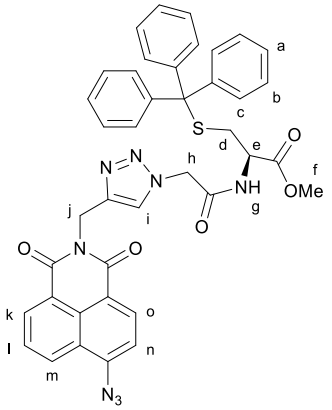

The compound **75** (157 mg, 0.202 mmol) was dissolved in DMF (2.0 mL) and NaN_3 (40.0 mg, 0.606 mol) was added to the solution. The mixture was stirred for 48 hours at room temperature. The reaction mixture was poured into water (20 mL) and the precipitate that formed was collected by filtration, washed with water (20 mL × 3) and dried *in vacuo* to obtain **76** (142 mg, 95%, M.p. 142-145 °C) as a yellow solid. ^{1}H NMR (400 MHz, $CDCl_3$) δ 8.51 (d, 1H, *J* = 6.6, H_k), 8.45 (d, 1H, *J* = 8.0, H_o), 8.31 (d, 1H, *J* = 8.4, H_m), 7.75 (s, 1H, H_i), 7.64 – 7.58 (m, 1H, H_l), 7.32 (d, 1H, *J* = 8.0, H_n), 7.28 – 7.09 (m, 15H, $H_{a\text{-}c}$), 6.44 (d, 1H, *J* = 7.6, H_g), 5.38 (s, 2H, H_j), 4.88 (d, 2H, *J* = 2.0, H_h), 4.38 – 4.30 (m, 1H, H_e), 3.53 (s, 3H, H_f), 2.61– 2.48 (m, 2H, H_d). ^{13}C NMR (101 MHz, $CDCl_3$) δ 170.2, 164.8, 163.7, 163.3, 144.2, 144.1, 143.8, 132.6, 132.1, 129.6, 129.3, 129.1, 128.2, 127.1, 127.0, 125.2, 124.4, 122.5, 118.7, 114.8, 67.2, 52.8, 52.6, 51.7, 35.2, 33.4. IR: (υ_{max}/cm^{-1}) 3322, 3063, 2959, 2123, 1745, 1695, 1659, 1583, 1440, 1344, 1286, 1237, 1178, 1032, 785, 699. HR-ESI MS (m/z) $[M+H]^+$ calcd for $C_{40}H_{33}N_8O_5S$ 737.2295, found 737.2239.

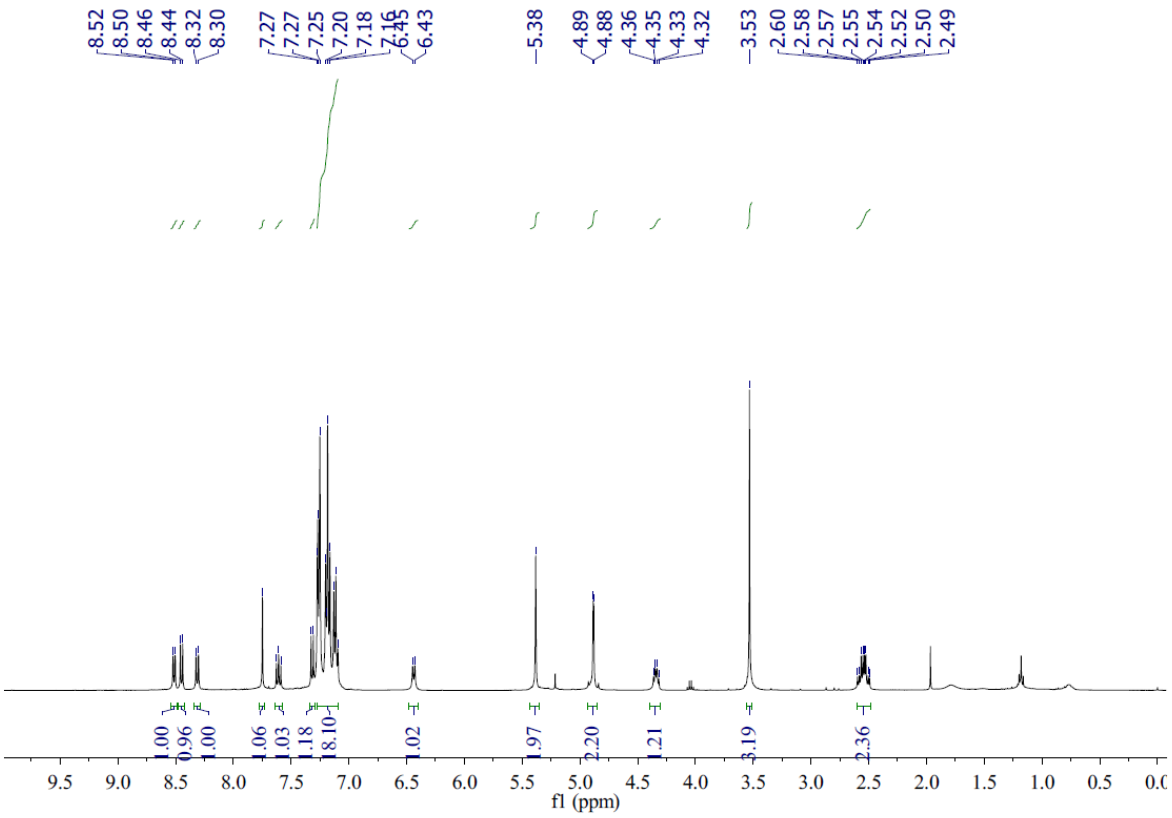
8.52
8.50
8.46
8.44
8.32
8.30
7.27
7.27
7.25
7.20
7.18
7.16
6.45
6.43
5.38
4.89
4.88
4.36
4.35
4.33
4.32
3.53
2.60
2.58
2.57
2.55
2.54
2.52
2.50
2.49
1.00
0.96
1.00
1.06
1.03
1.18
8.10
1.02
1.97
2.20
1.21
3.19
2.36
f1 (ppm)

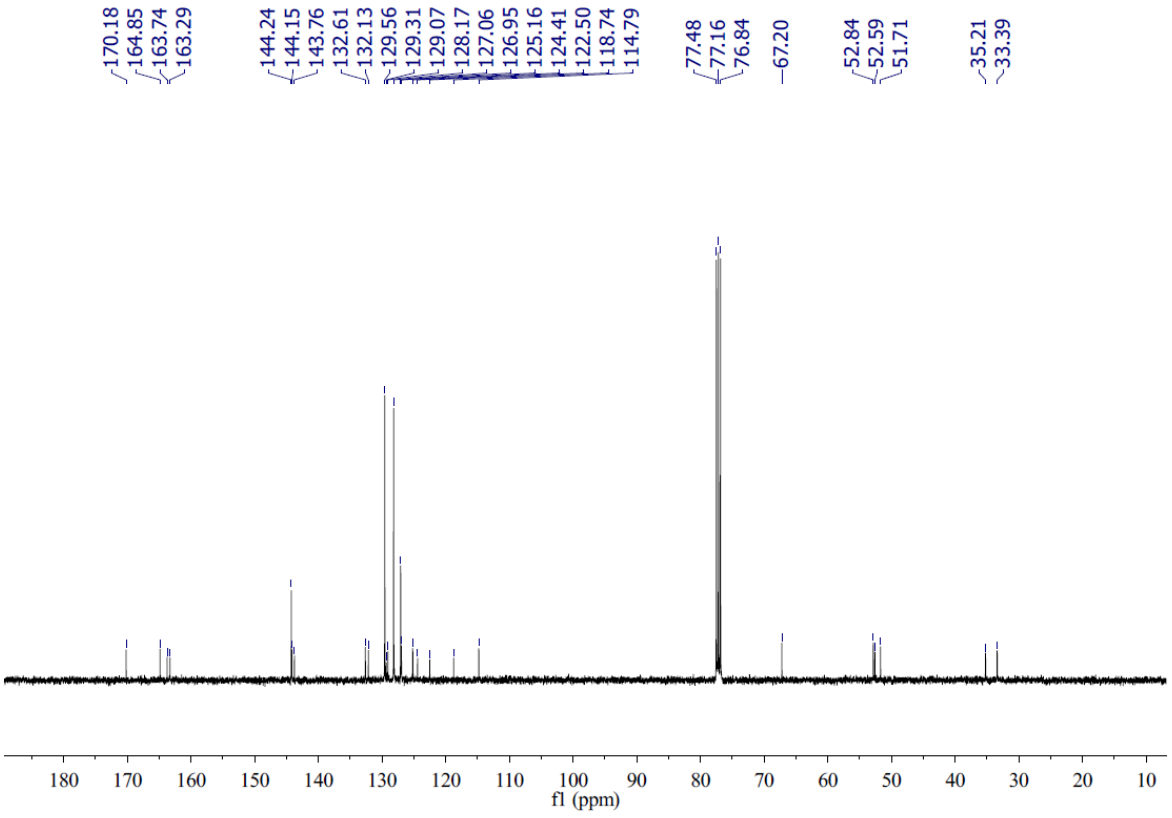
170.18
164.85
163.74
163.29
144.24
144.15
143.76
132.61
132.13
129.56
129.31
129.07
128.17
127.06
126.95
125.16
124.41
122.50
118.74
114.79
77.48
77.16
76.84
67.20
52.84
52.59
51.71
35.21
33.39
f1 (ppm)

Methyl N-(2-(4-((6-(4-((bis(pyridin-2-ylmethyl)amino)methyl)-1*H*-1,2,3-triazol-1-yl)-1,3-dioxo-1*H*-benzo[*de*]isoquinolin-2(3*H*)-yl)methyl)-1*H*-1,2,3-triazol-1-yl)acetyl)-*S*-trityl-L-cysteinate (**77**)

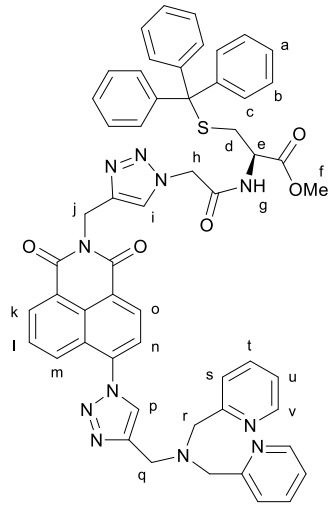

Under an atmosphere of nitrogen, **76** (110 mg, 0.150 mmol) and **54** (35.6 mg, 0.150 mmol) were dissolved in NMP (2.0 mL) and tetrakis(acetonitrile)copper(I) hexafluorophosphate (11.2 mg, 0.030 mmol) was added. The mixture was stirred at room temperature for 24 hours. After the reaction finished, saturated EDTA in 17% NH_3:H_2O (20 mL) was poured to the mixture and the precipitate was collected by filtration, and washed with water (30 mL). This crude product was purified by flash chromatography (eluent: DCM/MeOH 20:1) to give **77** as a brown solid (99.1 mg, 68%, M.p. 127-130 °C). ^{1}H NMR (400 MHz, $CDCl_3$) δ 8.58 – 8.52 (m, 2H, $H_{k,o}$), 8.46 (d, 2H, J = 4.2, H_v), 8.16 (d, 1H, J = 8.4, H_m), 8.11 (s, 1H, H_p), 7.80 (s, 1H, H_i), 7.71–7.64 (m, 2H, H_t), 7.62 – 7.57 (m, 2H, H_s), 7.55 – 7.57 (m, 2H, $H_{l,n}$), 7.28 – 7.06 (m, 17H, $H_{a\text{-}c,u}$), 6.70 (d, 1H, J = 7.5, H_g), 5.40 (s, 2H, H_j), 4.93 (s, 2H, H_h), 4.37 – 4.31 (m, 1H, H_e), 3.99 (s, 2H, H_q), 3.88 (s, 4H, H_r), 3.51 (s, 3H, H_f), 2.60 – 2.49 (m, 2H, H_d). ^{13}C NMR (101 MHz, $CDCl_3$) δ 170.2, 164.9, 163.4, 162.9, 159.0, 149.2, 145.1, 144.2, 143.7, 138.5, 136.7, 132.5, 131.1, 130.0, 129.5, 129.2, 128.6, 128.1, 127.0, 126.4, 125.8, 125.2, 123.5 (×2), 122.7, 122.3, 67.2, 59.9, 52.8, 52.5, 51.7, 48.6, 35.4, 33.4. IR: (υ_{max}/cm^{-1}) 3016, 2949, 1739, 1663, 1588, 1434, 1365, 1230, 1217,

1038, 996, 743, 699. HR-ESI MS (*m/z*) $[M+H]^+$ calcd for $C_{55}H_{48}N_{11}O_5S$ 974.3561, found 974.3483.

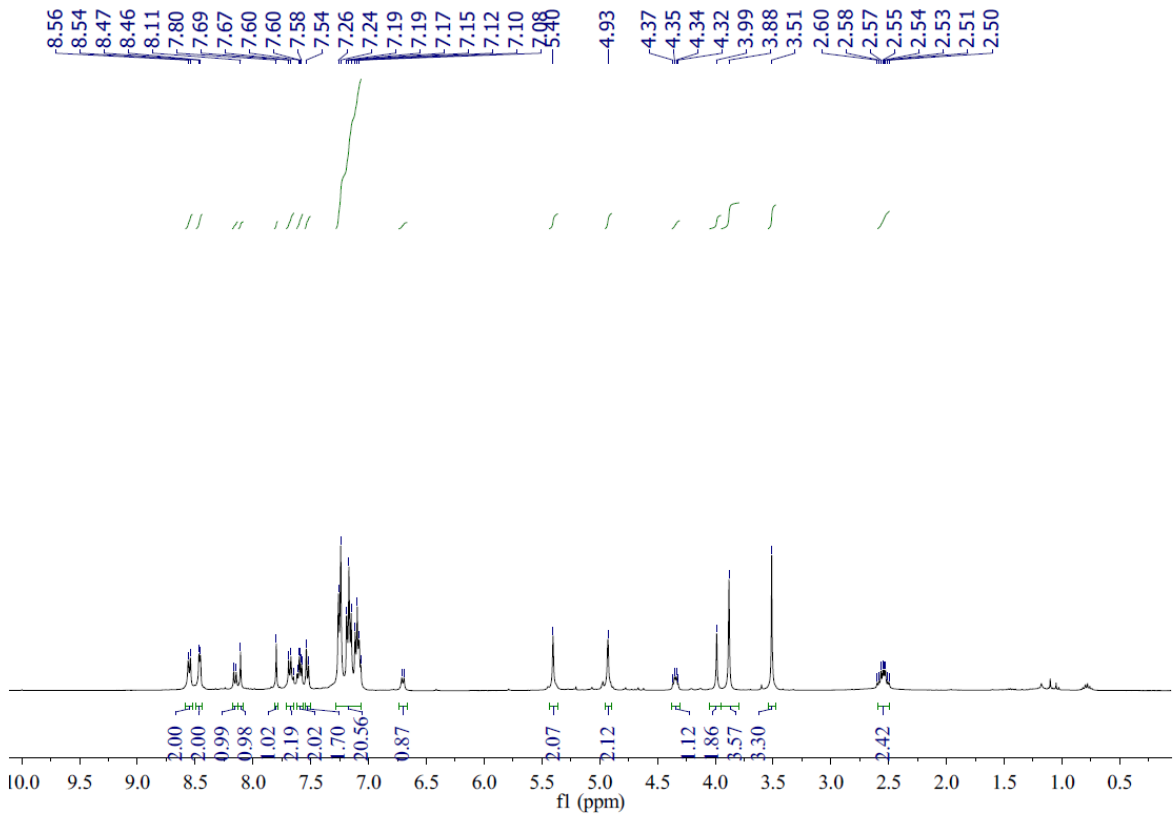
8.56
8.54
8.47
8.46
8.11
7.80
7.69
7.67
7.60
7.60
7.58
7.54
7.26
7.24
7.19
7.17
7.15
7.12
7.10
7.08
5.40
4.93
4.37
4.35
4.34
4.32
3.99
3.88
3.51
2.60
2.58
2.57
2.55
2.54
2.53
2.51
2.50
2.00
2.00
0.99
0.98
1.02
2.19
2.02
1.70
20.56
0.87
2.07
2.12
1.12
1.86
3.57
3.30
2.42
f1 (ppm)

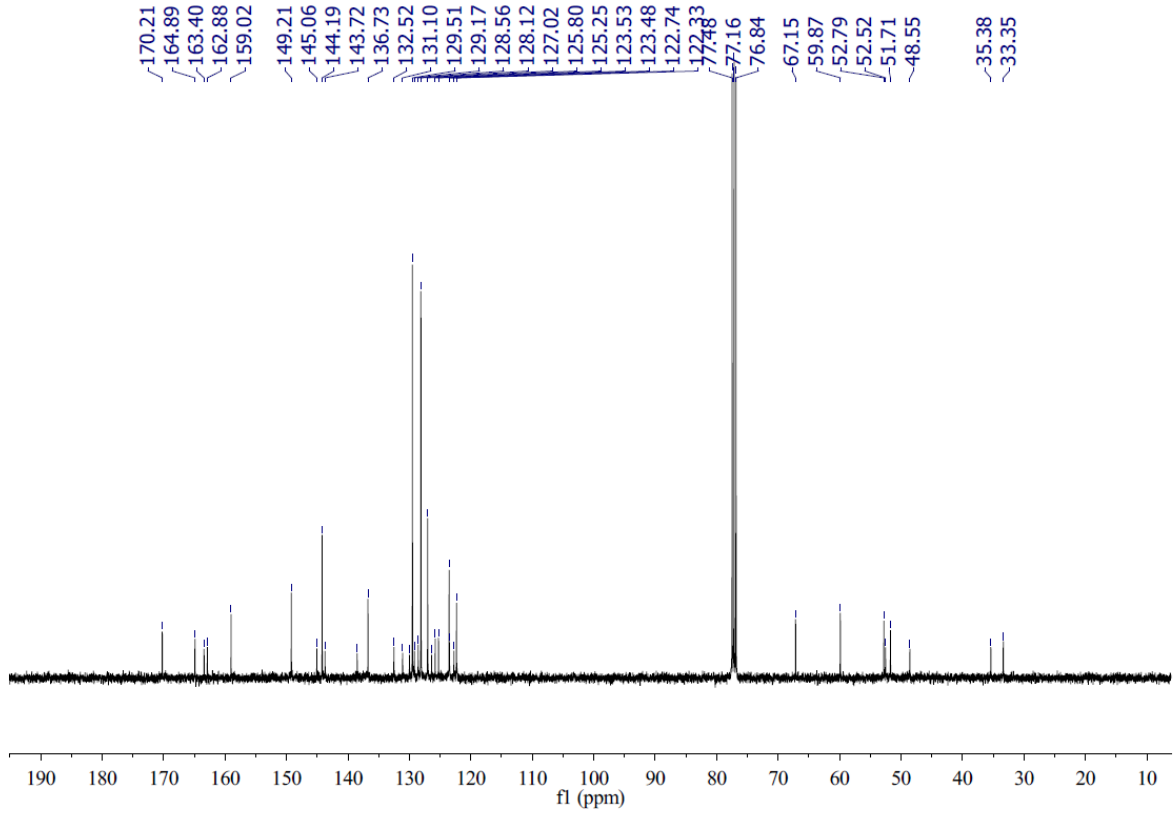
170.21
164.89
163.40
162.88
159.02
149.21
145.06
144.19
143.72
136.73
132.52
131.10
129.51
129.17
128.56
128.12
127.02
125.80
125.25
123.53
123.48
122.74
122.33
77.48
77.16
76.84
67.15
59.87
52.79
52.52
51.71
48.55
35.38
33.35
f1 (ppm)

Methyl (2-(4-((6-(4-((bis(pyridin-2-ylmethyl)amino)methyl)-1*H*-1,2,3-triazol-1-yl)-1,3-dioxo-1*H*-benzo[*de*]isoquinolin-2(3*H*)-yl)methyl)-1*H*-1,2,3-triazol-1-yl)acetyl)-L-cysteinate (**78**)

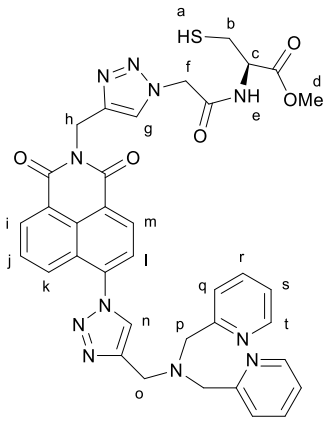

To a stirred solution of **77** (48.7 mg, 0.050 mmol) in CH_2Cl_2 (1.0 mL) at 0 °C was added trimethylsilane (35 µL, 0.025 mmol) and trifluoroacetic acid (35 µL, 0.050 mmol) and the resultant solution was stirred at room temperature overnight. After the reaction had finished, solid $NaHCO_3$ (42 mg, 0.50 mmol) was added and the mixture stirred for 10 minutes. The solution was then filtered and the collected solids washed with CH_2Cl_2 (3 mL × 3). The solid was then suspended in MeCN (10 mL) and stirred for 10 minutes, filtered and the filtrate was concentrated *in vacuo* to obtain **78** as a yellow solid (18.6 mg, 51%, M.p. 127-130 °C). ^{1}H NMR (400 MHz, $CDCl_3$: CD_3CN = 1:1) δ 8.66 – 8.60 (m, 2H, $H_{i,m}$), 8.55 (d, 2H, J = 4.2, H_t), 8.32 (s, 1H, H_n), 8.19 (d, 1H, J = 8.0, H_k), 7.86 (s, 1H, H_g), 7.85 – 7.76 (m, 4H, $H_{j,l,r}$), 7.63 (d, 2H, J = 7.8, H_q), 7.34 – 7.25 (m, 3H, $H_{e,s}$), 5.43 (s, 2H, H_h), 5.11 (d, 2H, J = 1.4, H_f), 4.70 – 4.64 (m, 1H, H_c), 4.09 (s, 2H, H_o), 4.06 (s, 4H, H_p), 3.67 (s, 3H, H_d), 2.92 – 2.86 (bs, 2H, H_b). ^{13}C NMR (101 MHz, $CDCl_3$: CD_3CN = 1:1) δ 171.3, 168.0, 166.8, 164.7, 164.2, 159.1, 149.6, 145.5, 144.9, 139.8, 139.3, 133.6, 132.3, 131.3, 130.4, 130.0, 128.0, 126.6, 125.4, 125.2, 124.3, 124.1, 60.4, 55.8, 54.0, 53.6, 50.1, 36.8, 27.6. IR: (υ_{max}/cm^{-1}) 3458, 3016, 1741, 1662, 1588, 1432, 1369, 1229, 1216, 1120, 1042, 996, 784, 765. HR-ESI MS (*m/z*) $[M+H]^+$ calcd for $C_{36}H_{34}N_{11}O_5S$ 732.2465, found 732.2415.

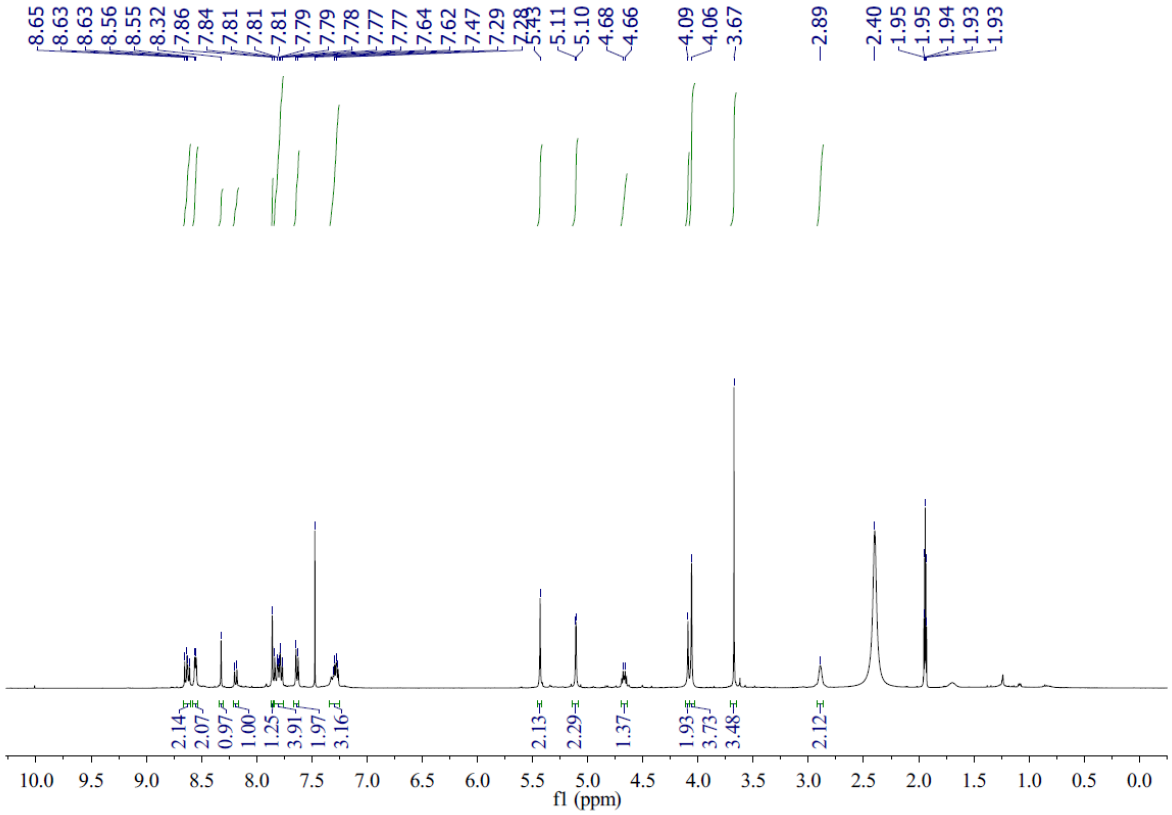
8.65
8.63
8.63
8.56
8.55
8.32
7.86
7.84
7.81
7.81
7.81
7.79
7.79
7.78
7.77
7.77
7.64
7.62
7.47
7.29
5.43
5.11
5.10
4.68
4.66
4.09
4.06
3.67
2.89
2.40
1.95
1.95
1.94
1.93
1.93
2.14
2.07
0.97
1.00
1.25
3.91
1.97
3.16
2.13
2.29
1.37
1.93
3.73
3.48
2.12
10.0 9.5 9.0 8.5 8.0 7.5 7.0 6.5 6.0 5.5 5.0 4.5 4.0 3.5 3.0 2.5 2.0 1.5 1.0 0.5 0.0
f1 (ppm)

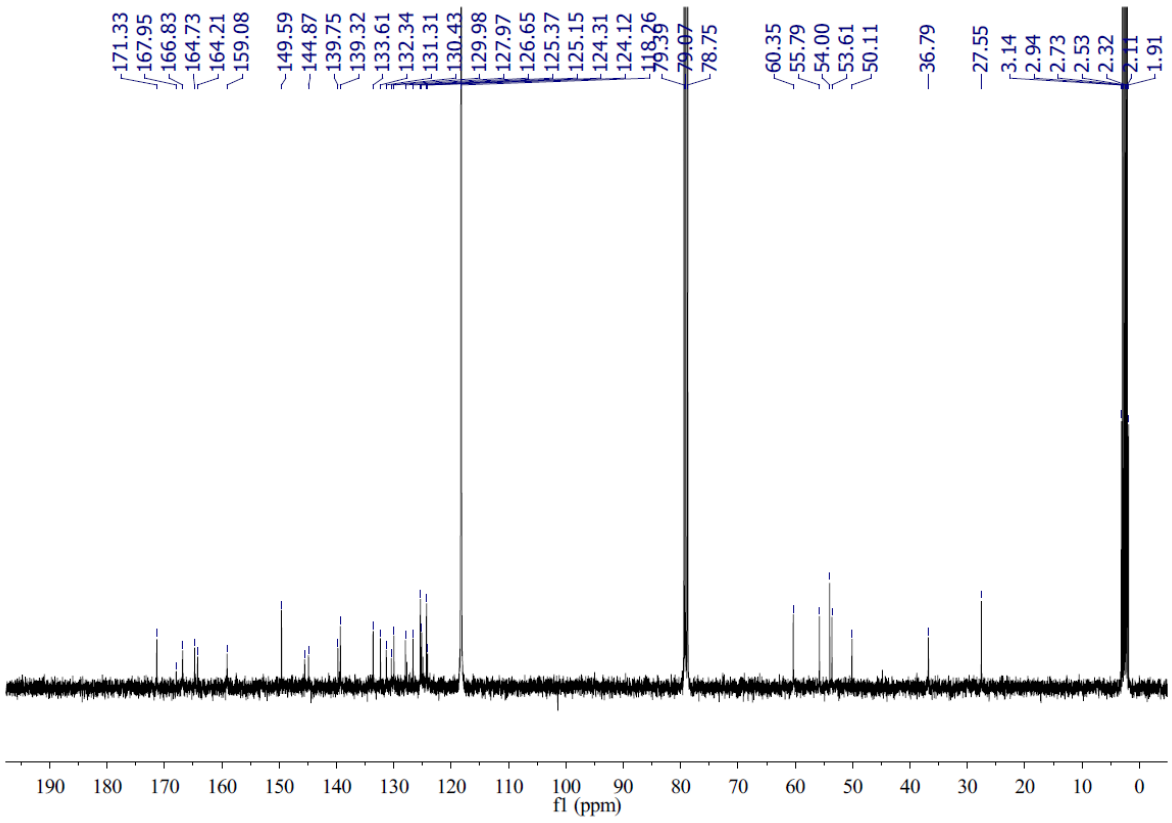
171.33
167.95
166.83
164.73
164.21
159.08
149.59
144.87
139.75
139.32
133.61
132.34
131.31
130.43
129.98
127.97
126.65
125.37
125.15
124.31
124.12
118.26
79.39
79.07
78.75
60.35
55.79
54.00
53.61
50.11
36.79
27.55
3.14
2.94
2.73
2.53
2.32
2.11
1.91
190 180 170 160 150 140 130 120 110 100 90 80 70 60 50 40 30 20 10 0
f1 (ppm)

2-Azidoethan-1-amine (**79**)

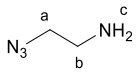

To a solution of 2-chloroethanamine hydrochloride (400 mg, 3.44 mmol) in H_2O (4.0 mL) wad added NaN_3 (672 mg, 10.36 mmol) at room temperature. After stirring at 80 °C for 24 h, the reaction was quenched with aqueous KOH solution (15%, 1.0 mL). Then the aqueous layer was extracted with diethyl ether (3 × 20 mL), the organic layers were combined and washed with brine (10 mL), dried over anhydrous $MgSO_4$, filtered and concentrated *in vacuo* to give **79** as a colourless oil (265 mg, 90 %). ^{1}H NMR (400 MHz, $CDCl_3$) δ 3.36 (t, 2H, J = 5.7, H_a), 2.90-2.85 (m, 2H, H_b), 1.49-1.41 (bs, 2H, H_c). All other spectroscopic data were consistent with those previously reported.[151]

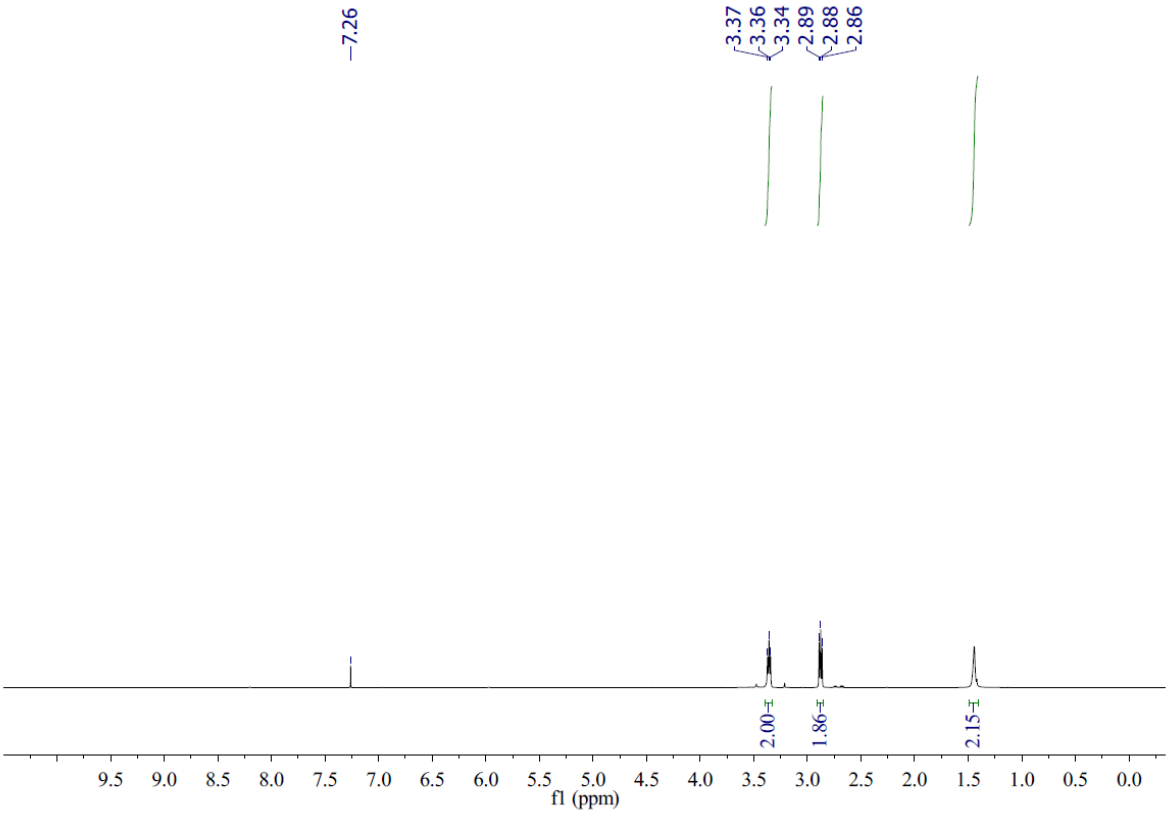
7.26
3.37
3.36
3.34
2.89
2.88
2.86
2.00
1.86
2.15
9.5 9.0 8.5 8.0 7.5 7.0 6.5 6.0 5.5 5.0 4.5 4.0 3.5 3.0 2.5 2.0 1.5 1.0 0.5 0.0
f1 (ppm)

N-(2-Azidoethyl)-4-methylbenzenesulfonamide **(80)**

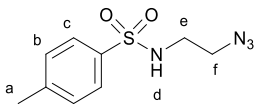

To a solution of **79** (265 mg, 3.08 mmol) in CH_2Cl_2 (4.0 mL), the 4-toluenesulfonyl chloride (587 mg, 3.08 mmol) was added at room temperature. The reaction mixture was stirred at the same temperature for 2 h and concentrated *in vacuo*. The residue was purified with flash column chromatography (petroleum ether: ethyl acetate = 5:1) to give **80** as a white solid (688 mg, 93 %, M.p. 67-69 °C). ^{1}H NMR (400 MHz, $CDCl_3$) δ 7.76 (d, 2H, *J* = 8.3, H_c), 7.32 (d, 2H, *J* = 8.3, H_b), 5.06 (t, 1H, *J* = 5.9, H_d), 3.39 (t, 2H, *J* = 5.9 Hz, H_f), 3.14-3.06 (m, 2H, H_e), 2.43 (s, 3H, H_a). ^{13}C NMR (101 MHz, $CDCl_3$) δ 143.9, 136.9, 130.0, 127.2, 51.0, 42.4, 21.6. IR: (υ_{max}/cm^{-1}) 3265, 2102, 1598, 1417, 1304, 1157, 1085, 939, 811, 685. HR-ESI MS (*m/z*) $[M-H]^-$ calcd for $C_9H_{11}N_4O_2S$ 239.0603, found 239.0621.

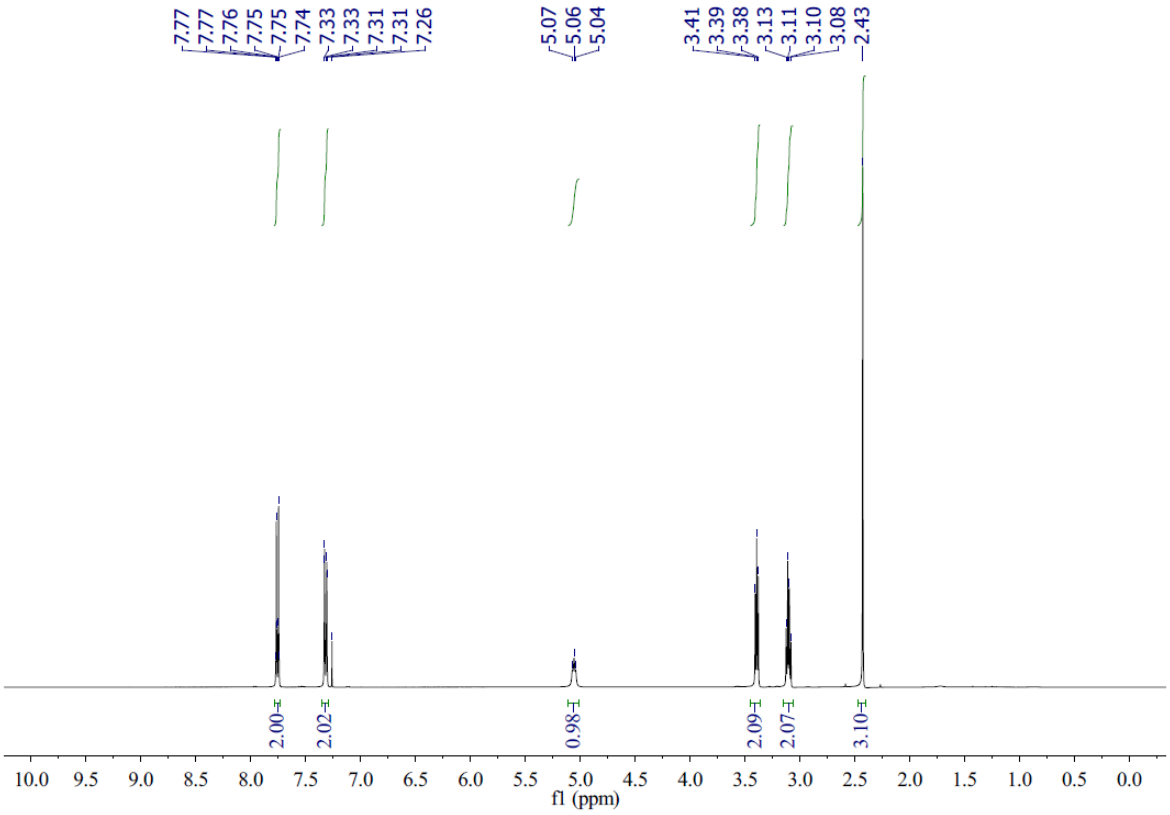
7.77
7.77
7.76
7.75
7.75
7.74
7.33
7.33
7.31
7.31
7.26
5.07
5.06
5.04
3.41
3.39
3.38
3.13
3.11
3.10
3.08
2.43
2.00
2.02
0.98
2.09
2.07
3.10
f1 (ppm)

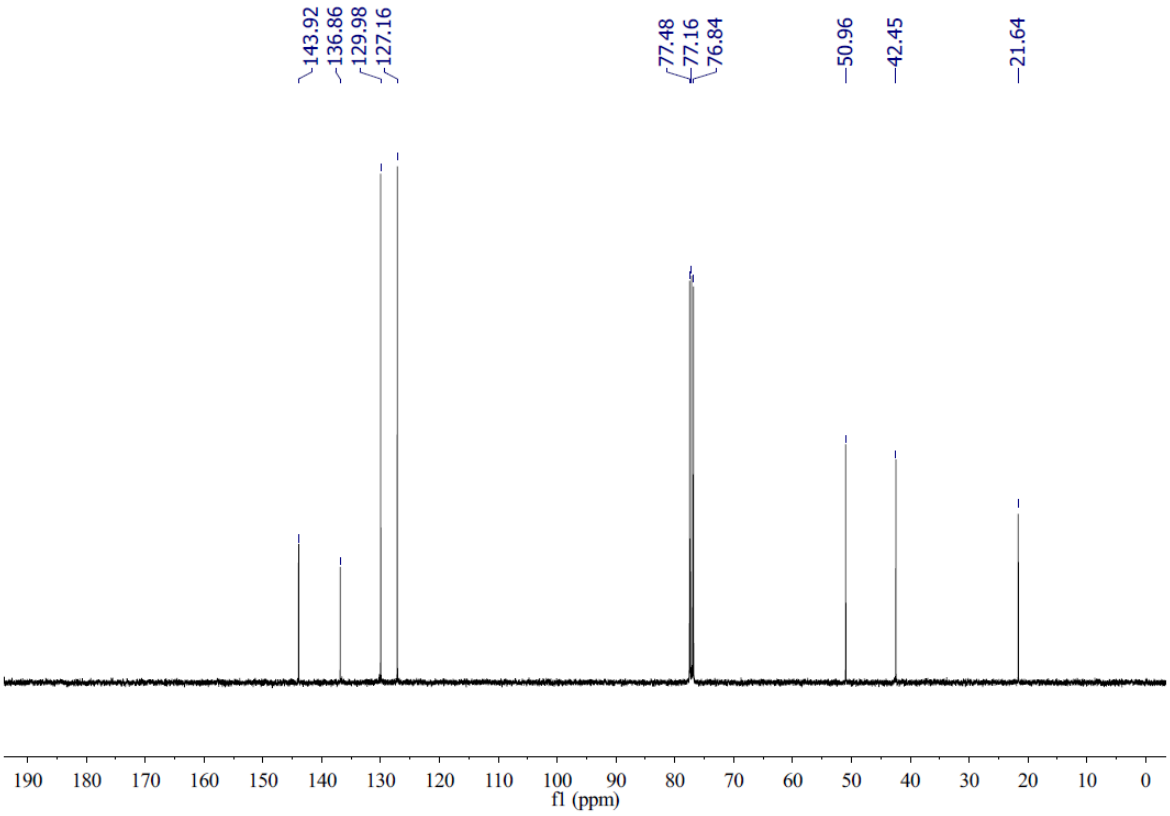
143.92
136.86
129.98
127.16
77.48
77.16
76.84
50.96
42.45
21.64
f1 (ppm)

(4-Azidobutyl)triphenylphosphonium bromide (**81**)

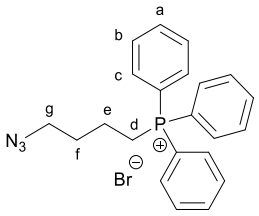

A solution of sodium azide (0.14 g, 2.20 mmol) and (4-bromobutyl)triphenylphosphonium bromide (0.96 g, 2.00 mmol) in EtOH/H_2O (1:1, 20 mL) was heated at reflux under N_2 overnight. The mixture was cooled and the solvent was evaporated under reduced pressure to afford a yellow oil. To the oil was added H_2O (2.0 mL) and the precipitate formed was collected by filtration and washed with water, dried *under vacuum* to afford **81** as a white solid (0.85 g, 87%). ^{1}H NMR (400 MHz, $CDCl_3$) δ 7.97-7.67 (m, 15H, $H_{a\text{-}c}$), 4.08-3.97 (m, 2H, H_d), 3.52-3.42 (m, 2H, H_g), 2.13-2.02 (m, 2H, H_e), 1.83-1.71 (m, 2H, H_f). ^{13}C NMR (101 MHz, $CDCl_3$) δ 135.1 (d, *J* = 3.0), 133.7 (d, *J* = 10.0), 130.6 (d, *J* = 12.6), 118.2 (d, *J* = 86.2), 50.7, 29.2 (d, *J* = 16.7), 22.3 (d, *J* = 50.8), 19.9 (d, *J* = 4.0). All other spectroscopic data were consistent with those previously reported.[152]

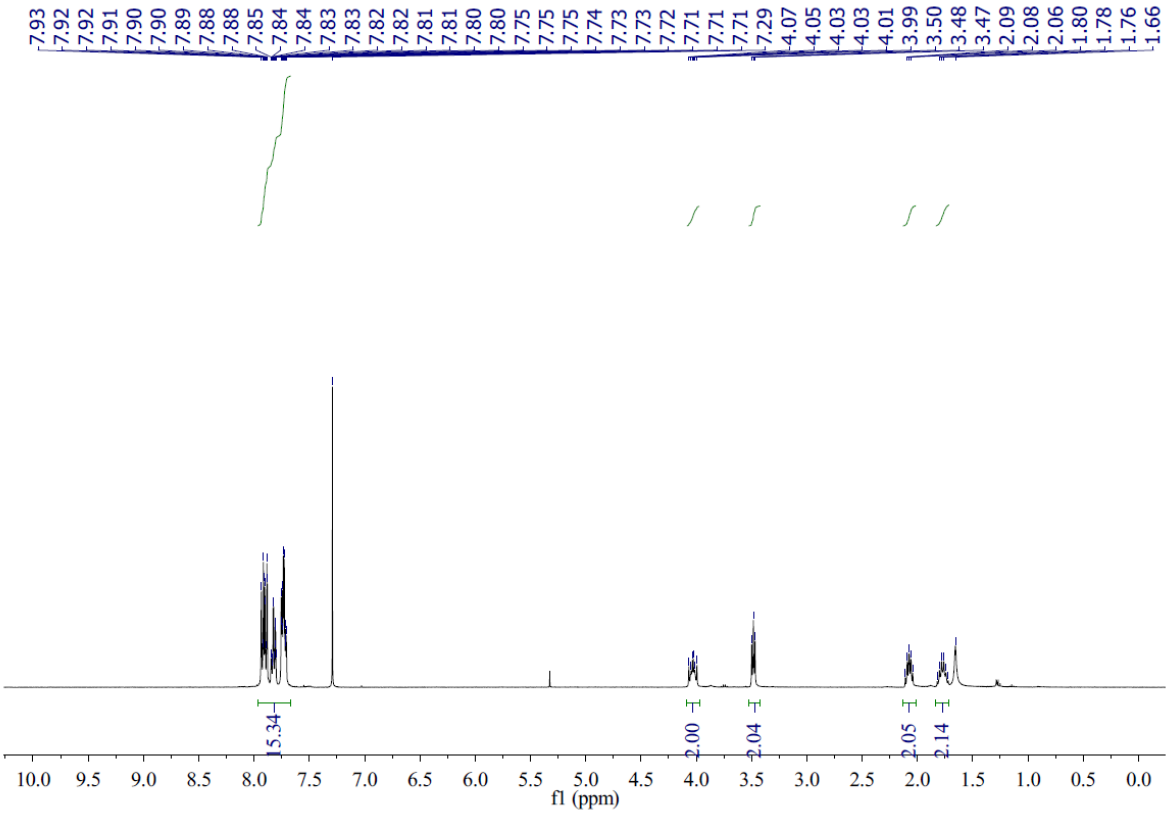
7.93 7.92 7.92 7.91 7.90 7.90 7.89 7.88 7.88 7.85 7.84 7.84 7.83 7.83 7.82 7.82 7.81 7.81 7.80 7.80 7.75 7.75 7.75 7.74 7.73 7.73 7.72 7.71 7.71 7.71 7.29 4.07 4.05 4.03 4.01 3.99 3.50 3.48 3.47 2.09 2.08 2.06 1.80 1.78 1.76 1.66
15.34
2.00
2.04
2.05
2.14
10.0 9.5 9.0 8.5 8.0 7.5 7.0 6.5 6.0 5.5 5.0 4.5 4.0 3.5 3.0 2.5 2.0 1.5 1.0 0.5 0.0
f1 (ppm)

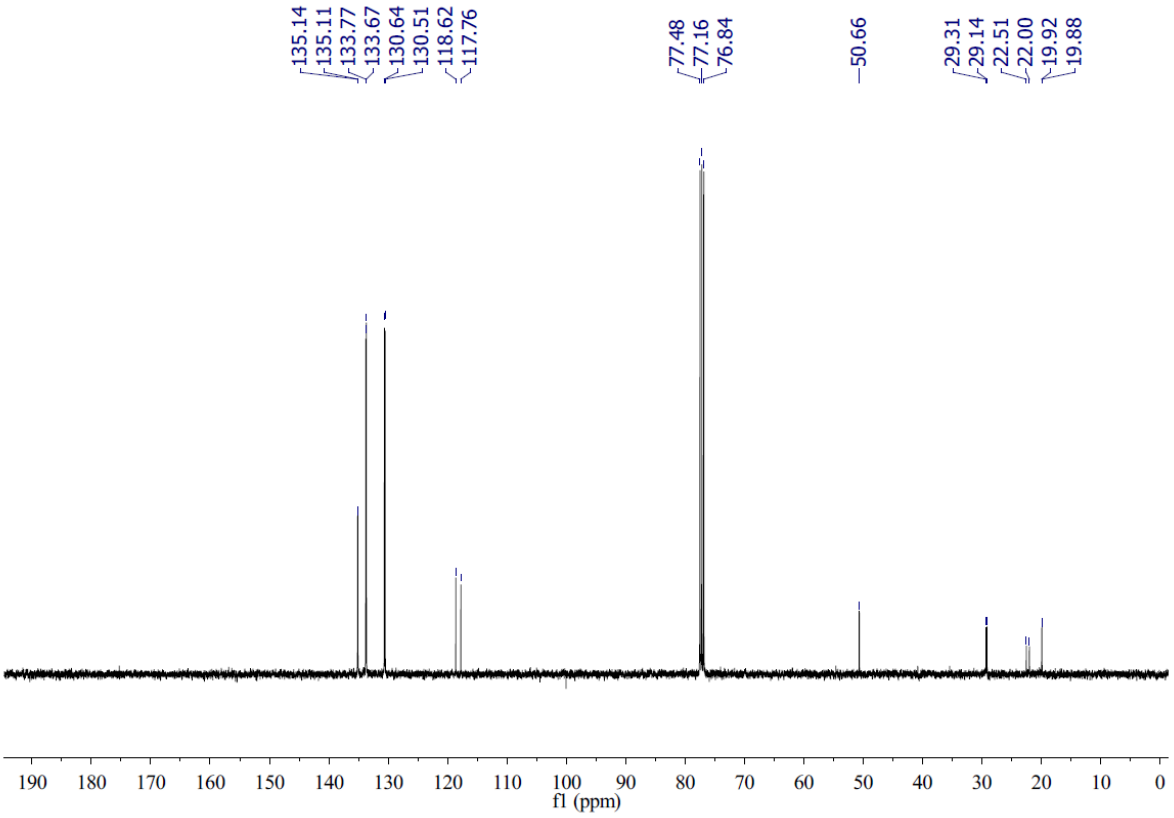
135.14 135.11 133.77 133.67 130.64 130.51 118.62 117.76
77.48 77.16 76.84
50.66
29.31 29.14 22.51 22.00 19.92 19.88
190 180 170 160 150 140 130 120 110 100 90 80 70 60 50 40 30 20 10 0
f1 (ppm)

(4-Azidobutyl)triphenylphosphonium tetrafluoroborate **(82)**

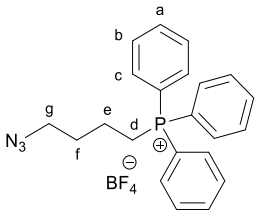

Compound **81** (2.27 g, 5.15 mmol) was dissolved in CH_2Cl_2 (40 mL). This solution was thoroughly washed with a saturated aqueous solution of ammonium tetrafluoroborate (3 × 50 mL). The organic phase was dried over $MgSO_4$ and the solvent was removed *in vacuo* to yield tetrafluoroborate **82** as a white solid (2.18 g, 95%).^{1}H NMR (400 MHz, $CDCl_3$) δ 7.81-7.64 (m, 15H, $H_{a\text{-}c}$), 3.38-3.22 (m, 4H, $H_{d,g}$), 1.89-1.79 (m, 2H, H_e), 1.74-1.63 (m, 2H, H_f). ^{13}C NMR (101 MHz, $CDCl_3$) δ 135.3 (d, *J* = 3.0), 133.4 (d, *J* = 9.9), 130.6 (d, *J* = 12.6), 117.9 (d, *J* = 86.4), 50.4, 29.1 (d, *J* = 16.9), 21.4 (d, *J* = 52.0), 19.8 (d, *J* = 3.8). ^{31}P NMR (162 MHz, $CDCl_3$) δ 23.64. ^{19}F NMR (377 MHz, $CDCl_3$) δ -152.16 (d, *J* = 19.8). All other spectroscopic data were consistent with those previously reported.[25]

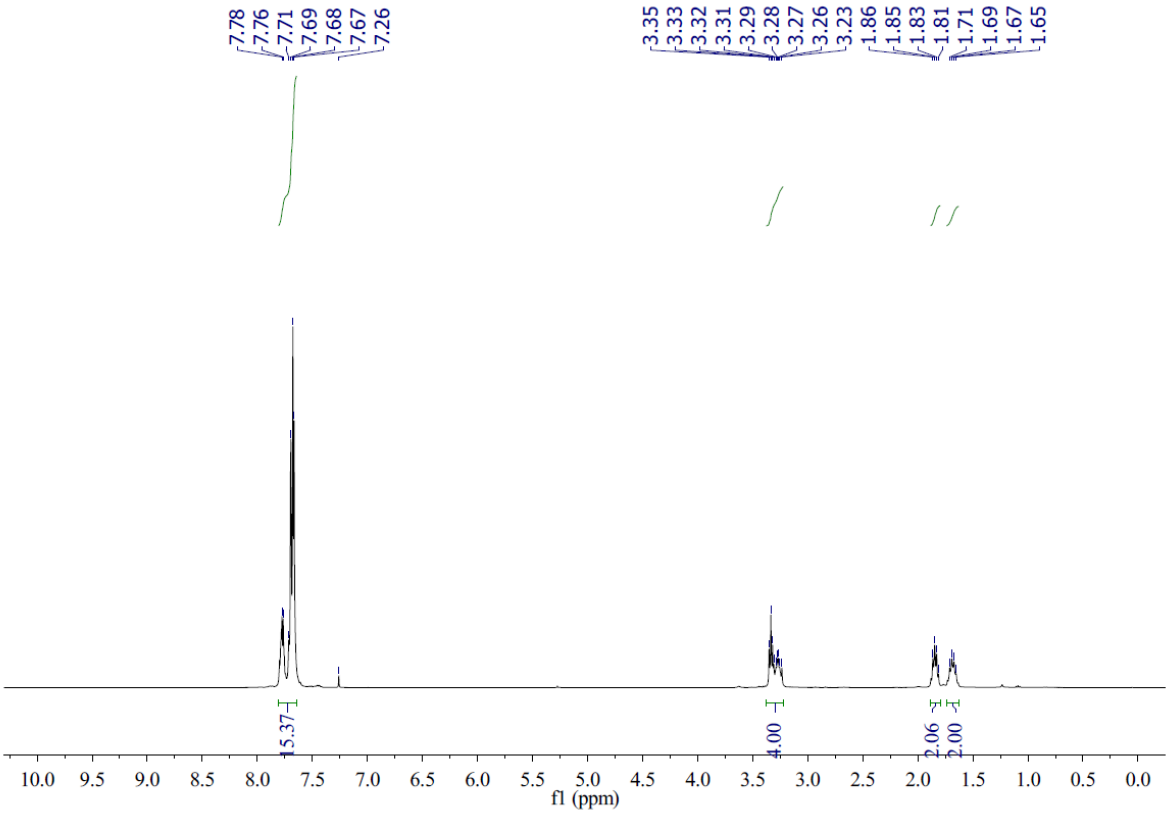
7.78
7.76
7.71
7.69
7.68
7.67
7.26
3.35
3.33
3.32
3.31
3.29
3.28
3.27
3.26
3.23
1.86
1.85
1.83
1.81
1.71
1.69
1.67
1.65
15.37
4.00
2.06
2.00
10.0 9.5 9.0 8.5 8.0 7.5 7.0 6.5 6.0 5.5 5.0 4.5 4.0 3.5 3.0 2.5 2.0 1.5 1.0 0.5 0.0
f1 (ppm)

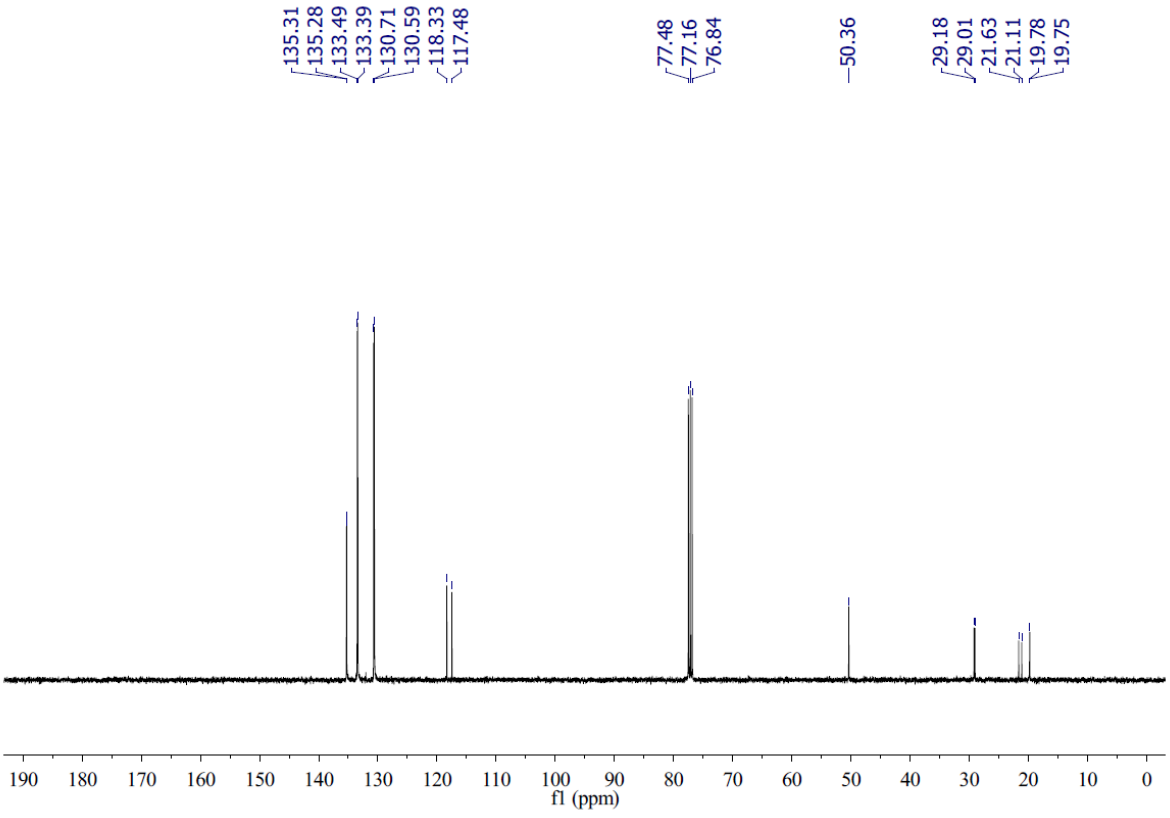
135.31
135.28
133.49
133.39
130.71
130.59
118.33
117.48
77.48
77.16
76.84
50.36
29.18
29.01
21.63
21.11
19.78
19.75
190 180 170 160 150 140 130 120 110 100 90 80 70 60 50 40 30 20 10 0
f1 (ppm)

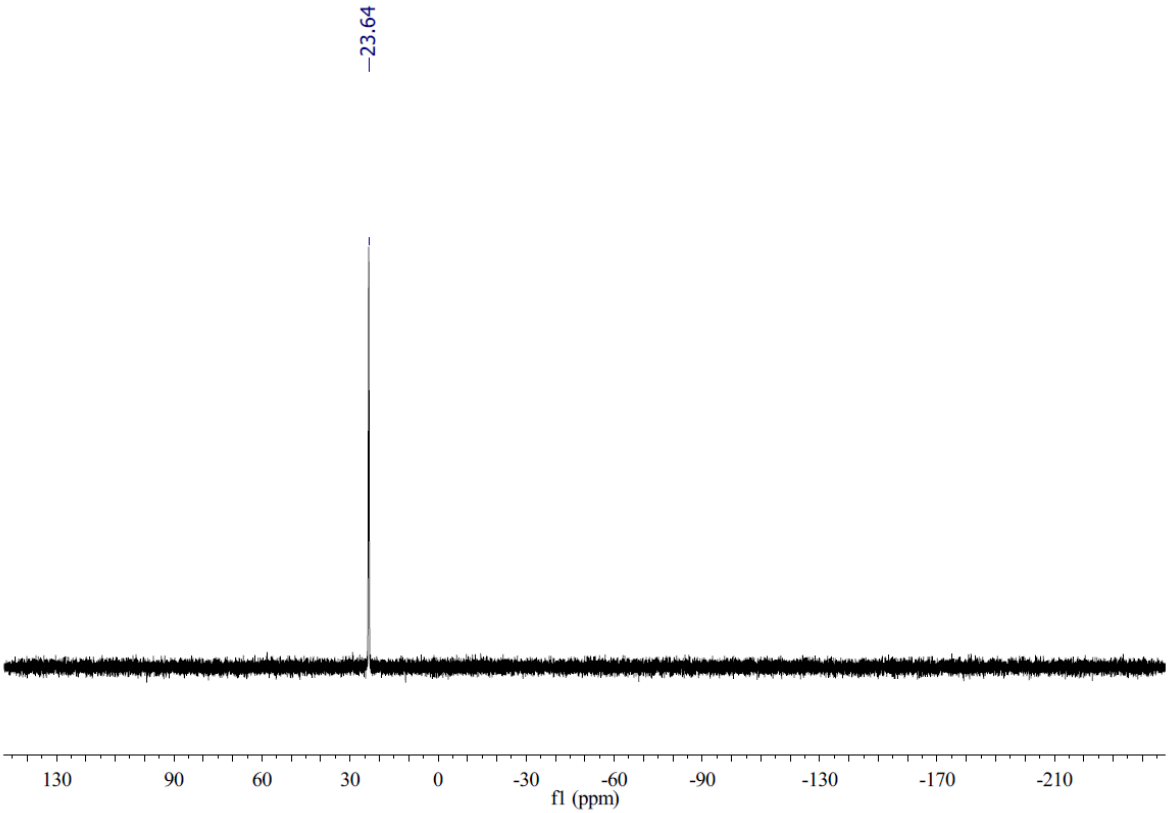
-23.64
130
90
60
30
0
-30
-60
-90
-130
-170
-210
f1 (ppm)

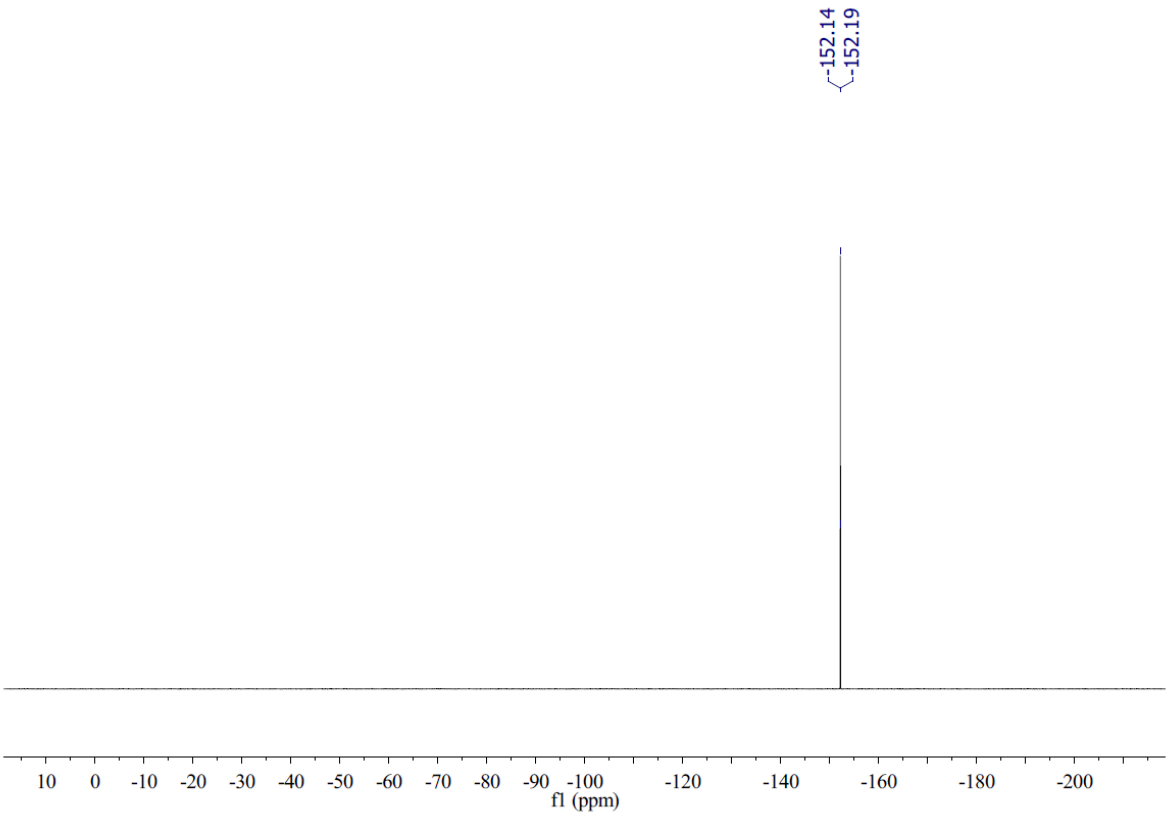
-152.14
-152.19
10
0
-10
-20
-30
-40
-50
-60
-70
-80
-90
-100
-120
-140
-160
-180
-200
f1 (ppm)

2-Chloro-*N*-(2-(dimethylamino)ethyl)acetamide hydrochloride (**83**)

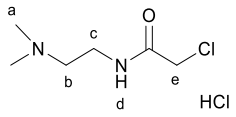

Chloroacetyl chloride (2.26 g, 20 mmol) in ethyl acetate (50 mL) was cooled in an ice/water bath to 0 °C and a solution of *N*,*N*-dimethylethylenediamine (1.77 g, 20 mmol) in ethyl acetate (50 mL) was added drop wise. The reaction was stirred at 0 °C for 1 h under nitrogen. The precipitate formed was collected by filtration, washed with diethyl ether and then dried *in vacuo* to yield the product in its hydrochloride form **83** (2.90 g, 72 %) as a white powder. ^{1}H NMR (400 MHz, DMSO-d_6) δ 8.72-8.64 (bs, 1H, H_d), 4.13 (s, 2H, H_e), 3.50-3.44 (m, 2H, H_c), 3.15 (t, 2H, J = 6.2, H_b), 2.76 (s, 6H, H_a). ^{13}C NMR (101 MHz, $CDCl_3$) δ 167.1, 55.8, 43.2, 42.7, 34.7. All other spectroscopic data were consistent with those previously reported.[153]

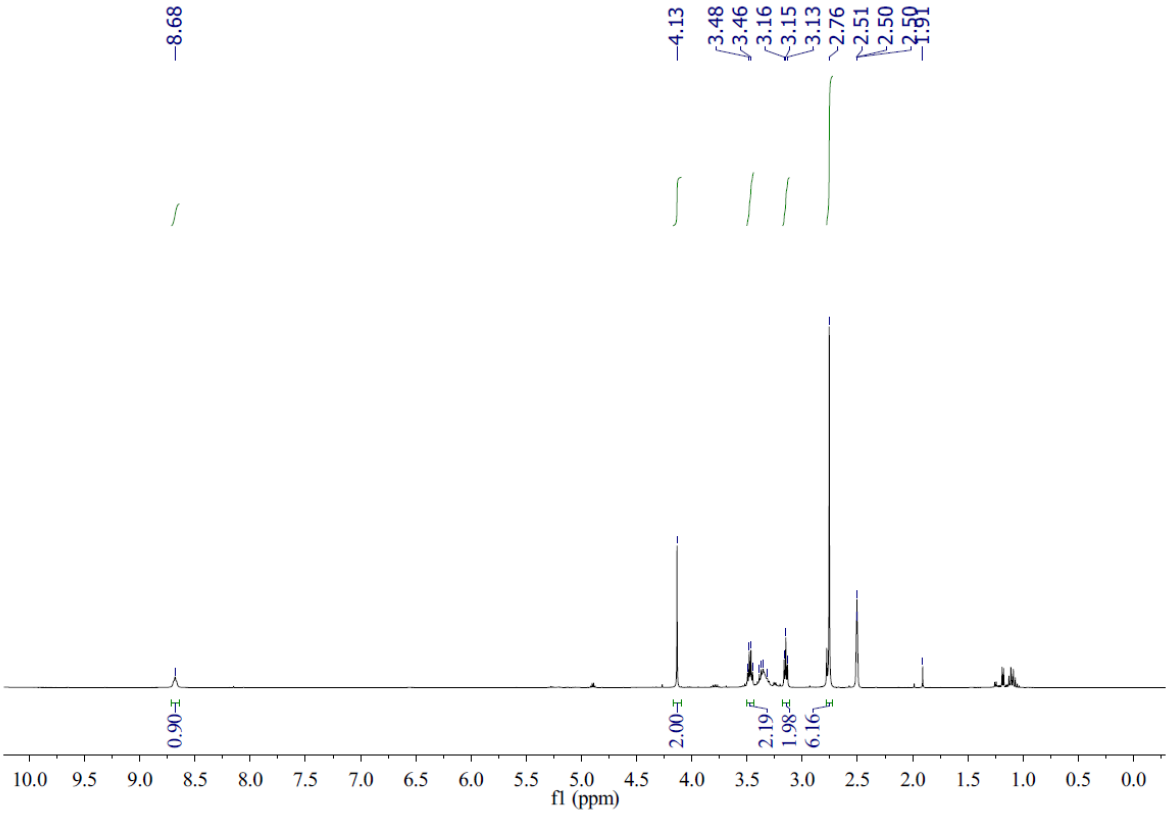
8.68
4.13
3.48
3.46
3.16
3.15
3.13
2.76
2.51
2.50
2.50
1.91
0.90
2.00
2.19
1.98
6.16
f1 (ppm)

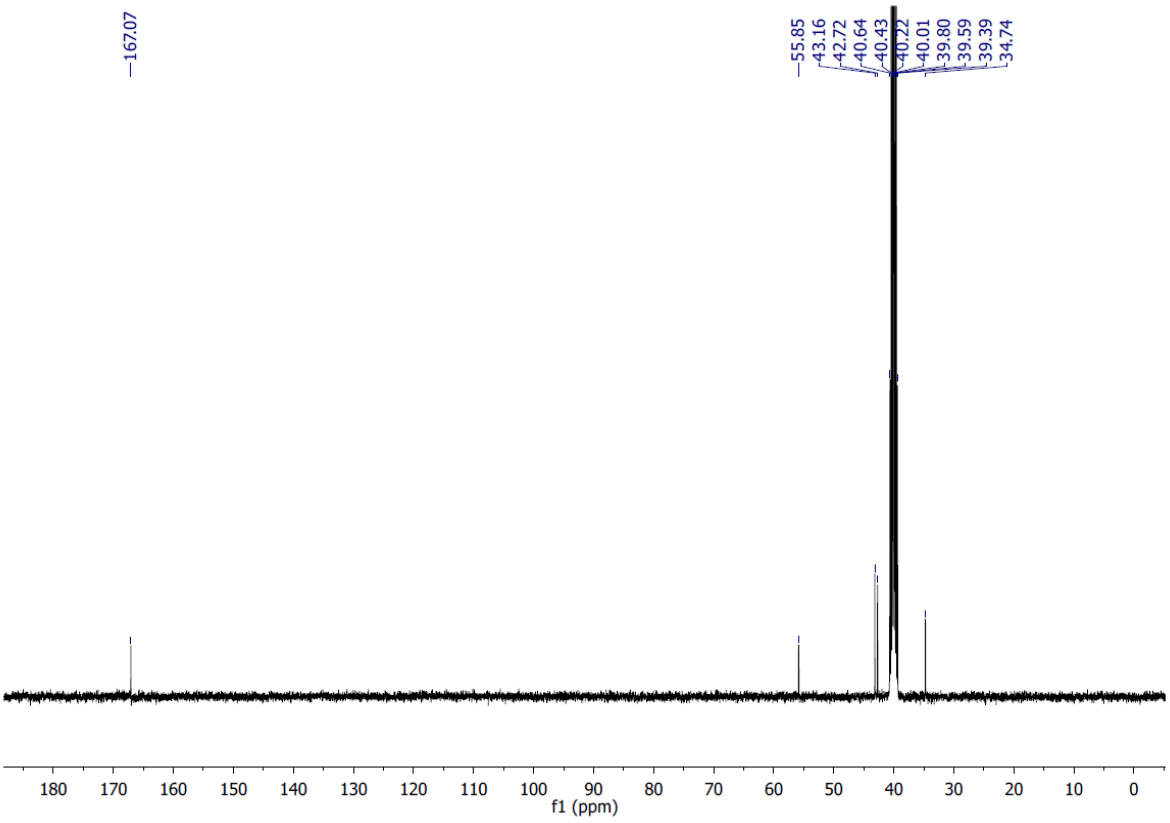
167.07
55.85
43.16
42.72
40.64
40.43
40.22
40.01
39.80
39.59
39.39
34.74
f1 (ppm)

2-Azido-*N*-(2-(dimethylamino)ethyl)acetamide **(84)**

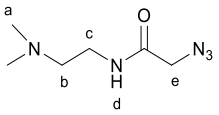

Compound **83** (1.01 g, 5.0 mmol) was dissolved in H_2O (25 mL), NaN_3 (1.96 g, 30 mmol) was added to the flask, and the reaction mixture stirred for 48 h at 65 °C. After cooling, the solution was adjusted to pH 10 using saturated aqueous $NaHCO_3$ and extracted with EtOAc (3 × 20 mL). The remaining aqueous layer was adjusted to pH 14 with aqueous NaOH (1.0 M), and extracted with EtOAc (3 × 20 mL). All organic extracts were combined, dried over $MgSO_4$ and the solvent was removed *in vacuo* to give azide **84** as a pale-yellow oil (0.71 g, 83%). ^{1}H NMR (400 MHz, $CDCl_3$) δ 6.91-6.65 (bs, 1H, H_d), 3.91 (s, 2H, H_e), 3.34-3.26 (m, 2H, H_c), 2.41-2.34 (m, 2H, H_b), 2.19 (s, 6H, H_a). ^{13}C NMR (101 MHz, $CDCl_3$) δ 166.7, 57.6, 52.7, 45.2, 36.8. All other spectroscopic data were consistent with those previously reported.[25]

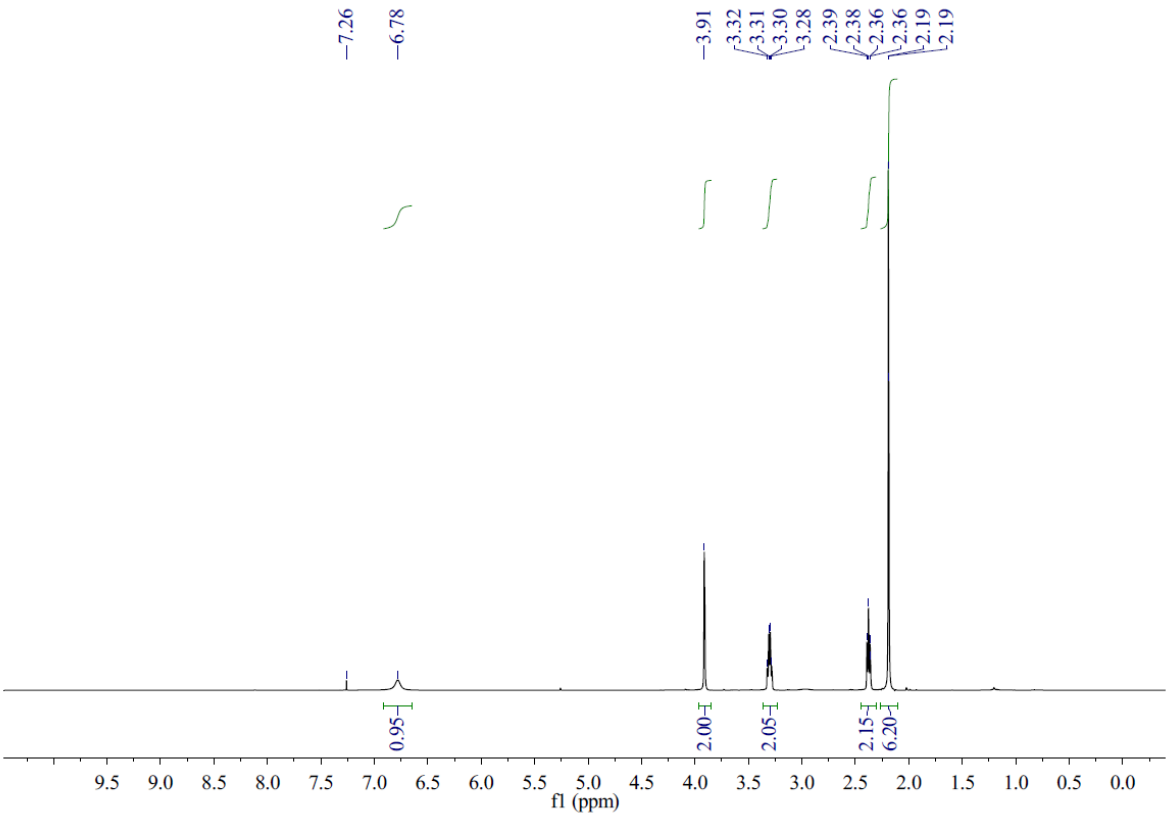
7.26
6.78
3.91
3.32
3.31
3.30
3.28
2.39
2.38
2.36
2.36
2.19
2.19
0.95
2.00
2.05
2.15
6.20
9.5 9.0 8.5 8.0 7.5 7.0 6.5 6.0 5.5 5.0 4.5 4.0 3.5 3.0 2.5 2.0 1.5 1.0 0.5 0.0
f1 (ppm)

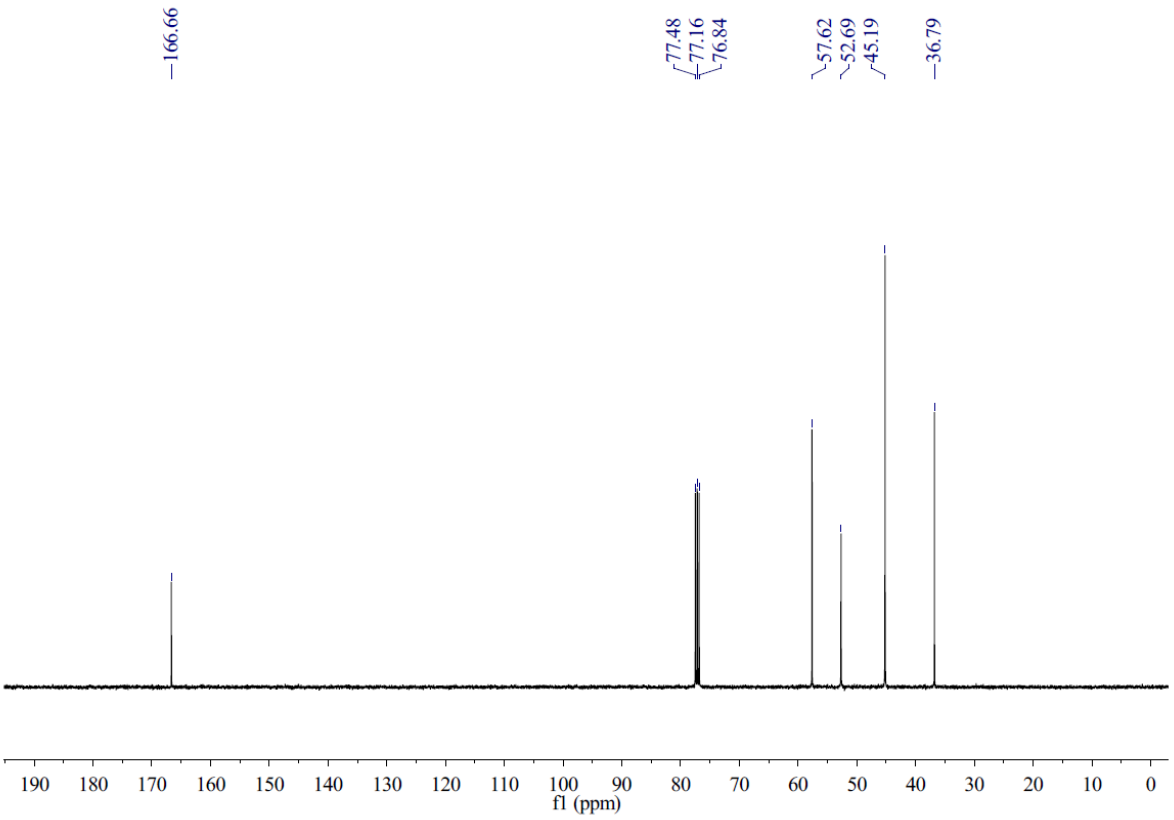
166.66
77.48
77.16
76.84
57.62
52.69
45.19
36.79
190 180 170 160 150 140 130 120 110 100 90 80 70 60 50 40 30 20 10 0
f1 (ppm)

General procedure of top click reaction to obtain **85**-**87**.

Under an atmosphere of nitrogen, alkyne **59** (51.4 mg, 0.10 mmol) and azide **80**, **82** or **84** (0.10 mmol) were dissolved in the mixture of NMP (1.0 mL) and EtOH (1.0 mL), tetrakis(acetonitrile)copper(I) hexafluorophosphate (7.5 mg, 0.020 mmol) was added. The mixture was stirred at room temperature for 24 hours. After the reaction had finished, saturated EDTA in 17% $NH_3 \cdot H_2O$ (10.0 mL) was poured into the mixture and the precipitate that formed was collected by filtration and washed with water (30 mL). The crude product was purified by flash chromatography on silica gel (eluent: CH_2Cl_2/MeOH 20:1) to give product **85**-**87** as brown solids.

N-(2-(1-((6-(4-((bis(pyridin-2-ylmethyl)amino)methyl)-1*H*-1,2,3-triazol-1-yl)-1,3-dioxo-1*H*-benzo[*de*]isoquinolin-2(3*H*)-yl)methyl)-1*H*-1,2,3-triazol-4-yl)ethyl)-4-methylbenzenesulfonamide (**85**)

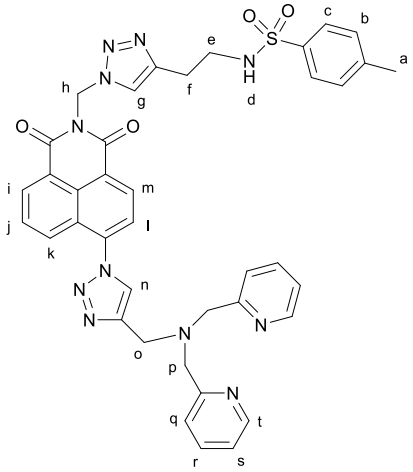

85 (67.1 mg, 89%, M.p. 103-107 °C). ^{1}H NMR (400 MHz, $CDCl_3$) δ 8.72-8.67 (m, 2H, $H_{i,m}$), 8.55 (d, 2H, J = 4.1, H_t), 8.28 (d, 1H, J = 7.8, H_k), 8.17 (s, 1H, H_n), 7.85-7.78 (m, 2H, $H_{j,l}$), 7.72-7.65 (m, 5H, $H_{c,g,r}$), 7.63-7.59 (m, 2H, H_q), 7.29 (d, 2H, J = 8.0, H_b), 7.21-7.15 (m, 2H, H_s), 5.50 (s, 2H, H_h), 5.18-5.09 (m, 1H, H_d), 4.45-4.38 (m, 2H, H_f), 4.08 (s, 2H, H_o), 3.96 (s, 4H, H_p), 3.51-3.45 (m, 2H, H_e), 2.41 (s, 3H, H_a). ^{13}C NMR (101 MHz, $CDCl_3$) δ 163.4, 162.90, 159.1, 149.2, 145.0, 143.8, 143.2, 138.5, 136.9, 136.8, 132.5, 131.1, 129.9, 129.0, 128.6, 127.1, 126.3, 125.8, 124.9, 123.5, 123.3, 122.6, 122.4, 59.9, 50.3, 48.6, 42.7, 35.4, 21.6. IR: (υ_{max}/cm^{-1}) 3073, 1704, 1662, 1589, 1432, 1329, 1233, 1157, 1041, 996, 786, 660. HR-NSI MS (*m/z*) $[M+H]^+$ calcd for $C_{39}H_{36}N_{11}O_4S$ 754.2667, found 754.2662.

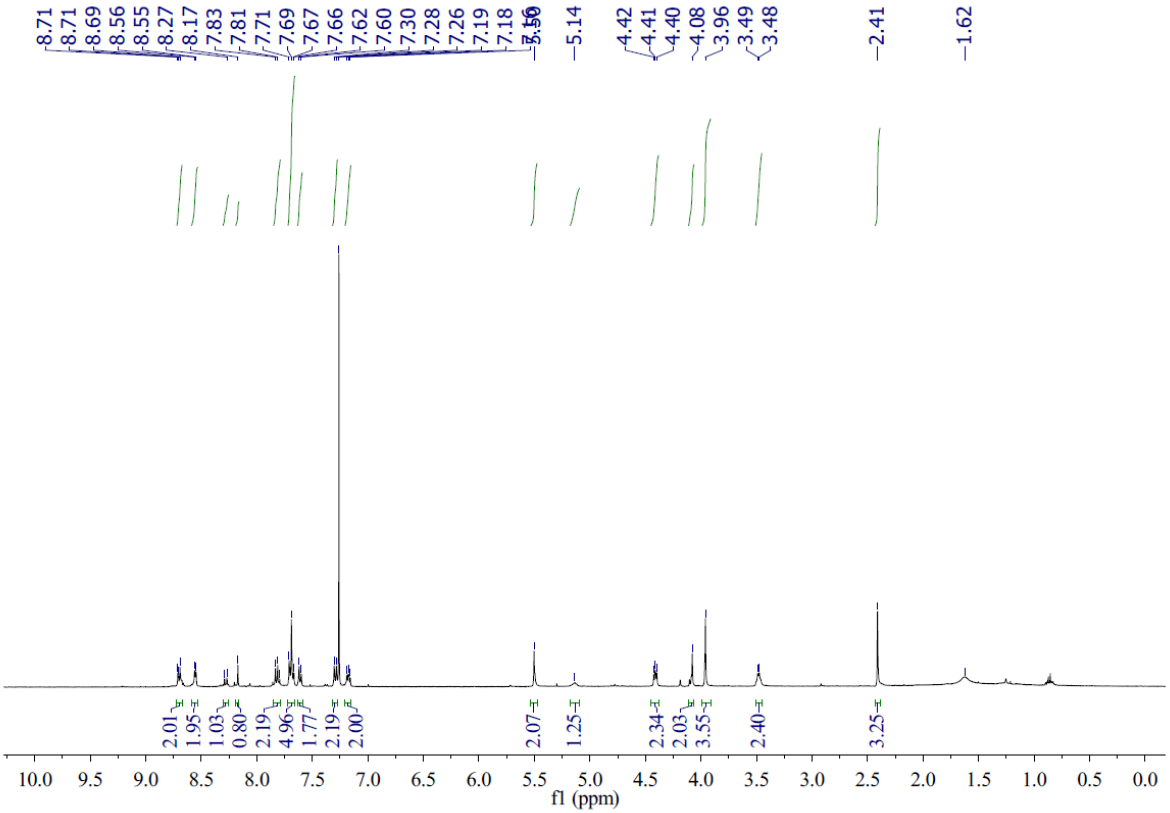
8.71
8.71
8.69
8.56
8.55
8.27
8.17
7.83
7.81
7.71
7.69
7.67
7.66
7.62
7.60
7.30
7.28
7.26
7.19
7.18
5.14
4.42
4.41
4.40
4.08
3.96
3.49
3.48
2.41
1.62
2.01
1.95
1.03
0.80
2.19
4.96
1.77
2.19
2.00
2.07
1.25
2.34
2.03
3.55
2.40
3.25
10.0 9.5 9.0 8.5 8.0 7.5 7.0 6.5 6.0 5.5 5.0 4.5 4.0 3.5 3.0 2.5 2.0 1.5 1.0 0.5 0.0
f1 (ppm)

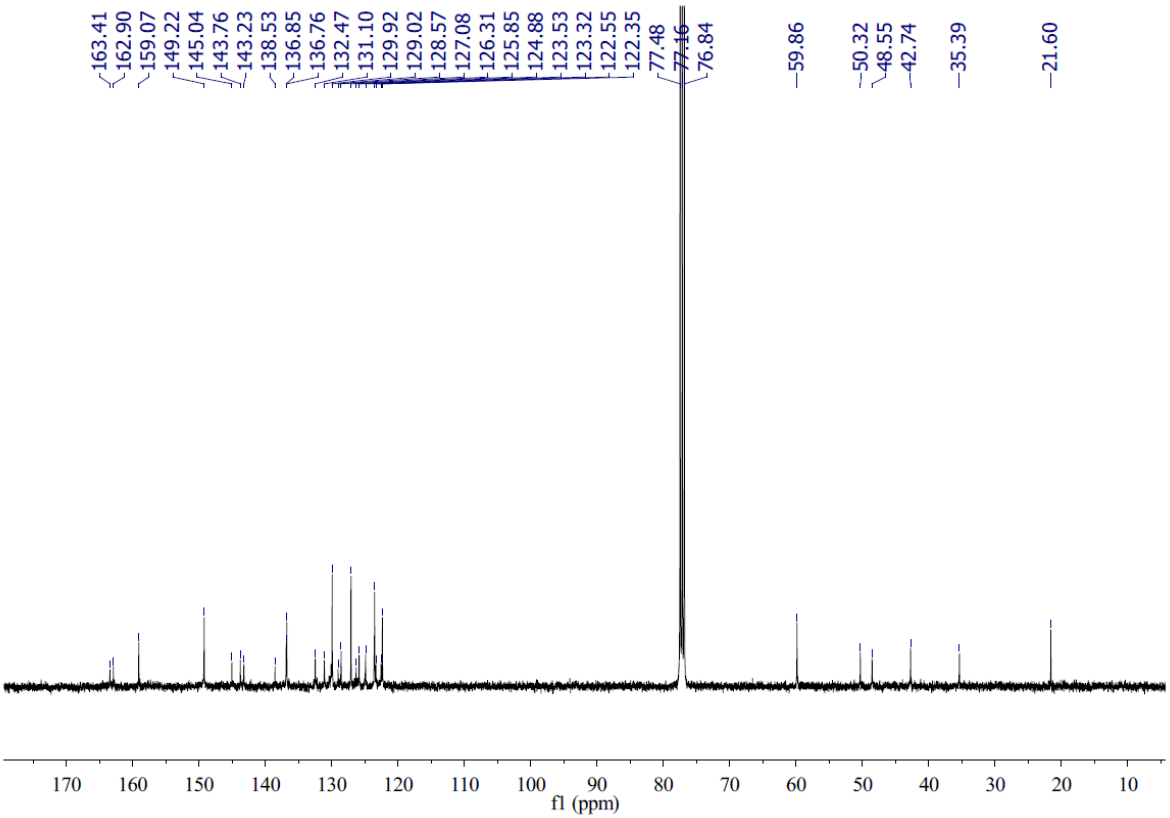
163.41
162.90
159.07
149.22
145.04
143.76
143.23
138.53
136.85
136.76
132.47
131.10
129.92
129.02
128.57
127.08
126.31
125.85
124.88
123.53
123.32
122.55
122.35
77.48
77.16
76.84
59.86
50.32
48.55
42.74
35.39
21.60
170 160 150 140 130 120 110 100 90 80 70 60 50 40 30 20 10
f1 (ppm)

(4-(1-((6-(4-((Bis(pyridin-2-ylmethyl)amino)methyl)-1*H*-1,2,3-triazol-1-yl)-1,3-dioxo-1*H*-benzo[*de*]isoquinolin-2(3*H*)-yl)methyl)-1*H*-1,2,3-triazol-4-yl)butyl)triphenylphosphonium tetrafluoroborate (**86**)

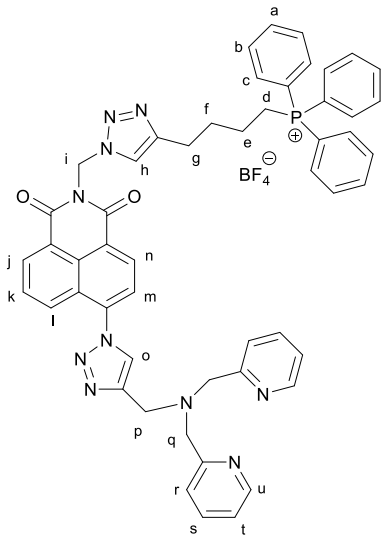

86 (130 mg, 68%, M.p. 131-135 °C). ^{1}H NMR (400 MHz, $CDCl_3$) δ 8.58-8.50 (m, 2H, $H_{j,n}$), 8.47 (d, 2H, J = 4.3, H_u), 8.22 (s, 1H, H_o), 8.17 (d, 1H, J = 8.5, H_l), 7.78-7.74 (m, 2H, $H_{k,m}$), 7.72-7.57 (m, 20H, $H_{a\text{-}c,g,r,s}$), 7.15-7.07 (m, 2H, H_t), 5.34 (s, 2H, H_i), 4.34 (t, 2H, J = 6.3, H_g), 4.01 (s, 2H, H_p), 3.90 (s, 4H, H_q), 3.30 (t, 2H, J = 14.3, H_d), 2.17-2.04 (m, 2H, H_f), 1.62-1.49 (m, 2H, H_e). ^{13}C NMR (101 MHz, $CDCl_3$) δ 163.3, 162.7, 159.0, 149.0, 145.1, 143.3, 138.4, 136.7, 135.1 (d, J = 2.8), 133.4 (d, J = 10.0), 132.3, 131.0, 130.5 (d, J = 12.6), 129.9, 129.0, 128.4, 126.3, 125.8, 123.6, 123.5, 123.4, 123.3, 122.6, 122.2, 117.8 (d, J = 85.8), 59.8, 53.5, 48.6, 35.5, 29.9 (d, J = 17.3), 21.1 (d, J = 53.5), 19.2. ^{31}P NMR (162 MHz, $CDCl_3$) δ 23.91. ^{19}F NMR (377 MHz, $CDCl_3$) δ −151.75. IR: (υ_{max}/cm^{-1}) 3067, 1738, 1585, 1436, 1366, 1232, 1112, 1037, 785, 689. HR-NSI MS (*m/z*) $[M - BF_4]^+$ calcd for $C_{52}H_{46}N_{10}O_2P$ 873.3537, found 873.3544.

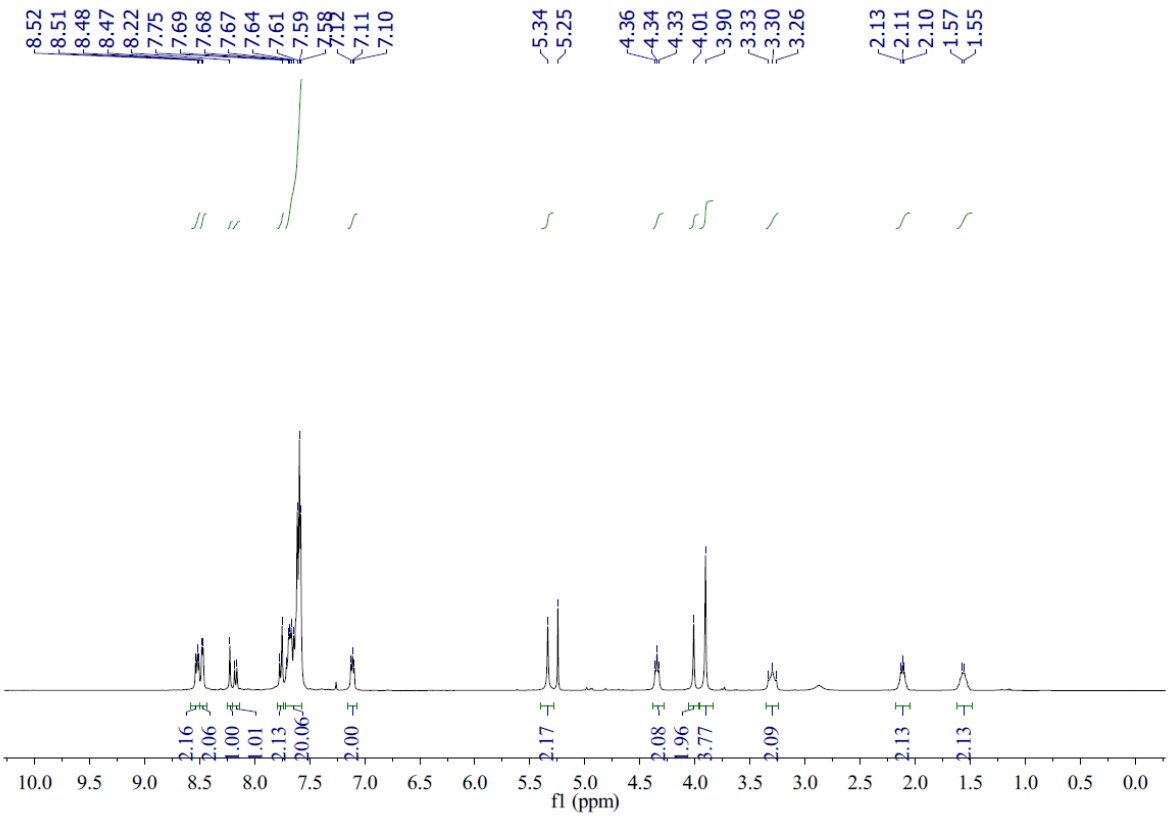
8.52
8.51
8.48
8.47
8.22
7.75
7.69
7.68
7.67
7.64
7.61
7.59
7.58
7.12
7.11
7.10
5.34
5.25
4.36
4.34
4.33
4.01
3.90
3.33
3.30
3.26
2.13
2.11
2.10
1.57
1.55
2.16
2.06
1.00
1.01
2.13
20.06
2.00
2.17
2.08
1.96
3.77
2.09
2.13
2.13
10.0 9.5 9.0 8.5 8.0 7.5 7.0 6.5 6.0 5.5 5.0 4.5 4.0 3.5 3.0 2.5 2.0 1.5 1.0 0.5 0.0
f1 (ppm)

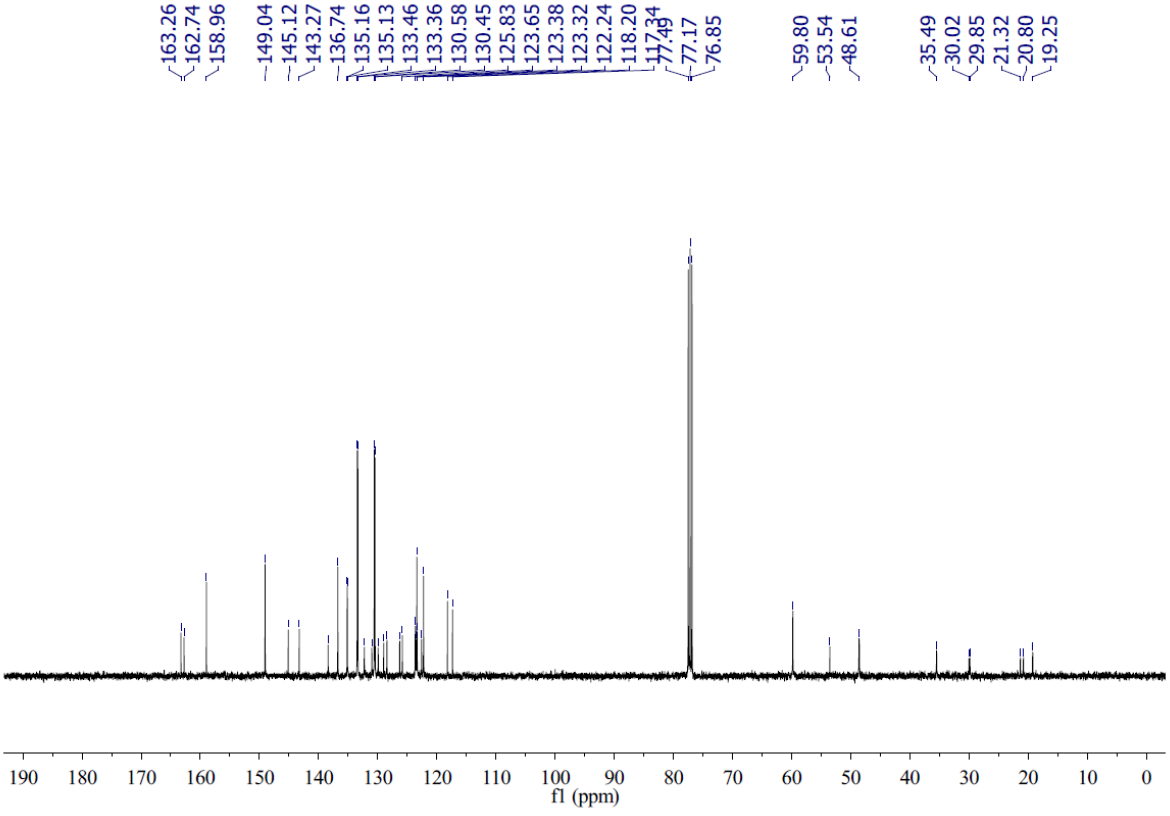
163.26
162.74
158.96
149.04
145.12
143.27
136.74
135.16
135.13
133.46
133.36
130.58
130.45
125.83
123.65
123.38
123.32
122.24
118.20
77.17
76.85
59.80
53.54
48.61
35.49
30.02
29.85
21.32
20.80
19.25
190 180 170 160 150 140 130 120 110 100 90 80 70 60 50 40 30 20 10 0
f1 (ppm)

^{31}P NMR:

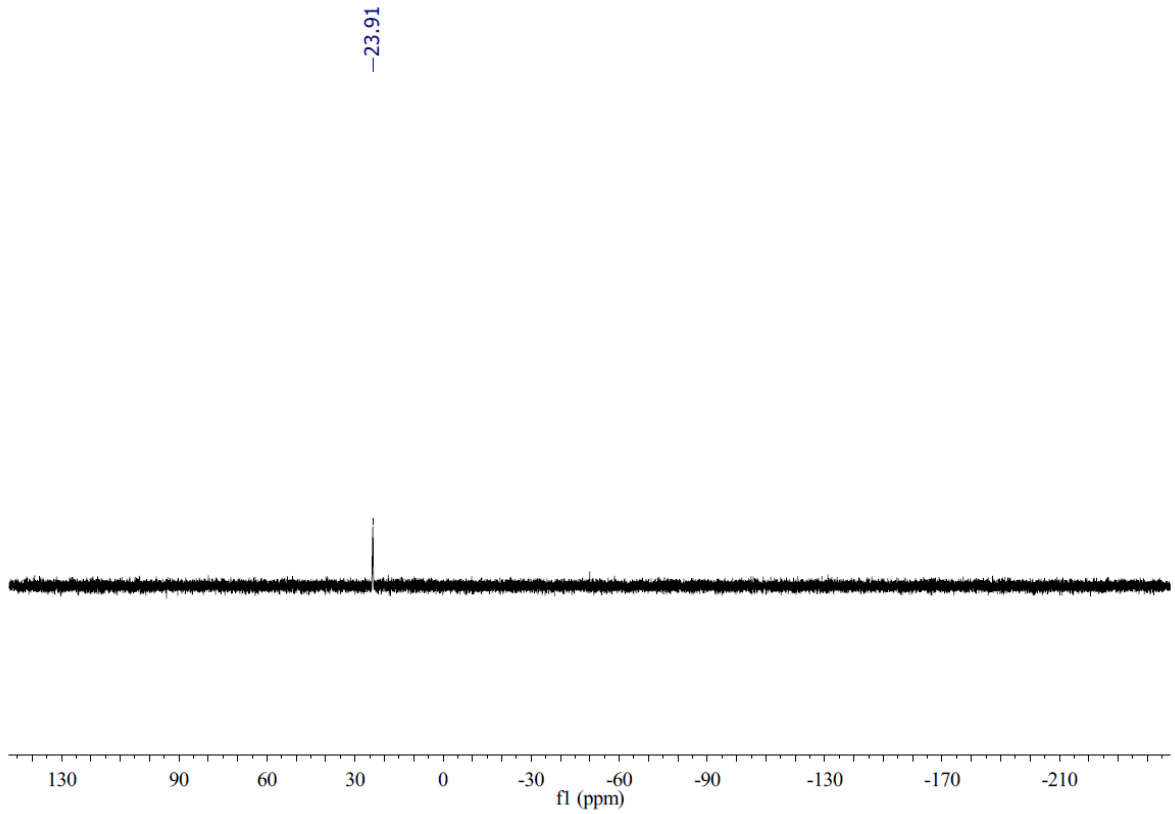

^{19}F NMR

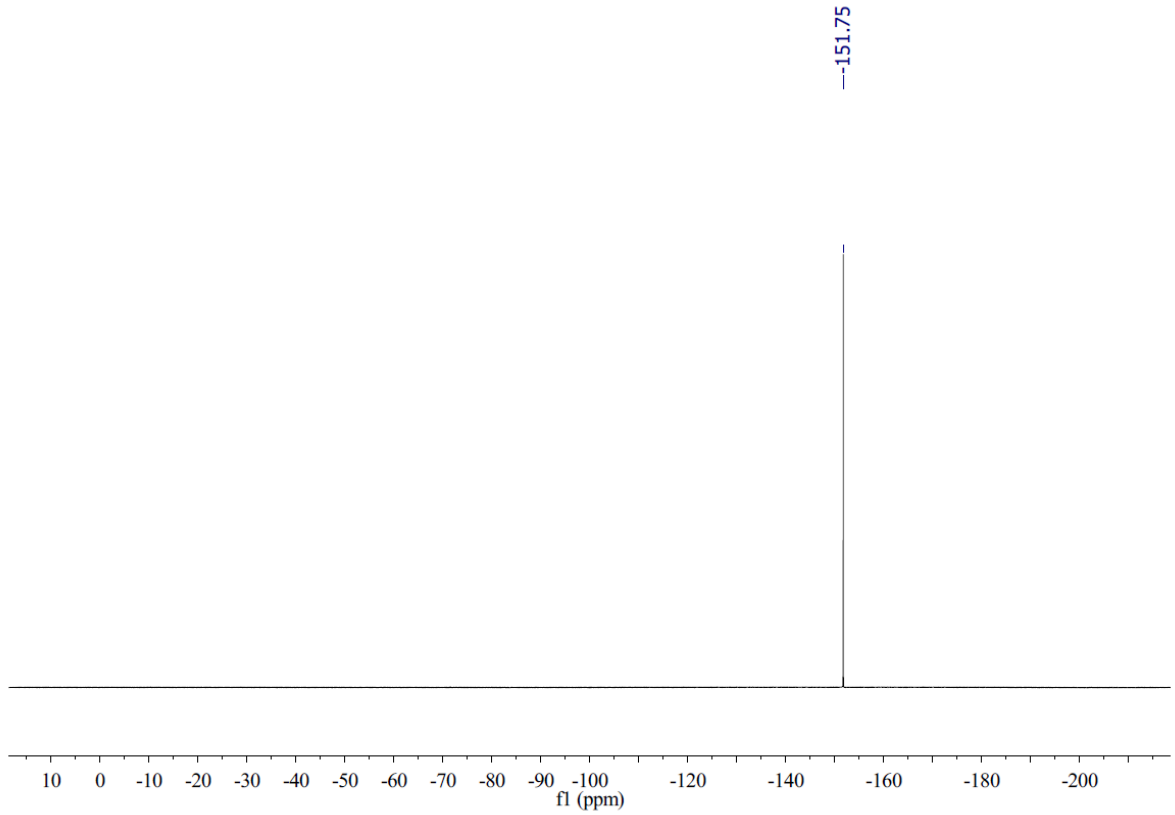

2-(1-((6-(4-((Bis(pyridin-2-ylmethyl)amino)methyl)-1*H*-1,2,3-triazol-1-yl)-1,3-dioxo-1*H*-benzo[*de*]isoquinolin-2(3*H*)-yl)methyl)-1*H*-1,2,3-triazol-4-yl)-*N*-(2-(dimethylamino)ethyl)acetamide (**87**)

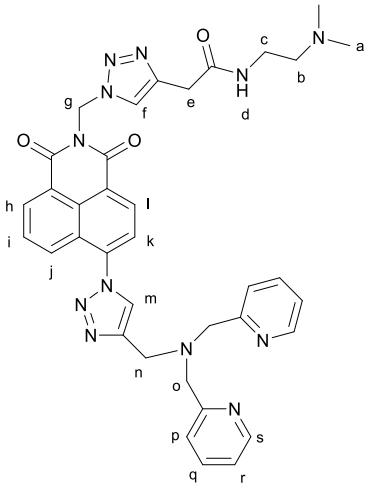

87 (92.4 mg, 90%, M.p. 113-117 °C). ^{1}H NMR (400 MHz, $CDCl_3$) δ 8.71-7.64 (m, 2H, $H_{h,l}$), 8.53 (d, 2H, J = 4.7, H_s), 8.26 (d, 1H, J = 8.6, H_j), 8.17 (s, 1H, H_m), 7.86 (s, 1H, H_f), 7.83-7.76 (m, 2H, $H_{i,k}$), 7.70-7.63 (m, 2H, H_q), 7.59 (d, 2H, J = 7.8, H_p), 7.18-7.12 (m, 2H, H_r), 6.70-6.58 (bs, 1H, H_d), 5.52 (s, 2H, H_g), 5.00 (s, 2H, H_e), 4.06 (s, 2H, H_n), 3.94 (s, 4H, H_o), 3.32-3.23 (m, 2H, H_c), 2.34 (t, 2H, J = 6.1, H_b), 2.13 (s, 6H, H_a). ^{13}C NMR (101 MHz, $CDCl_3$) δ 165.1, 163.3, 162.8, 159.0, 149.2, 145.0, 143.6, 138.5, 136.6, 132.4, 131.0, 130.0, 129.1, 128.5, 126.3, 125.7, 125.1, 123.4, 122.6, 122.2, 59.8, 57.4, 52.9, 48.5, 45.0, 37.2, 35.4. IR: (υ_{max}/cm^{-1}). HR-NSI MS (m/z) $[M+H]^+$ calcd for $C_{36}H_{37}N_{12}O_3$ 685.3106, found 685.3104.

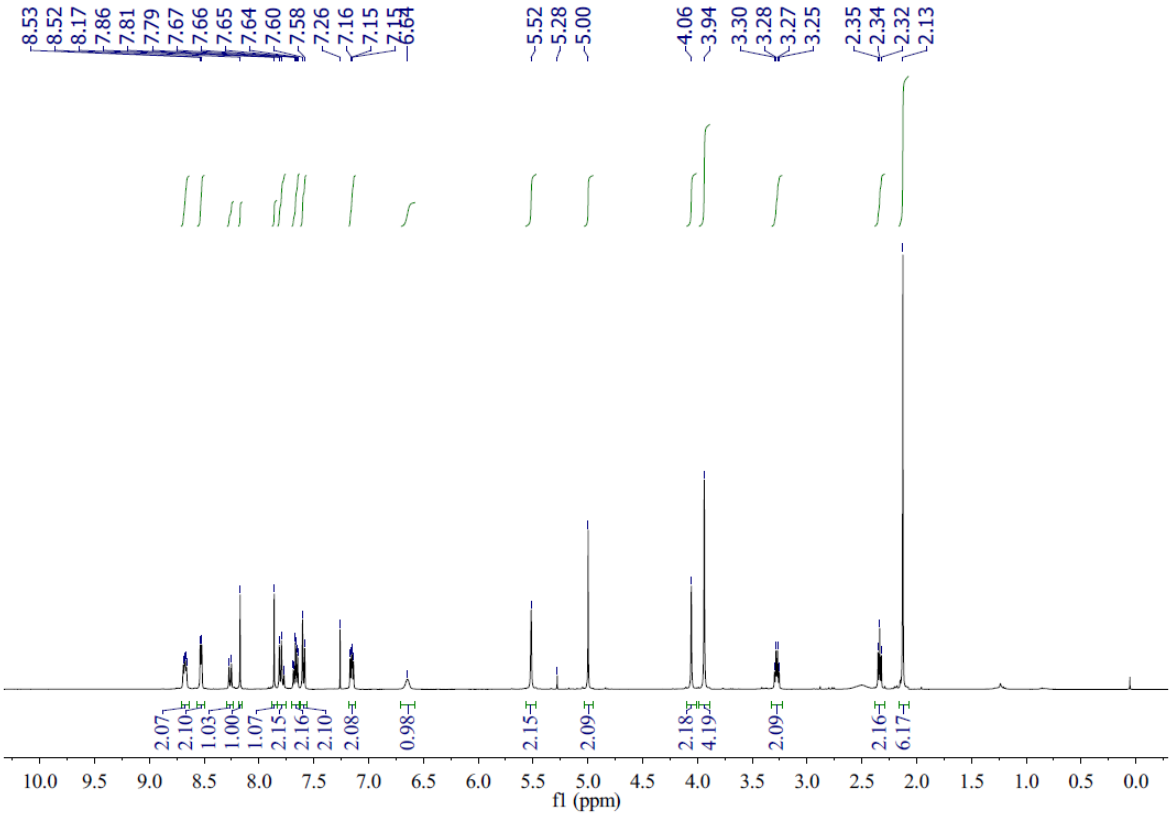
8.53
8.52
8.17
7.86
7.81
7.79
7.67
7.66
7.65
7.64
7.60
7.58
7.26
7.16
7.15
6.84
5.52
5.28
5.00
4.06
3.94
3.30
3.28
3.27
3.25
2.35
2.34
2.32
2.13
2.07
2.10
1.03
1.00
1.07
2.15
2.16
2.10
2.08
0.98
2.15
2.09
2.18
4.19
2.09
2.16
6.17
10.0 9.5 9.0 8.5 8.0 7.5 7.0 6.5 6.0 5.5 5.0 4.5 4.0 3.5 3.0 2.5 2.0 1.5 1.0 0.5 0.0
f1 (ppm)

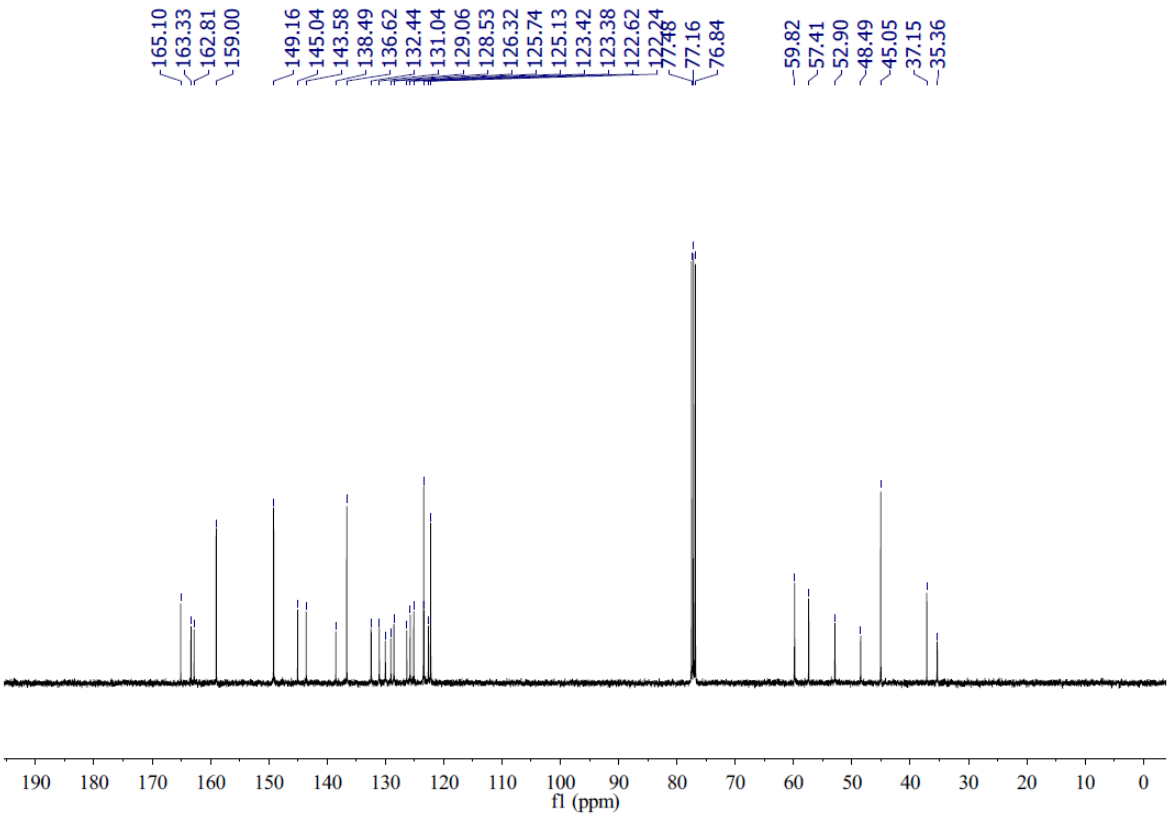
165.10
163.33
162.81
159.00
149.16
145.04
143.58
138.49
136.62
132.44
131.04
129.06
128.53
126.32
125.74
125.13
123.42
123.38
122.62
122.24
77.48
77.16
76.84
59.82
57.41
52.90
48.49
45.05
37.15
35.36
190 180 170 160 150 140 130 120 110 100 90 80 70 60 50 40 30 20 10 0
f1 (ppm)

6-Bromo-2-ethyl-1*H*-benzo[*de*]isoquinoline-1,3(2*H*)-dione (**88**)

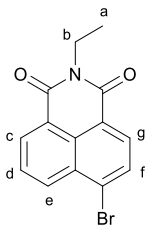

4-Bromo-1,8-naphthalic anhydride (0.55 g, 2.0 mmol) and ethylamine (70% solution in water, 0.14 mL, 2.4 mmol) was refluxed in dioxane (20 mL) for 7 hours. Then the reaction mixture was cooled to room temperature and a second aliquot of ethylamine (70% solution in water, 0.10 mL, 1.6 mmol) was added and the mixture was refluxed for another 7 hours. The solution was cooled to room temperature and poured into H_2O (100 mL) and the precipitate formed was collected by filtration, washed with H_2O (100 mL) and dried in vacuo to give **88** (0.58 g, 95%) as a yellow solid. ^{1}H NMR (400 MHz, $CDCl_3$) δ 8.66 (dd, 1H, *J* = 7.4, 0.8, H_c), 8.57 (d, 1H, *J* = 8.4, H_e), 8.42 (d, 1H, *J* = 7.9, H_g), 8.04 (d, 1H, *J* = 7.9, H_r), 7.84 (dd, 1H, *J* = 8.4, 7.4, H_d), 4.24 (q, 2H, *J* = 7.1, H_b), 1.34 (t, 3H, *J* = 7.1, H_a). ^{13}C NMR (101 MHz, $CDCl_3$) δ 163.4, 133.2, 132.0, 131.2, 131.1, 130.6, 130.2, 129.0, 128.1, 123.2, 122.4, 35.6, 13.3. All other spectroscopic data were consistent with those previously reported.[102]

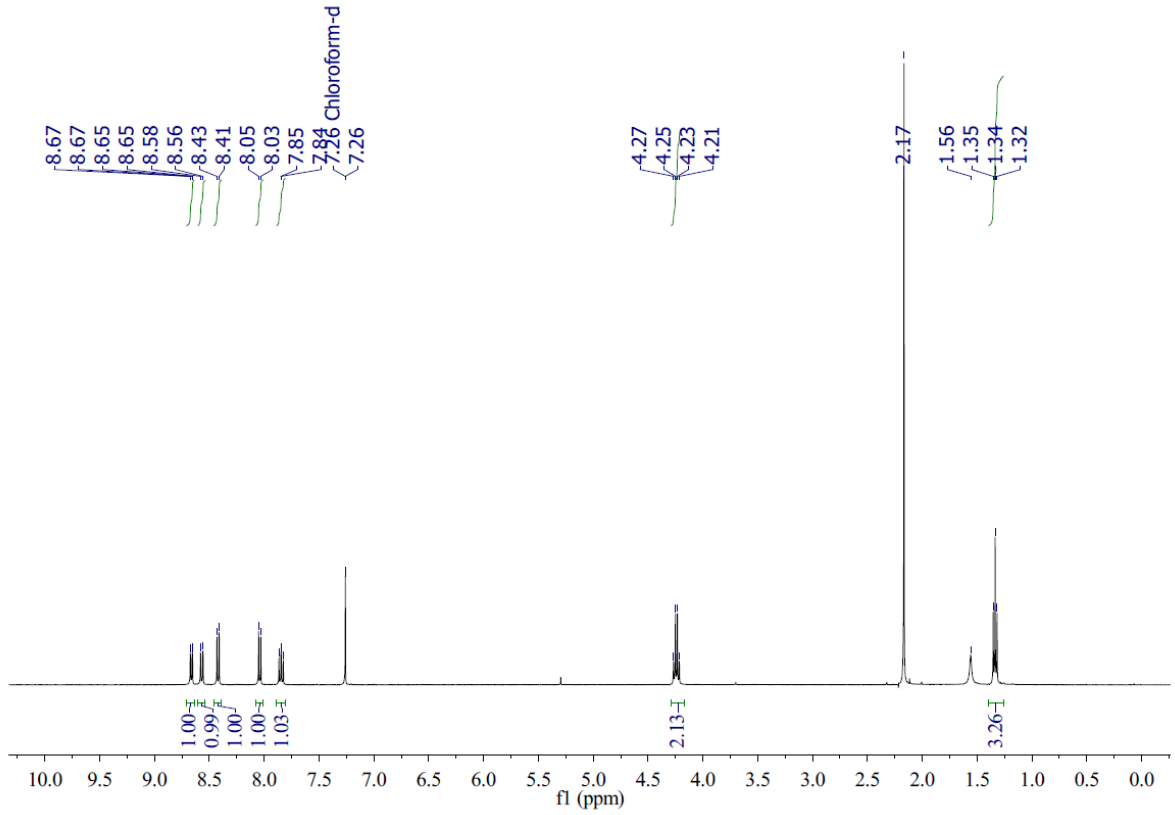
8.67
8.67
8.65
8.65
8.58
8.56
8.43
8.41
8.05
8.03
7.85
7.84
7.26
Chloroform-d
7.26
4.27
4.25
4.23
4.21
2.17
1.56
1.35
1.34
1.32
1.00
0.99
1.00
1.00
1.03
2.13
3.26
f1 (ppm)

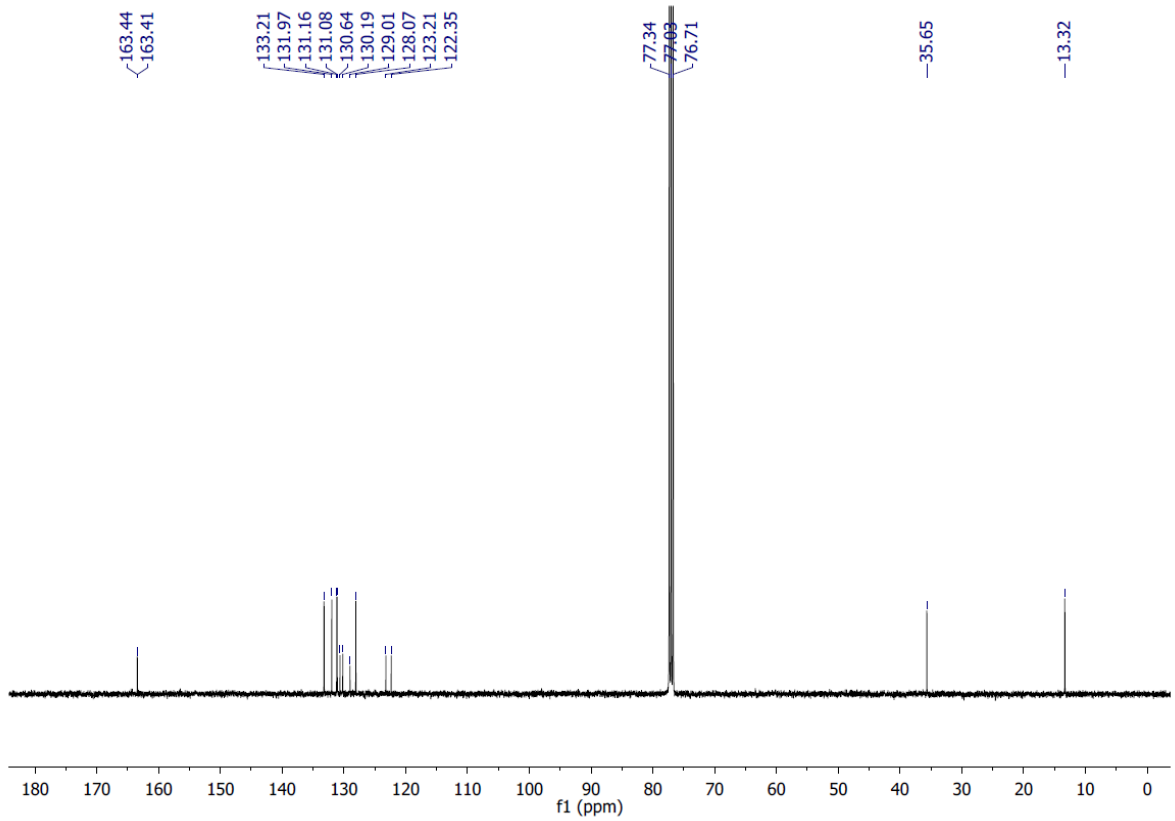
163.44
163.41
133.21
131.97
131.16
131.08
130.64
130.19
129.01
128.07
123.21
122.35
77.34
77.03
76.71
35.65
13.32
f1 (ppm)

6-Azido-2-ethyl-1*H*-benzo[*de*]isoquinoline-1,3(2*H*)-dione (**89**)

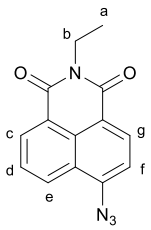

The bromide compound **88** (0.49 g, 1.6 mmol) was dissolved in *N*-methypyrrolidionone (5.0 mL) and sodium azide (0.13 g, 1.9 mmol) was added and the mixture was stirred at 40 °C for 24 h. The reaction mixture was diluted with H_2O (30 mL) and extracted with EtOAc (3 × 20 mL). The organic phase was washed with brine (30 mL) and dried over $MgSO_4$, concentrated *in vacuo* to give **89** (0.39 g, 91%) as a dark brown solid. ^{1}H NMR (400 MHz, $CDCl_3$) δ 8.64 (dd, 1H, *J* = 7.4, 1.0, H_c), 8.58 (d, 1H, *J* = 8.0, H_g), 8.43 (dd, 1H, *J* = 8.4, 1.0, H_e), 7.74 (dd, 1H, *J* = 8.4, 7.4, H_d), 7.46 (d, 1H, *J* = 8.0, H_f), 4.24 (q, 2H, *J* = 7.1, H_b), 1.33 (t, 3H, *J* = 7.1, H_a). ^{13}C NMR (101 MHz, $CDCl_3$) δ 163.8, 163.4, 143.4, 132.1, 131.6, 129.1, 128.7, 126.8, 124.4, 122.7, 119.0, 114.6, 35.5, 13.4. All other spectroscopic data were consistent with those previously reported.[102]

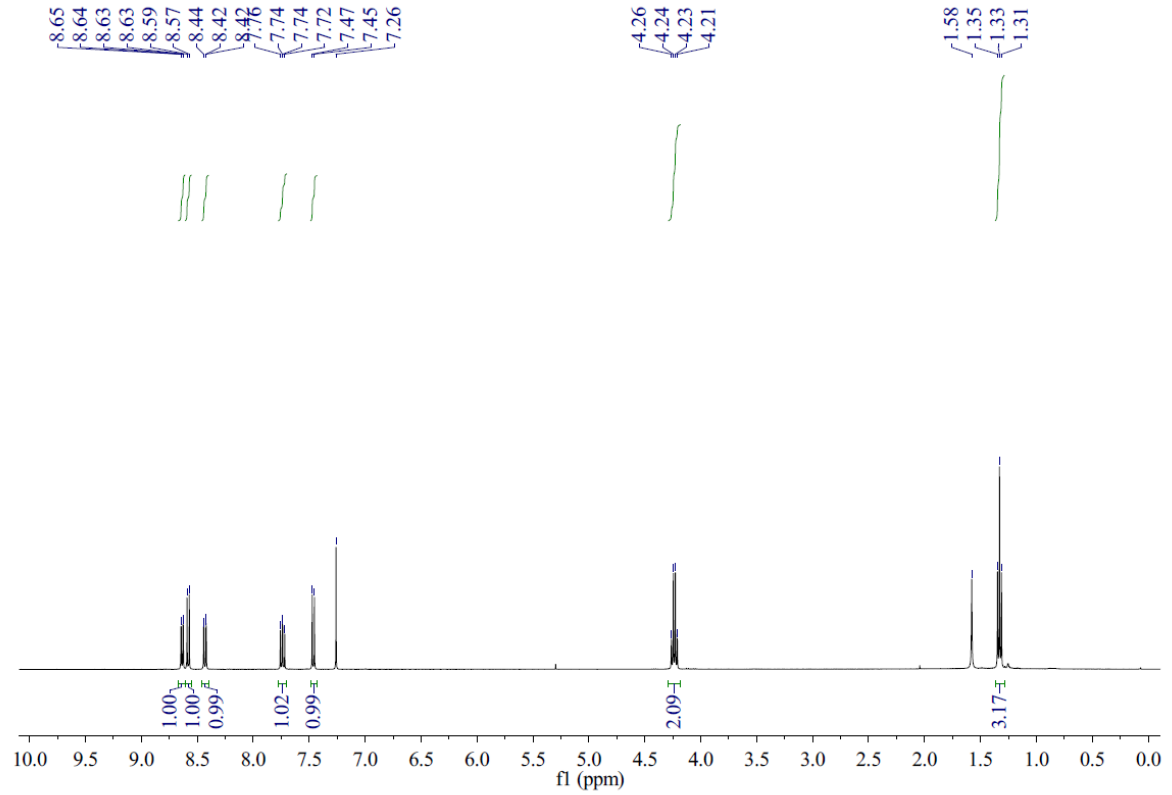
8.65
8.64
8.63
8.63
8.59
8.57
8.44
8.42
7.76
7.74
7.74
7.72
7.47
7.45
7.26
4.26
4.24
4.23
4.21
1.58
1.35
1.33
1.31
1.00
1.00
0.99
1.02
0.99
2.09
3.17
f1 (ppm)

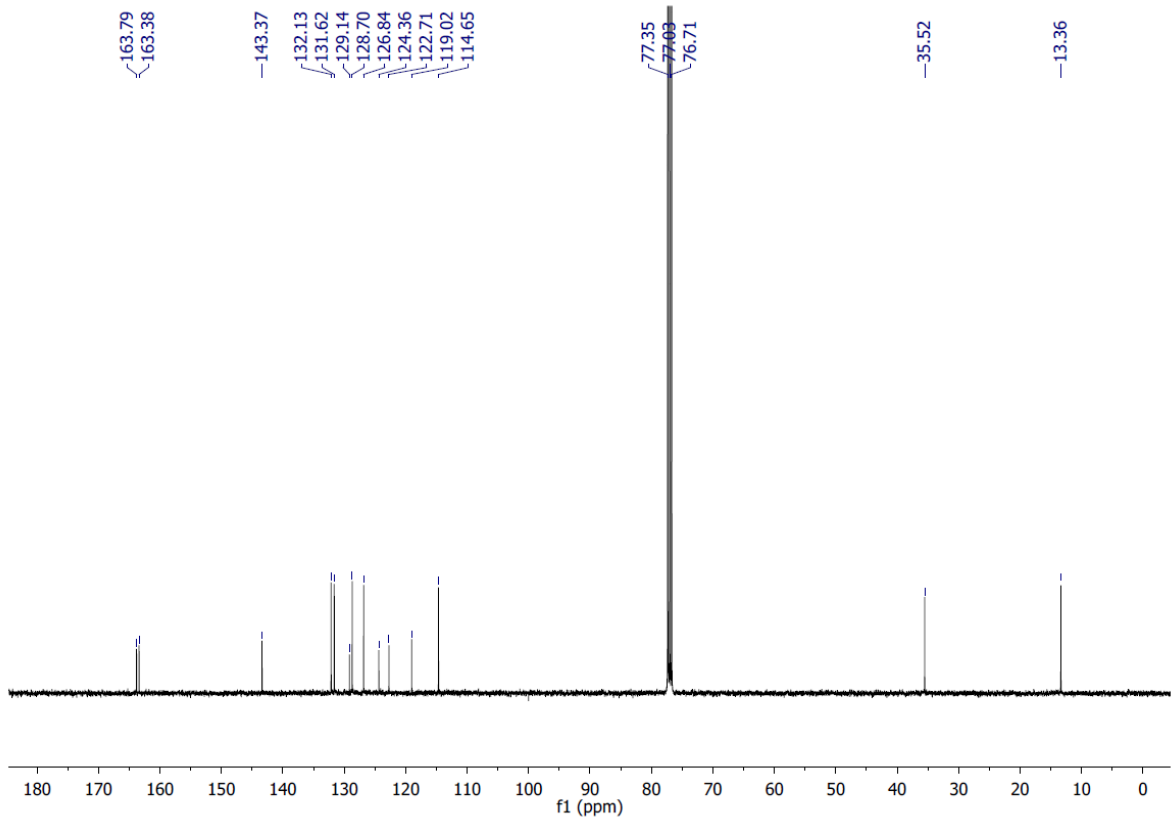
163.79
163.38
143.37
132.13
131.62
129.14
128.70
126.84
124.36
122.71
119.02
114.65
77.35
77.03
76.71
35.52
13.36
f1 (ppm)

6-(4-((Bis(pyridin-2-ylmethyl)amino)methyl)-1*H*-1,2,3-triazol-1-yl)-2-ethyl-1*H*-benzo[*de*]isoquinoline-1,3(2*H*)-dione (**90**)

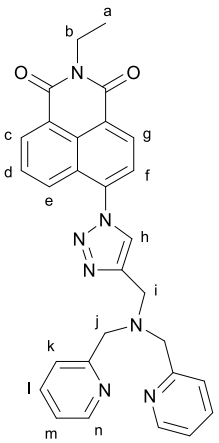

Under nitrogen atmosphere, the azide **89** (0.16 g, 0.62 mmol) and alkyne **54** (0.15 g, 0.62 mmol), DIPEA (62 µL, 0.35 mmol) was dissolved in the mixture of NMP (2.0 mL) and EtOH (2.0 mL). The tetrakis(acetonitrile)copper(I) hexafluorophosphate (46 mg, 0.12 mmol) was added to the above solution and the mixture was stirred at room temperature for 24 hours. After the reaction complete judged by TLC, saturated EDTA in 17% $NH_3 \cdot H_2O$ (20 mL) was poured to the mixture and the precipitate formed was collected by filtration, then washed with water (30 mL). This crude product was purified by flash chromatography (eluent: DCM/MeOH 20:1) to give **90** (0.29 g, 93%, M.p. 93-97 °C) as a brown solid. ^{1}H NMR (400 MHz, $CDCl_3$) δ 8.67-8.60 (m, 2H, $H_{c,g}$), 8.48 (dd, 2H, J = 4.9, 0.8, H_n), 8.19 (dd, 1H, J = 8.6, 1.0, H_e), 8.11 (s, 1H, H_h), 7.78-7.71 (m, 2H, $H_{d,f}$), 7.65-7.58 (m, 2H, H_l), 7.54 (d, 2H, J = 7.8, H_k), 7.13-7.07 (m, 2H, H_m), 4.20 (q, 2H, J = 7.1, H_b), 4.01 (s, 2H, H_i), 3.89 (s, 4H, H_j), 1.29 (t, 3H, J = 7.1, H_a). ^{13}C NMR (101 MHz, $CDCl_3$) δ 163.4, 162.9, 158.9, 149.1, 144.9, 138.2, 136.6, 132.0, 130.6, 129.5, 128.9, 128.5, 126.3, 125.7, 123.7, 123.4, 122.9, 122.2, 59.8, 48.4, 35.7, 13.3. IR: (υmax/cm^{-1}) 3196, 1703, 1611, 1551, 1473, 1427, 1365, 1230, 1119, 1037, 950, 726. HR-NSI MS (*m/z*) $[M+H]^+$ calcd for $C_{29}H_{26}N_7O_2$ 504.2142, found 504.2134.

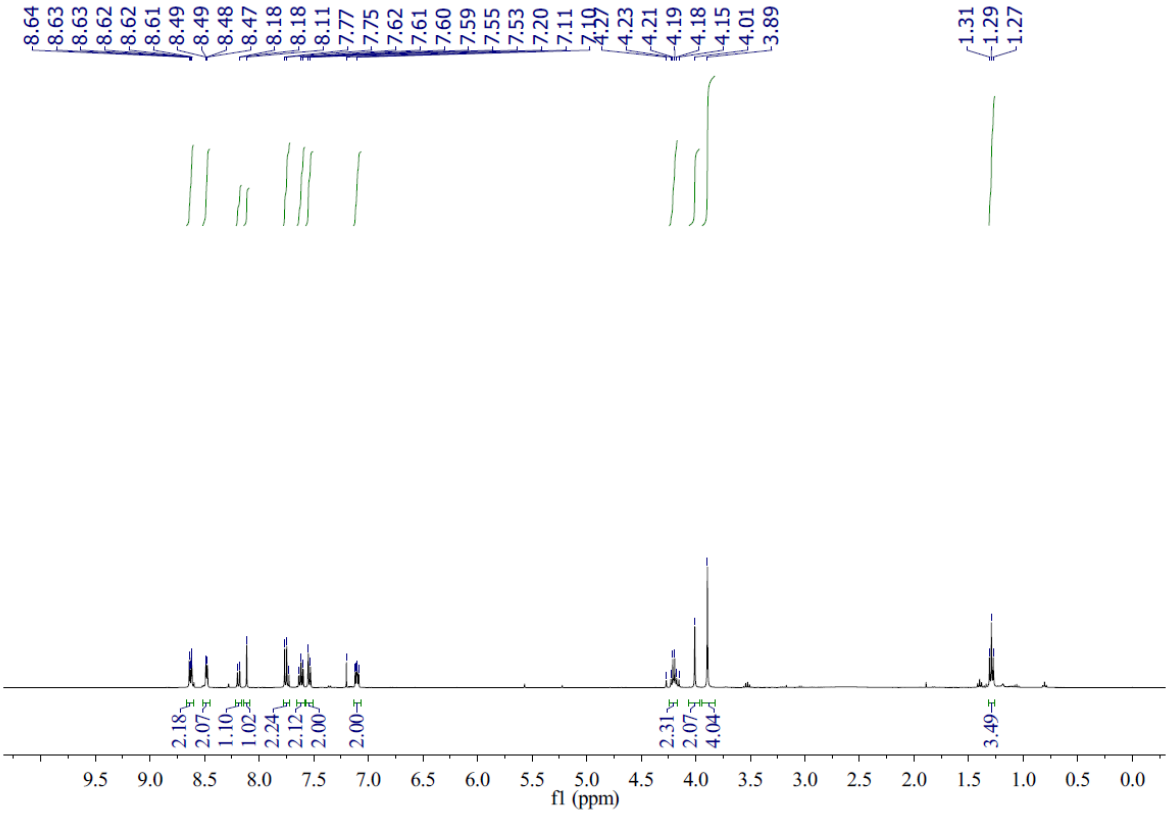
8.64
8.63
8.63
8.62
8.62
8.61
8.49
8.49
8.48
8.47
8.18
8.18
8.11
7.77
7.75
7.62
7.61
7.60
7.59
7.55
7.53
7.20
7.11
4.27
4.23
4.21
4.19
4.18
4.15
4.01
3.89
1.31
1.29
1.27
2.18
2.07
1.10
1.02
2.24
2.12
2.00
2.00
2.31
2.07
4.04
3.49
9.5 9.0 8.5 8.0 7.5 7.0 6.5 6.0 5.5 5.0 4.5 4.0 3.5 3.0 2.5 2.0 1.5 1.0 0.5 0.0
f1 (ppm)

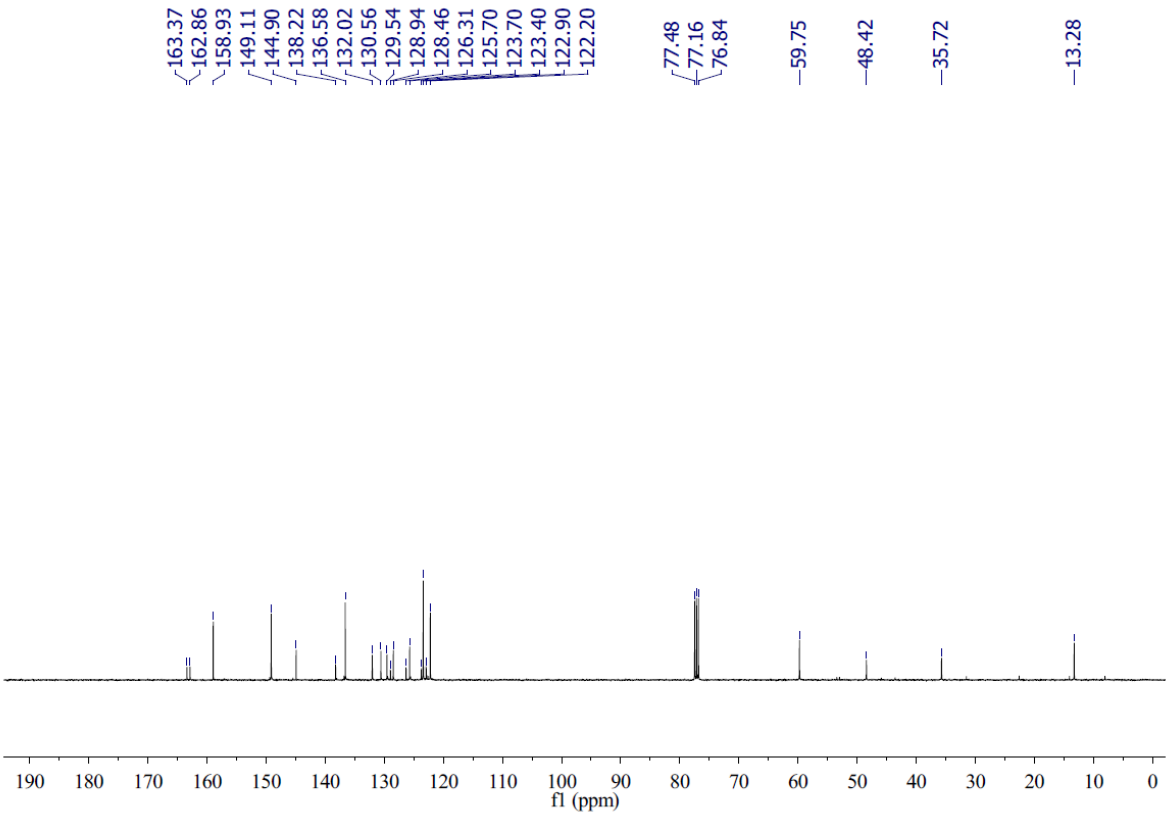
163.37
162.86
158.93
149.11
144.90
138.22
136.58
132.02
130.56
129.54
128.94
128.46
126.31
125.70
123.70
123.40
122.90
122.20
77.48
77.16
76.84
59.75
48.42
35.72
13.28
190 180 170 160 150 140 130 120 110 100 90 80 70 60 50 40 30 20 10 0
f1 (ppm)

References

1 N. M. Hooper, N. T. Watt and I. J. Whitehouse, *Int. J. Alzheimers. Dis.*, 2011, Article ID 971021, 10 pages.

2 L. C. Costello and R. B. Franklin, *Arch. Biochem. Biophys.*, 2016, **611**, 100–112.

3 P. Chabosseau and G. A. Rutter, *Arch. Biochem. Biophys.*, 2016, **611**, 79–85.

4 A. S. Prasad, *Curr. Opin. Clin. Nutr. Metab. Care*, 2009, **12**, 646–652.

5 W. Maret, *Metallomics*, 2015, **7**, 202–211.

6 A. Wedd, W. Maret, *Binding, Transport and Storage of Metal Ions in Biological Cells*, The Royal Society of Chemistry, 2014.

7 Y. Chen, Y. Bai, Z. Han, W. He and Z. Guo, *Chem. Soc. Rev.*, 2015, **44**, 4517–4546.

8 P. Chabosseau, J. Woodier, R. Cheung and G. A. Rutter, *Metallomics*, 2018, **10**, 229–239.

9 Z. Xu, J. Yoon and D. R. Spring, *Chem. Soc. Rev.*, 2010, **39**, 1996–2006.

10 Y. Wu, X. Peng, B. Guo, J. Fan, Z. Zhang, J. Wang, A. Cui and Y. Gao, *Org. Biomol. Chem.*, 2005, **3**, 1387–1392.

11 N. C. Lim, L. Yao, H. C. Freake and C. Brückner, *Bioorganic Med. Chem. Lett.*, 2003, **13**, 2251–2254.

12 Z. Liu, C. Zhang, Y. Chen, F. Qian, Y. Bai, W. He and Z. Guo, *Chem. Commun.*, 2014, **50**, 1253–1255.

13 S. Sahana, G. Mishra, S. Sivakumar and P. K. Bharadwaj, *J. Photochem. Photobiol. A Chem.*, 2018, **351**, 231–239.

14 Z. X. Han, X. B. Zhang, Z. Li, Y. J. Gong, X. Y. Wu, Z. Jin, C. M. He, L. X. Jian, J. Zhang, G. L. Shen and R. Q. Yu, *Anal. Chem.*, 2010, **82**, 3108–3113.

15 A. C. Sedgwick, L. Wu, H. H. Han, S. D. Bull, X. P. He, T. D. James, J. L. Sessler, B. Z. Tang, H. Tian and J. Yoon, *Chem. Soc. Rev.*, 2018, **47**, 8842–8880.

16 F. Huo, Q. wu, J. Kang, Y. Zhang and C. Yin, *Sensors Actuators, B Chem.*, 2018, **262**, 263–269.

17 Y. Hong, J. W. Y. Lam and B. Z. Tang, *Chem. Soc. Rev.*, 2011, **40**, 5361–5388.

18 H. Mehdi, W. Gong, H. Guo, M. Watkinson, H. Ma, A. Wajahat and G. Ning, *Chem. - A Eur. J.*, 2017, **23**, 13067–13075.

19 D. Escudero, *Acc. Chem. Res.*, 2016, **49**, 1816–1824.

20 Y. Tu, J. Liu, H. Zhang, Q. Peng, J. W. Y. Lam and B. Z. Tang, *Angew. Chemie*, 2019, **131**, 15053–15056.

21 W. J. Bettger and B. L. O'Dell, *J. Nutr. Biochem.*, 1993, **4**, 194–207.

22 B. L. O'Dell, *J. Nutr.*, 2000, **130**, 1432S–1436S.

23 S. Iyoshi, M. Taki and Y. Yamamoto, *Org. Lett.*, 2011, **13**, 4558–4561.

24 D. Li, S. Chen, E. A. Bellomo, A. I. Tarasov, C. Kaut, G. A. Rutter and W. -h. Li, *Proc. Natl. Acad. Sci.*, 2011, **108**, 21063–21068.

25 J. Pancholi, D. J. Hodson, K. Jobe, G. A. Rutter, S. M. Goldup and M. Watkinson, *Chem. Sci.*, 2014, **5**, 3528–3535.

26 N. R. Johnston, R. K. Mitchell, E. Haythorne, M. P. Pessoa, F. Semplici, J. Ferrer, L. Piemonti, P. Marchetti, M. Bugliani, D. Bosco, E. Berishvili, P. Duncanson, M. Watkinson, J. Broichhagen, D. Trauner, G. A. Rutter and D. J. Hodson, *Cell Metab.*, 2016, **24**, 389–401.

27 K. Rathore, C. S. Lim, Y. Lee, H. J. Park and B. R. Cho, *Asian J. Org. Chem.*, 2014, **3**, 1070–1073.

28 H. M. McBride, M. Neuspiel and S. Wasiak, *Curr. Biol.*, 2006, **16**, 551–560.

29 A. Atkinson, O. Khalimonchuk, P. Smith, H. Sabic, D. Eide and D. R. Winge, *J. Biol. Chem.*, 2010, **285**, 19450–19459.

30 D. Rajapakse, T. Curtis, M. Chen and H. Xu, *Oxid. Med. Cell. Longev.*, , DOI:10.1155/2017/6926485.

31 S. L. Sensi, D. Ton-That, P. G. Sullivan, E. A. Jonas, K. R. Gee, L. K. Kaczmarek and J. H. Weiss, *Proc. Natl. Acad. Sci.*, 2003, **100**, 6157–6162.

32 S. L. Sensi, D. Ton-That, J. H. Weiss, A. Rothe and K. R. Gee, *Cell Calcium*, 2003, **34**, 281–284.

33 E. M. Nolan, J. W. Ryu, J. Jaworski, R. P. Feazell, M. Sheng and S. J. Lippard, *J. Am. Chem. Soc.*, 2006, **128**, 15517–15528.

34 A. Loas, R. J. Radford and S. J. Lippard, *Inorg. Chem.*, 2014, **53**, 6491–6493.

35 H. M. Kim, C. S. Lim, G. Masanta, H. J. Kim, B. R. Cho and J. H. Han, *J. Am. Chem. Soc.*, 2011, **133**, 5698–5700.

36 N. Y. Baek, C. H. Heo, C. S. Lim, G. Masanta, B. R. Cho and H. M. Kim, *Chem. Commun.*, 2012, **48**, 4546–4548.

37 Y. L. and B. R. C. Kailash Rathore, Chang Su Lim, *Org. Biomol. Chem.*, 2014, **12**, 3406–3412.

38 Z. Liu, C. Zhang, Y. Chen, W. He and Z. Guo, *Chem. Commun.*, 2012, **48**, 8365–8367.

39 G. Grynkiewicz, M. Poenie and R. Y. Tsien, *J. Biol. Chem.*, 1985, **260**, 3440–3450.

40 L. Xue, G. Li, C. Yu and H. Jiang, *Chem. - A Eur. J.*, 2012, **18**, 1050–1054.

41 K. Sreenath, J. R. Allen, M. W. Davidson and L. Zhu, *Chem. Commun.*, 2011, **47**, 11730–11732.

42 W. Chyan, D. Y. Zhang, S. J. Lippard and R. J. Radford, *Proc. Natl. Acad. Sci.*, 2014, **111**, 143–148.

43 J. J. Hwang, S.-J. Lee, T.-Y. Kim, J.-H. Cho and J.-Y. Koh, *J. Neurosci.*, 2008, **28**, 3114–3122.

44 H. C. Roh, S. Collier, J. Guthrie, J. D. Robertson and K. Kornfeld, *Cell Metab.*, 2012, **15**, 88–99.

45 F. Qian, C. Zhang, Y. Zhang, W. He, X. Gao, P. Hu and Z. Guo, *J. Am. Chem. Soc.*, 2009, **131**, 1460–1468.

46 Q. Liu, D. Zhu, H. Jiang, L. Xue and G. Li, *Inorg. Chem.*, 2012, **51**, 10842–10849.

47 H. J. Lee, C. W. Cho, H. Seo, S. Singha, Y. W. Jun, K. H. Lee, Y. Jung, K. T. Kim, S. Park, S. C. Bae and K. H. Ahn, *Chem. Commun.*, 2016, **52**, 124–127.

48 H. Zhu, J. Fan, S. Zhang, J. Cao, K. Song, D. Ge, H. Dong, J. Wang and X. Peng, *Biomater. Sci.*, 2014, **2**, 89–97.

49 Z. Hu, G. Yang, J. Hu, H. Wang, P. Eriksson, R. Zhang, Z. Zhang and K. Uvdal, *Sensors Actuators, B Chem.*, 2018, **264**, 419–425.

50 K. Sreenath, Z. Yuan, A. Allen, M. W. Davidson and L. Zhu, *Chem. - A Eur. J.*, 2015, **21**, 867–874.

51 C. Du, S. Fu, X. Wang, A. C. Sedgwick, W. Zhen, M. Li, X. Li, J. Zhou, Z. Wang, H. Wang and J. L. Sessler, *Chem. Sci.*, 2019, **10**, 5699–5704.

52 D. S. Schwarz and M. D. Blower, *Cell. Mol. Life Sci.*, 2016, **73**, 79–94.

53 K. Mori, *Cell*, 2000, **101**, 451–454.

54 C. J. Stork and Y. V. Li, *J. Mol. Signal.*, 2010, **5**, 1–6.

55 C. Giunta, J. M. Walker, A. E. Palmer, J. Jeong, B. Steinmann, M. Rohrbach, D. J. Eide, J. G. Park and F. Wang, *Proc. Natl. Acad. Sci.*, 2012, **109**, E3530–E3538.

56 T. S. Le Nguyen, K. Kohno and Y. Kimata, *Biosci. Biotechnol. Biochem.*, 2013, **77**, 1337–1339.

57 K. Zhang and R. J. Kaufman, *Nature*, 2008, **454**, 455–462.

58 S. H. Back and R. J. Kaufman, *Annu. Rev. Biochem.*, 2012, **81**, 767–793.

59 C. Hetz and S. Saxena, *Nat. Rev. Neurol.*, 2017, **13**, 477–491.

60 W. Lin, D. Buccella and S. J. Lippard, *J. Am. Chem. Soc.*, 2013, **135**, 13512–13520.

61 X. Gan, P. Sun, H. Li, X. Tian, B. Zhang, J. Wu, Y. Tian and H. Zhou, *Biosens. Bioelectron.*, 2016, **86**, 393–397.

62 H. Xiao, P. Li, X. Hu, X. Shi, W. Zhang and B. Tang, *Chem. Sci.*, 2016, **7**, 6153–6159.

63 M. Yang, J. Fan, J. Zhang, J. Du and X. Peng, *Chem. Sci.*, 2018, **9**, 6758–6764.

64 J.-T. Hou, H. S. Kim, C. Duan, M. S. Ji, S. Wang, L. Zeng, W. Ren and J. S. Kim, *Chem. Commun.*, 2019, 2533–2536.

65 W. Lin, G. Xu, S. Gao, Y. Ma, Y. Tang and A. Xu, *Sci. Rep.*, 2017, **7**, 1–9.

66 H. Wu and J. Zhao, *Metallomics*, 2019, **11**, 1984–1987.

67 Y. V. Li, *Endocrine*, 2014, **45**, 178–189.

68 M. Aridor and L. A. Hannan, *Traffic*, 2000, **1**, 836–851.

69 G. K. Walkup, S. C. Burdette, S. J. Lippard and R. Y. Tsien, *J. Am. Chem. Soc.*, 2000, **122**, 5644–5645.

70 L. E. Mcquade and S. J. Lippard, *Inorg. Chem.*, 2010, **49**, 9535–9545.

71 C. Zhang, Y. Zhang, Y. Chen, Z. Xie, Z. Liu, X. Dong, W. He, C. Shen and Z. Guo, *Inorg. Chem. Commun.*, 2011, **14**, 304–307.

72 H. Singh, H. W. Lee, C. H. Heo, J. W. Byun, A. R. Sarkar and H. M. Kim, *Chem. Commun.*, 2015, **51**, 12099–12102.

73 R. W. Horobin and F. Rashid-Doubell, *Biotech. Histochem.*, 2013, **88**, 461–476.

74 R. S. Li, P. F. Gao, H. Z. Zhang, L. L. Zheng, C. M. Li, J. Wang, Y. F. Li, F. Liu, N. Li and C. Z. Huang, *Chem. Sci.*, 2017, **8**, 6829–6835.

75 W. Zhang, J. Zhang, P. Li, J. Liu, D. Su and B. Tang, *Chem. Sci.*, 2019, **10**, 879–883.

76 D. Aoki, N. Lee, N. Yamaguchi, C. Dubois and M. N. Fukuda, *Proc. Natl. Acad. Sci. U. S. A.*, 1992, **89**, 4319–4323.

77 Y. Maeda, G. V. Beznoussenko, J. Van Lint, A. A. Mironov and V. Malhotra, *EMBO J.*, 2001, **20**, 5982–5990.

78 L. Zhao, Z. Xia and F. Wang, *Front. Pharmacol.*, 2014, **5**, 1–23.

79 R. S. MacDonald, *J. Nutr.*, 2000, **130**, 1500S–1508S.

80 L. M. Green and J. M. Berg, *Proc. Natl. Acad. Sci. U. S. A.*, 1990, **87**, 6403–6407.

81 J. G. Miranda, A. L. Weaver, Y. Qin, J. G. Park, C. I. Stoddard, M. Z. Lin and A. E. Palmer, *PLoS One*, 2012, **7**, 1–10.

82 M. L. Zastrow, Z. Huang and S. J. Lippard, *ACS Chem. Biol.*, 2020, **15**, 396–406.

83 L. M. Canzoniero, D. M. Turetsky and D. W. Choi, *J. Neurosci.*, 1999, **19**, 1–6.

84 H. Haase and D. Beyersmann, *Biochem. Biophys. Res. Commun.*, 2002, **296**, 923–928.

85 C. Zhang, Z. Liu, Y. Li, W. He, X. Gao and Z. Guo, *Chem. Commun.*, 2013, **49**, 11430–11432.

86 B. J. Grattan and H. C. Freake, *Nutrients*, 2012, **4**, 648–675.

87 P. Huang, L. Feng, E. A. Oldham, M. J. Keating and W. Plunkett, *Nature*, 2000, **407**, 390–395.

88 S. C. Paski and Z. Xu, *Can. J. Physiol. Pharmacol.*, 2002, **80**, 790–795.

89 A. S. Prasad, F. W. J. Beck, L. Endre, W. Handschu, M. Kukuruga and G. Kumar, *J. Lab. Clin. Med.*, 1996, **128**, 51–60.

90 E. J. Margalioth, J. G. Schenker and M. Chevion, *Cancer*, 1983, **52**, 868–872.

91 R. B. Franklin, P. Feng, B. Milon, M. M. Desouki, K. K. Singh, A. Kajdacsy-Balla, O. Bagasra and L. C. Costello, *Mol. Cancer*, 2005, **4**, 1–13.

92 C. Matsui, T. Takatani-Nakase, Y. Hatano, S. Kawahara, I. Nakase and K. Takahashi, *FEBS Lett.*, 2017, **591**, 3348–3359.

93 K. M. Taylor, P. Vichova, N. Jordan, S. Hiscox, R. Hendley and R. I. Nicholson, *Endocrinology*, 2008, **149**, 4912–4920.

94 N. Kagara, N. Tanaka, S. Noguchi and T. Hirano, *Cancer Sci.*, 2007, **98**, 692–697.

95 J. F. Shi, P. Wu, Z. H. Jiang and X. Y. Wei, *Eur. J. Med. Chem.*, 2014, **71**, 219–228.

96 A. Doerflinger, N. N. Quang, E. Gravel, G. Pinna, M. Vandamme, F. Ducongé and E. Doris, *Chem. Commun.*, 2018, **54**, 3613–3616.

97 S. Chen, X. Zhao, J. Chen, J. Chen, L. Kuznetsova, S. S. Wong and I. Ojima, *Bioconjug. Chem.*, 2010, **21**, 979–987.

98 T. Kim, H. M. Jeon, H. T. Le, T. W. Kim, C. Kang and J. S. Kim, *Chem. Commun.*, 2014, **50**, 7690–7693.

99 N. Muhammad, N. Sadia, C. Zhu, C. Luo, Z. Guo and X. Wang, *Chem. Commun.*, 2017, **53**, 9971–9974.

100 S. Maiti, N. Park, J. H. Han, H. M. Jeon, J. H. Lee, S. Bhuniya, C. Kang and J. S. Kim, *J. Am. Chem. Soc.*, 2013, **135**, 4567–4572.

101 E. Tamanini, A. Katewa, L. M. Sedger, M. H. Todd and M. Watkinson, *Inorg. Chem.*, 2009, **48**, 319–324.

102 K. Jobe, C. H. Brennan, M. Motevalli, S. M. Goldup and M. Watkinson, *Chem. Commun.*, 2011, **47**, 6036–6038.

103 C. Corona, B. K. Bryant and J. B. Arterburn, *Org. Lett.*, 2006, **8**, 1883–1886.

104 D. James, J. M. Escudier, E. Amigues, J. Schulz, C. Vitry, T. Bordenave, M. Szlosek-Pinaud and E. Fouquet, *Tetrahedron Lett.*, 2010, **51**, 1230–1232.

105 P. Swietach, R. D. Vaughan-Jones, A. L. Harris and A. Hulikova, *Philos. Trans. R. Soc. B Biol. Sci.*, , DOI:10.1098/rstb.2013.0099.

106 C. Ripoll, M. Martin, M. Roldan, E. M. Talavera, A. Orte and M. J. Ruedas-Rama, *Chem. Commun.*, 2015, **51**, 16964–16967.

107 E. Tamanini, K. Flavin, M. Motevalli, S. Piperno, L. A. Gheber, M. H. Todd and M. Watkinson, *Inorg. Chem.*, 2010, **49**, 3789–3800.

108 J. O'Brien, I. Wilson, T. Orton and F. Pognan, *Eur. J. Biochem.*, 2000, **267**, 5421–5426.

109 W. Q. Ding and S. E. Lind, *IUBMB Life*, 2009, **61**, 1013–1018.

110 P. Jiang and Z. Guo, *Coord. Chem. Rev.*, 2004, **248**, 205–229.

111 S. Phaniraj, Z. Gao, D. Rane and B. R. Peterson, *Dye. Pigment.*, 2016, **135**, 127–133.

112 D. Greentree, É. Rousseau, J. Teijeira, K. Côté and L. Picard, *J. Mol. Cell. Cardiol.*, 2002, **34**, 1163–1172.

113 S. J. Kim, Y. Wi, J. S. Kim, J. E. Song, K. Sunwoo, H. Y. Yoon, G. Han, H. T. Le, P. Verwilst, C. Kang and T. W. Kim, *Chem. Commun.*, 2018, **54**, 8897–8900.

114 J. L. Challinor-Rogers, D. C. Kong, M. N. Iskander and G. A. McPherson, *J.Pharmacol.Exp.Ther.*, 1995, **273**, 778–786.

115 E. Yuriev, D. C. M. Kong and M. N. Iskander, *Eur. J. Med. Chem.*, 2004, **39**, 835–847.

116 K. R. Gee, Z. Zhou, S. L. Sensi and J. H. Weiss, *Cell Calcium*, 2002, **31**, 245–251.

117 T. Clive and R. Parkesh, *Org. Biomol. Chem.*, 2003, **1**, 3265–3267.

118 W. Goch and W. Bal, *Inorg. Chem.*, 2018, **57**, 9826−9838.

119 P. Thordarson, *Chem. Soc. Rev.*, 2011, **6**, 1305–1323.

120 D. B. Hibbert and P. Thordarson, *Chem. Commun*, 2016, **52**, 12792–12805.

121 L. Fang, G. Trigiante, C. J. Kousseff, R. Crespo-Otero, M. P. Philpott and M. Watkinson, *Chem. Commun.*, 2018, **54**, 9619–9622.

122 M. M. Wu, J. Llopis, S. Adams, J. M. McCaffery, M. S. Kulomaa, T. E. Machen, H. P. H. Moore and R. Y. Tsien, *Chem. Biol.*, 2000, **7**, 197–209.

123 J. Wang, Y. Xiao, Z. Zhang, X. Qian, Y. Yang and Q. Xu, *J. Mater. Chem.*, 2005, **15**, 2836–2839.

124 H. Su, X. Chen and W. Fang, *Anal. Chem.*, 2014, **86**, 891–899.

125 Y. Tu, J. Liu, H. Zhang, Q. Peng, J. W. Y. Lam and B. Z. Tang, *Angew. Chemie - Int. Ed.*, 2019, **58**, 14911–14914.

126 X. Zhang, Y. Yuan, L. Jiang, J. Zhang, J. Gao, Z. Shen, Y. Zheng, T. Deng, H. Yan, W. Li, W. W. Hou, J. Lu, Y. Shen, H. Dai, W. W. Hu, Z. Zhang and Z. Chen, *Autophagy*, 2014, **10**, 1801–1813.

127 H. Wang, Z. He, Y. Yang, J. Zhang, W. Zhang, W. Zhang, P. Li and B. Tang, *Chem. Sci.*, 2019, **10**, 10876–10880.

128 P. Coyle, P. D. Zalewski, J. C. Philcox, I. J. Forbes, A. D. Ward, S. F. Lincoln, I. Mahadevan and A. M. Rofe, *Biochem. J.*, 1994, **303**, 781–786.

129 J. Nanda, B. Adhikari, S. Basak and A. Banerjee, *J. Phys. Chem. B*, 2012, **116**, 12235–12244.

130 T. M. Vishwanatha, K. Kurpiewska, J. Kalinowska-Tłuścik and A. Dömling, *J. Org. Chem.*, 2017, **82**, 9585–9594.

131 L. Fang, G. Trigiante, R. Crespo-Otero, M. P. Philpott, C. R. Jones and M. Watkinson, *Org. Biomol. Chem.*, 2019, **17**, 10013–10019.

132 A. Asokan and M. J. Cho, *J. Pharm. Sci.*, 2002, **91**, 903–913.

133 L. Ercolani, J. L. Stow, J. F. Boyle, E. J. Holtzman, H. Lin, J. R. Grove and D. A. Ausiello, *Proc. Natl. Acad. Sci. U. S. A.*, 1990, **87**, 4635–4639.

134 B. Ruttkay-Nedecky, L. Nejdl, J. Gumulec, O. Zitka, M. Masarik, T. Eckschlager, M. Stiborova, V. Adam and R. Kizek, *Int. J. Mol. Sci.*, 2013, **14**, 6044–6066.

135 A. Hayata, H. Itoh, S. Matsutaka and M. Inoue, *Chem. - A Eur. J.*, 2016, **22**, 3370–3377.

136 T. Hirano, K. Kikuchi, Y. Urano, T. Higuchi and T. Nagano, *J. Am. Chem. Soc.*, 2000, **122**, 12399–12400.

137 E. B. Veale and T. Gunnlaugsson, *J. Org. Chem.*, 2008, **73**, 8073–8076.

138 F. Yang, N. G. Nickols, B. C. Li, G. K. Marinov, J. W. Said and P. B. Dervan, *Proc. Natl. Acad. Sci. U. S. A.*, 2013, **110**, 1863–1868.

139 N. G. Nickols and P. B. Dervan, *Proc. Natl. Acad. Sci. U. S. A.*, 2007, **104**, 10418–10423.

140 J. A. Raskatov, J. L. Meier, J. W. Puckett, F. Yang, P. Ramakrishnan and P. B. Dervan, *Proc. Natl. Acad. Sci. U. S. A.*, 2012, **109**, 1023–1028.

141 S. J. Lippard, E. Tomat, E. M. Nolan and J. Jaworski, *J. Am. Chem. Soc.*, 2008, **130**, 15776–+.

142 C. J. Fahrni and T. V. O. Halloran, *J. Am. Chem. Soc.*, 1999, **121**, 11448–11458.

143 M. Taki, J. L. Wolford and T. V. O. Halloran, *J. Am. Chem. Soc.*, 2004, **126**, 712–713.

144 C. Herrero, A. Quaranta, S. El Ghachtouli, B. Vauzeilles, W. Leibl and A. Aukauloo, *Phys. Chem. Chem. Phys.*, 2014, **16**, 12067–12072.

145 N. Umeda, T. Ueno, C. Pohlmeyer, T. Nagano and T. Inoue, *J. Am. Chem. Soc.*, 2011, **133**, 12–14.

146 Y. Zhou, K. Liu, J. Y. Li, Y. Fang, T. C. Zhao and C. Yao, *Org. Lett.*, 2011, **13**, 1290–1293.

147 A. K. Bandela, S. Bandaru and C. Pulla, *Chem.Eur.J*, 2015, **21**, 13364–13374.

148 T. Kühn and H. Schwalbe, *J. Am. Chem. Soc.*, 2000, **122**, 6169–6174.

149 M. Zhou, R. Dai and S. Tian, *Chem. Commun.*, 2018, **54**, 6036–6039.

150 A. Maisonial, P. Serafin, M. Traïkia, E. Debiton, V. Théry, D. J. Aitken, P. Lemoine, B. Viossat and A. Gautier, *Eur. J. Inorg. Chem.*, 2008, 298–305.

151 J. Dash, Z. A. E. Waller, G. D. Pantoş and S. Balasubramanian, *Chem. Eur. J.*, 2011, **17**, 4571–4581.

152 X. Chen, G. N. Khairallah, R. A. J. O'Hair and S. J. Williams, *Tetrahedron Lett.*, 2011, **52**, 2750–2753.

153 T. Gunnlaugsson, D. F. Brougham, A. M. Fanning, M. Nieuwenhuyzen, J. E. O'Brien and R. Viguier, *Org. Lett.*, 2004, **6**, 4805–4808.

154 S. Combemale, C. Santos, F. Rodriguez, V. Garcia, C. Galaup, C. Frongia, V. Lobjois, T. Levade, C. Baudoin-Dehoux, S. Ballereau and Y. Génisson, *RSC Adv.*, 2013, **3**, 18970–18984.

155 T. Yamamoto, H. Hasegawa, T. Hakogi and S. Katsumura, *Org. Lett.*, 2006, **8**, 5569–5572.

Appendix 1: Ceramide synthesis

As ceramide is used as a Golgi apparatus targeting unit in commercial dyes for this organelle, its synthesis was attempted following reported procedures.[154,155] As shown in Scheme A.1, the synthesis to azide functioned ceramide **107** was planned, which it was envisioned could then be incorporated into alkyne **59** through a 'click' reaction to generate a Golgi targeted Zn^{2+} probe. However, this synthesis failed at the last corss-metathesis step, despite multiple attempts to get the product **107** and as a result of the long multi-steps synthesis and low yields in some steps, an alternative Golgi targeting strategy was sought.

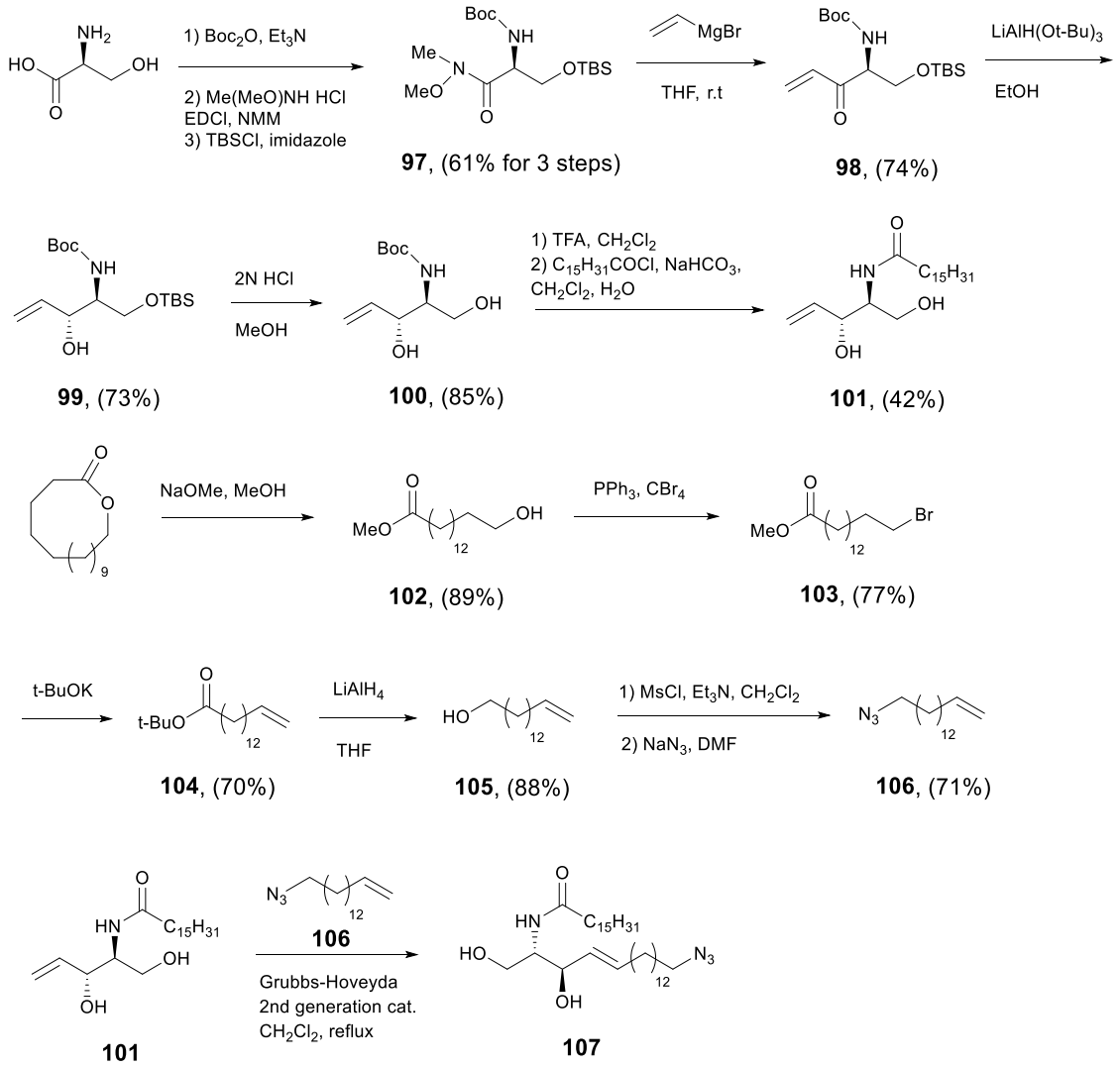

Scheme A.1 The synthetic route towards ceramide azide derivative, **107**.

Appendix 2: The unexpected by-product formed in the synthesis of 69

During the synthesis of **69** (see section 7.3) an unexpected by-product was identified as allene **108**. This presumably forms as a result of quaternisation of the nitrogen centre, increasing the acidity of the α-carbonyl proton, which after its removal, then allows a sigmatropic rearrangement to occur.

N,*N*-bis(2-ethoxy-2-oxoethyl)-*N*-(prop-2-yn-1-yl)propa-1,2-dien-1-aminium bromide (**108**)

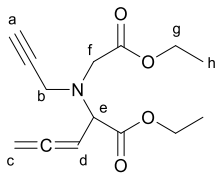

108 (1.32 g, 35%) as a red oil. ^{1}H NMR (400 MHz, $CDCl_3$) δ 5.22 (dd, 1H, *J* = 14.2, 6.7, H_d), 4.78 (dd, 2H, *J* = 6.7, 2.3, H_c), 4.15 - 4.06 (m, 5H, $H_{e,g}$), 3.60 (d, 2H, *J* = 2.4, H_b), 3.55-3.52 (m, 2H, H_f), 2.20 (t, 1H, *J* = 2.4, H_a), 1.23-1.16 (m, 6H, H_h). ^{13}C NMR (101 MHz, $CDCl_3$) δ 209.4, 170.6, 170.5, 87.2, 78.7, 77.0, 73.5, 64.3, 60.8, 60.5, 50.9, 41.3, 14.1 (×2). HR-NSI MS (*m/z*) $[M+H]^+$ calcd for $C_{14}H_{20}NO_4$ 266.1387, found 266.1383.

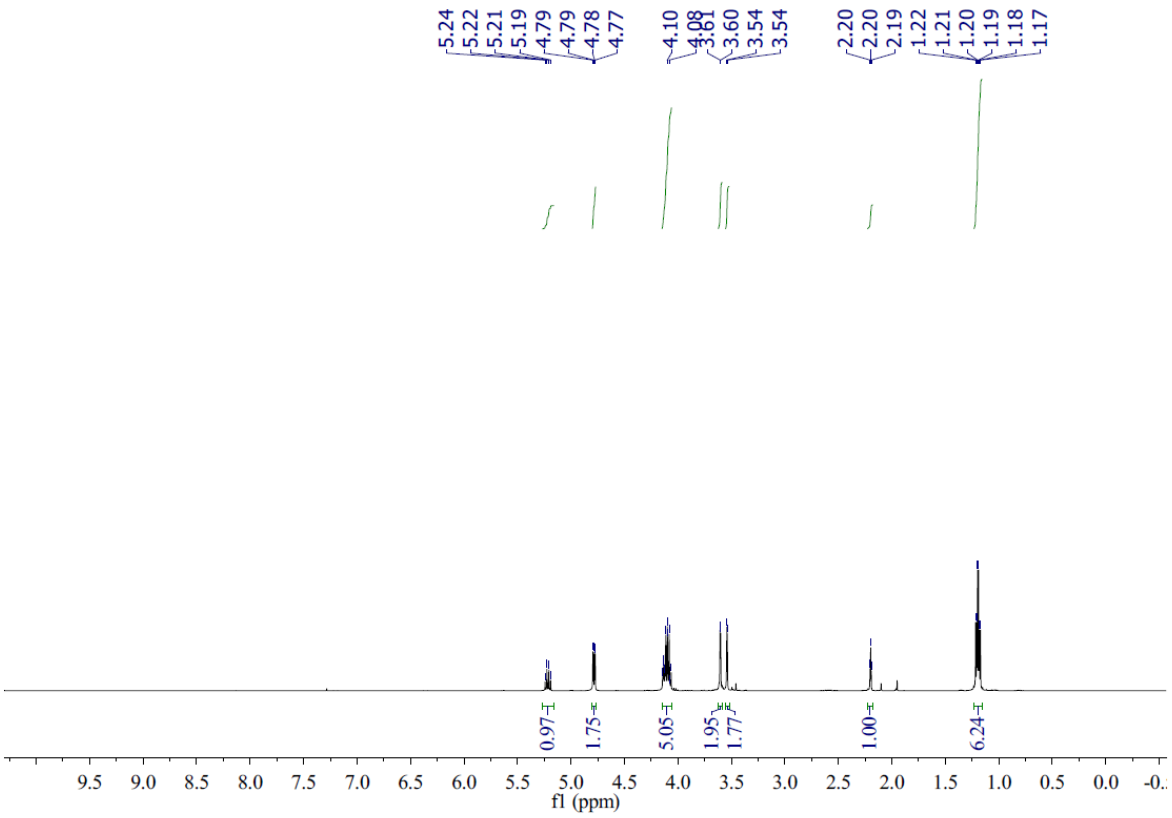
5.24
5.22
5.21
5.19
4.79
4.79
4.78
4.77
4.10
4.08
3.61
3.60
3.54
3.54
2.20
2.20
2.19
1.22
1.21
1.20
1.19
1.18
1.17
0.97
1.75
5.05
1.95
1.77
1.00
6.24
fl (ppm)

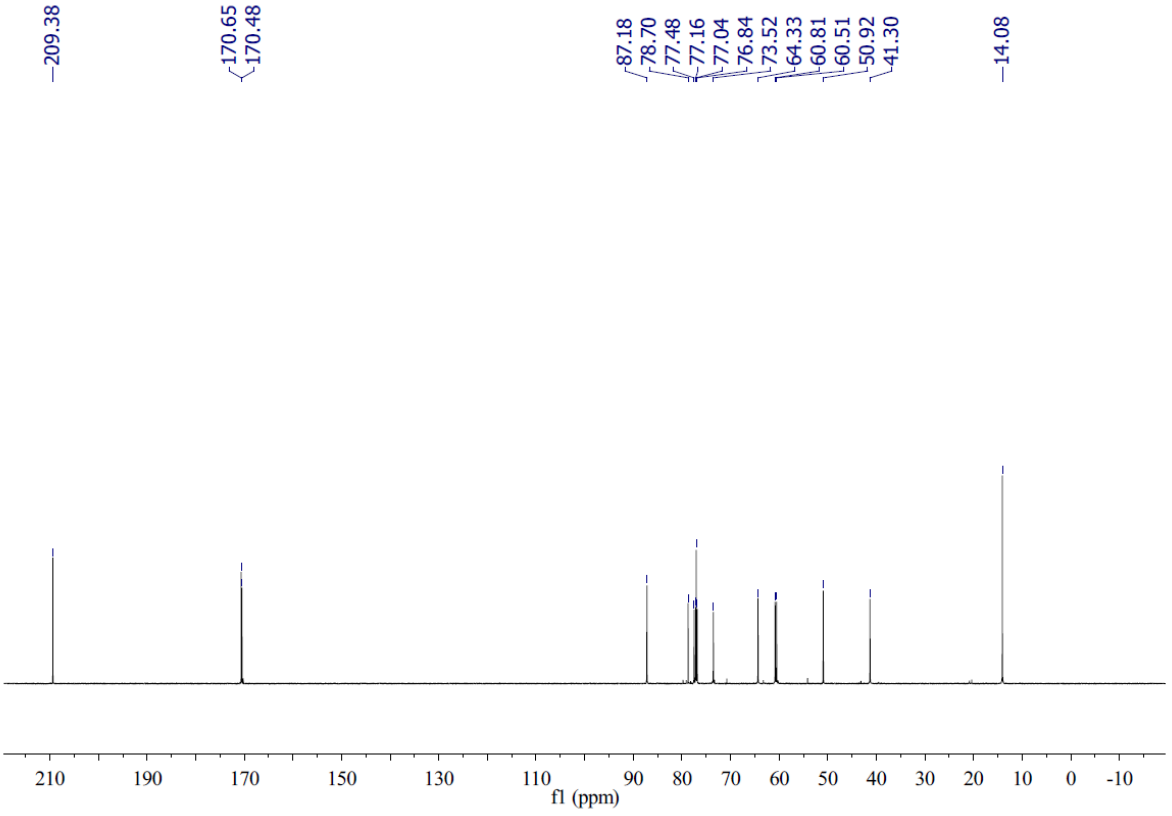
209.38
170.65
170.48
87.18
78.70
77.48
77.16
77.04
76.84
73.52
64.33
60.81
60.51
50.92
41.30
14.08
fl (ppm)